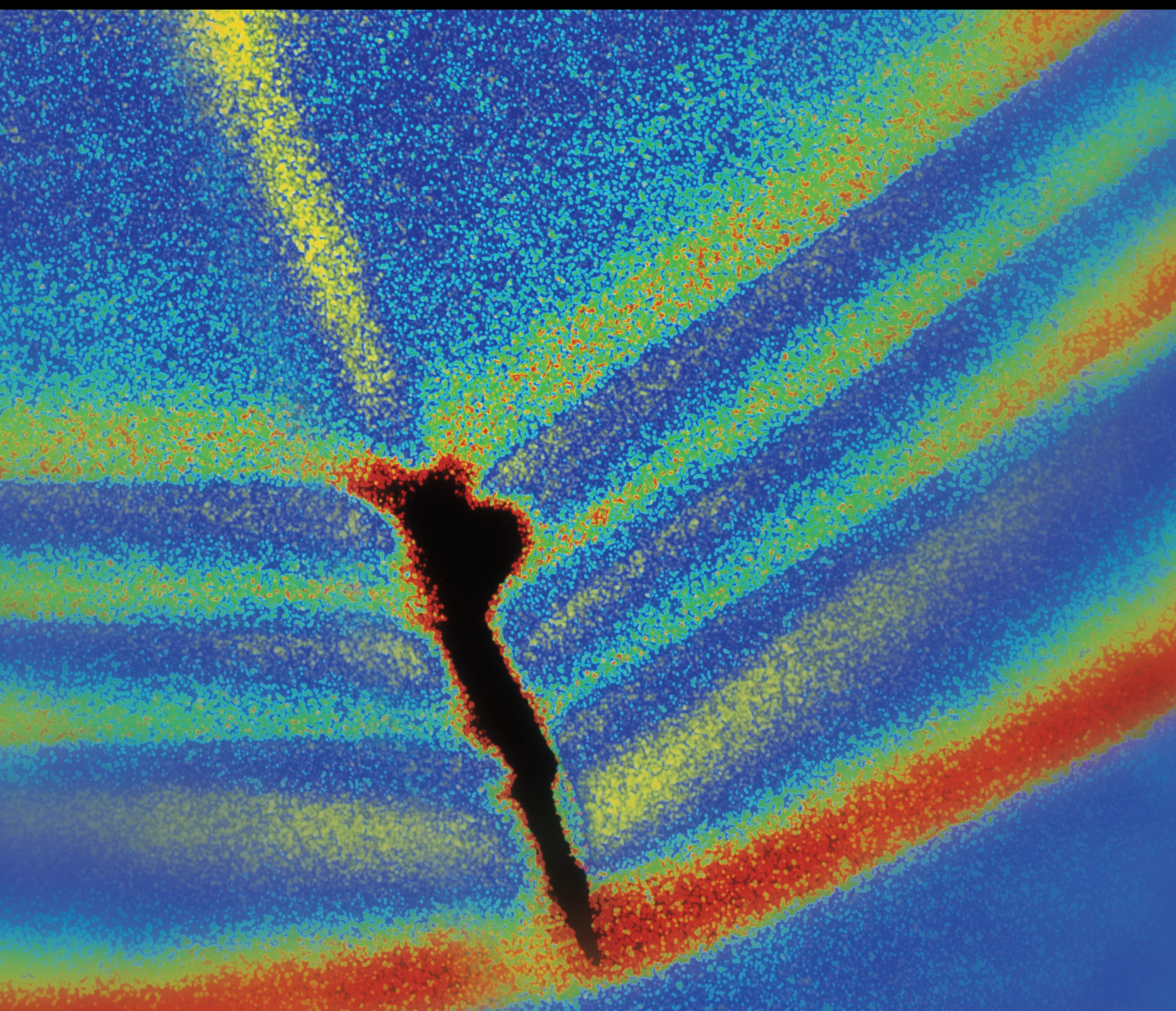


Shock and Vibration

# Effects of Shock and Vibration in Blasting

Lead Guest Editor: Nan Jiang

Guest Editors: Bangbiao Wu and Qi Zhao





---



# **Effects of Shock and Vibration in Blasting**



Shock and Vibration

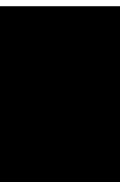
---

## **Effects of Shock and Vibration in Blasting**

Lead Guest Editor: Nan Jiang

Guest Editors: Bangbiao Wu and Qi Zhao





---

Copyright © 2022 Hindawi Limited. All rights reserved.

This is a special issue published in “Shock and Vibration.” All articles are open access articles distributed under the Creative Commons Attribution License, which permits unrestricted use, distribution, and reproduction in any medium, provided the original work is properly cited.



# Chief Editor

Huu-Tai Thai , Australia

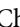
## Associate Editors

Ivo Calìo , Italy  
Nawawi Chouw , New Zealand  
Longjun Dong , China  
Farzad Ebrahimi , Iran  
Mickaël Lallart , France  
Vadim V. Silberschmidt , United Kingdom  
Mario Terzo , Italy  
Angelo Marcelo Tusset , Brazil

## Academic Editors

Omid A. Yamini , Iran  
Maher Abdelghani, Tunisia  
Haim Abramovich , Israel  
Desmond Adair , Kazakhstan  
Manuel Aenlle Lopez , Spain  
Brij N. Agrawal, USA  
Ehsan Ahmadi, United Kingdom  
Felix Albu , Romania  
Marco Alfano, Italy  
Sara Amoroso, Italy  
Huaming An, China  
P. Antonaci , Italy  
José V. Araújo dos Santos , Portugal  
Lutz Auersch , Germany  
Matteo Aureli , USA  
Azwan I. Azmi , Malaysia  
Antonio Batista , Brazil  
Mattia Battarra, Italy  
Marco Belloli, Italy  
Francisco Beltran-Carbajal , Mexico  
Denis Benasciutti, Italy  
Marta Berardengo , Italy  
Sébastien Besset, France  
Giosuè Boscato , Italy  
Fabio Botta , Italy  
Giuseppe Brandonisio , Italy  
Francesco Bucchi , Italy  
Rafał Burdzik , Poland  
Salvatore Caddemi , Italy  
Wahyu Caesarendra , Brunei Darussalam  
Baoping Cai, China  
Sandro Carbonari , Italy  
Cristina Castejón , Spain

Nicola Caterino , Italy  
Gabriele Cazzulani , Italy  
Athanasios Chasalevris , Greece  
Guoda Chen , China  
Xavier Chimentin , France  
Simone Cinquemani , Italy  
Marco Civera , Italy  
Marco Cocconcelli , Italy  
Alvaro Cunha , Portugal  
Giorgio Dalpiaz , Italy  
Thanh-Phong Dao , Vietnam  
Arka Jyoti Das , India  
Raj Das, Australia  
Silvio L.T. De Souza , Brazil  
Xiaowei Deng , Hong Kong  
Dario Di Maio , The Netherlands  
Raffaella Di Sante , Italy  
Luigi Di Sarno, Italy  
Enrique Lopez Droguett , Chile  
Mădălina Dumitriu, Romania  
Sami El-Borgi , Qatar  
Mohammad Elahinia , USA  
Said Elias , Iceland  
Selçuk Erkaya , Turkey  
Gaoliang Fang , Canada  
Fiorenzo A. Fazzolari , United Kingdom  
Luis A. Felipe-Sese , Spain  
Matteo Filippi , Italy  
Piotr Fołga , Poland  
Paola Forte , Italy  
Francesco Franco , Italy  
Juan C. G. Prada , Spain  
Roman Gabl , United Kingdom  
Pedro Galvín , Spain  
Jinqiang Gan , China  
Cong Gao , China  
Arturo García García-Perez, Mexico  
Rozaimi Ghazali , Malaysia  
Marco Gherlone , Italy  
Anindya Ghoshal , USA  
Gilbert R. Gillich , Romania  
Antonio Giuffrida , Italy  
Annalisa Greco , Italy  
Jiajie Guo, China

Amal Hajjaj , United Kingdom  
Mohammad A. Hariri-Ardebili , USA  
Seyed M. Hashemi , Canada  
Xue-qiu He, China  
Agustin Herrera-May , Mexico  
M.I. Herreros , Spain  
Duc-Duy Ho , Vietnam  
Hamid Hosano , Japan  
Jin Huang , China  
Ahmed Ibrahim , USA  
Bernard W. Ikuu, Kenya  
Xingxing Jiang , China  
Jiang Jin , China  
Xiaohang Jin, China  
MOUSTAFA KASSEM , Malaysia  
Shao-Bo Kang , China  
Yuri S. Karinski , Israel  
Andrzej Katunin , Poland  
Manoj Khandelwal, Australia  
Denise-Penelope Kontoni , Greece  
Mohammadreza Koopialipour, Iran  
Georges Kouroussis , Belgium  
Genadijus Kulvietis, Lithuania  
Pradeep Kundu , USA  
Luca Landi , Italy  
Moon G. Lee , Republic of Korea  
Trupti Ranjan Lenka , India  
Arcanjo Lenzi, Brazil  
Marco Lepidi , Italy  
Jinhua Li , China  
Shuang Li , China  
Zhixiong Li , China  
Xihui Liang , Canada  
Tzu-Kang Lin , Taiwan  
Jinxin Liu , China  
Ruonan Liu, China  
Xiuquan Liu, China  
Siliang Lu, China  
Yixiang Lu , China  
R. Luo , China  
Tianshou Ma , China  
Nuno M. Maia , Portugal  
Abdollah Malekjafarian , Ireland  
Stefano Manzoni , Italy

Stefano Marchesiello , Italy  
Francesco S. Marulo, Italy  
Traian Mazilu , Romania  
Vittorio Memmolo , Italy  
Jean-Mathieu Mencik , France  
Laurent Mevel , France  
Letícia Fleck Fadel Miguel , Brazil  
FuRen Ming , China  
Fabio Minghini , Italy  
Marco Miniaci , USA  
Mahdi Mohammadpour , United Kingdom  
Rui Moreira , Portugal  
Emiliano Mucchi , Italy  
Peter Múčka , Slovakia  
Fehmi Najar, Tunisia  
M. Z. Naser, USA  
Amr A. Nassr, Egypt  
Sundararajan Natarajan , India  
Toshiaki Natsuki, Japan  
Miguel Neves , Portugal  
Sy Dzung Nguyen , Republic of Korea  
Trung Nguyen-Thoi , Vietnam  
Gianni Niccolini, Italy  
Rodrigo Nicoletti , Brazil  
Bin Niu , China  
Leilei Niu, China  
Yan Niu , China  
Lucio Olivares, Italy  
Erkan Oterkus, United Kingdom  
Roberto Palma , Spain  
Junhong Park , Republic of Korea  
Francesco Pellicano , Italy  
Paolo Pennacchi , Italy  
Giuseppe Petrone , Italy  
Evgeny Petrov, United Kingdom  
Franck Poisson , France  
Luca Pugi , Italy  
Yi Qin , China  
Virginio Quaglini , Italy  
Mohammad Rafiee , Canada  
Carlo Rainieri , Italy  
Vasudevan Rajamohan , India  
Ricardo A. Ramirez-Mendoza , Mexico  
José J. Rangel-Magdaleno , Mexico


Didier Rémond , France  
Dario Richiedi , Italy  
Fabio Rizzo, Italy  
Carlo Rosso , Italy  
Riccardo Rubini , Italy  
Salvatore Russo , Italy  
Giuseppe Ruta , Italy  
Edoardo Sabbioni , Italy  
Pouyan Roodgar Saffari , Iran  
Filippo Santucci de Magistris , Italy  
Fabrizio Scozzese , Italy  
Abdullah Seçgin, Turkey  
Roger Serra , France  
S. Mahdi Seyed-Kolbadi, Iran  
Yujie Shen, China  
Bao-Jun Shi , China  
Chengzhi Shi , USA  
Gerardo Silva-Navarro , Mexico  
Marcos Silveira , Brazil  
Kumar V. Singh , USA  
Jean-Jacques Sinou , France  
Isabelle Sochet , France  
Alba Sofi , Italy  
Jussi Sopanen , Finland  
Stefano Sorace , Italy  
Andrea Spaggiari , Italy  
Lei Su , China  
Shuaishuai Sun , Australia  
Fidelis Tawiah Suorineni , Kazakhstan  
Cecilia Surace , Italy  
Tomasz Szolc, Poland  
Iacopo Tamellini , Italy  
Zhuhua Tan, China  
Gang Tang , China  
Chao Tao, China  
Tianyou Tao, China  
Marco Tarabini , Italy  
Hamid Toopchi-Nezhad , Iran  
Carlo Trigona, Italy  
Federica Tubino , Italy  
Nerio Tullini , Italy  
Nicolò Vaiana , Italy  
Marcello Vanali , Italy  
Christian Vanhille , Spain

Dr. Govind Vashishtha, Poland  
F. Viadero, Spain  
M. Ahmer Wadee , United Kingdom  
C. M. Wang , Australia  
Gaoxin Wang , China  
Huiqi Wang , China  
Pengfei Wang , China  
Weiqiang Wang, Australia  
Xian-Bo Wang, China  
YuRen Wang , China  
Wai-on Wong , Hong Kong  
Yuanping XU , China  
Biao Xiang, China  
Qilong Xue , China  
Xin Xue , China  
Diansen Yang , China  
Jie Yang , Australia  
Chang-Ping Yi , Sweden  
Nicolo Zampieri , Italy  
Chao-Ping Zang , China  
Enrico Zappino , Italy  
Guo-Qing Zhang , China  
Shaojian Zhang , China  
Yongfang Zhang , China  
Yaobing Zhao , China  
Zhipeng Zhao, Japan  
Changjie Zheng , China  
Chuanbo Zhou , China  
Hongwei Zhou, China  
Hongyuan Zhou , China  
Jiaxi Zhou , China  
Yunlai Zhou, China  
Radoslaw Zimroz , Poland







# Contents

## **Classification Method and Application of Rock Fracture Ability by Supercritical CO<sub>2</sub> Blasting**

Xiaohong Zhu, Jianhong Jia , and Zhongwei Cai






Research Article (11 pages), Article ID 7973016, Volume 2022 (2022)

## **Dynamic Response Characteristic of Building Structure under Blasting Vibration of underneath Tunnel**

Ru He , Nan Jiang , Dong-Wei Li , and Jian-Feng Qi 

Research Article (13 pages), Article ID 9980665, Volume 2022 (2022)

## **The Vibration Characteristics of Ground of Rock Blasting in Silt-Rock Strata**

Tao Yin , Chuanbo Zhou , Changqing Zheng , Jugen Fu , and Ziru Guo 


Research Article (14 pages), Article ID 3318965, Volume 2021 (2021)

## **Influence of In-Situ Stress on the Energy Transmission of Blasting Stress Wave in Jointed Rock Mass**

Qian Dong , XinPing Li , and TingTing Liu 


Research Article (17 pages), Article ID 6822317, Volume 2021 (2021)

## **Experimental Investigation on Influencing Factors of Rock Fragmentation Induced by Carbon Dioxide Phase Transition Fracturing**

Bo Gao, Youjiang Yang, Weilong Xue, Anhui Guo, and Xuedong Luo 



Research Article (9 pages), Article ID 6674485, Volume 2021 (2021)

## **Numerical Analysis of the Influence of Foundation Pit Blasting on a Nearby Metro Tunnel**

Haibo Wang , Yaoyao Wang, Mengxiang Wang, and Qi Zong


Research Article (15 pages), Article ID 5585726, Volume 2021 (2021)

## **Prediction of Bench Blasting Vibration on Slope and Safety Threshold of Blasting Vibration Velocity to Undercrossing Tunnel**

Li He , Dongwang Zhong, Yihe Liu , and Kun Song

Research Article (14 pages), Article ID 9939361, Volume 2021 (2021)

## **Research on Damage Characteristics of Brick Masonry under Explosion Load**

Jifeng Wei , Zhixin Du, Yonghui Zheng, and Oundavong Ounhueane


Research Article (11 pages), Article ID 5519231, Volume 2021 (2021)

## **Rheological Properties of Argillaceous Intercalation under the Combination of Static and Intermittent Dynamic Shear Loads**

Xin Zhang , Qian Dong , Xiangping Zhang , Ming Lang , Suzhi Zhao , Zhuoang Chen , and Jinshan Sun 




Research Article (12 pages), Article ID 5533086, Volume 2021 (2021)

## **Experimental Study on Physical and Dynamic Mechanical Properties of Temperature-Water Coupled Sandstone**

Qi Ping , Dezhi Qi, Qi Diao, Chuanliang Zhang, Qi Gao, and Yulin Wu


Research Article (12 pages), Article ID 6568436, Volume 2021 (2021)

**Random Dynamic Response Characteristics of Pipeline Subjected to Blasting Cylindrical SH Waves**

Shiwei Lu , Heng Zhang , and Ling Ji 








Research Article (9 pages), Article ID 5592858, Volume 2021 (2021)

**Numerical and Experimental Approach for Failure Analysis of Soil Subjected to Surface Explosion Loading**

Iau-Teh Wang 

Research Article (12 pages), Article ID 4981507, Volume 2021 (2021)

**Study on Dynamic Evolution Law of Blasting Cracks in Elliptical Bipolar Linear Shaped Charge Blasting**

Bo Wu , Shixiang Xu , Guowang Meng , Junhua Cai , Han Wei , Hualong Li , and Jinglong Zhang 

Research Article (10 pages), Article ID 5272878, Volume 2021 (2021)

**Research on Energy Dissipation Laws of Coal Crushing under the Impact Loads**

Dengke Xu , Chaomin Mu , Wenqing Zhang, and Zhongqing Li

Research Article (13 pages), Article ID 5563196, Volume 2021 (2021)

**Energy Action Mechanism of Coal and Gas Outburst Induced by Rockburst**

Wenqing Zhang , Chaomin Mu , Dengke Xu, and Zhongqing Li


Research Article (14 pages), Article ID 5553914, Volume 2021 (2021)

**Blasting Vibration Control Using an Improved Artificial Neural Network in the Ashele Copper Mine**

Shida Xu , Tianxiao Chen , Jiaqi Liu , Chenrui Zhang , and Zhiyang Chen 



Research Article (11 pages), Article ID 9949858, Volume 2021 (2021)

**Testing Method for the Range of Fracture Zone of Rock Slope under Blasting Load**

Zhide Wang, Zuyao Ma, Yuanyou Xia, Xiong Zhou, Manqing Lin, Jie Li, and Jinyuan Wang 






Research Article (12 pages), Article ID 5574696, Volume 2021 (2021)

**Strength Weakening Effect of High Prestatically Loaded Marble Subjected to Low-Frequency Dynamic Disturbance under Point Load**

Wuxing Wu , and Fengqiang Gong 


Research Article (12 pages), Article ID 5529897, Volume 2021 (2021)

**Study on the Propagation Law of Water Hammer Wave in Underwater Blasting and the Reducing Effect of Air Curtain on Water Hammer Wave**

Chao Qi , Zuxiang Hu , Suihong Wang, Zhixiong Jiang , Haoyuan Wu , and Zhiqiang Yin 

Research Article (15 pages), Article ID 9994071, Volume 2021 (2021)

**Sabot Discard Characteristics under Different Spin Rates of the Rifled Barrel Launching APFSDS**

Chengqing Zhang, Huiyuan Wang , Ting Liu, and Yingxian Duo

Research Article (18 pages), Article ID 9951989, Volume 2021 (2021)






## Contents

### **Rockburst Prediction on the Superimposed Effect of Excavation Accumulation Energy and Blasting Vibration Energy in Deep Roadway**

Qingwen Li  and Ben Xiang









Research Article (10 pages), Article ID 6644590, Volume 2021 (2021)

### **Dynamic Splitting Behavior and the Constitutive Relationship of Frozen Sandstone Containing a Single Fissure**

Tao Zhao , Gengshe Yang , Lei Wang , Hailiang Jia , and Yuzhe Qiao 

Research Article (13 pages), Article ID 6661037, Volume 2021 (2021)

### **Experimental Study on Injuries to Animals Caused by a Gas Explosion in a Large Test Laneway**

Runzhi Li , Zhigang Zhang , Rongjun Si , Lei Wang , Shengnan Li , Weidong Wu , Jia Cao , and Wenjie Ren 



Research Article (9 pages), Article ID 6632654, Volume 2021 (2021)

### **Investigation and Control of the Blasting-Induced Ground Vibration under Cold Condition**

Yingguo Hu, Zhaowei Yang , Erlei Yao, Meishan Liu, and Yu Rao

Research Article (13 pages), Article ID 6660729, Volume 2021 (2021)

### **Influence of Cavity Width on Attenuation Characteristic of Gas Explosion Wave**

Dengke Xu , Chaomin Mu , Zhongqing Li, and Wenqing Zhang

Research Article (12 pages), Article ID 6634754, Volume 2021 (2021)

### **Time-Frequency Analysis and Application of a Vibration Signal of Tunnel Excavation Blasting Based on CEEMD-MPE-HT**

Chen-yang Ma , Li Wu , Miao Sun , and Qing Yuan 

Research Article (10 pages), Article ID 6672942, Volume 2021 (2021)

### **Modelling on Shock-Induced Energy Release Behavior of Reactive Materials considering Mechanical-Thermal-Chemical Coupled Effect**

Baoyue Guo , Kerong Ren , Zhibin Li , and Rong Chen 

Research Article (12 pages), Article ID 6669573, Volume 2021 (2021)



## Research Article

# Classification Method and Application of Rock Fracture Ability by Supercritical CO<sub>2</sub> Blasting

Xiaohong Zhu,<sup>1</sup> Jianhong Jia ,<sup>2</sup> and Zhongwei Cai<sup>3</sup>

<sup>1</sup>Wuchang University of Technology, Wuhan, Hubei, 430223, China

<sup>2</sup>Three Gorges Geotechnical Consultants Co., Ltd., Wuhan, Hubei, 430074, China

<sup>3</sup>China International Water & Electric Corporation, Beijing 100120, China

Correspondence should be addressed to Jianhong Jia; swc@cug.edu.cn

Received 28 May 2021; Revised 14 November 2021; Accepted 3 December 2021; Published 11 January 2022

Academic Editor: Bangbiao Wu

Copyright © 2022 Xiaohong Zhu et al. This is an open access article distributed under the Creative Commons Attribution License, which permits unrestricted use, distribution, and reproduction in any medium, provided the original work is properly cited.

In order to study the fracture ability classification of rock mass under the cracking action of supercritical CO<sub>2</sub> phase transition, based on the classification theory of rock mass in blasting engineering, an analytic hierarchy process (AHP)-entropy weight method (EWM) and the cloud model classification method for rock mass cracking under CO<sub>2</sub> phase transformation are proposed. In this method, rock density, rock tensile strength, rock wave impedance, and rock mass integrity coefficient are used as the factors to determine the level of rock mass fracturing, and the evaluation index system of rock mass fracturing is established. Through this evaluation method, the rock mass in a reconstruction project section of Nyingchi, Tibet, is classified and evaluated. The results present that this new classification method of rock mass fracture ability uses AHP-EWM to carry out the weight distribution of the classification index. In addition, it is combined with the cloud model for the classification division, overcoming the traditional classification method fixed with appraisal pattern flaw. Therefore, it has validity and feasibility. According to the characteristics of fracture ability, the rock masses in the area to be rebuilt on the Tibet Highway are divided into grade II, grade III, and grade IV, which provides scientific guidance for the construction of the project.

## 1. Introduction

At present, blasting is still the most important means of rock crushing excavation in open pit mining and underground engineering construction. In traditional blasting engineering, vibration, shock wave, flying stone, and other hazards are inevitably caused. In addition, there are certain safety hazards when applied in coal seams with a high concentration of gas. In order to overcome the above shortcomings of blasting, it is necessary to actively develop gas blasting excavation technology with high safety as a supplementary means of blasting excavation. Gas explosion excavation technology is the most widely used CO<sub>2</sub> phase change fracturing technology. This technology originated at the beginning of the last century and was initially used to increase the permeability and mining of coal seams in British coal mines [1]. Subsequently, it was widely used in coal mines in many countries [2]. Nowadays, CO<sub>2</sub> phase change

fracturing has once again attracted attention due to the advantages of rock-soil blasting and excavation in complex environments [3–5]. Wang et al. [6] studied the phase change fracturing process of liquid CO<sub>2</sub> from theoretical analysis and numerical simulation, established a mathematical model of coal seam fracturing pressure, and analyzed the fracturing influence range. Li et al. [7] investigated a new liquid CO<sub>2</sub> rock breaking technology through a series of field tests and successfully applied the technology to rock excavation at the construction site of a subway station. At present, in the research of CO<sub>2</sub> phase change fracturing and rock breaking, in order to ensure efficient fracturing of the target rock mass, it is necessary to carry out the fracture grading evaluation for various target rock masses existing in different geological environments, which can help in the parameter design and crack scheme optimization.

Rock mass fracture ability refers to the difficulty of rock mass cracking under high pressure in the process of CO<sub>2</sub>

phase transformation. At present, there is no relevant classification evaluation standard for rock mass cracking in the CO<sub>2</sub> of phase change fracturing and rock breaking at home and abroad. However, the explosive classification of rock mass corresponding to commonly used explosives such as emulsion explosives has formed a relatively complete system. The blastability classification methods of rock mass can be divided into two main categories. The first category uses a single comprehensive index such as rock Platts coefficient and rock explosive unit consumption for blastability classification [8–10]. However, rock blastability classification is a comprehensive classification, it is necessary to comprehensively consider multiple factors such as rock density, tensile strength, and rock integrity coefficient. Therefore, the effect of this single index evaluation method is not ideal. The second category uses soft mathematical calculation methods such as set pair analysis, neural network, cluster analysis, matter element extension method, and gray correlation analysis for comprehensive blastability classification [11–16]. Zhou et al. [17] proposed a multifactor index system of rock mass blastability consisting of density, wave impedance, uniaxial compressive strength, and uniaxial tensile strength. Based on the system engineering theory, an improved multidimensional blastability classification model was established. On the basis of gray correlation theory and entropy weight theory, Gao et al. [18] established a comprehensive evaluation model of tunnel collapse risk based on entropy weight and gray correlation degree. Furthermore, the grade of collapse risk of the tunnel was obtained combined with the correction coefficient of tunnel construction according to rainfall conditions. Tao et al. [19] created the evaluation model of rock mass blastability based on the principle of cluster analysis and applied it to the classification of rock mass blastability in practical engineering. Zheng et al. [20] built a rock burst prediction model based on the entropy weight gray correlation BP neural network and utilized the model to the rock burst prediction of a tunnel project. The prediction results obtained were in good agreement with the actual conditions, which verified the feasibility and effectiveness of the model in the rock burst prediction.

The above research provides guidance for the classification evaluation of rock mass under blasting load, but the proposed models still have limitations. Moreover, due to the obvious difference between CO<sub>2</sub> phase change induced fracture rock and explosive blasting, the existing rock mass explosive classification method cannot be directly applied to the evaluation of rock mass fracture behavior under CO<sub>2</sub> phase change induced fracture. Therefore, it is necessary to carry out the evaluation of rock mass fracture behavior under phase change induced fracture. On the basis of the theory and idea of explosive classification of rock mass and considering the characteristics of rock breaking caused by CO<sub>2</sub> phase transformation, this paper proposes a rock mass fracture ability classification evaluation method based on AHP–EWM and the cloud model and evaluates the fracture ability of the rock mass of a reconstruction project in Milin County, Tibet. This method provides a reliable reference for the safe and effective construction of the project.

## 2. Methodology

**2.1. CO<sub>2</sub> Phase Change Fracturing Method.** The CO<sub>2</sub> phase change fracturing (liquid CO<sub>2</sub> liquid-gas phase cracking) rock breaking method is to put the crack tube with liquid carbon dioxide as shown in Figure 1 into the hole of the required rock mass drilled in advance. In the process of CO<sub>2</sub> phase change fracturing and rock breaking, a CO<sub>2</sub> storage tank is first used to fill the liquid CO<sub>2</sub> into the liquid storage tube of the fracturing tube, and then the heater is energized on the tube to generate heat so that the liquid CO<sub>2</sub> in the tube absorbs heat into a supercritical state. The supercritical carbon dioxide absorbs heat and heats up, and the internal pressure of the liquid storage tube continues to rise. When the pressure in the tube exceeds the rated pressure of the rupture disc, the shearing piece will be instantly broken, and the supercritical CO<sub>2</sub> will instantly relieve the pressure and expand and transform into high-pressure gas. At the same time, the high-pressure CO<sub>2</sub> gas is instantly released from the explosion vent nozzle set on the discharge head to provide the energy required for deformation of the rock mass medium, thereby causing the rock mass medium to produce relative displacement and create cracks.

**2.2. Classification Method of AHP–EWM and the Cloud Model.** This paper introduces a classification method based on the analytic hierarchy process (AHP)–entropy weight method (EWM) and cloud model, which can classify the difficulty of rock mass fracture under CO<sub>2</sub> phase change fracture. This method first assigns subjective and objective weights to the selected rock mass fracturing grading evaluation indicators through the analytic hierarchy process and the entropy weight method and then optimizes the weights through the Lagrange multiplier method to obtain the combined weight of each factor in the classification of rock mass fracturing in the whole classification process. After that, the cloud model of the selected classification factors is established, and the different evaluation factors of rock mass fracture ability correspond to the membership degree of different fracture grades through the digital characteristics of cloud. Finally, combined with the weight of the evaluation factor and the membership degree of each factor, the grade of the rock mass fracture ability is determined. The flowchart of the method is shown in Figure 2.

**2.2.1. Theory of Analytic Hierarchy Process (AHP).** Hierarchical analysis is a systematic analysis method proposed by American operations research scientist T. L. Saaty in the 1970s [21]. This method combines qualitative and quantitative methods to decompose complex problems into several levels and several factors and then compares each factor in pairs to obtain the weights corresponding to different problem solutions, thereby providing a theoretical basis for the choice of the best method. In the analytic hierarchy process, the selected evaluation indicators are first determined, the selected factors in pairs are compared, and they are scored according to the degree of influence of the

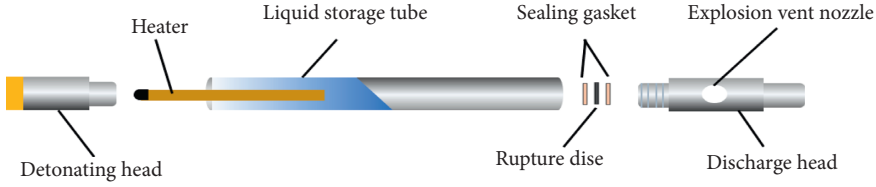


FIGURE 1: Structure diagram of the carbon dioxide phase change fracturing tube.

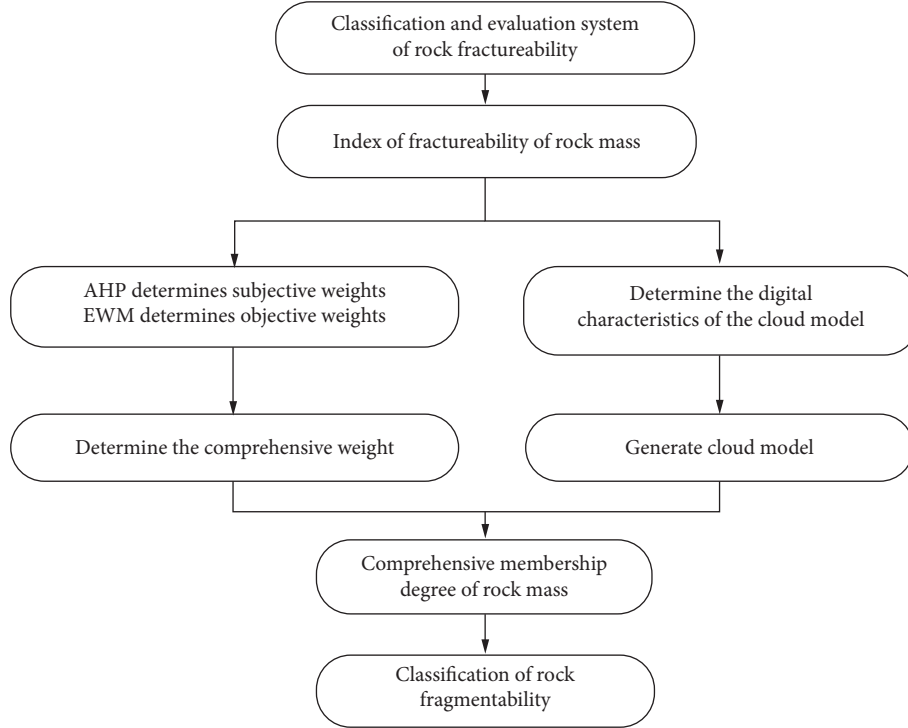


FIGURE 2: Flow chart of cracking classification.

comparison factor on the target factor. The scoring scale is 1–9, as shown in Table 1.

After scoring according to the numerical value, a judgment matrix  $A = (a_{ij})_{n \times n}$  can be constructed, where  $a_{ij}$  represents the importance of the  $i$ -th index relative to the  $j$ -th index. Afterwards, the consistency test of the judgment matrix is performed to determine whether the consistency of the judgment matrix is within the recognized range, that is, whether the judgment matrix is reasonable.

The consistency of the matrix can be tested by the following formula:

$$CI = \frac{\lambda_{\max} - n}{n - 1}, \quad (1)$$

$$CR = \frac{CI}{RI}, \quad (2)$$

where  $n$  represents the order of matrix  $A$ ;  $\lambda_{\max}$  represents the largest eigenvalue of matrix  $A$ ; and  $RI$  represents the average random consistency index, which takes a value according to the size of  $n$ . If  $CR < 0.1$ , it can be considered that the judgment matrix satisfies the consistency. When the judgment matrix cannot pass the consistency test, it is necessary

to reassign the degree of mutual importance between the indicators until it passes the matrix consistency test.

After checking the consistency of the matrix, the weight  $\mu_j$  of each evaluation index can be obtained according to formula (3) of the weight value, that is, the degree of influence of each grading index with respect to the fracture ability of the rock mass.

$$\mu_j = \frac{\sum_{i=1}^n a_{ji} / \sum_{k=1}^n a_{ki}}{n} \quad (j = 1, 2, 3, \dots, n) \quad (3)$$

**2.2.2. Theory of the Entropy Weight Method (EWM).** Entropy is originally derived from the definition in thermodynamics and represents the uniformity of the distribution of energy in space. At the end of the 1940s, C.E. Shannon first introduced entropy into the field of information theory and then put forward a broader concept of information entropy. Now, information theory has been successfully applied in many fields. The information entropy theory reflects the degree of information disorder and can be used to evaluate the amount of information. The more information an index carries, the greater the impact on

TABLE 1: Numerical scales of factor contribution.

Numerical scales	Meaning and explanation
1	Comparing the two factors, the target factor is as important as the comparison factor
3	Comparing the two factors, the target factor and the comparison factor are slightly more important
5	Comparing the two factors, the target factor and the comparison factor are strongly important
7	On comparison of two factors, the target factor and the comparison factor are more strongly important
9	On comparison of two factors, the target factor and the comparison factor are extremely important
2, 4, 6, 8	The intermediate values reflect an intermediate position of importance
Reciprocals (i.e., 1, 1/3, 1/5, . . . , 1/9)	The reciprocal number reflects the reverse comparison positions of the above

decision making and the greater the weight. Through the information entropy theory, the objective weight of each evaluation index can be determined.

The EWM is a method of calculating the objective weight of the evaluation factor, which is different from the AHP. The first step is to set up  $m$  evaluation objects and  $n$  evaluation indicators when EWM is used to determine the index weight [22, 23]. Then, the  $j$ -th index of the  $i$ -th object as  $x_{ij}$  should be defined so that the data matrix  $X = (x_{ij})_{m \times n}$  about the original index of the object can be obtained.

The data in the matrix  $X$  can be further normalized by the following formula to obtain a new matrix  $Y = (y_{ij})_{m \times n}$ :

$$y_{ij} = \frac{x_{ij} - \min x_j}{\max x_j - \min x_j}. \quad (4)$$

Afterwards, the entropy value  $H_j$  is calculated according to each group of data in the matrix  $Y = (y_{ij})_{m \times n}$ , and the definition of the entropy value is shown in formula (5). After obtaining the entropy value  $H_j$ , the objective weight  $\omega_j$  of the grading index can be obtained by formula (6):

$$H_j = -\frac{1}{\ln m} \sum_{i=1}^m \frac{y_{ij}}{\sum_{i=1}^m y_{ij}} \ln \frac{y_{ij}}{\sum_{i=1}^m y_{ij}}, \quad (5)$$

$$\omega_j = \frac{1 - H_j}{n - \sum_{j=1}^n H_j}. \quad (6)$$

The objective weight  $\omega_j$  of each grading index is obtained by the entropy weight method. Combined with the subjective weight  $\mu_j$  of each grading index obtained by AHP in the previous section, the final combined weight  $V_j$  of each index is obtained by the Lagrange multiplier method. The formula of  $V_j$  is as follows:

$$v_j = \frac{(u_j \omega_j)^{0.5}}{\sum_{j=1}^m (u_j \omega_j)^{0.5}}. \quad (7)$$

**2.2.3. Theory of Cloud Model.** The cloud model was first proposed by Li and Shi in 1995 [24]. It is a mathematical model to deal with the conversion of quantitative numerical value and qualitative concept uncertainty. It can effectively solve the problem of fuzzy concept quantification and has been widely used in various fields. In the

grading of rock mass fracturing caused by CO<sub>2</sub> phase change, semiquantitative and semiquantitative analysis methods are mostly used, and subjective factors are inevitably involved in the qualitative description of rock blasting characteristics. Therefore, the cloud model theory is used to analyze the complexity and fuzziness of the classification of rock mass fracturing caused by CO<sub>2</sub> phase change, which has excellent applicability. The theoretical principles of the cloud model are as follows:

- (1) Definition of cloud: suppose  $X$  is a quantitative set represented by precise values,  $X = \{x\}$ , called domain. Any element  $x$  in the set has a stable number  $\mu_c(x)$ , called the degree of membership of  $x$  to  $C$ , where  $C$  is called the fuzzy set in the universe of set  $X$ . The distribution of the membership degree on  $X$  is called the membership cloud. The membership cloud generator generates a membership degree for each element  $x$  in the universe of discourse, called a cloud drop, denoted by  $(x, \mu_c(x))$ . In the process of data processing of fuzzy sets, the degree of membership corresponding to  $x$  in the universe of discourse is not fixed, but its changes will not change the overall characteristics of the membership cloud.
- (2) Digital characteristics of the cloud: the core of the cloud model is to construct a cloud generator and realize the mapping between qualitative and quantitative digital feature values through the generator, reflecting the quantitative features of qualitative concepts. The cloud generator is divided into two forms: the forward and the backward cloud generators. The forward cloud generator uses the digital characteristics of the cloud: expectation  $E_x$ , entropy  $E_n$ , and hyperentropy  $H_e$  to produce membership degrees corresponding to different values of evaluation indicators, namely, cloud drops. The backward cloud generator is opposite to the forward cloud generator. According to the distribution of  $n$  cloud droplets in the cloud, the digital feature expectation  $E_x$ , entropy  $E_n$ , and hyperentropy  $H_e$  are determined. This paper uses a forward cloud generator to generate a cloud model, and the expected curve of its subordinate cloud is approximately a normal distribution, as shown in Figure 3. Expectation  $E_x$  is the domain value corresponding to the area centroid in the cloud model diagram, which expresses the



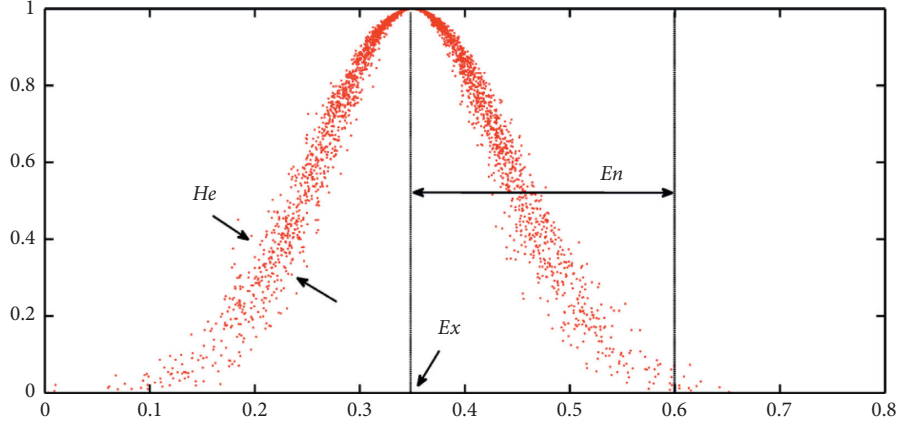


FIGURE 3: Diagram of forward cloud generator.

average value of the fuzzy concept. Entropy  $E_n$  represents the range of the evaluated index and also reflects the fuzziness and randomness of the evaluated index. The smaller the  $E_n$ , the smaller the fuzziness and randomness of the evaluation index. Hyperentropy  $H_e$  is the uncertainty measure of entropy, which describes the degree of dispersion of cloud drops in the curve.

In each grade of fracture ability, the evaluation index is a quantitative range, which has upper and lower limits ( $C_{\min}$ ,  $C_{\max}$ ), and the characteristic values of expectation  $E_x$ , entropy  $E_n$ , and hyperentropy  $H_e$  can be calculated by the following formula:

$$\begin{cases} E_x = (C_{\min} + C_{\max})/2 \\ E_n = (C_{\max} - C_{\min})/2, \\ H_e = k \end{cases} \quad (8)$$

where  $C_{\max}$  and  $C_{\min}$  are the maximum and minimum boundary values of the corresponding grade standard, respectively, and  $k$  is constant, which is taken according to the stability of the evaluation index.

The fracture ability classification of rock mass adopts a forward cloud generator, and the expected curve formed by  $n$  cloud droplets generated by the forward cloud generator satisfies the normal distribution  $(x, \mu_c(x))$ , which is defined as

$$\mu_c(x) = e^{-(x_i - E_x)^2 / 2(E_n')^2}, \quad (9)$$

where  $\mu_c(x)$  is the degree of certainty;  $x_i$  is the variable value;  $E_x$  is the expectation; and  $E_n'$  is the entropy,  $E_n' \sim N(E_n, H_e^2)$ .

According to the definition of the forward cloud generator, the specific steps to generate a normal cloud model are as follows: firstly, a normal random number  $x_i$  with expected value  $E_x$  and standard deviation  $E_n'$  is generated. Secondly, a normal random number  $E_n'$  with expected value  $E_n$  and standard deviation  $H_e$  is generated. Then,  $(x, \mu_c(x))$  is substituted as the cloud drop into equation (9). Afterwards, the above steps are repeated

until  $n$  cloud drops are generated. Finally, the forward cloud generator is used to generate a normal cloud model.

### 3. Rock Mass Fracturing Classification Model Based on AHP-EWM and the Cloud Model

**3.1. Fracture Ability Classification Index.** Reasonable selection of rock mass fracturing index is the prerequisite for establishing the classification model. In the process of  $\text{CO}_2$  phase transformation, the rock breaking effect is controlled by the physical and mechanical properties of the rock, the geological structure characteristics of the rock mass, and other factors. Therefore, there are many indicators that can be used to reflect the fracturing evaluation of the rock mass. This paper refers to the evaluation indexes selected by the relevant research on the explosive classification of existing rock mass and considers that the selected evaluation indexes should have the characteristics of low correlation, easy to measure, and representative. After comprehensive consideration, rock density, rock tensile strength, rock wave impedance, and rock mass integrity coefficient are selected as the classification indexes of rock mass fracture ability [25].

After selecting the evaluation index of the fracture ability of the rock mass, the classification standard of each index is further determined. According to the  $\text{CO}_2$  phase change fracturing effect in the field test and the parameter properties of the on-site rock mass, combined with the classification standard in the literature of related rock mass blasting classification, the rock mass fracturing ability is divided into 5 grades [26–28]. The fracture ability classification standard is shown in Table 2.

**3.2. AHP-EWM to Determine the Weight.** AHP was used to compare the importance of each parameter in Table 2, referring to relevant blastability literature and experts to evaluate the importance of each index and compare the impact of each factor on the grading of rock mass fracturing according to the evaluation criteria in Table 1. The degree of importance and the comparison result of importance are shown in Table 3.

TABLE 2: Numerical scales of factor contribution.

Fracture ability grade	Rock mass density (g·cm <sup>-3</sup> )	Tensile strength (MPa)	Wave impedance of rock (×10 <sup>6</sup> kg·m <sup>-2</sup> ·s <sup>-1</sup> )	Intactness index of rock mass	Fracturing description
Grade I	<2.5	<8.0	<5.0	<0.05	Extremely easy to fracture
Grade II	2.5 ~ 2.8	8.0 ~ 13.0	5.0 ~ 8.0	0.05 ~ 0.35	Easy to fracture
Grade III	2.8 ~ 3.1	13.0 ~ 18.0	8.0 ~ 12.0	0.35 ~ 0.55	Medium
Grade IV	3.1 ~ 3.4	18.0 ~ 23.0	12.0 ~ 15.0	0.55 ~ 0.75	Hard to fracture
Grade V	>3.4	>23.0	>15.0	>0.75	Extremely hard to fracture

TABLE 3: Comparison of the importance of each index of rock fracture ability classification.

Evaluation index	Rock mass density	Tensile strength	Wave impedance of rock	Intactness index of rock mass
Rock mass density	1	1/5	1/4	1/3
Tensile strength	5	1	2	3
Wave impedance of rock	4	1/2	1	2
Intactness index of rock mass	3	1/3	1/2	1

From Table 3, a judgment matrix  $A = (a_{ij})_{n \times n}$  can be obtained ( $a_{ij}$  represents the importance of the  $i$ -th index relative to the  $j$ -th index, and  $n$  is the number of evaluation indexes). The maximum eigenvalue  $\lambda$  of matrix  $A$  is calculated by MATLAB. After that, the consistency of the judgment matrix is tested by formulas (1) and (2). The calculated  $CI$  value is 0.017, the  $CR$  value is  $0.019 < 0.1$ , and the consistency of the matrix is within the recognized range, so the evaluation of grading indicators is reasonable in Table 3. And according to the calculation formula (3) of the index weight of the analytic hierarchy process, the corresponding weight of each index is obtained, as shown in Table 4.

Table 4 shows the subjective weights of the grading indicators determined by AHP. According to the AHP-EWM comprehensive weight determination method, the objective weights of the indicators need to be determined by EWM. In this regard, in combination with related literature, five typical rock mass samples that are representative in classification are selected. The index parameters of the samples are shown in Table 5.

According to Table 5, a data matrix  $X = (x_{ij})_{m \times n}$  can be constructed ( $x_{ij}$  represents the  $j$ -th index value of the  $i$ -th sample,  $m$  is the number of samples, and  $n$  is the number of evaluation indexes). According to formula (4), the matrix  $X$  is normalized to obtain the matrix  $Y = (y_{ij})_{m \times n}$ . Then, the entropy value and weight of each evaluation index are calculated according to formulas (5) and (6), as shown in Table 6.

According to the weights of each index in Tables 4 and 6, combined with formula (7), the final combined weight of each index is obtained, as shown in Table 7.

**3.3. Building a Cloud Model.** According to the rock mass fracture ability classification evaluation index and the cloud digital feature expectation  $E_x$ , entropy  $E_n$ , and hyperentropy  $H_e$  calculation methods, the cloud digital feature calculation method of the fracture ability classification evaluation index can be obtained, as shown in Table 8. Among them, the superentropy  $H_e$  is 0.01. Combining the grading indexes and

standards in Table 2, the cloud digital characteristics corresponding to the grading evaluation indexes of rock mass fracturing under CO<sub>2</sub> phase change fracturing can be obtained, as shown in Table 9.

The cloud digital features of the evaluation indexes in Table 9 are input into the forward cloud generator to generate the cloud model of the membership degree corresponding to different indexes of rock mass crackability, as shown in Figure 4.

When evaluating the fracturing grade of a rock mass in a certain area, it is only needed to input the measured data of each grading index of the rock mass into the forward cloud generator, and the membership degree of each index of the rock mass for the crackability of I ~ V grades can be obtained.

Then, combined with the weight of each evaluation index in Table 7, the comprehensive membership degree of the rock mass with respect to the fracture ability of grades I ~ V can be obtained. The calculation formula is as shown in the following formula:

$$U_i = \sum_{j=1}^m \mu_{ij}(x) v_j, \quad (10)$$

where  $U_i$  is the comprehensive membership degree of the rock mass to the  $i$ -th grade;  $\mu_{ij}(x)$  is the membership degree of the rock mass to the  $j$ -th index in the  $i$ -th grade; and  $v_j$  is the weight of the corresponding evaluation index.

Finally, the fracturing grade of the rock mass can be determined by comparing the magnitude of each  $U_i$  value.

$$i = \max\{U_i | i = 1, 2, 3, 4, 5\}, \quad (11)$$

where the value of  $i$  is the fracturing grade corresponding to the evaluated rock mass (1, 2, 3, 4, and 5, respectively, represent Grade I, II, III, IV, and V).

## 4. Engineering Application Analysis

**4.1. Research Area.** In order to apply this classification method to engineering practice, the K6+000–K8+000 and K13+000–K15+393 sections of a reconstruction

TABLE 4: Weight obtained by AHP.

Grading index	Rock mass density ( $\text{g}\cdot\text{cm}^{-3}$ )	Tensile strength (MPa)	Wave impedance of rock ( $\times 10^6 \text{ kg}\cdot\text{m}^{-2}\cdot\text{s}^{-1}$ )	Intactness index of rock mass
Weight	0.0729	0.4728	0.2844	0.1699

TABLE 5: Parameters of the sample rock mass.

Number of the rock mass sample	Rock mass density ( $\text{g}\cdot\text{cm}^{-3}$ )	Tensile strength (MPa)	Wave impedance of rock ( $\times 10^6 \text{ kg}\cdot\text{m}^{-2}\cdot\text{s}^{-1}$ )	Intactness index of rock mass
1	1.5	12	3	0.04
2	2.7	10	7	0.2
3	3.0	15	10	0.4
4	3.2	19	13	0.6
5	3.8	24	27	0.8

TABLE 6: Entropy and weight obtained by EWM.

Grading index	Rock mass density ( $\text{g}\cdot\text{cm}^{-3}$ )	Tensile strength (MPa)	Wave impedance of rock ( $\times 10^6 \text{ kg}\cdot\text{m}^{-2}\cdot\text{s}^{-1}$ )	Intactness index of rock mass
Entropy	0.8438	0.7417	0.7296	0.7822
Weight	0.1730	0.2861	0.2995	0.2412

TABLE 7: Comprehensive weight of rock mass fracturing evaluation index.

Grading index	Rock mass density ( $\text{g}\cdot\text{cm}^{-3}$ )	Tensile strength (MPa)	Wave impedance of rock ( $\times 10^6 \text{ kg}\cdot\text{m}^{-2}\cdot\text{s}^{-1}$ )	Intactness index of rock mass
Weight	0.1154	0.3774	0.2995	0.2077

TABLE 8: Calculation method about digital characteristics of the cloud.

Fracture ability grade	Range of evaluation indicators	Expectation $E_x$	Entropy $E_n$	Hyperentropy $H_e$
Grade I	(0, a)	$E_{x1} = (0 + a)/2$	$E_{n1} = (a - 0)/6$	0.01
Grade II	(a, b)	$E_{x2} = (a + b)/2$	$E_{n2} = (b - a)/6$	0.01
Grade III	(b, c)	$E_{x3} = (b + c)/2$	$E_{n3} = (c - b)/6$	0.01
Grade IV	(c, d)	$E_{x4} = (c + d)/2$	$E_{n4} = (d - c)/6$	0.01
Grade V	(d, +∞)	$E_{x5} = d$	$E_{n5} = E_{n4}$	0.01

project in Milin County, Linzhi City, Tibet, are taken as the research objects of rock mass fracturing classification. These two sections belong to the piedmont colluvial slope, and the strata are dominated by quaternary loose colluvial layer breccia and intercalated rocks. The main mineral composition of strata rock mass is feldspar, quartz, and hornblende, which have high compressive strength and belong to hard rock. Commonly used mechanical excavation methods cannot effectively destroy the rock mass, so it is planned to use  $\text{CO}_2$  phase change fracturing technology to break the rock. According to the strength, the rocks in this project area can be divided into three types: feldspar quartz sandstone (A), feldspar quartz fine sandstone (B), and diorite (C). In order to determine the crackability grades of the three types of rock masses in the construction area of the project and to provide theoretical guidance for the actual fracturing project, firstly, the three types of rock masses in the construction area were sampled. The rock

samples are shown in Figure 5. Subsequently, an on-site investigation of the engineering geological conditions of the area was carried out; combined with the indoor test of the rock samples obtained in the engineering area, the parameters of the fracturing evaluation index of the rock mass in the engineering area were obtained, as shown in Table 10.

**4.2. Research Area Analysis of Rock Fracture Ability in the Engineering Area.** By inputting the data from Table 10 into the forward cloud model, the membership degree of each evaluation index of nine rock mass samples in I~V grade rock masses can be obtained. According to Table 4, the comprehensive weights of rock density, tensile strength, wave impedance of rock, and intactness index of rock mass are 0.1154, 0.3774, 0.2995, and 0.2077, respectively. According to the membership degree calculation formula

TABLE 9: Cloud digital characteristics of fracture ability evaluation index.

Fracture ability grade	Rock mass density ( $\text{g}\cdot\text{cm}^{-3}$ )			Tensile strength (MPa)		
	$E_x$	$E_n$	$H_e$	$E_x$	$E_n$	$H_e$
Grade I	1.25	0.42	0.01	4.00	1.33	0.01
Grade II	2.65	0.05	0.01	10.50	0.83	0.01
Grade III	2.95	0.05	0.01	15.50	0.83	0.01
Grade IV	3.25	0.05	0.01	20.50	0.83	0.01
Grade V	3.40	0.05	0.01	23.00	0.83	0.01

Fracture ability grade	Wave impedance of rock ( $\times 10^6 \text{ kg}\cdot\text{m}^{-2}\cdot\text{s}^{-1}$ )			Intactness index of rock mass		
	$E_x$	$E_n$	$H_e$	$E_x$	$E_n$	$H_e$
Grade I	2.50	0.83	0.01	0.025	0.008	0.01
Grade II	6.50	0.50	0.01	0.20	0.05	0.01
Grade III	10.00	0.67	0.01	0.45	0.033	0.01
Grade IV	13.50	0.50	0.01	0.65	0.033	0.01
Grade V	15.00	0.50	0.01	0.75	0.033	0.01

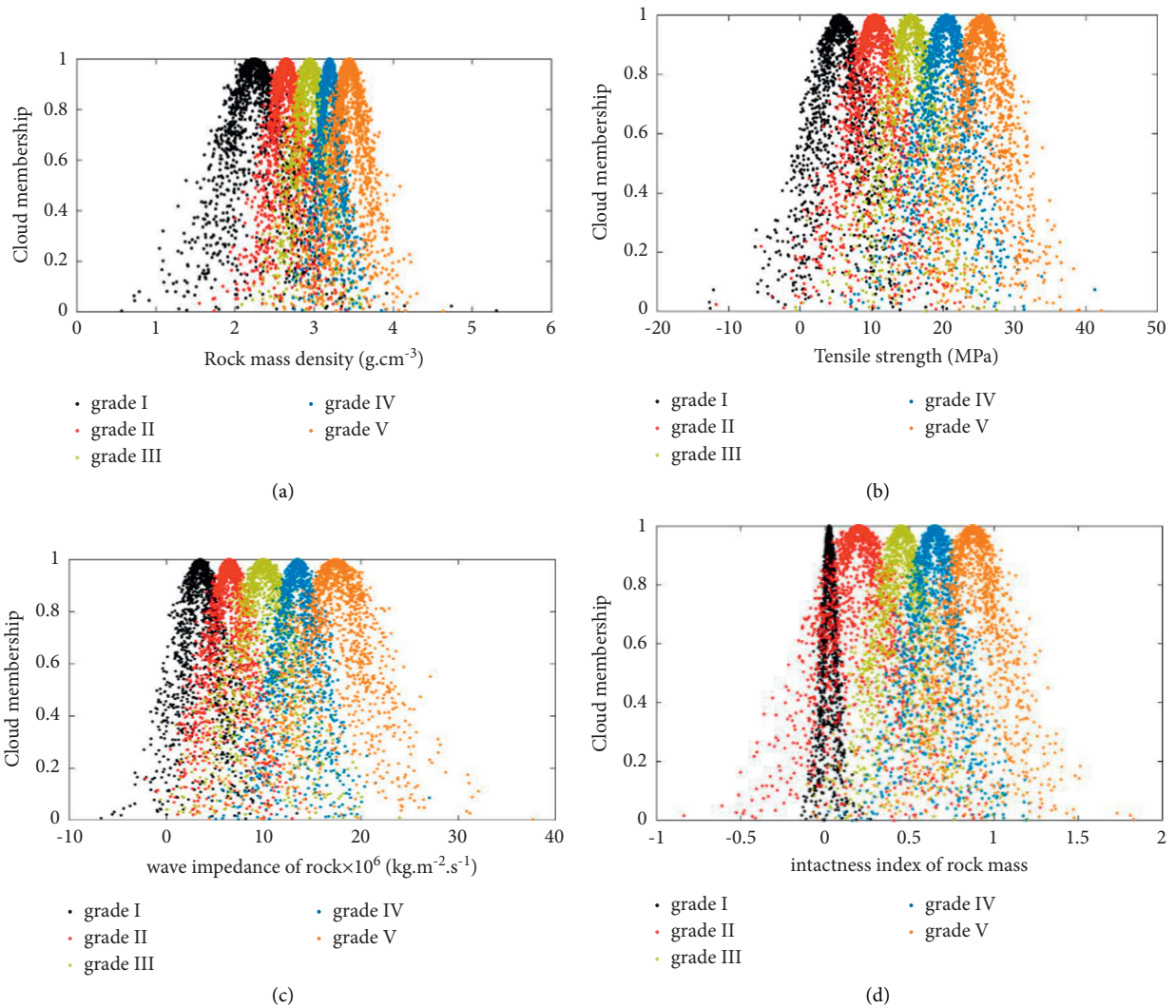


FIGURE 4: Cloud model diagram of different graded indexes of rock mass fracturing. (a) Rock mass density. (b) Tensile strength. (c) Wave impedance of rock. (d) Intactness index of rock mass.



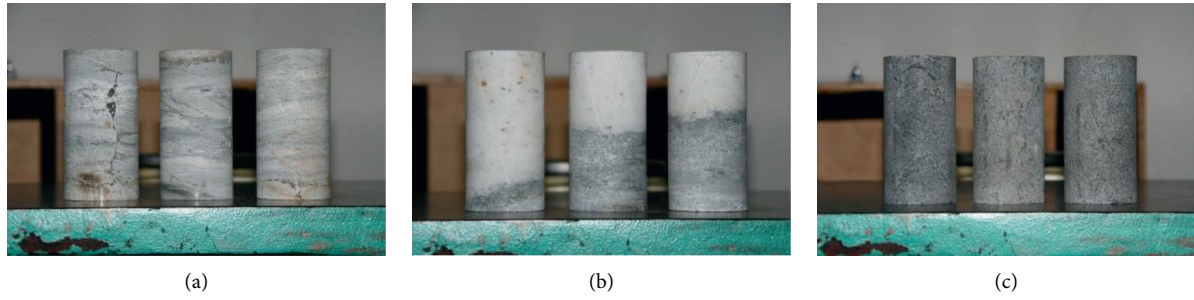


FIGURE 5: Rock samples in the engineering area. (a) Rock sample A, (b) rock sample B, and (c) rock sample C.

TABLE 10: Parameters of rock samples in the engineering area.

Rock samples	Rock mass density ( $\text{g}\cdot\text{cm}^{-3}$ )	Tensile strength (MPa)	Wave impedance of rock ( $\times 10^6 \text{ kg m}^{-2} \text{ s}^{-1}$ )	Intactness index of rock mass
A <sub>1</sub>	2.64	9.8	8.950	0.786
A <sub>2</sub>	2.68	9.6	8.788	
A <sub>3</sub>	2.65	10.1	8.984	
B <sub>1</sub>	2.73	14.2	10.303	0.636
B <sub>2</sub>	2.75	14.8	11.226	
B <sub>3</sub>	2.71	15.1	11.062	
C <sub>1</sub>	3.06	22.4	13.020	0.732
C <sub>2</sub>	3.05	23.8	12.978	
C <sub>3</sub>	3.06	23.6	12.491	

TABLE 11: Fracture ability classification results of rock mass.

Rock samples	Comprehensive membership					Fracture ability grade
	U <sub>1</sub>	U <sub>2</sub>	U <sub>3</sub>	U <sub>4</sub>	U <sub>5</sub>	
A <sub>1</sub>	0.3357	0.6772	0.5012	0.3306	0.3654	Grade II
A <sub>2</sub>	0.2623	0.5969	0.4351	0.3439	0.2972	Grade II
A <sub>3</sub>	0.3173	0.6561	0.4614	0.4331	0.2941	Grade II
B <sub>1</sub>	0.0989	0.4975	0.7171	0.5158	0.2104	Grade III
B <sub>2</sub>	0.1474	0.3019	0.7991	0.3841	0.2017	Grade III
B <sub>3</sub>	0.1423	0.4314	0.8634	0.5538	0.2959	Grade III
C <sub>1</sub>	0.0501	0.1568	0.5479	0.8991	0.5712	Grade IV
C <sub>2</sub>	0.1478	0.1659	0.6010	0.8636	0.6599	Grade IV
C <sub>3</sub>	0.1087	0.2003	0.3251	0.7490	0.5879	Grade IV

(10), the comprehensive membership degree of each rock mass sample for different grades can be obtained, and the results are shown in Table 11.

From the membership degree of different rock samples in Table 11, the fracture ability grades of the three types of rock masses in the engineering area are as follows: the grade of the fracture ability of rock mass A (A<sub>1</sub>~A<sub>3</sub>) is grade II, that of rock mass B (B<sub>1</sub>~B<sub>3</sub>) is grade III, and that of rock mass C (C<sub>1</sub>~C<sub>3</sub>) is grade IV. The rock mass in the construction area is generally in the range of easy to fracture to hard to fracture.

Through AHP-EWM and the cloud model method, the CO<sub>2</sub> phase transformation rock breaking fracture ability classification of the rock in the engineering area is carried out, the rock mass parameters of the engineering area are scientifically and reliably analyzed, and the actual blasting work guidance is provided for the regional blasting construction work.

## 5. Conclusions

This paper puts forward the concept of rock mass fracturing under the action of CO<sub>2</sub> phase change rock breaking. On the basis of the rock mass blastability classification theory, a CO<sub>2</sub> phase change fracturing based on AHP-EWM and the cloud model is proposed, and the classification method is applied to a reconstruction project in Tibet. The main conclusions obtained are as follows:

- (1) Based on the classification theory of rock mass blastability, AHP-EWM and cloud model classification for rock mass fracturing were proposed, which can effectively classify and evaluate rock mass fracturing. Moreover, the method is simple and easy to implement, overcomes the shortcomings of the traditional grading method's fixed evaluation mode, and has strong applicability.

- (2) When using AHP–EWM and the cloud model to classify the rock mass, the classification evaluation index of rock mass fracture ability is determined first. The subjective weight and objective weight are given to the selected evaluation indexes by AHP and EWM, and the combined weight is obtained by optimizing the weights of the two by the Lagrange multiplier method. Then, the cloud model of evaluation index is established, and the membership degree of different fracture grades corresponding to different grade evaluation indexes of rock mass fracture ability is determined by the digital characteristics of the cloud. Finally, different final membership degrees are obtained by using the product of the weight of evaluation index and the membership degree of each index.
- (3) The grading evaluation method is applied to the rock mass in a reconstruction project in Milin County, Tibet. The rock mass in the area is classified in terms of fracture ability. It is obtained that the three main rock masses in the area are fracturing relative to each grade. Among the three types of rock mass, feldspar quartz sandstone is divided into grade II, which is easy to fracture rock mass; feldspar quartz fine sandstone is divided into grade III, which belongs to medium hard to fracturing rock mass; diorite is divided into grade IV, which is difficult to the fracture rock mass. This method provides scientific guidance for engineering construction by classifying the crackability of the rock mass.

## Data Availability

All data, models, and codes generated or used during the study appear in the submitted article.

## Conflicts of Interest

The authors declare that they have no conflicts of interest.

## References

- [1] D. R. Schooler, *The Use of Carbon Dioxide for Dislodging Coal in Mines*, Curtis Laws Wilson Library, MO USA, 1944.
- [2] R. Holmberg and T. White, "Cardox system brings benefits in the mining of large coal," *International Journal of Rock Mechanics and Mining Science & Geomechanics Abstracts*, vol. 32, no. 5, p. 231, 1995.
- [3] J. Xia, B. Dou, H. Tian, J. Zheng, G. Cui, and M. Kashif, "Research on initiation of carbon dioxide fracturing pipe using the liquid carbon dioxide phase-transition blasting technology," *Energies*, vol. 14, no. 3, p. 521, 2021.
- [4] X. Liu, Z. Wang, D. Song, X. He, and T. Yang, "Variations in surface fractal characteristics of coal subjected to liquid CO<sub>2</sub> phase change fracturing," *International Journal of Energy Research*, vol. 44, no. 11, pp. 8740–8753, 2020.
- [5] Z. Liao, X. Liu, D. Song et al., "Micro-structural damage to coal induced by liquid CO<sub>2</sub> phase change fracturing," *Natural Resources Research*, vol. 30, pp. 1613–1627, 2021.
- [6] H. Wang, Z. Cheng, Q. Zou et al., "Elimination of coal and gas outburst risk of an outburst-prone coal seam using controllable liquid CO<sub>2</sub> phase transition fracturing," *Fuel*, vol. 284, Article ID 119091, 2021.
- [7] Q.-Y. Li, G. Chen, D.-Y. Luo, H.-P. Ma, and Y. Liu, "An experimental study of a novel liquid carbon dioxide rock-breaking technology," *International Journal of Rock Mechanics and Mining Sciences*, vol. 128, Article ID 104244, 2020.
- [8] C. P. Wen and R. Li, "Attribute measurement model and application for classification of rock blastability," *Engineering Blasting*, no. 03, pp. 14–17, 2007.
- [9] T. Y. Wu, N. Jiang, C. B. Zhou, X. D. Luo, H. B. Li, and Y. Q. Zhang, "Experimental and numerical investigations on damage assessment of high-density polyethylene pipe subjected to blast loads," *Engineering Failure Analysis*, vol. 131, Article ID 105856, 2022.
- [10] N. Jiang, B. Zhu, C. B. Zhou et al., "Blasting vibration effect on the buried pipeline: a brief overview," *Engineering Failure Analysis*, vol. 129, Article ID 105709, 2021.
- [11] S. Xiao, K. Li, X. Ding, and T. Liu, "Rock mass blastability classification using fuzzy pattern recognition and the combination weight method," *Mathematical Problems in Engineering*, vol. 2015, no. 12, 11 pages, Article ID 724619, 2015.
- [12] X. H. Ding, W. J. Yuan, Z. Jie et al., "Classification and identification of rock blastability in open-pit minebased on comprehensive weighted cloud model," *Coal Science and Technology*, vol. 47, no. 10, pp. 96–101, 2019.
- [13] S. Wu, S. Yang, and Q. Wang, "Classification of open pit iron mine rock mass blastability based on concept lattice and rough set," *Geotechnical & Geological Engineering*, vol. 38, no. 1, pp. 449–458, 2020.
- [14] A. Alipour, M. Mokharian, and S. Chehrehgani, "An application of fuzzy sets to the blastability index (BI) used in rock engineering," *Periodica Polytechnica: Civil Engineering*, vol. 62, no. 3, pp. 1–10, 2018.
- [15] N. Jiang, Y. Q. Zhang, T. Y. Wu, Y. K. Yao, and X. D. Luo, "Determination of blasting vibration safety criterion for HDPE pipeline using vibration and strain data in a coastal metro line," *Sensors*, vol. 21, p. 7252, 2021.
- [16] G. Y. Zhao, M. L. Gong, W. Z. Liang, and C. S. Hong, "Rock mass blastability classification using the combination of PSM and CM," *Mining and metallurgy engineering*, vol. 36, no. 03, pp. 21–25, 2016.
- [17] T. Zhou, J. H. Hu, Y. Kuang, and R. D. Huang, "Improved rock engineering system (RES)-Multidimensional cloud evaluation model and its application to the rock mass blastability," *IEEE Access*, vol. 7, no. 99, pp. 1100305–100317, 2019.
- [18] C.-l. Gao, S.-c. Li, J. Wang, L.-p. Li, and P. Lin, "The risk assessment of tunnels based on grey correlation and entropy weight method," *Geotechnical & Geological Engineering*, vol. 36, no. 3, pp. 1621–1631, 2018.
- [19] T. J. Tao, P. Huang, J. Li, J. Zhou, and H. Yu, "Blastability classification of fractured rock mass based on weighted clustering analysis," *Chemical Engineering Transactions (CET Journal)*, vol. 62, pp. 469–474, 2017.
- [20] Y. Zheng, H. Zhong, Y. Fang, W. Zhang, K. Liu, and J. Fang, "Rockburst prediction model based on entropy weight integrated with grey relational BP neural network," *Advances in Civil Engineering*, vol. 2019, Article ID 3453614, 8 pages, 2019.
- [21] K. Zhao, N. Jiang, C. B. Zhou, H. B. Li, B. Zhu et al., "Dynamic behavior and failure of buried gas pipeline considering the pipe connection form subjected to blasting seismic waves," *Thin-Walled Structures*, vol. 170, Article ID 108495, 2022.
- [22] A. Xi, L. A. Wei, A. Lz, and X. Guo, "Risk assessment for long-distance gas pipelines in coal mine gobbs based on structure

- entropy weight method and multi-step backward cloud transformation algorithm based on sampling with replacement,” *Journal of Cleaner Production*, vol. 227, pp. 218–228, 2019.
- [23] H. Xu, C. Ma, J. Lian, K. Xu, and E. Chaima, “Urban flooding risk assessment based on an integrated k-means cluster algorithm and improved entropy weight method in the region of Haikou, China,” *Journal of Hydrology*, vol. 563, pp. 975–986, 2018.
- [24] D. Y. Li and X. M. Shi, “Membership clouds and membership cloud generators,” *Computer research and development*, vol. 32, no. 06, pp. 15–20, 1995.
- [25] S. J. Yu, M. Y. Xin, S. L. Mao et al., “Correlation analysis of rock mass explosibility index,” *Journal of rock mechanics and engineering*, vol. 24, no. 003, pp. 468–473, 2005.
- [26] S. J. Li, Y. P. Zhang, H. Z. Zhu, and J. J. Xuan, “Blasting classification of rock mass based on clustering analysis of comprehensive weight,” *Engineering blasting*, vol. 21, no. 03, pp. 18–22, 2015.
- [27] B. Zhu, N. Jiang, C. Zhou, X. Luo, Y. Yao, and T. Wu, “Dynamic failure behavior of buried cast iron gas pipeline with local external corrosion subjected to blasting vibration,” *Journal of Natural Gas Science and Engineering*, vol. 88, Article ID 103803, 2021.
- [28] N. Jiang, B. Zhu, X. He, C. Zhou, X. Luo, and T. Wu, “Safety assessment of buried pressurized gas pipelines subject to blasting vibrations induced by metro foundation pit excavation,” *Tunnelling and Underground Space Technology*, vol. 102, Article ID 103448, 2020.

## Research Article

# Dynamic Response Characteristic of Building Structure under Blasting Vibration of underneath Tunnel

Ru He <sup>1</sup>, Nan Jiang <sup>2</sup>, Dong-Wei Li <sup>1</sup> and Jian-Feng Qi <sup>2</sup>

<sup>1</sup>School of Civil and Architecture Engineering, East China University of Technology, Nanchang 330013, Jiangxi, China

<sup>2</sup>Faculty of Engineering, China University of Geosciences, Wuhan 430074, Hubei, China

Correspondence should be addressed to Dong-Wei Li; [dwli2005@163.com](mailto:dwli2005@163.com)

Received 5 March 2021; Revised 6 June 2021; Accepted 16 December 2021; Published 4 January 2022

Academic Editor: Shan Gao

Copyright © 2022 Ru He et al. This is an open access article distributed under the Creative Commons Attribution License, which permits unrestricted use, distribution, and reproduction in any medium, provided the original work is properly cited.

The vibration induced by blasting excavation of the subway tunnel in complex urban environments may cause harmful effects on adjacent buildings. Investigating the dynamic response of adjacent buildings is a key issue to predict and control blasting hazards. In this paper, the blasting excavation of the subway tunnel right below a building was selected as a case study, and the blast vibrations in the field were monitored. The Hilbert–Huang Transform (HHT) model was used to extract and analyze the time-frequency characteristic parameters of blasting dynamic response signals. By substituting intrinsic mode functions (IMF) component frequency and instantaneous energy for main frequency and blasting total input energy, respectively, the characteristics of time-instantaneous frequency-instantaneous energy of buildings under blasting seismic load were analyzed, and the concept of effective duration of vibration was proposed.

## 1. Introduction

Subway is a key tool to facilitate new urban areas growth and renovate the old urban areas. With the further expansion and encryption of the subway network, the tunnels excavated under the existing buildings will spring up in complex urban environments. The drilling and blasting method, as a cost-saving and efficient excavation method for hard-rock tunnel, has been widely used in the excavation of urban metro tunnels. However, the blasting seismic wave will inevitably cause dynamic disturbance to adjacent buildings. Once the construction is not standardized or the vibration control is insufficient, the blasting seismic wave may lead to the cracking or local damage of the building structure. In order to evaluate and control the blasting dynamic damage of buildings reasonably, the dynamic response characteristics of buildings under the blasting vibration of the short-distance underneath tunnel should be evaluated, and potentially dynamic damage should be minimized.

The problem-analyzing perspectives mainly include peak particle vibration velocity (PPV) [1–4], the dominant frequency [5–8], and energy [9], and the safety regulations for

blasting (GB6722-2014) stipulates the safety threshold of PPV for adobe houses, civil buildings, commercial buildings, tunnels, etc. Due to the complexity and transient nature of blasting seismic waves, PPV and the dominant frequency cannot reflect the variation characteristics of structural blasting dynamic response in the time domain well and cannot fully meet the needs of practical engineering.

The blasting dynamic response of structure can be considered as the propagation and transformation of blasting energy, so energy can comprehensively express the characteristic of building structure and the complexity of blasting seismic wave. At present, the energy analysis methods of blasting seismic wave mainly include Fourier transform and Hilbert–Huang transform (HHT). The Fourier transform's idea is to decompose signal into the weighted sum of sinusoidal signals, and each sinusoidal signal corresponds to a fixed frequency and a fixed amplitude. Therefore, it is very effective for a stable signal whose frequency does not change with time, but not for the nonstationary signal whose frequency varies with time. For example, the blasting energy based on Fourier transform is a total cumulative energy during the duration of blasting

vibration, which cannot reflect the specific occurrence time of the maximum energy. The time variation of signal cannot be reflected.

HHT is an adaptive signal processing method with stronger time-frequency properties than Fourier transform and wavelet transform. It is composed of empirical mode decomposition (EMD) and Hilbert spectrum analysis (HSA). As the most important step in HHT, EMD was proposed by Huang in 1998 [10], which can decompose complex signal into a series of intrinsic mode functions (IMF) adaptively according to the characteristics of the given signal itself. It fundamentally breaks through the limitations of Fourier transform and establishes the signal analysis method based on instantaneous frequency for the first time [11]. For the complex transient wave such as blasting seismic wave, HHT transform can more clearly and accurately show the specific distribution of energy at any time and frequency, and accurately depict the signal characteristics at any time.

HHT method is mainly applied to damage monitoring and modal identification of construction in civil engineering [12–14]. Until recently, however, HHT and its variants were gradually introduced into blasting vibration signal analysis, and the instantaneous energy and the instantaneous frequency of blasting seismic wave began to be valued [15,16]. Zong et al. [17] studied the blasting seismic wave signal frequency spectrum characteristics and energy distribution of coalmine roadway excavation by the HHT method and EMD. Liu et al. [18] analyzed the instantaneous total energy of the four charge structures of conventional charge, water interval charge at both ends, water interval charge at the orifice, and water interval charge at the hole bottom. Li et al. [19] proposed here an improved HHT method combined with a wavelet packet to extract the energy spectrum feature of a blast wave. By using instantaneous energy spectrum, Yuan et al. [20] analyzed the blasting vibration signals in a lead-zinc mine in south China by three-dimensional Hilbert spectrum, marginal spectrum, and instantaneous energy spectrum, and the results indicate that the blasting frequencies lie mainly within 0~200 Hz, which consists of more than 90% of the total signal energy. Chen et al. [21] studied the propagation laws of blasting vibration waves in weak rock tunnels using HHT and found that with a given charge quantity, as the distance from the explosion source increases, the spectrum width of the blasting vibration frequency becomes narrower, and the overall energy is more concentrated. Fei [22] processed blasting vibration signals by the HHT method and analyzed the propagation law of blasting vibration under the ancient ruins. Yang et al. [23] explored the propagation attenuation characteristics of blasting during tunnel excavation in the grade change area of surrounding rock and analyzed the distribution laws of instantaneous energy in time domain and frequency domain. Most of the existing blasting energy studies focus on the analysis of the blasting seismic wave propagation.

The structural blasting dynamic response is not only related to the propagation law of blasting seismic wave but also should consider the working condition and the characteristics of the building itself. Due to diverse architectural features, such as structure types, building stories, foundation

types, and construction measures, the blasting seismic wave of the same or similar working conditions used to produce the different structural dynamic disturbance response characteristics. Therefore, it is the key to analyze the blasting dynamic response characteristics of buildings with different structural types, obtain the variation law of the blasting dynamic response characteristics, and enrich the blasting safety regulations. Comparing with other analysis methods, like Fourier transformation and the wavelet, the HHT not only extracts the real information of structural dynamic response in the time domain but also effectively removes noise from monitoring signals. However, it is very rare to use HHT to analyze the instantaneous characteristics of the structural dynamic response signals [24], and the report of time-instantaneous frequency-instantaneous energy study of structural dynamic response under blasting vibration of underneath tunnel is not available yet.

Based on the monitoring data, HHT is introduced into the dynamic response characteristic analysis of multi-storey frame structure under blasting vibration of underneath tunnel, using the dominant instantaneous frequency and the instantaneous energy to replace the dominant frequency and the total input energy, respectively, the time-instantaneous frequency-instantaneous energy variation law of multistorey frame concrete building under tunnel blasting excavation is analyzed. The maximum instantaneous energy in the vibration duration and the blasting instantaneous energy at the peak vibration velocity are compared. The curves of horizontal radial, horizontal tangential, and vertical instantaneous energy along the direction of floor height are obtained, respectively. The frequency components and energy contribution percentages of the structural response signals are studied with time. The concept of effective vibration time length is put forward. The concept of effective vibration time length, that is, the duration when the instantaneous energy exceeds a certain limit energy control value in a single blasting, is put forward, which can describe the characteristic law of vibration energy more directly and reliably than the relative duration.

The innovations and main contributions of this paper are described as follows:

HHT is successfully introduced into the analysis of blasting vibration response characteristics of building structures. The effectiveness and superiority of HHT is verified by the analysis and comparison of conventional vibration parameters and instantaneous parameters.

Substituting the IMF component frequency and instantaneous energy for main frequency and total input energy, respectively, the variation law and characteristics of time-instantaneous frequency-instantaneous energy is analyzed. The variation of the main frequency components of the structural response signal and its energy contribution percentage with time is given, which is of great practical values to guide the blasting operations.

The concept of effective duration of vibration is proposed, which can be defined as the duration when the instantaneous energy exceeds a certain energy control value in a single blasting, and is of great theoretical values to enrich the current blasting safety regulations and the methods evaluating the safety of structures.

## 2. Overview of Undercrossing Tunnel Engineering

The undercrossing tunnel is located between Zhifang Road Station to Qinglongshan Ditiexiaozen Station of the Wuhan Metro Line 8. The total length of the tunnel is 1274.11 m. This is a single-hole-double-track tunnel with a horseshoe cross section and a size of 11.8 m  $\times$  9.6 m (span  $\times$  height). In this project, the tunnel roof is buried at a depth of 15 m. As the tunnel is embedded in rock of high grade, the drilling and blasting method is adopted. The distribution of the underlying stratum is shown in Figure 1(b). There are 3.5 m thick plain fill, followed by 8.5 m thick of clay and then moderately weathered limestone from top to bottom.

Right above the tunnel, there is a newly constructed building, which consists of a basement and two above ground levels. As illustrated in Figure 1(a), the tunnel is parallel to the long axis of building.

The building is a kindergarten teaching building. The foundation of the building is pile foundation, and there is a basement, which makes the soil-structure dynamic interaction more obvious and results in stronger dynamic response.

The hard-rock tunnel is constructed by center diaphragm (CD) excavation method using 2# rock emulsion explosive with the cyclical footage of about 1.5 m. According to the design requirements, a shallow hole millisecond blasting method should be used for the construction of the tunnel, and multiperiod nonelectric millisecond detonators control the explosions.

According to the requirements of the project site, the PPV of the ground surface node should not exceed 2 cm·s<sup>-1</sup>. The maximum charge for the same section is 24.57 kg. The single-period charge placed within each cut hole, relief hole, and perimeter hole are 0.8 kg, 0.4 kg, and 0.2 kg, respectively. Wedge-shaped cutting is adopted for tunnel excavation. The design depth of the wedge cut eye and the central straight eye is 2.2 m. The diameters of the holes are all 42 mm and the distance between the cut holes, relief holes, and perimeter holes are 350 mm, 400 mm, and 300 mm, respectively.

## 3. Blasting Dynamic Response Monitoring Test and Analysis

The TC-4850 blasting vibration recorder system was used to carry out field monitoring of the blasting vibration response signal of building. The monitoring system consists of a vibration sensor and a vibration recorder. The time-history curve of particle vibration at the monitoring point can be obtained, from which PPV can be extracted, namely, the maximum absolute value of the velocity of particle vibration

around the equilibrium position when disturbed by blasting earthquake, as well as the frequency of main vibration, namely, the frequency with the maximum amplitude in the vibration response.

During the test, the blasting vibration test was carried out when the tunnel face was consistent with the short axis of the building. Blasting vibration meters were placed at the outer wall corner, and all measuring points were placed along the height direction. A0, A1, and A2 are vibration measuring points, as shown in Figure 1(b).

The sensor directions were arranged as  $X$  direction along the long axis of the building, that is, consistent with the direction of the tunnel,  $Y$  direction along the short axis of the building and tangent to the direction of the tunnel, and  $Z$  direction was vertical direction.

**3.1. Blasting Vibration Characteristics.** 12 sets of blasting vibration monitoring data of three measuring points in the building under four times blasting were recorded during the process of excavation blasting of tunnel. The PPV and maximum main frequency recorded for each data set are shown in Table 1. Among them, blasting no. 1 and blasting no. 3 refer to the blasting excavation of the lower bench, while blasting no. 2 and no. 4 refer to the blasting excavation of the upper bench.

Figure 2 shows the variation law of the PPV in the  $X$  direction, in the  $Y$  direction, and in the  $Z$  direction with different heights in the same blasting. The peak response velocity in the  $X$  direction  $V_X$  and in the  $Y$  direction  $V_Y$  increases first and then decreases with the increase of floors, which is contrary to the response results of three-story ground buildings without basement in existing studies [25].

The vertical peak velocity  $V_Z$  is consistent with the measured results of the response of three-story ground buildings without basement in existing studies [25], showing a trend of decreasing first and then increasing. It can be seen that the basement could make the blasting seismic dynamic response different from that of nonbasement buildings.

Figure 3 shows the variation of the  $V_Z$  to  $V_X$  ratio and the  $V_Z$  to  $V_Y$  ratio in the same blasting with the floor. The higher the ratio is, the more obvious the vibration response of the building is in the vertical direction. Different from natural earthquakes, the  $V_Z$  to  $V_X$  ratio and the  $V_Z$  to  $V_Y$  ratio are basically greater than 1 under the blasting vibration of tunnel excavation, that is, the vertical PPV is always higher than the horizontal radial and horizontal tangential PPV. In general, the long-axis stiffness of the building is greater than the short-axis stiffness, so the natural vibration frequency building in the vertical direction is closer to the main vibration frequency of the blasting seismic wave.

Figures 3(a) and 3(b) show the ratios of vertical and horizontal PPV decrease from basement to the first floor and increase from the first floor to the second floor. At the 1st floor which has the same elevation with the ground surface, the difference between the vertical and horizontal structural response velocities is the smallest, and the difference between the vertical and horizontal PPV increases with the distance from the ground surface.



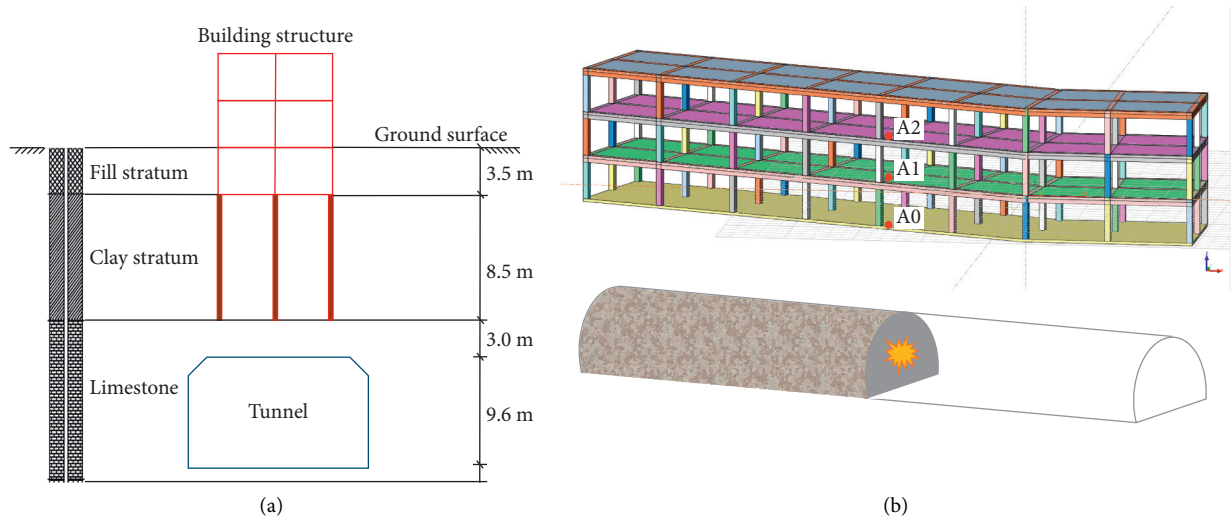


FIGURE 1: Positional relationship of the tunnel and building and layout of the monitoring points. (a) Profile graph. (b) 3D graph.

TABLE 1: Vibration monitoring points PPV and maximum main frequency statistics.

Blasting number	Vibration measuring point number	PPV $V/(cm \cdot s^{-1})$			Maximum main frequency $f/(Hz)$		
		$V_X$	$V_Y$	$V_Z$	$f_X$	$f_Y$	$f_Z$
No. 1	A0	0.44	0.63	0.589	18.141	20.779	18.265
No. 1	A1	0.693	0.794	0.574	23.19	20.25	27.3
No. 1	A2	0.572	0.652	0.702	21.68	16.33	30.2
No. 2	A0	0.70	1.872	3.79	24.54	27.304	44.944
No. 2	A1	1.592	2.812	3.341	23.6	26.94	36.7
No. 2	A2	1.187	3.138	5.323	16.495	22.92	34.48
No. 3	A0	1.104	2.14	4.14	38.095	24.096	11.065
No. 3	A1	0.99	2.10	3.65	34.19	21.11	27.68
No. 3	A2	0.605	2.29	5.96	18.78	21.56	33.06
No. 4	A0	0.44	0.69	1.58	38.84	20.31	24.77
No. 4	A1	0.50	0.70	1.185	33.33	23.39	26.23
No. 4	A2	0.35	0.71	1.788	23.6	23.53	29.52

The frequencies of the three main vibration directions of the structure can reflect the dynamic response of building. As shown in Figure 4, the vibration frequency range of the structure response is between 11 Hz and 44 Hz subject to the blasting vibration of the underpass tunnel, and the dominant frequency of the speed signal is vertical > horizontal. Under the same blasting, the bandwidths of the dominant frequency band of the velocity response signal in the three directions have the trend that: the first floor < 2nd floor < basement. As the floors increase, the main frequencies in the X direction and Y direction gradually attenuate and tend to the natural frequency of the structure, while the main frequency of vertical signal increases with increasing height.

**3.2. Instantaneous Characteristics of Blasting Vibration.** Introducing the HHT analysis method to the analysis of structural dynamic response, the complicated blasting vibration is turned into the combined action of multiple IMF components. Substituting the IMF component frequency and instantaneous energy for main frequency and total input energy, respectively, the variation law and characteristics of

time-instantaneous frequency-instantaneous energy is analyzed [26, 27].

Taking the vertical response signals of blasting vibration of the measuring point A0 in the basement of blasting no. 1 as an example, the variation of its vertical instantaneous frequency, instantaneous amplitude, and instantaneous energy characteristics are analyzed.

The vertical velocity time-history curve is shown in Figure 5(a), and the Fourier frequency spectrum is shown in Figure 5(b). The instantaneous energy and instantaneous frequency time-history curve can be obtained through HHT transformation of the data, as shown in Figures 5(c) and 5(d), respectively.

Figure 5 shows that the dominant frequency of the vertical vibration signal is 18.265 Hz. For the vertical blasting vibration signal, the vertical real-time frequency varies dramatically during the vibration duration, and the instantaneous frequency at the moment of maximum velocity is not consistent with that at the moment of maximum instantaneous energy. Furthermore, the peak time of vibration velocity is not consistent with that of instantaneous energy peak.

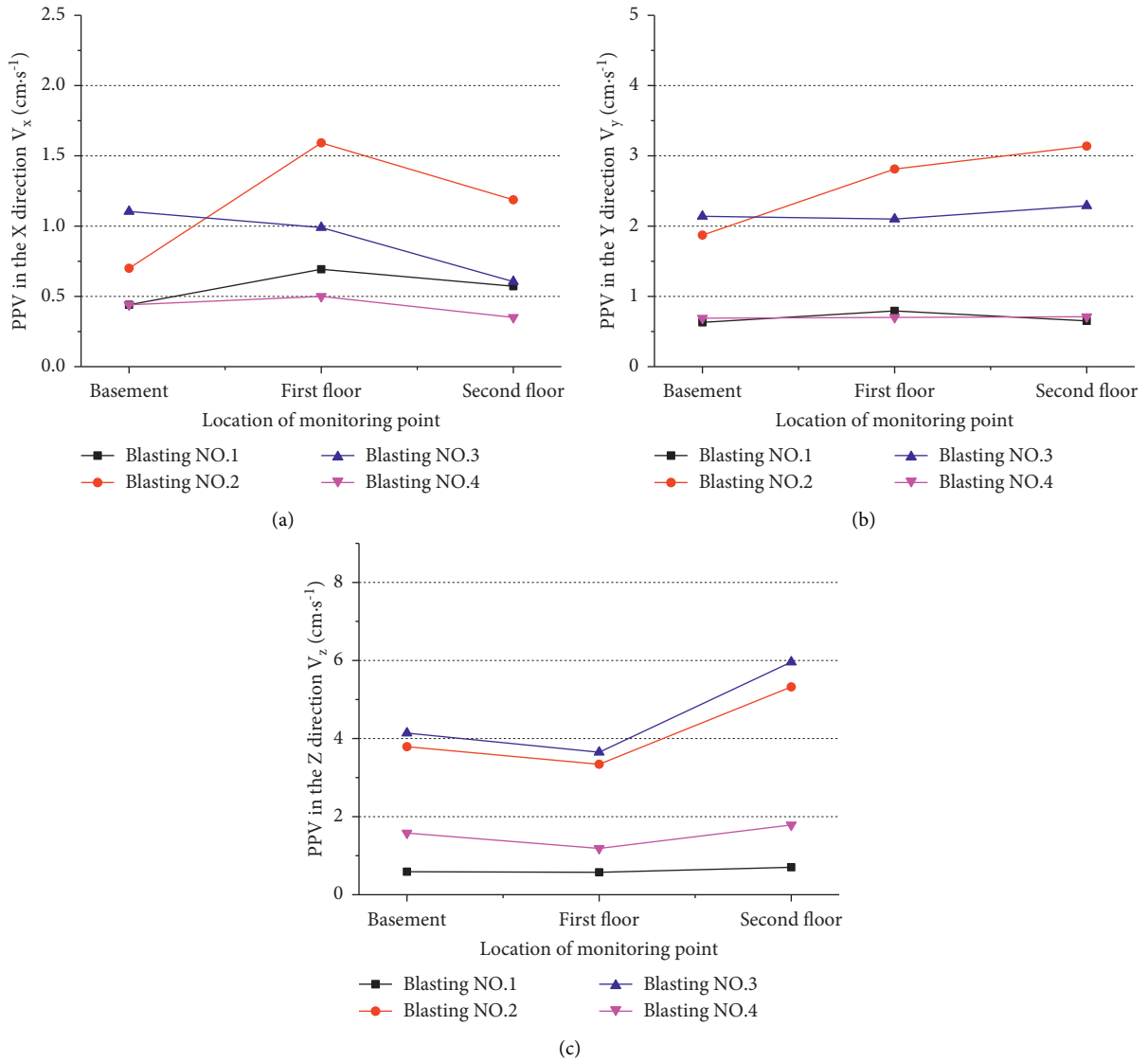


FIGURE 2: PPV curves with different heights. (a) PPV in the X direction. (b) PPV in the Y direction. (c) PPV in the Z direction.

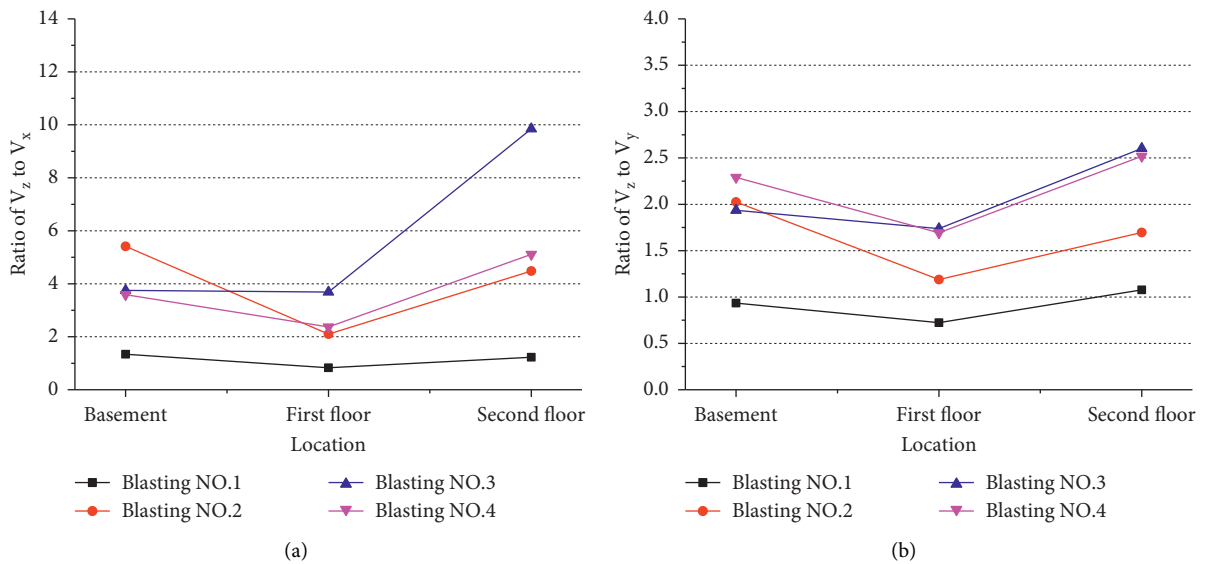


FIGURE 3: PPV ratio curves with different heights. (a) The  $V_z$  to  $V_x$  ratio. (b) The  $V_z$  to  $V_y$  ratio.

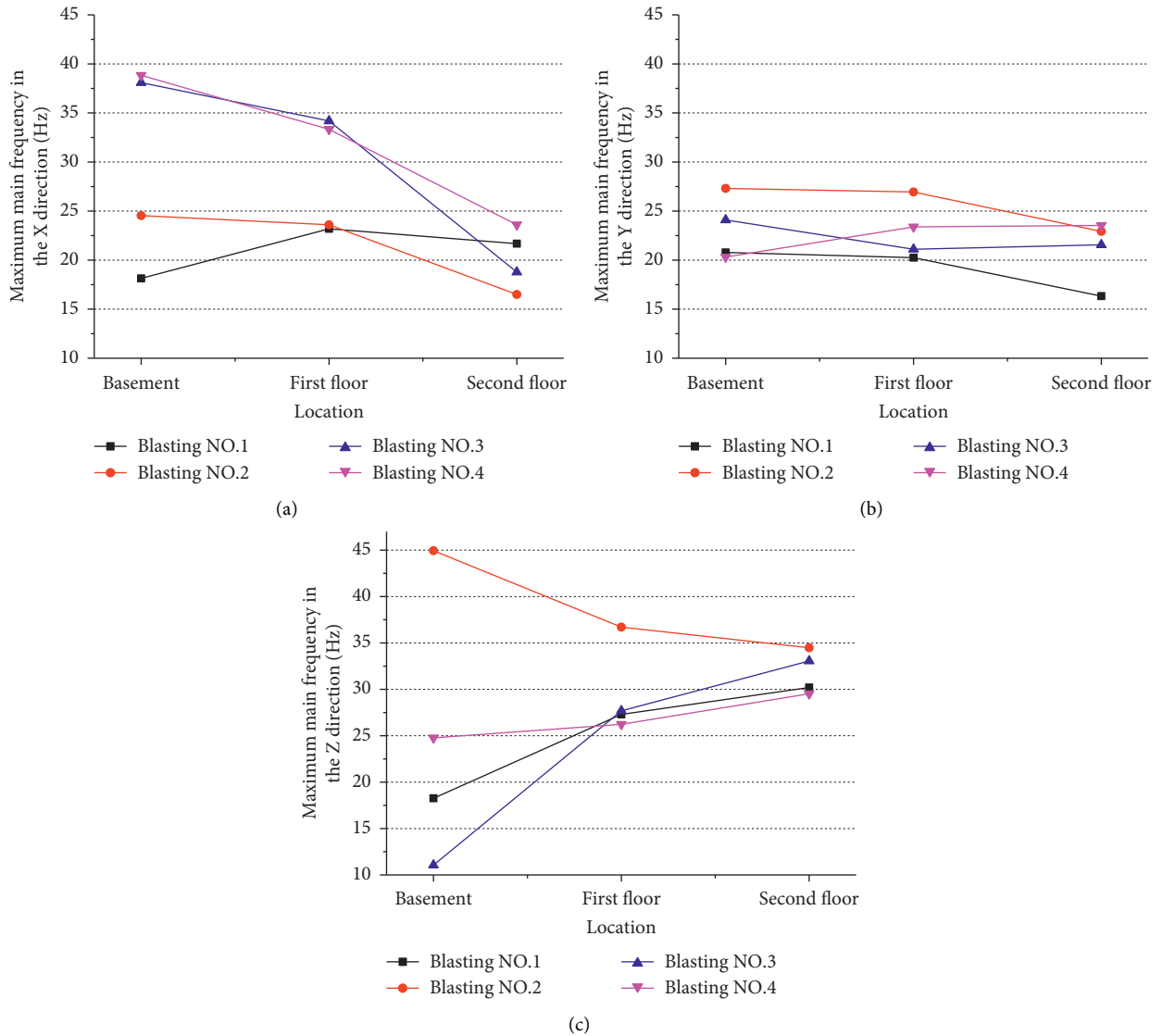


FIGURE 4: Main frequency curves with different heights. (a)  $f_{X-max}$ . (b)  $f_{Y-max}$ . (c)  $f_{Z-max}$ .

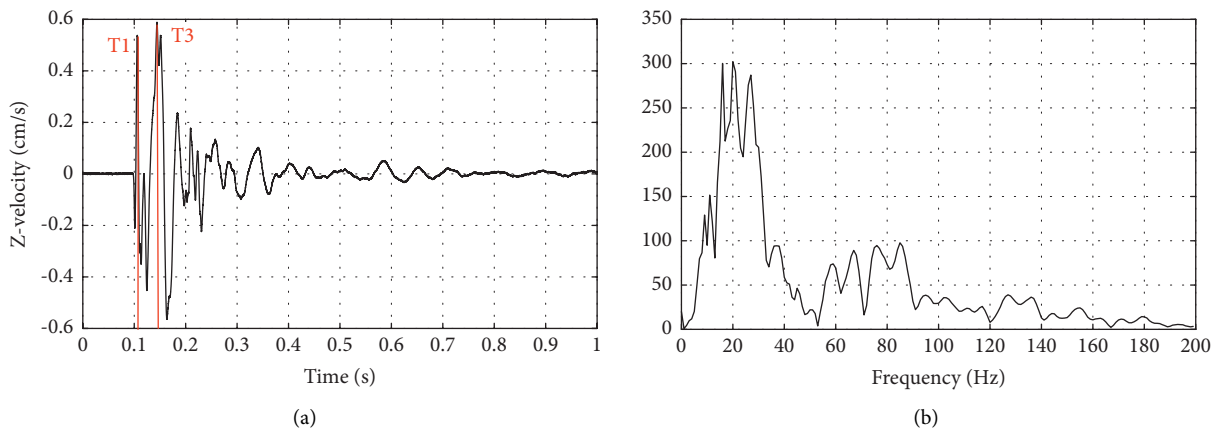


FIGURE 5: Continued.

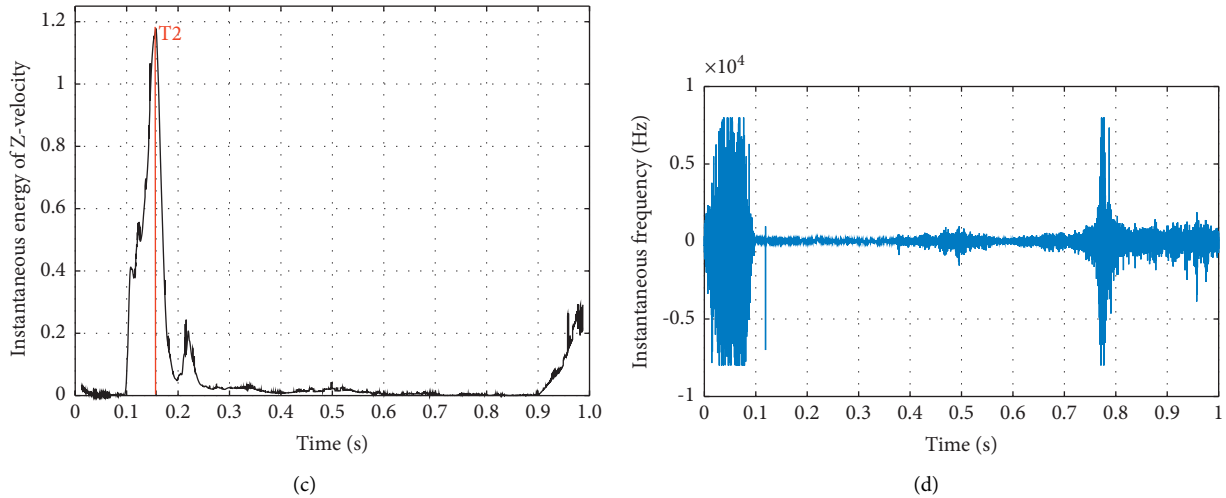


FIGURE 5: Vertical response signals of the measuring point A0 of blasting no. 1. (a) The vertical velocity time-history curve. (b) The Fourier frequency spectrum. (c) The instantaneous energy. (d) The instantaneous frequency.

During the vibration process, the particle vibration velocity has two similar peak values, and the instantaneous energy has one peak value. Take the occurrence time of the maximum vibration velocity, the maximum instantaneous energy and the secondary vibration velocity, respectively, as the critical moment  $T1 = 0.1442$  s,  $T2 = 0.1573$  s, and  $T3 = 0.1633$  s.

The instantaneous energy at the three critical moments is shown in Figure 6. It can be seen that the energy at time T2 is 44.52% higher than that at time T1.

By EMD decomposition of vertical vibration velocity signals, 13 IMF components can be obtained. The corresponding instantaneous frequencies and instantaneous amplitudes of the 13 IMF components can be obtained by HHT. The instantaneous frequencies and instantaneous amplitudes at the three critical moments are extracted in Table 2.

As White noise and signal drift, IMF1 and IMF13, have extremely small energy, they are ignored and not included in statistics.

IMF component instantaneous frequency at the three critical moments is shown in Figure 7. According to the analysis and results in Figure 5, the dominant frequency of the vertical vibration signal is 18.265 Hz. Vertical blasting vibration response signals have a rich frequency spectrum, most of which are distributed within 90 Hz, and the dominant frequency spectrum of the signals is within 13.57 Hz~20.71 Hz. The IMF components (IMF4 and IMF5) of the intermediate frequency have entered the dominant frequency range of the vertical vibration and are decreasing continuously, which is close to the main frequency 18.265 Hz. The low-frequency IMF components (IMF6~IMF12) enter the range of the structure's natural vibration frequencies (2 Hz~10 Hz). In this region, the instantaneous frequencies of the three critical moments vary slightly around the IMF dominant frequency.

Power spectral density (PSD) defines how to distribute the power of a signal or time series with frequency. The

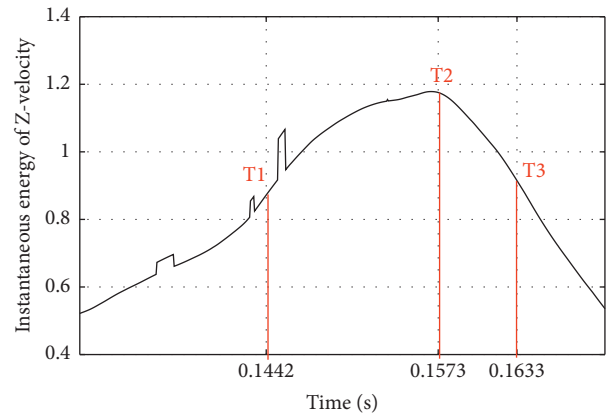


FIGURE 6: Instantaneous energy at the three critical moments.

maximum value of PSD is usually used to represent the important feature information of frequency extracted [28]. According to PSD value of the vertical velocity response signals, its relative advantage in the vertical main frequency band can be shown in Figure 8. Among these IMF components, IMF5 (20 Hz, PSD = 275.5), IMF8 (7 Hz, PSD = 116.88), and IMF4 (58 Hz, PSD = 80.43) contribute to the vertical dominant frequency significantly.

IMF5, which is closest to the vibration dominant frequency, contributes the most to the dominant frequency. The low frequency IMF8 in the natural frequency range of the component dominant frequency structure has the second contribution. The contribution of intermediate frequency IMF4 cannot be ignored. Especially for the intermediate frequency IMF4, its instantaneous frequency is much higher than the IMF dominant frequency at the three critical moments. In velocity analysis and energy analysis, the dominant frequency of IMF4 cannot replace the instantaneous frequency.

Based on the instantaneous energy spectrum of HHT, the instantaneous energy of each IMF component at three

TABLE 2: The instantaneous frequency of the IMF component at three critical moments.

IMF	Main frequency of IMF (Hz)	Instantaneous frequency (Hz)			Instantaneous amplitudes		
		T1	T2	T3	T1	T2	T3
2	849	700	1007	2891	0.001	0.0018	0.0011
3	131	122.77	348	906.6	0.0829	0.0009	0.0009
4	58	137.32	76.76	92	0.0227	0.1382	0.1064
5	20	16.55	22.50	23.75	0.5463	0.6408	0.5639
6	16	17.447	20.55	22.43	0.0211	0.0393	0.0489
7	15	16.77	20.5	23.82	0.0071	0.0045	0.0038
8	7	6.09	5.74	5.52	0.0369	0.0436	0.0464
9	16	2.24	1.81	0.75	0.0019	0.00213	0.0021
10	7	2.79	3.32	3.64	0.0982	0.0108	0.0113
11	4	3.32	3.34	3.41	0.0052	0.0051	0.0051
12	3	2.33	2.29	2.32	0.0059	0.0059	0.0059

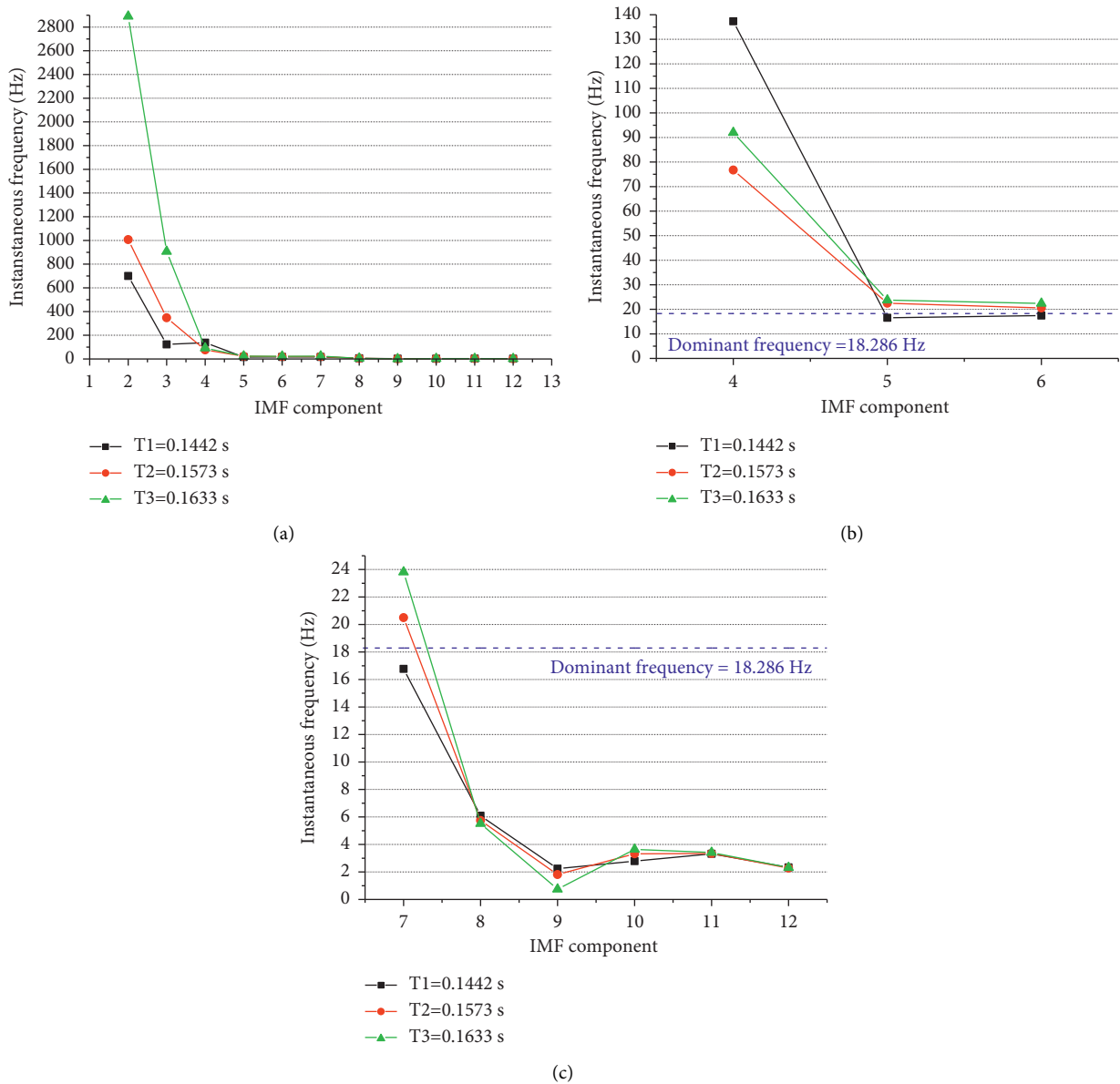


FIGURE 7: IMF component instantaneous frequency at the three critical moments. (a) Instantaneous frequency. (b) Intermediate instantaneous frequency. (c) Low instantaneous frequency.

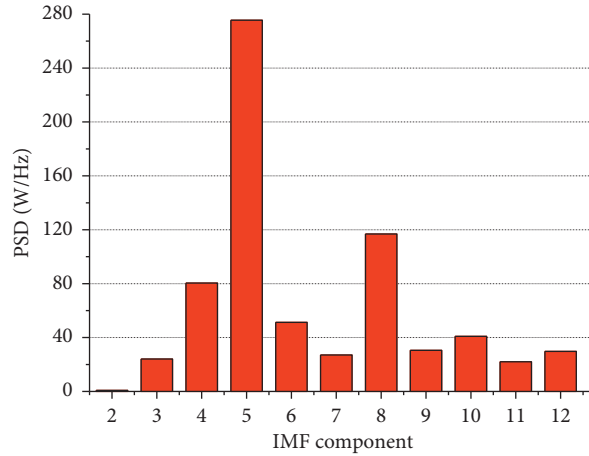


FIGURE 8: The PSD value of IMF component.

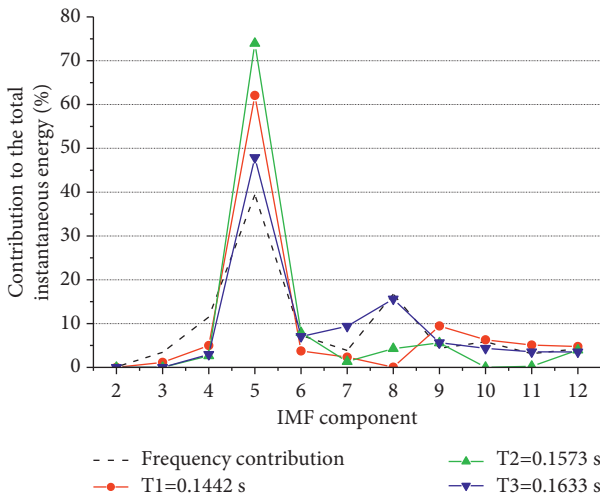


FIGURE 9: Ratio of IMF instantaneous energy to the total vertical instantaneous energy.

critical moments and its percentage in the total vertical instantaneous energy can be obtained. As shown in Figure 9, the contributions of IMF components to instantaneous energy are inconsistent with the contributions to vertical vibration main frequency at the three critical time points.

The IMF5 has the most obvious effect on the vertical vibration dominant frequency and the maximum instantaneous energy. The main frequency of IMF5 (20 Hz) is the closest one to the vibration dominant frequency (18.265 Hz). The IMF component with the second largest energy contribution to the instantaneous energy is not fixed. The second largest energy contribution to T1, T2, and T3 is IMF9, IMF6, and IMF8, respectively. The frequency band spans the low frequency and the middle frequency, and the frequency values differ greatly.

**3.3. Instantaneous Energy Varies with Different Heights.** As mentioned above, the HHT analysis method is used to process 36 sets of data under four blasting, and the variation curves of peak instantaneous energy caused by

vibration in X, Y, and Z direction along the height are obtained.

As shown in Figure 10, the instantaneous energy curves of X direction and Y direction basically show a trend of increasing first and then decreasing, and the maximum energy appears on the first floor. The instantaneous energy curves in the Z direction are the polar opposite of X and Y direction, that is, the minimum vertical energy occurs on the first floor.

The vibration duration in blasting engineering includes two concepts: single blasting vibration duration and total blasting vibration duration. The duration of single blasting vibration is the duration from the beginning of particle vibration to the complete stop, and the total duration of blasting vibration is the sum of the duration of each blasting vibration.

When blasting seismic wave propagates in a given structure, its input energy constantly transforms between system kinetic energy, system damping energy dissipation, and system deformation energy with the change of time. That is, the maximum instantaneous input energy corresponds to the maximum strain and maximum displacement of the structure.

Therefore, in this paper, consider the maximum instantaneous energy as signs of the first dynamic damage under blasting seismic wave and define the  $t_{m-e-z}$  as relative occurrence time of maximum instantaneous energy ( $E_{i-max}$ ). The  $t_{m-e-z}$  curves of change with the floor are shown in Figure 11.

As can be seen from Figure 11, the occurrence time of the maximum instantaneous energy of each floor varies greatly, and it can appear at 5.7% of the total vibration duration at the earliest and 97% of the total vibration duration at the latest.

The influence of vibration duration on building vibration response is mainly in the nonlinear response stage rather than the elastic stage. The impact of vibration duration is mainly manifested in two aspects that are the reduction of elastic limit so that the material can easily enter the plastic state and increase the cumulative damage plastic deformation.



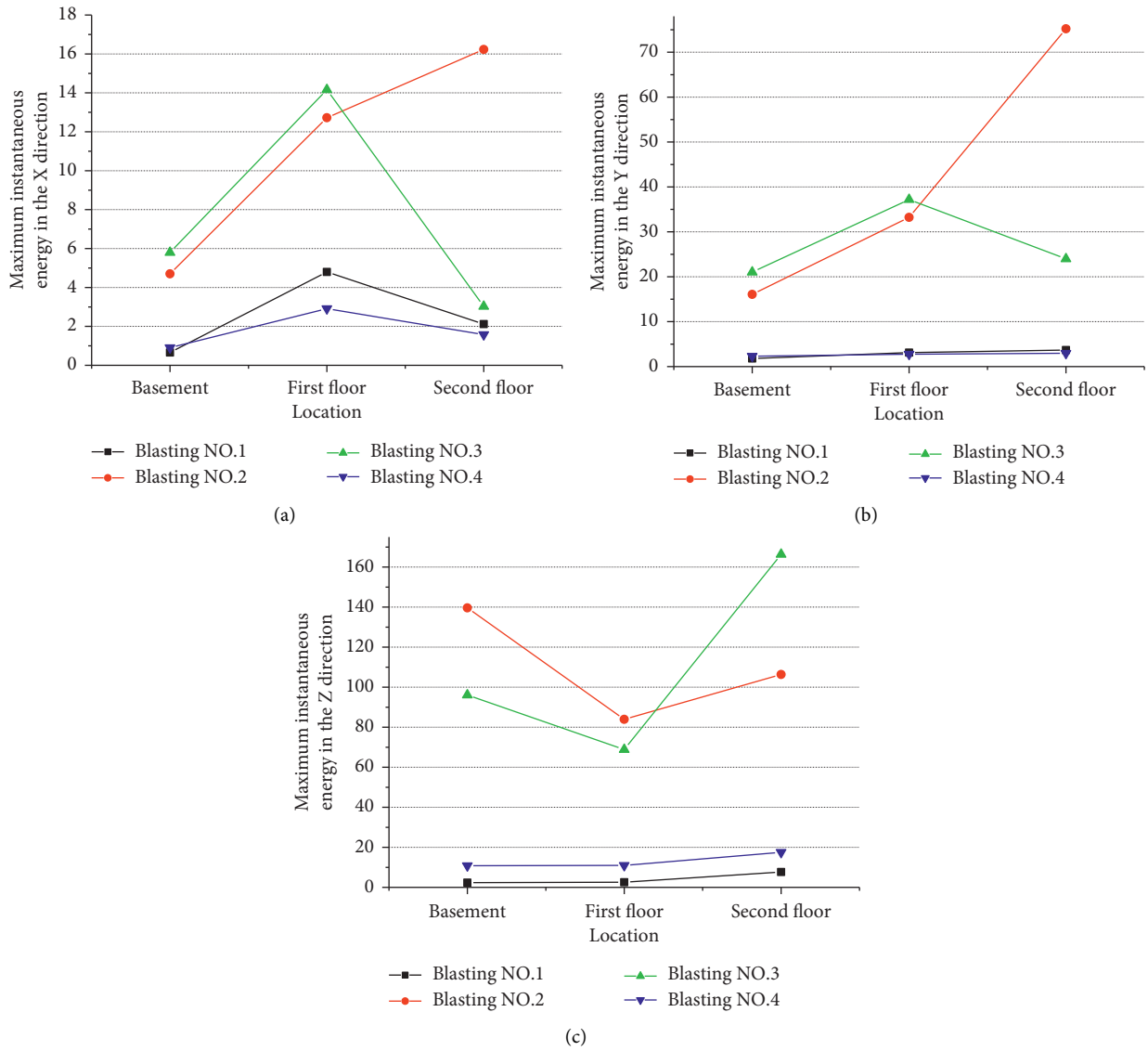


FIGURE 10: Maximum instantaneous energy curves with different heights. (a) In the X direction. (b) In the Y direction. (c) In the Z direction.

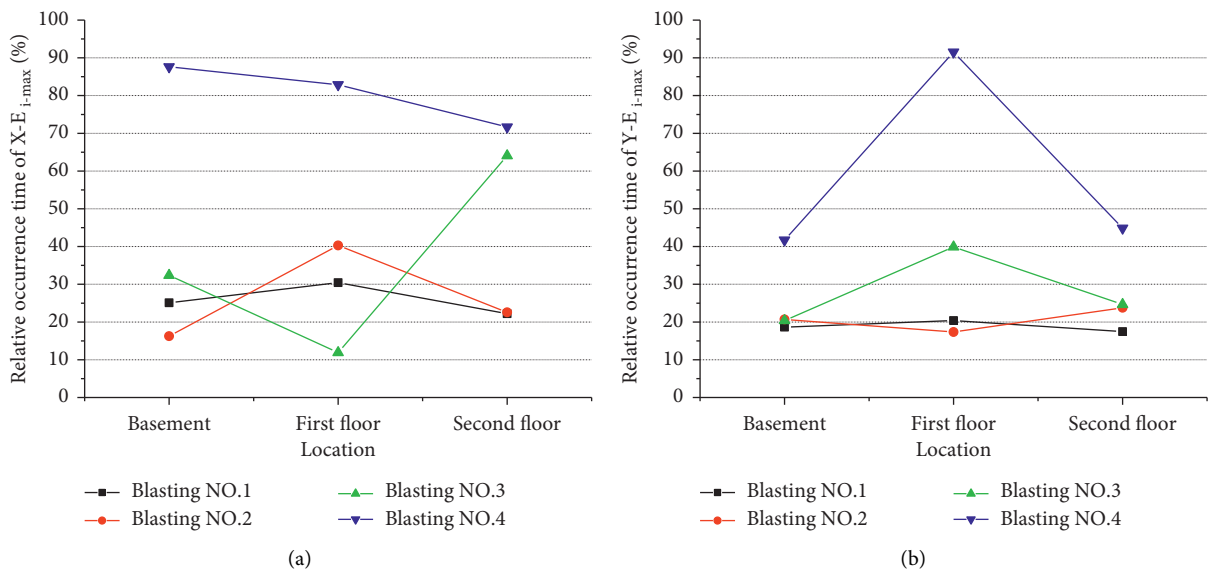


FIGURE 11: Continued.

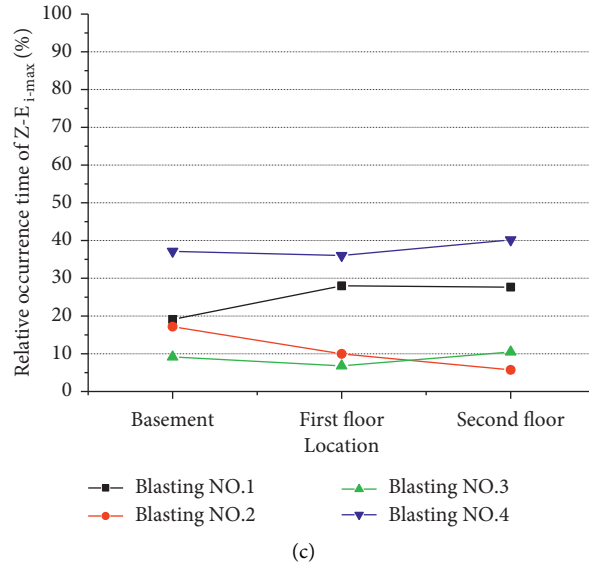


FIGURE 11: The  $t_{m-e-z}$  curves of change with the floor. (a) In the X direction. (b) In the Y direction. (c) In the Z direction.

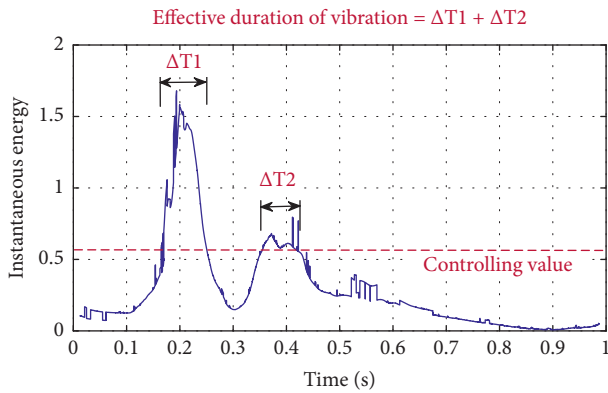


FIGURE 12: Schematic of effective duration of vibration.

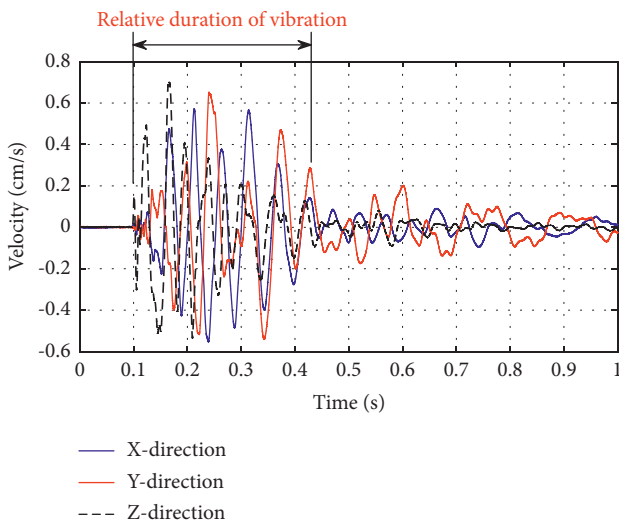


FIGURE 13: Schematic of relative duration of vibration.

Therefore, the duration when the instantaneous energy exceeds a certain energy control value in a single blasting can be defined as the effective duration of vibration in this paper (see Figure 12). Compared with the relative vibration duration, which means the time from the beginning of particle vibration to the time when the amplitude of vibration wave attenuates to 1/3 of its maximum value in actual engineering (see Figure 13). In the dynamic response analysis of the structure, the effective duration of vibration can be more accurate and scientific than the relative duration of vibration. Especially in the study of dynamic response based on instantaneous energy or maximum impulse the effective duration of vibration can describe the characteristic law of vibration energy more objectively and directly than the vibration duration.

### 4. Conclusions

In this paper, a building adjacent to the excavation blasting of underpass tunnel is taken as a case study. Substituting the IMF component frequency and instantaneous energy for main frequency and total input energy, respectively, the variation law and characteristics of time-instantaneous frequency-instantaneous energy is analyzed. The main conclusions are as follows:

- (1) Under the blasting vibration induced by undercrossing tunnel excavation,  $V_X$  and  $V_Y$  increases first and then decreases with the increase of the floor.  $V_Z$  is firstly decreased and then increased, and  $V_Z$  is always higher than  $V_X$  and  $V_Y$ . At the 1st floor which has the same elevation with the ground surface, the difference between the vertical and horizontal structural response velocities is the smallest.
- (2) The horizontal radial and horizontal tangential instantaneous energy increase firstly and then decrease with the increase of floor under blasting vibration,

whereas the vertical instantaneous energy variation has the contrary feature.

- (3) The instant of maximal peak value of instantaneous energy does not accord with the peak vibration velocity. The frequency and energy contribution of structural response signal change with time and differ considerably from main vibration frequency. Therefore, the main vibration frequency derived from PSD frequency spectrums cannot precisely represent the structural dynamic response under blasting seismic wave.
- (4) Effective duration of vibration is defined as the duration when the instantaneous energy exceeds a certain energy control value in a single blasting, which could describe the instantaneous energy or maximum impulse more accurately and effectively in the structure dynamic response analysis under blasting vibration.

Effective duration of vibration is related to the control value of this instantaneous input blasting energy, which is related to the characteristics of the building structure. Due to the diversity of structure, how to effectively link the various parameters of the building structure with the control value of instantaneous input blasting energy is our next work.

## Data Availability

All data included in this study are available upon request by contacting the corresponding author.

## Conflicts of Interest

The authors declare that there are no conflicts of interest regarding the publication of this paper.

## Acknowledgments

This research work was supported by the National Natural Science Foundation of China (Grant nos. 41807265 and 41977236), the Open Research Fund Program of Engineering Research Center of Rock and Soil Drilling and Excavation and Protection of Ministry of Education (Grant no. 202004), and the PhD Funds of East China University of Technology (Grant no. DHBK2019236).

## References

- [1] N. Jiang, B. Zhu, X. He, C. Zhou, X. Luo, and T. Wu, "Safety assessment of buried pressurized gas pipelines subject to blasting vibrations induced by metro foundation pit excavation," *Tunnelling and Underground Space Technology*, vol. 102, Article ID 103448, 2020.
- [2] K. Zhao, N. Jiang, C. Zhou, H. Li, Z. Cai, and B. Zhu, "Dynamic behavior and failure of buried gas pipeline considering the pipe connection form subjected to blasting seismic waves," *Thin-Walled Structures*, vol. 170, Article ID 108495, 2022.
- [3] C. Lin, M. Huang, F. Nadim, and Z. Liu, "Tunnelling-induced response of buried pipelines and their effects on ground settlements," *Tunnelling and Underground Space Technology*, vol. 96, Article ID 103193, 2020.
- [4] Y.-Q. Xia, N. Jiang, Y.-K. Yao, and C.-B. Zhou, "Dynamic responses of a concrete pipeline with bell-and-spigot joints buried in a silty clay layer to blasting seismic waves," *Explosion and Shock Waves*, vol. 40, no. 4, Article ID 043302, 2020.
- [5] B. Zhu, N. Jiang, Y.-S. Jia, and C. Zhou, "Field experiment on blasting vibration effect of underpass gas pipelines," *Chinese Journal of Rock Mechanics and Engineering*, vol. 38, no. 12, pp. 122–132, 2020.
- [6] D. Liu, W.-B. Lu, and M. Chen, "Study on the main frequency attenuation formula of blasting vibration of tunnel drilling and blasting excavation," *Chinese Journal of Rock Mechanics and Engineering*, vol. 37, no. 9, pp. 2015–2026, 2018.
- [7] D. Kong, Y. Xu, and C. Song, "Dynamic response of composite steel lining structure under blast loading," *Shock and Vibration*, vol. 2020, no. 12, 12 pages, 2020.
- [8] B. Zhu, N. Jiang, C. Zhou, X. Luo, Y. Yao, and T. Wu, "Dynamic failure behavior of buried cast iron gas pipeline with local external corrosion subjected to blasting vibration," *Journal of Natural Gas Science and Engineering*, vol. 88, no. 2, Article ID 103803, 2021.
- [9] H. Wei, J. Chen, J. Zhu, X. Yang, H. Chu, and X. Liu, "A new zoning method of blasting vibration based on energy proportion and its SVM classification models," *Shock and Vibration*, vol. 2021, no. 4, 13 pages, Article ID 6697682, 2021.
- [10] N. E. Huang, Z. Shen, S. R. Long et al., "The empirical mode decomposition and the Hilbert spectrum for nonlinear and non-stationary time series analysis," *Proceedings of the Royal Society of London. Series A: Mathematical, Physical and Engineering Sciences*, vol. 454, no. 1971, pp. 903–995, 1998.
- [11] C.-Y. Ma, Li Wu, M. Sun, and Q. Yuan, "Time-frequency analysis and application of a vibration signal of tunnel excavation blasting based on CEEMD-MPE-HT," *Shock and Vibration*, vol. 2021, Article ID 6672942, 2021.
- [12] Y.-L. Zhang and R.-X. Li, "Identification of structural parameters based on HHT and NExT," *Frontiers Research of Architecture and Engineering*, vol. 4, no. 1, 2021.
- [13] H. Sun, Q.-R. Si, N. Chen, and S.-Q. Yuan, "HHT-based feature extraction of pump operation instability under cavitation conditions through motor current signal analysis," *Mechanical Systems and Signal Processing*, vol. 139, Article ID 106613, 2019.
- [14] A. A. Mousavi, C. Zhang, S. F. Masri, and G. Gholipour, "Structural damage localization and quantification based on a CEEMDAN hilbert transform neural network approach: a model steel truss bridge case study," *Sensors*, vol. 20, no. 5, p. 1271, 2020.
- [15] X. Li, H. Hu, L. He, and K. Li, "An analytical study of blasting vibration using deep mining and drilage rules," *Cluster Computing*, vol. 20, no. 1, pp. 109–120, 2017.
- [16] G. Hu, H.-L. Fei, S.-J. Bao, and Z.-G. Yang, "Blasting damage accumulative effect of tunnel surrounding rock structure on HHT," *Tunnelling and Underground Space Technology*, vol. 16, no. 1, pp. 249–259, 2020.
- [17] Q. Zong, H.-B. Wang, Y. Xu, and J.-G. Fu, "Coalmine roadway excavation blasting seismic wave signal analysis based on HHT method," *Journal of Vibration and Shock*, vol. 32, no. 15, pp. 6–120, 2013.
- [18] J.-C. Liu, W.-X. Gao, and J. Jiang, "Vibration signal analysis of water seal blasting based on wavelet threshold denoising and HHT transformation," *Advances in Civil Engineering*, vol. 2020, no. 1, 14 pages, Article ID 4381480, 2020.

- [19] L. Li, F. Wang, F. Shang, Y. Jia, C. Zhao, and D. Kong, "Energy spectrum analysis of blast waves based on an improved Hilbert-Huang transform," *Shock Waves*, vol. 27, no. 3, pp. 487–494, 2017.
- [20] H. Yuan, X. Liu, Y. Liu, H. Bian, W. Chen, and Y. Wang, "Analysis of acoustic wave frequency spectrum characters of rock mass under blasting damage based on the HHT method," *Advances in Civil Engineering*, vol. 2018, Article ID 9207476, 8 pages, 2018.
- [21] L. Chen, J. Chen, Y. Luo et al., "Propagation laws of blasting seismic waves in weak rock mass: a case study of muzhailing tunnel," *Advances in Civil Engineering*, vol. 2020, no. 9, 15 pages, Article ID 8818442, 2020.
- [22] Y.-P. Fei, "Prediction model and safety limit of tunnel blasting vibration under the ancient ruins," *Engineering Blasting*, vol. 26, no. 5, pp. 42–51, 2020.
- [23] Z.-G. Yang, Y.-P. Fei, and G. Hu, "HHT analysis on influence of blasting vibration during tunnel excavation on surrounding rock," *Journal of Safety Science and Technology*, vol. 15, no. 9, pp. 121–127, 2019.
- [24] Z.-S. Wu, Q. Liu, Q.-p. Hou, and Z.-T. Li, "Study on impacted parameters of blasting vibration on brick concrete structure based on HHT method," *Chinese Journal of Underground Space and Engineering*, vol. 15, pp. 449–453, 2019.
- [25] S.-H. Chen, H.-X. Wei, R.-Q. Du, and A.-K. Zhang, *Analysis of Blasting Seismic Effect of Building Structure*, China Coal Industry Publishing House, Beijing, China, 2011.
- [26] N. E. Huang and N. O. Attoh Okine, *The Hilbert-Huang Transform in Engineering*, CRC Press, Boca Raton, FL, USA, 2005.
- [27] N. E. Huang and S. S. P. Shen, *Hilbert-huang Transform and its Applications*, World Scientific Publishing Company, Singapore, 2nd edition, 2014.
- [28] H.-M. Zhao, H.-D. Liu, Y. Jin, X. Dang, and W. Deng, "Feature extraction for data-driven remaining useful life prediction of rolling bearings," *IEEE Transactions on Instrumentation and Measurement*, vol. 70, Article ID 3511910, 2021.

## Research Article

# The Vibration Characteristics of Ground of Rock Blasting in Silt-Rock Strata

Tao Yin <sup>1</sup>, Chuanbo Zhou <sup>2</sup>, Changqing Zheng <sup>3</sup>, Jugen Fu <sup>1</sup> and Ziru Guo <sup>4</sup>

<sup>1</sup>School of Civil Engineering and Architecture, Anhui University of Science and Technology, No. 168 Taifeng Street, Huainan 232001, Anhui, China

<sup>2</sup>Faculty of Engineering, China University of Geosciences, No. 388 Lumo Road, Wuhan 430074, Hubei, China

<sup>3</sup>Zhuhai Baopoxin Research & Development Co., Ltd, No. 2099 Fenghuang North Road, Zhuhai 519099, Guangdong, China

<sup>4</sup>School of Chemical Engineering, Anhui University of Science and Technology, No. 168 Taifeng Street, Huainan 232001, Anhui, China

Correspondence should be addressed to Tao Yin; [taoyin@aust.edu.cn](mailto:taoyin@aust.edu.cn)

Received 6 May 2021; Revised 6 October 2021; Accepted 6 November 2021; Published 30 November 2021

Academic Editor: Vasudevan Rajamohan

Copyright © 2021 Tao Yin et al. This is an open access article distributed under the Creative Commons Attribution License, which permits unrestricted use, distribution, and reproduction in any medium, provided the original work is properly cited.

As the shield section passes through the silt-rock strata, the rock stratum of the tunnel section has to be blasted into blocks in advance, and the diameter of the blocks should be less than 30 cm after breaking, and then, the blocks could smoothly enter the soil cabin through the opening of the tunnel boring machine (TBM) cutter head and finally be discharged through the screw machine. The geology of rock blasting in silt-rock strata is complex, and the vibrations caused by blasting threaten the safety of buildings around the blasting area. According to the measured data of blasting vibrations at the sites, the waveform duration of vibration acceleration and the distribution characteristics of dominant frequency of vibration velocity were analyzed, the energy characteristics of vibration velocity were researched by wavelet analysis, and the attenuation laws of vibration velocity were studied by dimensional analysis (DA). The dominant frequency bands of vibration energy of ground are in the range of 0–15.625 Hz, and the distribution characteristics of frequency bands of vibration energy in different directions of the ground are similar to each other, but the energy magnitude is different from each other. The research results could provide a reference for the safe blasting distance of buildings under similar geological conditions.

## 1. Introduction

With the fast economic growth in China, the demand for urban underground space engineering is growing rapidly. By 2020, there have been 33 cities with 177 subway lines in China [1]. In the construction of metro tunnel shield method, the silt-rock strata often encounter in the range of section, such as Shenzhen Metro Line 11 [2], Xiamen Metro Line 2 [3], Shenzhen Metro Line 5 [4], and Fuzhou Metro Line 1 [5], and when the shield machine passes through the silt-rock strata, the rock stratum in the lower part is not easy to break, while the silt stratum in the upper part is easy to enter into the soil cabin, especially the silt stratum, which is rich in groundwater. Once the soil pressure in the sealed soil cabin is unbalanced, it is easy to cause soil loss, large

settlement, and collapse accident. Many scientists had researched to solve this problem [1–5]. They concluded that when the rock stratum of the tunnel section was blasted into blocks in advance, and the diameter of the blocks should be less than 30 cm after breaking, then the blocks could smoothly enter the soil cabin through the opening of the TBM cutter head and finally be discharged through the screw machine.

There are many studies about blasting in rock, soil, air, and water, but few researches about rock blasting in the silt-rock strata. The removing and replacing silt layer by explosion has been investigated comprehensively in China. For example, Yang et al. [6] studied the propagation laws of blast waves in silt, which were similar to that in water and satisfied the geometrical similarity law. Li et al. [7] researched the

vibration effect of removing and replacing silt layer by explosion in deep silt and obtained that the high tide level could reduce the negative effect of blasting vibrations and the low tide level had a positive impact on the peak velocity of blasting vibrations. Xu et al. [8] applied the regression analysis by Sadowski's formula and obtained the attenuation laws of peak particle velocity (PPV) with distance in the removing and replacing silt layer by explosion. W. Wei [9] adopted many blasting tests in soft marine silt clay at the sites of Ningbo and obtained the time history of blast wave pressure, excess pore water pressure, and temperature of soft soil under different buried depths of explosive. Some foreign researchers had conducted a lot of experiments to compact soil by blasting. C. WA et al. [10] studied that the blasting vibrations could cause the liquefaction of saturated soil; however, the liquefaction caused by blasting load was different from that caused by seismic load. Mikulyak [11] modeled the blasting by computer in geological conditions of soft soil and investigated the formation characteristics of two kinds of spherical cavities by different blasting schemes.

Some scientists studied the blasting vibration waveform by wavelet analysis. D. Huang [12] analyzed the time-frequency characteristics of measured vibration signal of the mountain tunnel by the Fourier transform and the wavelet packet transform. Y. Yang [13] studied the blasting vibration signals of different elevations and explosion distances of an open-pit mine based on the wavelet packet theory. Józef Pyra [14] used various methods of time and frequency to analyze the vibration induced by blasting works carried out in open-cast mines.

Other scientists have studied the propagation law of blasting vibration by DA. M. Khandelwal [15] performed a DA technique to propose a new formula for the prediction of the PPV. Dehghani [16] evaluated and calculated the blast-induced ground vibration by artificial neural networks and DA techniques. Olarewaju [17] used the finite element method to study the dynamic dimensionless behaviors of underground pipes due to blast loads.

The analysis of vibration characteristics of ground of rock blasting in silt-rock strata by wavelet analysis and DA has been less reported at present. This study relied on the rock blasting engineering in silt-rock strata in the shield section of Zhuhai Metro, the waveform and the distribution characteristics of frequency of blasting vibrations were analyzed, the energy characteristics of blasting vibrations in different frequency bands were studied by wavelet analysis, and the attenuation laws of vibration velocity were fitted by DA. The dominant frequency bands of vibration energy of ground are in the range of 0–15.625 Hz, and the distribution characteristics of frequency bands of vibration energy in different directions of the ground are similar to each other, but the energy magnitude is different from each other. The research results could provide a reference for the safe blasting distance of buildings under similar geological conditions.

## 2. Project Overview

The shield section between Hengqinbei Railway Station and Hengqin Railway Station of Zhuhai-Zhuhai Airport Inter-city Railway is located in the Economic Development Zone

of Hengqin Island, Zhuhai City, as shown in Figure 1. It runs along the coastline of South China Sea, with a total length of 2.656 km, all of which is constructed by the shield method.

As the shield section passes through the silt-rock strata, the rock stratum of the tunnel section has to be blasted into blocks in advance, and the diameter of the blocks should be less than 30 cm after breaking, and then, the blocks could smoothly enter the soil cabin through the opening of the cutter head and finally be discharged through the screw machine. The diagram of charging on field is shown in Figure 2. The rock cores before blasting and after blasting are shown in Figure 3.

The blasting area is located in the artificial reclamation area, and there are three strata from the ground surface to the subway tunnel. (1) The first stratum is artificial fill. It is yellowish-brown, slightly wet, mainly in saturated loose state, and slightly compacted, and the artificial fill is mostly pavement concrete with a thickness of 20–35 cm, and the layer thickness is in the range of 0.30–15.10 m, and the average layer thickness is 2.82 m. (2) The second stratum is silt. It is from gray to dark gray, saturated, and in flow plastic state, with uniform and fine soil, locally enriching with shell debris and sand. The layer thickness is in the range of 0.50–30.30 m. (3) The third stratum is rock. It is weakly weathered granite. It is brown-yellow, gray-brown, gray-white, and other colors, medium-coarse grain structure, and massive structure. The joint fissures are developed relatively. The rock quality is hard. The buried depth of the layer fluctuates greatly, and the distribution is discontinuous. The physical and mechanical parameters of artificial fill, silt, and rock are listed in Tables 1 and 2, respectively.

The length of the blasting area is 960 cm, and the width of the blasting area is 160 cm. The casing drilling method is used for drilling blastholes, and the PVC casing with a diameter of 7.5 cm is installed immediately after the blasthole is formed for protecting the blasthole wall. The spacing and row spacing of blastholes are both 80 cm, the diameter of blastholes is 14.6 cm, and the depth of blastholes is 3400 cm. Three rows of blastholes are detonated each time, 13 blastholes are arranged in a row, and the millisecond blasting network in the blasthole is adopted. The millisecond sections of three rows of blastholes are 6, 7, and 8 in turn, and the delay time is 50 ms. The layouts of blastholes are shown in Figure 4.

After drilling the blastholes, the blastholes are filled with underground water immediately, and the blastholes are water coupling charge. The diameter of the explosive roll is 6 cm, and the density of the explosive is 1.061 kg/m<sup>3</sup>. The continuous charge is adopted, the charge length is the depth of the rock at the tunnel section, and the thickness of the rock to be blasted is in the range of 1–8 m. The blastholes are stemmed with gravels of 1–1.5 cm diameter, and the stemming length is 1000 cm.

## 3. Test Points of Blasting Vibrations

The TC-4850 self-recording instrument (developed and manufactured by Zhongke (Chengdu) Instruments Company Limited) was used as the blasting vibrations measuring





FIGURE 1: Zhuhai-Zhuhai Airport Intercity Railway.



FIGURE 2: Diagram of charging on field.

instrument during the blasting, each instrument had three channels, and it could be collected in parallel. The arrangement of blasting vibration meters is shown in Figure 5.

Three acceleration measuring points and six velocity measuring points were arranged in total. The measuring points were arranged along the ray with the explosion source



FIGURE 3: Rock cores (a) before blasting and (b) after blasting.

TABLE 1: Physical and mechanical parameters of artificial fill.

Density $\rho$ ( $\text{g}/\text{cm}^3$ )	Poisson's ratio $u$	Cohesion (KPa)	Shear modulus (MPa)	Angle of internal friction (rad)
1.98	0.35	100	150	0.31

TABLE 2: Physical and mechanical parameters of rock and silt.

	Density $\rho$ ( $\text{g}/\text{cm}^3$ )	Elastic modulus $E$ (GPa)	Poisson's ratio $u$	P wave velocity (m/s)	Yield strength (MPa)	Tangent modulus (GPa)	Hardening parameter	Strain rate parameter $C$
Rock	2.5	0.74	0.25	5357	3.0e-5	0.042	1.0	0.06
Silt	1.63	3.3e-5	0.45	1250	4.0e-9	0.0	—	—

as the center. The schematic diagram of explosion source and measuring points is shown in Figure 6.

#### 4. Analysis of the Characteristics of Blasting Vibrations of Ground

*4.1. Analysis of the Characteristics of Vibration Acceleration.* The first blasting was carried out at 10:00 a.m. on March 31, 2016, and the second blasting was carried out at 3:00 p.m. on March 31, 2016, with an interval of 10 days, and the third blasting was carried out at 10:00 a.m. on April 10, 2016. The vibration acceleration test points were all 10 meters away from the explosion source, and the results of three tests of blasting are shown in Table 3.

The waveform duration of vibration accelerations of three blasting is shown in Figure 7.

As shown in the acceleration waveform of blasting vibrations from Figure 7, the peak particle acceleration of the three blasting vibrations has little difference to each other; the duration of acceleration waveform is about 0.4 s at 10:00 a.m. on March 31, 2016, in the first blasting, and about 0.8 s at 3:00 p.m. on March 31, 2016, in the second blasting, which is 0.4 s longer than the duration of the first blasting, with an interval of 10 days, and in the third blasting at 10:00 a.m. on April 10, 2016, the duration of acceleration waveform is about 0.5 s, which is close to the duration of the first blasting.

The above data show that the silt has a good structural strength during the first blasting, but after the disturbance of the blasting load, the silt has been thixotropic liquefied [18]. During the second blasting with a short time interval, the explosive gas generates a cavity in the silt after the explosion. When the pressure of the explosive gas is less than the

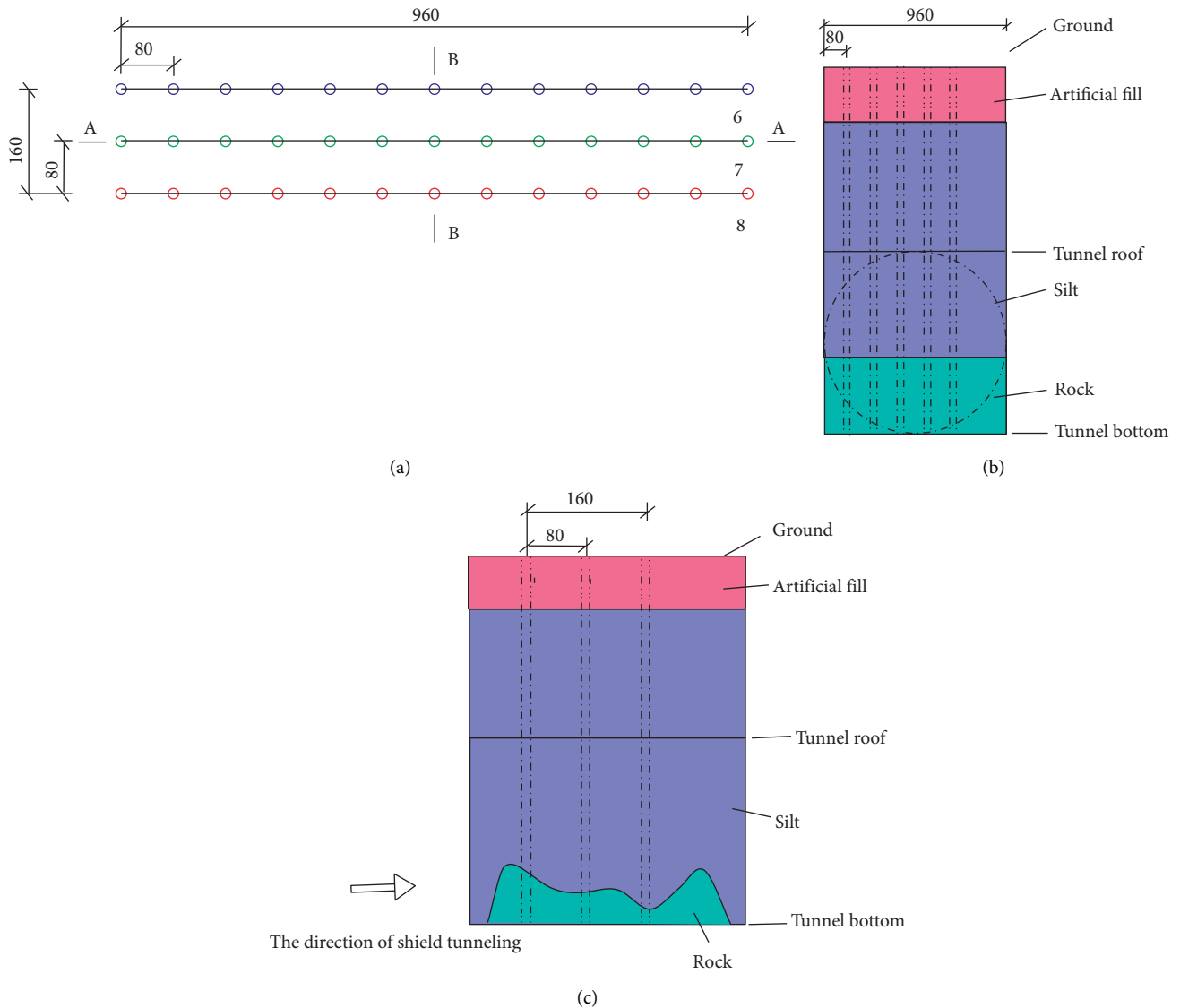


FIGURE 4: Sketch map of blastholes (cm). (a) Planar graph, (b) cross section of A-A, and (c) cross section of B-B.



FIGURE 5: Arrangement of blasting vibration meters.

pressure of the silt outside the cavity, the silt around the cavity begins to compress into the cavity, and then, the cavity comes into being. The cavity is overcompressed, and then, the cavity expands again to work on the silt. In the process of

pulsation, the water and stemming materials in the blast hole are continuously pushed out of the blast hole until they reach the orifice and escape when they come into contact with the atmosphere, which results in the extension of the waveform duration of acceleration in the second blasting. During the third blasting, the duration of acceleration waveform is close to that of the first blasting, which indicates that after a period of sedimentation, the silt has recovered a certain structural strength.

4.2. Analysis of the Distribution Characteristics of the Dominant Frequency of Blasting Vibration Velocity. Based on the analysis of the dominant frequency of vibration velocity of the three blasting tests in Table 3, it is concluded that the dominant frequency of vibration velocity of the first blasting is between 30 and 60 Hz, which indicates that the silt has good structural strength; during the second blasting, the silt undergoes thixotropic liquefaction after the disturbance

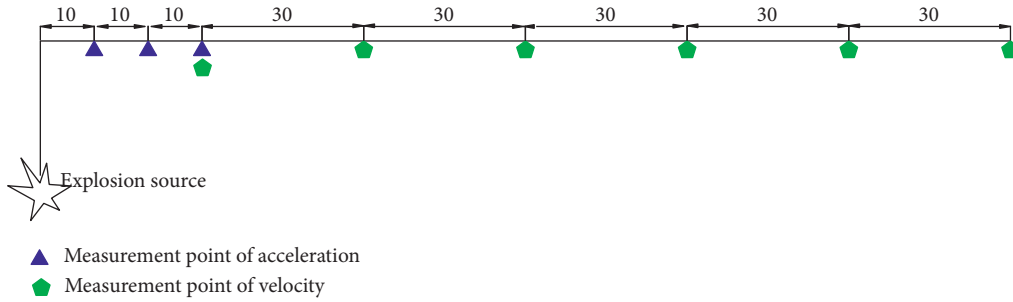


FIGURE 6: Schematic diagram of explosion source and measuring points *m*.

TABLE 3: Results of three tests of blasting.

	The total explosives (kg)	The maximum charge of one section (kg)	Sections	The dominant frequency (Hz)	
				X	Y
The first blasting	43.2	34.8	5,6,7	X	47.06
				Y	55.56
				Z	36.04
The second blasting	432.0	150.0	5,6,7	X	10.34
				Y	8.32
				Z	14.60
The third blasting	331.2	115.2	5,7,8	X	36.70
				Y	37.38
				Z	66.67

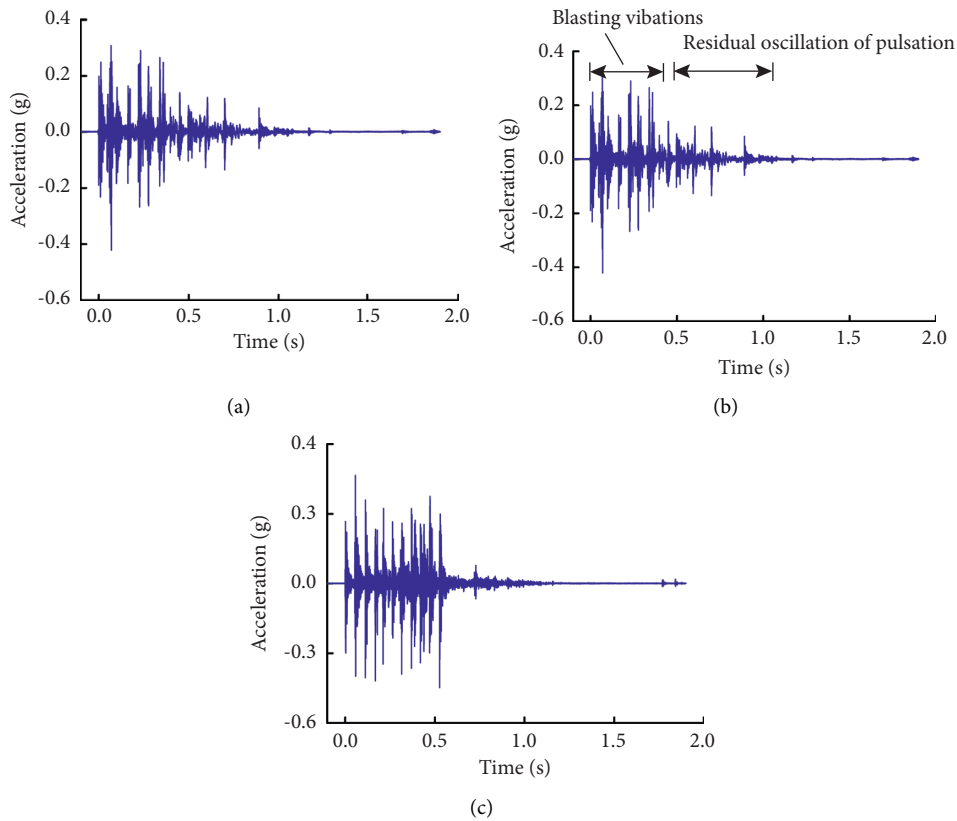


FIGURE 7: Acceleration waveform of blasting vibrations, (a) acceleration waveform of the first blasting, (b) acceleration waveform of the second blasting, and (c) acceleration waveform of the third blasting.



of the first blasting load. The dominant vibration frequency of dynamic velocity is reduced to 5–15 Hz, which is close to the natural vibration frequency of the building, and it is easy to cause the building resonance. At 10:00 am on April 10, 2016, the dominant frequency of the blasting vibration velocity is between 30 and 70 Hz during the third blasting, and the analysis shows that the structural strength of the silt has been restored due to 10 days from the last blasting. Therefore, the continuous blasting operation should be avoided in the field blasting. Each blasting operation should be separated for a period of time, and the next blasting will be beneficial to reduce the vibration damage until the silt recovers structural strength.

**4.3. Energy Percentage of Each Frequency Bands of Blasting Vibrations.** Taking a typical test data of blasting vibrations as an example, the field monitoring data of blasting vibrations are shown in Table 4, and the time history curves of velocity of measured blasting vibration signals are shown in Figure 8.

**4.3.1. Reconstruction Error.** The signals of blasting vibrations belonged to random signals. At present, the db8 wavelet basis function was widely used to analyze the nonstationary vibration signal [19–21]. The error of wavelet reconstruction signal based on db8 is shown in Figure 9.

It could be seen from Figure 9 that using db8 wavelet basis function to decompose the vibration signals in 8 layers, the relative error magnitude between the reconstructed signal and the original signal was  $10^{-11}$ , which met the analysis requirements.

**4.3.2. Decomposition and Reconstruction.** Using db8 wavelet basis function to decompose the signal of blasting vibrations with the scale of 8, the wavelet coefficients of 9 frequency bands were obtained [22]. During blasting vibration monitoring, the sampling frequency of the signal was set to 8000 Hz (2 s sampling 16000 points). According to the Shannon sampling theorem [21], the Nyquist frequency of sampling was 4000 Hz. According to the principle of wavelet decomposition [23], the bandwidth of nine wavelets was a8: 0–15.625 Hz, d8: 15.625–31.25 Hz, d7: 31.25–62.5 Hz, d6: 62.5–125 Hz, d5: 125–250 Hz, d4: 250–500 Hz, d3: 500–1000 Hz, d2: 1000–2000 Hz, and d1: 2000–4000 Hz. The blasting vibration components of different wavelet frequency bands are shown in Figure 10.

**4.3.3. Percentage of Energy per Frequency Band.** The statistics of energy percentage of each wavelet band of blasting vibration signals in different directions are shown in Table 5.

During blasting rock in silt-rock strata, the frequency bands of ground vibration energy are wide, but the frequency bands are mainly concentrated in 0–15.625 Hz, 31.25–62.5 Hz, and 62.5–125 Hz, which are accounting for more than 90% of the total signal energy. The dominant frequency bands of blasting vibration energy are in 0–15.625 Hz, which are close to the natural frequency of

buildings and have a great impact on the vibration damage of surface buildings.

The high-frequency signals above 125 Hz continue the whole monitoring period, which are represented by noise signal, with relatively small energy, and limited impact on surface buildings.

**4.4. The Energy of Each Frequency Bands of Blasting Vibrations.** Taking the test data of the first blasting vibrations on the morning of March 31, 2016, as an example, the distance between the test point and the explosion source was 60 m, and the energy distributions of each wavelet band in different directions are shown in Figure 11.

It can be seen from Figure 11 that the distribution characteristics of the frequency bands of blasting vibration energy in different directions of the ground are similar to each other, but the energy magnitudes are different from each other.

The wavelet energy analysis was carried out on the six test data of blasting vibrations of rock blasting in silt-rock strata, and the directions of the maximum energy are shown in Table 6.

According to Table 6, when the distance of the test points from the explosion source is in the range of 30–60 m, the number of times of maximum energy in Z direction is 8, and the number of times of maximum energy in X direction is 4.

According to the analysis, because of the end effect of the cylindrical charge, there is air above the ground, without clamping effect, and there are more times of maximum energy in the Z direction; when the amount of cylindrical charge is less, the end effect is not obvious, and the explosion stress waves propagate outward in the form of cylinder, 13 blastholes in a row produce a cylinder wave, and the cylinder wave would overlap at the measuring point, so there are 4 times in the X direction.

When the distance of the test point from the explosion source is in the range of 90–180 m, the number of times of maximum energy is 15 in the Z direction, 4 in the X direction, and 3 in the Y direction. It is considered that the maximum number of times of energy in the X direction and Y direction is the most due to the influence of pinch effect on explosion stress wave in the Z direction.

The times of the maximum energy in the Z direction are the most, followed by the X direction when the distance of the test point from the explosion source is in the range of 30–60 m. Because the vibration energy in the Z direction is the largest and easy to cause up and down vibration damage to the building, the blasting vibration energy in the Z direction should be focused on analysis, followed by the X direction.

The vibration energy in the Z direction is mainly analyzed when the distance of the test point from the explosion source is in the range of 90–180 m.

**4.5. Attenuation Laws of Vibration Velocity of Rock Blasting in Silt-Rock Strata.** To study the attenuation laws of vibration velocity of rock blasting in the silt-rock strata, four vibration velocity tests were carried out in the blasting area. Six

TABLE 4: Field monitoring data of blasting vibrations.

The total explosives (kg)	The maximum charge of one section (kg)	Sections	The distance from explosion source (m)	PPV (cm/s)		
				X	Y	Z
432	150	5,6,7	130	0.15	0.13	0.10

Note. X was the horizontal direction pointing to the explosion source, Y was the horizontal direction perpendicular to X, and Z was the vertical direction.

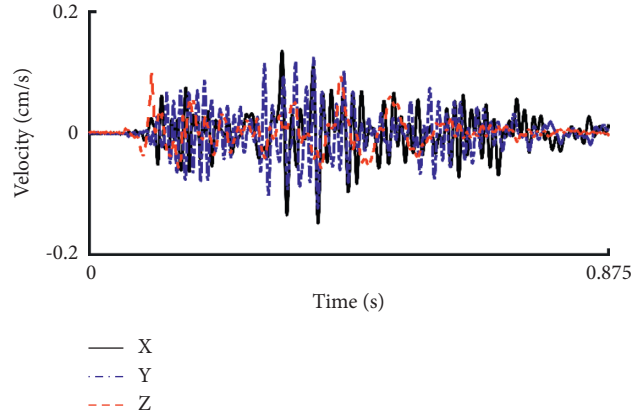


FIGURE 8: Time history curves of velocity of measured blasting vibrations.

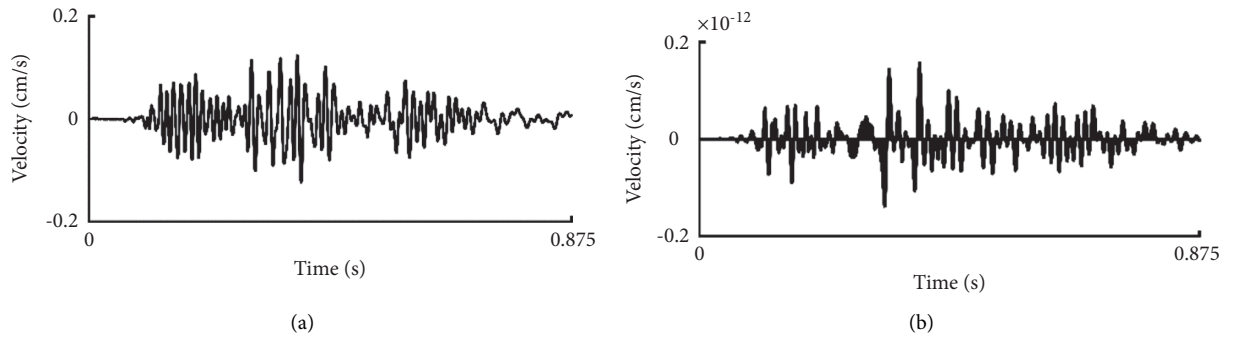


FIGURE 9: Wavelet reconstruction and error based on db8. (a) Original blasting vibration signals and (b) error of reconstructed signals.

measuring points of vibration velocity were arranged for each test. The test results of blasting vibration velocity are shown in Table 7.

**4.5.1. Prediction Model of Blasting Vibration Velocity Based on DA.** Natural phenomena and engineering problems could be described by a series of physical quantities. To find the laws between these physical quantities, firstly, we could list the physical quantities that involved in these problems, ignore some physical quantities with less influence, and then classify the physical quantities involved according to their attributes; secondly, we could find out the interrelations between different physical quantities; and finally, we could find out the causal relationship between some physical quantities and the other physical quantities.

There were relations among all kinds of physical quantities, which showed that their structure must be composed of several unified basic components. This basic

component of physical quantity was called dimension. Because physics studied the evolution and movement of matter in space and time, all quantitative problems could not be separated from the three basic quantities of mass ( $M$ ), time ( $T$ ), and length ( $L$ ). Therefore,  $M$ ,  $T$ , and  $L$  were the most suitable dimensions for these three basic quantities. The dimensions of all other derived quantities could be expressed as the combination of these three basic quantities according to the definition or objective laws.

The attenuation of seismic wave was affected by the factors of explosion source, geological conditions, distance of explosion source, and depth of explosion source when the blasting seismic wave propagated in silt-rock strata [24, 25]. There were 9 physical quantities involved in propagation velocity in silt-rock strata [26, 27], as shown in Table 8.

Based on the DA of Buckingham's theorem ( $\pi$  theorem), the PPV  $v$  of the ground during the rock blasting in the silt-rock strata could be expressed as follows:

$$v = \Phi(S, \rho, H, a, f, t, Q, r, c). \quad (1)$$



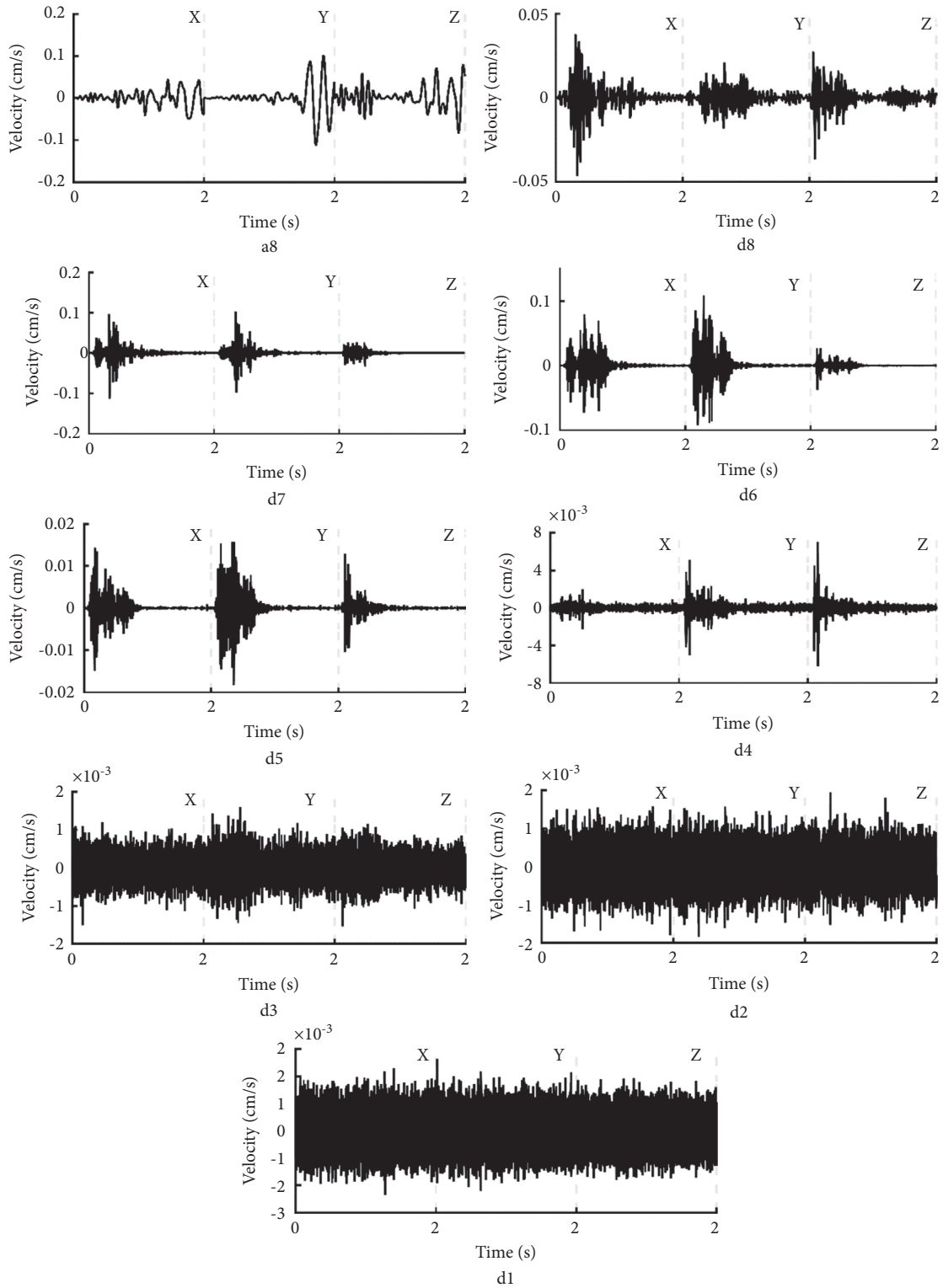


FIGURE 10: Stratified reconstruction of signals by wavelet decomposition.

TABLE 5: Energy percentage of each frequency band in different directions (%).

Frequency bands	a8	d8	d7	d6	d5	d4	d3	d2	d1
X	43.80	9.69	24.94	21.12	0.38	0.01	0.01	0.02	0.04
Y	67.02	1.81	11.25	19.41	0.46	0.01	0.01	0.01	0.02
Z	88.91	4.93	4.13	1.80	0.15	0.03	0.01	0.02	0.03

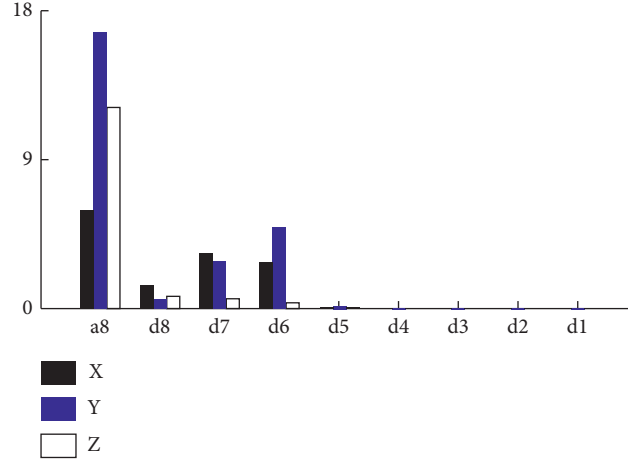
FIGURE 11: Energy of each frequency bands in different directions (cm/s)<sup>2</sup>.

TABLE 6: Directions of the maximum energy.

The distance from explosion source (m)	The first blasting	The second blasting	The third blasting	The forth blasting	The fifth blasting	The sixth blasting
30	X	Z	Z	Z	X	Z
60	Z	X	Z	Z	X	Z
90	Z	Z	Z	Z	X	Z
120	Y	Y	X	X	Z	Z
150	The instrument was not triggered	Z	Z	Z	Y	Z
180	Z	Z	X	The instrument was not triggered	Z	Z

Note. X was the horizontal direction pointing to the explosion source, Y was the horizontal direction perpendicular to X, and Z was the vertical direction.

According to the  $\pi$  theorem, where independent dimensions were  $Q$ ,  $r$ , and  $c$ , and  $\pi$  represents dimensionless quantities, then,

$$\left\{ \begin{array}{l} \pi = \frac{v}{Q^\alpha r^\beta c^\gamma}, \pi_1 = \frac{S}{Q^{\alpha_1} r^{\beta_1} c^{\gamma_1}}, \pi_2 = \frac{\rho}{Q^{\alpha_2} r^{\beta_2} c^{\gamma_2}}, \\ \pi_3 = \frac{H}{Q^{\alpha_3} r^{\beta_3} c^{\gamma_3}}, \pi_4 = \frac{a}{Q^{\alpha_4} r^{\beta_4} c^{\gamma_4}}, \\ \pi_5 = \frac{f}{Q^{\alpha_5} r^{\beta_5} c^{\gamma_5}}, \pi_6 = \frac{t}{Q^{\alpha_6} r^{\beta_6} c^{\gamma_6}}. \end{array} \right. \quad (2)$$

where  $\alpha$ ,  $\beta$ , and  $\gamma$  were undetermined coefficients. According to the dimensional homogeneous theorem, there were as follows:

$$\left\{ \begin{array}{l} \pi = \frac{v}{c}, \pi_1 = \frac{S}{r}, \pi_2 = \frac{\rho}{Qr^{-3}}, \\ \pi_3 = \frac{H}{r}, \pi_4 = \frac{a}{r^{-1}c}, \\ \pi_5 = \frac{f}{r^{-1}c}, \pi_6 = \frac{t}{rc^{-1}}. \end{array} \right. \quad (3)$$

Substituting (3) into (1) could obtain the following:

$$\frac{v}{c} = \Phi \left( \frac{S}{r}, \frac{\rho}{Qr^{-3}}, \frac{H}{r}, \frac{a}{r^{-1}c^2}, \frac{f}{r^{-1}c}, \frac{t}{rc^{-1}} \right). \quad (4)$$

Since the product and power of different dimensionless numbers  $\pi$  were still dimensionless,  $\pi_2$  and  $\pi_3$  are combined as follows to get a new dimensionless number  $\pi_7$ :

TABLE 7: Testing results of blasting vibration velocity.

Test times	The maximum charge of one section Q (kg)	No. of measuring point	Vibration velocity			Resultant	
			The distance from explosion source (m)	The X direction	The Y direction		The Z direction
No. 1	34.8	ZC1	30	1.67	1.32	1.93	1.94
		ZC2	60	0.37	0.39	0.49	0.54
		ZC3	90	0.18	0.17	0.33	0.34
		ZC4	130	0.15	0.13	0.1	0.2
		ZC5	170	0.04	0.06	0.09	0.1
No. 2	150	ZC1	30	4.68	3.2	8.1	8.58
		ZC2	60	6.97	3.87	4.22	7.6
		ZC3	90	0.46	0.47	0.97	1.01
		ZC4	120	1.11	1.14	0.81	1.36
		ZC5	150	0.34	0.39	0.62	0.63
No. 3	165.6	ZC6	180	0.34	0.14	0.48	0.49
		ZC1	30	4.95	3.1	15.3	15.36
		ZC2	60	2.37	1.75	8.05	8.25
		ZC3	90	1.22	0.84	2.09	2.09
		ZC4	120	0.73	0.36	0.83	0.87
No. 4	54	ZC5	150	0.01	0.017	0.0057	0.017
		ZC1	30	2.13	0.68	0.63	0.63
		ZC2	60	0.57	0.68	0.38	1.41
		ZC3	90	1.6	0.82	0.5	1.61
		ZC4	120	0.37	0.26	2.1	2.12
		ZC5	150	0.22	0.18	1.02	1.03
		ZC6	180	0.18	0.12	0.63	0.63

TABLE 8: Physical quantities involved in blasting vibration velocity in silt-rock strata.

	Variables	Dimensions
The dependent variables	Particle vibration displacement S	L
	PPV $v$	LT <sup>-1</sup>
	Peak particle acceleration $\alpha$	LT <sup>-2</sup>
	Frequency of particle vibration $f$	T <sup>-1</sup>
The independent variables	Quality of explosives Q	M
	Horizontal distance between the test point and the explosion source $r$	L
	Depth of explosion source $H$	L
	Density of rock $\rho$	ML <sup>-3</sup>
	Propagation velocity of vibration wave $c$	LT <sup>-1</sup>
	Detonation time $t$	T

Note. L, T, and M were dimensions of length, time, and mass, respectively.

$$\pi_7 = (\pi_2^{1/3})^{\beta_1} \pi_3^{\beta_2} = \left( \frac{\sqrt[3]{\rho r}}{\sqrt[3]{Q}} \right)^{\beta_1} \left( \frac{H}{r} \right)^{\beta_2}, \quad (5)$$

where  $\beta_1$  and  $\beta_2$  were the indexes of  $\pi_2$  and  $\pi_3$ , respectively.

At the same site,  $\rho$  and  $c$  could be approximately constant. Therefore, from (5), it could be considered that  $v$  and  $(\sqrt[3]{Q}/r)^{\beta_1} (H/r)^{\beta_2}$  had a functional relationship.

To sum up, this functional relationship could be expressed as follows:

$$\ln v = \left[ \alpha_1 + \beta_1 \ln \left( \frac{\sqrt[3]{Q}}{r} \right) \right] + \left[ \alpha_2 + \beta_2 \ln \left( \frac{H}{r} \right) \right]. \quad (6)$$

If  $\ln v_0 = \alpha_1 + \beta_1 \ln(\sqrt[3]{Q}/R)$ , there were as follows:

$$\ln v_0 = \alpha_1 + \frac{(\beta_1 \ln Q)}{3} - \beta_1 \ln r. \quad (7)$$

In equation (6),  $\alpha_1$  and  $\alpha_2$  were the coefficients given in the process of function transformation;  $-\beta_1 \ln r$  was the attenuation of blasting vibration velocity with distance  $r$ ;  $\beta_1$  was the attenuation index, which mainly reflected the effect of site medium conditions; and  $\alpha_1 + (\beta_1 \ln Q)/3$  comprehensively reflected the contribution of site medium conditions and explosive quantity to the PPV of ground.

If  $\ln k_1 = \ln \alpha_1$ , there were as follows:

$$v_0 = k_1 \left( \frac{\sqrt[3]{Q}}{r} \right)^{\beta_1}. \quad (8)$$

Equation (8) was Sadovskii's equation. without the effect of the depth of explosion source. Substituting (8) into (6), we could get the following:

TABLE 9: Prediction model of attenuation laws of blasting vibration velocity.

Direction	Equation (8)	Correlation coefficient	Equation (11)	Correlation coefficient
X	$v = 152.93 (\sqrt[3]{Q}/r)^{1.89}$	0.60	$v = 237.46 (\sqrt[3]{Q}/r)^{2.13} (H/r)^{-0.28}$	0.62
Y	$v = 63.43 (\sqrt[3]{Q}/r)^{1.67}$	0.63	$v = 92.76 (\sqrt[3]{Q}/r)^{1.88} (H/r)^{-0.24}$	0.65
Z	$v = 107.77 (\sqrt[3]{Q}/r)^{1.66}$	0.38	$v = 340.36 (\sqrt[3]{Q}/r)^{2.30} (H/r)^{-0.73}$	0.42
Resultant	$v = 114.43 (\sqrt[3]{Q}/r)^{1.59}$	0.43	$v = 333.62 (\sqrt[3]{Q}/r)^{2.19} (H/r)^{-0.68}$	0.47

$$\ln v = \ln v_0 + \left[ \alpha_2 + \beta_2 \ln \left( \frac{H}{r} \right) \right]. \quad (9)$$

If  $\ln k_1 = \ln \alpha_1$ , then (9) could be changed into the following:

$$v = k_1 k_2 \left( \frac{\sqrt[3]{Q}}{r} \right)^{\beta_1} \left( \frac{H}{r} \right)^{\beta_2}. \quad (10)$$

If  $k = k_1 k_2$ , the mathematical model of the attenuation laws of blasting vibration velocity in silt-rock strata considering the effect of burial depth was established as follows:

$$v = k \left( \frac{\sqrt[3]{Q}}{r} \right)^{\beta_1} \left( \frac{H}{r} \right)^{\beta_2}, \quad (11)$$

where  $k$  was the site effect coefficient,  $\beta_1$  was the attenuation coefficient of blasting vibrations, and  $\beta_2$  was the effect coefficient of explosion source depth.

**4.5.2. Comparative Analysis of Prediction Results of Blasting Vibration Velocity.** The explosion source was below the ground surface during blasting rock in silt-rock strata, while measuring points of blasting vibration velocity were often located on the ground surface, which was also the key content of the analysis of attenuation laws of blasting vibrations. Therefore, this study selected the ground data for analysis and established the prediction model of vibration velocity of rock blasting in silt-rock strata. According to Z. C. Zhang's research [28], the attenuation laws of vibration velocity near blasting zone were different from the attenuation laws of vibration velocity far blasting zone.  $\bar{R} = r/Q^{1/3}$  was the scaled distance,  $r$  was the horizontal distance between the test point and the explosion source, and  $Q$  was the quality of explosives. The  $\bar{R} < 5.0$  was in the near blasting zone. The  $\bar{R}$  of monitoring data in this paper is greater than 5.0, and the monitoring data were not within the range of near blast area. The monitoring data could be used to analyze the attenuation law. Equation (11) in Section 4.5.1 is used for regression fitting analysis of the blasting vibration data listed in Table 7 to obtain the prediction model of vibration velocity of rock blasting in the silt-rock strata.

In regression analysis, the correlation coefficient was an indicator to measure the linear correlation between variables. The larger the correlation coefficient was, the smaller the error was, the higher the linear correlation between variables was, the higher the reliability of the prediction model was, and vice versa. To determine the accuracy of the established mathematical model, the established mathematical model (11) was compared with the traditional Sadowski's formula (8) and the prediction accuracy of the

two eqns. for blasting vibration velocity was evaluated according to the correlation coefficient of the fitting curve. The analysis results are shown in Table 9.

It can be concluded from Table 9:

- (1) According to the obtained prediction model of vibration velocity considering the explosion depth, using the control variable method, it can be found that with the increase in horizontal distance, the PPV decreases; with the increase in explosive quantity, the PPV increases; and with the increase in explosion depth, the PPV decreases; this is consistent with the results of the paper analysis and common sense. It is shown that the prediction model of vibration velocity of rock blasting in silt-rock strata established is effective in predicting PPV of ground.
- (2) The correlation coefficient obtained by fitting 4.5 section blasting vibration velocity data by using the vibration velocity prediction model (equation (11)) considering explosion depth is greater than that of traditional Sadowski's formula (equation (8)), which indicates that the attenuation laws of ground blasting vibrations in silt-rock strata are more complex, and the mathematical prediction model established in this study can better reflect the effect of rock blasting vibrations on the ground in silt-rock strata.

## 5. Conclusions

Based on the analysis of vibration characteristics of rock blasting in silt-rock strata, the following conclusions are drawn:

- (1) In the first blasting, the silt has good structural strength, and in the second blasting with an interval of 5 hours, the silt is subject to thixotropic liquefaction after the disturbance of blasting load. When the third blasting is carried out with an interval of 10 days, the waveform duration of acceleration is close to that of the first blasting waveform, and the dominant frequency of blasting vibration velocity is close to that of the first blasting too. It is considered that after a period of sedimentation, the silt recovered to a certain structural strength, and the residual oscillation of pulsation is weakened.
- (2) The distribution of frequency bands of vibration energy is wide, but they are mainly concentrated in the range of 0–15.625 Hz, 31.25–62.5 Hz, and 62.5–125 Hz, and they are accounting for more than 90% of the total energy of signals during blasting

rock. The dominant frequency bands of blasting vibration energy are in the range of 0–15.625 Hz.

- (3) The distribution characteristics of frequency bands of blasting vibration energy in different directions are similar to each other during blasting rock, but the energy magnitudes are different from each other. The times of maximum energy in  $Z$  direction are the most, followed by  $X$  direction when the distance from the explosion source is in the range of 30–60 m. The blasting vibration energy in  $Z$  direction should be selectively analyzed, followed by  $X$  direction. The blasting vibration energy in  $Z$  direction should be mainly analyzed when the distance from the explosion source is in the range of 90–180 m.
- (4) The correlation coefficients of the prediction model based on the DA are greater than that of the traditional Sadovskii's formula through fitting the measured blasting vibration data.

## Data Availability

The processed data required to reproduce these findings cannot be shared at this time as the data also form part of an ongoing study.

## Conflicts of Interest

The authors declare that they have no conflicts of interest.

## Acknowledgments

This study was sponsored by the National Natural Science Foundation of China (Grant no. 41972286), the Fund for Talent Introduction, Anhui University of Science and Technology (no. 13190208), and the Program for Innovation Training (no. S202110361067).

## References

- [1] Z.-L. Chen, J.-Y. Chen, H. Liu, and Z.-F. Zhang, "Present status and development trends of underground space in Chinese cities: evaluation and analysis," *Tunnelling and Underground Space Technology*, vol. 71, pp. 253–270, 2018.
- [2] L. Chong, "Study on construction technology of deep hole blasting pretreatment for shield passing through upper soft and lower hard strata," *Technology and Market*, vol. 8, no. 8, pp. 32–35, 2015.
- [3] Z. Q. Wu, "Key construction technology of boulder and bedrock bulge treatment in cross sea shield tunnel," *Jiangxi Building Materials*, vol. 3, no. 5, pp. 181–183, 2016.
- [4] X. L. Pan and Q. H. Ren, "Application of deep hole blasting technology without free face in subway construction," *Construction and Architecture*, vol. 8, pp. 70–71, 2011.
- [5] L. J. Zheng, "Shield tunneling technology in boulder stratum," *Railway Construction Technology*, vol. 7, pp. 11–13, 2014.
- [6] Z. S. Yang, W. F. Xing, and J. S. Ren, "The propagation law of shock wave in silt under explosion," in *Proceedings of the 4th National Engineering Blasting Academic Conference*, Metallurgical industry press, Beijing, China, 1989.
- [7] X. Li, J. Ma, H. Y. Li, L. Fan, and Z. J. Wen, "Analysis of vibration effects to deep and thick silt by blasting compaction," *Hydro-Science and Engineering*, vol. 2, pp. 71–77, 2016.
- [8] X. Y. Xu, R. Wang, Q. S. Meng, and J. Hao, "Monitoring and controlling technology for vibration effect due to deep and thick silt by blasting compaction," *Rock and Soil Mechanics*, vol. 29, pp. 3256–3259, 2016.
- [9] W. Wei, *The Transmission Characteristics of Blast Shock Wave in Soft Soil*, Ningbo University, Ningbo, China, 2015.
- [10] C. Wa and J. Martin, "Blast induced liquefaction potential influence of unsaturated conditions," *Blast Induced Liquefaction Potential Influence of Unsaturated Conditions*, pp. 1–32, 1979.
- [11] S. V. Mikulyak, "Calculation of the formation processes of underground cavities by blasting method," *Journal of Mining Science*, vol. 36, no. 2, pp. 133–140, 2000.
- [12] D. Huang, S. Cui, and X. Li, "Wavelet packet analysis of blasting vibration signal of mountain tunnel," *Soil Dynamics and Earthquake Engineering*, vol. 117, pp. 72–80, 2019.
- [13] Y. Yang, W. Sun, and S. F. Li, "Research to blasting vibration distribution of an open pit mine based on wavelet packet theory," *Applied Mechanics and Materials*, vol. 130–134, pp. 1547–1555, 2011.
- [14] J. Pyra and A. Sołtys, "Method for studying the structure of blast-induced vibrations in open-cast mines," *Journal of Vibroengineering*, vol. 18, no. 6, pp. 3829–3840, 2016.
- [15] M. Khandelwal and M. Saadat, "A dimensional analysis approach to study blast-induced ground vibration," *Rock Mechanics and Rock Engineering*, vol. 48, no. 2, pp. 727–735, 2014.
- [16] H. Dehghani and M. Ataee-Pour, "Development of a model to predict peak particle velocity in a blasting operation," *International Journal of Rock Mechanics and Mining Sciences*, vol. 48, no. 1, pp. 51–58, 2011.
- [17] A. J. Olarewaju, *A Study on the Dynamic Dimensionless Behaviors of Underground Pipes Due to Blast Loads Using Finite Element Method*, Earthquake engineering, London, United Kingdom, 2015.
- [18] N. H. Yang, *Blasting Vibration Theory and Control Technology*, China Railway Publishing House, China, 2014.
- [19] C. Wu, C. B. Zhou, N. Jiang et al., "Wavelet energy analysis of blasting vibration of mining slope in open pit to underground transition," *Blasting*, vol. 32, pp. 104–108, 2015.
- [20] J. W. Yan, Y. Long, X. Fang, and Z. C. Hua, "Analysis on features of energy distribution for blasting seismic wave based on wavelet transform," *Explosion and Shock Waves*, vol. 27, no. 5, pp. 405–410, 2007.
- [21] X. Tian, Z. Song, and J. Wang, "Study on the propagation law of tunnel blasting vibration in stratum and blasting vibration reduction technology," *Soil Dynamics and Earthquake Engineering*, vol. 126, p. 105813, 2019.
- [22] C. H. Hu, *System Analysis and Design Based on MATLAB: Wavelet Analysis*, Xidian University Press, Warsaw, China, 1999.
- [23] Y. P. Zou and X. Li, *Signal Conversion and Processing*, Huazhong University of Technology Press, Wuhan, city, 1993.
- [24] S. W. Lu, *Propagation Characteristics of Blasting Vibration in Slopes Subjected to Open-Pit to Underground Mining and Safety Criterion*, China University of Geosciences, China, 2017.
- [25] N. Jiang, C. Zhou, S. Lu, and Z. Zhang, "Propagation and prediction of blasting vibration on slope in an open pit during underground mining," *Tunnelling and Underground Space Technology*, vol. 70, pp. 409–421, 2017.

- [26] H. Tang, *Experimental and Theoretical Study on Effect of Topography on Propagation of Blasting Waves*, Graduate School of the Chinese Academy of Sciences(Wuhan Institute of Rock and Soil Mechanics), Wuhan, China, 2007.
- [27] N. Jiang, B. Zhu, X. He, C. Zhou, X. Luo, and T. Wu, "Safety assessment of buried pressurized gas pipelines subject to blasting vibrations induced by metro foundation pit excavation," *Tunnelling and Underground Space Technology*, vol. 102, Article ID 103448, 2020.
- [28] Z. C. Zhang, C. M. Lin, Z. B. Huang, and B. Y. Ge, "Prediction of blasting vibration of area near tunnel blasting source," *Explosion and Shock Waves*, vol. 34, no. 3, pp. 367–372, 2014.



## Research Article

# Influence of In-Situ Stress on the Energy Transmission of Blasting Stress Wave in Jointed Rock Mass

Qian Dong <sup>1,2</sup>, XinPing Li <sup>3</sup>, and TingTing Liu <sup>3</sup>

<sup>1</sup>Hubei Key Laboratory of Blasting Engineering, Jiangnan University, Wuhan, Hubei 430056, China

<sup>2</sup>Hubei (Wuhan) Institute of Explosion Science and Blasting Technology, Jiangnan University, Wuhan, Hubei 430056, China

<sup>3</sup>Hubei Key Laboratory of Road-Bridge and Structure Engineering, Wuhan University of Technology, Wuhan, Hubei 430070, China

Correspondence should be addressed to Qian Dong; [dongqian@jhun.edu.cn](mailto:dongqian@jhun.edu.cn)

Received 1 June 2021; Accepted 15 September 2021; Published 12 October 2021

Academic Editor: Bangbiao Wu

Copyright © 2021 Qian Dong et al. This is an open access article distributed under the Creative Commons Attribution License, which permits unrestricted use, distribution, and reproduction in any medium, provided the original work is properly cited.

The study of influence of in-situ stress on energy transmission of blasting stress wave in jointed rock mass is the basis for improving the utilization rate and optimizing the distribution of explosive energy in underground rock mass during blasting excavation. Thus, a model test was carried out to explore the energy transmission of blasting stress wave in jointed rock mass under different in-situ stresses, and the energy transmitting coefficients of the blasting stress wave were derived. Then, the influencing factors such as the scale and distribution of in-situ stresses and the angle and number of joints were discussed, respectively. The results showed that the energy transmission of blasting stress wave in jointed rock mass was affected by both the intact rock and joints, and the energy transmitting coefficients first increased and then decreased with the rise of static load and lateral static load coefficient, indicating that the lower in-situ stress can enhance the energy transmission of stress wave in rock mass to some extent. While the in-situ stress was relatively large, the stress wave energy dissipation in intact rock was dominant. The number and angle of joints also had a remarkable impact on the energy attenuation of the stress wave; when the stress wave was vertically incident on the joints, the energy transmitting coefficient was the largest. For underground engineering, the orientation of the dominant structural plane and the in-situ stress state of rock mass should be determined firstly, and the blasting parameters can be optimized to improve the utilization of explosive energy and achieve the designed blasting effect.

## 1. Introduction

In the natural or human activities such as earthquake, mining and blasting excavation in the underground rock mass, different magnitude of stress waves will be produced. Meanwhile, joints that widely exist in the natural rock mass significantly affect the stress wave propagation [1]. The propagation of stress wave in jointed rock mass is always accompanied by energy transmission, attenuation, and dissipation. Moreover, underground rock mass is inevitably located in a certain in-situ stress environment. Hence, the exploration of energy transmission of stress wave across the in-situ stressed jointed rock mass is of great significance to improve the utilization rate and optimize the distribution of

the explosive energy in underground rock mass during blasting excavation.

Natural rock masses contain massive joints, which often control their mechanical behavior and have a great impact on the propagation of stress wave simultaneously [2–4]. To date, considerable theoretical researches on the stress wave propagation through joints of rock mass had been conducted, which can be roughly divided into two categories [5]. The first one is based on the theory of Discontinuous Deformation Method (DDM) [6], which supposed that the stresses on both sides of the joint are continuous during the passage of the stress wave, while the displacements are discontinuous. The DDM had been widely applied to investigate stress wave passing across linear and nonlinear

deformational rock joints [7–9], one single joint and multiple parallel joints [10–12]. Other scholars combined the DDM with another analysis method, such as the method of characteristic line [13], scattering matrix method [14], and so on. Recently, the Layered Medium Model (LMM) was proposed for wave propagation across filled joints with the assumption that both displacements and stresses were continuous across the interface of two media [15, 16]. The other category method is based on the Equivalent Medium Method (EMM), where effective elastic moduli were calculated and used to represent the jointed medium, such as virtual wave source method [17, 18]. However, these theoretical methods rarely took into account the effect of initial stress.

On the other hand, experimental researches on the stress wave propagation in the rock mass were mainly through the Split Hopkinson Pressure Bar (SHPB) apparatus [19–21]. Meanwhile, to consider the effect of initial stress on stress wave propagation, some scholars had added the confining pressure and axial pressure loading device to the conventional SHPB apparatus, and the related studies had focused on the effect of in-situ stress on the dynamic mechanical properties of the rock mass [22, 23]. Nevertheless, few works had been carried out on the propagation and attenuation of stress waves in jointed rock mass under initial stress by experimental means.

Underground rock masses are initially subjected to in-situ stress before blasting excavation, and the presence of in-situ stress affects mechanical properties of joints and intact rock and the stress wave propagation [24, 25]. The existence of initial stress not only affects the propagation of stress wave in intact rock but also alters the stress state of the joints, thus changing the stress wave propagation in rock mass. Fan and Sun [26] used the nonlinear Barton-Bandis model to simulate the deformation characteristic of the joints, and utilized the DDM to study the seismic wave propagation through an in-situ stressed rock mass. Cheng et al. [27] investigated the effect of increasing static stress on attenuation mechanism and energy dissipation of stress wave in sandstone by an improved SHPB apparatus.

For some critical issues in blasting excavation of natural rock mass, such as low utilization rate of explosive energy and unclear distribution of explosive energy in rock mass, so that the rock mass cannot be fragmented effectively and adequately. To solve the above problems, the energy transmission of the blasting stress wave in the jointed rock mass should be clarified, and the blasting excavation parameters of the rock mass can be optimized. Thus, it is necessary to survey the energy transmission of the stress wave in jointed rock mass to fully understand stress wave propagation and attenuation mechanism. Some scholars studied the energy transmission and attenuation of stress wave in jointed rock mass by theoretical or experimental approaches [28–30]. However, researches on the effect of static stress on the stress wave energy transmission in jointed rock mass were comparatively scarce, especially through experimental methods.

Therefore, in the present study, a model test of stress wave propagation in jointed rock mass under different in-

situ stresses (equal and unequal biaxial static loading) was carried out. Based on the stress and strain time-history curves measured at different positions in the model test samples and the stress wave propagation theory, the energy transmitting coefficient of stress wave was derived; consequently, the energy transmission of blasting stress wave in intact rock and jointed rock mass under different in-situ stresses was comparative analyzed. Furthermore, the influencing factors of the stress wave energy transmission, such as the scale and distribution of static loads, the angle and the quantity of joints were discussed, respectively.

## 2. Model Test of Stress Wave Propagation

**2.1. Static Loading Apparatus.** The multifunctional testing machine for rock and soil was adopted to provide steady and uniformly distributed static boundary loads in the model test, as shown in Figure 1. Meanwhile, the length, height, and thickness of the model test sample are 1600 mm, 1300 mm, and 400 mm, respectively, and the schematic diagram of the static loads applied to the sample during the test is shown in Figure 2, in which the  $P_V$  and  $P_H$  represent the vertical and horizontal boundary static loads, respectively.

**2.2. Mechanical Properties of the Intact Rock and Joint Simulation Material.** It is well known that the natural rock masses are composed of intact rock and discontinuities such as joints and fissures, and these discontinuities are considered as the weak planes in terms of mechanical properties compared with intact rock, and the mechanical behavior of the rock masses are often controlled by the discontinuities. Therefore, the mechanical strength of the intact rock simulation material should be greater than that of the joint simulation material in the model test. To accurately simulate geological structure characteristics of underground rock masses, cement mortars and mica plates were adopted as simulation materials of intact rock and joints, respectively, to investigate the effect of in-situ stress on the stress wave energy transmission in jointed rock mass. The detailed determination process of similarity coefficients and simulation materials in model test can refer to the literature [31, 32], and is only briefly described in this paper, as follows:

- (1) The stress similarity coefficient  $C_\sigma$  between the intact rock simulation material and the prototype of deep-buried underground engineering surrounding the rock was 20, and the physical and mechanical parameters of the prototype are presented in Table 1.
- (2) In order to avoid the influence of nonuniform aggregate in concrete materials on the propagation of blasting stress wave, the low strength cement mortar without aggregate was selected as the intact rock simulation material.
- (3) In the model test, the mixture ratio of cement mortar in accordance with the similarity theory was determined through the orthogonal tests, which were cement: sand: water: plasticizer = 1 : 4 : 1.2 : 0.0267. Through a series of tests, the mechanical parameters



FIGURE 1: Multifunctional testing machine for rock and soil.

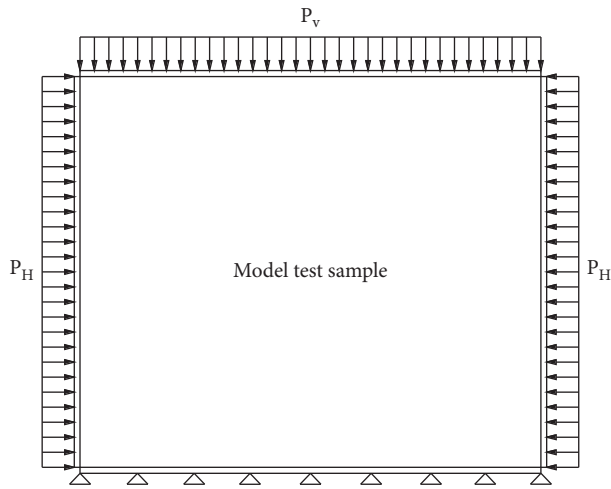


FIGURE 2: The schematic diagram of the static loads applied to the test sample.

TABLE 1: Physical and mechanical parameters of similar materials and prototype of intact rock.

Parameters	Prototype	Similar material
Uniaxial compressive strength $R_c$ (MPa)	120	5.864
Tensile strength $\sigma_t$ (MPa)	12	0.613
Elastic modulus $E$ (GPa)	50	5.226
Internal friction angle $\varphi$ ( $^\circ$ )	30	23.2
Cohesion $c$ (MPa)	30	1.49
Poisson ratio $\mu$	0.223	0.203
Density $\rho$ ( $\text{kg/m}^3$ )	2600	1980

of the cement mortar material of the chosen mixture ratio are shown in Table 1.

- (4) The joints in the in-situ stressed rock mass are in a closed state of compression, so the joints in the model test samples were made into closed joints. While the wave length of the blasting stress wave is greater than the joint thickness, the influence of the joint thickness on the stress wave propagation can be

ignored. Therefore, in the model test samples, the mica plates with a thickness of 1 mm were used to be the joint simulation material, as shown in Figure 3(a).

- (5) The typical relationship curve between the normal stress and the compressive deformation of mica plates was obtained through the normal compression test, as shown in Figure 3(b). It can be observed that the normal stress and deformation of joint simulation material shows a nonlinear relationship, which is consistent with the mechanical properties of joints in the in-situ stressed rock mass [8].

**2.3. Design and Fabrication of Model Test Samples.** The energy transmission of the blasting stress wave in jointed rock mass is related to the angle, quantity, and mechanical properties of joints, and also affected by the scale and distribution of in-situ stress. Hence, three different model samples, named  $T_1$ ,  $T_2$ , and  $T_3$ , respectively, were designed to study the effect of in-situ stress on the energy transmission of blast stress wave in intact rock and rock mass with different angles and numbers of joints, as shown in Figure 4.

Based on the structural characteristics of the cylindrical charge of the model samples, it can be probably considered that the original blasting stress wave generated from the blast source in the model samples is the same in all directions. Consequently, to take full advantage of the model samples and improve the test efficiency, four measuring lines were arranged in each model test sample, respectively, which were along the line direction of the blast source and the midpoint of the four sides of the test samples. For example, the designed  $T_1$  test sample was used to study the energy transmission of blasting stress wave vertical incident jointed rock mass under different in-situ stresses. As a contrast, the energy transmission of the stress wave in intact rock without joints was also considered. According to the number of joints in the four measuring lines, the corresponding research objects are intact rock, single-joint rock mass, double-joints rock mass, and triple-joints rock mass. Besides, the  $T_2$  and  $T_3$  test samples were designed to study the energy transmission of blasting stress wave in intact rock and rock mass containing joints with different numbers and angles. Refer to the  $T_1$  test sample, the corresponding research objects of the  $T_2$  and  $T_3$  test samples are intact rock and single-joint and double-joints rock masses of  $30^\circ$ ,  $60^\circ$  and  $90^\circ$ , respectively.

In addition, all the measuring lines contained in the three model test samples were arranged with the strain sensors and the PVDF (Polyvinylidene fluoride) stress sensors, which were located at 150 mm and 350 mm from the blasting source along the radial propagation direction of the stress wave in each measuring line, as shown in Figure 4. The strain sensors and the PVDF stress sensors were self-made, and the fabrication process of a single strain sensor was as follows: The BE120-5AA resistance strain gauge was firstly bonded to the polyethylene sheet with the size of 8 mm (length)  $\times$  8 mm (width) and then connected to the shielding wires. At the same time, the surface of the strain gauge was coated

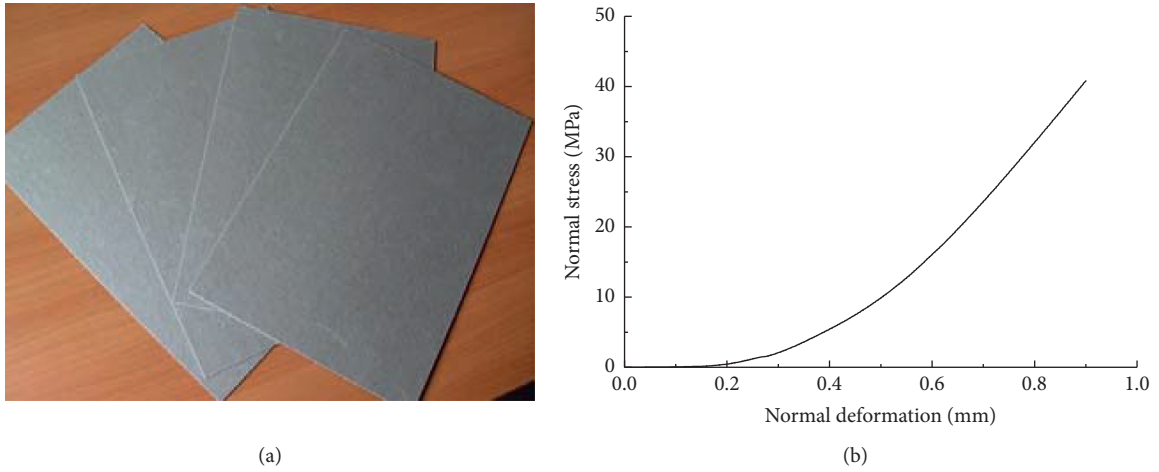


FIGURE 3: Joint simulation material and its mechanical properties. (a) The mica plates. (b) Normal stress and deformation curve.

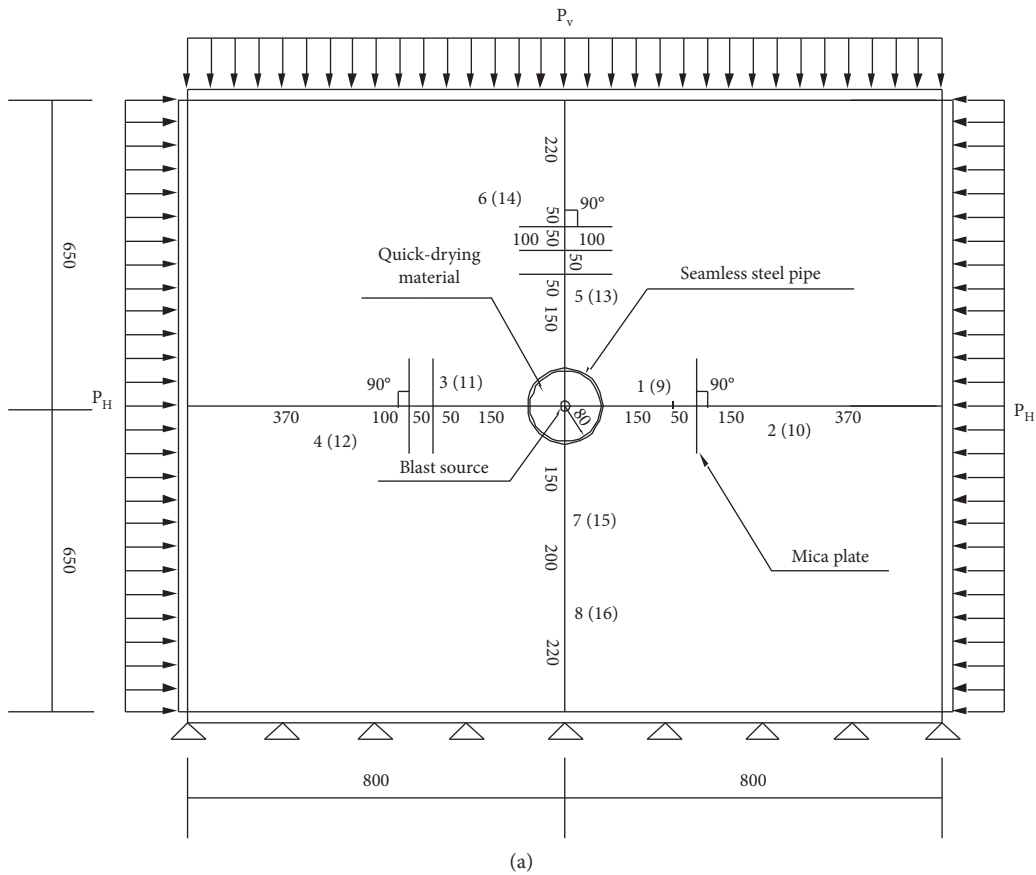
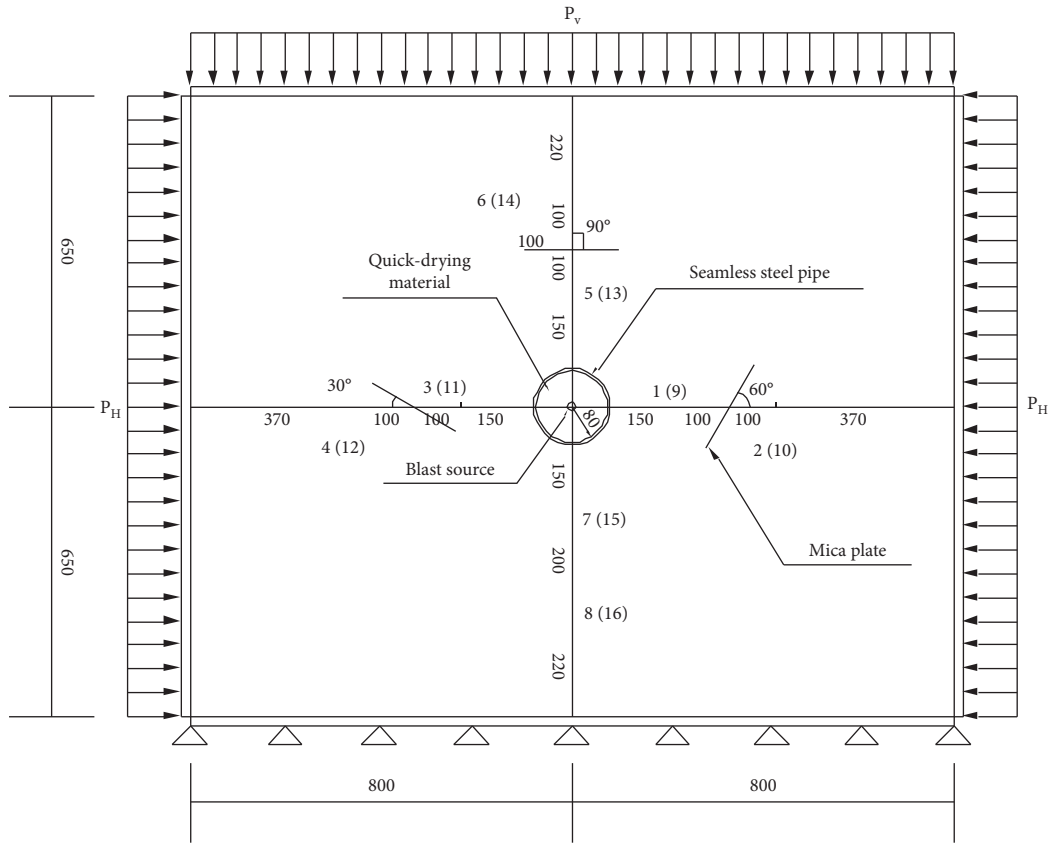
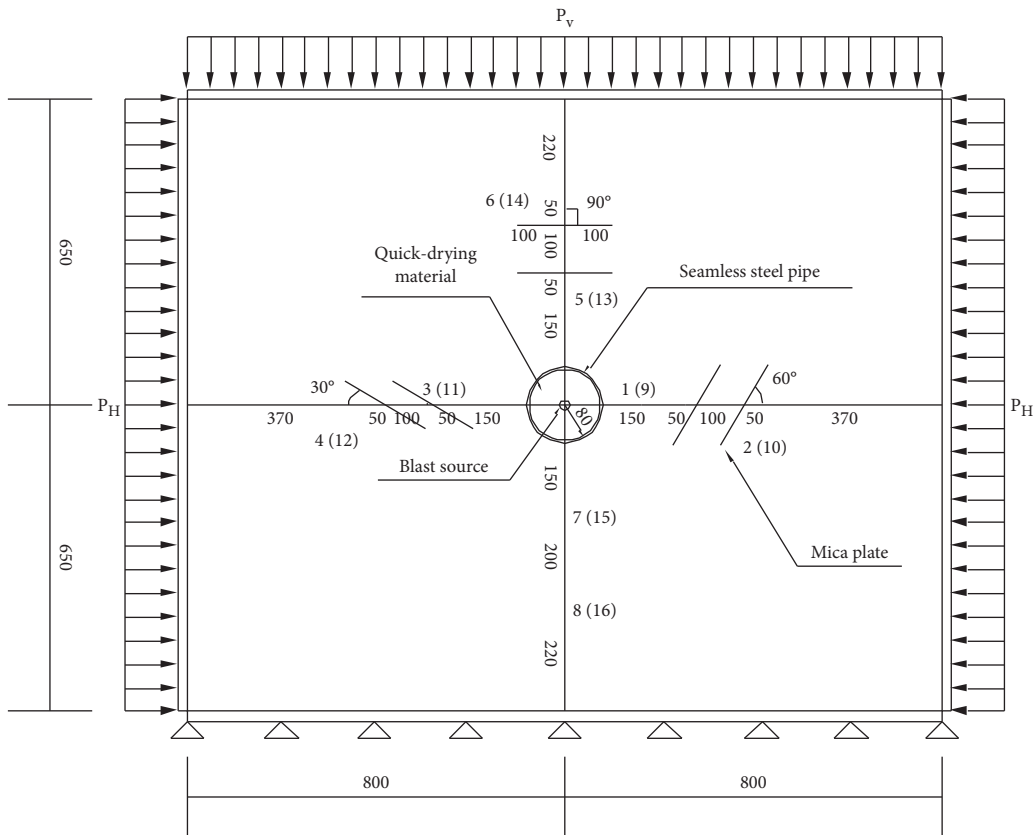


FIGURE 4: Continued.



(b)



(c)

FIGURE 4: Layout of measuring points and joints of model test samples (unit: mm). (a) T1 sample. (b) T2 sample. (c) T3 sample.



with epoxy resin and evenly adhered with the sand. The purpose of this treatment is to avoid the influence of water on the strain gauge during the casting of the model samples, and to increase the match between the strain sensor and the model sample materials as shown in Figure 5(a). On the other hand, the PVDF stress sensors were based on the piezoelectric effect principle of the polyvinylidene fluoride to measure external pressure changes. Meanwhile, to protect the sensitive components and ensure the stress uniformity of the sensor structure, a circular protective substrate made of stainless steel was designed. The fabricated PVDF stress sensor had a diameter of 40 mm, a thickness of 5 mm, and a maximum range of 50 MPa, which was also connected by shielded cables as shown in Figure 5(b).

Due to the different piezoelectric effect of polyvinylidene fluoride sensitive components, it is necessary to calibrate the sensitivity coefficient of each PVDF stress sensor, and the instruments used for the calibration were an oil pressure tank, an oil pump, a charge amplifier and a voltmeter. The calibration process was as follows: the PVDF stress sensors were firstly connected to the charge amplifier and placed in the oil pressure tank, while different oil pressures were applied by using the oil pump, and several sets of pressure values and the corresponding voltage values were recorded to obtain the sensitivity coefficients, which ranged from 1761 to 2290 pC/MPa for the PVDF stress sensors used in the model test. Moreover, the strain sensors fabricated were based on conventional resistive strain gauges as sensitive elements, and the factory-calibrated sensitivity factor of 2.12 for the resistive strain gauges was adopted during the dynamic testing.

In each test sample, the number of the strain and stress measuring points varied from 1 to 8 and 9 to 16 illustrated in Figure 4, respectively. According to the cylindrical charge structure of test samples, the stress and strain test sections were set at different thickness of samples. Meanwhile, the stress and strain measurement points at the same distance from the blasting source are ensured to be projected in the direction of the thickness of the test samples. Each model test sample was divided into three layers for pouring, and the thickness of the first layer was 150 mm and cured for 1 day. When the layer surface reached the certain strength, the self-made PVDF pressure sensors were embedded. Then, the second layer with the thickness of 100 mm was poured, and resistive strain sensors were embedded on its surface after 1 day's maintenance. Finally, the third layer with a thickness of 150 mm was poured. After 28 days of maintenance, the fabricated model test samples can be applied to the explosive loads. The blasting stress wave imposed in the model test samples was generated by four detonating cords with a total length of 1.6 m, and the TNT (Trinitrotoluene) equivalence is about 17.6 g. The detonating cords were fixed in the seamless steel pipe in the center of the test samples through the wooden centering stent, as shown in Figure 6.

**2.4. Model Test Procedure.** In order to improve the efficiency of the model test, the method of repeatedly applying blasting load on a single model test sample was adopted, and different

initial static load conditions were set simultaneously. The detailed test steps are as follows:

Firstly, the fabricated and cured model test samples were hoisted to the multifunctional testing machine for rock and soil (seen in Figure 1), and the four detonating cords were fixed in the center of the seamless steel pipe of the test samples through the wooden centering stent (seen in Figure 6). Quick-drying materials were selected as the filling material and loading core of seamless steel pipes in the test samples, subsequently poured into the pipes and cured for 1 day to reach the strength similar to the model test material.

Secondly, the static loads of different scales and distributions were applied to the model test samples by static loading apparatus, and to ensure the strain uniformity of the model test samples, the static loads were applied to the preset value in two steps, and stabilized for 15 and 30 minutes, respectively.

Thirdly, after the static loads were applied, the dynamic data acquisition instrument DH 5960 was set to the state to be triggered, and then the detonating cords were detonated by the electric detonator, and the dynamic stress and strain data of different positions in the model test samples were collected synchronously with the sampling frequency of 2 MHz.

Finally, after data acquisition, the quick-drying materials in the seamless steel pipes in each model test sample can be broken and cleaned out by an electric drill. Then, the new detonating cords and quick-drying materials were placed in the steel pipes, and the next blasting test can be carried out.

In the model test, according to the distribution of the in-situ stresses of the underground engineering surrounding the rock mass and the stress similarity coefficient, 20 blasting tests under static loading conditions of different scales and distributions were carried out on the three model test samples, as shown in Table 2. The symbols  $P_V$  and  $P_H$  represented the vertical and horizontal boundary static loads exerted to the samples as shown in Figure 4, and the corresponding lateral static load coefficient was the ratio of  $P_H$  to  $P_V$ . The static loads applied to the  $T1$  test sample were from NO.1 to NO.4, designing for the equal biaxial static loading. While for the  $T2$  and  $T3$  samples, the static loads were from NO.1 to NO.8 in Table 2, including the equal and unequal biaxial static loading.

### 3. Energy Transmitting Coefficient of Blasting Stress Wave

According to the theory of stress wave propagation, in each test sample, when the blasting stress wave produced by the detonating cords propagates to the stress and strain measurement point before the joint, a small area  $dA$  on the stress wave front around the measuring point was selected as the research object. Assuming in a small time  $dt$ , stress wave radial propagation distance  $dL = cdt$ ,  $c$  is the propagation velocity of the stress wave, as shown in Figure 7.

The energy  $E_I$  of the incident stress wave in a small volume  $dV$  near the measuring point before the joint is:





FIGURE 5: Stress and strain sensors in the model test samples. (a) Strain sensors. (b) A PVDF stress sensor.



FIGURE 6: Schematic diagram of charge structure.

TABLE 2: Boundary static loads of model test samples.

No.	Static loads (MPa)		In-situ stresses (MPa)	
	$P_V$	$P_H$	Vertical	Horizontal
1	0	0	0	0
2	0.75	0.75	15	15
3	1.5	1.5	30	30
4	3	3	60	60
5	0.75	1.5	15	30
6	1.5	0.75	30	15
7	1.5	3	30	60
8	3	1.5	60	30

$$\begin{aligned}
 E_I &= \int \int \int_V \sigma_I(t) \varepsilon_I(t) dV = \int_0^{l_n} \sigma_I(t) \varepsilon_I(t) dA dl \\
 &= dA \int_0^{t_n} \sigma_I(t) \varepsilon_I(t) c dt,
 \end{aligned} \quad (1)$$

where  $t_n$  and  $l_n$  denote the propagation time and distance of the incident stress wave, respectively, and  $\sigma_I(t)$  and  $\varepsilon_I(t)$  are the stress and strain time-history curves of the measuring point before the joints. The energy intensity  $I_I$  of the incident stress wave near the measuring point is

$$I_I = \int_0^{t_n} \sigma_I(t) \varepsilon_I(t) c dt. \quad (2)$$

In the same way, the energy intensity  $I_T$  of the transmitted stress wave is

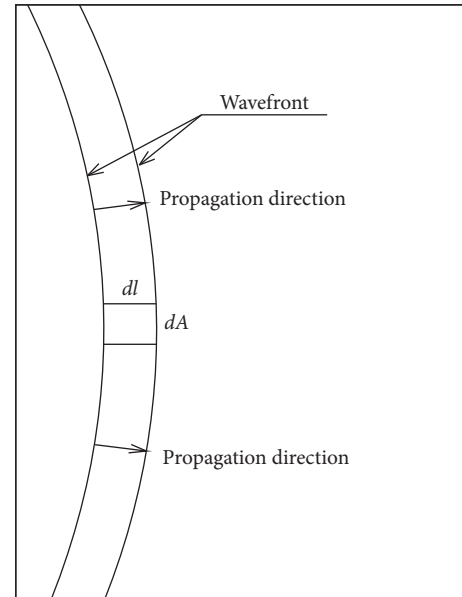


FIGURE 7: Sketch of blasting stress wave propagation near the measuring point.

$$I_T = \int_0^{t_m} \sigma_T(t) \varepsilon_T(t) c dt, \quad (3)$$

where,  $t_m$  denotes the propagation time of the transmitted stress wave, and  $\sigma_T(t)$  and  $\varepsilon_T(t)$  are the stress and strain time-history curves of the measuring point after the joints.

To eliminate the effect of variation of the incident stress wave amplitude, the energy intensity ratio of the transmitted and the incident stress wave is defined as the energy transmitting coefficient  $\eta$  of the stress wave passing through the jointed rock mass, as given below:

$$\eta = \frac{\int_0^{t_m} \sigma_T(t) \varepsilon_T(t) dt}{\int_0^{t_n} \sigma_I(t) \varepsilon_I(t) dt}. \quad (4)$$

#### 4. Energy Transmission of Blasting Stress Wave in the In-Situ Stressed Intact Rock

As a comparison, the energy transmission of the blasting stress wave in intact rock under different in-situ stresses was analyzed first.

*4.1. Effect of the Equal Biaxial Static Loads.* Based on the stress and strain time-history curves obtained from the intact rock section in the three model test samples, the energy transmission of the blasting stress wave in the intact rock was investigated. To compare with the follow-up studies in the jointed rock mass, only the head waves of the stress and strain time-history curves were adopted for analysis. The energy intensity ratio of the head wave measured by strain measuring point 7 (stress measuring point 15) and strain measuring point 8 (stress measuring point 16) was defined as the energy transmitting coefficient of blasting stress wave in the intact rock. The strain and stress time-history curves of intact rock in three test samples were obtained under different equal biaxial static loads, and the typical stress and strain time-history curves are shown in Figure 8.

Figure 8 showed a part of the strain and stress time-history curves of the incident and transmitted waves in the intact rock section of the T1 sample when the static load was 0 MPa, the curves all started at the same time, and lasted for 2 ms. It can be seen from Figure 8 that the time when the blasting stress wave propagated to the strain measuring point 7 and stress measuring point 15, and the point 8 and 16 was almost consistent, meanwhile the head wave durations of the corresponding measuring points were almost the same. Hence, based on the head wave of the time-history curves recorded at the strain measuring point 7 and the stress measuring point 15, the energy intensity of the incident stress wave can be obtained by the equation (4). Similarly, the energy intensity of transmitted stress wave can be obtained through the head wave of the curves recorded at the strain measuring point 8 and the stress measuring point 16.

After removing the outliers, the average values of the incident and transmitted stress wave energy intensity of the intact rock in three test samples under different equal biaxial static loads were sorted out. When the equal biaxial static loads were 0, 0.75, 1.5, and 3 MPa, the incident wave energy intensities were 23.91, 18.47, 14.15, and 7.76 J/m<sup>2</sup>, respectively, and the energy intensities of the transmitted wave

were 9.08, 7.94, 6.51, and 2.56 J/m<sup>2</sup>, respectively. The energy intensities of incident and transmitted stress wave in intact rock under different equal biaxial static loads are shown in Figure 9.

It can be observed in Figure 9 that the energy intensities of the incident and transmitted stress waves in the intact rock decrease with the increasing of the equal biaxial static load. The reason for the above phenomenon is that the larger the static stress, the stronger the interaction forces between particles of intact rock, so the vibration of intact rock induced by dynamic disturbance was more inhibited. Thus, the greater the static load, the smaller the dynamic response of the intact rock caused by the blasting stress wave, and the smaller the energy of the stress wave in the intact rock simultaneously. Meanwhile, the energy transmitting coefficients of the blasting stress wave in intact rock under different equal biaxial static loads are as shown in Figure 10.

When the static loads were 0, 0.75, 1.5, and 3 MPa, the blasting stress wave energy transmitting coefficients were 0.38, 0.43, 0.46, and 0.33, respectively. It is reported that the energy transmitting coefficient of stress wave increases first and then decreases with the increase of static loads. In the model test, there were no obvious cracks and damage on the surface of the samples after explosive loading, so it is unnecessary to consider the stress wave energy dissipation caused by the fragment of the samples. Therefore, the energy dissipation of the blasting stress wave in the intact rock can be divided into two parts. The first part was the energy dissipation due to the geometrical dispersion of the stress wave front. Meanwhile, there were numerous micro-cracks inside the intact rocks, and when the stress wave propagates in them, it will drive the micro-cracks to slide overcoming the frictional forces, and another part of the stress wave energy was dissipated.

When the equal biaxial static load was less than 1.5 MPa (i.e., 25.6% of the uniaxial compressive strength  $R_c$ ), with the increase of static load, the micro-cracks in the intact rock were closed, the dynamic stress required for the sliding of the micro-cracks was increased simultaneously, and the quantity of micro-cracks that can slip under the stress wave was also reduced, so the energy dissipation of the stress wave decreased. When the static load reached a certain extent, and continued growing, the closed micro-cracks were expanded and new micro-cracks were initiated. Finally, the quantity of micro-cracks that can slip increased, so the energy dissipation of the stress wave was raised accordingly. It can be speculated that there was a critical static load  $R_{cr}$  (25.6%  $R_c < R_{cr} < 51.2\% R_c$ ); when the static load was greater than  $R_{cr}$ , the number of micro-cracks in the intact rock grew, resulting in the fall of stress wave energy transmitting coefficients.

*4.2. Effect of the Lateral Static Load Coefficient.* When subjected to biaxial unequal static loading, the intact rock is in a state of differential stress loading, and the evolution of micro-cracks in the intact rock is closely related to the differential stress [33]. The influence of the lateral static load

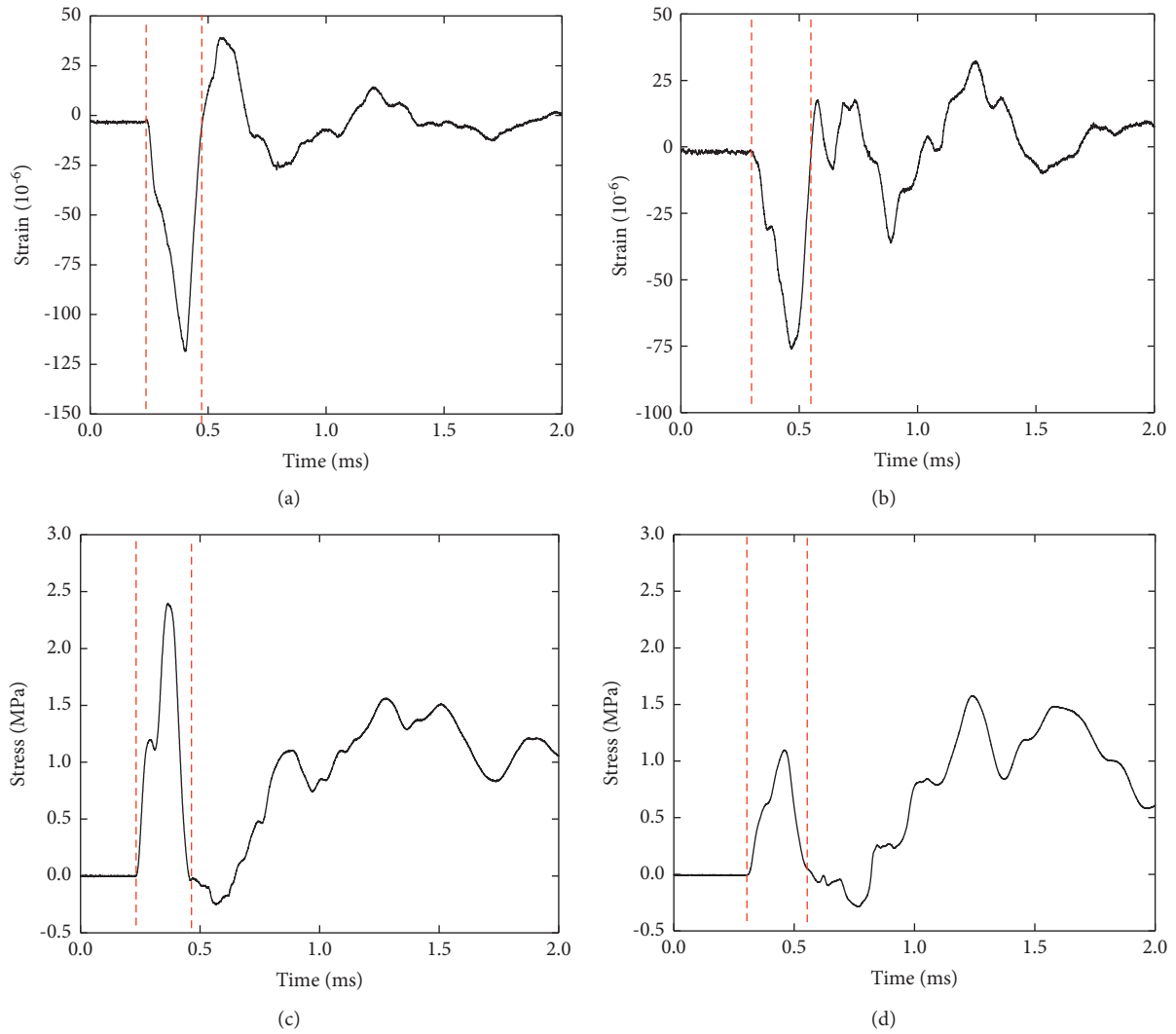


FIGURE 8: Typical incident and transmitted stress wave strain and stress time-history curves in intact rock. (a) Strain measuring point. (b) Strain measuring point 8. (c) Stress measuring point 15. (d) Stress measuring point 16.

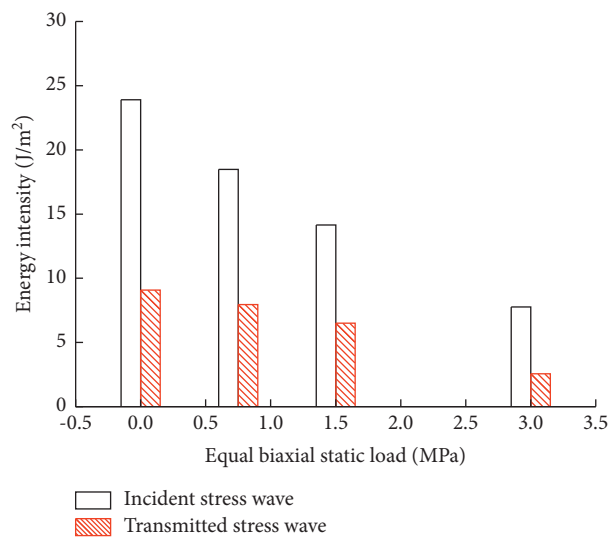


FIGURE 9: Energy intensities of incident and transmitted stress wave in intact rock under different equal biaxial static loads.

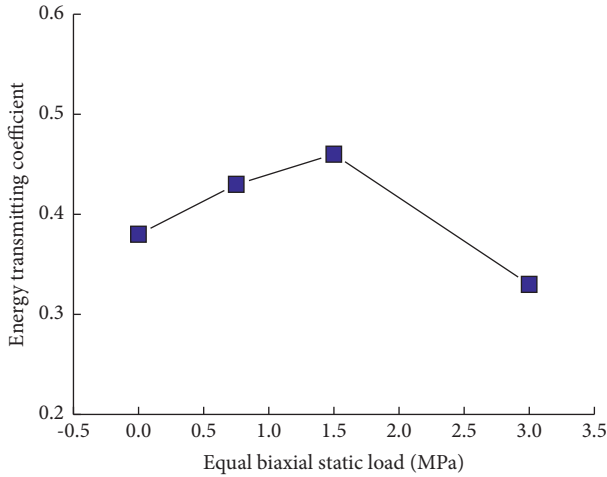


FIGURE 10: Energy transmitting coefficients of blasting stress wave in intact rock under different equal biaxial static loads.

coefficient on the stress wave energy transmission of the intact rock was studied under the static loading conditions of vertical loads of 1.5 MPa and lateral coefficients of 0.5, 1, and 2, respectively. The energy intensities of incident and transmitted stress waves under different lateral static load coefficients are shown in Figure 11.

It can be seen from Figure 11 that the energy intensity of the incident and transmitted stress waves decreased as the lateral static coefficient increased. The reason is that when the vertical static load was constant, the greater the lateral static load, the stronger the constraint on the vibration of the particles in the intact rock, so the energy of the blasting stress wave was smaller. According to the data in Figure 11, the energy transmitting coefficients of stress wave were 0.429, 0.460, and 0.371, respectively, when the lateral static load coefficients were 0.5, 1, and 2. The energy transmitting coefficient of the stress wave in the intact rock increased first and then decreased with the increase of the lateral static load coefficient. When the lateral static load coefficients were 0.5, 1, and 2, the differential stresses for intact rock were 0.75, 0, and 1.5 MPa, respectively. The energy transmitting coefficients of stress wave under different differential stresses are shown in Figure 12.

Figure 12 shows that when the intact rock was subjected to biaxial unequal static loading, the energy transmitting coefficient of the stress wave decreased with the increase of differential stress. The reason is that the quantity of micro-cracks in the intact rock increased with the differential stress, and the quantity of micro-cracks that can slide under stress wave grew simultaneously, so the energy dissipation of the stress wave increased, and finally the energy transmitting coefficient of the stress wave continued to decline.

In summary, the test results implied that the change of static loading state will affect the development and evolution of micro-cracks in the intact rock, thus changing the energy transmission of the blasting stress wave.

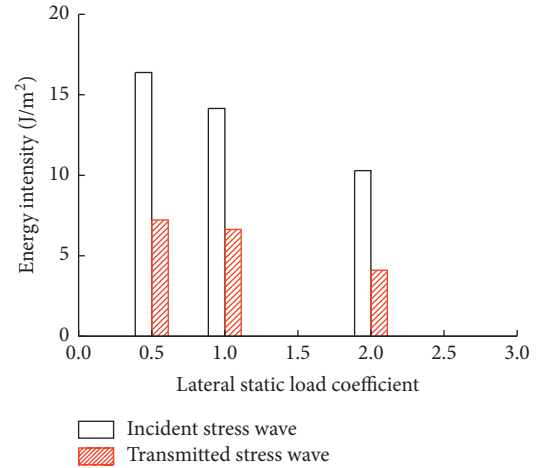


FIGURE 11: Energy intensities of incident and transmitted stress waves in intact rock under different lateral static load coefficients.

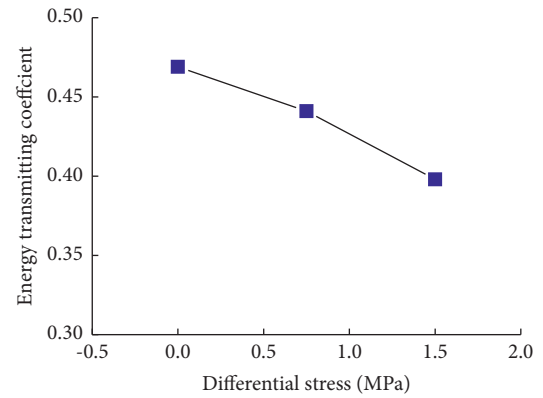


FIGURE 12: Energy transmitting coefficients of stress wave in the intact rock under different differential stresses.

## 5. Energy Transmission of Blasting Stress Wave Normal Incident In-Situ Stressed Rock Mass

**5.1. Effect of the Equal Biaxial Static Loads.** Based on the test results of T1 sample, the energy transmission of blasting stress wave normal incident jointed rock mass under different in-situ stresses can be obtained. The energy intensities of the blasting stress wave normal incident rock mass containing various numbers of joints under different equal biaxial static loads are shown in Table 3, and the abbreviations ISW and TSW represented incident and transmitted stress wave, respectively.

Table 3 manifested that the incident wave energy intensities of rock mass containing different numbers of joints were relatively close in the T1 sample, indicating that the propagation of the blasting stress waves produced by the detonating fuses in all directions were uniform under equal biaxial static loads. Compared with the transmitted wave energy intensities in the intact rock under the same equal biaxial static loads, it can be found that the transmitted wave energy intensities of jointed rock mass and intact rock were

TABLE 3: Energy intensities of incident and transmitted stress wave under different equal biaxial static loads.

Static loads (MPa)	Single-joint rock mass		Double-joints rock mass		Triple-joints rock mass	
	ISW ( $J/m^2$ )	TSW ( $J/m^2$ )	ISW ( $J/m^2$ )	TSW ( $J/m^2$ )	ISW ( $J/m^2$ )	TSW ( $J/m^2$ )
0	22.54	4.33	24.76	3.32	21.23	2.02
0.75	16.32	5.63	19.41	5.30	17.59	3.99
1.5	14.85	6.29	13.19	4.89	15.78	5.18
3	8.43	2.68	6.65	2.01	6.33	1.80

quite different, illustrating that the existence of joints will dissipate the energy of stress wave. Meanwhile, the greater the quantity of joints, the smaller the energy intensities of the transmitted wave. To conclude, with the increase of static loads, the energy intensities of incident and transmitted wave in rock mass containing different numbers of joints showed a decreasing trend, while the energy intensities of transmitted wave increased at first and then decreased.

The energy transmitting coefficients of blasting stress wave in single-joint, double-joints, triple-joints rock mass and the intact rock under different equal static loads are plotted in Figure 13.

It can be seen from Figure 13 that the energy transmitting coefficients of stress wave in the intact rock under the same static load were larger than that in the jointed rock mass, and coefficients decreased with the increase of the joint number. With the rise of static loads, the stress wave energy transmitting coefficients of the intact rock and jointed rock mass both increased first and then decreased. It was also found that with the growth of static loads, the difference of stress wave energy transmitting coefficients of the intact rock and jointed rock mass reduced gradually.

The energy dissipations in the blasting stress wave propagation in rock mass were mainly composed of the following two parts: the first one was the energy dissipation produced by the friction between the micro-cracks and the stress wave front diffusion in the intact rock; the other part was the energy dissipation when the stress wave was propagating at joints. In order to quantitatively study the energy dissipation of stress waves at joints, it was assumed that the two parts of energy dissipations in the jointed rock masses were independent. In Figure 13, the ratio of the stress wave energy transmitting coefficient between the jointed rock mass and the intact rock under the same biaxial equal static load was the energy transmitting coefficient of the stress wave passing through the joints, as shown in Figure 14.

Figure 14 shows that the more the number of joints, the smaller the energy transmitting coefficients of the stress wave, and coefficients increased with the static loads. The reason for this phenomenon was that the greater the static load, the greater the normal and tangential stresses on the joints, and the joints usually satisfy the nonlinear stress deformation relationship [4, 9]. Therefore, the normal and tangential stiffness of joints increased with the static loads, so the dissipation of the stress wave energy was reduced accordingly.

In summary, combined with Figures 10 and 14, the variation of stress wave energy transmitting coefficient with the increase of static loads in the jointed rock mass in

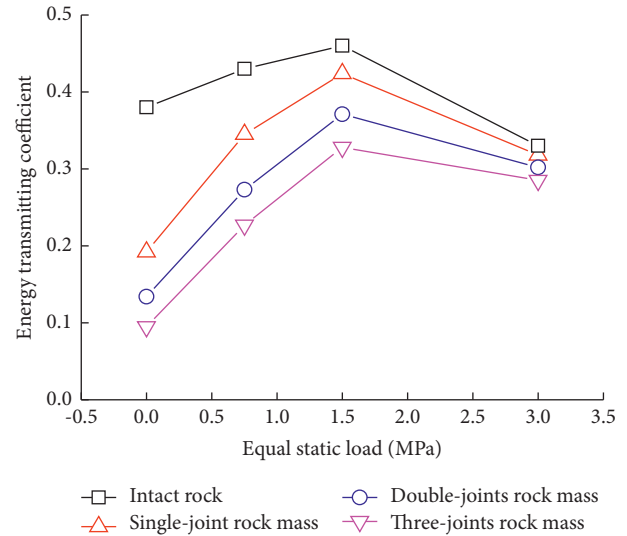


FIGURE 13: Energy transmitting coefficients of stress wave in intact rock and rock mass under different equal static loads.

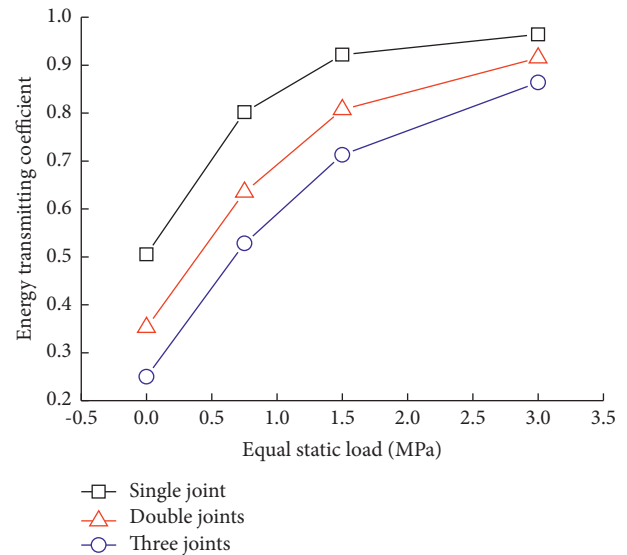


FIGURE 14: Energy transmitting coefficients of stress wave at joints under different equal static loads.

Figure 13 can be interpreted as follows: when the static load increased from 0 to 1.5 MPa, the energy transmission of stress wave in the intact rock and joints both grew, so the energy transmitting coefficient of the stress wave in jointed



rock mass increased accordingly. With the increase of the static load, the energy transmission of stress wave at joints continued to improve, while the energy transmission in the intact rock declined sharply, which eventually led to the decrease of the energy transmitting coefficient.

**5.2. Effect of the Number of Joints.** The variation of energy transmitting coefficients of the stress wave in rock mass containing various numbers of joints under different equal biaxial static loads is shown in Figure 15.

Energy dissipation occurred when the stress wave propagating through each joint and the energy transmitting coefficients of the stress wave decreased with the increase of the joint number under the same static loads. Figure 15 shows that when the static loads were 0, 0.75, 1.5, and 3 MPa, and the number of joints increased from 0 to 3, the decrements of stress wave energy transmitting coefficients were 75%, 47.2%, 28.7%, and 13.6%, respectively. The results showed that when the static load increased, the reduction of the energy transmitting coefficient decreased with the increment of the number of joints.

The reason for the above results was that as the static loads increased, the stiffness of the joints rose, and the blasting stress wave energy transmission in the jointed rock mass increased. At the same time, when the blasting wave passed through the jointed rock mass, multiple transmission reflections occurred between the joints, which will enlarge the energy transmitting coefficient to some extent, and the larger the static load, the stronger the multiple transmission reflections effect. Therefore, with the growth of static load, the energy transmitting coefficients of stress wave passing through intact rock and jointed rock gradually became close.

The results showed that the larger the in-situ stress, the lower the influence of the number of joints on the energy transmission of the blasting stress wave, while the evolution of the micro-cracks in the intact rock played a leading role in the attenuation of the stress wave energy.

## 6. Energy Transmission of Blasting Stress Wave Obliquely Incident In-Situ Stressed Rock Mass

**6.1. Effect of the Equal Biaxial Static Load.** In the T2 and the T3 test samples, the energy intensities of the incident and transmitted wave passing through rock masses with different angles and quantities of joints under various equal biaxial static loads are shown in Tables 4 and 5, and the abbreviations ISW and TSW represent incident and transmitted stress wave, respectively.

Tables 4 and 5 indicated that with the increase of static loads, the transmitted wave energy intensities of the jointed rock mass with the same angle and number showed a trend of increasing first and then decreasing. Under the equivalent static load, the transmitted wave energy intensities had no obvious change with the raise of the joint angle. Based on the data in Tables 4 and 5, the energy transmitting coefficients of stress wave in single-joint and double-joints rock masses

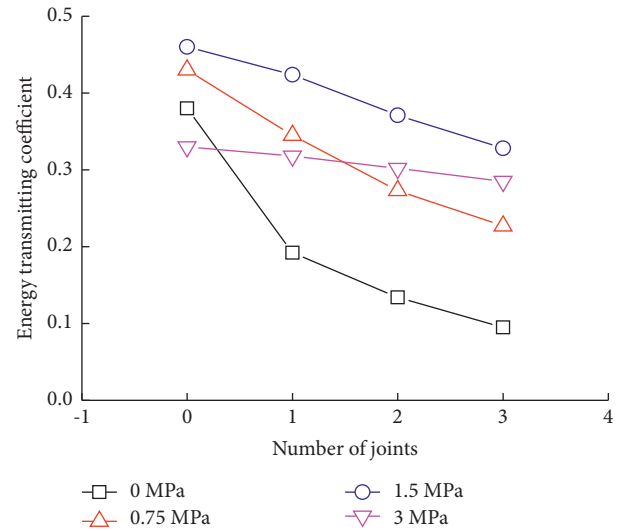


FIGURE 15: Influence of joint number on stress wave energy transmitting coefficients under different static loads.

with different angles under equal biaxial static loads are shown in Figure 16.

According to the joints layout diagram of the T2 and T3 test samples in Figure 4, the incident angles of stress wave in the 30°, 60°, and 90° single-joint and double-joint rock masses were 60°, 30°, and 0°, respectively. Figure 16 shows that the energy transmitting coefficients increased at first and then decreased with the growth of static loads, while the coefficients dropped with the increase of the joint number under the same static load. Compared with Figure 13, it can be seen that as the static load rose from 0, the jointed rock mass with different angles and numbers all showed a trend of first increasing and then decreasing, and the reason for this phenomenon is explained in Section 5.1.

**6.2. Effect of the Lateral Static Load Coefficient.** To compare with the test results of the intact rock, the variation of energy transmitting coefficients of the blasting stress wave in rock mass with different angles and quantities of joints was obtained, under unequal biaxial static loads, with the vertical static loading of 1.5 MPa and lateral static load coefficients of 0.5, 1, and 2 respectively, as shown in Figure 17.

It can be seen from Figure 17 that with the rise of the lateral static load coefficient, the stress wave energy transmitting coefficients of the intact rock and jointed rock mass both first increased and then decreased. That was because the normal and tangential stresses on joints increased with the lateral static load coefficients, so the normal and tangential stiffness of joints grew simultaneously due to the nonlinear deformation characteristics of the joint. Therefore, with the increase of the lateral static load coefficient, the energy transmission of the stress wave at the joints was more efficient.

However, according to the analysis of Section 4.2, due to the change of differential stress, the energy transmission of stress wave in the intact rock mass increased first and then decreased with the growth of the lateral pressure



TABLE 4: Energy intensities of incident and transmitted stress wave in single-joint rock mass under different equal biaxial static loads.

Static loads (MPa)	Single-joint rock mass					
	30°		60°		90°	
	ISW (J/m <sup>2</sup> )	TSW (J/m <sup>2</sup> )	ISW (J/m <sup>2</sup> )	TSW (J/m <sup>2</sup> )	ISW (J/m <sup>2</sup> )	TSW (J/m <sup>2</sup> )
0	20.12	4.73	23.45	5.14	22.43	4.60
0.75	17.92	5.41	15.27	4.86	16.87	5.67
1.5	13.68	5.32	12.53	5.08	12.76	5.59
3	7.54	2.02	5.93	1.69	6.67	2.06

TABLE 5: Energy intensities of incident and transmitted stress wave in double-joints rock mass under different equal biaxial static loads.

Static loads (MPa)	Double-joints rock mass					
	30°		60°		90°	
	ISW (J/m <sup>2</sup> )	TSW (J/m <sup>2</sup> )	ISW (J/m <sup>2</sup> )	TSW (J/m <sup>2</sup> )	ISW (J/m <sup>2</sup> )	TSW (J/m <sup>2</sup> )
0	22.87	3.45	21.36	2.82	23.54	2.92
0.75	17.54	4.46	18.43	4.90	16.42	4.71
1.5	14.65	5.02	15.28	5.47	14.73	5.77
3	7.21	1.87	5.62	1.53	6.33	1.84

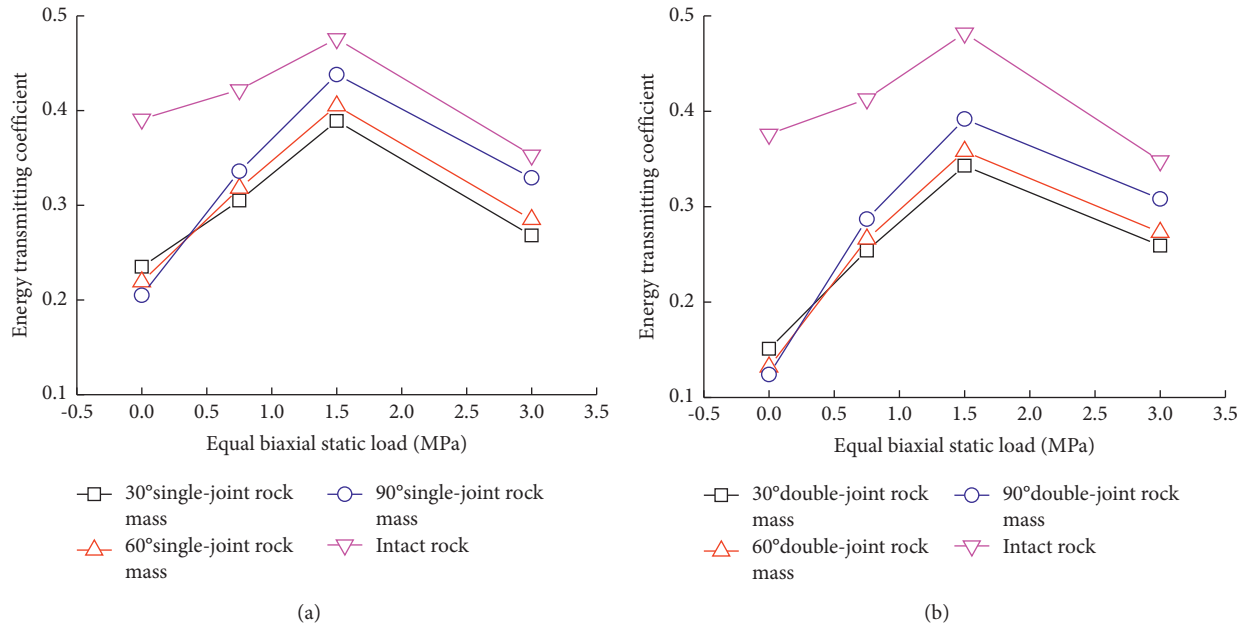


FIGURE 16: Energy transmitting coefficients of stress wave in jointed rock masses with different angles and numbers under equal biaxial static loads. (a) Single-joint rock mass. (b) Double-joints rock mass.

coefficient, as shown in Figure 17. It also can be found that the variations of stress wave energy transmitting coefficient of the intact rock and jointed rock mass were identical with the increment of the lateral coefficient, indicating that when the differential stress increased, the stress wave energy dissipation in the intact rock was dominant in the process of stress wave passing through jointed rock mass.

6.3. *Effect of the Joint Angle.* In the blasting excavation of underground engineering, the spatial distribution of joints in the surrounding rock mass was commonly random, so it

is necessary to study the effect of the joint angle on stress wave energy transmission. Based on the data in Tables 4 and 5, the influence of the joint angle on the energy transmission of the stress wave under equal biaxial static loads is shown in Figure 18.

Figure 18 shows that when the static load was zero, the stress wave energy transmitting coefficients decreased with the increase of joint angle (i.e., the decrease of the stress wave incident angle), while when the static load was greater than zero, the coefficients increased with the joint angle. The reason may be that the normal and tangential stiffness of the joint varied with the joint angle under the equal biaxial static loads and blasting stress wave.

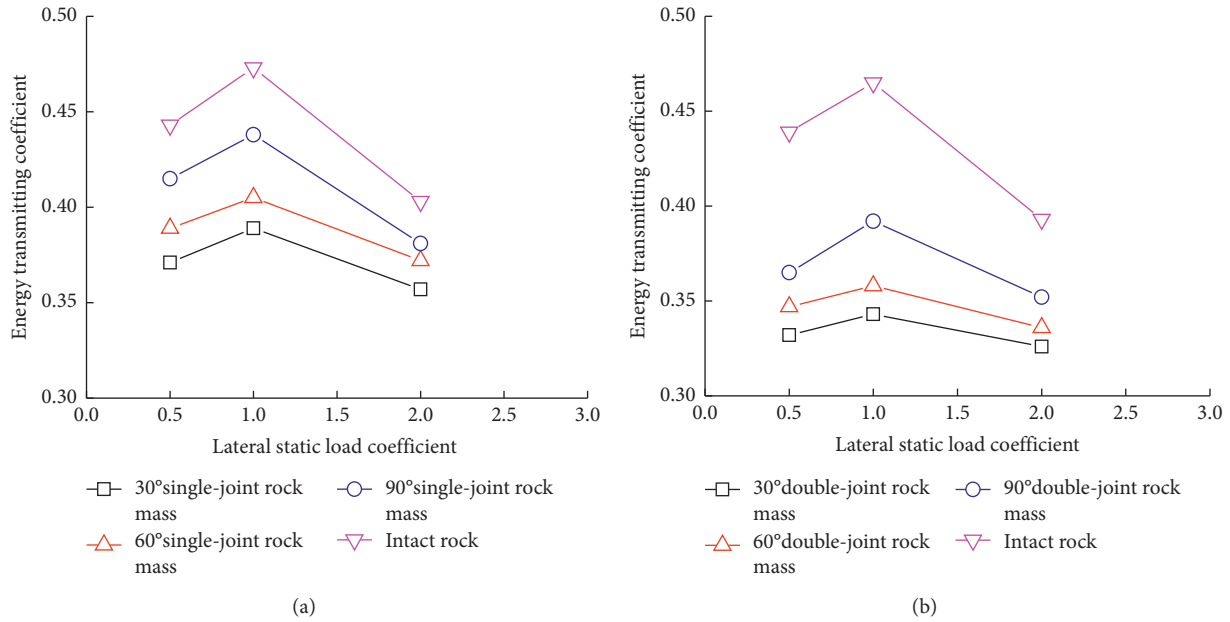


FIGURE 17: Energy transmitting coefficients of blasting stress wave in jointed rock masses under different lateral static load coefficients. (a) Single-joint rock mass. (b) Double-joints rock mass.

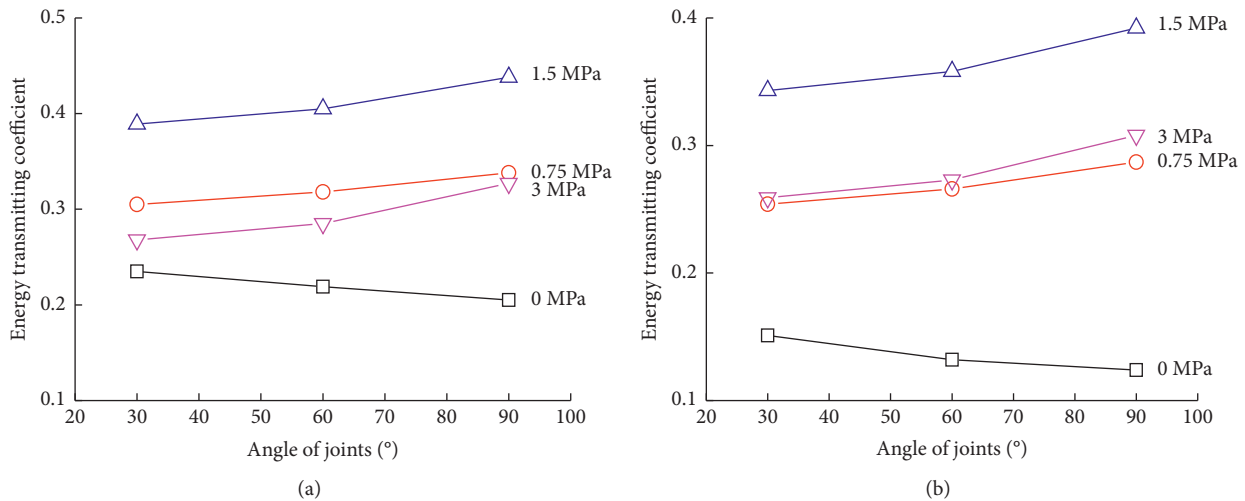


FIGURE 18: Influence of joint angle on energy transmitting coefficient of stress wave under equal biaxial static loads. (a) Single-joint rock mass. (b) Double-joints rock mass.

For the unequal biaxial static loading, the loading condition with vertical static load of 1.5 MPa was selected, and the effects of the joint angle on the energy transmission of the stress wave in jointed rock mass are shown in Figure 19.

It can be seen from Figure 19 that the energy transmitting coefficients of the stress wave increased with the joint angle under the same lateral static load coefficient. When the lateral static load coefficient and the angle of joint were constant, the energy transmitting coefficient decreased with the increase of the number of joints.

The above results showed that the energy transmitting coefficients of stress wave in the jointed rock mass increased with the increase of the angle of joint (i.e., the decrease of the angle of incident stress wave), and while the static loads were greater than 0, the energy transmitting coefficient was the largest when the stress wave normal incident the joints. For the practical underground engineering, the state of in-situ stress was highly complex, and the spatial distribution of joints in the rock mass was also complicated. Due to the high cost of dynamic test, the joint angles set in the test were only 30°, 60°, and 90°, which may lead to the effects of joint angle

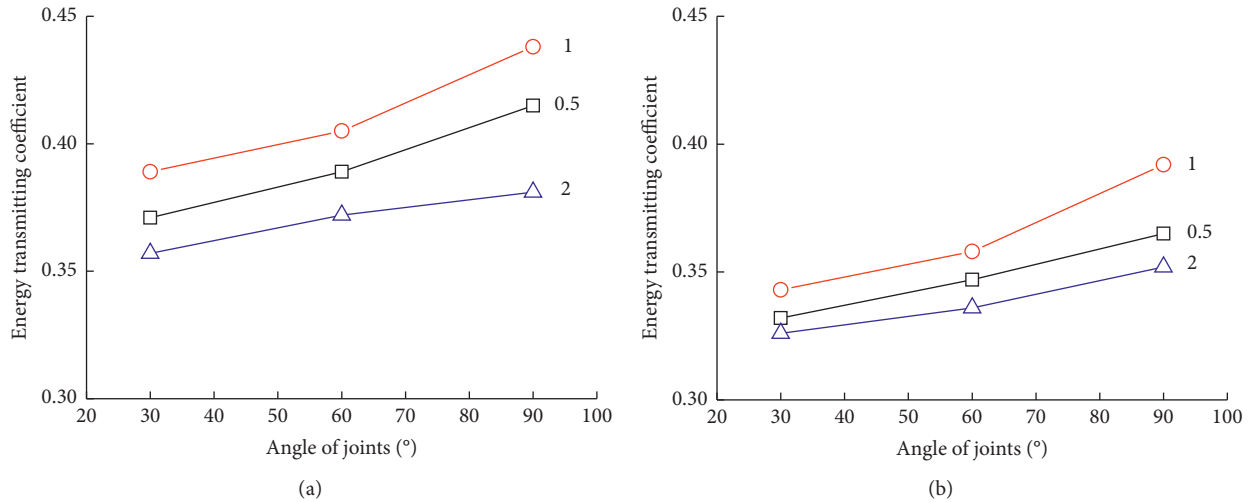


FIGURE 19: Influence of joint angle on energy transmitting coefficient of stress wave under unequal biaxial static loads. (a) Single-joint rock mass. (b) Double-joints rock mass.

on the energy transmission of blasting stress wave under different in-situ stress states and cannot reflect the actual situation. Furthermore, theoretical and numerical simulation research should be carried out for more quantitative analysis.

## 7. Conclusion

- (1) The energy transmission of the blasting stress wave in the intact rock was closely related to the evolution of internal micro-cracks. Under equal biaxial static loading, when the static load was less than 25.6% of the uniaxial compressive strength  $R_c$ , the micro-cracks in the intact rock were closed, resulting in the increase of the stress wave energy transmitting coefficients with the static load. Meanwhile, there was a critical static load  $R_{cr}$  ( $25.6\% R_c < R_{cr} < 51.2\% R_c$ ), when the static load was greater than  $R_{cr}$ , the number of micro-cracks in the intact rock had grown, resulting in the decrease of stress wave energy transmitting coefficients. Under unequal biaxial static loading, with the rise of differential stress, the number of micro-cracks in the intact rock continued to grow, resulting in the decline of stress wave energy transmitting coefficients, and the coefficients increased first and then decreased with the lateral pressure coefficient.
- (2) The energy transmission of the blasting stress wave in jointed rock mass was affected by both the intact rock and joints. Due to the nonlinear deformation characteristics of joints, the energy transmission of the stress wave increased with the in-situ stress, but the increment declined gradually. The energy transmitting coefficients of the jointed rock mass firstly increased and then decreased with the rise of static load and lateral static load coefficient. It is indicated that when the in-situ stress was low, the presence of in-situ stress can enhance the energy transmission of the stress wave in the rock mass to some extent, so as to optimize the explosive energy distribution in the rock mass during blasting excavation, which was beneficial to the full fragment of rock mass. When the in-situ stress was relatively large, the stress wave energy dissipation in the intact rock was dominant in the process of stress wave passing through jointed rock mass, whereas the effect of joints on energy transmission of the stress wave was reduced, and the charge of blasting excavation should be increased to achieve the blasting effect.
- (3) When the stress wave incident the rock mass containing different angles and numbers of joints, the energy transmitting coefficients of the stress wave dropped with the growth of the number of joints, and the larger the in-situ stress, the lower the influence of the number of joints on the energy transmission of the blasting stress wave. The stress wave energy transmitting coefficients in the jointed rock mass increased with the angle of joint (i.e., the decrease of the angle of incident stress wave) under static loading; when the stress wave vertically incident the joints, the energy transmitting coefficient was the largest. Therefore, in the blasting excavation of the underground rock mass, the connection line of blast holes should be perpendicular to the dominant joints in the rock mass, to ensure the efficient transmission of blasting energy.
- (4) In the blasting excavation of the underground rock mass, the in-situ stress and the spatial distribution of joints were complicated and significantly affect the energy transmission of the blasting stress wave, especially for long tunnels and caverns. Therefore, in underground engineering, the orientation of the dominant structural plane and the in-situ stress state of the surrounding rock mass should be determined first, and the blasting parameters can be optimized

accordingly, so as to improve the utilization of explosive energy and achieve the designed blasting effect.

In this paper, due to the limitation of test conditions and the complexity of influence factors, the in-situ stress state and the distribution of joints in the rock mass were relatively simple. However, for practical engineering, the situation is more complicated, which is also the focus of further research.

## Data Availability

The data used to support the findings of this study are available from the corresponding author upon request.

## Conflicts of Interest

The authors declare that they have no conflicts of interest.

## Acknowledgments

This study was supported by the Natural Science Foundation of Hubei Province, China (2020CFB428), Innovation Group Project of the Natural Science Foundation of Hubei Province, China (2020CFA043), Key Research and Development Project of Hubei Province, China (2020BCA084), the National Natural Science Foundation of China (51774222), Open Research Fund of Hubei Key Laboratory of Blasting Engineering (HKLBEF202006), and the Research Start-Up Foundation of Jiangnan University (1027-06020001).

## References

- [1] Ö. Aydan, *ISRM Book Series 3: Rock Dynamics*, CRC Press, Boca Raton, FL, USA, 2017.
- [2] L. J. Pyrak-Nolte, L. R. Myer, and N. G. W. Cook, "Transmission of seismic waves across single natural fractures," *Journal of Geophysical Research Solid Earth*, vol. 95, no. B6, pp. 8617–8638, 1990.
- [3] L. J. Pyrak-Nolte, L. R. Myer, and N. G. W. Cook, "Anisotropy in seismic velocities and amplitudes from multiple parallel fractures," *Journal of Geophysical Research Atmospheres*, vol. 95, no. B7, pp. 11345–11358, 1990.
- [4] J. Zhao and J. G. Cai, "Transmission of elastic P-waves across single fractures with a nonlinear normal deformational behavior," *Rock Mechanics and Rock Engineering*, vol. 34, no. 1, pp. 3–22, 2001.
- [5] A. Perino, J. B. Zhu, J. C. Li, G. Brala, and J. Zhao, "Theoretical methods for wave propagation across jointed rock masses," *Rock Mechanics and Rock Engineering*, vol. 43, no. 6, pp. 799–809, 2010.
- [6] M. Schoenberg, "Elastic wave behavior across linear slip interfaces," *Journal of the Acoustical Society of America*, vol. 68, no. 5, pp. 1516–1521, 1980.
- [7] J. Zhao, X. B. Zhao, and J. G. Cai, "A further study of P-wave attenuation across parallel fractures with linear deformational behavior," *International Journal of Rock Mechanics and Mining Sciences*, vol. 43, pp. 776–788, 2006.
- [8] X. B. Zhao, J. Zhao, and J. G. Cai, "P-wave transmission across fractures with nonlinear deformational behaviour," *International Journal for Numerical and Analytical Methods in Geomechanics*, vol. 30, no. 11, pp. 1097–1112, 2006.
- [9] J. C. Li and G. W. Ma, "Analysis of blast wave interaction with a rock joint," *Rock Mechanics and Rock Engineering*, vol. 43, no. 6, pp. 777–787, 2010.
- [10] B. L. Gu, R. Suárez-Rivera, K. T. Nihei, and L. R. Myer, "Incidence of plane waves upon a fracture," *Journal of Geophysical Research: Solid Earth*, vol. 101, pp. 25337–25346, 1996.
- [11] J. G. Caj and J. Zhao, "Effects of multiple parallel fractures on apparent attenuation of stress waves in rock masses," *International Journal of Rock Mechanics and Mining Sciences*, vol. 37, no. 4, pp. 661–682, 2000.
- [12] J. C. Li, H. B. Li, G. W. Ma, and J. Zhao, "A time-domain recursive method to analyse transient wave propagation across rock joints," *Geophysical Journal International*, vol. 188, no. 2, pp. 631–644, 2012.
- [13] J. Zhao, J. G. Cai, X. B. Zhao, and H. B. Li, "Dynamic model of fracture normal behaviour and application to prediction of stress wave attenuation across fractures," *Rock Mechanics and Rock Engineering*, vol. 41, no. 5, pp. 671–693, 2008.
- [14] A. Perino, R. Orta, and G. Barla, "Wave propagation in discontinuous media by the scattering matrix method," *Rock Mechanics and Rock Engineering*, vol. 45, no. 6, pp. 901–918, 2012.
- [15] J. C. Li, W. Wu, H. B. Li, J. B. Zhu, and J. Zhao, "A thin-layer interface model for wave propagation through filled rock joints," *Journal of Applied Geophysics*, vol. 91, pp. 31–38, 2013.
- [16] J. C. Li, H. B. Li, Y. Y. Jiao, Y. Q. Liu, X. Xia, and C. Yu, "Analysis for oblique wave propagation across filled joints based on thin-layer interface model," *Journal of Applied Geophysics*, vol. 102, pp. 39–46, 2014.
- [17] J. B. Zhu, X. B. Zhao, J. C. Li, G. F. Zhao, and J. Zhao, "Normally incident wave propagation across a joint set with the virtual wave source method," *Journal of Applied Geophysics*, vol. 73, pp. 283–288, 2011.
- [18] J. B. Zhu and J. Zhao, "Obliquely incident wave propagation across rock joints with virtual wave source method," *Journal of Applied Geophysics*, vol. 88, pp. 23–30, 2013.
- [19] H. Kolsky, "Stress waves in solids," *Journal of Sound and Vibration*, vol. 1, no. 1, pp. 88–110, 1964.
- [20] Y. Ju, L. Sudak and H. P. Xie, "Study on stress wave propagation in fractured rocks with fractal joint surfaces," *International Journal of Solids and Structures*, vol. 44, no. 13, pp. 4256–4271, 2007.
- [21] J. J. Feng, E. Y. Wang, L. Chen, X. L. Li, Z. Y. Xu, and G. A. Li, "Experimental study of the stress effect on attenuation of normally incident P-wave through coal," *Journal of Applied Geophysics*, vol. 132, pp. 25–32, 2016.
- [22] X. B. Li, Z. L. Zhou, T. S. Lok, L. Hong, and T. Yin, "Innovative testing technique of rock subjected to coupled static and dynamic loads," *International Journal of Rock Mechanics and Mining Sciences*, vol. 45, no. 5, pp. 739–748, 2008.
- [23] J. F. Jin, X. B. Li, T. B. Yin, and X. J. Zhou, "Effect of axial static stress of elastic bar on incident stress wave under axial impact loading," *Engineering mechanics*, vol. 30, no. 11, pp. 21–27, 2013, in Chinese.
- [24] M. D. Sharma and N. J. Garg, "Wave velocities in a prestressed anisotropic elastic medium," *Journal of Earth System Science*, vol. 115, no. 2, pp. 257–265, 2006.
- [25] A. N. Guz, V. M. Nazarenko, and V. L. Bogdanov, "Combined analysis of fracture under stresses acting along cracks," *Archive of Applied Mechanics*, vol. 83, no. 9, pp. 1273–1293, 2013.
- [26] L. F. Fan and H. Y. Sun, "Seismic wave propagation through an in-situ stressed rock mass," *Journal of Applied Geophysics*, vol. 121, pp. 13–20, 2015.

- [27] Y. Cheng, Z. P. Song, J. F. Jin, J. B. Wang, and T. Wang, "Experimental study on stress wave attenuation and energy dissipation of sandstone under full deformation condition," *Arabian Journal of Geosciences*, vol. 12, pp. 736–749, 2019.
- [28] T. T. Liu, J. C. Li, H. B. Li, and S. B. Chai, "Energy analysis of stress wave propagation across parallel nonlinear joints," *Chinese Journal of Rock Mechanics and Engineering*, vol. 32, no. 8, pp. 1610–1617, 2013, in Chinese.
- [29] W. H. Wang, H. Hao, X. B. Li, Z. Yan, and F. Q. Gang, "Effects of a single open joint on energy transmission coefficients of stress waves with different waveforms," *Rock Mechanics and Rock Engineering*, vol. 48, no. 5, pp. 2157–2166, 2015.
- [30] J. C. Li, L. F. Rong, H. B. Li, and S. N. Hong, "An SHPB test study on stress wave energy attenuation in jointed rock masses," *Rock Mechanics and Rock Engineering*, vol. 52, no. 2, pp. 403–420, 2018.
- [31] Q. Dong, "Model test study on propagation law of plane stress wave in jointed rock mass under different in-situ stresses," *IOP Conference Series: Earth and Environmental Science*, vol. 100, Article ID 012009, 2017.
- [32] Q. Dong, X. P. Li, and J. H. Huang, "Model test study on cylindrical blasting stress wave propagation across jointed rock mass with different initial stresses," *Advances in Civil Engineering*, vol. 2020, Article ID 8881302, 13 pages, 2020.
- [33] M. Cai, P. K. Kaiser, and Y. Tasaka, "Generalized crack initiation and crack damage stress thresholds of brittle rock masses near underground excavations," *International Journal of Rock Mechanics and Mining Sciences*, vol. 41, no. 5, pp. 833–847, 2004.

## Research Article

# Experimental Investigation on Influencing Factors of Rock Fragmentation Induced by Carbon Dioxide Phase Transition Fracturing

Bo Gao,<sup>1</sup> Youjiang Yang,<sup>1</sup> Weilong Xue,<sup>1</sup> Anhui Guo,<sup>1</sup> and Xuedong Luo<sup>2</sup> 

<sup>1</sup>CCCC Second Highway Consultants Co., Ltd., Wuhan 430056, China

<sup>2</sup>Faculty of Engineering, China University of Geosciences, Wuhan 430074, China

Correspondence should be addressed to Xuedong Luo; [luoxd@cug.edu.cn](mailto:luoxd@cug.edu.cn)

Received 5 January 2021; Revised 23 January 2021; Accepted 22 August 2021; Published 7 September 2021

Academic Editor: Roman Gabl

Copyright © 2021 Bo Gao et al. This is an open access article distributed under the Creative Commons Attribution License, which permits unrestricted use, distribution, and reproduction in any medium, provided the original work is properly cited.

Carbon dioxide phase transition fracturing is a novel physical blasting technique, which is gradually used in mining and underground space engineering. The improvement of its rock breaking efficiency is the key concern in the application. In this paper, field experiments of CO<sub>2</sub> phase transition fracturing were conducted. Based on the strain monitoring and fracturing crater volume measuring, the variation of CO<sub>2</sub> filling amount and shear sheet thickness on rock fragmentation of CO<sub>2</sub> phase transition fracturing was investigated. The experimental results indicated that the fracturing crater is shaped as an elliptical cone that is longer in the jet direction and shorter in the vertical jet direction. With the increase of the CO<sub>2</sub> filling amount, the excavated crater volume gradually increases, but the growth rate gradually decreases. The powder factor is constant within a certain charge amount, and after exceeding this charge amount, the powder factor of CO<sub>2</sub> increases significantly. As the shear sheet thickness increases, although the consultant peak stress gradually increases, its growth rate is still unchanged. The crater volume and its growth rate gradually increase in the same situation. Moreover, with the shear sheet thickness increase, the CO<sub>2</sub> powder factor decreases continuously, and the decline rate remains unchanged.

## 1. Introduction

Due to the harmful effects like blasting seismic waves, noise, flying rocks, and harmful gases, the use of explosives in inflammable and combustible, sensitive areas is limited [1, 2]. Therefore, there is an urgent need for a safe, environmentally friendly, and efficient nonexplosive rock breaking method. As a new type of physical rock breaking technology, CO<sub>2</sub> phase transition fracturing breaks the rock mass by the expansion energy of CO<sub>2</sub> liquid-gas phase transition. The whole fracturing process is nonsparking, and the phase transition product is a flame-retardant harmless gas [3, 4]. In general, its safety and environmental protection are far better than blasting, and this technique has a broad application prospect as an alternative technology for blasting.

In 1914, the British company Cardox developed a system for the permeability and recovery of low-breathing

and high-gas coal seams, reducing coal dust and reducing the gas explosion risk. And it is called the Cardox tube system. Shortly hereafter, Cardox tube system was widely used for coal mining in the United States, Germany, Britain, France, and other countries. Due to the rapid development of coal mining technology and mechanized production of coal mines, coal mines gradually stopped using the Cardox tube system. In recent years, CO<sub>2</sub> phase transition fracturing has been widely used in the field of rock excavation due to its multiple advantages [5], such as pile-well excavation [6], gas drainage [7–9], coal roadway excavation [10, 11], and coal mining face mining [12].

Rock fragmentation is essential for evaluating a new rock excavation method. Through the tests in Bulawayo gold mine, Singh [13] confirmed that the combined detonation effect of two CO<sub>2</sub> fracturing pipes was the same as that of five boreholes filled with explosives, indicating that this



technique was a good rock breaking method. Some scholars have also explored the rock fragmentation with different initial parameters. Zhan [14] investigated the influence of different CO<sub>2</sub> filling amounts on the effective damage range in coal through numerical simulation, indicating that damage radius and depth are positively correlated with the filling amount. Zhang et al. [15, 16] carried out the fracturing tests on the concrete block, established the peridynamics model to study the evolution of cracks, and indicated that gas impact and gas wedge are both important to rock fragmentation, and the direction of crack propagation was perpendicular to that of carbon dioxide release. Zhou et al. [4] got a similar conclusion with them through the field test and numerical simulation and indicated that the fracturing crack propagation speed decreased with time. Tao et al. [17] compared the rock breaking mechanism between the carbon dioxide phase transition fracturing and blasting and drew the conclusion that there are no crushing zones after CO<sub>2</sub> phase transition fracturing; thus, the explosive energy utilization rate is correspondingly improved. Tian [18] investigated the influence of confining pressure on the number and shape of cracks and pointed out that the number of cracks produced by CO<sub>2</sub> phase transition fracturing is more than that of hydraulic fracturing.

Previous studies on the influencing factors of rock fragmentation for CO<sub>2</sub> phase transition fracturing almost carried out on the rock mass with good quality, complete concrete block and soil, the crack evolution process were investigated. The rock fragmentation characteristics of fractured rock masses which are induced by CO<sub>2</sub> phase transition fracturing are not yet clear. Moreover, there are few studies on the influence of initial parameters of fracturing on rock fragmentation characteristics. Through the in situ tests, this paper investigates the influence of CO<sub>2</sub> filling amount and shear sheet thickness for rock fragmentation on fractured mudstone, with dynamic strain monitoring and crater volume measurement. The test results may provide the reference for drill hole design on fractured rock masses.

## 2. Principle of CO<sub>2</sub> Phase Transition-Induced Rock Fragmentation

CO<sub>2</sub> phase transition fracturing pipe consists of a detonator, a heating tube, a liquid storage pipe, a gasket, a shear sheet, and an energy drain head. When we conduct the CO<sub>2</sub> fracturing, we should first fill the liquid carbon dioxide into the liquid storage pipe, and then the filled CO<sub>2</sub> fracturing pipe is inserted into the predrilled hole with signal line reserved and the hole sealed. Then, the heating tube will be energized by current and immediately release a lot of heat in a short time. While the liquid carbon dioxide absorbs heat and transfers to the supercritical state, the pressure in the storage pipe is continually rising. When the inner pressure of the storage pipe exceeds the shear sheet strength, the shear sheet is broken. Supercritical carbon dioxide quickly transfers to high-pressure gas and releases from the outlet of the energy drain head. At the same time, the high-pressure gas instantly brings the strong destructive force; the surrounding rock in the jet direction is firstly be compressed

under the shock stress, resulting in a certain number of cracks. Then, the high-pressure gas enters the impact cracks; these cracks propagate forward again under the high-pressure gas wedge [18, 19]. During this process, the thickness of shear sheet determines the peak compressive stress; the filling amount of carbon dioxide determines the total amount of high-pressure gas and the duration of the gas wedge, both of which have a decisive influence on rock fragments. The rock breaking process for the CO<sub>2</sub> phase transition fracturing is shown in Figure 1.

Nowadays, when describing the power of CO<sub>2</sub> phase transition fracturing, the CO<sub>2</sub> phase transition fracturing is often equivalent to the pressure vessel explosion. When we calculate the physical explosion energy of pressure vessels, the explosion energy calculation method of liquefied gas and high-temperature saturated water container and the explosion energy calculation method of high-pressure gas and saturated water vapor container are widely used. The former method is mainly used to describe superheated liquid, and liquid carbon dioxide is not a superheated liquid; thus, this method is not suitable for this fracturing technique. In contrast, the existence state of carbon dioxide in the liquid storage pipe and the explosion trigger conditions are consistent with the explosion energy calculation method of high-pressure gas and saturated water vapor container, so this method is the most widely recognized. The corresponding equation of this method is given by

$$E_g = \frac{pV}{K-1} \left[ 1 - \left( \frac{0.1013}{p} \right)^{(K-1)/K} \right] \times 10^3, \quad (1)$$

where  $E_g$  is the total explosive energy of the carbon dioxide, kJ;  $p$  is the maximum inner pressure of fracturing pipe, MPa;  $V$  is the effective volume for the storage pipe, m<sup>3</sup>; and  $K$  is the adiabatic index of carbon dioxide, taken as 1.295.

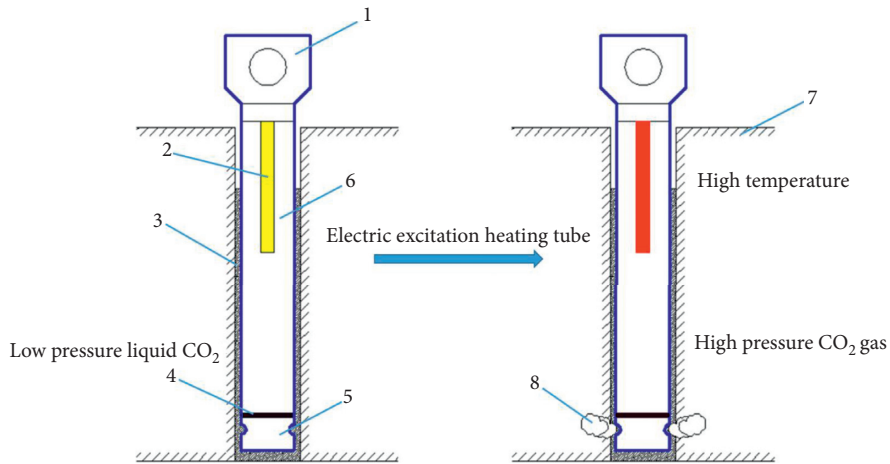
## 3. Effect of Carbon Dioxide Filling Amount on Rock Fragments

**3.1. Field Test.** Strong-to-medium weathered mudstone with basic quality grade V was chosen as fracturing medium in this experiment; its uniaxial compressive strength was less than 10 MPa, belonging to extremely soft rock. To investigate the effect of carbon dioxide filling amount on rock fragments, five kinds of fracturing pipes with different capacities were chosen, as is shown in Figure 2(a).

During the process of liquid carbon dioxide filling, when the inner pressure in the fracturing pipe reaches a preset value, the filling machine could not press liquid carbon dioxide into the fracturing pipe. At that time, we should remove the fracturing pipe from the filling shelf and measure the mass of filled carbon dioxide. The filling equipment of CO<sub>2</sub> fracturing pipe and the platform scale for weighting the fracturing pipe before and after the filling are shown in Figures 2(b) and 2(c).

After drilling, the filled fracturing pipes were put into the drill hole, and medium-coarse sand and small pieces of gravel were chosen as stemming materials to prevent the





1-draw bar ; 2-heating tube ; 3-stemming materials ; 4-shear sheet ; 5- energy drain head ; 6- liquid storage pipe ; 7-rock mass ; 8- gaseous carbon dioxide

FIGURE 1: Principle of carbon dioxide phase transition fracturing.

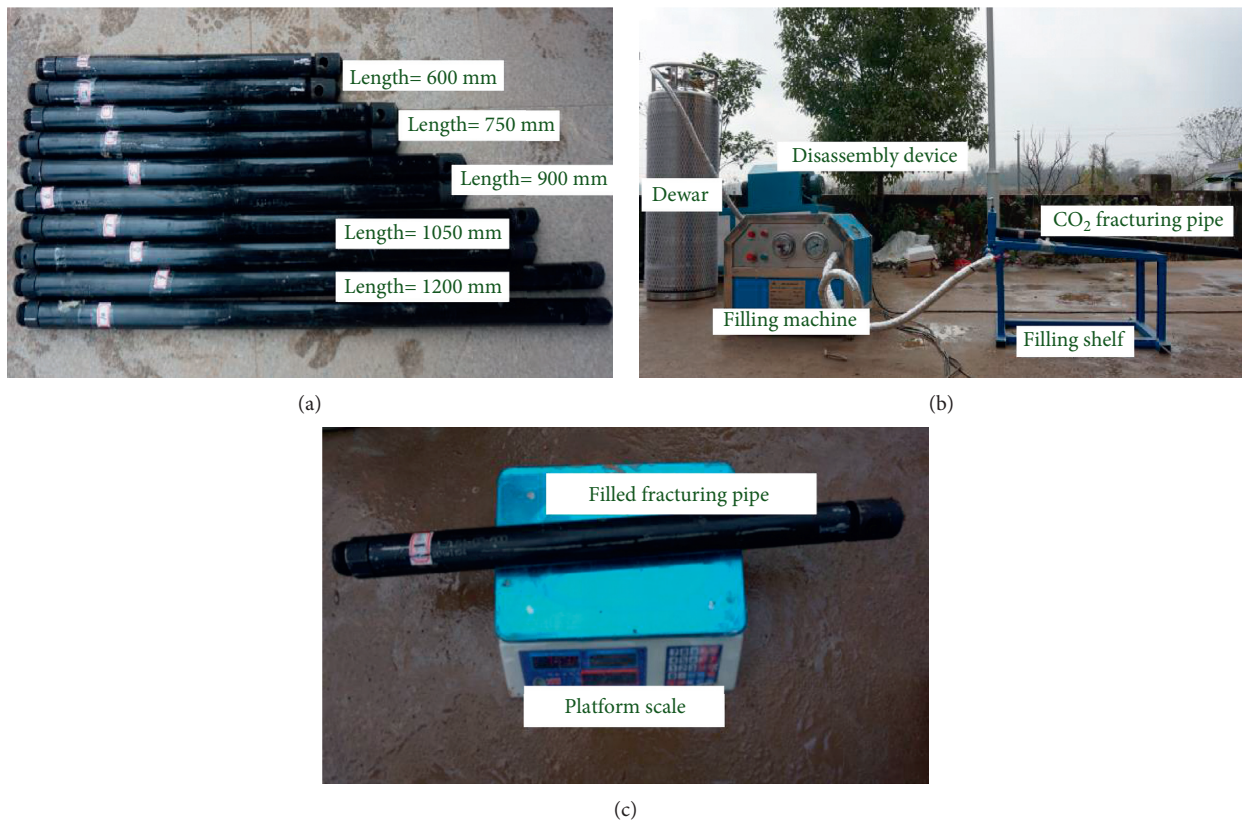


FIGURE 2: Equipment of carbon dioxide phase transition fracturing. (a) CO<sub>2</sub> fracturing pipes with different capacities. (b) Filling equipment of CO<sub>2</sub> fracturing pipe. (c) Platform scale for measuring the filled fracturing pipe.

pipe from flying. Despite the fact that the drill hole was stemmed, we also connected the steel strand to the lifting head for double protection of the fracturing pipe. The heating tube is then connected, the fuse is led to a safe range, and five fracturing pipes of different filling amounts were detonated in sequence.

Moreover, since too little carbon dioxide mass and too thick the shear sheet may cause the fracturing pipe to fail to detonate, a test fracturing with 460 g carbon dioxide and 3.5 mm shear sheet was carried out before the formal tests to explore whether the fracturing pipe in this situation can be detonated. The results showed that the 3.5 mm shear sheet

could be destroyed even with the smallest capacity fracturing pipe. Therefore, the CO<sub>2</sub> filling amounts in these tests were 460 g, 585 g, 760 g, 870 g, and 960 g, respectively. Furthermore, among all the tests, the shear sheet thickness was 3.5 mm, and the drill hole depth and diameter were 900 mm and 115 mm, respectively.

**3.2. Test Results.** After the fracturing pipe was detonated, a large amount of fog remained in the fracturing crater, which is due to the vaporization and heat absorption of liquid carbon dioxide, leading to a decrease in the surrounding temperature and the condensation of water vapor in the air into small water droplets and the formation of fog. Moreover, the morphology for CO<sub>2</sub> phase transition crater is significantly different from blasting, and the crater shape is longer in jet direction. The reason is that the high-pressure carbon dioxide can only be released from two symmetrical release holes due to the special structure for fracturing pipe, resulting in a Mohaupt effect in the jet direction. The load in the jet direction is much higher than that of other directions; the surrounding rock in this direction is firstly damaged

induced the dynamic stress, resulting in a large number of initial cracks. Then, the high-pressure CO<sub>2</sub> expands into the initial cracks, leading them to continue to propagate. Since the borehole in jet direction firstly undergoes the jet, the corresponding axis length for CO<sub>2</sub> phase transition crater was longer, as is shown in Figure 3. By contrast, the blasting crater follows the Livingston blasting crater principle, and because the blasting energy is released in every direction, there are all the circular craters; the surrounding rocks in all directions get the same degree of fragmentation.

To quantitatively analyse the influence of different CO<sub>2</sub> filling amounts on rock fragments, the plane perpendicular to the axis of the drill hole was chosen as the reference plane. The debris in the fracturing crater was cleaned up; the distance between the contour of the crater and the reference plane is measured on a 100 mm × 100 mm grid to find out the crater depth at each measuring point. The area  $S_i$  of each cross section of fracturing crater was calculated through the Simpson equation, and the crater volume  $V$  was obtained by the prism volume formula:

$$S_i = \frac{B}{3} [(Y_0 + Y_n) + 2(Y_2 + Y_4 + \dots + Y_{2i} + \dots) + 4(Y_1 + Y_3 + \dots + Y_{2i+1} + \dots)],$$

$$V = \frac{B}{3} \left[ (s_1 + s_n) + 2(s_2 + s_4 + \dots + s_i + \dots + s_n) + \sum_{i=1}^n \sqrt{s_i s_{i+1}} \right],$$
(2)

where  $S_i$  is the area of the crater cross section, m<sup>2</sup>;  $B$  is the horizontal distance between two adjacent measured points,  $B = 0.1$  m; and  $Y_i$  is the fracturing crater depth of measuring point  $i$ , m.

After cleaning up the broken rocks in the fracturing crater, the boundary of the fracturing crater was determined. Since the CO<sub>2</sub> phase transition fracturing crater is elliptical, taking the drill hole as the center, the crater diameter is measured at 45° intervals. The length of the long axis and the short axis of the ellipse were counted, as Figure 4 shows.

From Figure 4, it can be seen that as the CO<sub>2</sub> filling amount increases, the long axis length of the fracturing crater gradually increases, but the short axis length first increases and then decreases. With the CO<sub>2</sub> filling amount increasing, the crater volume gradually grew; the CO<sub>2</sub> powder factor remained unchanged within a certain filling amount, beyond which it increases significantly, as shown in Figure 5. When the CO<sub>2</sub> filling amount increases from 460 g to 970 g, even if the growth rate of crater volume slows down, its value gradually increases. It can also be found that after the CO<sub>2</sub> filling amount exceeds a certain value, its influence on the crater volume growth becomes smaller but becomes significantly larger on the powder factor. The reason for that is that the CO<sub>2</sub> filling amount is not the only factor that affects the crater volume; the shear sheet thickness limits the peak pressure in CO<sub>2</sub> phase transition fracturing and also controls the rock fragmentation. While the peak pressure is

constant, if only the CO<sub>2</sub> filling amount increases, there is a clear threshold for fracturing crater volume. When the crater volume reaches the threshold value, it is meaningless to further increase the filling amount, which will only increase the cost of construction and reduce the economic efficiency. To better improve the energy utilization ratio of rock fragmentation, it is necessary to further explore the influence of shear sheet thickness on rock fragmentation.

## 4. Effect of Shear Sheet Thickness on Rock Fragments

**4.1. Field Test.** It is acknowledged that the shear sheet is the most important component to influence the peak shock force. When the absolute pressure in fracturing pipe exceeds the shear sheet strength, high-pressure carbon dioxide gas will be ejected through the energy drain head [20]. The thickness of the shear sheet is the determining factor in determining its failure pressure, and it is generally accepted that the thicker the shear sheet, the higher the corresponding failure pressure. To control the thickness as a single variable, all shear sheets were made by Q235a steel in these tests. Shear sheets with thicknesses of 1.5 mm, 2.0 mm, 2.5 mm, 3.0 mm, and 3.5 mm were selected; a fracturing pipe with the length of 900 mm was used. The CO<sub>2</sub> filling amount for the five tests is 755 g, 760 g, 760 g, 755 g, and 750 g, respectively. Although there was some variation in the amount of CO<sub>2</sub>

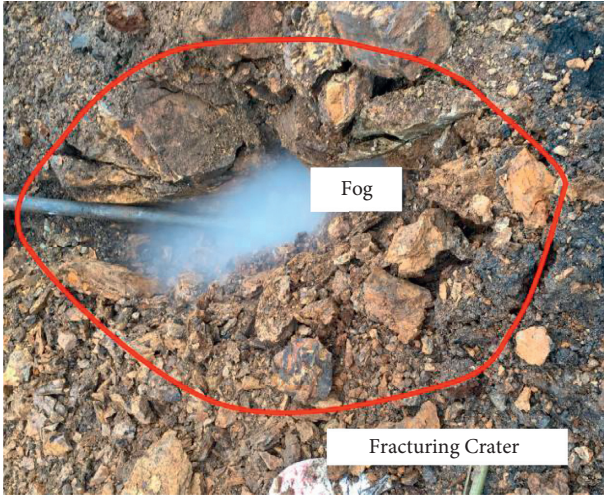


FIGURE 3: Shape of the fracturing crater.

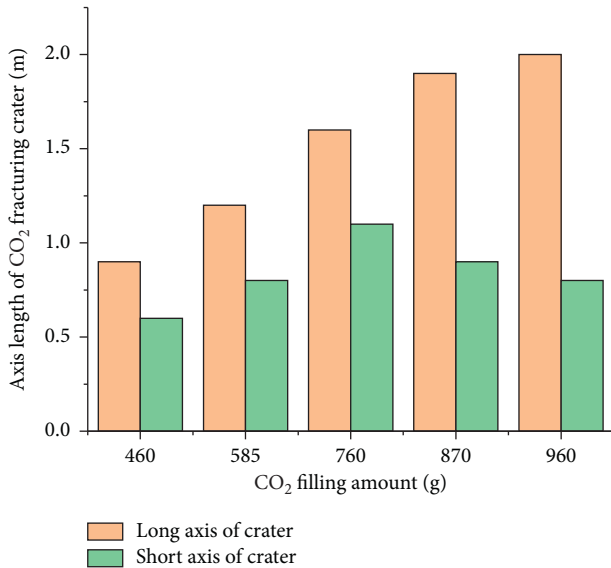


FIGURE 4: Long and short axes length of CO<sub>2</sub> fracturing crater with different CO<sub>2</sub> filling amounts.

filled between the different pipes, this variation was within a negligible margin of error.

Different from the previous tests, since the shear sheet greatly affected the peak stress in the rock mass, the strain test was added. Considering that the higher impact appears in the jet direction, all the self-made strain testing devices were installed at a distance of 2 m from the drill hole in the jet direction. The strain signals at the monitoring points are collected using dynamic strain testing apparatus DH5960. The schematic sketch of strain measuring test design was shown in Figure 6; the procedure for preparing and installing self-made strain testing devices is as follows:

- (1) Prepare several plain bars and iron sheets and weld three iron sheets X, Y, and Z at the underside of the plain bar. Three iron sheets are perpendicular to each

other; the sheet Z has a long side in the same direction as the long axis of the plain bar.

- (2) Make the gypsum strain block, pour the stirred quick-setting gypsum into the strip mold, take it out after the gypsum solidifies, and polish the block surface to make it smooth enough.
- (3) Before attaching the strain gauges to the strain block, the resistance of strain gauges shall be measured; then the epoxy resin shall be used to attach the strain gauges for ensuring that the strain gauge is firmly bonded with strain block and the adhesive layer is uniform. Then, paste the gypsum strain block on each iron sheet.
- (4) Connect the strain gauges to the wires via terminals, and number the wires. Since the insulation resistance and bonding strength of the strain gauge will be reduced when it is affected with damp, add painted gypsum as a protective layer in the surface of strain gauges. Moreover, the above treatment can avoid damage caused by friction with the drill hole when the strain testing device is installed.
- (5) Bury the strain testing device in the predrilled measuring hole, and ensure that the strain gauges are at the same depth as the gas outlet of the fracturing pipe and the X sheet is pointing towards the fracturing pipe; then stem the drill hole with quick-setting gypsum.

As shown in Figure 7, when we started to conduct CO<sub>2</sub> phase transition fracturing, the self-made strain testing device was first installed as described above, and then the fracturing pipe was buried. It should be noted that the direction of the line connecting the two symmetrical gas outlets should be in the same line with the long axis of X sheet when installing the fracturing pipe.

## 4.2. Test Results

### 4.2.1. Peak Stress with Different Shear Sheet Thicknesses.

During these tests, DH5960 super dynamic signal test system was used to record the micro strain. The DH5960 super dynamic signal test system, with 20 MHz maximum transient sampling rate and 1 MHz frequency response, is designed for impact and blasting test. Moreover, Gigabit Ethernet switch is adopted to expand; only one computer can also realize unlimited multichannel super dynamic signal parallel synchronous testing and analysis. To meet the dynamics requirements of strain measurement, in these tests, we set a measuring frequency of 20000 Hz. Since the strain real-time curve in the field experiment can be interfered by a series of field factors such as electromagnetic, the WNOISE function was utilized to denoise field strain data to get more realistic strain signals. This method processes wavelet decomposition coefficient to separate signal and noise with the help of different characteristics of signal and noise in wavelet transform.

These electric resistance strain gauges only measured the strain in a certain direction at the measuring point. To obtain

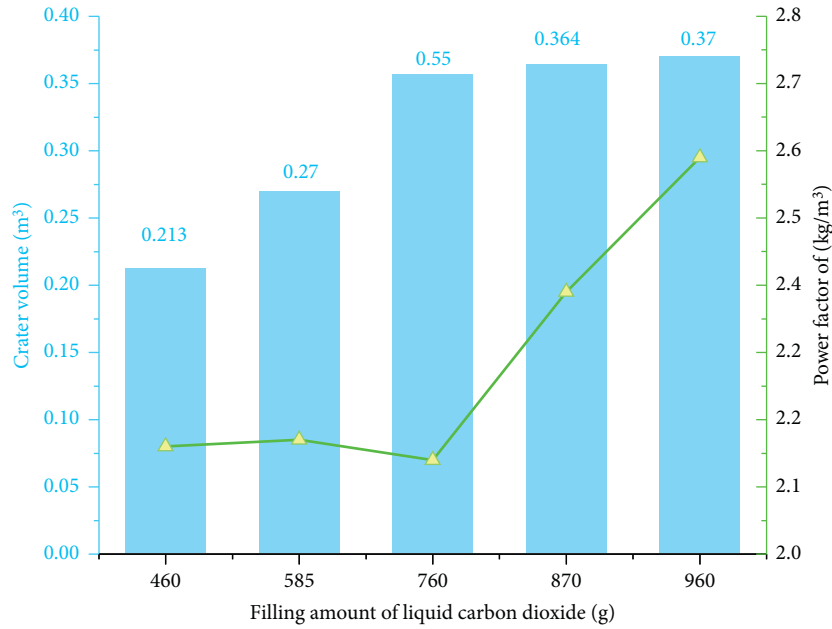


FIGURE 5: Variation of crater volume and powder factor with varying CO<sub>2</sub> filling amounts.

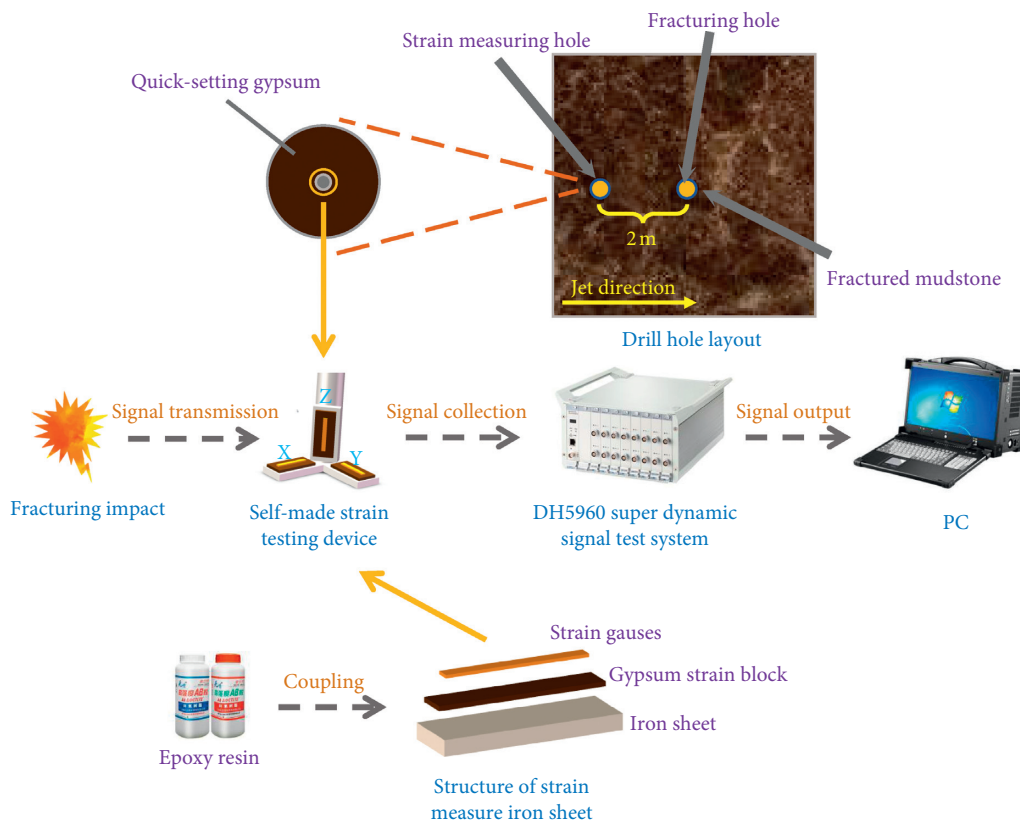


FIGURE 6: Schematic sketch of the strain measuring test design.

the peak dynamic stress, the strain value obtained needs to be converted [21–23]. Since the monitoring point was in a state of three-dimensional stress state, three perpendicular strain gauges were pasted along with the three principal

stress directions. Assuming that the principal strain in the radial, tangential, and vertical directions of the measuring point is  $\epsilon_x$ ,  $\epsilon_y$ , and  $\epsilon_z$ , respectively, according to the generalized Hooke's law, the corresponding principal stresses  $\sigma_x$ ,





FIGURE 7: Installation process of the fracturing pipe and strain testing device.

$\sigma_y$ , and  $\sigma_z$  of radial, tangential, and vertical direction are as follows:

$$\begin{cases} \sigma_x = \frac{E}{1+\nu} \left( \frac{\nu}{1-2\nu} \theta + \varepsilon_x \right) \\ \sigma_y = \frac{E}{1+\nu} \left( \frac{\nu}{1-2\nu} \theta + \varepsilon_y \right), \\ \sigma_z = \frac{E}{1+\nu} \left( \frac{\nu}{1-2\nu} \theta + \varepsilon_z \right) \end{cases} \quad (3)$$

where  $\theta$  is the volumetric strain,  $\theta = \varepsilon_x + \varepsilon_y + \varepsilon_z$ ,  $E$  is the dynamic modulus of elasticity, and  $\nu$  is the dynamic Poisson's ratio.

To investigate the relationship between the shear sheet thickness and the peak stress, the peak strains of five tests were recorded; then the peak strain in each test is converted to peak stress by equation (3), as shown in Figure 8.

From Figure 8, it can be seen that when the shear sheet thickness is the same, the peak stress in the vertical direction (Z-direction) of the measuring point is the largest, and the peak stress in the radial (X-direction) and tangential (Y-direction) directions does not differ much, indicating that the dominant stress direction is the vertical direction. As the

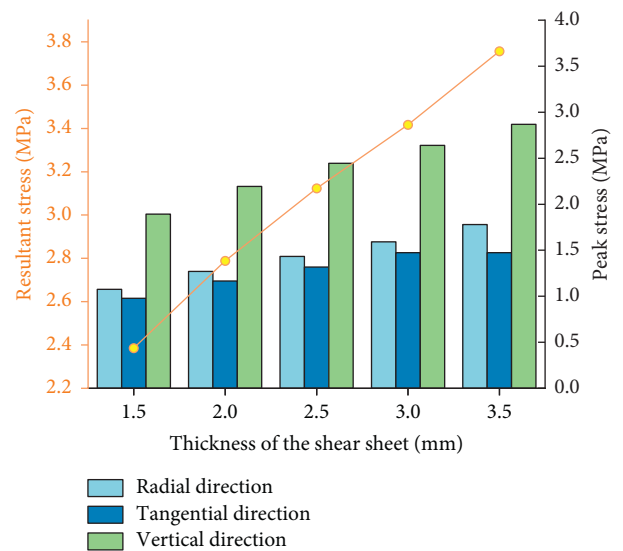


FIGURE 8: Variation of peak stress in different directions and resultant stress with varying thickness of the shear sheet.

shear sheet thickness increases, the resultant stress also grows continuously. When the shear sheet thickness varies from 1.5 mm to 3.5 mm, the resultant stress increases by 1.371 MPa. It can be seen that the peak stress increases with

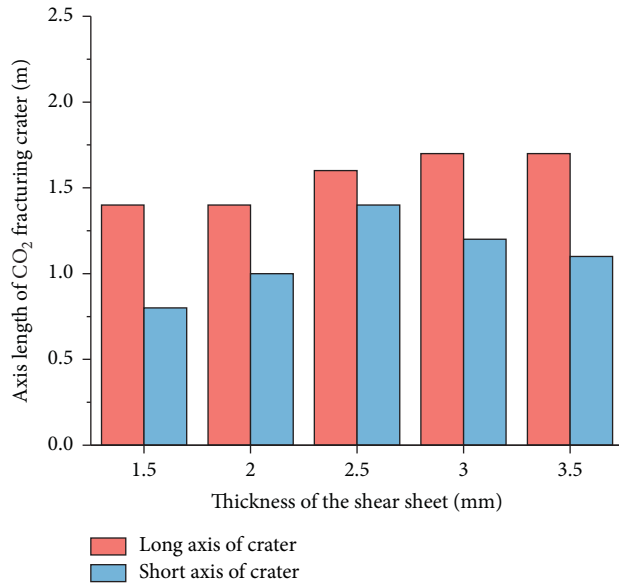


FIGURE 9: Long and short axes length of CO<sub>2</sub> fracturing crater with different thickness of shear sheet.

the growth of the shear sheet strength, and its growth rate is unchanged. The measured peak stress can reflect the peak stress of the drill hole wall in the direction of the air outlet of the fracturing. It is indicated that the thicker the shear sheet, the larger the peak stress.

**4.2.2. Crater Volume with Different Shear Sheet Thicknesses.** The previous measuring method for crater volume and crater morphology was utilized in the tests with variable shear sheet thickness. Furthermore, the CO<sub>2</sub> powder factors were obtained by these five tests. The results are shown in Figures 9 and 10.

It can be seen that as the shear sheet thickness increases, the crater volume and long axis length of the fracturing crater gradually increase, the CO<sub>2</sub> powder factor decreases, while the length of the short axis first grows and then declines. Moreover, when the CO<sub>2</sub> filling amount is equivalent in these five tests, the peak stress in the jet direction gradually increases with the shear sheet thickness increases, resulting in the growth of the effective damage range of the rock mass.

When the shear sheet thickness varies from 1.5 mm to 2.5 mm, the crater volume increases by 0.059 m<sup>3</sup> and the powder factor decreases by 1.19 kg/m<sup>3</sup>. As the shear sheet thickness is changed from 2.5 mm to 3.5 mm, the crater volume increases by 0.132 m<sup>3</sup>, and the powder factor decreases by 1.30 kg/m<sup>3</sup>. It is indicated that with the increase of shear sheet thickness, the growth rate of crater volume increases, but the decline rate of powder factor remains unchanged.

Comparing the test results for different CO<sub>2</sub> filling amount levels and different shear sheet thickness, it can be seen that the crater volume changes with variable CO<sub>2</sub> filling are smaller than the crater volume with variable shear sheet thicknesses. Moreover, a conclusion can be drawn from the

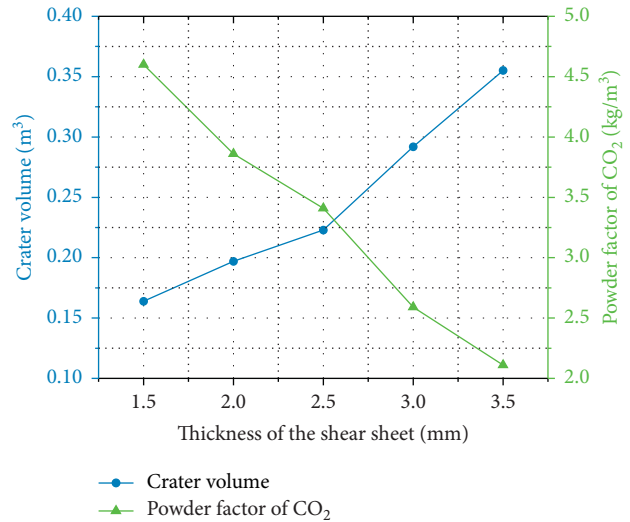


FIGURE 10: Crater volume and powder factor of CO<sub>2</sub> with variable shear sheet thickness.

evaluation indicators, such as powder factor and crater radius, that the effect of shear sheet thickness on the rock fragments is obviously larger than the amount of liquid carbon dioxide.

## 5. Conclusions

In this paper, the fracturing craters volume were counted, and the effects of CO<sub>2</sub> filling amount and shear sheet thickness on rock fragments were investigated through the in situ rock breaking test. Moreover, the dynamic strain test under the impact of CO<sub>2</sub> phase transition fracturing was carried out. The following conclusions are obtained:

- (1) The fracturing crater of CO<sub>2</sub> phase transition fracturing is significantly different from the blasting and is longer in the jet direction and shorter in the vertical jet direction. It is shaped like an ellipsoidal cone.
- (2) As the CO<sub>2</sub> filling amount increases, the crater volume gradually increases, and its growth rate gradually decreases. The powder factor of CO<sub>2</sub> remains constant within a certain CO<sub>2</sub> filling amount and increases significantly beyond that value. The length of the long axis of the crater gradually increases with the increasing CO<sub>2</sub> filling amounts, but the length of the short axis first grows and then decreases.
- (3) When the shear sheet thickness increases, the corresponding resultant stress grows, but the grow slope is constant. Even if the powder factor decreases, the value of crater volume and its growth rate continually increase with the growing shear sheet thickness. The change pattern of long and short axis length in variable shear sheet thickness is the same as that in variable CO<sub>2</sub> filling amounts. Overall, shear sheet thickness has a greater effect on rock fragmentation than CO<sub>2</sub> filling amount.

Although the change characteristics of the strains we measured are consistent with the existing understanding, it should be noted that the above conclusions were obtained by a limited number of tests. To get a more universal statistical law, more tests in different fractured rock masses need to be carried out in the future. The influence of rock properties and confining pressures on rock fragmentations should be further explored in fractured rock masses, which is significant for rock excavation in deep rock engineering.

## Data Availability

The data used to support the findings of this study are included within the article.

## Conflicts of Interest

The authors declare that there are no conflicts of interest regarding the publication of this study.

## Acknowledgments

This study was sponsored by the National Natural Science Foundation of China (Grant nos. 42072309, 41807265, and 41972286) and the Hubei Key Laboratory of Blasting Engineering Foundation (Grant nos. HKLBEF202002 and HKLBEF202001).

## References

- [1] T. S. Bajpayee, T. R. Rehak, G. L. Mowrey, and D. K. Ingram, "Blasting injuries in surface mining with emphasis on flyrock and blast area security," *Journal of Safety Research*, vol. 35, no. 1, pp. 47–57, 2004.
- [2] N. Jiang, B. Zhu, X. He, C. Zhou, X. Luo, and T. Wu, "Safety assessment of buried pressurized gas pipelines subject to blasting vibrations induced by metro foundation pit excavation," *Tunnelling and Underground Space Technology*, vol. 102, Article ID 103448, 2020.
- [3] T. Caldwell, *A Comparison of Non-explosive Rock Breaking Techniques*, The University of Queensland, Brisbane, Australia, 2004.
- [4] S. Zhou, N. Jiang, X. He, and X. Luo, "Rock breaking and dynamic response characteristics of carbon dioxide phase transition fracturing considering the gathering energy effect," *Energies*, vol. 13, no. 6, p. 1336, 2020.
- [5] N. Vidanovic, S. Ognjanovic, and N. Ilincic, "Application of unconventional methods of underground premises construction in coal mines," *Technics Technologies Education Management*, vol. 6, no. 4, pp. 861–865, 2011.
- [6] X. Xie, X. Li, Q. Lii, and H. Ma, "Liquid CO<sub>2</sub> phase-transforming rock fracturing technology in pile-well excavation," *Journal of Central South University*, vol. 49, no. 8, pp. 2031–2038, 2018.
- [7] T. Lu, Z. Wang, H. Yang, P. Yuan, Y. Han, and X. Sun, "Improvement of coal seam gas drainage by under-panel cross-strata stimulation using highly pressurized gas," *International Journal of Rock Mechanics and Mining Sciences*, vol. 77, pp. 300–312, 2015.
- [8] Y. Fan, B. Qin, Q. Zhou, Q. Shi, D. Ma, and J. Wu, "Liquid CO<sub>2</sub> phase transition fracturing technology and its application in enhancing gas drainage of coal mines," *Adsorption Science and Technology*, vol. 38, no. 9-10, pp. 393–412, 2020.
- [9] H. Chen, Z. Wang, L. Qi, and F. An, "Effect of liquid carbon dioxide phase change fracturing technology on gas drainage," *Arabian Journal of Geosciences*, vol. 10, no. 14, pp. 1–9, 2017.
- [10] Z. Nie, "Application of cardox dioxide blasting technique in coal mines," *Coal Technology*, vol. 26, no. 8, pp. 36–37, 2007.
- [11] Z. Du and X. Yufei, "Study on carbon dioxide blasting mining and driving equipment and technology," *Coal Science and Technology*, vol. 44, no. 9, pp. 36–42, 2016.
- [12] Y. B. Zhang, E. Q. Li, J. W. Liu, X. J. Leng, and W. G. Li, "Applications of carbon dioxide cannon blasting on the problem of triangular flap top in coal mine handling mechanized mining face," *Applied Mechanics and Materials*, vol. 256-259, pp. 71–74, 2012.
- [13] S. P. Singh, "Non-Explosive applications of the PCF concept for underground excavation," *Tunnelling and Underground Space Technology*, vol. 13, no. 3, pp. 305–311, 1998.
- [14] D. S. Zhan, *Carbon Dioxide Filling Capacity and Cracking Effect Simulation Analysis*, China Coal Research Institute, Beijing, China, 2017.
- [15] Y. Zhang, J. Deng, B. Ke, H. Deng, and J. Li, "Experimental study on explosion pressure and rock breaking characteristics under liquid carbon dioxide blasting," *Advances in Civil Engineering*, vol. 2018, Article ID 7840125, 2018.
- [16] Y. Zhang, J. Deng, H. Deng, and B. Ke, "Peridynamics simulation of rock fracturing under liquid carbon dioxide blasting," *International Journal of Damage Mechanics*, vol. 28, no. 7, pp. 1038–1052, 2018.
- [17] M. Tao, H. T. Zhao, X. B. Li, and A. Ma, "Comprehensive comparative analysis of liquid CO<sub>2</sub> phase change fracturing and explosive rock fracturing," *Blasting*, vol. 35, no. 2, pp. 41–49, 2018.
- [18] Z. C. Tian, *Crack Form and Influencing Factors of Liquid Carbon Dioxide Phase Transition Fracturing*, China University of Mining and Technology, Xuzhou, China, 2018.
- [19] X. H. Zhou, J. L. Men, and D. P. Song, "Research on optimal borehole parameters of antireflection in coal seam by liquid CO<sub>2</sub> blasting," *Chinese Journal of Rock Mechanics and Engineering*, vol. 35, no. 3, pp. 524–529, 2106.
- [20] K. P. Zhou, B. Ke, J. L. Li, Y. N. Zhang, and L. Cheng, "Pressure dynamic response and explosion energy of liquid carbon dioxide blasting system," *Blasting*, vol. 34, no. 3, pp. 7–13, 2017.
- [21] J. Y. Li, *Experimental Study on the Morphology of Blasting Crater with Different Strength Concrete*, Southwest University of science and technology, Mianyang, China, 2018.
- [22] H. B. Chu, X. L. Yang, A. J. Hou, and Y. Yu, "A simulation-based experimental study on explosion stress wave propagation and attenuation in coal," *Explosion and Shock Waves*, vol. 32, no. 2, pp. 185–189, 2012.
- [23] J. P. Zhao, "Experiment study on measurement and separation of explosive wave signals near blast hole in concrete," *Blasting*, vol. 29, no. 2, pp. 4–9+18, 2012.



## Research Article

# Numerical Analysis of the Influence of Foundation Pit Blasting on a Nearby Metro Tunnel

Haibo Wang , Yaoyao Wang, Mengxiang Wang, and Qi Zong

*School of Civil Engineering and Architecture, Anhui University of Science and Technology, Huainan 232001, Anhui, China*

Correspondence should be addressed to Haibo Wang; wanghb\_aust@163.com

Received 15 June 2021; Revised 11 August 2021; Accepted 12 August 2021; Published 7 September 2021

Academic Editor: Qi Zhao

Copyright © 2021 Haibo Wang et al. This is an open access article distributed under the Creative Commons Attribution License, which permits unrestricted use, distribution, and reproduction in any medium, provided the original work is properly cited.

It is important to guarantee the safety of adjacent underground structures during the foundation pit blasting excavation of modern city construction. The blasting excavation construction of a large, deep foundation pit near an existing metro station of Guangzhou Metro Line 3 is used as the example in this study. Based on blasting vibration field test results, the influence of blasting dynamic load on the lining of an adjacent metro tunnel is numerically analyzed in simulation using Fast Lagrangian Analysis of Continua 3D (FLAC3D), and the relationships between the blasting vibration velocity and stress and the displacement of the metro tunnel lining are obtained. The results show that the stress of lining structure is within the allowable range under the experimental blasting conditions, the lining displacement increases linearly with the applied dynamic vibration velocity, and the vertical displacement of the lining is more obviously affected than the horizontal displacement by the dynamic load. This study can be used as a basis for the control of blasting vibration in a complex urban environment. Its practical application shows that the proposed blasting plan and parameters are reasonable and effective.

## 1. Introduction

Blasting is an efficient and fast excavation method for hard rock mass, and it has been widely used in the excavation of urban building foundation pits. With the continuous construction of urban metro in China, dangers associated with the blasting excavation of foundation pits adjacent to existing urban metro often arise. Most metro tunnels are lined with reinforced concrete segments. When the blasting vibration exceeds a certain limit, it can cause catastrophic damage to the lining. In order to ensure the safety and stability of the adjacent metro tunnel, the influence of the blasting vibration should be evaluated, and potentially damaging effects should be minimized. The abovementioned issue is a key technical issue in realizing the safe and efficient implementation of build foundation pit construction in complex urban environments.

At present, research on the response characteristics of foundation pit on a metro tunnel has been widely considered by scholars [1–5]. However, most of these studies focus on the displacement and stability of foundation pit, and less

attention has been paid to blasting engineering and blasting seismic wave influence on a metro tunnel. Xia et al. researched the impact of the cavity effect on tunnel excavation blasting vibration by a series of blast tests. The results suggested that the cavity effect on the ground only worked within a limited scope in shallow tunnel excavations, and an empirical equation was proposed to calculate the amplifying coefficient [6]. Koneshwaran et al. used a fully coupled technique involving smooth particle hydrodynamics and finite element techniques to investigate the blast response of segmented bored tunnels [7]. El Koursi et al. devised technological improvements to the structure and critical systems of the vehicle and tested in real situation, focused particularly on the behavior of people in blast situation, and presented the related improvements of the vehicles' design in order to improve resilience and survivability to blast [8]. Shin et al. modified the detonation pressure equation based on the results of field tests. Tunnel behavior due to blast-induced vibration was investigated in terms of particle velocity, displacement, and stress of the linings, and guidelines for a blast protection zone were proposed [9]. Ozer analyzed

the field-testing results of ground vibration induced by blasting during the construction of the Istanbul Kadikoy-Kartal metro tunnel. The empirical relationships between the scaled distance and peak particle velocity were established in order to predict the influence on neighboring buildings and structures [10]. Ocak and Bilgin studied the performance of a roadheader, impact hammer and drilling and blasting method in the excavation of metro station tunnels in Istanbul and gained machine utilization time and average net cutting rate of each machine [11]. De et al. studied the effects of a surface explosion through a combination of physical model tests and numerical modeling. The influence of the barrier thickness in reducing the explosion-induced strains, stresses, and pressures on the tunnel was analyzed [12]. Park and Jeon proposed an air-deck method to reduce blast-induced vibration in the direction of tunneling, and its effect was investigated through numerical and experimental studies [13]. Masoudi and Sharifzadeh studied the reinforcement selection for deep, high-stress tunnels in preliminary design stages using a ground demand and support capacity approach. This covered methods to measure the energy dissipation capacities of rockbolts, and the applicable range of each type of rockbolt was presented [14]. Feldgun et al. presented a comprehensive approach to simulate the effects of an explosion in a buried infrastructure tunnel on the soil surface and nearby tunnels. This simulation considered all stages of this complex process, including the detonation of the internal explosive charge, the shock wave propagation through the air in the tunnel, and the following interaction with the cavity lining. The simulation then examined the soil-structure dynamic interaction [15]. Lin et al. proposed a novel fuzzy model for identifying high-risk factors during excavations in urban karst geological environments [16]. Qin and Zhang analyzed the influence of the maximum charge on the vibration speed of the existing tunnel by comparing the influence of adjacent tunnel blasting team on the existing tunnel simulated by ANSYS LS-DYNA with the actual monitoring results [17]. Jiang et al. focused on safety of buried pressurized gas pipelines subject to blasting vibrations induced by metro foundation pit excavation [18, 19]. In order to control boulder deep-hole blasting-induced vibrations to a neighboring metro shaft, the damping hole and the isolation hole and changing the charging layout of the blasting areas were applied [20]. Also, Liu et al. optimized blasting scheme of metro stations subsurface excavating oblique through pile foundations of existing elevated light rail lines [21].

This paper focuses on the blasting excavation of the Taiguhui foundation pit in Guangzhou, China. This pit is adjacent to Shipaiqiao Station of Guangzhou Metro Line 3. Vibration of blasting excavation with small quantity of explosives is tested, and a typical vibration curve of blasting seismic wave is gained. The three-dimensional numerical calculation model of rock mass and metro lining is established by the finite difference software FLAC3D. On that base, the dynamic response characteristics of metro lining and rock mass under different load conditions are calculated and analyzed. The relationships between maximum displacement and vibration velocity of lining under different

dynamic load conditions are calculated and analyzed. The prediction formula of metro lining PPV is established, which can guide the parameters' design of foundation pit blasting.

## 2. Overview of Foundation Pit Blasting Construction

*2.1. General Engineering Situation.* The foundation pit is at the northwest corner of the intersection of Tianhe Road and Tianhe East Road in Guangzhou City, China. The project consists of a podium building and three towers of 30, 45, and 31 stories. The building basement is four stories deep, and the foundation pit is 260 m × 160 m. The excavation depth of the foundation pit is 27 m. The enclosure structure of the foundation pit is a continuous concrete wall. The building's foundation is the enlarged foundation of a manual digging pile, the diameter of the building pile foundation ranges from 1.5 to 2.8 m, and the pile diameter of the towers is larger than that of the podium building. According to the geological data of this project, it would be difficult to excavate the foundation pit and pile foundation of the buildings in the middle weathered rock stratum using a machine, so a blasting method is needed.

The foundation pit is in a complex environment. The east side is on Tianhe East Road, which is a busy road. The south side is on Tianhe Road, which is a main road with many municipal pipelines laid underneath. Shipaiqiao Station of Guangzhou Metro Line 3 is about 32–36 m from the side of the foundation pit. It is about 10 m between the pedestrian channel and the pit. Therefore, the harmful effect of the blasting construction must be controlled.

The surrounding environment is shown in Figure 1. The enclosure structure and the rock and soil conditions of the foundation pit are shown in Figure 2.

The geological survey results show that the buried depth of static groundwater level is 0.8~4.6 m. The main aquifers of the site are the pore water in miscellaneous fill soil, silt layer, and bedrock fissure water. The pore water in miscellaneous fill is perched water, and the water level fluctuates with seasons. The silt layer is confined water, which is vertically infiltrated by the upper stagnant water and laterally supplied by this layer. Bedrock fissure water mainly exists in strongly weathered and moderately weathered rock strata, which belongs to confined water and is mainly supplied by fissure water laterally. Meanwhile, lateral seepage is the main form of drainage.

*2.2. Blasting Program.* The excavation blasting construction mainly includes manual excavation pile blasting and foundation pit blasting of stone. Different blasting methods are adopted according to their respective engineering characteristics.

*2.2.1. Manual Digging Pile Blasting Plan.* Short-hole bench blasting can be used for the weathered bedrock section of a manual hole digging pile. The holes should be arranged as central cut, caving, and contour holes. Accounting for the blasting damage and convenience of construction, the

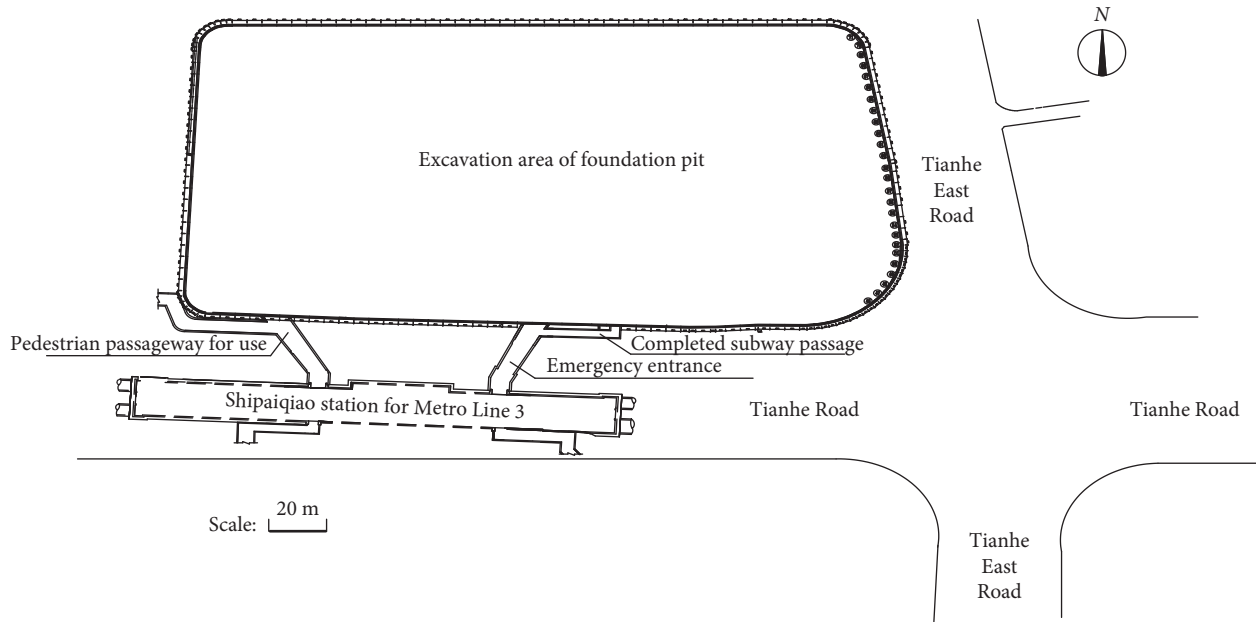
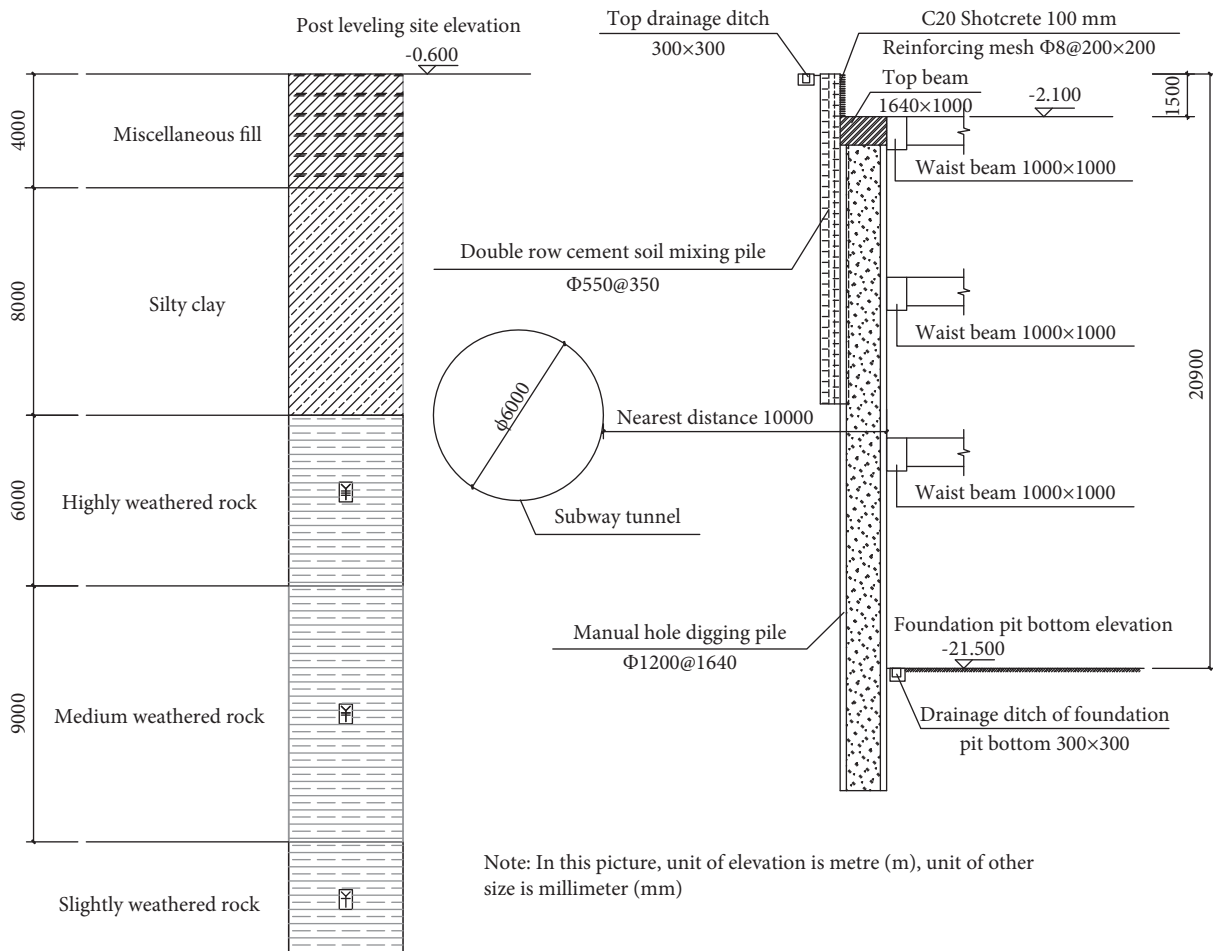


FIGURE 1: Surrounding engineering environment.



Note: In this picture, unit of elevation is metre (m), unit of other size is millimeter (mm)

FIGURE 2: Enclosure structure and rock and soil conditions of the foundation pit.

opening position of the contour hole is 0.2–0.3 m from the design outline. A millisecond-delay detonator is used to achieve millisecond-controlled blasting, and protective measures should be taken to cover the pile wellhead to avoid flying stones.

**2.2.2. Foundation Pit Blasting Plan.** The foundation pit is in the downtown area. There are buildings, roads, and underground pipelines around the blasting site. Blasting vibration and flying stones should be strictly controlled, and short-hole bench blasting with 2.0–3.0 m in depth should be adopted.

According to the rock strata exposure condition of the foundation pit, the blasting area is divided into two regions. The position of the bench in the center of the foundation pit, the drill, and the blast with a hand-held drilling rig are selected to form a small bench, around which blasting excavation occurs. Because the resistance lines of the bench blasting all point to the wider area of the foundation pit center, it is beneficial to reduce the production of flying stones.

To ensure the safety of nearby metro station, harmful effects of blasting must be controlled, a protective layer should be reserved at a distance of 2.0 m from the retaining structure of the foundation pit, and the rock should be broken by a crushing hammer to ensure the stability of the retaining structure.

The excavation sequence of the foundation pit is shown in Figure 3. For blasting vibration controlling, A region and B region were divided into several detonations.

**2.3. Blasting Parameters.** Air leg drill with the model of YT-28 is adopted for blast hole drill, and the diameter of the drill hole is 42 mm.

Dynamite: emulsion explosive is used, and the diameter of the roll is 32 mm.

The bench height of short-hole bench blasting is 2–3 m, the borehole depth is 2.2–3.2 m, the borehole spacing is 1.0–1.2 m, the row spacing is 0.9–1.2 m, and the front and rear rows are formed using a plum blossom pattern hole.

The blasting hole depth of the manual digging pile is 1.0 m, the cutting hole and hollow hole depths are both 1.2 m, and the blasting hole circle distance ranges from 0.3 to 0.5 m.

A millisecond detonator and a hole bottom continuous charge structure are used, a detonation charge pack is placed in the middle or lower part of the charge section, and the noncharge section is plugged with rock powder.

**2.4. Blasting Vibration Monitoring and Research.** In the construction site, the upper ground is soil and the lower ground is weathered rock, causing the propagation of the blasting vibration wave to attenuate rapidly. The blasting vibration is monitored by the vibrations of NUBOX-6016 according to a field test and regression analysis, and the blasting vibration attenuation law is

$$v = 160 \left( \frac{\sqrt[3]{Q}}{R} \right)^{1.7}, \quad (1)$$

where  $v$  is the vibration velocity,  $Q$  is the charge quantity, and  $R$  is the distance between the blasting area and blasting vibration measuring point.

A typical curve of the vibration velocity time history is shown in Figure 4.

For the blasting construction of the surrounding buildings and roads, the allowable vibration velocity of Guangzhou City is less than 2.0 mm/s.

The maximum amounts of charge at different distances, as calculated by equation (1), are shown in Table 1.

The minimum distance between the exit passage entrance of Shipaiqiao Station of Metro Line 3 and the side of the foundation pit is approximately 10 m. According to Table 1, the maximum charge per blasting section is 0.44 kg, which seriously affects the construction schedule. However, the allowable velocity of the traffic tunnel in the *technical specification for retaining and protection of building foundation excavations in Guangzhou area* is less than 15.0 cm/s [22]. According to equation (1), the maximum amount of the corresponding single section is 15.34 kg, which is quite different from the values in Table 1.

Based on this, the stress and deformation of the metro tunnel under different blasting dynamic loads are analyzed with FLAC3D software according to the typical time history curve of the vibration velocity obtained from the test. The numerical simulation results can guide blasting engineering practice.

### 3. Numerical Simulation Analysis of the Influence of a Blasting Dynamic Load on an Adjacent Tunnel

#### 3.1. Basic Assumptions.

- (1) The tunnel lining is a whole reinforced concrete structure; the formation distribution of the rock and soil is stratified
- (2) The tunnel lining is in close contact with the surrounding strata
- (3) Ignoring the influence of the rheological characteristics of the rock and the soil mass, as well as joints, fractures, and possible water in the rock mass, the rock mass and lining are taken as a uniform, continuous, isotropic medium

#### 3.2. Calculation Model and Parameters

**3.2.1. Calculation Model.** The metro tunnel outside diameter is 6.0 m, the inner diameter is 5.4 m, the lining thickness is 0.3 m, the tunnel center buried depth is 12 m, and the space between the tunnel center and the foundation pit edge is calculated as 10 m for safety. The relationships are shown in Figure 5.

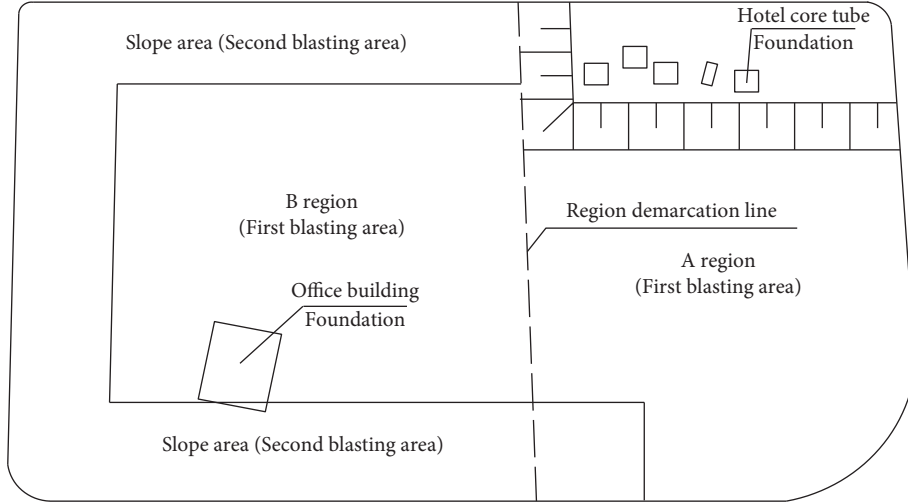


FIGURE 3: Blasting subsequence of the foundation pit.

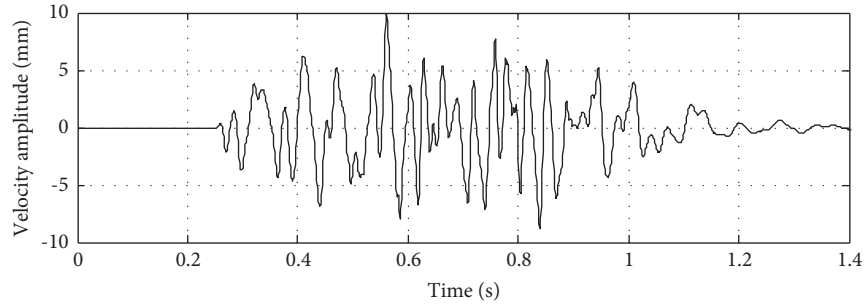


FIGURE 4: Typical vibration curve of a blasting seismic wave.

TABLE 1: Permitted maximum charge of one section.

Distance (m)	10	12	16	18	20	25	30
Charge (kg)	0.44	0.76	1.79	2.56	3.51	6.85	11.83

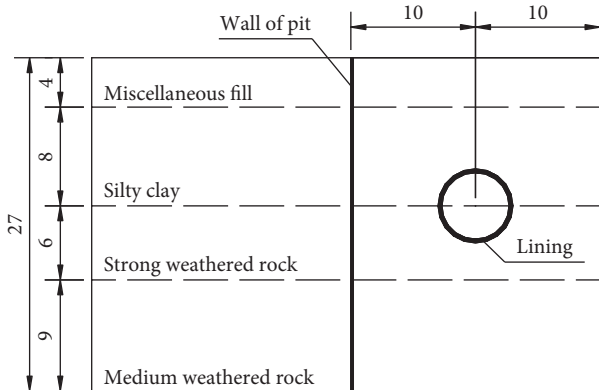


FIGURE 5: Position relationships between the tunnel and the pit (unit: m).

The effect of the blasting dynamic load on the metro tunnel lining, regardless of the foundation pit supporting structure, is modeled using only the tunnel lining, soil, and rock mass, as shown in Figure 6.

The coordinate system in the calculation model is set according to the following conditions. The center of the metro tunnel is taken as the original point (0, 0, 0). The trending direction of the tunnel is set as the Y axis, and the direction oriented perpendicular to the paper is set as positive. The direction perpendicular to the tunnel trending direction is set as the X axis, and the right direction is set as positive. The vertical direction of gravity is set as the Z axis, and the upward direction is set as positive. The model size is 10 m × 20 m × 27 m (trending length × width × height). According to the abovementioned parameters, the calculation model of the metro tunnel and rock mass is established as shown in Figure 6.

During the calculation, the rock mass is modeled using the Mohr–Coulomb elastic-plastic constitutive model. The principal stress in three directions of the rock and soil can be assumed to be  $\sigma_1$ ,  $\sigma_2$ , and  $\sigma_3$ , with  $\sigma_1 > \sigma_2 > \sigma_3$ , so the Mohr–Coulomb yield criterion is expressed as

$$\begin{cases} f^s = \sigma_1 - \sigma_3 N_\phi + 2c\sqrt{N_\phi} \\ f^t = \sigma_3 - \sigma^t \end{cases}, \quad (2)$$

where  $\sigma_1$  is the maximum principal stress,  $\sigma_3$  is the minimum principal stress,  $\phi$  is the internal friction angle,  $c$  is the cohesion,  $\sigma^t$  is the tensile strength,  $\sigma_{\max}^t = c/\tan \phi$ , and  $N_\phi = 1 + \sin(\phi)/1 - \sin(\phi)$ . When  $f^s = 0$ , the material will



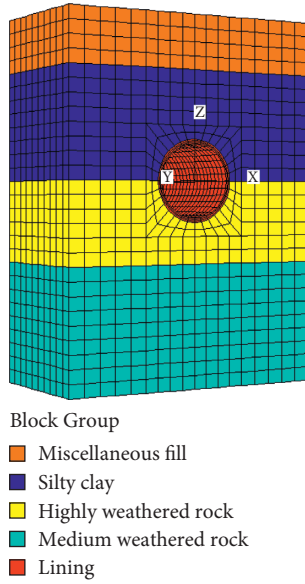


FIGURE 6: Calculation model of FLAC3D.

experience shear failure; when  $f^t = 0$ , the material will experience tensile failure.

**3.2.2. Boundary Condition.** The FLAC3D dynamic calculation is based on the results of a static calculation whose calculation boundaries are set as follows. The Z-direction constraints are imposed on the bottom of the model, and the other five surfaces are set as free boundaries. During the dynamic calculation, the X-direction constraints are imposed on either side of the model for incident wave absorption. The Y-direction constraints are imposed in the tunnel trending direction. The Z-direction constraints are imposed for the model. The stress boundary condition is controlled using the upper section of the model, and the static boundary model is used for dynamic reflection boundary conditions.

**3.2.3. Selection of Damping.** When excavation blasting is performed, the blasting seismic wave propagation in the formation causes the vibration energy to gradually decay due to damping, and the rock particle vibration eventually stops. During the dynamic analysis, Rayleigh damping is used, with a minimum critical damping ratio of 0.1 and a minimum center frequency of 10 Hz.

**3.2.4. Application of Blasting Seismic Wave Load.** A separation of the wave and field technique is adopted for the applied dynamic load. The blasting seismic load is translated to an equivalent load and applied directly to the artificial boundary. A blasting vibration velocity wave can be transformed to a stress wave as follows [11]:

$$\sigma_n = 2(\rho C_p)v_n, \quad (3)$$

$$\sigma_s = 2(\rho C_s)v_s, \quad (4)$$

where  $\sigma_n$  is the applied normal stress,  $\sigma_s$  is the applied shear stress,  $\rho$  is the density of the transmission medium,  $C_p$  is the longitudinal wave propagation of the medium,  $C_s$  is the transverse wave velocity, and  $v_n$  and  $v_s$  are, respectively, the normal and tangential particle vibration velocities of the imposed blasting vibration load.

In Figure 4, the peak velocity of the curve is about 1.0 cm/s, and four kinds of construction conditions are designed. The blasting vibration velocity amplitude of each condition and the corresponding maximum charge quantity can be calculated according to equation (1). The calculated results are shown in Table 2.

Because of the blasting construction on the medium weathered stratum in Figure 1, the dynamic load is applied in the lower-left (medium weathered rock) section of the model. According to equations (3) and (4), the blasting vibration velocity changes to a stress wave, the blasting seismic wave curve of Figure 4 is set as a benchmark, and the dynamic loads of different working conditions are multiplied by the appropriate factors.

**3.2.5. Physical and Mechanical Parameters.** The physical and mechanical parameters of the lining, soil, and rock mass for the numerical calculation are shown in Table 3.

## 4. Numerical Simulation Results and Analysis

**4.1. Numerical Simulation Results and Analysis of the Static Load.** According to the abovementioned model and parameters, the displacement and stress contour charts of the stratum and metro tunnel lining in static load are determined, as shown in Figures 7 and 8.

Figure 7 shows the X (horizontal) and Z (vertical) directions of the strata and tunnel lining contour chart. From this figure, the following conclusions can be drawn:

- (1) Under the action of self-weight stress, the excavation of the metro tunnel accelerates stratum consolidation, causing both horizontal and vertical displacements. The displacement of each stratum layer is different. Miscellaneous fill develops maximum displacement, and rock strata develop minimum displacement. The maximum horizontal and vertical displacements of the miscellaneous fill are 3.363 mm and 65.952 mm, respectively. Silty clay has maximum horizontal and vertical displacements of 3.0 mm and 50.0 mm, respectively. The horizontal and vertical displacements of the strata below the medium weathered rock are less than 1.0 mm and 10 mm, respectively.
- (2) Because of the self-weight stress of the upper layer and the lining itself, the horizontal displacement of the lining's left side is greater than in the right side. The maximum horizontal displacement is 0.925 mm, and the horizontal displacement in the top and bottom of the lining is low. The vertical displacement of the lining top is 5 mm. Because of the highly weathered rock at the bottom, the displacement of the lining bottom is in the range of 2.56–2.75 mm.



TABLE 2: Vibration velocities and maximum charges of signal shots for different conditions.

Condition	Vibration velocity of tunnel (cm/s)	Vibration velocity of pit edge (cm/s)	Maximum charge of signal shot (kg)
1st condition	5	105.154	3.814
2nd condition	10	210.309	12.961
3rd condition	15	315.463	26.508
4th condition	20	420.617	44.041

TABLE 3: Calculation parameters for rock, soil, and lining.

Name of stratum	Depth (m)	Density (kg/m <sup>3</sup> )	Poisson's ratio	C (kPa)	$\Phi$ (°)	Bulk modulus (MPa)	Shear modulus (MPa)	Tensile strength (kPa)
Miscellaneous fill	4	1800	0.35	10	10	5.0	1.7	
Silty clay	8	1900	0.34	25	15	16.7	6	25
Highly weathered rock	6	2200	0.3	120	25	416.7	192.3	500
Medium weathered rock	9	2400	0.27	500	28	1449.3	787.4	1600
Lining	0.3	2600	0.17	3200	62	17424.2	14743.6	1800

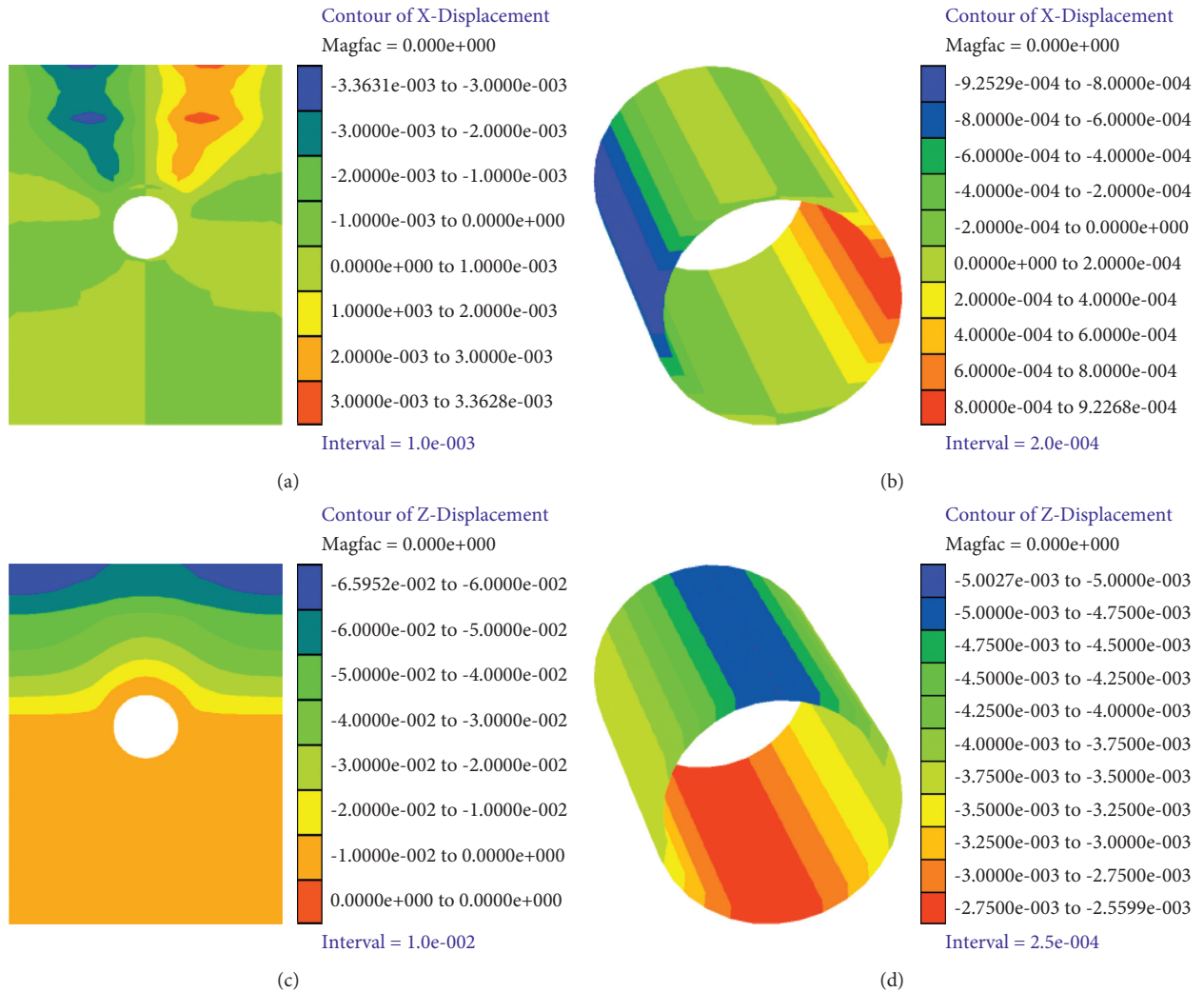


FIGURE 7: Displacement contour chart of static load. (a) X-displacement of rock mass. (b) X-displacement of lining. (c) Z-displacement of rock mass. (d) Z-displacement of lining.

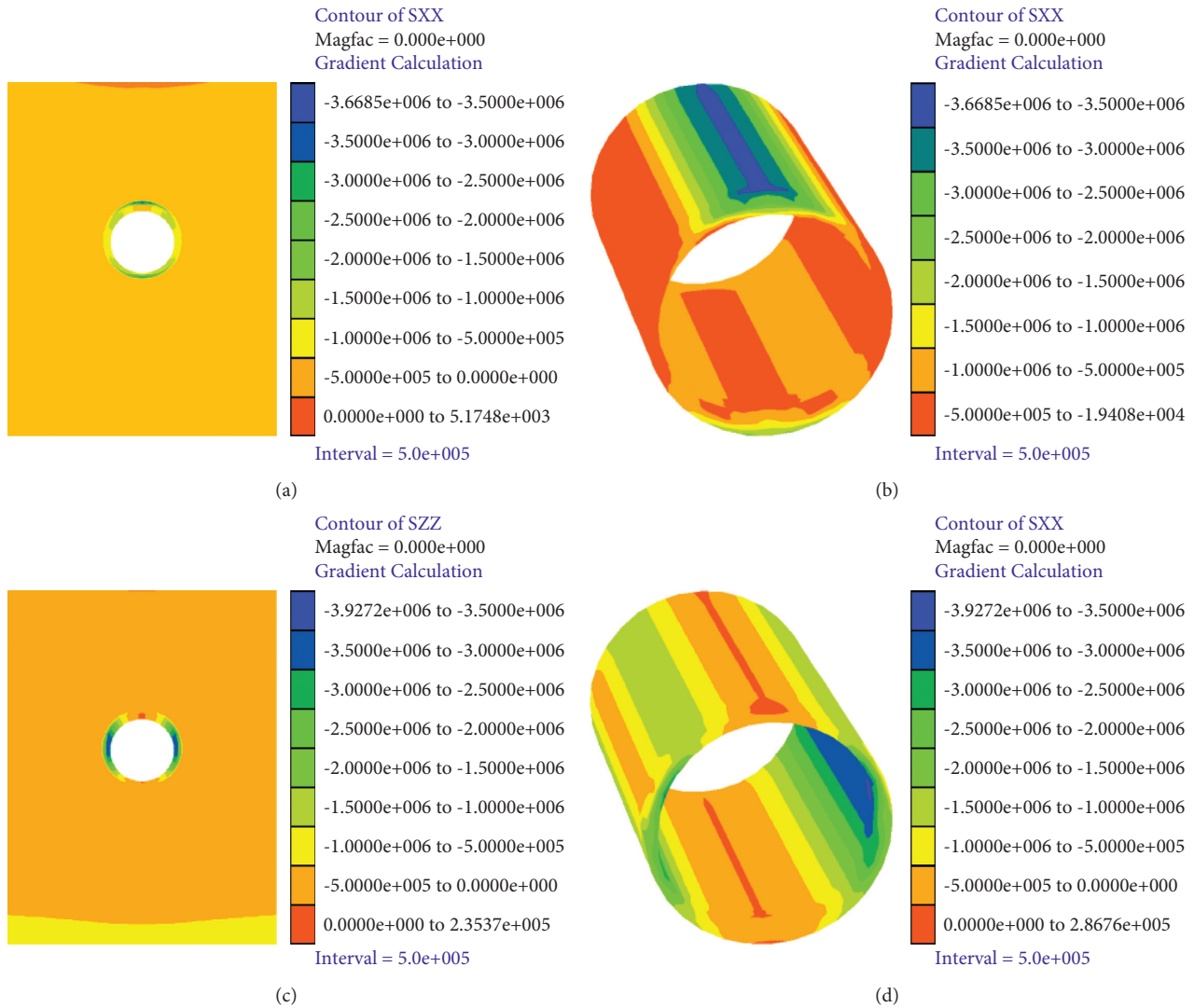


FIGURE 8: Stress contour chart of static load. (a) X-direction stress of rock mass. (b) X-direction stress of lining. (c) Z-direction stress of rock mass. (d) Z-direction stress of lining.

This deformation can meet the requirements of the *Code for Design of Metro for China* [23].

Figure 8 is the stress distribution contour chart of the X (horizontal) and Z (vertical) directions of the strata and the tunnel lining. The contour shows the strata and the tunnel lining, the compression force, and the distributed symmetry with the central vertical line of the lining. The maximum stress of the strata in the X and Z directions is 500 kPa, and the maximum horizontal stress at the top of the miscellaneous fill is only 5.175 kPa.

In Figure 8(b) and 8(d), the horizontal direction stress of the lining's outside wall is greater than that of the inner wall, and the maximum stress at the lining top and bottom sides is 3.669 MPa. The vertical direction stress of the lining's inner wall is greater than that of the outside wall, with a maximum value of 3.927 MPa. Both stresses are far less than the compressive strength of concrete.

It can be seen that the stress and deformation of the stratum and tunnel lining are in the safe range under the action of the self-weight stress.

**4.2. Numerical Simulation Results and Analysis of Dynamic Load.** The geotechnical engineering dynamic analysis using FLAC3D is based on the static analysis results. Before the dynamic calculation, the displacement of each direction is set to zero. Then, the boundary conditions are set, the blasting dynamic load is applied, and the calculation is carried out. The stress and displacement of the rock mass and lining under different blasting dynamic loads are calculated. There are too many images of calculation results for four kinds of conditions, and the distribution law is almost quite similar. Therefore, only the calculations of the results for the first and fourth conditions are listed, as shown in Figures 9 and 10.

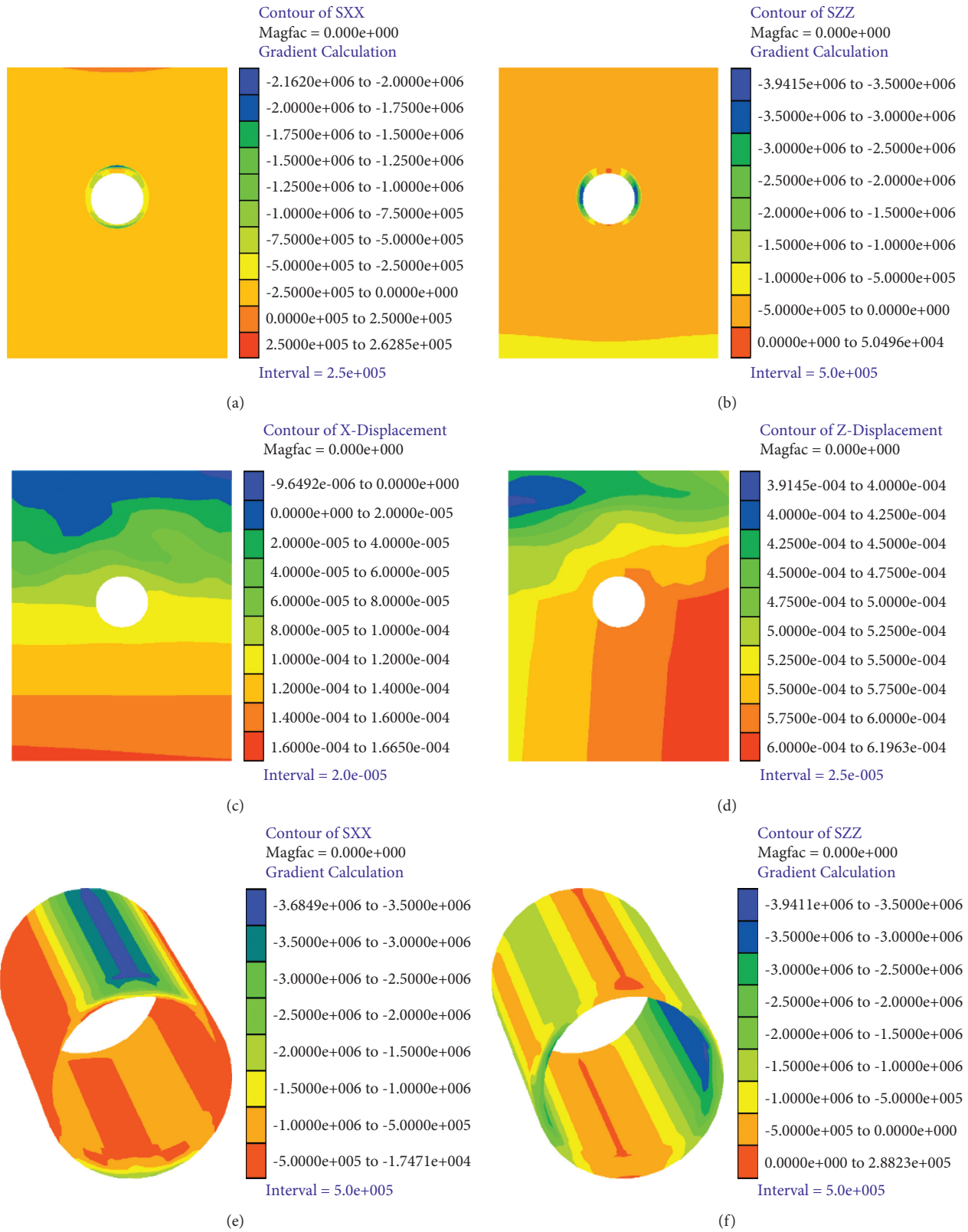


FIGURE 9: Continued.

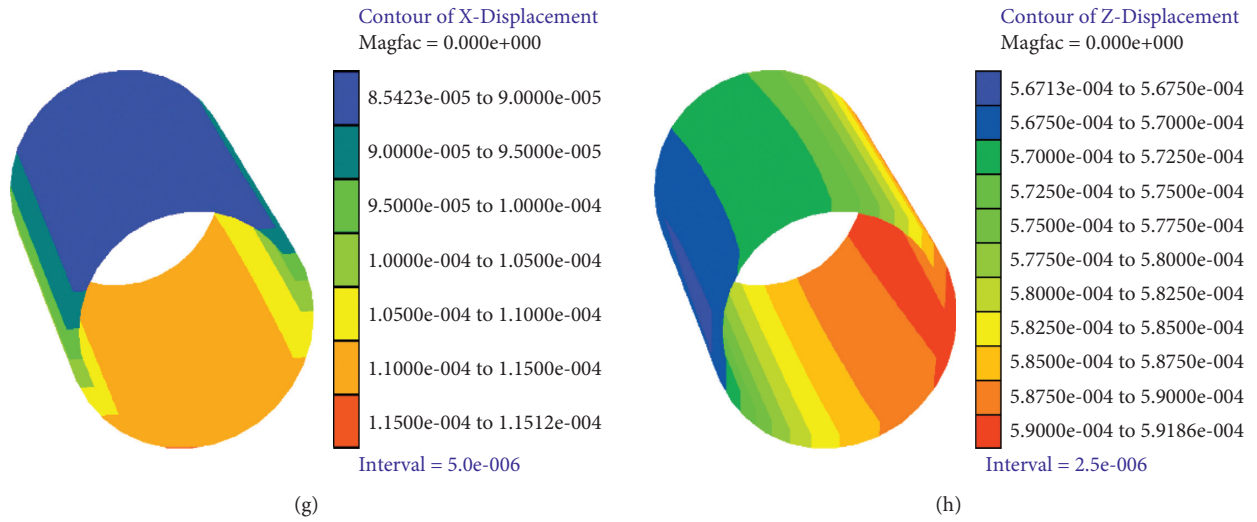


FIGURE 9: Displacement and stress contour chart of the 1st condition. (a) X-direction stress of the model. (b) Z-direction stress of the model. (c) X-displacement of the model. (d) Z-displacement of the model. (e) X-direction stress of the lining. (f) Z-direction stress of the lining. (g) X-displacement of the lining. (h) Z-displacement of the lining.

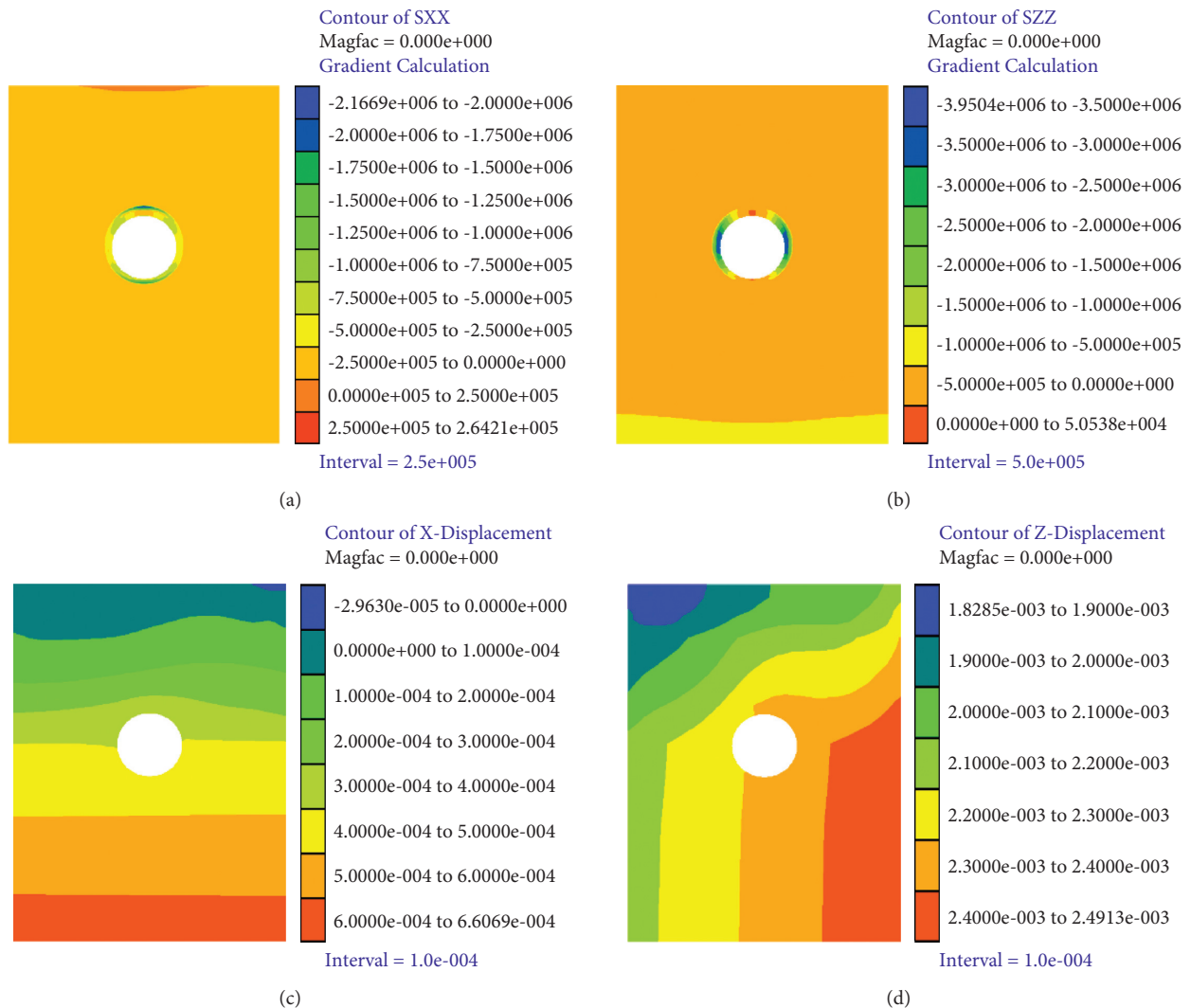


FIGURE 10: Continued.

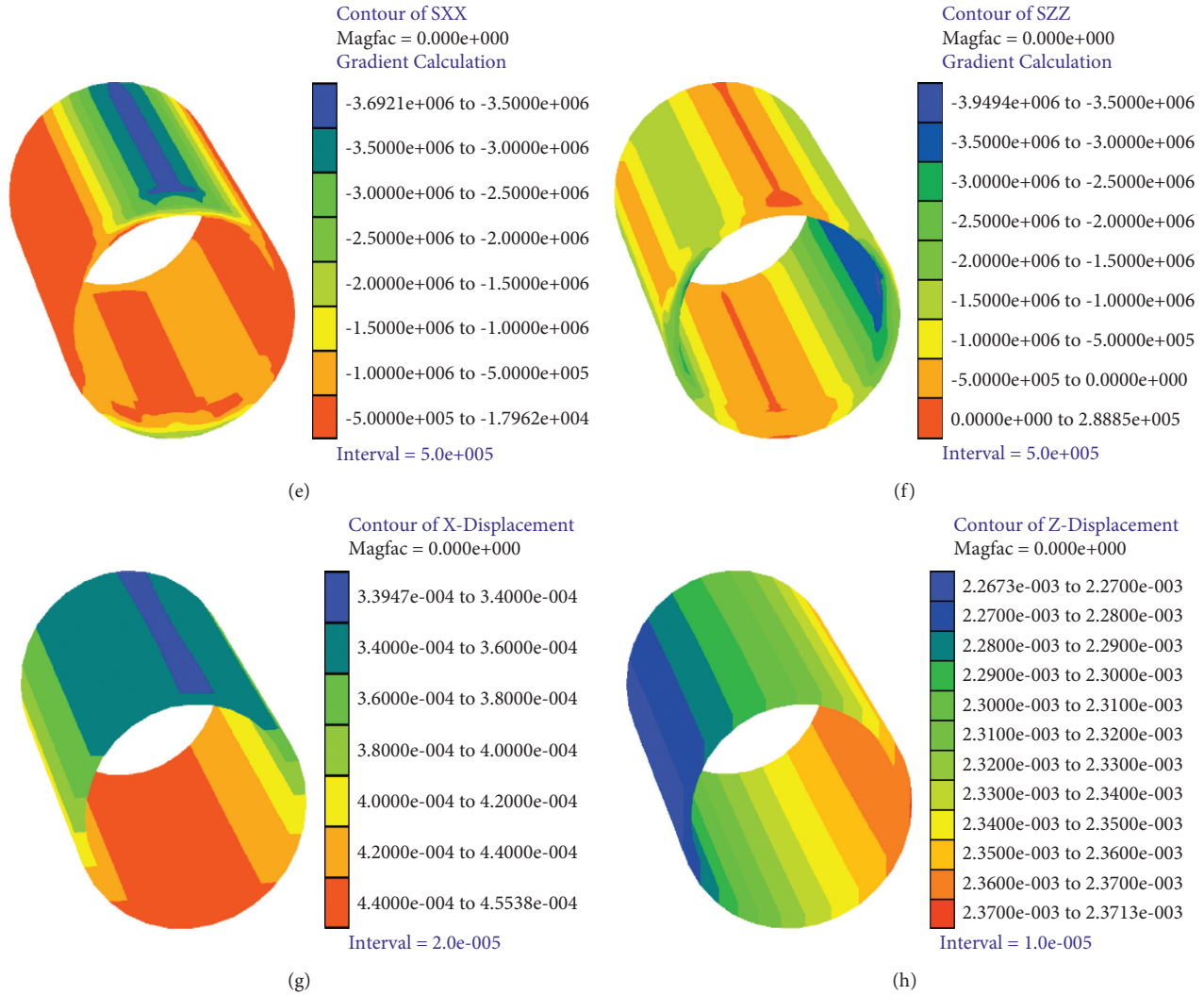


FIGURE 10: Stress contour chart of the fourth condition. (a) X-direction stress of the model. (b) Z-direction stress of the model. (c) X-displacement of the model. (d) Z-displacement of the model. (e) X-direction stress of the lining. (f) Z-direction stress of the lining. (g) X-displacement of the lining. (h) Z-displacement of the lining.

Figure 9 shows that after applying the blasting dynamic load, the deformation of the metro tunnel lining in the geotechnical engineering model is quite small, with a magnitude of  $10^{-4}$  m, so the deformation will not have an adverse effect. For the rock mass, because of the dynamic load in the lower-left part of the model, a relatively large displacement appears in the region, with maximum horizontal and vertical displacements of  $1.666 \times 10^{-4}$  m and  $6.196 \times 10^{-4}$  m, respectively.

For the metro tunnel lining, because of the blasting dynamic load applied in the bottom left of the model, the deformations around the inside and outside of the lining are not the same.

- (1) The horizontal displacement is greater at the top, and the displacement at the bottom of the outer wall is greater than that of the wall. The maximum horizontal displacement is  $1.153 \times 10^{-4}$  m, and at the bottom of the inside, the displacement is  $1.151 \times 10^{-4}$  m.

- (2) For the vertical displacement, the right side is larger than the left. For the right side wall, the maximum displacement of outer is  $5.924 \times 10^{-4}$  m and the maximum displacement of inner is  $5.912 \times 10^{-4}$  m, the maximal displacement of the left side is  $5.675 \times 10^{-4}$  m.

As shown in Figure 10, after applying the blasting dynamic load, the metro tunnel lining, rock, and soil mass are mainly compressive stress. The stresses around the interior and exterior walls are different. The maximum horizontal stress is 3.685 MPa on the top of the lining walls and 2.575 MPa for the lining at the bottom of the outer wall. The maximum vertical stress in the lining of the left side is 3.941 MPa, and the compressive stress for the lining of the right side is 3.941 MPa.

4.3. Analysis of Numerical Simulation Results in Different Conditions. To analyze the relationship between the applied

blasting dynamic load and the maximum displacement, we summarize the stress of the tunnel lining, the maximum displacement, and the stress of the lining under static conditions and a dynamic load in Table 4, from which we can see the following:

- (1) The stress and displacement of the metro tunnel lining increase as long as the blasting dynamic load strength improves.
- (2) Compared to the static load, after applying the blasting dynamic load, the displacements of the subway tunnel lining are positive. This is shown in the tunnel lining toward the right and upward from the blasting dynamic load. The displacement of the 4th condition is the largest, with a vertical displacement of  $23.719 \times 10^{-4}$  m and a horizontal displacement of  $4.554 \times 10^{-4}$  m, both within the allowable range [13].
- (3) After applying the blasting dynamic load, the maximum stress of the lining increases slightly. The maximum stress growth rates for the different conditions are shown in Table 5, from which we see that the growth rate of the horizontal stress on the top is greatly influenced by the blasting dynamic load compared to the rate of the other stress and the growth rate of the horizontal stress in the bottom is less affected by the blasting dynamic load.

The relationship between the tunnel lining maximum displacement and the vibration velocity for different conditions is shown in Figure 11, from which we can see that the vertical displacement is more vulnerable than the horizontal displacement to the impact of the blasting dynamic load.

According to Figure 11, the displacement of the tunnel lining increases linearly with the vibration velocity.

The vertical displacement of the lining right side is

$$\delta_{z-r} = 1.1884v - 0.0251 \text{ (correlation coefficient is 0.99),} \quad (5)$$

the vertical displacement of the lining left side is

$$\delta_{z-l} = 1.1365v \text{ (correlation coefficient is 0.99),} \quad (6)$$

the horizontal displacement of the lining bottom is

$$\delta_{x-b} = 0.2271v - 0.0131 \text{ (correlation coefficient is 0.99),} \quad (7)$$

and the horizontal displacement of the lining top is

$$\delta_{x-t} = 0.1677v - 0.0526 \text{ (correlation coefficient is 0.99),} \quad (8)$$

where  $\delta_{z-r}$  is the vertical displacement in the right side of the lining,  $10^{-4}$  m;  $\delta_{z-l}$  is the vertical displacement in the left side of the lining,  $10^{-4}$  m;  $\delta_{x-b}$  is the horizontal displacement in the bottom of the lining,  $10^{-4}$  m;  $\delta_{x-t}$  is the horizontal displacement in the top of lining,  $10^{-4}$  m; and  $v$  is the blasting vibration velocity of the lining, cm/s.

From Figure 11 and equations (5)–(8), it can be found that the vertical displacement of the right side of the metro tunnel lining increases when the blasting vibration velocity is fastest, so the vertical displacement of the lining top can be used as a control index of the influence of the blasting construction on the metro tunnel. As calculated by equation (5), the corresponding vibration velocity of the lining displacement of 1.0 mm is 8.436 cm/s, and the maximum initiation explosive charge is 5.556 kg. It is more manageable than equation (1) according to the allowable limit vibration speeds; in equation (1), the charge can only be calculated according to the allowable vibration velocity limit of 2.0 cm/s or 15.0 cm/s.

## 5. Optimization of Blasting Parameters

During blasting construction, the maximum initiation explosive charge for the design of the blasting parameters is 5.0 kg.

### 5.1. Blasting Parameters for the Manual Digging Pile

**5.1.1. Blast Holes Layout.** The diameters of the manual digging piles range from 1.50 to 2.80 m, and their thickness is 0.3 m. The diameter of the blasting space ranges from 1.80 m to 3.10 m.

Depth of hole:  $L = 1.0$  m.

Depth of cut hole:  $L_1 = (1.2 \sim 1.4)$   $L = 1.2 \sim 1.4$  m. The chosen value is 1.2 m.

**5.1.2. Calculation of Explosive Charge.** The explosive charge is calculated as follows:

$$Q_1 = q_1 S L \eta, \quad (9)$$

where  $Q_1$  is the charge of a single blast in the pile in kg,  $q_1$  is the explosive consumption of the unit volume rock in  $\text{kg/m}^3$ ,  $S$  is the blast area in  $\text{m}^2$ ,  $L$  is the depth of the blast hole in m, and  $\eta$  is the blast hole utilization ratio.

The explosive diameter is 32 mm in the field. Taking the 1.50 m diameter of the manual digging pile as an example (the excavation diameter is 1.8 m), the explosive consumption of rock is  $2.0 \text{ kg/m}^3$ , so the total charge of a single blast is calculated as follows:

$$Q_1 = 2.0 \times 2.54 \times 1.2 \times 0.85 = 4.32 \text{ kg.} \quad (10)$$

In actual construction, blasting parameters are shown in Table 6, and Figure 12 shows holes' arrangement.

**5.1.3. Charge Structure and Initiation Style.** Boring priming is adopted. A reasonable initiation time can improve the blasting effect and reduce blasting vibration. The initiation sequence is as follows: the delay time is 25 ms for cut holes, 75 and 110 ms for cut spreader holes, and 200–460 ms for contour holes.



TABLE 4: Maximum displacement and stress of linings for different conditions.

Condition	Velocity (cm/s)	Vertical displacement ( $10^{-4}$ m)		Horizontal displacement ( $10^{-4}$ m)		Z-direction stress (MPa)		X-direction stress (MPa)	
		Top	Bottom	Left	Right	Top	Bottom	Left	Right
Static load	0	-50.03	-27.5	-9.253	9.239	-3.927	-3.927	-3.669	-2.568
1st condition	5	5.675	5.924	0.9	1.153	-3.942	-3.941	-3.685	-2.575
2nd condition	10	11.35	11.821	1.70	2.275	-3.945	-3.944	-3.686	-2.577
3rd condition	15	17.1	17.855	2.60	3.429	-3.950	-3.949	-3.692	-2.579
4th condition	20	22.7	23.719	3.395	4.554	-3.950	-3.949	-3.692	-2.579

TABLE 5: Stress growth rates of linings for different conditions (unit: %).

Condition	Z-direction stress		X-direction stress	
	Left	Right	Top	Bottom
1st condition	0.369	0.354	0.447	0.277
2nd condition	0.458	0.438	0.477	0.374
3rd condition	0.593	0.568	0.632	0.460
4th condition	0.596	0.565	0.643	0.463

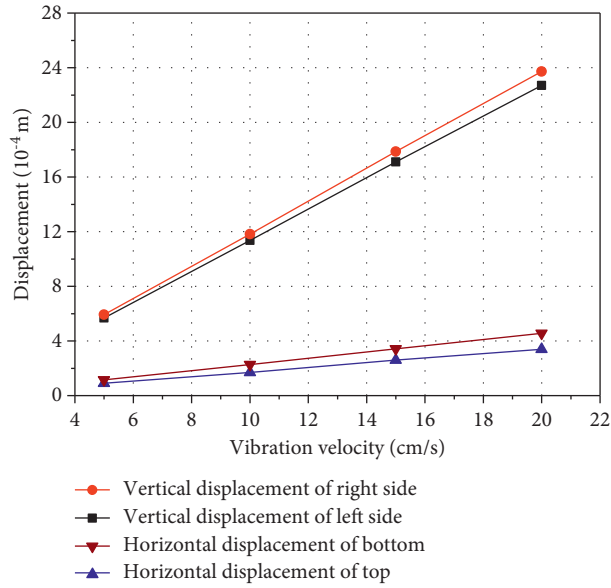


FIGURE 11: Relationship between maximum displacement and vibration velocity of the lining.

TABLE 6: Blasting parameters of a pile with net diameters of 1.5 m.

No. of circle	No. of hole	Diameter of circle (mm)	Depth of hole (m)	Distance of hole (mm)	Distance of circle (mm)	Quantity of hole (unit)	Charge of unit hole (kg)
I	1-4	800	1.20	560		4	0.50
II	5-12	1600	1.0	530	300	8	0.30
Total						12	4.40

## 5.2. Blasting Parameters for Foundation Pit Rock Mass

5.2.1. *Blast Hole Layout.* Short-hole bench blasting of 2.0–3.0 m in height is adopted for foundation pit excavation, and the holes of nearby rows form a triangle.

5.2.2. *Calculation of Explosive Charge.* The explosive charge is calculated as follows:

$$Q_2 = q_2 abH, \quad (11)$$

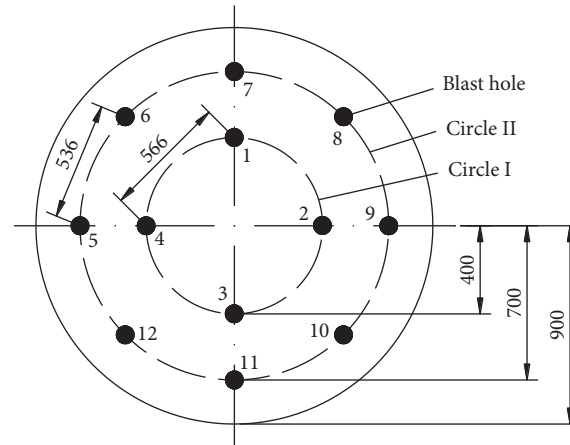


FIGURE 12: Blast-hole layout of a pile with net diameters of 1.5 m (unit: mm).

TABLE 7: Blasting parameters of the foundation pit.

Depth of hole (m)	$a \times b$ (m)	$q_2$ ( $\text{kg}\cdot\text{m}^{-3}$ )	Charge of unit hole (kg)	Length of stemming (m)
2.0	$1.0 \times 0.9$	0.45	0.8	1.2
2.5	$1.1 \times 0.9$	0.45	1.1	1.4
3.0	$1.2 \times 1.0$	0.45	1.6	1.4

where  $Q_2$  is the charge of a single blast in the foundation pit in kg,  $q_2$  is the explosive consumption of the unit volume rock in  $\text{kg}/\text{m}^3$ ,  $a$  is the distance between the blast holes in  $m$ ,  $b$  is the distance between nearby rows in  $m$ , and  $H$  is the depth of the blast hole in  $m$ .

Blasting parameters of different depths can be calculated using equation (11). These are shown in Table 7.

The parameters are adjusted during construction according to the properties of the rock, blasting effect, and blasting vibration.

## 6. Conclusions

In this paper, a metro tunnel lining adjacent to the excavation blasting of a foundation pit is taken as a case study. Through the combination of vibration monitoring and numerical calculation, the effects of foundation pit blasting on metro tunnel lining are studied and analyzed. The main conclusions are as follows:

- (1) Under the blasting dynamic load, the tunnel lining displacement is within the allowable range, and the displacement increases linearly with the vibration velocity of the dynamic load. The vertical displacement is greater than the horizontal displacement and is influenced more by the blasting dynamic load.
- (2) Compared to the static load condition, the stress amplitude of the dynamic load condition increases by 0.227%–0.643%. The horizontal stress at the top of the tunnel lining is greatly influenced by the blasting dynamic load, and the horizontal stress at the bottom is less affected by the blasting dynamic load.
- (3) The tunnel lining vertical displacement is proposed as the control index of the influence of blasting construction on the metro tunnel.

- (4) The prediction formula of metro lining PPV is established; according to the formula, blast hole layout and explosive charge of unit hole for the manual digging pile and foundation pit rock mass are optimized.

## Data Availability

The data used to support the findings of this study are available from the corresponding author upon request.

## Conflicts of Interest

The authors declare that there are no known conflicts of interest associated with this publication.

## Acknowledgments

This work was supported by the National Natural Science Foundation of China (no. 51404010), the Natural Science Foundation of Anhui Province (no. 2008085ME163), and the Postdoctoral Science Foundation of Anhui Province (no. 2018B282).



## References

- [1] S.-S. Lin, S.-L. Shen, A. Zhou, and Y.-S. Xu, "Risk assessment and management of excavation system based on fuzzy set theory and machine learning methods," *Automation in Construction*, vol. 122, Article ID 103490, 2021.
- [2] S.-L. Shen, Y.-X. Wu, and A. Misra, "Calculation of head difference at two sides of a cut-off barrier during excavation dewatering," *Computers and Geotechnics*, vol. 91, pp. 192–202, 2017.
- [3] K. Elbaz, S.-L. Shen, Y. Tan, and W.-C. Cheng, "Investigation into performance of deep excavation in sand covered karst: a

- case report,” *Soils and Foundations*, vol. 58, no. 4, pp. 1042–1058, 2018.
- [4] Y.-F. Jin, Z.-Y. Yin, W.-H. Zhou, and X. Liu, “Intelligent model selection with updating parameters during staged excavation using optimization method,” *Acta Geotechnica*, vol. 15, no. 9, pp. 2473–2491, 2020.
  - [5] Q.-L. Cui, S.-L. Shen, Y.-S. Xu, H.-N. Wu, and Z.-Y. Yin, “Mitigation of geohazards during deep excavations in karst regions with caverns: a case study,” *Engineering Geology*, vol. 195, pp. 16–27, 2015.
  - [6] X. Xia, H. Li, Y. Liu, and C. Yu, “A case study on the cavity effect of a water tunnel on the ground vibrations induced by excavating blasts,” *Tunnelling and Underground Space Technology*, vol. 71, pp. 292–297, 2018.
  - [7] S. Koneswaran, D. P. Thambiratnam, and C. Gallage, “Blast response of segmented bored tunnel using coupled SPH-FE method,” *Structure*, vol. 2, no. 2, pp. 58–71, 2015.
  - [8] E. M. El Koursi, J.-L. Bruyelle, R. Seddon, and C. O’Neill, “Design solutions to improve resilience of metro vehicle to blast events,” *Transportation Research Part A: Policy and Practice*, vol. 118, pp. 280–291, 2018.
  - [9] J.-H. Shin, H.-G. Moon, and S.-E. Chae, “Effect of blast-induced vibration on existing tunnels in soft rocks,” *Tunnelling and Underground Space Technology*, vol. 26, no. 1, pp. 51–61, 2011.
  - [10] U. Ozer, “Environmental impacts of ground vibration induced by blasting at different rock units on the Kadikoy-Kartal metro tunnel,” *Engineering Geology*, vol. 100, no. 1–2, pp. 82–90, 2008.
  - [11] I. Ocak and N. Bilgin, “Comparative studies on the performance of a roadheader, impact hammer and drilling and blasting method in the excavation of metro station tunnels in Istanbul,” *Tunnelling and Underground Space Technology*, vol. 25, no. 2, pp. 181–187, 2010.
  - [12] A. De, A. N. Morgante, and T. F. Zimmie, “Numerical and physical modeling of geofoam barriers as protection against effects of surface blast on underground tunnels,” *Geotextiles and Geomembranes*, vol. 44, no. 1, pp. 1–12, 2016.
  - [13] D. Park and S. Jeon, “Reduction of blast-induced vibration in the direction of tunneling using an air-deck at the bottom of a blasthole,” *International Journal of Rock Mechanics and Mining Sciences*, vol. 47, no. 5, pp. 752–761, 2010.
  - [14] R. Masoudi and M. Sharifzadeh, “Reinforcement selection for deep and high-stress tunnels at preliminary design stages using ground demand and support capacity approach,” *International Journal of Mining Science and Technology*, vol. 28, no. 4, pp. 573–582, 2018.
  - [15] V. R. Feldgun, Y. S. Karinski, and D. Z. Yankelevsky, “The effect of an explosion in a tunnel on a neighboring buried structure,” *Tunnelling and Underground Space Technology*, vol. 44, pp. 42–55, 2014.
  - [16] S.-S. Lin, S.-L. Shen, A. Zhou, and Y.-S. Xu, “Novel model for risk identification during karst excavation,” *Reliability Engineering & System Safety*, vol. 209, Article ID 107435, 2021.
  - [17] Q. Qin and J. Zhang, “Vibration control of blasting excavation of large cross-section highway tunnel over metro line,” *Arabian Journal of Geosciences*, vol. 13, no. 17, Article ID 868, 2020.
  - [18] N. Jiang, T. Gao, C. Zhou, and X. Luo, “Effect of excavation blasting vibration on adjacent buried gas pipeline in a metro tunnel,” *Tunnelling and Underground Space Technology*, vol. 81, pp. 590–601, 2018.
  - [19] N. Jiang, B. Zhu, X. He, C. Zhou, X. Luo, and T. Wu, “Safety assessment of buried pressurized gas pipelines subject to blasting vibrations induced by metro foundation pit excavation,” *Tunnelling and Underground Space Technology*, vol. 102, Article ID 103448, 2020.
  - [20] Z. Zhang, Y. Li, S. Wang, H. Zhang, and Y. Qian, “Assessing and controlling of boulder deep-hole blasting-induced vibrations to minimize impacts to a neighboring metro shaft,” *Archives of Civil and Mechanical Engineering*, vol. 21, no. 2, Article ID 66, 2021.
  - [21] S. Liu, H. Su, and X. Si, “Optimization study on blasting scheme of metro stations subsurface excavating oblique through pile foundations of existing elevated light rail lines,” *Advances in Mechanical Engineering*, vol. 12, no. 6, Article ID 1687814020933063, 2020.
  - [22] Standard of Guangzhou, *Technical Specification for Retaining and Protection of Building Foundation Excavations in Guangzhou Area (GJB 02-98)*, (in China), p. 76, Guangzhou Institute of Geochemistry, Guangzhou, China Guangzhou Institute of Geochemistry, 1998.
  - [23] Standard of Guangzhou, *Code for Design of Metro for China*, Guangzhou Institute of Geochemistry, Guangzhou, China, in China, 2013.

## Research Article

# Prediction of Bench Blasting Vibration on Slope and Safety Threshold of Blasting Vibration Velocity to Undercrossing Tunnel

Li He <sup>1,2</sup>, Dongwang Zhong,<sup>2</sup> Yihe Liu <sup>2</sup> and Kun Song<sup>1</sup>

<sup>1</sup>Key Laboratory of Geological Hazards on Three Gorges Reservoir Area, Ministry of Education, China Three Gorges University, Yichang 443002, China

<sup>2</sup>Hubei Province Key Laboratory of Systems Science in Metallurgical Process, Wuhan University of Science and Technology, Wuhan 430065, China

Correspondence should be addressed to Yihe Liu; liuyihe96@163.com

Received 6 May 2021; Accepted 19 August 2021; Published 7 September 2021

Academic Editor: Nan Jiang

Copyright © 2021 Li He et al. This is an open access article distributed under the Creative Commons Attribution License, which permits unrestricted use, distribution, and reproduction in any medium, provided the original work is properly cited.

The reconstruction and expansion project of oil reserve base often faces the excavation and blasting of the slope and undercrossing tunnel at the same time. Due to the flammable and explosive liquid storage nearby, the tight construction period, and the high requirements of collaborative construction, once the blasting accident occurs, the consequences are unimaginable. To facilitate safe and timely cooperative blasting construction of the slope and undercrossing tunnel, a vibration monitoring test of the slope and tunnel surrounding rock is conducted. The vibration response characteristics of the rock surrounding the slope and tunnel are analyzed, and a mathematical prediction model for the peak particle velocity (PPV) with consideration of the influence of the relative slope gradient ( $H/D$ ) is established based on dimension analysis theory, which improves the prediction accuracy of PPV at the slope surface. ANSYS/LS-DYNA is used to establish a 3D finite element model for the slope and tunnel, and the dynamic response of the tunnel surrounding rock under blasting load is verified through field monitoring data. A linear statistical relationship between PPV and effective tensile stress (ETS) of the tunnel surrounding rock is established. The PPV safety criterion of the tunnel surrounding rock under blasting load is proposed to be 10 cm/s according to the first strength theory, and hence, the minimum safety distance from the tunnel working face to the slope surface is calculated to be 36 m. Finally, the excavation timing arrangement of the slope and tunnel is proposed, which has been successfully applied to the expansion project, and the construction period has been effectively shortened by 45 days while ensuring construction safety. The research results have great guiding significance to similar cooperative blasting excavation engineering for high slope and adjacent tunnel with safety and efficiency.

## 1. Introduction

Strategic petroleum reserves are the most important links in a national energy security system. As of 2015, China has built eight national petroleum reserve bases with a total reserve capacity of 28.6 million cubic meters, including seven surface and one underground oil storage depots. With the undertaking of large-scale construction projects related to these petroleum reserves, large numbers of adjacent petroleum pipeline tunnels passing through open high-steep slopes continue to emerge. During the excavation of the high-steep slope and petroleum pipeline tunnel, blasting, as a fast and efficient excavation method for hard rock masses,

has been widely used. Reasonable and proper evaluation of the impact of the blasting vibration and control of the detrimental effects of the vibration are the key technical issues to ensure the safety and stability of the slope and tunnel during blasting excavation, thus realizing the safe and efficient construction of national strategic petroleum reserve projects.

There are many extensive studies on the impact of rock blasting excavations on open-pit slopes and tunnels [1–3]. For example, Jiang et al. established a mathematical model to describe the attenuation of the PPV on open-pit slopes subjected to underground mining blasting [4]. Li et al. proposed a method to predict the time history of blast

vibration on high slopes, from which a blast vibration spectral control scheme was presented [5]. Mohammadi Azizabadi et al. modeled the effect of blast vibration on slope stability in jointed rock masses by coupling waveform superposition and numerical methods [6]. Ma et al. proposed an integrated method of microseism energy density and the magnitude-frequency relation based on microseismic monitoring to analyse the slope stability [7]. Huang et al. discussed the time-frequency characteristics and multifrequency band energy distribution characteristics of tunnel blasting vibration signals by using Fourier transform and wavelet packet transform [8]. Lu et al. derived analytical solutions for the particle velocity response of the surrounding rock of a circular tunnel subjected to cylindrical  $P$ -waves [9]. Li and Li presented a mathematical method to calculate the relative velocity around a circular tunnel induced by blasting loads and theoretically analyzed the influence of the wavelength-to-tunnel-diameter ratio on the dynamic response of underground tunnels [10]. Jiang and Zhou proposed an approach to mathematically model the influences of blasting vibration on the tunnel structure and finally provided blasting vibration safety criteria [11]. In recent years, with the development of computer technology, numerical simulation methods are frequently adopted to study the influence of blasting on slopes and tunnels [12–16]. However, construction projects related to the national petroleum reserve bases usually involve cooperative blasting excavation of high-steep slopes and undercrossing tunnels, which is the key constraint on the construction period and engineering safety of the project [17]. The unreasonable schedule of the slope and tunnel construction directly affects the progress of the overall construction project. Therefore, it is necessary to conduct an in-depth study on the schedule design of the construction of the upper slope and undercrossing tunnel to guide the overall project construction.

In this paper, we focus on the expansion project of the national petroleum reserve base of Aoshan Island in Zhoushan City (Section 2). First, based on the field monitoring and analysis of the blasting vibration, a mathematical model is established to describe the attenuation law of PPV on the slope surface affected by bench blasting (Section 3 and Section 4). Second, a 3D numerical model is established to analyze the vibration response of the slope subjected to bench blasting by using the dynamic finite element software ANSYS/LS-DYNA. In addition, the reliability of the numerical simulation results is verified using the field monitoring data (Section 5 and Section 6). Then, the dynamic response of the undercrossing tunnel subjected to bench blasting was analyzed by numerical simulations, and a PPV safety criterion of the tunnel surrounding rock is proposed (Section 7 and Section 8). Finally, based on these primary results, we calculated key nodes for the cooperative blasting construction of the high-steep slope and undercrossing tunnel and proposed an excavation timing arrangement of the upper slope and undercrossing tunnel (Section 9).

## 2. Engineering Background

The Zhoushan National Petroleum Reserve Base Expansion Project is located in the west of Aoshan Island, Zhoushan City, Zhejiang Province. The project is located at  $29^{\circ}56'42''$ – $29^{\circ}59'00''$ N in latitude and  $122^{\circ}8'12''$ – $122^{\circ}9'20''$ E in longitude. The estimated rock excavation volume of the project is 3.05 million cubic meters, and the designed reserve of petroleum is 2.4 million cubic meters. The project construction involves cooperative blasting excavation of a high-steep rock slope and undercrossing oil pipeline tunnel, as shown in Figure 1.

The slope to be excavated is steep in height with a slope angle of 35–45 degrees and gentle at the lower part with a slope angle of 20–30 degrees. The highest excavation elevation is +128 m, and the lowest excavation elevation is +8.0 m. In order to ensure the stability of the undercrossing tunnel surrounding rock, tunneling is stopped when the tunnel working face is 30–50 m away from slope surface. At this time, the blasting excavation elevation of the upper high-steep slope is approximately 40 m. Moreover, there are enlarged tunnel sections with a length of 14 m, at 94 m and 294 m from the designed tunnel entrance, as shown in Figure 2.

The surface of the slope body is mostly silty clay, and downwards are strong weathering, moderate weathering, and slightly weathering crystal debris vitreous tuff, with medium hardness in most rock masses. The width of each stage platform is 3 m (Figure 2). The slope is excavated by the bench presplitting blasting method. Table 1 lists the parameters of bench blasting. Figure 3 shows the arrangement of the blast holes and the design of delay detonators.

The tunnel is excavated by the drilling-and-blasting method. Figure 4 shows the arrangement of the blast holes and the design of delay detonators, and Table 2 lists the parameters of the blast holes.

## 3. Field Blasting Vibration Test

**3.1. Layout of Blasting Vibration Monitoring Points.** To accurately evaluate the dynamic response of the upper slope and undercrossing tunnel, 8 locations are designated as the blasting vibration monitoring points according to the blasting characteristics of the slope excavation, to monitor and analyze the vibration of the blasting construction, as shown in Figure 2. In order to ensure the authenticity of the vibration data, considering the influence of the loosening of the tunnel surrounding rock on the particle vibration, a 2–2.5 m deep hole is drilled at the measuring point and a threaded steel bar with a diameter of 18 mm is inserted and densified by grouting. A steel plate of 10 cm × 10 cm × 1.5 cm in size is welded horizontally on the exposed end of the steel bar, as shown in Figure 5(a). For the measuring point on the slope surface, the ground is smoothed with cement mortar after the surface slag and gravel were removed, and the steel plate with prefabricated threaded holes is wedged horizontally. The vibration velocity transducer is fixed on the steel plate with screws tightened to establish a rigid



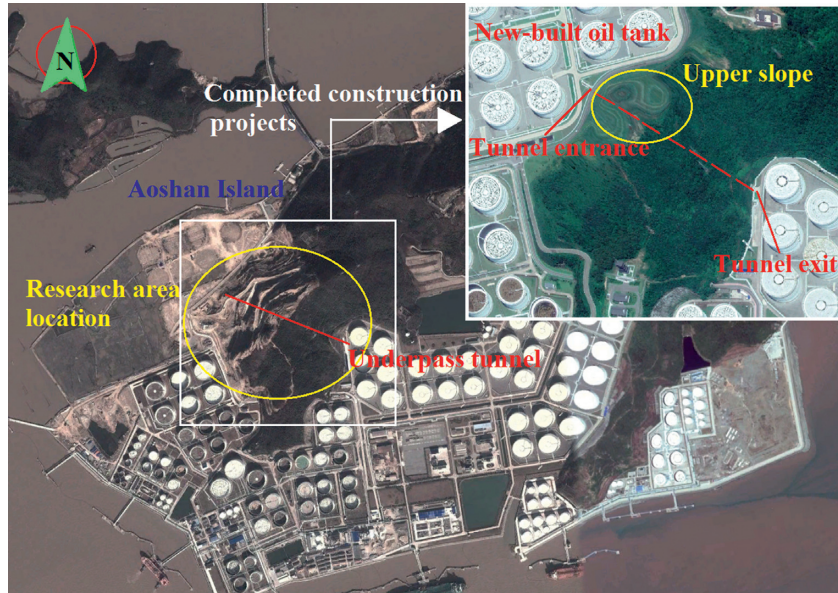


FIGURE 1: Layout of the national petroleum reserve base in Zhoushan.

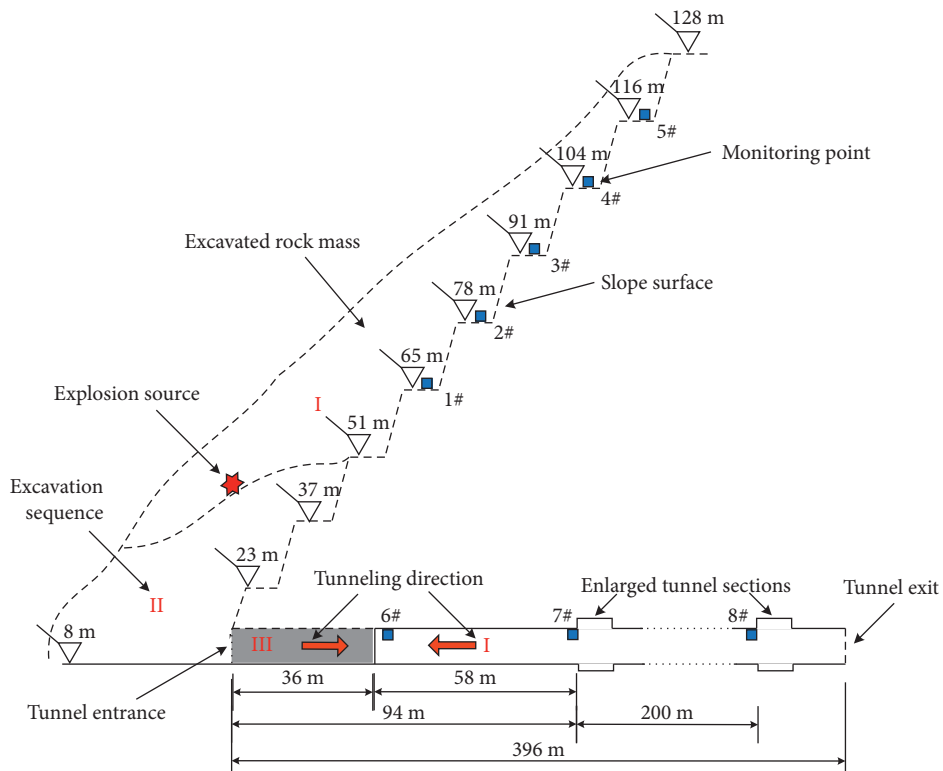


FIGURE 2: Schematic diagram of the spatial distribution of the upper slope and undercrossing tunnel.

TABLE 1: Blast hole parameters in bench blasting.

Classification	Hole spacing (m)	Hole row-spacing (m)	Minimum burden (m)	Stemming length (m)	Single hole charge (kg)
Presplitting hole	1.5	4	—	2.5	12–16.4
Main blast hole	4	3.6	3.6	2.5–4	75–108

Note. The type of explosive is emulsion explosive, the detonation velocity is 3500 m/s, the charge density is 1000 kg/m<sup>3</sup>, the equivalent charge diameter is 0.072~0.084, the bench height is 12–15 m, the hole depth is 14–17 m, the borehole diameter is 115 mm, the specific consumption of the explosives is 0.3 kg/m<sup>3</sup>, the maximum charge per delay is 108–376 kg, and the total charge of each blasting is 0.94–4.8 t.



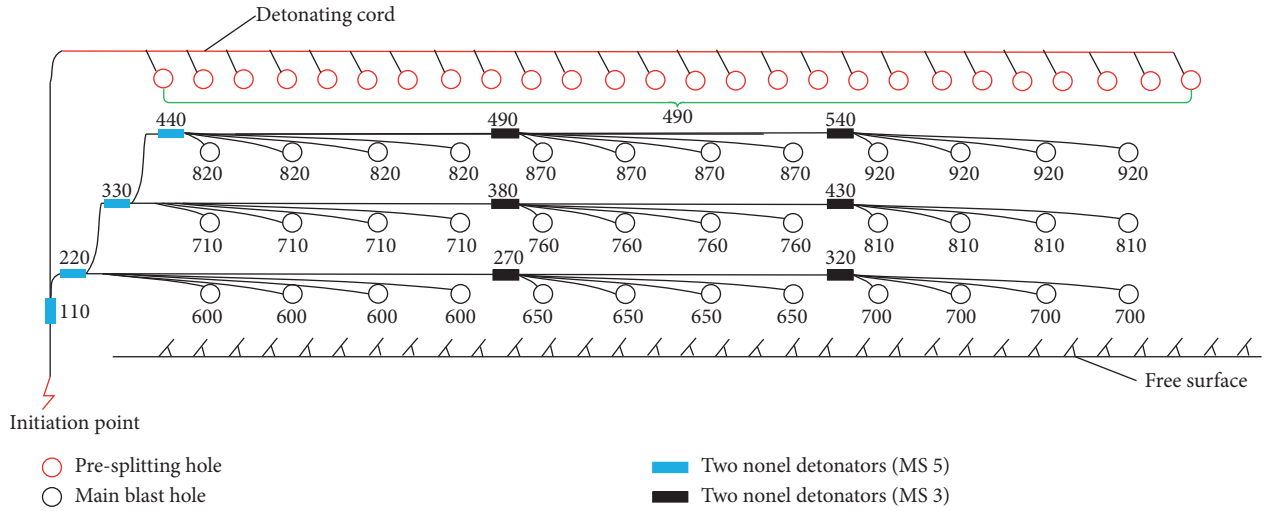


FIGURE 3: Schematic diagram of the arrangement of blast holes in bench blasting (each blast hole is equipped with two nonel detonators (MS10)).

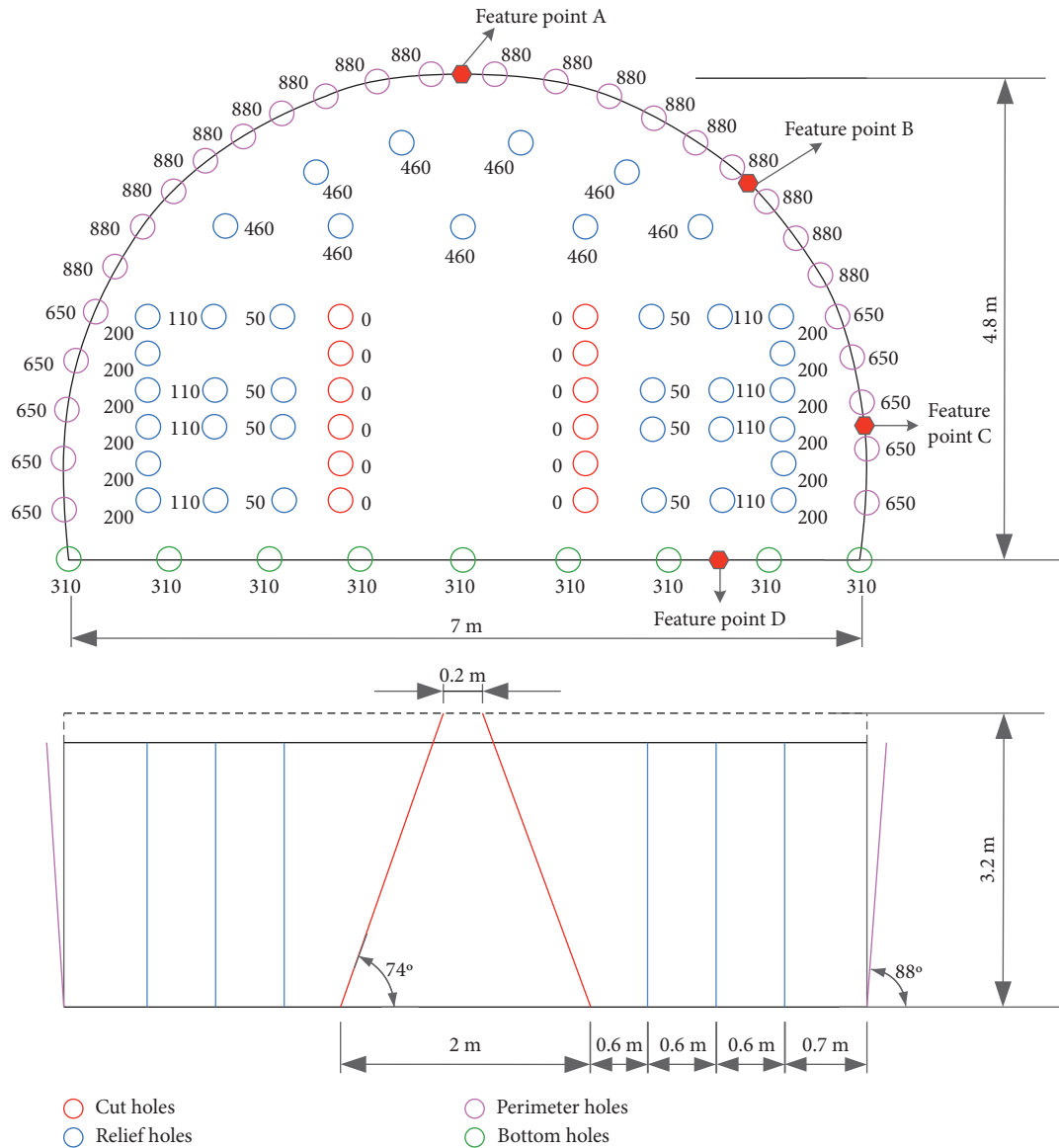


FIGURE 4: Schematic diagram of the arrangement of blast holes in tunnel blasting.

TABLE 2: Blast holes' parameters in tunnel blasting.

Classification	Blast hole angle (°)	Hole depth (m)	Number	Single hole charge (kg)
Cut holes	74° oblique hole	3.2	12	2.5
Relief holes	Vertical hole	3	37	1.8
Perimeter holes	88° oblique hole	3	28	1.1
Bottom holes	Vertical hole	3	9	2

Note. The cross-sectional area is 29 m<sup>2</sup>, the total number of blast holes is 86, the total charge is 145 kg, the maximum charge per delay is 18.9 kg, and the specific consumption of the explosives is 1.6 kg/m<sup>3</sup>.



FIGURE 5: Photographs of installed sensors. (a) Measuring point in the tunnel. (b) Measuring point on the slope surface.

connection between the transducer and the slope surface, as shown in Figure 5(b).

**3.2. Vibration Monitoring Results and Analysis.** During the slope excavation, 10 sets of effective field blasting vibration tests on the slope surface and 10 sets of effective field blasting vibration tests on the tunnel surrounding rock were carried out. In order to better study the blasting vibration response of the upper slope and tunnel surrounding rock, the formula for the peak velocity vector sum (PVS) is defined as follows [18]:

$$PVS = \max \sqrt{V_x^2 + V_y^2 + V_z^2}, \quad (1)$$

where  $V_x$ ,  $V_y$ , and  $V_z$  are time-history functions of vibration velocity in  $x$ ,  $y$ , and  $z$  directions, respectively.

PVS comprehensively covers the time history information on the particle vibration velocity in three directions, although the occurrence moment of PVS is not strictly consistent with the moment of PPV in all directions ( $x$ ,  $y$ , and  $z$ ).

PPV and PVS data are listed in Table 3 and 4.

It can be seen from Table 3 and 4 that PPV is the largest in the  $z$  direction at most measuring points on the slope surface. However, there is no obvious rule for the maximum PPV direction of the measured points in the tunnel. Therefore, when evaluating the influence of the blasting vibration velocity on the tunnel surrounding rock, the maximum PPV should be selected.

Frequency analyses show that approximately 94% of the monitoring data contain vibration frequencies of 25–100 Hz for the upper slope, with main vibration frequencies

concentrated in the range of 25–60 Hz and 50–150 Hz for the three directions and in the range of 50–100 Hz for the undercrossing tunnel. The blasting vibration frequency of the slope excavation is relatively high compared with the natural frequency of the upper slope and undercrossing tunnel. Therefore, resonance of the blasting vibration with the upper slope and undercrossing tunnel is difficult to achieve.

#### 4. Attenuation Rule and Prediction Model of PPV

Previous studies have shown that, during the propagation of the blasting seismic waves along the slope surface, the attenuation of seismic waves is affected by many factors such as explosion source, propagation medium, rock properties, and distance from the explosion source [12, 19, 20]. Multiple PPV prediction models are proposed as follows:

$$\left\{ v = K \left( \frac{\sqrt[3]{Q}}{R} \right)^\alpha, \quad (2a) \right.$$

$$\left. \left\{ v = K \left( \frac{\sqrt[3]{Q}}{R} \right)^\alpha \left( \frac{\sqrt[3]{Q}}{H} \right)^\beta, \quad (2b) \right. \right.$$

$$\left. \left\{ v = K \left( \frac{\sqrt[3]{Q}}{R} \right)^\alpha \left( \frac{R}{D} \right)^\beta, \quad (2c) \right. \right.$$

$$\left. \left\{ v = K \left( \frac{\sqrt[3]{Q}}{D} \right)^\alpha \left( \frac{\sqrt[3]{Q}}{H} \right)^\beta, \quad (2d) \right. \right.$$

TABLE 3: Monitoring data on the slope surface.

Blasting times	Horizontal distance (m)	Vertical distance (m)	Maximum charge per delay (kg)	PPV (cm/s)			PVS (cm/s)
				$x$	$y$	$z$	
1	69	25	250	6.9	2.5	7.2	7.9
2	97	51	250	4.2	3	4.8	5.4
3	98	39	315	3.4	0.9	3.6	3.8
4	367	65	315	0.4	0.3	0.5	0.6
5	193	28	108	1.3	1.4	1.6	2.1
6	219	41	108	0.6	0.9	0.4	1.0
7	155	54	108	1.1	1.3	1.3	1.6
8	133	28	108	1.7	1.4	1.8	1.9
9	61	39	310	7.6	5.8	7.7	7.9
10	306	65	310	0.7	0.7	0.9	1.1

TABLE 4: Monitoring data on the tunnel surrounding rock.

Blasting times	Horizontal distance (m)	Vertical distance (m)	Maximum charge per delay (kg)	PPV (cm/s)			PVS (cm/s)
				$x$	$y$	$z$	
1	304	38	310	0.7	0.7	0.6	0.9
2	365	28	315	0.5	0.3	0.4	0.6
3	94	28	315	3.5	0.9	1	3.8
4	88	17	243	5.8	4.5	5	6.2
5	85	16	174	6.9	9.5	8.5	13.3
6	109	15	168	4.6	7	8.4	9.4
7	109	29	168	1.4	1.8	1.9	2.5
8	111	29	168	4.7	3.8	2.7	5.9
9	58	15	165	4.4	7.1	7.1	7.3
10	98	15	252	7.9	8.9	9.3	12.1

$$\left\{ v = K \left( \frac{\sqrt[3]{Q}}{R} \right)^\alpha \left( \frac{H}{R} \right)^\beta, \right. \quad (2e)$$

where  $K$  is the field influence coefficient,  $Q$  is the maximum charge per delay,  $D$  is the horizontal distance,  $H$  is the vertical distance,  $\alpha$  is the PPV attenuation coefficient,  $\beta$  is the influence coefficient of elevation difference, and  $R$  is the distance from the explosion source.

The relative slope gradient ( $H/D$ ) affects the propagation of the blasting seismic waves in the rock and soil because of the propagation path of the blasting seismic waves along the slope surface. Table 5 summarizes the main variables involved in the propagation attenuation of the blasting seismic waves on the slope surface.

The functional relationship between the variables can be expressed as

$$v = \Phi(\rho, D, H, \mu, C_p, E, Q, f), \quad (3)$$

where variables  $D$ ,  $Q$ , and  $C_p$  are independent and satisfy the following formulas according to Buckingham's Pi theorem in dimensional analysis [21]:

$$\left\{ \begin{array}{l} \pi_1 = \frac{v}{D^{\alpha_1} Q^{\beta_1} C_p^{\gamma_1}}, \\ \pi_2 = \frac{\rho}{D^{\alpha_2} Q^{\beta_2} C_p^{\gamma_2}}, \\ \pi_3 = \frac{H}{D^{\alpha_3} Q^{\beta_3} C_p^{\gamma_3}}, \\ \pi_4 = \frac{\mu}{D^{\alpha_4} Q^{\beta_4} C_p^{\gamma_4}}, \\ \pi_5 = \frac{E}{D^{\alpha_5} Q^{\beta_5} C_p^{\gamma_5}}, \\ \pi_6 = \frac{f}{D^{\alpha_6} Q^{\beta_6} C_p^{\gamma_6}}, \end{array} \right. \quad (4)$$

where  $\pi_n$  denotes the dimensionless form of the dependent variables,  $n = 1, 2, \dots, 6$ , and the exponents  $\alpha_n$ ,  $\beta_n$ , and  $\gamma_n$  are dimensional exponents.  $\pi_n$  can be calculated as follows:

TABLE 5: Variables related to PPVs on the slope surface subjected to blasting excavation.

Variables	Symbol	Dimension
PPV	$v$	$LT^{-1}$
Density of rock mass	$\rho$	$ML^{-3}$
Horizontal distance	$D$	$L$
Vertical distance	$H$	$L$
Poisson ratio	$\mu$	$1$
P-wave velocity	$C_p$	$LT^{-1}$
Elastic modulus	$E$	$ML^{-1}T^{-2}$
Maximum charge per delay	$Q$	$M$
Frequency	$f$	$T^{-1}$

Note.  $M$  is the mass,  $L$  is the length, and  $T$  is the time.

$$\left\{ \begin{array}{l} \pi_1 = \frac{v}{C_p}, \\ \pi_2 = \frac{\rho}{QD^{-3}}, \\ \pi_3 = \frac{H}{D}, \\ \pi_4 = \mu, \\ \pi_5 = \frac{D^3 E}{QC_p^2}, \\ \pi_6 = \frac{fD}{C_p}. \end{array} \right. \quad (5)$$

Substituting (5) into (3) gives

$$\frac{v}{C_p} = \Phi \left( \frac{\rho}{QD^{-3}}, \frac{H}{D}, \mu, \frac{D^3 E}{QC_p^2}, \frac{fD}{C_p} \right). \quad (6)$$

For the excavation blasting operation of the same site,  $E$ ,  $\rho$ ,  $\mu$ , and  $C_p$  of the propagation medium can be regarded as constants. Therefore, (6) can be simplified to

$$\frac{v}{C_p} = \Phi \left( \frac{Q}{D^3}, fD, \frac{H}{D} \right). \quad (7)$$

Therefore, the similarity criterion equation of PPV can be written as follows:

$$v = K \left( \frac{\sqrt[3]{Q}}{D} \right)^{\alpha_7} (fD)^{\beta_7} \left( \frac{H}{D} \right)^{\gamma_7}, \quad (8)$$

where  $\alpha_7$ ,  $\beta_7$ , and  $\gamma_7$  are the coefficient related to engineering geological conditions.

The frequency of PPV caused by the blasting seismic wave is influenced by the properties of the propagation medium, propagation distance, and mass of the explosives. Assuming that the rock property and mass of the explosives are constant, the frequency can be calculated as follows [22]:

$$\begin{aligned} f &= k_f \left( \frac{C_s^7}{QR^2} \right)^{1/5} \\ &= \frac{k_f C_s^{7/5}}{Q^{1/3}} \left( \frac{Q^{1/3}}{R} \right)^{2/5}, \end{aligned} \quad (9)$$

where  $k_f$  is the frequency coefficient,  $k_f = 0.01-0.03$ , and  $C_s$  is the shear wave velocity.

Substituting (9) into (8) gives

$$v = K \left( \frac{\sqrt[3]{Q}}{D} \right)^{\alpha_8} \left( \frac{\sqrt[3]{Q}}{R} \right)^{\beta_8} \left( \frac{H}{D} \right)^{\gamma_8}, \quad (10)$$

where  $\alpha_8$  and  $\beta_8$  are the PPV attenuation coefficient and  $\gamma_8$  is the influence coefficient of the relative slope gradient.

Regression analyses of the test results listed in Table 3 using (10) lead to the prediction model of PPV and PVS on the slope surface of bench blasting. In addition, to validate the established prediction model, its prediction accuracy is compared with that obtained using (2), based on the fitting coefficients of the fitting curves, as shown in Table 6.

- The fitting correlation coefficients of PPV and PVS at the monitoring points on the slope surface obtained using the established mathematical model, (10), are all larger than those obtained using previous classical formulas, (2), indicating that the propagation attenuation of PPV and PVS on the slope surface is more complicated and is affected by the relative slope gradient. The mathematical prediction model established by considering the influence of the relative slope gradient can better describe the propagation attenuation of the bench blasting vibration on the slope surface.
- The regression analysis results show that the prediction formula of PVS obtained by using the established mathematical prediction model has a high prediction accuracy with a correlation coefficient of 0.953. Additionally, the PVS comprehensively considers the vibration effect in all directions. Thus, it can better reflect the vibration response characteristics of the PPV of the slope surface. Therefore, the following prediction formula can be used to predict the PVS of the slope surface particles when the bench blasting vibration propagates to the slope surface:

$$v = 85.03 \left( \frac{\sqrt[3]{Q}}{D} \right)^{7.72} \left( \frac{\sqrt[3]{Q}}{R} \right)^{-6.16} \left( \frac{H}{D} \right)^{-0.87}. \quad (11)$$

## 5. Numerical Modeling and Parameter Selection

The dynamic finite element software ANSYS/LS-DYNA is used to establish the numerical model of the cooperative blasting construction of the upper slope and undercrossing tunnel according to the actual engineering of the blasting excavation, as shown in Figure 2. The coordinates are defined as follows: the radial direction of the undercrossing

TABLE 6: Prediction formulas of PPV on the slope surface.

Category	Formula form	PPV prediction equation	Correlation coefficient	Formula form	PPV prediction equation	Correlation coefficient
$x$		$v = 516.98 (\sqrt[3]{Q/R})^{1.73}$	0.959		$v = 609.11 (\sqrt[3]{Q/R})^{1.65} (\sqrt[3]{Q/H})^{0.22}$	0.956
$y$		$v = 29.64 (\sqrt[3]{Q/R})^{0.96}$	0.611		$v = 27.09 (\sqrt[3]{Q/R}) (\sqrt[3]{Q/H})^{-0.12}$	0.502
$z$	Equation (2a)	$v = 528.48 (\sqrt[3]{Q/R})^{1.71}$	0.909	Equation (2b)	$v = 582.89 (\sqrt[3]{Q/R})^{1.66} (\sqrt[3]{Q/H})^{0.13}$	0.898
PVS		$v = 314.19 (\sqrt[3]{Q/R})^{1.49}$	0.924		$v = 355.31 (\sqrt[3]{Q/R})^{1.43} (\sqrt[3]{Q/H})^{0.16}$	0.915
$x$		$v = 391.11 (\sqrt[3]{Q/R})^{1.66} (R/D)^{0.97}$	0.954		$v = 448.09 (\sqrt[3]{Q/D})^{1.49} (\sqrt[3]{Q/H})^{0.36}$	0.962
$y$		$v = 8.94 (\sqrt[3]{Q/R})^{0.67} (R/D)^{4.16}$	0.538		$v = 22.58 (\sqrt[3]{Q/D})^{0.92} (\sqrt[3]{Q/H})^{-0.04}$	0.515
$z$	Equation (2c)	$v = 343.44 (\sqrt[3]{Q/R})^{1.6} (R/D)^{1.49}$	0.899	Equation (2d)	$v = 427.95 (\sqrt[3]{Q/D})^{1.51} (\sqrt[3]{Q/H})^{0.28}$	0.904
PVS		$v = 193.45 (\sqrt[3]{Q/R})^{1.37} (R/D)^{1.69}$	0.917		$v = 272.87 (\sqrt[3]{Q/D})^{1.29} (\sqrt[3]{Q/H})^{0.28}$	0.923
$x$		$v = 609.11 (\sqrt[3]{Q/R})^{1.87} (H/R)^{-0.22}$	0.956		$v = 179.47 (\sqrt[3]{Q/D})^{6.67} (\sqrt[3]{Q/R})^{-4.84} (H/D)^{-0.83}$	0.965
$y$		$v = 27.09 (\sqrt[3]{Q/R})^{0.88} (H/R)^{0.12}$	0.502	Equation (10)	$v = 4.13 (\sqrt[3]{Q/D})^{9.82} (\sqrt[3]{Q/R})^{-8.98} (H/D)^{-0.82}$	0.666
$z$	Equation (2e)	$v = 583.47 (\sqrt[3]{Q/R})^{1.79} (H/R)^{-0.13}$	0.898		$v = 170.03 (\sqrt[3]{Q/D})^{6.64} (\sqrt[3]{Q/R})^{-4.87} (H/D)^{-0.75}$	0.931
PVS		$v = 355.31 (\sqrt[3]{Q/R})^{1.59} (H/R)^{-0.16}$	0.915		$v = 85.03 (\sqrt[3]{Q/D})^{7.72} (\sqrt[3]{Q/R})^{-6.16} (H/D)^{-0.87}$	0.953

The following conclusions can be obtained from the results shown in Table 6.

tunnel is the  $x$ -axis, the axial direction of the undercrossing tunnel is the  $y$ -axis, and the vertical direction is the  $z$ -axis. In order to avoid the boundary effect of the model, the lengths along the tunnel axis direction ( $y$  direction) and horizontal radial direction ( $x$  direction) are set to 250 m and 200 m, respectively, and the vertical direction ( $z$  direction) is set to 157 m. The 8-node SOLID164 solid element is used to establish the model, including 307708 units and 323265 nodes. According to the characteristics of the project site, the top surface of the numerical model is considered as a free constrained boundary and the other surfaces are nonreflecting boundaries. Moreover, displacement constraints are applied to the bottom of the model. The numerical model is shown in Figure 6.

The diameter of the blasting holes used in the blasting excavation of the upper open-pit slope is 70–115 mm, which is very small compared with the size of the numerical calculation model. Therefore, if the numerical calculation model of the blasting hole is established according to the actual blasting parameters and the explosive material model or the equivalent load is applied on the wall of the blasting hole, the number of numerical calculation model elements will be large, which may prevent the calculation process from completing. In this paper, the equivalent approximate blasting load is applied to the slope surface above the undercrossing tunnel with an elevation of +40 m. The numerical calculation is based on the following basic assumptions [23]:

- The blasting impact load is equivalent to the triangular load
- The boosting time of the triangular load is  $100 \mu\text{s}$ , and the positive pressure acting time of the triangular load is  $600 \mu\text{s}$
- The blasting impact load acts on the slope in the form of uniform vertical pressure

The peak value of the equivalent blasting load is calculated through the following formula [24]:

$$P_{\max} = \frac{1}{8} \rho_e D^2 k_d^{-6} \eta, \quad (12)$$

where  $\rho_e$  is the charge density,  $D$  is the explosive detonation velocity,  $k_d$  is the decoupling charge coefficient,  $k_d = d_b/d_c$ ,  $d_b$  and  $d_c$  are the blast hole diameter and equivalent charge diameter, respectively, and  $\eta$  is the increasing multiples of detonation pressure,  $\eta = 8\sim 11$ .

The peak value of the blasting load is calculated by using equation (12), and the bench blasting parameters is 730 MPa. Figure 7 shows the time-history curve of the blasting load on the slope surface [25, 26].

The numerical calculation parameters are selected based on the results of indoor mechanical tests. The surrounding rock in the research area is simplified to be homogenous without considering the influence of cracks and weak planes. The \*MAT\_PLASTIC\_KINEMATIC material model is used for the surrounding rock [27]. The physical and mechanical parameters of the surrounding rock are listed in Table 7.

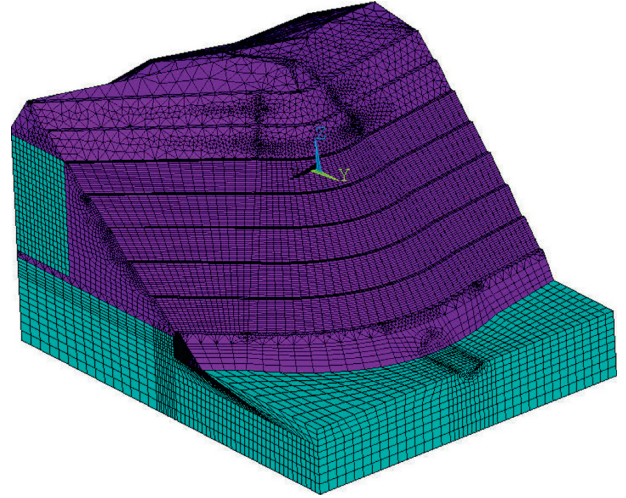


FIGURE 6: Numerical calculation model.

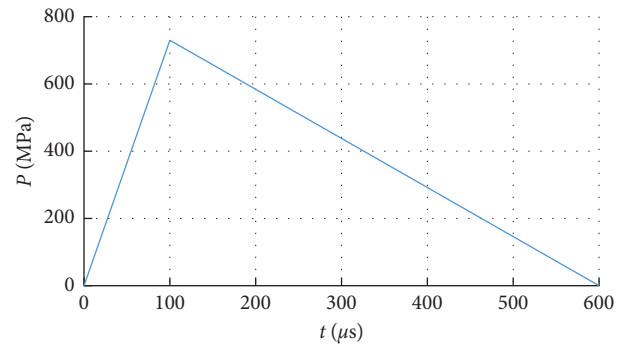


FIGURE 7: Time-history curve of the blasting load on the slope surface.

## 6. Numerical Calculations and Verification

The Rayleigh damping parameters in the numerical calculation are determined by repeated trial calculation and comparison. In this paper, the numerical calculation results of PPV on the slope surface caused by bench blasting are compared with the field measured data, and then, the Rayleigh damping parameters are adjusted manually step by step according to the comparative analysis results until the relative error between the numerical calculation results and the field measured results is less than 5%. Finally, the reasonable Rayleigh damping parameters are determined to be  $\alpha_0 = 0.4$  and  $\beta_0 = 0.0003$ .

To validate the numerical calculation results, 5 field monitoring points are set up on the slope surface, as shown in Figure 2, and the monitoring points in the numerical model are set up at the same locations. The time-history curves of monitoring points in the numerical model are obtained; one typical curve is shown in Figure 8.

The numerically simulated and measured PPVs at each monitoring point are listed in Table 8.

From Table 8, it is evident that the simulated PPVs are slightly higher than but similar to those obtained by field monitoring, and the maximum relative error of PPV is



TABLE 7: Physical and mechanical parameters of the surrounding rock.

Surrounding rock type	Parameters					
	Elastic modulus $E$ (GPa)	Poisson's ratio $\mu$	Frictional angle $\varphi$ ( $^{\circ}$ )	Cohesion $c$ (MPa)	Density $\rho$ ( $\text{kg}\cdot\text{m}^{-3}$ )	Dynamic tensile strength $f_c^t$ (MPa)
III	40	0.3	50	1.5	2500	3.7
IV	30	0.33	39	0.7	2400	3.3

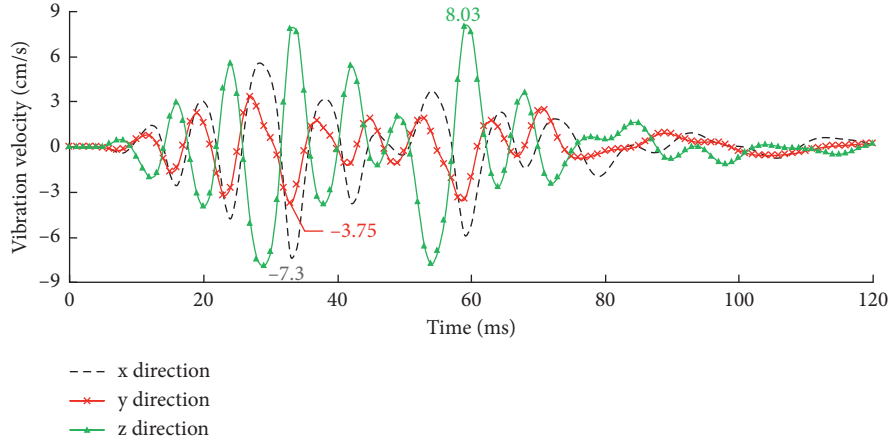


FIGURE 8: Time-history curve of the numerically simulated particle velocity at 1# monitoring point.

TABLE 8: PPVs of field monitoring and numerical simulation at monitoring points.

Monitoring points	PPV of field monitoring (cm/s)			PPV of numerical simulation (cm/s)			Relative error of PPV (%)		
	$x$	$y$	$z$	$x$	$y$	$z$	$x$	$y$	$z$
1#	6.94	3.61	7.48	7.3	3.75	8.03	5.19	3.88	7.35
2#	4.76	2.18	4.8	5.04	2.25	5.05	5.88	3.21	5.21
3#	3.16	1.87	2.98	3.34	2.06	3.13	5.70	10.16	5.03
4#	2.17	1.3	2.34	2.32	1.42	2.46	6.91	9.23	5.13
5#	1.32	1.08	1.65	1.42	1.17	1.54	7.58	8.33	-6.67

10.16%. The particle vibration frequencies of 45.25–120.5 Hz at each monitoring point obtained by numerical simulations are slightly higher than those obtained by in situ monitoring points. The main reason for the above phenomenon is that the particle vibration frequencies of the numerical simulations are obtained without considering the attenuation and dissipation of the blasting seismic waves caused by joints and weakening faces in the rock mass [28, 29].

In summary, the comparison between numerical simulation and field monitoring data shows that the three-dimensional model and model parameters adequately describe the field data. Therefore, a study of the dynamic response and safety effects of the undercrossing tunnel subjected to upper slope excavation is feasible by numerical simulations.

## 7. Tunnel Dynamic Response Caused by Bench Blasting

The reliability of the numerical model was verified using the field monitoring data. On this basis, the dynamic response

characteristics of the undercrossing tunnel subjected to bench blasting can be analyzed based on numerical calculations. The rock surrounding the undercrossing tunnel in the expansion project is of high grade and good stability. Initial shotcrete and anchor support were carried out for the undercrossing tunnel during blasting construction on the slope. In order to avoid increases in the numerical calculation time due to excessive numbers of numerical model elements, the initial shotcrete and anchor support of the undercrossing tunnel is not modeled separately in the modeling process. Therefore, considering this actual situation, the safety control standards of the surrounding rock are used to analyze the influence of blasting vibration on the tunnel.

According to the theory of seismic wave propagation, the surrounding rock and its enlarged section are most affected when the blasting area is closest to the tunnel. Therefore, the specific calculation condition in this section is the blasting area which is located on the bench directly above the tunnel, and the distance from the explosive source is 25.8 m.

To evaluate the influence of bench blasting on the surrounding rock of the tunnel, the safety measure stipulated in the initial scheme of the project blasting design is used, i.e., tunnel blasting is suspended when the tunnel working face is 21 m from the slope surface. Therefore, four featured points A, B, C, and D on the tunnel section 21 m from the slope surface are selected, respectively corresponding to the vault crown, arch lumbar, midpoint of the side wall, and bottom of the tunnel wall, as shown in Figure 4.

The distribution of PPVs and the effective tensile stress (ETS) at each inspection point of the tunnel section are listed in Table 9.

The data in Table 9 show that PPVz and PPVy are the largest at the vault crown and gradually decrease moving downward along the tunnel section. PPVx is small at the vault crown because of the radial symmetry constraint, followed by an increase, and then decreases moving downward along the tunnel section. The attenuation speed of PPVz is evidently faster than those in the other two horizontal directions. It can be seen that the stress wave generated by the blasting load initially propagates downward with a high-strength longitudinal wave and gradually attenuates with an increase in distance. The surface wave formed at the free surface has a slower attenuation speed than that of the longitudinal wave. The maximum PPV of the tunnel section appears at the vault crown, which is 13.92 cm/s.

The distribution of ETS at each inspection point shows that ETS gradually decreases along the tunnel section, and the attenuation speed gradually decreases. PPV and ETS both produce maximum values at the vault crown of the tunnel, which are 13.92 cm/s and 4.78 MPa, respectively. Therefore, the safety and stability of the tunnel are evaluated according to the dynamic response of the surrounding rock at the vault crown. The maximum ETS at the vault crown reaches 4.78 MPa, exceeding the tensile strength standard, which is the dynamic tensile strength (3.7 MPa) shown in Table 7. Therefore, the surrounding area of the tunnel is not safe according to the maximum tensile strength theory.

## 8. PPV Safety Criterion of Tunnel Surrounding Rock

To further study the dynamic response of the tunnel, ETS and PPVs at different measuring points are calculated by numerical simulation and listed in Table 10.

The numerical simulation results indicate that ETS are different from PPVs. A statistical relationship model between PPV and ETS is established and shown in Figure 9.

The linear statistical relationship between PPV and ETS shown in Figure 9 is established as follows:

$$\sigma_t = 0.3615PPV - 0.0529. \quad (13)$$

Equation (13) indicates that a linear relationship exists between PPV and ETS [23, 30]. Based on the first strength theory, ETS exceeds the dynamic tensile strength (3.7 MPa) of the tunnel surrounding rock when PPV reaches

TABLE 9: The distribution of PPVs and ETS.

No.	PPV of numerical simulation (cm/s)			ETS (MPa)
	x	y	z	
A	3.44	5.07	13.92	4.78
B	4.15	4.91	7.38	2.72
C	2.05	2.63	2.16	0.92
D	1.16	2.57	1.34	0.83

TABLE 10: Values of ETS and PPV from numerical simulations.

No.	1	2	3	4	5	6	7	8	9
PPV (cm/s)	7.41	5.73	3.89	1.45	6.79	4.91	2.11	1.01	3.18
ETS (MPa)	2.82	1.95	1.57	0.41	2.14	1.71	0.52	0.38	1.21

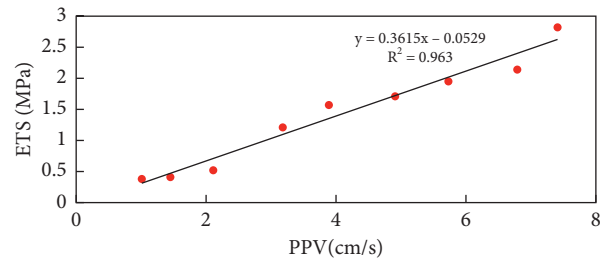


FIGURE 9: Relationship between PPV and ETS.

10.38 cm/s. To be more practical, the PPV safety criterion of the tunnel surrounding rock is determined to be 10 cm/s.

## 9. Excavation Timing Arrangement of the Upper Slope and Undercrossing Tunnel

Based on the simulation calculations, the relationship between PPV at the vault crown and the length of retained rock mass during bench blasting directly above the tunnel entrance is obtained, as shown in Figure 10.

It can be seen from Figure 10 that PPVz decrease with an increase in the axial distance, and their attenuation speed is faster than that of PPVx and PPVy. The attenuation speed in the excavated direction of the tunnel is less than that in the direction of no excavation. The horizontal vibration velocity (PPVx and PPVy) increases first, then decreases in the excavated direction, and decreases rapidly in the direction of no excavation. PPVs in the three directions increased slightly adjacent to the slope surface and then tended to become stable. The reason for that is mainly due to the coupling effect of the increase in the propagation distance and the decrease in the original rock stress constraint.

To ensure construction progress and the stability of the tunnel surrounding rock, PPV of the tunnel vault crown shall not exceed 10 cm/s and the length of the retained rock mass at the tunnel entrance shall not be less than 36 m; these values can be obtained from Figure 10. Therefore, tunnel blasting is suspended when the distance from the tunnel working face to the slope surface is less than 36 m, and all the

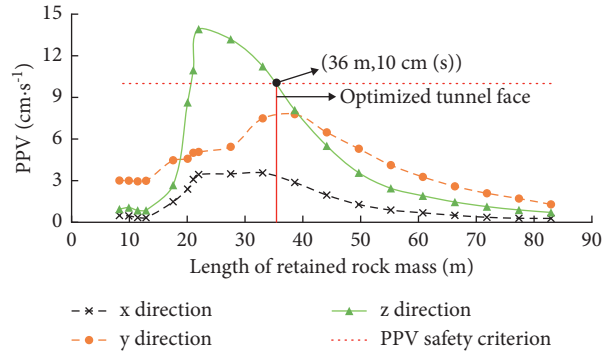


FIGURE 10: Relationship between PPV and the length of the retained rock mass at the tunnel entrance.



FIGURE 11: Map of the project site. (a) Formation of the rock slope. (b) Slope greening map.

working faces are transferred to slope excavation at this time. Subsequently, the tunnel is excavated from the slope surface to the slope body until tunnel hole-through is reached, after the excavation and reinforcement of the slope at the tunnel entrance have been completed. The excavation timing arrangement of the upper slope and undercrossing tunnel is shown in Figure 2.

The research results have been successfully applied to the blasting project of the expansion project of the Zhoushan national petroleum reserve base. The cooperative blasting construction of the open-pit slope and undercrossing tunnel has been effectively guided with good results, and the construction period is shortened by 45 days while ensuring construction safety. The project site is shown in Figure 11.

## 10. Conclusions

- (a) The mathematical prediction model established herein with consideration of the influence of the relative slope gradient can better describe the propagation attenuation of bench blasting vibration on the slope surface. The PPV and PVS formula for the propagation of the bench blasting vibration is proposed as follows:

$$v = 85.03 \left( \frac{\sqrt[3]{Q}}{D} \right)^{7.72} \left( \frac{\sqrt[3]{Q}}{R} \right)^{-6.16} \left( \frac{H}{D} \right)^{-0.87}. \quad (14)$$

- (b) A 3D numerical calculation model is established to analyze the dynamic response of the tunnel surrounding rock subjected to bench blasting. A comparison of the numerical simulation data and the field measurement data shows that the numerical model and the selected parameters adequately describe the field data, and therefore, the numerical calculation model is feasible for studies on the dynamic response of the tunnel surrounding rock to bench blasting vibration.
- (c) A linear statistical relationship between PPV and ETS for the tunnel surrounding rock is established. Based on the first strength theory, the PPV safety criterion of the tunnel surrounding rock is determined to be 10 cm/s. The minimum safe distance from the tunnel working face to the slope surface, obtained by simulation calculations, is 36 m.
- (d) The excavation timing arrangement of the upper slope and undercrossing tunnel is proposed, which has been successfully applied to the expansion project of the Zhoushan national petroleum reserve base. The engineering application results show that the construction period is shortened by 45 days while ensuring construction safety. The research results have great guiding significance to similar cooperative blasting excavation engineering for high slope and adjacent tunnel with safety and efficiency.

## Data Availability

No data were used to support the findings this study.

## Conflicts of Interest

The authors declare that there are no conflicts of interest regarding the publication of this paper.

## Acknowledgments

This research was supported by the Open Fund of Key Laboratory of Geological Hazards on Three Gorges Reservoir Area, Ministry of Education (Grant no. 2017KDZ02), National Natural Science Foundation of China (Grant no. 51904210), Open Fund of Key Laboratory of Systems Science in Metallurgical Process, Hubei Province (Grant no. Z202001), and Key R&D Projects in Hubei Province (Grant no. 2020BCA084).

## References

- [1] H. Zheng, T. Li, J. Shen, C. Xu, H. Sun, and Q. Lü, "The effects of blast damage zone thickness on rock slope stability," *Engineering Geology*, vol. 246, pp. 19–27, 2018.
- [2] H. K. Verma, N. K. Samadhiya, M. Singh, R. K. Goel, and P. K. Singh, "Blast induced rock mass damage around tunnels," *Tunnelling and Underground Space Technology*, vol. 71, pp. 149–158, 2018.
- [3] B. Duan, H. Xia, and X. Yang, "Impacts of bench blasting vibration on the stability of the surrounding rock masses of roadways," *Tunnelling and Underground Space Technology*, vol. 71, pp. 605–622, 2018.
- [4] N. Jiang, C. Zhou, S. Lu, and Z. Zhang, "Propagation and prediction of blasting vibration on slope in an open pit during underground mining," *Tunnelling and Underground Space Technology*, vol. 70, pp. 409–421, 2017.
- [5] P. Li, W. B. Lu, X. X. Wu, M. Chen, P. Yan, and Y. G. Hu, "Spectral prediction and control of blast vibrations during the excavation of high dam abutment slopes with millisecond-delay blasting," *Soil Dynamics and Earthquake Engineering*, vol. 94, pp. 116–124, 2017.
- [6] H. R. Mohammadi Azizabadi, H. Mansouri, and O. Fouché, "Coupling of two methods, waveform superposition and numerical, to model blast vibration effect on slope stability in jointed rock masses," *Computers and Geotechnics*, vol. 61, pp. 42–49, 2014.
- [7] K. Ma, C. A. Tang, Z. Z. Liang, D. Y. Zhuang, and Q. B. Zhang, "Stability analysis and reinforcement evaluation of high-steep rock slope by microseismic monitoring," *Engineering Geology*, vol. 218, pp. 22–38, 2017.
- [8] D. Huang, S. Cui, and X. Li, "Wavelet packet analysis of blasting vibration signal of mountain tunnel," *Soil Dynamics and Earthquake Engineering*, vol. 117, pp. 72–80, 2019.
- [9] S. Lu, C. Zhou, Z. Zhang, and N. Jiang, "Particle velocity response of surrounding rock of a circular tunnel subjected to cylindrical P-waves," *Tunnelling and Underground Space Technology*, vol. 83, pp. 393–400, 2019.
- [10] C. Li and X. Li, "Influence of wavelength-to-tunnel-diameter ratio on dynamic response of underground tunnels subjected to blasting loads," *International Journal of Rock Mechanics and Mining Sciences*, vol. 112, pp. 323–338, 2018.
- [11] N. Jiang and C. Zhou, "Blasting vibration safety criterion for a tunnel liner structure," *Tunnelling and Underground Space Technology*, vol. 32, pp. 52–57, 2012.
- [12] X. Song, J. C. Zhang, X. B. Guo, and Z. X. Xiao, "Influence of blasting on the properties of weak intercalation of a layered rock slope," *International Journal of Minerals, Metallurgy and Materials*, vol. 16, no. 1, pp. 7–11, 2009.
- [13] J.-H. Shin, H.-G. Moon, and S.-E. Chae, "Effect of blast-induced vibration on existing tunnels in soft rocks," *Tunnelling and Underground Space Technology*, vol. 26, no. 1, pp. 51–61, 2011.
- [14] J. H. Yang, W. B. Lu, Z. G. Zhao, P. Yan, and M. Chen, "Safety distance for secondary shotcrete subjected to blasting vibration in Jinping-II deep-buried tunnels," *Tunnelling and Underground Space Technology*, vol. 43, pp. 123–132, 2014.
- [15] C. A. Tang, L. Li, N. Xu, and K. Ma, "Microseismic monitoring and numerical simulation on the stability of high-steep rock slopes in hydropower engineering," *Journal of Rock Mechanics and Geotechnical Engineering*, vol. 7, no. 5, pp. 493–508, 2015.
- [16] H. Yu, Y. Yuan, G. Yu, and X. Liu, "Evaluation of influence of vibrations generated by blasting construction on an existing tunnel in soft soils," *Tunnelling and Underground Space Technology*, vol. 43, pp. 59–66, 2014.
- [17] L. He, L. Wu, and D. W. Zhong, "Impact from blasting construction of open-air slope on expanding section of existing under-crossing tunnel," *Water Resources and Hydropower Engineering*, vol. 49, no. 9, pp. 18–24, 2018.
- [18] L. He, D. W. Zhong, C. Chen, and H. Xiong, "Monitoring and analysis of blasting vibration in high rocky slope excavation," *Minimally Invasive Neurosurgery*, vol. 1, pp. 6–10, 2017.
- [19] M. Chen, W. B. Lu, P. Li, and M. Liu, "Elevation amplification effect of blasting vibration velocity in rock slope," *Chinese Journal of Rock Mechanics and Engineering*, vol. 30, no. 11, pp. 2189–2195, 2011.
- [20] N. Jiang, T. Gao, C. Zhou, and X. Luo, "Effect of excavation blasting vibration on adjacent buried gas pipeline in a metro tunnel," *Tunnelling and Underground Space Technology*, vol. 81, pp. 590–601, 2018.
- [21] H. L. Langhaar, *Dimensional Analysis and Theory of Models*, Wiley, New York, NY, USA, 1951.
- [22] D. W. Zhong, L. He, P. Cao, and X. W. Huang, "Experimental study of reducing vibration intensity based on controlled blasting with precise time delay," *Journal of China Coal Society*, vol. 40, no. S1, pp. 107–112, 2015.
- [23] D. P. Zhao, M. N. Wang, and L. L. Jia, "Research on influence of excavating road trench slope on adjacent existing tunnel," *Rock and Soil Mechanics*, vol. 30, no. 5, pp. 1399–1402+1408, 2009.
- [24] Y. H. Zhang, G. H. Yang, P. Liu, and Y. C. Zhang, "An Equivalent approach for acting blasting load in dynamic numerical simulation of blasting vibration," *Chinese Journal of Underground Space and Engineering*, vol. 8, no. 1, pp. 56–64, 2012.
- [25] W. B. Lu, J. H. Yang, M. Chen, and Z. C. Bing, "Mechanism and equivalent numerical simulation of transient release of excavation load for deep tunnel," *Chinese Journal of Rock Mechanics and Engineering*, vol. 30, no. 6, pp. 1089–1096, 2011.
- [26] H. T. Xu, W. B. Lu, and X. H. Zhou, "Equivalent application method of blasting load in finite element simulation of blasting vibration field," *Eng J Wuhan Univ*, vol. 41, no. 1, pp. 67–71, 2008.
- [27] J. O. Hallquist, *LS-DYNA Keyword User's Manual*, Softw Technol Corp, Livermore, CA, USA, 2007.

- [28] B. Zhu, N. Jiang, C. Zhou, X. Luo, Y. Yao, and T. Wu, "Dynamic failure behavior of buried cast iron gas pipeline with local external corrosion subjected to blasting vibration," *Journal of Natural Gas Science and Engineering*, vol. 88, Article ID 103803, 2021.
- [29] N. Jiang, B. Zhu, X. He, C. Zhou, X. Luo, and T. Wu, "Safety assessment of buried pressurized gas pipelines subject to blasting vibrations induced by metro foundation pit excavation," *Tunnelling and Underground Space Technology*, vol. 102, Article ID 103448, 2020.
- [30] M. Chen, W. B. Lu, L. Wu, and H. Xu, "Safety threshold of blasting vibration velocity to high rock slope of Xiaowan hydropower station," *Chinese Journal of Rock Mechanics and Engineering*, vol. 26, no. 1, pp. 51–56, 2007.

## Research Article

# Research on Damage Characteristics of Brick Masonry under Explosion Load

Jifeng Wei , Zhixin Du, Yonghui Zheng, and Oundavong Ounhueane

State Key Laboratory of Explosion Science and Technology, Beijing Institute of Technology, Beijing 100081, China

Correspondence should be addressed to Jifeng Wei; [weijifeng@bit.edu.cn](mailto:weijifeng@bit.edu.cn)

Received 3 March 2021; Revised 16 June 2021; Accepted 23 July 2021; Published 26 August 2021

Academic Editor: Bangbiao Wu

Copyright © 2021 Jifeng Wei et al. This is an open access article distributed under the Creative Commons Attribution License, which permits unrestricted use, distribution, and reproduction in any medium, provided the original work is properly cited.

As the main structural component of partition wall or load-bearing wall, brick masonry has been widely used in construction engineering. However, brick and mortar are all brittle materials prone to crack. Nowadays, fireworks, gas stoves, high-pressure vessels, and other military explosives may explode to damage nearby structures. Many explosion casualties had shown that the load-bearing capacity of brick masonry decreased dramatically and cracks or fragments appeared. Previous studies mainly focused on noncontact explosion in which shock wave is the main damage element. In fact, the response and damage effect of brick masonry wall under contact explosion are more complex, which attracts more attention now. In order to explore the damage characteristics of brick masonry under explosion load, a series of simulations and verification experiments are conducted. RHT and MO granular material models are introduced to describe the behaviour of brick and masonry, respectively, in simulation. The combination effect of front compressive wave and back tensile wave are main factors influencing the breakage of masonry wall. The experimental results are well in accordance with the simulation results. The front cross section dimension of crater is closely related to the radius of spherical explosive charge. A power function predictive model is developed to express the relationship between the radius of hole and the radius of explosive. Furthermore, with increasing the quantity of explosive charge, the number and ejection velocity of fragments are all increased. The relationship between maximum ejection velocity and the quantity of explosive also can be expressed as a power function model.

## 1. Introduction

Brick masonry is a composite structure which consists of brick, mortar, and brick-mortar interfaces. With lots of advantages of easy availability, good durability, low-cost building material, and sound and insulation properties, it has been widely used in civil constructions. However, masonry materials (sintered bricks and mortar) are brittle materials with low ductility which is easy to crack under severe impact or explosion [1–3]. Failure of a masonry wall is likely to be sudden and severe that poses significant debris hazard to building occupants when subjected to blast loads. According to the analysis of human casualties and property losses in explosion accidents, it had been found that the fragmentation of brick masonry also can cause damage to whether human or surrounding devices except high overpressure [4–6].

Previous research studies had paid more attention to experiments. Varma et al. [7] tested on several masonry panels with different thickness subjected to near-field and far-field explosions. Gabrielsen et al. [8] investigated experimentally the response of building walls to blast loading from large nuclear weapons. Davidson et al. [9] conducted three explosive tests that involved a sprayed-on polymer to increase blast resistance of unreinforced concrete masonry walls. Dennis et al. [10] conducted both five dynamic experiments to analyse the response and failure of one-way 1/4-scale reinforced masonry walls to blast loads. Ahmad et al. [11] carried out six tests to study the resistance of brick masonry wall exposed to varying blast load at different scaled distances. Keys et al. [12] carried out two experimental trials to obtain a baseline set of results for the breakage mechanisms and debris distribution and developed a new method to predict the spatial debris distribution. Norén-Cosgriff



et al. [13] observed the onset of cracking of building and measured air blast overpressure and vibrations on the ground surface.

By far many simulations on damage behaviours and phenomena of brick masonry under dynamic loads had been done. Zhou et al. [14] simulated the damage and fragmentation of a typical masonry wall under blast loading at different scaled distances. Keys et al. [15] used applied element method to calculate the breakage and debris distribution of masonry subjected to long duration blast loading. Shadlou et al. [16] presented a brief discussion about the main challenges on modelling the reinforced concrete frames, masonry infills, and interaction between them for structures located in seismic zones. Some scholars [17–20] used brick masonry discrete model to explore the details of damage development process of the masonry and the damage phenomenon at the interface between the brick and the mortar. However, this method would consume lots of central processing unit (CPU) and memory resources of computer during calculations [21]. Other scholars [22–26] adopted equivalent homogenized material model to characterize the overall properties of masonry walls.

By now, few researches had been done to study the response of brick masonry under contact explosion loads. In the present study, a series of numerical simulations and experiments are carried out to study the structural response and damage characteristics of brick masonry wall under contact explosion loads. Different explosive charges are deployed in the same contact position to compare the difference among them. The relationship between the dimension of crater and the radius of explosive is obtained. The damage mechanism of brick masonry under explosion load is analysed. Furthermore, the fragmentation and maximum ejection velocities of brick masonry under different conditions are studied.

## 2. Computational Model

**2.1. Physical Model and Algorithm.** The brick masonry wall is composed of mortar and regularly arranged bricks. A separate model is used to establish the brick wall; that is, the brick and mortar are used as independent components. This type of modelling method is intuitive and can accurately simulate the bond between the mortar and the brick. Here, the size of brick is 240 mm (length)  $\times$  115 mm (width)  $\times$  53 mm (thick). 6 pieces are placed in the length direction of the wall ( $X$ -direction), 22 pieces are placed in the height direction ( $Y$ -direction), 2 pieces are placed in the thickness direction ( $Z$ -direction), and the thickness of mortar is 10 mm. So, the total size of brick wall is 1250 mm  $\times$  1490 mm  $\times$  240 mm.

Both brick and mortar are all divided with Lagrange cells. In Lagrange algorithm, the material is attached to the grid to trace the flow of each mass point. The grid and the material are deformed together and the coordinates move with the material, which is one of the most widely used methods to solve the explosion and impact problems. The boundaries of brick wall are all imposed six degrees of freedom constraints, as shown in Figure 1. The spherical

composition 4 (C4) explosive is established by Smoothed Particle Hydrodynamics (SPH). As a meshless discretization method, the main advantage of SPH method has advantage to avoid severe problems associated with mesh tangling and distortion which usually occur in Lagrangian analysis involving large deformation impact and explosive loading events. The explosive is attached to the geometric centre of front surface of brick masonry wall and is detonated from the centre of itself. In order to obtain the pressure on the wall and trace the damage zone, a series of gauge points are set along the horizontal and vertical directions of front and back surfaces. The established simulation model is shown in Figure 2.

**2.2. Material Model and Parameters.** There are two materials in this study, C4 explosives (main charge) and brick masonry (including brick and mortar). The material models and parameters used in these materials are described, respectively.

**2.2.1. C4 Explosive.** As a plastic explosive, C4 is composed of RDX (hexogen), plastic binder, and plasticizer. RDX is the main component of it, about 91%. It is easy to be kneaded into various shapes at will which is often used in breaching obstacles or demolition of large structures. Although this kind of explosive is powerful, it is very safe to use. Even if it is shot directly, it is hard to explode. It can only be detonated with a detonator.

The equation of state (EOS) of detonation products is essential for describing the detonation properties of explosives, and it is the core parameter in simulations of detonation process of explosives. In AUTODYN numerical simulation program, there are three EOS suitable for explosives: Becker–Kistiakowsky–Wilson (BKW) EOS, Jones–Wilkins–Lee (JWL) EOS, and Lee–Tarver EOS. Among them, JWL EOS can accurately describe the characteristics of the detonation product volume, pressure, temperature, and energy during the detonation process [27–29]. The main parameters of JWL EOS for C4 explosive are shown in Table 1. Besides, its loading density  $\rho_e$ , detonation velocity  $D_e$ , and CJ pressure  $P_{CJ}$  are 1.60 g·cm<sup>-3</sup>, 8193 m·s<sup>-1</sup>, and 28 GPa, respectively.

The expression of JWL EOS is as follows:

$$P = A \left( 1 - \frac{\omega}{R_1 V} \right) e^{-R_1 V} + B \left( 1 - \frac{\omega}{R_2 V} \right) e^{-R_2 V} + \frac{\omega E_0}{V}, \quad (1)$$

where  $P$  is the pressure,  $E_0$  is the initial specific energy,  $V$  is the relative volume of the detonation product, and  $A$ ,  $B$ ,  $R_1$ ,  $R_2$ , and  $\omega$  are constants. The parameters  $A$  and  $B$  have dimensions of pressure, while  $R_1$ ,  $R_2$ , and  $\omega$  are dimensionless.

**2.2.2. Brick Masonry.** Brick masonry is a solid entity composed of many blocks that are bonded by mortar as a whole. RHT strength and failure model is chosen to describe the behaviour of brick material, while Mo granular strength model is used to describe the behaviour of mortar material.

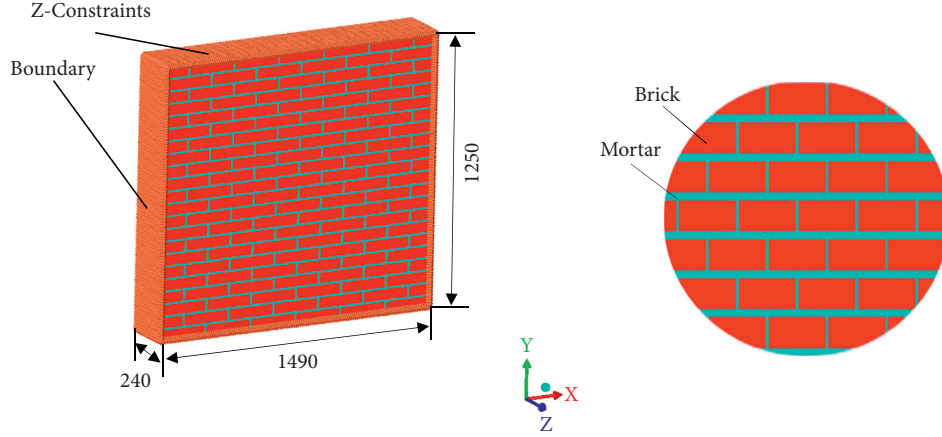


FIGURE 1: Finite element model of brick masonry.

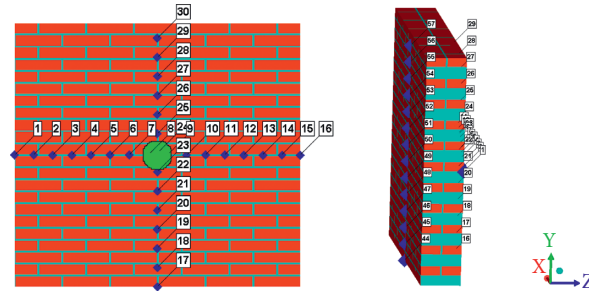


FIGURE 2: The layout of gauge points.

TABLE 1: Parameters of JWL EOS for C4 explosive.

Parameter	$A$ (GPa)	$B$ (GPa)	$R_1$	$R_2$	$\omega$	$E_0$ (J·m <sup>-3</sup> )	$\rho_e$ (g·cm <sup>-3</sup> )	$D_e$ (m·s <sup>-1</sup> )	$P_{CJ}$ (GPa)
Value	609.77	12.95	4.5	1.4	0.25	$9.0 \times 10^9$	1.6	8193	28

RHT model, first proposed by Riedel, Hiemaier, and Thoma, has developed and been widely used in the numerical simulation of explosion shock and other fields. This model is expressed in terms of three stress limit surfaces, namely, initial elastic yield surface, failure surface, and residual strength surface [30, 31]. While the surfaces account for reduction in strength along different meridians as well as strain rate effects, the static compressive meridian surfaces are depicted in Figure 3. The failure surface is formed from material parameters including compressive, tensile, and shear strength of the brick. The model is elastic until the stress reaches the initial yield surface, beyond which plastic strains evolve. When the stress reaches the failure surface, a parameterized damage model governs the evolution of damage, driven by plastic strain, which in turn represents the post-failure stress limit surface by interpolating between failure surface and residual friction surface. There are three stages of linear strengthening and damage softening, as shown in Figure 3.

The failure surface  $Y_{\text{fail}}^*$  is expressed as a function of the normalized pressure  $p$ , the Lode angle  $\theta$ , and strain rate  $\dot{\epsilon}$ :

$$Y_{\text{fail}}^* = Y_{\text{TXC}}^*(p) \cdot R_3(\theta) \cdot F_{\text{RATE}}(\dot{\epsilon}), \quad (2)$$

where  $Y_{\text{TXC}}^*(p)$  represents the compression meridian intensity,  $R_3(\theta)$  is introduced to describe the reduced strength on shear and tensile meridian, and  $F_{\text{RATE}}(\dot{\epsilon})$  represents the dynamic increase factor (DIF) as a function of the strain rate.

The moving elastic limit surface  $Y_{\text{ela}}^*$  can be described as follows:

$$Y_{\text{ela}}^* = Y_{\text{fail}}^* F_{\text{CAP}}(p), \quad (3)$$

where  $F_{\text{CAP}}(p)$  is a function that limits the elastic deviatoric stresses under hydrostatic compression.

In order to describe the strength of the completely crushed material, a residual failure surface  $Y_{\text{res}}^*$  is defined as

$$Y_{\text{res}}^* = B \times (p^*)^M, \quad (4)$$

where  $B$  is the residual failure surface constant,  $p^*$  is the normalized hydrostatic pressure, and  $M$  represents the residual failure surface exponent.

The main parameters of brick material are shown in Table 2.

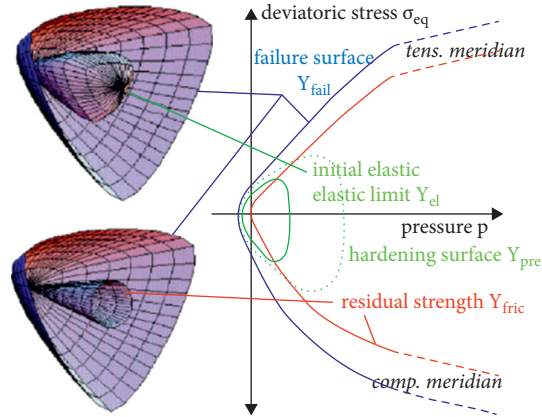


FIGURE 3: The reference spatial distribution and meridian of RHT constitutive elastic limit surface, failure surface, and residual strength surface.

TABLE 2: Main parameters of brick material.

Density ( $\text{g}\cdot\text{cm}^{-3}$ )	Compressive strength (MPa)	Volume modulus (GPa)	Shear modulus (GPa)	Damage constant $D_1$	Damage constant $D_2$	Tensile strength (MPa)
2.25	2.6	11.0	4.4	0.014	1.0	6.0

MO granular continuum model, proposed by Moxnes et al. in 1999, is an extension of the Drucker–Prager model that considers the effects associated with granular materials [32, 33]. The model uses a hydrostatic compaction curve as a function of the density, a model for the yield stress as a function of pressure and elastic modulus as a function of density. The model does not include any strain rate dependency of yield stress. The parameters are constructed by using a quasistatic unilateral compression test and validated by using a high-speed piston (up to 300 m/s) impacting a granular pyrotechnic bed. The yield stress can be described as

$$\sigma_y = \sigma_p + \sigma_\rho \cdot F, \quad (5)$$

where  $\sigma_y$ ,  $\sigma_p$ , and  $\sigma_\rho$  denote the total yield stress, the pressure yield stress, and the density yield stress, respectively, and  $F$  is initially supplied by the user as the initial fraction of yield. Failure occurs if the von Mises stress is greater than both the total yield stress  $\sigma_y$  and  $F_S P$ , where  $F_S$  is the user defined variable slope and  $P$  is pressure. The material parameters of mortar are shown in Table 3.

### 3. Results and Discussion

**3.1. Analysis of the Fracture Process of Brick Masonry.** When an explosive is detonated, the expansion of the hot gases at extremely high pressures causes a shock wave to form, moving outward at high velocity. Nearby structures will suffer some degree of damage from it. If the explosive is put on the surface of the structure to explode, higher-pressure, shorter load durations will be obtained. At this time, a part of the shock wave will penetrate into contacted brick masonry. This part of shock wave is so called transmission shock wave. It will also be affected

by a reverse incoming sparse wave. This reflected wave will form a reflected shock wave load. The propagation of shock waves not only causes dynamic stress to the medium, but also causes the movement, deformation, or destruction of the medium. Shock wave cannot be supplemented with energy during its propagation process, so it will gradually weaken and finally disappear.

When the brick masonry is impacted by the explosion of 2.0 kg C4 spherical charge, the zone suffered from severe impact is damaged to form a crater. Figure 4 shows successive frames of fracture development after explosion on the front surface of brick masonry. It can be seen that the dimensions of crater increase gradually; finally, a big hole is formed.

The stress contours of brick masonry under explosion loads are shown in Figure 5(a). The closer to the centre the element is, the larger the stress is. Accordingly, the larger the strain gets. When the strains of elements are up to failure strain, the elements will be eroded, such as gauge #8, gauge #9, and gauge #23 on the front surface close to the centre of brick masonry (in Figure 5(b)). The strains of other gauges are lower than failure strain, so they do not fail. The zone with a large number of continuous eroded elements is called a crater. The more the effective strains of elements reach failure strain, the larger the crater is. Figure 5(c) shows that the compression behaviour of different gauges. When the value of compression is below zero, the gauges suffer from the effect of tensile stress. When the crater breaks, a few fragments will be extruded from it. The maximum ejection velocity is about  $16.2 \text{ m}\cdot\text{s}^{-1}$ , as shown in Figure 5(d).

Figure 6 presents the dimensions change of damage zone on the front surface when brick masonry wall is damaged by 2.0 kg C4 spherical charge. With the increase of time, three dimensions become larger and larger. The 240 mm thickness

TABLE 3: Main parameters of mortar material.

Density ( $\text{g}\cdot\text{cm}^{-3}$ )	Poisson's coefficient	Volume modulus (GPa)	Shear strength residual coefficient (GPa)	Failure principal tensile stress (MPa)
1.7	0.10	5.9	2.2	1.0

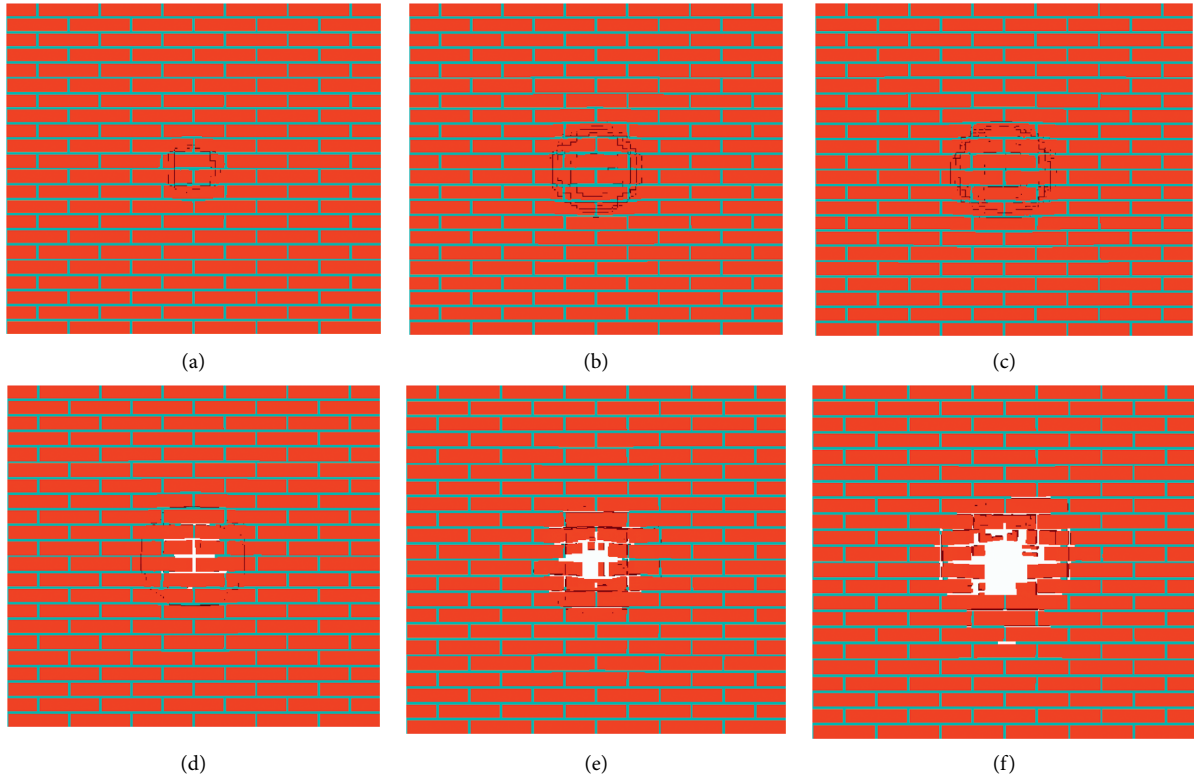


FIGURE 4: The fracture development of brick masonry by 2.0 kg C4 explosive. (a) 0.1 ms. (b) 0.5 ms. (c) 1.0 ms. (d) 2.0 ms. (e) 4.0 ms. (f) 6.0 ms.

wall cracks at about 2.0 ms while the crater reaches its maximum cross section at about 5 ms. Before the crater breaks, it has reached the maximum cross section surface, beyond 400 mm. The growth rates of  $X$  and  $Y$  dimensions are almost the same, which are larger than that of  $Z$  dimension. So, the shape of cross section of crater is close to be circular.

### 3.2. Damage Zone of Brick Masonry under Different Charges.

In order to study the damage characteristics of the brick masonry under different explosion loads, five C4 spherical charges, 0.5 kg, 1.0 kg, 2.0 kg, and 4.0 kg, are designed. The radii of these charges are 42.10 mm, 53.04 mm, 66.82 mm, and 84.19 mm, respectively. These charges are all placed on the centre of front surface of brick masonry wall to explode.

Figure 7 gives damaged pattern of the back of brick masonry wall subjected to different explosion loads. As we know, shock wave will be produced when explosive is detonated and then turns to compression wave in brick masonry. When stress wave transmits to the back free surface of brick masonry, a reverse tensile wave is inevitably formed to stretch the back to go farther. When the quantity

of charge is smaller, such as 0.5 kg, a small crater is found on the front face just at the contact position. Seen from the back surface of the wall, there is a small hole and few fragments are extruded. When the quantity of charge increases to 1.0 kg, a larger crater is formed on the front. Viewing from the back, the mortar in the centre is extended to form a larger hole and a few fragments are ejected. At the same time, it can be found that left and right sides of masonry wall are slightly affected by such a high explosion. That may be due to the bond strength of transverse mortar layer being lower than that of longitudinal brick-mortar interaction. If 2.0 kg explosive charge is used, deeper crater appears with more distinct bulge on the back. The crater breaks to form more fragments and two sides of masonry wall are heavily affected along transverse mortar layers. When the charge reaches 4.0 kg, an even larger crater appears. The sizes of back fracture zone and hole are all larger than above results.

Next, two experiments were conducted to investigate the damage characteristics of masonry wall. 1.0 kg and 2.0 kg spherical explosive charge were chosen to be detonated on the surface of masonry wall. Crater holes are formed under such two equivalent explosives, as shown in Figure 8.

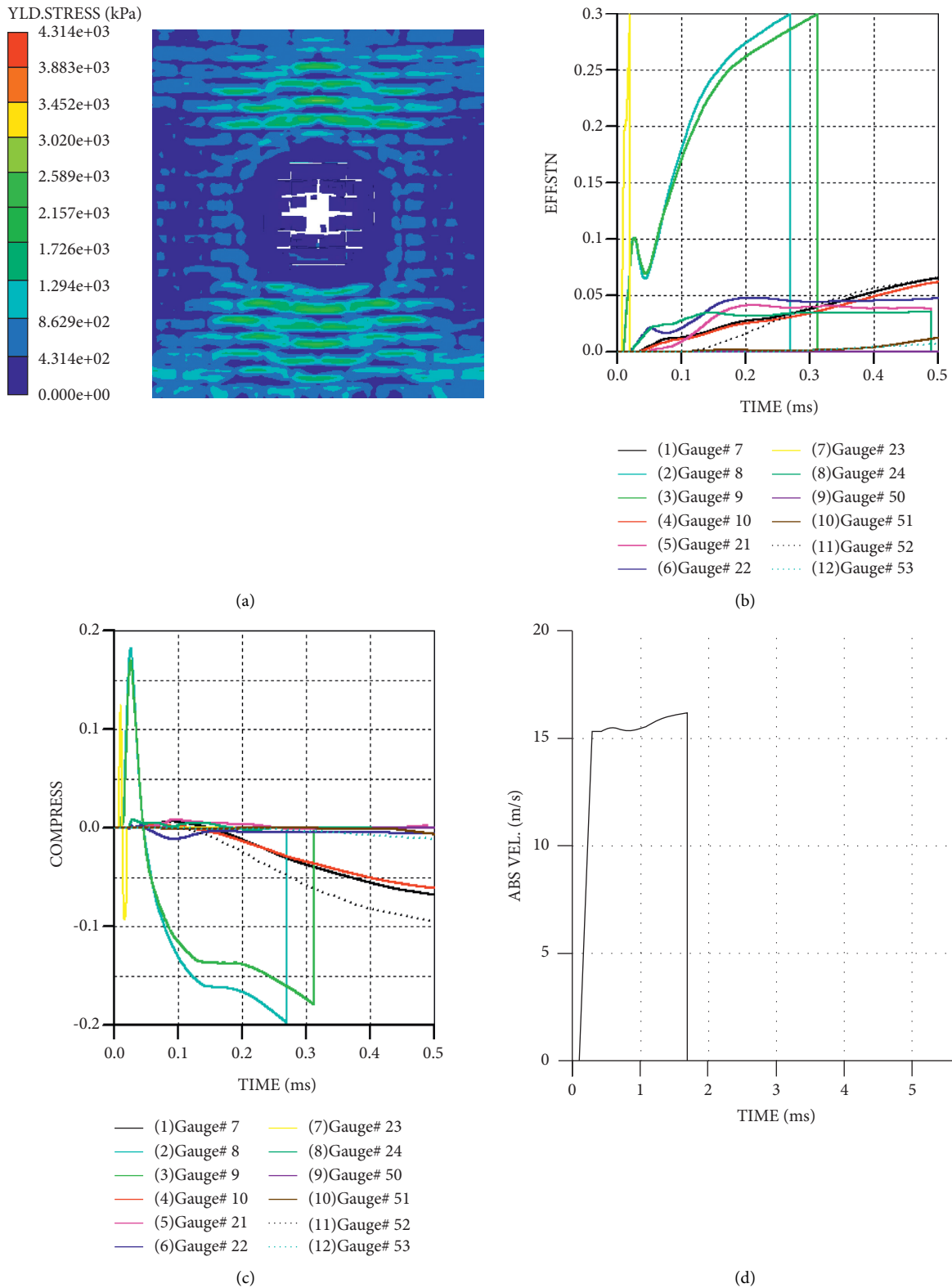


FIGURE 5: Simulation results of 2.0 kg C4 explosion load. (a) Contour of stress distribution. (b) Effective strains of gauges. (c) Compression behaviour of gauges. (d) Ejection velocity of fragments.

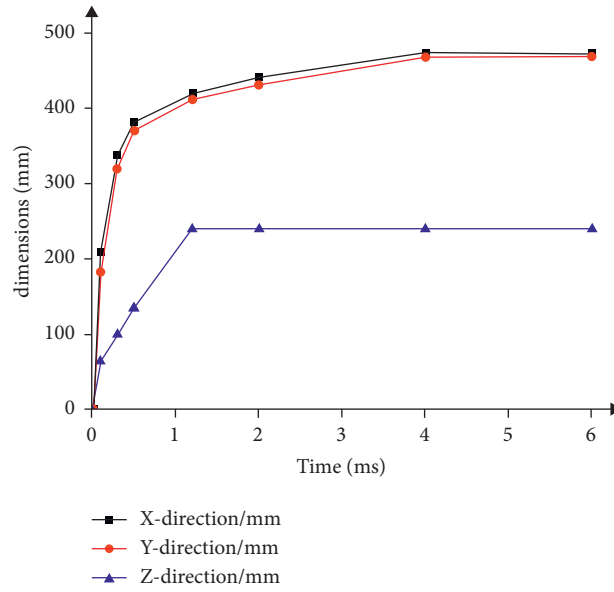


FIGURE 6: The dimensions in three directions of crater for 2.0 kg C4 explosion load.

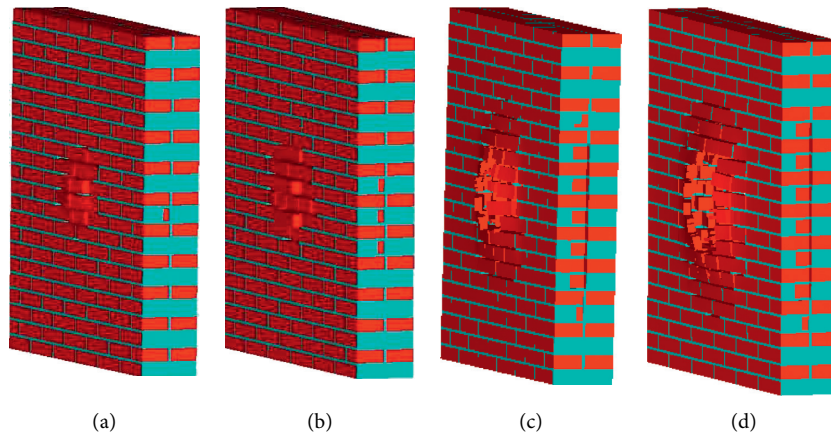


FIGURE 7: Destruction diagram of brick masonry under different explosive loads. (a) 0.5 kg. (b) 1.0 kg. (c) 2.0 kg. (d) 4.0 kg.

Compared with the simulation results in Figure 9, the experimental results are in good agreement with them.

Table 4 shows the dimensions of damage zones of brick masonry wall under different explosion loads. With the increase of the quantity of explosive, the lengths in  $X$ -direction and  $Y$ -direction increase. Moreover, the size of crater on front surface is smaller than that of fracture zone on back surface. When explosive is attached to brick masonry, released energy would be absorbed by masonry wall and thus compressive stress wave would spread in it. Once compressive stress wave reaches the back free surface, an enhanced tensile stress wave will appear due to impedance mismatch between wall and air. The reflected tensile wave from free surface encounters the inbound compressive stress resulting in total stress that is subtractive. When the total stress is tensile (tensile stress greater than inbound compressive stress) and exceeds the tensile strength of any point in the masonry matrix, cracks or fractures will occur. For

brittle brick masonry material, the damage area on the back free surface can be larger than that on the front incident surface.

*3.3. A Simple Predictive Model of the Dimensions of Hole.* When the spherical explosive is detonated on the surface of masonry wall, according to the simulation and experiments, the crater hole is basically determined by the radius of the explosive. The simplified model can be described in Figure 10.

Since the explosion energy is released on the front surface of contact point and evenly in all directions, the radius of crater hole is merely controlled by the radius of explosive charge. However, the relationship between these two radii is not given clearly.

$$r_d \propto r_0. \quad (6)$$



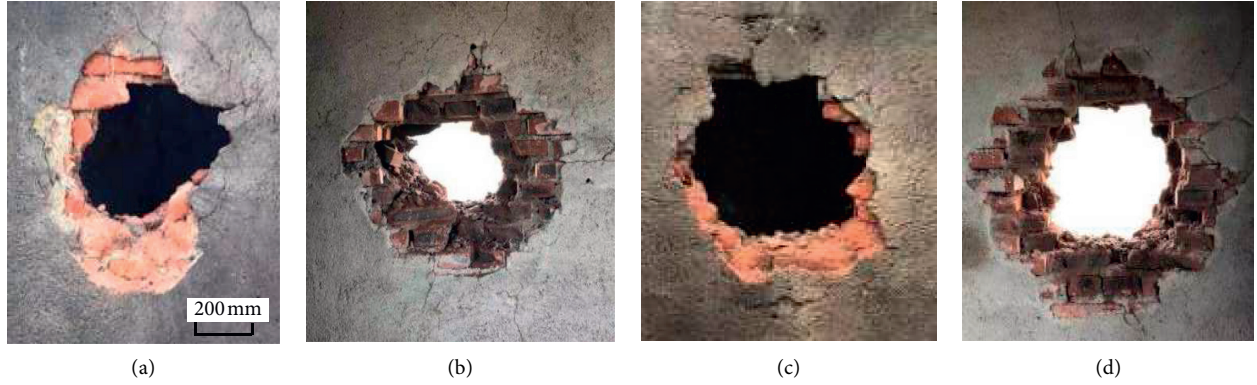


FIGURE 8: Experimental results under two different explosion loads. (a) Front view of 1.0 kg. (b) Back view of 1.0 kg. (c) Front view of 2.0 kg. (d) Back view of 2.0 kg.

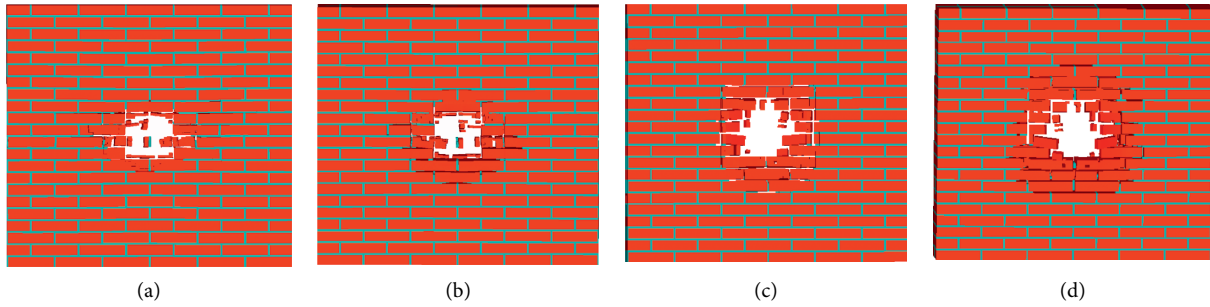


FIGURE 9: Simulation results under two different explosion loads. (a) Front view of 1.0 kg. (b) Back view of 1.0 kg. (c) Front view of 2.0 kg. (d) Back view of 2.0 kg.

TABLE 4: The damaged zones of brick masonry under different conditions.

Case no.	Charge (kg)	Crater in front surface		Fracture in back surface	
		X-direction (mm)	Y-direction (mm)	X-direction (mm)	Y-direction (mm)
I	0.5	266	252	366	338
II	1.0	364	347	524	447
III	2.0	473	468	604	618
IV	4.0	637	630	755	751

According to Table 4, the dimensions of front surface are drawn in Figure 11(a).

The ratios of radius of holes to the radius of explosive charges for four cases increase monotonously from 6.32 to 7.57. When fitting these data in Figure 11(b), it can be expressed as

$$r_d = 1.2859r_0^{1.24306}. \quad (7)$$

Thus, a power function predicting model of the radius of hole is found.

**3.4. A Simple Fitting Model of Maximum Fragment Velocity.** With the increase in the quantity of the explosive, more and more cracks along the longitudinal direction are noticed. Once the hole is formed, the damaged bricks will be blown out

to produce a number of fragments. Seen from the viewpoint of energy, the more quantity of explosive is used, the higher explosive energy loading on the surface of masonry wall is produced, and the higher the velocity of fragment gets. That is to say, the ejection velocities of fragments are determined by the radius of explosive too for spherical explosive charge. The fragment with maximum ejection velocity is found at the centre of crater or the apex of crater before breakup.

The maximum velocity of fragment  $V_{\max}$  is proportional to the radius of spherical explosive:

$$V_{\max} \propto r_0. \quad (8)$$

Figure 12 presents the maximum ejection velocity of fragments under different conditions. Adding coordinate point (0, 0), there are five groups of data. It is found that a power function curve fits these data well.

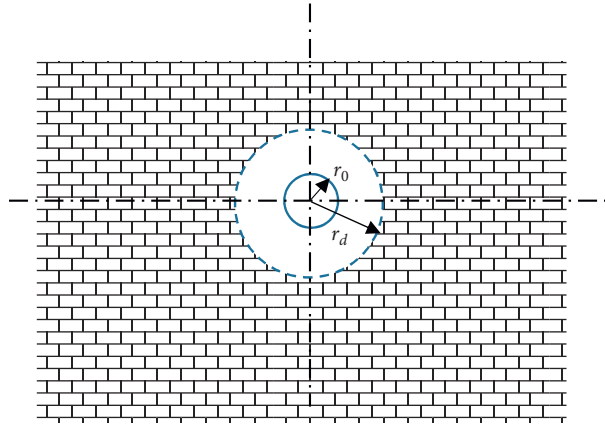


FIGURE 10: The relationship between the radius of crater hole and the radius of explosive.

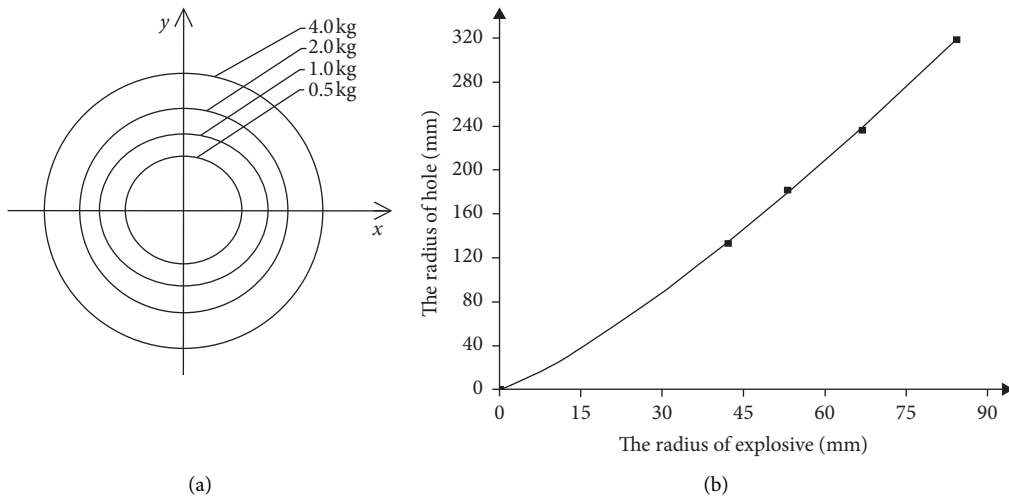


FIGURE 11: Crater on front surface under different charges. (a) Dimensions of holes. (b) Fitting curve.

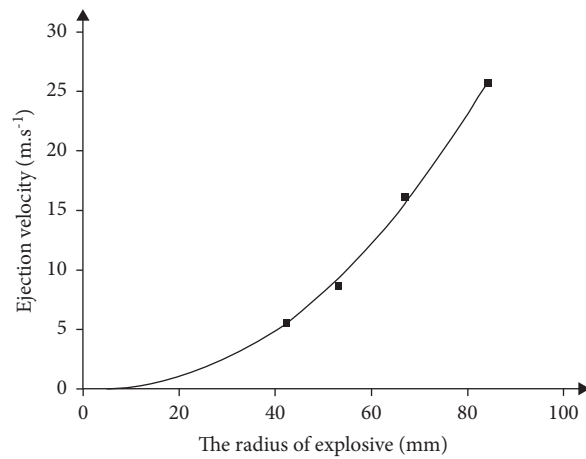


FIGURE 12: The maximum ejection velocities of fragments under different charges and fitting curve.

Now, the maximum ejection velocity is power function to the radius of explosive.

$$V_{\max} = 0.00139r_0^{2.21747}. \quad (9)$$

When the explosive is 4.0 kg, the maximum ejection velocity can reach about 26 m/s, which may cause severe damage to surrounding equipment or personnel.

#### 4. Conclusions

In this paper, numerical simulation and verification experiments of damage response of brick masonry under different amounts of C4 spherical charges are carried out. The following conclusions are obtained:

- (1) When constrained brick masonry is exposed to contact explosion by spherical charge, a crater is formed on the front. The shape of cross section of crater is almost circular. The cross section dimension of crater increases monotonously with the radius of spherical explosive charge. For four cases in this study, the ratios of radial lengths to the radius of explosive charge increase from 6.32 to 7.57.
- (2) Explosion energy releases compressive wave directly on the front surface, and then stress wave (transmission wave) will travel to the back to make brickwork cracked. The combination effect of front compressive wave and back tensile wave are the main factors influencing the crack of brick masonry wall. When the back tensile wave is beyond the tensile strength of brick masonry, fracture zone will be pulled out to form a hole. The radius of hole is directly determined by the radius of the explosive. A power function predictive model is obtained to estimate the size of hole for C4 explosive detonated on the surface of 240 mm thickness masonry wall.
- (3) The fragments can get higher velocities under larger explosion load, which may cause lethal damage to surrounding equipment or personnel. In the region of research, there is a power function relationship between maximum ejection velocity and the radius of explosive.

#### Data Availability

The data used to support the findings of this study are included within the article.

#### Conflicts of Interest

The authors declare that there are no conflicts of interest regarding the publication of this study.

#### Acknowledgments

The authors acknowledge the financial support for this work provided by the National Key R&D Program of China (2017YFC0822105).

#### References

- [1] F. Parisi, C. Balestrieri, and D. Asprone, "Blast resistance of tuff stone masonry walls," *Engineering Structures*, vol. 113, pp. 233–244, 2016.
- [2] A. T. Edwards and T. D. Northwood, "Experimental studies of the effects of blasting on structures," *The Engineer*, vol. 30, pp. 538–546, 1960.
- [3] C. W. Wong and M. Karamanoglu, "Modelling the response of masonry structures to gas explosions," *Journal of Loss Prevention in the Process Industries*, vol. 12, pp. 199–205, 1999.
- [4] L. A. De Be'jar, L. Simmons, and J. L. Davis, "Standoff-mortar fragment velocity characterization before and after perforating conventional building walls," *International Journal of Impact Engineering*, vol. 35, pp. 1043–1052, 2008.
- [5] P. W. Sielicki and T. Lodygowski, "Masonry wall behaviour under explosive loading," *Engineering Failure Analysis*, vol. 104, pp. 274–291, 2019.
- [6] S. Shi, D. Du, W. Xu, and S. Wang, "Theoretical and experimental study on an innovative seismic retrofit solution for old brick masonry buildings," *Engineering Structures*, vol. 225, Article ID 111296, 2020.
- [7] R. K. Varma, C. P. S. Tomar, S. Parkash, and V. S. Sethi, "Damage to brick masonry panel walls under high explosive detonations," *Pressure Vessels and Piping Division ASME*, vol. 351, pp. 207–216, 1997.
- [8] B. Gabrielsen, C. Wilton, and K. Kaplan, "Response of arching walls and debris from interior walls caused by blast loading," Tech. Rep. AD-A014 957, URS Research Company, San Mateo, CA, USA, 1975.
- [9] J. S. Davidson, J. R. Porter, R. J. Dinan, L. H. Michael, and D. C. James, "Explosive testing of polymer retrofit masonry walls," *Journal of Performance of Constructed Facilities*, vol. 18, pp. 100–106, 2004.
- [10] S. T. Dennis, J. T. Baylot, and S. C. Woodson, "Response of 1/4-scale concrete masonry unit (CMU) walls to blast," *Journal of Engineering Mechanics*, vol. 128, no. 2, pp. 134–142, 2002.
- [11] S. Ahmad, A. Elahi, and H. Pervaiz, "Experimental study of masonry wall exposed to blast loading," *Materiales De Construcción*, vol. 64, no. 313, Article ID e007, 2014.
- [12] R. A. Keys and S. K. Clubley, "Establishing a predictive method for blast induced masonry debris distribution using experimental and numerical methods," *Engineering Failure Analysis*, vol. 82, pp. 82–91, 2017.
- [13] K. M. Norén-Cosgriff, N. Ramstad, A. Neby, and C. Madshus, "Building damage due to vibration from rock blasting," *Soil Dynamics and Earthquake Engineering*, vol. 138, no. 106331, pp. 1–13, 2020.
- [14] X. Q. Zhou, H. Hao, and A. J. Deeks, "Numerical modeling of response and damage of masonry walls to blast loading," *Transactions of Tianjin University*, vol. 12, no. 1, pp. 132–137, 2006.
- [15] R. Keys and S. Clubley, "Modeling debris distribution of masonry panels subject to blast loads using experimental & applied element methods," in *Proceedings of the 15th International Symposium on the Interaction of the Effects of Munitions with Structures*, Potsdam, Germany, September 2013.
- [16] M. Shadlou and M. M. Kashani, "A review on the current trends on computational modelling of masonry-infilled reinforced concrete frames," *Journal of Physics Conference Series*, vol. 1264, Article ID 012044, 2019.
- [17] X. Wei and R. G. Stewart, "Model validation and parametric study on the blast response of unreinforced brick masonry

- walls,” *International Journal of Impact Engineering*, vol. 37, pp. 1150–1159, 2010.
- [18] C. S. Meyer, “Development of brick and mortar material parameters for numerical simulations,” *Dynamic Behavior of Materials*, vol. 1, pp. 351–359, 2011.
- [19] N. Gebbeken, T. Linse, and T. Araujo, “Masonry under dynamic actions - experimental investigations, material modeling and numerical investigations,” *Advances in Protective Structures Research*, Taylor & Francis Group London CRC Press, London, UK, pp. 131–162, 2012.
- [20] L. Chen, Q. Fang, J. Fan, Y. Zhang, H. Hao, and J. Liu, “Responses of masonry infill walls retrofitted with CFRP, steel wire mesh and laminated bars to blast loadings,” *Advances in Structural Engineering*, vol. 17, no. 6, pp. 817–836, 2014.
- [21] S. Pietruszczak and X. Niu, “A mathematical description of macroscopic behavior of brick masonry,” *International Journal of Solids and Structures*, vol. 29, pp. 531–546, 1992.
- [22] G. Ma, H. Hao, and Y. Lu, “Homogenization of masonry using numerical simulations,” *Journal of Engineering Mechanics*, vol. 127, no. 5, pp. 421–431, 2001.
- [23] G. Milani, P. B. Lourenco, and A. Tralli, “Homogenized rigid-plastic model for masonry walls subjected to impact,” *International Journal of Solids and Structures*, vol. 46, no. 22-23, pp. 4133–4149, 2009.
- [24] X. Wei and H. Hao, “Numerical derivation of homogenized dynamic masonry material properties with strain rate effects,” *International Journal of Impact Engineering*, vol. 36, pp. 522–536, 2009.
- [25] C. Wu and H. Hao, “Derivation of 3D masonry properties using numerical homogenization technique,” *International Journal for Numerical Methods in Engineering*, vol. 66, no. 11, pp. 1717–1737, 2010.
- [26] C. Silva Luís, B. Lourenço Paulo, and M. Gabriele, “Rigid block and spring homogenized model (HRBSM) for masonry subjected to impact and blast loading,” *International Journal of Impact Engineering*, vol. 109, pp. 14–28, 2017.
- [27] B. Li, B. Chang, and L. Zhang, “Influence of charge density on JWL equation of state of explosives,” *Journal of Ordnance Equipment Engineering*, vol. 42, no. 1, pp. 174–178, 2021.
- [28] S. Koli, P. Chellapandi, L. B. Rao, and A. Sawant, “Study on JWL equation of state for the numerical simulation of near-field and far-field effects in underwater explosion scenario,” *Engineering Science and Technology, an International Journal*, vol. 23, pp. 758–768, 2020.
- [29] L. Michael and N. Nikiforakis, “A multi-physics methodology for the simulation of the two-way interaction of reactive flow and elastoplastic structural response,” *Journal of Computational Physics*, vol. 367, pp. 1–27, 2018.
- [30] T. Borrvall and W. Riedel, “The RHT concrete model in LS-DYNA,” in *Proceedings of the 8th European LS-DYNA Conference*, Strasbourg, France, January 2011.
- [31] C. Hecktner and J. Sievers, “Comparison of the RHT concrete material model in LS-DYNA and ANSYS AUTODYN,” in *Proceedings of the 11th European LS-DYNA Conference*, Salzburg, Austria, May 2017.
- [32] J. F. Moxnes, G. Ødegårdstuen, A. Atwood, and P. Curran, “Mechanical properties of a porous material studied in a high speed piston driven compaction experiment,” in *Proceedings of the 30th International Annual Conference of the ICT*, Fraunhofer ICT, Karlsruhe, Germany, June 1999.
- [33] D. Ambrosini and B. Luccioni, “Effects of underground explosions on soil and structures,” *Underground Space*, vol. 5, no. 4, pp. 324–338, 2019.

## Research Article

# Rheological Properties of Argillaceous Intercalation under the Combination of Static and Intermittent Dynamic Shear Loads

Xin Zhang <sup>1</sup>, Qian Dong <sup>2,3</sup>, Xiangping Zhang <sup>1</sup>, Ming Lang <sup>1</sup>, Suzhi Zhao <sup>1</sup>,  
Zhuoang Chen <sup>2,3</sup> and Jinshan Sun <sup>2,3</sup>

<sup>1</sup>China Railway 18 Bureau Group Co.,Ltd, Tianjin 300222, China

<sup>2</sup>Hubei Key Laboratory of Blasting Engineering, Jiangnan University, Wuhan, Hubei 430056, China

<sup>3</sup>Hubei (Wuhan) Institute of Explosion Science and Blasting Technology, Jiangnan University, Wuhan, Hubei 430056, China

Correspondence should be addressed to Jinshan Sun; [sunjinshan@cug.edu.cn](mailto:sunjinshan@cug.edu.cn)

Received 21 January 2021; Accepted 28 July 2021; Published 9 August 2021

Academic Editor: Francesco Bucchi

Copyright © 2021 Xin Zhang et al. This is an open access article distributed under the Creative Commons Attribution License, which permits unrestricted use, distribution, and reproduction in any medium, provided the original work is properly cited.

The construction and long-term operation stage of the rock slope with argillaceous interlayer will be subjected to intermittent dynamic loads, such as blasting and earthquake. For the argillaceous interlayer in the rock slope, its rheological properties are not only related to the initial stress state caused by the gravity of the overlying rock mass but also affected by intermittent dynamic loads. In order to investigate the rheological properties of argillaceous intercalation under the combination of static and intermittent dynamic shear loads, the rheological tests of argillic intercalated soil samples under static shear, static and cyclic dynamic shear, and static and intermittent dynamic shear were carried out, and the rheological deformation characteristics of soil samples under different shear conditions were analyzed. The results show that when the soil specimens in the static shear rheological process are disturbed by intermittent dynamic shearing load, the intermittent dynamic disturbances might have no remarkable influence on the rheological deformation of the specimens if the initial static shearing stress and intermittent dynamic shearing stress were comparatively low. However, low-intensity intermittent dynamic disturbances might accelerate the rheological deformation process of the specimens remarkably if the initial static shearing stress state was close to their shearing strength. There was a stress threshold when the soil specimens failed under the static and cycling dynamic shear and static and intermittent dynamic shear, which is determined by the sum of static shear stress and dynamic shear stress peak. For rock slopes controlled by rheological weak structural planes and influenced by long-term blasting vibrations, the transient and long-term dynamic stability should be comprehensively analyzed.

## 1. Introduction

There are inevitably a certain number of weak structural planes in natural rock slope, which control their mechanical response and stability [1–5]. Under the natural actions, such as self-weight, rainfall, and earthquake, rock slopes often slide along these weak structural planes and induce landslide disaster. Usually, these weak structural planes have obvious rheological properties, and their mechanical parameters will deteriorate under dynamic loads such as earthquake and blasting excavation, which lead to rheological deformation and progressive instability of rock slope [6, 7]. Therefore, it is of great theoretical and practical significance to study the

rheological properties of weak structural planes under dynamic loads for improving the long-term stability of rock slope and avoiding landslide failure.

It is well known that the vibration induced by blasting excavation has adverse effects on the surrounding buildings and equipment [8, 9]. At the same time, the dynamic loads of rock slope, such as earthquake or blasting excavation, are mostly long-term or periodic [10, 11]. In sum, the effects of intermittent dynamic loads on weak interlayer are mainly the accumulation of instantaneous damage and the change of long-term deformation characteristics.

Intensive research had been carried out on the cumulative damage of rock or structural planes caused by

intermittent or multiple dynamic loads [12–16]. For example, Li et al. [17] adopted the restart function of the finite element software ANSYS/LS-DYNA to explore the evolution mechanism and distribution law of rock cumulative damage under cyclic blasting. Liu et al. [18] studied the cumulative damage and failure mode of horizontal layered rock slope subjected to seismic loads. Cao et al. [19] built on the HJC constitutive model to study the effects of cyclic blast loading on shared rock in a neighborhood tunnel. Chai et al. [20] conducted a dynamic impact test to study on dynamic compression characteristics of rock with filled joints after cumulative damage. Song et al. [21] utilized the ground penetrating radar to detect the surrounding rock cumulative damage during tunnel blasting excavation.

On the other hand, because the rheology of weak discontinuities has a great influence on the long-term stability of geotechnical engineering, some scholars had systematically studied the rheological characteristics of weak discontinuities under static loads [22–24], but there are few studies on its rheology under dynamic disturbance. For example, Šancer et al. [25] presented some results of the laboratory tests on the time-dependent behavior of three types of sandstone and focused on the rheological rock properties during vibration (cyclic) loading. Hu et al. [26, 27] studied the dynamic rheological parameters of sludge soft soil through dynamic shear tests, and the rheological mechanism characteristics and rheological parameters of sludge soft soil under dynamic loading were deduced.

To sum up, the rock slopes formed by the open-pit mine, water conservancy and hydropower engineering, large-scale building foundation pit, and so on are often disturbed by blasting seismic effect for a long time. However, there are few studies on the influence of dynamic disturbances on the rheological process of weak structural planes of slope, so that the static evaluation methods are still mainly used to evaluate the long-term stability of rock slope, and only the transient stability analysis method is used to evaluate the dynamic stability of slope. For this reason, this paper has carried out preliminary laboratory test research on the rock slope controlled by the weak structural planes under the long-term disturbances of blasting excavation, and the shear rheological characteristics of the weak mud interlayer under the intermittent cyclic dynamic load were analyzed.

## 2. Influence Mechanism Analysis

The weak structural planes generally refer to the geological structural planes with weak shear strength, such as fault fracture zones and weak interlayers. There are many types of soft structural planes, and their properties are complex. Among them, the filling weak structures planes have wide distribution, low strength, and significant rheological properties and are sensitive to blasting vibration.

Therefore, the representative thin-layered muddy interlayers were selected in this paper. In the rock slope, the soft structural planes are always subjected to the gravity of the overlying strata, which can lead to normal stress and tangential stress on the structural planes. When the production blasting excavation was carried out in a rock slope as

shown in Figure 1(a), the incidental blasting seismic waves will cause the overlying rock mass on the structural surface to bear two horizontal and one vertical seismic inertial forces. If the intensity of blasting excavation is high, or under the action of long-term cyclic blasting loads, the strength of muddy interlayers will be decreased, which will eventually lead to landslide hazard on the slope, as shown in Figure 1(b). After the seismic inertial forces are applied to the soft structural plane, additional dynamic stresses in the normal and tangential directions can be formed as shown in Figure 2, where  $\sigma_s$ ,  $\sigma_d$ ,  $\tau_s$  and  $\tau_d$  denote initial normal stress, additional dynamic normal stress, initial shear stress, and additional dynamic shear stress of the argillized interlayer.

The seismic inertial forces and additional dynamic stresses are mainly affected by the velocity and acceleration of rock mass vibration caused by blasting. At present, according to the Blasting Safety Regulation (GB6722-2014) in China, the safe allowable particle vibration velocity of permanent rock slope is 5~15 cm/s (vibration frequency 10~100 Hz). According to the theoretical conversion, the relation between vibration velocity  $v$  and acceleration  $a$  is as follows:

$$a = 2\pi f v, \quad (1)$$

where  $\pi$  and  $f$  are the circumference ratio and the frequency of particle vibration velocity. The corresponding safety allowable rock mass particle acceleration value should be approximately 3~15 m/s<sup>2</sup>. Generally, in order to ensure the stability of the rock slope, after the blasting charge is controlled, the measured particle acceleration on the surface of slope is generally about 0~3 m/s<sup>2</sup> (area far away from the explosion source). That is, the additional seismic inertial forces are about 0~0.3 times the weight of the overlying rock mass, so the peak value of the additional dynamic stresses in the normal and tangential directions is also about 0~0.3 times the static normal and tangential stresses.

## 3. Experimental Methods

In order to study the influence of blasting vibration on the soft argillaceous intercalations, argillic intercalated circular cake saturated soil samples were made, and rheological tests under static shear, static and cyclic dynamic shear, and static and intermittent dynamic shear were carried out on those samples with a direct-shear rheometer attached with dynamic loads.

**3.1. Test Instrument.** The ZLB-1 triple rheological direct shear tester (Figure 3) produced by Nanjing Soil Instrument Factory was used in the test. The instrument applies certain normal pressures on the soil samples and a shear force on the shear surface to test the shear deformation of the samples. The diameter and height of the specimen corresponding to the equipment are 61.8 mm and 20 mm, respectively, and the maximum shear and normal force provided by the instrument are both 1.8 kN. An electromagnet controlled by a signal generator was installed at the bottom of the instrument weight to apply a simple harmonic vibration load, and an additional dynamic shear stress can be applied to the samples.



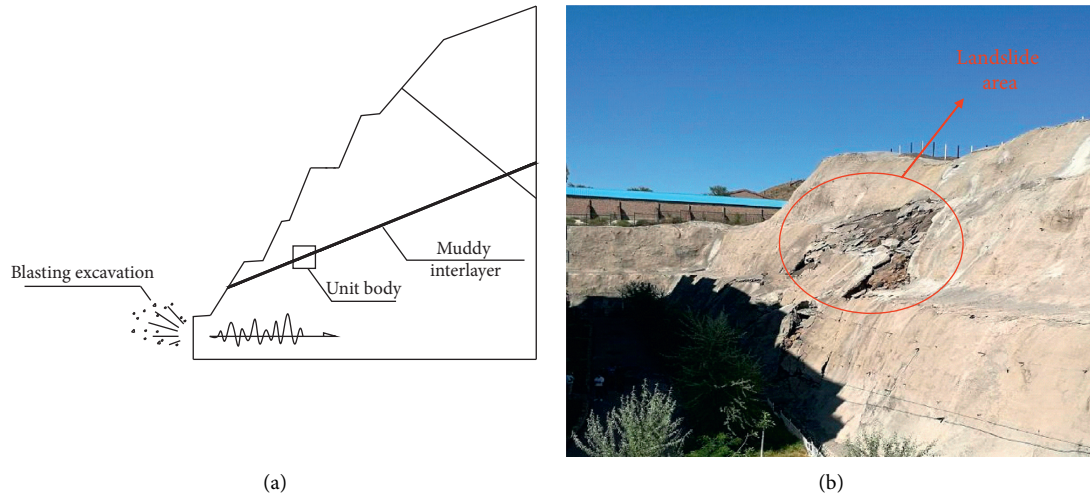


FIGURE 1: Rock slope with an argillaceous intercalation under blasting influence. (a) Force analysis of slope. (b) Landslide hazard.

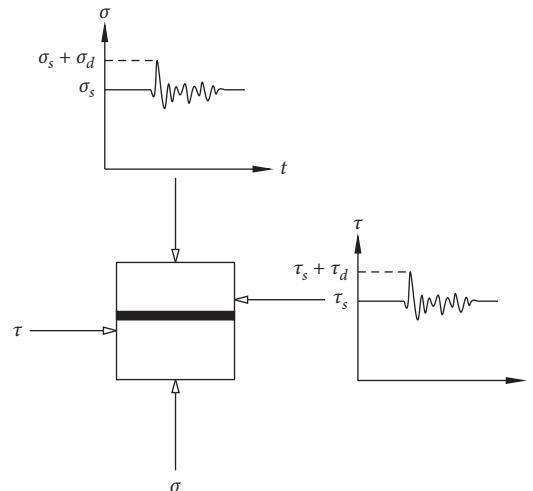


FIGURE 2: Stress diagram of the argillized interlayer element under blasting loads.

**3.2. Soil Samples' Preparation.** The soil samples were taken from a clay-like argillaceous interlayer with a thickness of 5 cm~20 cm in a quartz sandstone formation in Wuhan, a piece of it shown in Figure 4(a), and the standard shear test specimens with the diameter  $D=61.8$  mm and the thickness  $H=20$  mm were made matching with test equipment as shown in Figure 4(b). The physical and mechanical parameters of the soil samples are shown in Table 1.

**3.3. Experimental Procedure.** Shear rheological tests under static shear, static and cyclic dynamic shear, and static and intermittent dynamic shear were conducted for the prepared soil specimens. Before the test, apply pressure to the specimens in the shear box of the rheological direct shear apparatus for consolidation, and it lasts for 24 h. The detailed procedure of the three experiments conducted is shown below.

- (1) Static shear rheological test: three soil samples were made, and the permeable rocks were immersed in water. Rubber film was sandwiched between the permeable rocks and the samples. After the samples were consolidated for 24 hours under a shear stress of 22.5 kPa and a normal pressure of 150 kPa, the shear stress increased to 25 kPa, 32 kPa, and 38 kPa, which are 60%, 75%, and 90% of its ultimate shear stress, respectively. The rheological deformation characteristics of the samples were observed after the static loads were applied and remained unchanged.
- (2) Static and cyclic dynamic shear rheological test: three sets of three soil samples were made, a total of nine specimens. After consolidation for 24 hours under the stress state of 150 kPa normal pressure and 22.5 kPa shear stress, the shear stress of three groups of samples is loaded to its ultimate shear stress at 60%, 75%, and 90%, respectively, and then each



FIGURE 3: The ZLB-1 creep shear apparatus.

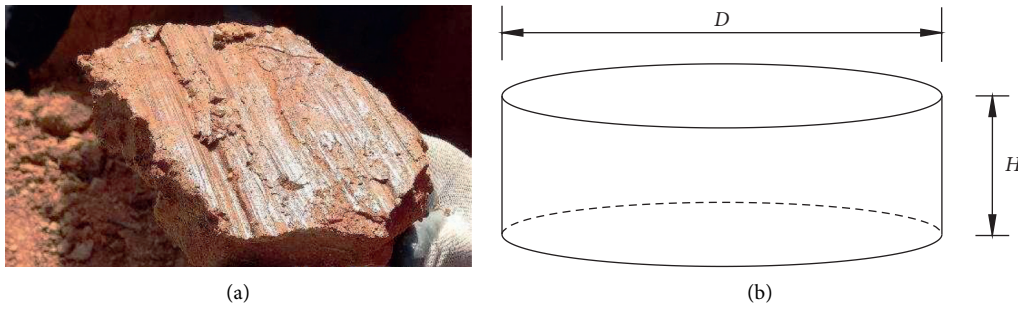


FIGURE 4: Preparation of soil samples. (a) A piece of the argillaceous interlayer. (b) Soil sample size illustration.

TABLE 1: Parameters of the soil specimens.

Parameters	Values
Density	1.85 g/cm <sup>3</sup>
Void ratio	0.82
Moisture content	24.8%
Saturation	81.9%
Cohesive force	5.0 kPa
Friction angle	14°

group of samples exerted the dynamic shear loads of 30 Hz frequency, and the corresponding peak values were 2.1 kPa, 4.2 kPa, and 8.5 kPa in the form of a sine wave, so the peak shear stresses caused by the dynamic loads were approximately 5%, 10%, and 20% of the ultimate shear stress, respectively. The maximum deformation was measured after applying the dynamic loads for 30 s and suspended for another 30 s.

- (3) Static and intermittent dynamic shear rheological stress: the preparation and consolidation process of

the soil samples and the initial static shear state were the same as the static and cyclic dynamic shear rheological test. Then, the 30 Hz frequency dynamic shear loads of the peak values were 2.1 kPa, 4.2 kPa, and 8.5 kPa, and in the form of a sine wave, they were applied. In the practical engineering, the dynamic disturbance of blasting was generally once a day. In order to shorten the test time, the dynamic disturbances were five times a day at 9:00, 12:00, 15:00, 18:00, and 21:00, respectively, and the duration time of each disturbance was 1 s.

## 4. Results and Analysis

**4.1. Static Shear Rheological Characteristics of Argillaceous Intercalation.** According to the test scheme, after the soil specimens were consolidated for 24 hours under the action of normal pressure and shear stress, the deformation was measured after the shear stress increased, and then the value of strain is 0. Therefore, the shear deformation curves (Figure 5) contain the elastic deformation increment of

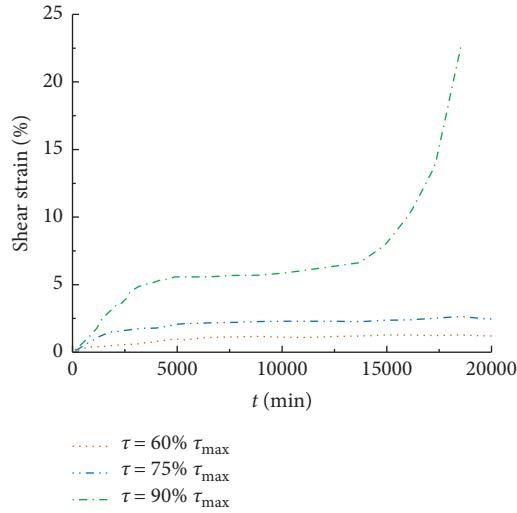


FIGURE 5: Strain of specimens under static shear load.

samples. However, in the test process, the shear strain of the three samples also increased rapidly after the sudden increase of shear stress. Because the shear stress increment was relatively small, the sudden increase of deformation increment was within 0.03 mm, and the shear strain was within 0.5%, so the elastic deformation increment was small, which was not significant. Therefore, the rheological deformation of the samples can be shown in Figure 5.

After the elastic deformation stage, two specimens with shear stress  $\tau$  of 60%  $\tau_{\max}$  (ultimate shear stress) and 75%  $\tau_{\max}$ , the deformation gradually increased with the time passing within the first 5000 mins, and the shear strain was less than 2%. After 5000 mins, the increase of deformation is not significant, and the specimens did not break during the test, so their deformation may be mainly viscoelastic deformation.

When the specimen shear stress  $\tau$  is 90%  $\tau_{\max}$ , the shear strain of the specimen in the first 5000 mins continues to increase, dominated by the viscoelastic deformation. The increase in strain is lower during 5000 mins~15000 mins, but the strain increases rapidly after 15000 mins until the specimen was broken, and the deformation at this stage is mainly plastic deformation.

According to the shear rheological curves, the deformation increments of the samples were counted every 10 mins to obtain the rheological rate curves of the samples (Figure 6). Since the elastic deformation is small, it is included in the deformation increment of the first 10 mins and counted together. The statistical results show that the deformation rate of the three samples within the first 1000 mins is relatively fast, and the deformation rate of the sample with  $\tau$  of 90%  $\tau_{\max}$  is the fastest, and the sample with  $\tau$  of 60%  $\tau_{\max}$  is the slowest.

Subsequently, the rheological rate of the samples decreased rapidly. After 10,000 mins, the rheological rate of the sample with  $\tau=60\% \tau_{\max}$  was close to 0, while the rheological rates of the samples with  $\tau=75\% \tau_{\max}$  and  $\tau=90\% \tau_{\max}$  were still higher and become closer. The strain rate of the specimen with shear stress  $\tau=90\% \tau_{\max}$  increased

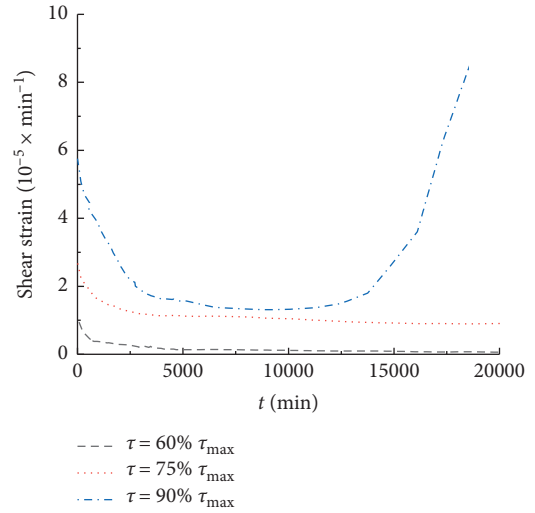


FIGURE 6: Rheological strain rate curves of specimens under static shear stress.

rapidly after 15,000 mins and had been in an accelerated deformation state before failure, while the strain rate of specimen with  $\tau=75\% \tau_{\max}$  continued to decrease.

It can be preliminarily inferred from the test results that when the normal stress is 150 kPa, the long-term shear strength  $\tau_{cr}$  of the soil samples may be a value between 75%  $\tau_{\max}$  and 90%  $\tau_{\max}$ , namely,

$$75\% \tau_{\max} < \tau_{cr} < 90\% \tau_{\max}. \quad (2)$$

However, due to the limitations of the quantity of test samples and the static loading capacity of the instrument, this value cannot be further determined accurately. When the shear stress is less than the critical value, the attenuative creep will occur, and only when the static load is greater than the critical value, it will lead to the final failure.

**4.2. Static and Cyclic Dynamic Shear Rheological Characteristics of Argillaceous Intercalation.** In the static and cyclic dynamic shear test, additional dynamic shear stresses of different strength were applied to the samples in different static shear stress states, and the strain of soil samples varied with the increase of cyclic times. The shear strain of soil samples is closely related to the cyclic dynamic shear stress and their initial static shear stress state.

When the initial shear stress of the specimens is low, such that its initial shear stress is 60% of the ultimate strength, namely, the  $\tau=60\% \tau_{\max}$  (shown in Figure 7(a)), and the cyclic dynamic shear stress for the ultimate shear strength of 5% and 10%, namely,  $\Delta\tau_p=5\% \tau_{\max}$  and  $\Delta\tau_p=10\% \tau_{\max}$ , the shear strain of the soil samples increased rapidly after the first few cycles of loading and then remained stable. When  $\Delta\tau_p=20\% \tau_{\max}$ , the increment of strain firstly increased rapidly and then slowed down. After 120,000 disturbances were applied, no damage occurred, and the total strain was less than 1%.

When the initial shear stress of the specimens is high, such as 90% of the ultimate strength, namely,  $\tau=90\% \tau_{\max}$ , even if the cyclic shear stress peak value  $\Delta\tau_p$  is small, such as

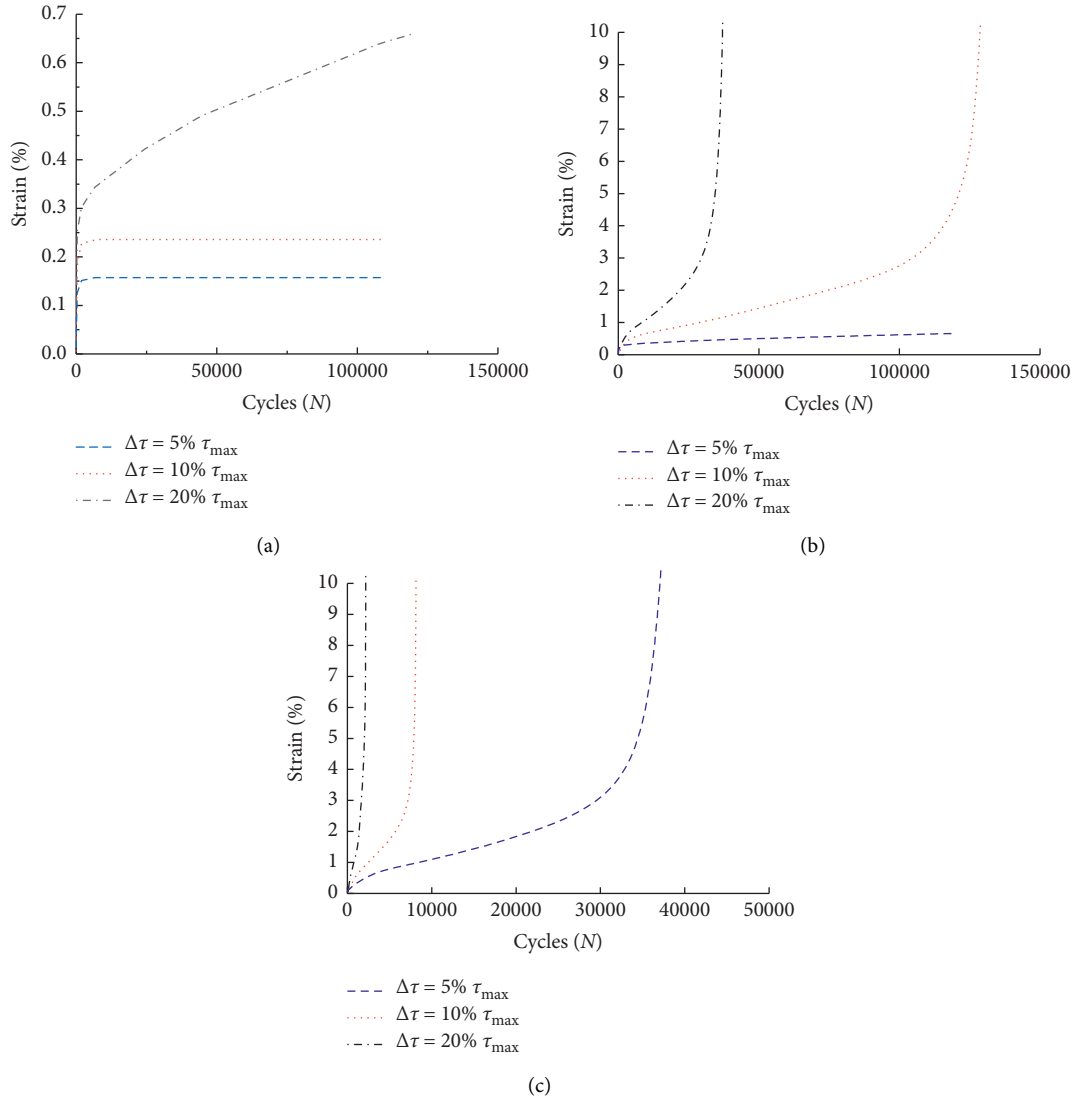


FIGURE 7: Rheological shearing strain curves under static and cyclic dynamic shear loads. (a) Specimen of  $\tau = 60\% \tau_{\max}$ . (b) Specimen of  $\tau = 75\% \tau_{\max}$ . (c) Specimen of  $\tau = 90\% \tau_{\max}$ .

5% of its ultimate shear strength ( $\Delta\tau_p = 5\% \tau_{\max}$ ) (shown in Figure 7(c)), the soil samples will also be damaged after enough cyclic times, and their strain increased slowly first and then rapidly. When the dynamic stress is relatively high, such as  $\Delta\tau_p = 20\% \tau_{\max}$  (as shown in Figure 7(c)), the strain basically maintained a trend of continuous acceleration.

When the initial shear stress of the samples is at a medium level, for example, 75% of the ultimate strength (Figure 7(b)), that is,  $\tau = 75\% \tau_{\max}$ , the strain variation of soil samples was more sensitive to the change of cyclic dynamic shear stress. When the dynamic shear stress is small (such as  $\Delta\tau_p = 5\% \tau_{\max}$ ), the strain of the soil samples increased slowly, and the final strain rate decreased to 0. When the dynamic shear stress is high (such as  $\Delta\tau_p = 20\% \tau_{\max}$ ), the soil samples may undergo shear failure quickly.

The test results showed that when the frequency of the dynamic shear stress is the same, and the sum of the initial static stress and the peak dynamic stress of the samples is

close, the deformation characteristics of the samples were also similar. For example, the specimens with  $\tau = 60\% \tau_{\max}$ ,  $\Delta\tau_p = 20\% \tau_{\max}$  and  $\tau = 75\% \tau_{\max}$ ,  $\Delta\tau_p = 5\% \tau_{\max}$ , after 120,000 times cyclic shear dynamic loads, the strains were 0.66% and 0.82%, respectively, while the specimens with  $\tau = 75\% \tau_{\max}$ ,  $\Delta\tau_p = 20\% \tau_{\max}$  and  $\tau = 90\% \tau_{\max}$ ,  $\Delta\tau_p = 5\% \tau_{\max}$  were failed after 37,800 and 33,000 times cyclic shear dynamic loads, respectively, and the variations of specimens strain were also similar.

Secondly, the failure of the samples under cyclic dynamic shear also had a certain critical value of stress state, and the samples breakage under additional dynamic stress can only occur if the total shear stress is larger than this critical value. The stress critical value (the sum of static shear stress and dynamic shear stress peak) of the soil samples should be between 70% and 80% of the shear strength, namely,

$$70\% \tau_{\max} < (\tau + \Delta\tau_p)cr < 80\% \tau_{\max}. \quad (3)$$

4.3. *Static and Intermittent Dynamic Shear Rheological Characteristics of Argillaceous Intercalation.* Intermittent dynamic shear loads were applied 5 times a day to the soil samples under different initial static stress states, and the rheological deformation characteristics of samples were observed. Compared with static rheological process, the deformation process of the samples after intermittent dynamic shear loads changed significantly.

- (1) When the initial static shear stress and the intermittent dynamic shear stress were relatively low, the rheological process of the samples is similar to the static rheological process, as shown in Figure 8(a) for the sample with  $\tau = 60\% \tau_{\max}$  and  $\Delta\tau_p = 5\% \tau_{\max}$ . In this way, after the rapid increase of strain in the initial stage, with the increase of time and the times of intermittent dynamic disturbances, the shear strain of the specimens had no obvious increasing trend. When the initial static shear stress was low, but the dynamic shear stress peak was relatively high, as shown in Figure 8(a), the samples with  $\tau = 60\% \tau_{\max}$ , while  $\Delta\tau_p = 10\% \tau_{\max}$  and  $\Delta\tau_p = 20\% \tau_{\max}$ , with the passing of time and increase of the number of disturbances, the strain continued to increase, and eventually failure occurred, while the specimens under static and cyclic dynamic shear did not fail, indicating that the intermittent dynamic shear loads changed the overall deformation of the specimens.
- (2) When the initial static shear stress is at a medium stress level, such as  $\tau = 75\% \tau_{\max}$ , the rheological deformation process of specimens was more sensitive to intermittent dynamic disturbances. When the dynamic shear stress peak is low, as shown in Figure 8(b), for the sample with  $\Delta\tau_p = 5\% \tau_{\max}$ , the deformation rate in the early stage increased slowly, but it increased rapidly after a long period of time. Compared with the curves of static shear test and static and cyclic dynamic shear test, it showed a typical three-stage deformation characteristic.
- (3) When the initial static shear stress is close to its ultimate strength, such as  $\tau = 90\% \tau_{\max}$ , the rheological deformation process of soil specimens was very sensitive to intermittent dynamic disturbances; even when the dynamic shear stress peak is low, as shown in Figure 8(c), for the sample with  $\Delta\tau_p = 5\% \tau_{\max}$ , the deformation rate of the specimen continued to grow rapidly, indicating that when it is close to the limit equilibrium, even a weak intermittent dynamic load can quickly destroy its equilibrium state.
- (4) By comparing the deformation curves of each sample in Figure 8, it can be found that the dynamic shear stress also changed the rheological process of the samples. The deformation curves of the samples subjected to low static shear stress and low intermittent dynamic shear stress were relatively smooth, and it is difficult to visually distinguish the moment of disturbance on the deformation curves. However, when the samples are subjected to high static shear

stress or high intermittent dynamic shear stress, the deformation of the samples jumped significantly, and the deformation curves showed a more obvious step-like shape.

The average rheological rate in the process of intermittent disturbances was analyzed by statistical the strain variables before and after the disturbance and the duration of the disturbance. When the initial static shear stress or the peak value of intermittent dynamic shear stress is small (as shown in Figure 9(a)), the rheological rate of the samples was higher at the initial stage and then remains at a lower level with irregular abrupt changes at some moments and increased to a higher level near the failure stage. With the increase of the initial static shear stress or intermittent dynamic shear stress peak (as shown in Figure 9(b)), the strain rate was relatively high at the initial stage and at the time of dynamic disturbance and gradually showed a certain regularity. However, when the initial shear stress was close to the ultimate strength, or the intermittent dynamic shear stress peak is high (as shown in Figure 9(c)), the rheological rate of the sample gradually increased, and the strain rate increased sharply during the dynamic disturbance. The time and numbers of intermittent dynamic disturbances can be clearly identified from the rheological rate curve.

In addition, when the intermittent dynamic shear stress of the samples is relatively large (as shown in Figure 9(c)), the static rheological rate between two adjacent intermittent disturbances was basically unchanged at the initial stage of the disturbance rheology, showing a stable rheological state. In the later stage of the disturbance rheological process, when the deformation speed of the specimens was accelerated, the dynamic deformation rate during disturbances increased gradually, and the static rheological rate between two adjacent disturbances also increased significantly, which was different from the smaller intermittent disturbance peak (as shown in Figure 9(a)).

Calculate the strain increment at a certain moment when the specimens were about to fail. Under the same initial static stress state, the strain increment of the static and intermittent dynamic shear rheological test and the sum strain increment of the static shear rheological test and static and cyclic dynamic shear rheological test were compared. For example, the strain at 17280 min of the sample with initial static shear stress  $\tau = 60\% \tau_{\max}$  and intermittent cyclic dynamic shear stress peak  $\Delta\tau_p = 5\% \tau_{\max}$  was sorted out, and the sample deformed for a total of 12 days and withstood 1800 dynamic disturbances. At the same time, the strain of the static rheological sample at 17280 min and the cyclic dynamic shear sample after 1800 cycles under the same initial static shear stress state were correspondingly sorted out, comparing the sum of the above strain with the static and intermittent disturbance rheological strain.

The statistical results showed (as shown in Figure 10) that when the static stress state, flow time, and number of dynamic disturbances were the same, the deformation of the sample under the static and intermittent cyclic dynamic shear disturbance was greater than the sum deformation of the static shear and static and cyclic dynamic

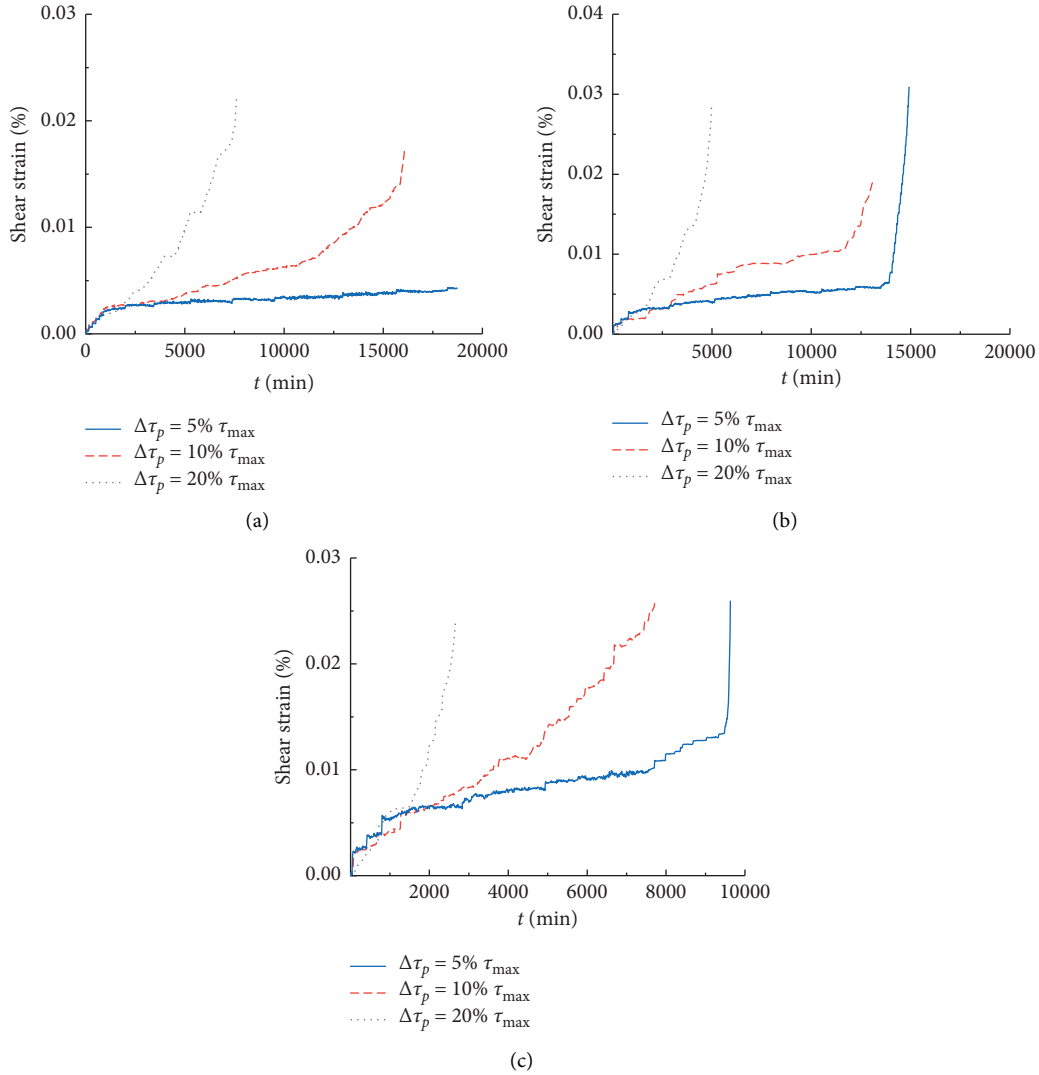


FIGURE 8: Rheological strain curves under static and intermittent dynamic shear loads. (a) Specimen of  $\tau = 60\% \tau_{max}$ . (b) Specimen of  $\tau = 75\% \tau_{max}$ . (c) Specimen of  $\tau = 90\% \tau_{max}$ .

shear. Moreover, when the samples were finally damaged, the intermittent disturbance rheological strain increment was several times that of the latter, and the closer it was to the failure moment, the more significant the difference was.

The results showed that static shear rheological deformation and intermittent cyclic dynamic shear deformation influence and promote each other. When the soil specimens approach failure, both static shear and intermittent dynamic shear promote soil damage and reduce its strength, thus making their accelerating deformation effect stronger. It can be seen that the small and transient dynamic disturbance may have a significant promoting effect on the rheological process of the argillite soft structural planes, and the greater the disturbance load is, the stronger the influence will be; meanwhile, the soil samples are more sensitive to the intermittent dynamic disturbance as it approaches the ultimate bearing state.

The duration time of the soil samples from the beginning of rheology to complete failure was defined as the rheological life time  $t_f$ . During the test, because the deformation of the samples after breakage was different, when the strain in the accelerated rheological stage reached 15%, the samples were considered to have reached their rheological life.

The relationship curves of the rheological life time  $t_f$  with the static loads and intermittent cyclic dynamic shear loads of soil samples showed that (as shown in Figure 11) the rheological life time  $t_f$  of the samples decreases with the increase of their static shear stress and intermittent dynamic shear stress, indicating that there is also a certain critical stress state that controls whether the samples can eventually be destroyed during the tests. From Figures 11 and 8(a), it can be found that when the peak value sum of static shear stress and intermittent dynamic shear stress of the soil samples is about 65% to 70% of its ultimate shear strength, the samples may eventually be damaged, namely,



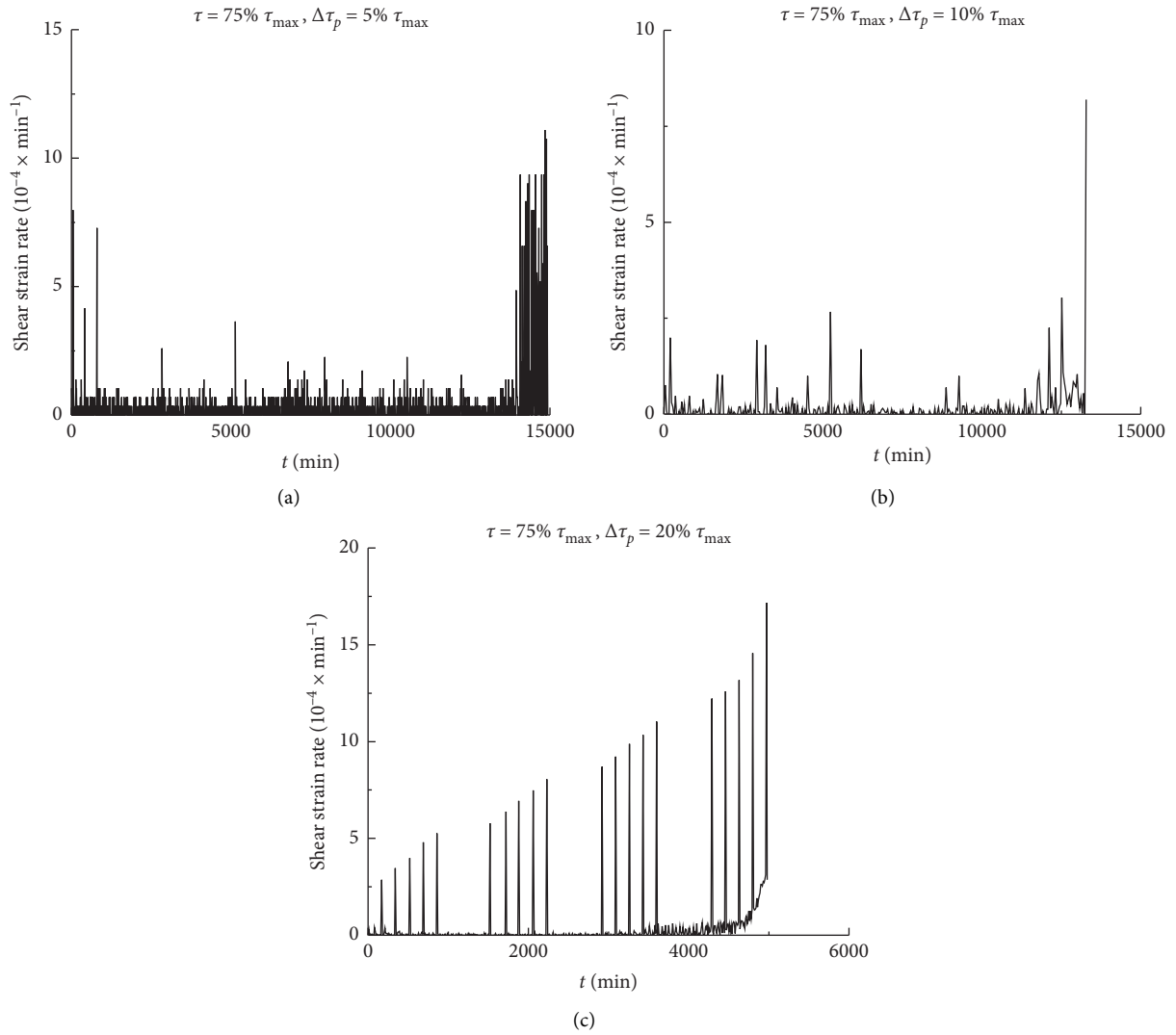


FIGURE 9: Rheological strain rate curves of specimens under static and intermittent dynamic shear loads ( $\tau = 75\% \tau_{\text{max}}$ ). (a)  $\Delta\tau_p = 5\% \tau_{\text{max}}$ . (b)  $\Delta\tau_p = 10\% \tau_{\text{max}}$ . (c)  $\Delta\tau_p = 20\% \tau_{\text{max}}$ .

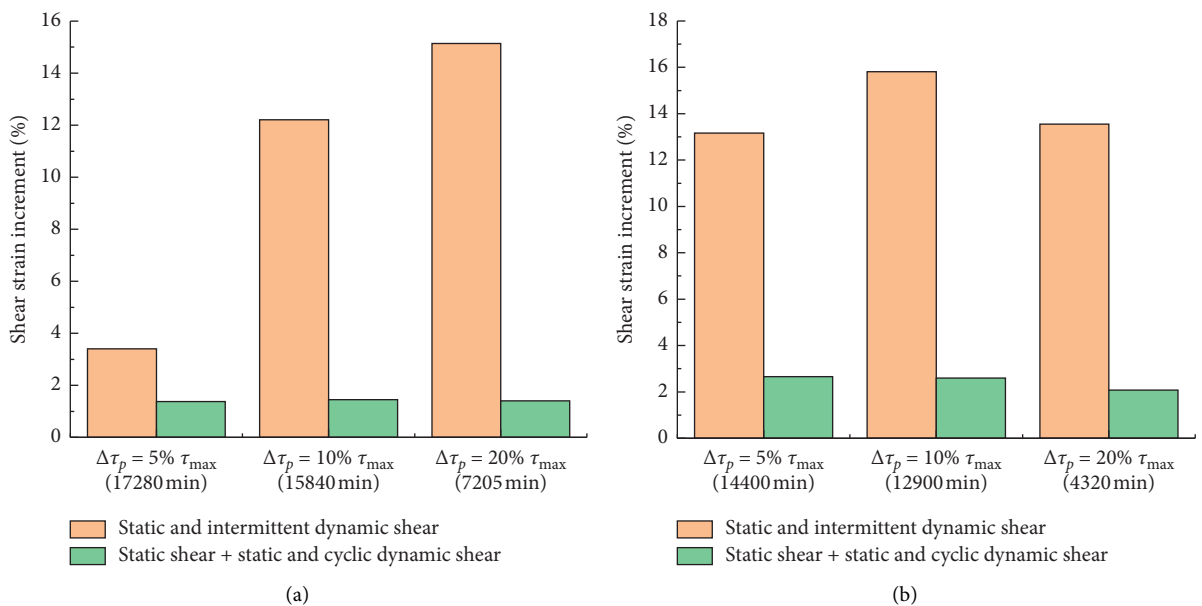


FIGURE 10: Continued.

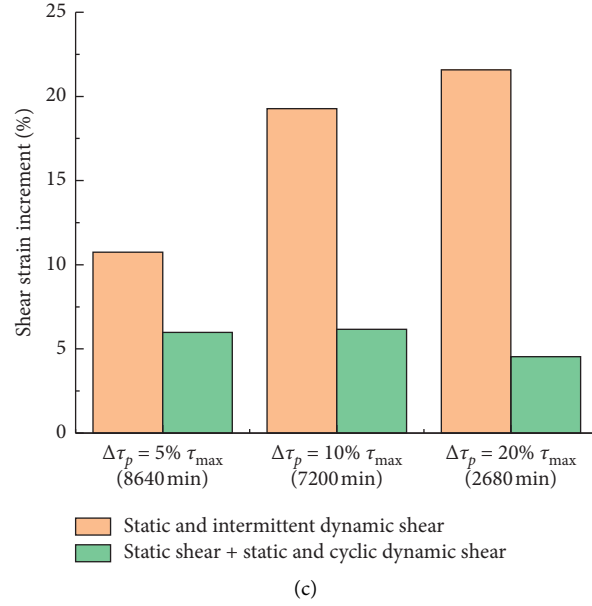


FIGURE 10: Comparison of the rheological strain increment in different shear tests. (a) Specimen of  $\tau = 60\% \tau_{\max}$ . (b) Specimen of  $\tau = 75\% \tau_{\max}$ . (c) Specimen of  $\tau = 90\% \tau_{\max}$ .

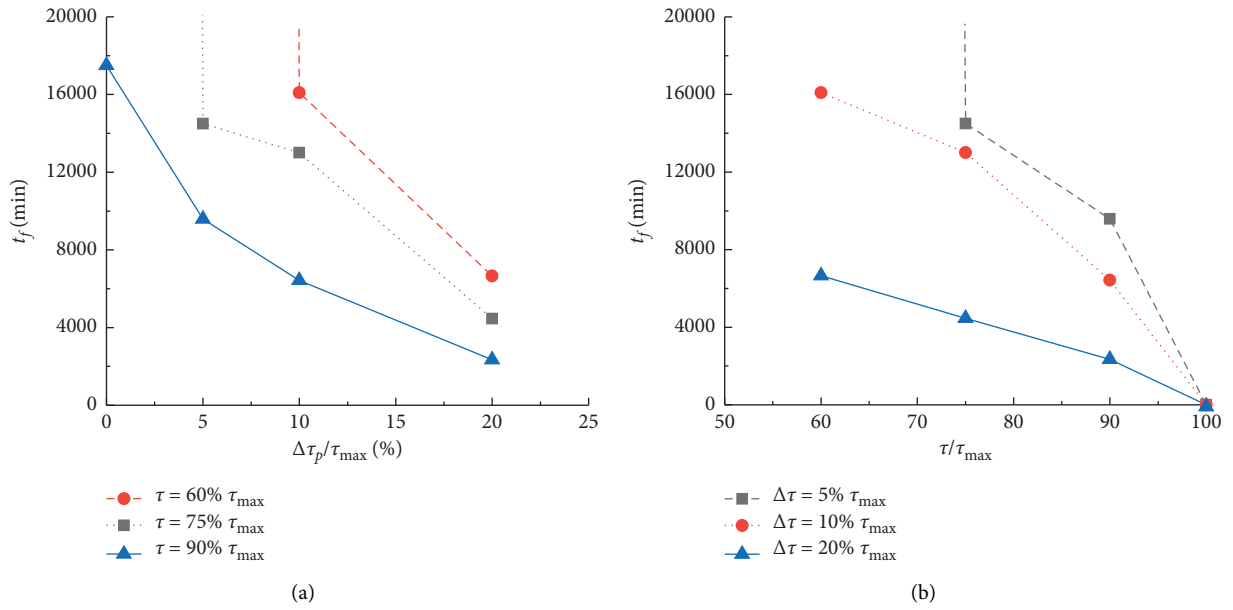


FIGURE 11: Rheological life of specimens versus static shear stress and peak value of dynamic stress. (a) Peak value of intermittent dynamic shear stress. (b) Static shear stress.

$$65\% \tau_{\max} < (\tau + \Delta\tau_p) M_{cr} < 70\% \tau_{\max}. \quad (4)$$

The combined stress threshold value may be slightly lower than that of the static shear test and static and cyclic dynamic shear test. The reason of this phenomenon is that, in the static and cyclic dynamic shear test, the cyclic dynamic shear loading of 30 Hz frequency was applied for 30 s and suspended for another 30 s, so 1800 cyclic dynamic shear loads can be applied per minute. Meanwhile, the test results showed that most of the soil samples had been destroyed

within 150,000 cyclic dynamic shear loads, and the corresponding failure time was about 83.3 mins. However, in the static and intermittent dynamic shear test, the failure time of most soil samples was more than 5000 mins, which is about 60 times that of the static and cyclic dynamic shear test, indicating that the time of soil samples to reach failure increased obviously. In this process, static shear and intermittent dynamic shear influence and promote each other, and both induce soil damage and reduce its strength, thus making the long-term shear strength under static and

intermittent dynamic shear lower than that of static and cyclic dynamic shear. Of course, due to the discrete of the samples, the combined stress threshold value should be verified by a large number of experiments.

## 5. Discussion

The experimental results showed that the long-term strength and creep life of the argillaceous interlayer may be reduced under intermittent cyclic dynamic disturbances. Therefore, the dynamic disturbance caused by intermittent blasting excavation may have a significant impact on the sliding surface parameters, the overall stability, and the local stability of the rock slope controlled by the argillaceous interlayer.

However, at present, the dynamic stability analysis of large rock slopes mainly focuses on the stability at a certain moment, and this methodology is reasonable when the dynamic disturbances are weak and the static safety factor of rock slope is relatively high, but it is not suitable for the case when the rock slopes are controlled by the weak structural plane or sliding surface, and its static stability safety factor is poor. Thus, a comprehensive analysis of transient and long-term dynamic stability should be carried out for rock slopes controlled by rheological weak structural surfaces and significantly affected by blasting vibration effect.

## 6. Conclusion

- (1) Under the static and cyclic dynamic shearing, the strain of the argillaceous interlayer samples varies with the increase of cyclic times. When the initial static shear stress and the cyclic dynamic shear stress peak are small, the influence of dynamic disturbance on their deformation is not significant. When the initial shear stresses of the samples are high, the soil strain may increase rapidly with the increase of cyclic times, even if the cyclic dynamic shear stresses are small.
- (2) If the static shear stress and the peak value of the intermittent cyclic dynamic shear stress are low, the dynamic disturbance has no significant influence on the rheological deformation process of soil samples. If the initial shear stress is close to its shear strength, weak intermittent dynamic disturbance can also significantly promote the rapid growth of their rheological deformation.
- (3) Under the same initial static shear stress state, the rheological deformation under the intermittent dynamic shear disturbance is greater than the sum of the static shear and static and cyclic dynamic shear, and the rheological life of the soil samples under intermittent dynamic shear disturbance may be lower than that under static shear flow.
- (4) When soil samples are finally disturbed by rheological failure, there exists a stress threshold value, which is determined by the sum of static shear stress and dynamic shear stress peak values.

- (5) It is suggested to totally evaluate the transient and long-term dynamic stability of rock slopes under the long-term influence of blasting excavation and controlled by rheological weak structural planes such as argillaceous interlayers.

## Data Availability

The data used to support the findings of this study are available from the corresponding author upon request.

## Conflicts of Interest

The authors declare that they have no conflicts of interest.

## Acknowledgments

This study was supported by the Natural Science Foundation of Hubei Province, China (2020CFB428), Innovation Group Project of the Natural Science Foundation of Hubei Province, China (2020CFA043), and Key Research and Development Project of Hubei Province, China (2020BCA084).

## References

- [1] W. G. Pariseau, S. Puri, and S. C. Schmelter, "A new model for effects of impersistent joint sets on rock slope stability," *International Journal of Rock Mechanics and Mining Sciences*, vol. 45, no. 2, pp. 122–131, 2008.
- [2] H. Wang, B. Zhang, G. Mei, and N. Xu, "A statistics-based discrete element modeling method coupled with the strength reduction method for the stability analysis of jointed rock slopes," *Engineering Geology*, vol. 264, pp. 1–14, Article ID 105247, 2020.
- [3] D. Song, Z. Chen, H. Chao, Y. Ke, and W. Nie, "Numerical study on seismic response of a rock slope with discontinuities based on the time-frequency joint analysis method," *Soil Dynamics and Earthquake Engineering*, vol. 133, pp. 1–13, Article ID 106112, 2020.
- [4] K. Ma, G. Liu, L. Guo, D. Zhuang, and D. S. Collins, "Deformation and stability of a discontinuity-controlled rock slope at Dagangshan hydropower station using three-dimensional discontinuous deformation analysis," *International Journal of Rock Mechanics and Mining Sciences*, vol. 130, pp. 1–19, Article ID 104313, 2020.
- [5] L. Zhao, C. Yu, X. Cheng, S. Zuo, and K. Jiao, "A method for seismic stability analysis of jointed rock slopes using Barton-Bandis failure criterion," *International Journal of Rock Mechanics and Mining Sciences*, vol. 136, pp. 1–13, Article ID 104487, 2020.
- [6] X. Song, J. C. Zhang, X. B. Guo et al., "Influence of blasting on the properties of weak intercalation of a layered rock slope," *International Journal of Minerals, Metallurgy and Materials*, vol. 16, no. 1, pp. 7–11, 2009.
- [7] Y. Chen, J. Xu, X. Huo, and J. Wang, "Numerical simulation of dynamic damage and stability of a bedding rock slope under blasting load," *Shock and Vibration*, vol. 2019, Article ID 9616859, 13 pages, 2019.
- [8] N. Jiang, B. Zhu, X. He, C. Zhou, X. Luo, and T. Wu, "Safety assessment of buried pressurized gas pipelines subject to blasting vibrations induced by metro foundation pit excavation," *Tunnelling and Underground Space Technology*, vol. 102, Article ID 103448, 2020.

- [9] B. Zhu, N. Jiang, C. Zhou, X. Luo, Y. Yao, and T. Wu, "Dynamic failure behavior of buried cast iron gas pipeline with local external corrosion subjected to blasting vibration," *Journal of Natural Gas Science and Engineering*, vol. 88, Article ID 103803, 2021.
- [10] T. Y. Wu, C. B. Zhou, N. Jiang et al., "Stability analysis for high-steep slope subjected to repeated blasting vibration," *Arabian Journal of Geosciences*, vol. 13, no. 828, pp. 1–12, 2020.
- [11] Y.-G. Hu, M.-S. Liu, X.-X. Wu, G. Zhao, and P. Li, "Damage-vibration couple control of rock mass blasting for high rock slopes," *International Journal of Rock Mechanics and Mining Sciences*, vol. 103, pp. 137–144, 2018.
- [12] M. Ramulu, A. K. Chakraborty, and T. G. Sitharam, "Damage assessment of basaltic rock mass due to repeated blasting in a railway tunnelling project - a case study," *Tunnelling and Underground Space Technology*, vol. 24, no. 2, pp. 208–221, 2009.
- [13] N. Erarslan and D. J. Williams, "The damage mechanism of rock fatigue and its relationship to the fracture toughness of rocks," *International Journal of Rock Mechanics and Mining Sciences*, vol. 56, pp. 15–26, 2012.
- [14] L. X. Xie, W. B. Lu, Q. B. Zhang, Q. H. Jiang, G. H. Wang, and J. Zhao, "Damage evolution mechanisms of rock in deep tunnels induced by cut blasting," *Tunnelling and Underground Space Technology*, vol. 58, pp. 257–270, 2016.
- [15] L. X. Xie, Q. B. Zhang, J. C. Gu et al., "Damage evolution mechanism in production blasting excavation under different stress fields," *Simulation Modelling Practice and Theory*, vol. 97, pp. 1–14, Article ID 101969, 2019.
- [16] H. Han, D. Fukuda, H. Liu et al., "FDEM simulation of rock damage evolution induced by contour blasting in the bench of tunnel at deep depth," *Tunnelling and Underground Space Technology*, vol. 103, pp. 1–16, Article ID 103495, 2020.
- [17] Y. Z. Li, Z. L. Wang, Y. P. Huang et al., "Numerical study of cumulative damage effect of rock under cyclic blast loading," *Blasting*, vol. 36, no. 2, pp. 47–53, 2019.
- [18] X. R. Liu, Z. Y. Deng, Y. Q. Liu et al., "Study of cumulative damage and failure mode of horizontal layered rock slope subjected to seismic loads," *Rock and Soil Mechanics*, vol. 40, no. 7, pp. 2507–2516, 2019.
- [19] F. Cao, T. H. Ling, J. Li et al., "Cumulative damage feature analysis for shared rock in a neighborhood tunnel under cyclic explosion loading," *Journal of Vibration and Shock*, vol. 37, no. 23, pp. 141–148, 2018.
- [20] S. B. Chai, H. Wang, Y. L. Jing et al., "Experimental study on dynamic compression characteristics of rock with filled joints after cumulative damage," *Chinese Journal of Rock Mechanics and Engineering*, vol. 39, no. 10, pp. 2025–2037, 2020.
- [21] X. L. Song, W. X. Gao, J. M. Ji et al., "Influence of blasting vibration on cumulative damage of surrounding rock," *Journal of Vibration and Shock*, vol. 39, no. 24, pp. 54–62, 2020.
- [22] Y. J. Cao, R. Q. Huang, H. M. Tang et al., "Experimental research on rheological characteristics of weak structural planes of high slopes in coal strata in a hydropower station," *Chinese Journal of Rock Mechanics and Engineering*, vol. 27, no. s2, pp. 3732–3739, 2008.
- [23] H. J. Hou and M. R. Shen, "Rheological properties of rock mass discontinuities and trial research of its long-term strength," *Geotechnical Engineering Technique*, vol. 6, pp. 324–326, 2003.
- [24] T. H. Yang, Y. Q. Rui, W. C. Zhu et al., "Rheological characteristics and long-term strength of siltized intercalation interbedded in peat mudstone," *Journal of Experimental Mechanics*, vol. 5, pp. 396–402, 2008.
- [25] J. Šancer, M. Štrejbar, and A. Maleňáková, "Effects of cyclic loading on the rheological properties of sandstones," *Central European Journal of Geosciences*, vol. 3, no. 2, pp. 207–214, 2011.
- [26] H. Hu, "Rheological model and rheological equation of sillage soft soil under dynamic loading," *Rock and Soil Mechanics*, vol. 28, no. 2, pp. 237–240, 2007.
- [27] H. Hu, H. X. Gu, and D. R. Yu, "Research on dynamic rheological characteristics and rheologic parameters of sludge soft soil," *Rock and Soil Mechanics*, vol. 29, no. 3, pp. 696–700, 2008.

## Research Article

# Experimental Study on Physical and Dynamic Mechanical Properties of Temperature-Water Coupled Sandstone

Qi Ping <sup>1,2,3</sup>, Dezhi Qi,<sup>2,3</sup> Qi Diao,<sup>2,3</sup> Chuanliang Zhang,<sup>2,3</sup> Qi Gao,<sup>2,3</sup> and Yulin Wu<sup>2,3</sup>

<sup>1</sup>State Key Laboratory of Mining Response and Disaster Prevention and Control in Deep Coal Mine, Anhui University of Science and Technology, Huainan, Anhui 232001, China

<sup>2</sup>Engineering Research Center of Mine Underground Projects, Ministry of Education, Anhui University of Science and Technology, Huainan, Anhui 232001, China

<sup>3</sup>School of Civil Engineering and Architecture, Anhui University of Science and Technology, Huainan, Anhui 232001, China

Correspondence should be addressed to Qi Ping; [ahpingqi@163.com](mailto:ahpingqi@163.com)

Received 22 April 2021; Accepted 8 July 2021; Published 3 August 2021

Academic Editor: Bangbiao Wu

Copyright © 2021 Qi Ping et al. This is an open access article distributed under the Creative Commons Attribution License, which permits unrestricted use, distribution, and reproduction in any medium, provided the original work is properly cited.

In order to study the influence characteristics of water bath at different temperatures on rock physical and dynamic mechanical properties, a total of 15 groups of temperature-water bath treatment were carried out on coal mine roadway sandstone at 25°C~95°C, and the basic physical parameters were tested. The impact compression test was carried out using the split Hopkinson pressure bar (SHPB) device. The results show that, with the increase of water bath temperature, the particle gap on the specimen surface increases. The volume, mass, and density of the specimens all increased with the increase of water bath temperature, and the increase was closely related to the water bath temperature. The dynamic compressive strength increases as a quadratic function of the water bath temperature, and the rate of increase is different before and after 45°C. The dynamic peak strain and average strain rate showed a quadratic function with the water bath temperature. The dynamic peak strain before 45°C decreased with the temperature increasing, and the dynamic peak strain after 45°C increased with the temperature increasing. The dynamic elastic modulus increased first and then decreased with the increase of water bath temperature and reached the maximum at 45°C. The failure pattern of sandstone is spalling. With the increase of water bath temperature, the fracture degree of the specimen gradually decreases.

## 1. Introduction

In recent years, with increasing excavation depth of underground space, the ground temperature is also getting higher [1]. Deep rock mass excavation is often in a special environment full of water [2]. Blasting excavation is one of the main excavation methods of deep rock mass engineering. Deep rock mass is subjected to impact load during excavation. Underground rock mass is mostly in the state of immersion, and different depth corresponding to the water temperature is different. Therefore, it is of great engineering value to carry out the experimental study on the dynamic mechanical properties of sandstone under the coupled action of temperature and water.

Many scholars have used TAW-2000 or RMT-150B rock mechanics test system to carry out static load test research on

rocks under or after high-temperature treatment. Qin et al. [3] carried out uniaxial compression tests on sandstone specimens treated at 200°C to 800°C and analyzed its stress-strain curve characteristics. Yu et al. [4] studied the variation characteristics of mass and longitudinal wave velocity with temperature after limestone was subjected to a high temperature of 20°C to 650°C and carried out uniaxial compression tests under static load. Jin et al. [5] compared two ways of natural cooling and water cooling after sandstone was subjected to a high temperature of 100°C to 800°C. Wu and Wang [6] carried out uniaxial compression and Brazil splitting tests on granites subjected to a high temperature of 250°C to 600°C, to analyze the stress-strain curve and load-radial displacement curve of granites. Rohan et al. [7] studied the effects of pretreatment on UPV and rock microstructure after treated at 100°C to 600°C. Yu et al. [8]

conducted uniaxial compression tests on sandstone after high-temperature treatment at 100°C to 600°C and under a high-temperature condition and analyzed the uniaxial compressive strength of sandstone after high-temperature cooling and under high-temperature condition. Su et al. [9] used the RMT-150B testing machine to analyze the deformation characteristics, strength characteristics, and acoustic emission characteristics of hard coal samples treated at 100°C to 500°C. Wei et al. [10] carried out static uniaxial compression on anthracite samples after high-temperature treatment at 20°C to 500°C and analyzed the change of coal sample density and porosity with temperature. Chen et al. [11] carried out uniaxial compression tests on granite specimens under a high temperature of 25°C to 1000°C at five loading rates. Split Hopkinson pressure bar (SHPB) device is the most commonly used loading device in the study of rock dynamic physical and mechanical properties. Ping et al. [12–15] analyzed the variation rule of the dynamic stress-strain curve of sandstone under a high temperature of 25°C to 1000°C. In addition, the effects of temperature on dynamic compressive strength, dynamic peak strain and strain rate, dynamic elastic modulus, and failure mode were investigated. Xu et al. [16] carried out dynamic uniaxial compression tests at three loading rates on sandstone subjected to a high temperature ranging from 25°C to 700°C. Zhang [17] analyzed the variation of dynamic stress, strain, strain rate, fractal dimension, failure mode, and damage degree with a temperature of sandstone subjected from -15°C to 800°C. Chen et al. [18] carried out a dynamic uniaxial compression test on sandstone subjected to a high temperature of 100°C to 1000°C. Liu and Xu [19] carried out dynamic compression tests on granite under a high-temperature action of 25°C to 1000°C and analyzed the variation law of peak stress and strain of granite with temperature. Yang et al. [20] conducted triaxial compression tests on granites subjected to a high temperature of 200°C~800°C and found that thermal cracks were generated and the cohesion between crystals was reduced.

Scholars at home and abroad mainly focus on the static and dynamic physical and mechanical properties of rocks in water. Xie et al. [21] used MTS815 testing machine to conduct uniaxial and triaxial compression tests on red-bed soft rocks under natural and saturated conditions and analyzed its strength and deformation characteristics. Liu et al. [22] used Rock-600-50 triaxial rheometer to analyze the mechanical behavior and energy evolution rule of yellow sandstone under the action of pore water. Duan and Ren [23] carried out static uniaxial compression tests on five kinds of sandstone with different water contents and analyzed the law of various physical parameters changing with water content. Zhang et al. [24] carried out a uniaxial compression acoustic emission test on saturated granite. Fang et al. [25] conducted uniaxial compression tests on four kinds of argillaceous siltstones and discussed the strength damage evolution characteristics of argillaceous siltstones under the influence of water content. Teng et al. [26] carried out uniaxial compression tests on four kinds of layered shales with water content and analyzed that the damage of water to shale was mainly due to adsorption of water and

capillary pressure. Su et al. [27] carried out uniaxial compression tests on natural and saturated sandstone and analyzed the deformation, strength, and energy characteristics of the specimens. Zhang [28] analyzed the water-rock interaction of shale and obtained the microscopic nature of the deterioration of water-rock interaction of shale. Fu et al. [29] carried out uniaxial compression tests on rock samples under natural state, saturated water action, and dry-wet cycle, to analyze the uniaxial compressive strength and elastic modulus of sandstone. Yang et al. [30] carried out uniaxial compression tests on siltstone samples soaked in water at 50°C and 100°C and discussed the infrared radiation characteristics of siltstone in the rupture process soaked at different water temperatures. Gao et al. [31] carried out uniaxial dynamic compression loading tests on marble under four damage gradients and dry and saturated states, to analyze the relationship between dynamic compressive strength and water content. Wang et al. [32] carried out a uniaxial dynamic compression test and dynamic splitting test on fine sandstone in a natural and saturated state and analyzed the effects of water and loading rate on dynamic tensile and compressive strength of fine sandstone and their differences. Zhao et al. [33] carried out dynamic tensile tests on sandstone specimens with different water contents and studied the variation rule of dynamic tensile strength of sandstone specimens with different water content under different loading rates. Zhou et al. [34] carried out dynamic compression, splitting, and fracture tests on dry and saturated sandstone and analyzed the relationship between rock strength and fracture toughness with water and loading rate. Chu et al. [35] carried out uniaxial dynamic compression tests on sandstone samples with three different water-bearing states and analyzed the stress-strain curves of the rock samples. Wang et al. [36] conducted uniaxial dynamic compression tests on four kinds of red sandstone with different water-bearing states and analyzed the rock failure micromechanism. Guo et al. [37] conducted an experimental study on the thermal conductivity of sandstone at different temperatures and water content and found that the thermal conductivity of sandstone in a saturated state decreased with the increase of temperature. Yu et al. [38] conducted uniaxial compression mechanical tests on granite after hydrothermal cycling and analyzed its appearance morphology and stress-strain curve. Hashiba and Fukui [39] carried out tensile tests on five kinds of rocks and found that the strength of rocks decreases after being saturated with water. Wong and Jong [40] studied the effect of water on the tensile strength of gypsum and found that water can reduce the tensile strength of gypsum. Karakul and Ulusay [41] conducted tensile tests on rock and found that the tensile strength of rocks decreased with the increase of water saturation. An et al. [42] carried out experimental research on rocks under the coupling action of high temperature and dynamic load, carried out dynamic and static tests on rocks, and obtained the relationship curves among loading rate, strain, temperature, compressive strength, and tensile strength. Wen et al. [43] conducted a dynamic compressive test study on sandstone under the coupling action of low temperature and dynamic load, analyzed the fracture morphology



characteristics, and obtained the dynamic failure law of sandstone. Wang et al. [44] conducted dynamic compression tests on Huashan granite to study the effects of treatment temperature and strain rate on the mechanical behavior of granite.

It can be seen that there are many researches on the static and dynamic physical and mechanical properties of sandstone under the action of high temperature and water rock. The researches on the physical and mechanical properties of sandstone under the action of temperature-water coupling mainly focus on the static load test, while the dynamic load test needs to be further studied. For studying physical and dynamic mechanical properties of sandstone is influenced by temperature and water coupling rules, the basic physical parameters of sandstone specimens after water bath at 25°C, 30°C, 35°C, 40°C, 45°C, 50°C, 55°C, 60°C, 65°C, 70°C, 75°C, 80°C, 85°C, 90°C, and 95°C were measured, and the color, mass, volume, and density of the specimens were compared and analyzed. The impact compression tests of sandstone specimens subjected to different water bath temperatures were carried out under similar loading conditions by using SHPB equipment. The correlation between dynamic characteristics of the specimens, such as peak stress strength, dynamic elastic modulus, average strain rate, and failure mode, and the change of water bath temperature was studied.

## 2. Sample Preparation and SHPB Test Device after Water Bath

**2.1. Processing of Sandstone Specimen.** Rock specimens used in this test are all taken from the deep roadway sandstone of Gubei Coal Mine of Huainan Mining Group in Anhui Province. In order to increase the contrast between the test specimens, the test specimens are all selected from the same rock block. According to the relevant provisions of “Methods for Determination of Physical and Mechanical Properties of Coal and Rock” [45], rock coring machine, cutting machine, and end grinding machine were used to grind the specimen into a cylinder specimen with a diameter of 50 mm and a length-diameter ratio of about 0.5.

**2.2. Preparation of Specimens after Water Bath.** The box-type water bath box is used to heat the sandstone specimen in the water bath, as shown in Figure 1. The size of the box is 420 mm × 200 mm × 105 mm, and the maximum heating temperature is 99°C.

First of all, the sandstone test pieces are evenly placed in the water bath box, with a certain gap between the test pieces and the door of the box closed. After heating to the corresponding temperature, keep the temperature with a constant value and water bath for 48 h [46]. Finally, turn off the water bath heating system, open the box cover, remove the specimen from the water bath box, wipe the moisture on the surface of the specimen with a dry towel, and measure the mass, diameter, thickness, and longitudinal wave velocity of the specimen.



FIGURE 1: Water bath.

**2.3. SHPB Test Device.** The test equipment in this paper is the SHPB test device of the State Key Laboratory of Mining Response and Disaster Prevention and Control in Deep Coal Mine, as shown in Figure 2. The impact compression test is carried out on sandstone specimens subjected to different water bath temperatures.

The SHPB test device shown in Figure 2 is mainly composed of an impact bar, an incident bar, a transmission bar, an absorbing bar, an oscilloscope, and a CS dynamic resistance strain gauge. The diameter of the incident bar, transmission bar, and absorption bar is 50 mm, bar length is 2000 mm, 1500 mm, and 1000 mm, respectively, with a material density of 7636 kg/m<sup>3</sup>, Poisson ratio is 0.28, elastic longitudinal wave velocity is 5190 m/s, and the impact rod adopts spindle shape. Before installation, a thin layer of Vaseline is evenly applied to the contact area between the pressure bar and the end face of the specimen as a lubricant to reduce the friction between the sandstone specimen and the end face of the pressure bar. In order to compare the influence law of water bath action at different temperatures on the dynamic characteristics of sandstone specimens, it is necessary to ensure the same impact loading conditions for each impact compression test in SHPB; that is, the same impact pressure is used to load specimens. The experimental principle is to measure the incident wave and reflected wave in the incident bar and the transmitted pulse in the transmission bar by using a strain gauge and obtain the stress-strain relationship according to the stress wave theory [47].

## 3. Physical Properties of Sandstone before and after Water Bath

**3.1. Color and Apparent Morphology of Specimens after Water Bath.** The color and apparent morphological changes of sandstone specimens subjected to different water bath temperatures are shown in Figure 3.

As can be seen from Figure 3, the surface color of sandstone specimens after water bath at 25°C~95°C did not change significantly and was mainly grayish-white. After water bath at 25°C~45°C, the particles on the surface of sandstone are dense. After water bath at 45°C~95°C, the particle gap on the surface of the specimen increases. It can be inferred that, with the increase of temperature, water gradually enters the specimen through the cracks on the surface, and water molecules weaken the binding effect between mineral particles and promote the particles to fall off, thus increasing the pores of sandstone. This indicates



FIGURE 2: SHPB test device.

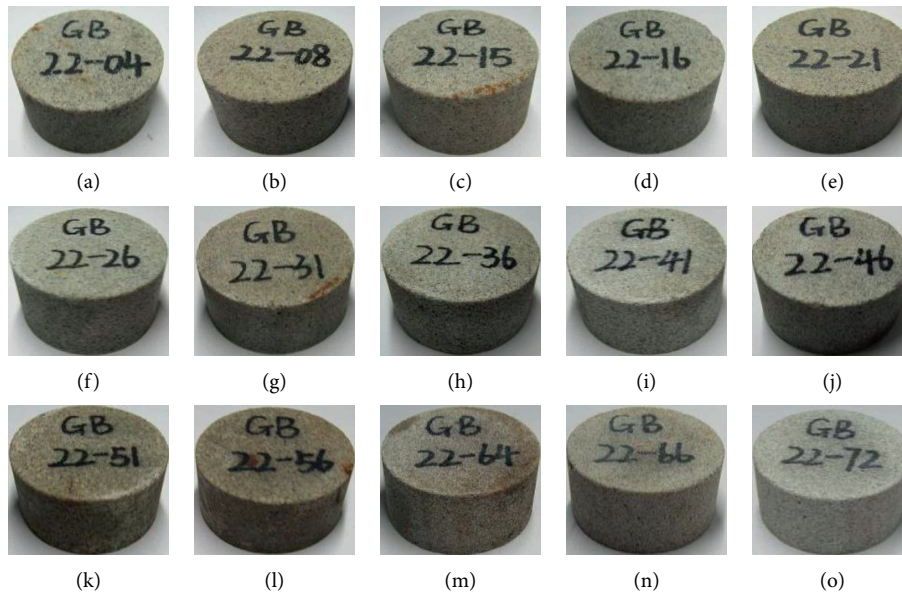


FIGURE 3: Apparent morphology of sandstone specimens after water bath at different temperatures. (a) 25°C. (b) 30°C. (c) 35°C. (d) 40°C. (e) 45°C. (f) 50°C. (g) 55°C. (h) 60°C. (i) 65°C. (j) 70°C. (k) 75°C. (l) 80°C. (m) 85°C. (n) 90°C. (o) 95°C.

that when the temperature is between 25°C and 45°C, a small amount of water enters the interior of the sandstone, and the internal structure of the sandstone specimen is mainly the combination between particles. After 45°C, more water enters the sandstone, and the internal structure of sandstone specimen is mainly composed of a water-particle combination.

**3.2. Measurement and Results of Basic Physical Parameters.** After the specimen taken out of the water bath box is wiped clean with a dry towel, the size and mass of the sandstone specimen are measured one by one, and the volume and density are calculated. The C61 nonmetallic ultrasonic detector was used to measure the elastic wave propagation time between the two end faces of the specimen, and longitudinal wave velocity was calculated. The basic physical parameters of sandstone specimens before and after water bath are shown in Table 1.

**3.3. Changes in Volume, Mass, and Density of Specimens.** After water bath at different temperatures, the sandstone specimens showed volume expansion and mass increase, and the volume expansion rate increased with the increase of water bath temperature, as shown in Figure 4.

As can be seen from Figure 4, the volume expansion rate of sandstone specimen was not affected by the change of water bath temperature in the range of 25°C~45°C, and the increased value varied from 0.39% to 0.45%. The volume expansion rate showed a slight increase, and the volume expansion rate was the smallest at 25°C, only 0.39%. This may be because the water bath caused the volume expansion of the mineral particles composed of sandstone, which first occupied the original micropores and microcracks in the specimen, so the volume expansion of the specimen was relatively small. When the water bath temperature rose to 45°C, new microcracks sprouted inside the sandstone specimen, leading to the appearance volume expansion of the specimen, and the volume expansion rate increased

TABLE 1: Physical parameters of sandstone before and after water bath.

Specimen number	Without the water bath					After the water bath							
	Diameter (mm)	Thickness (mm)	Mass (g)	Volume (cm <sup>3</sup> )	Density (g·cm <sup>-3</sup> )	Longitudinal wave velocity (m·s <sup>-1</sup> )	Temperature (°C)	Diameter (mm)	Thickness (mm)	Mass (g)	Volume (cm <sup>3</sup> )	Density (g·cm <sup>-3</sup> )	Longitudinal wave velocity (m·s <sup>-1</sup> )
GB22-03	49.68	24.96	121.09	48.4	2.502	2600		49.69	25.05	122.78	48.6	2.527	2319
GB22-04	49.69	25.17	122.86	48.8	2.517	2860	25	49.84	25.19	124.34	49.1	2.530	2422
GB22-05	49.72	25.24	123.51	49.0	2.521	2868		49.71	25.34	125.21	49.3	2.540	2437
GB22-07	49.73	25.00	122.81	48.5	2.530	2976		49.70	25.11	124.26	48.7	2.551	2511
GB22-08	49.72	25.01	121.57	48.5	2.504	2718	30	49.71	25.05	123.10	48.6	2.532	2319
GB22-09	49.73	25.06	121.78	48.7	2.502	2610		49.76	25.06	123.26	48.7	2.529	2321
GB22-13	49.72	25.09	123.05	48.7	2.526	2987		49.81	25.15	124.25	49.0	2.535	2418
GB22-14	49.71	24.94	122.12	48.4	2.524	2834	35	49.71	24.97	123.45	48.5	2.547	2401
GB22-15	49.58	24.83	119.63	47.9	2.496	2821		49.62	24.79	121.14	47.9	2.528	2430
GB22-16	49.70	25.08	121.37	48.6	2.495	2612		49.80	25.17	123.09	49.0	2.511	2247
GB22-17	49.65	25.01	121.87	48.4	2.518	2718	40	49.74	25.19	123.25	48.9	2.518	2209
GB22-18	49.76	25.10	123.85	48.8	2.537	2988		49.81	25.19	124.99	49.1	2.546	2377
GB22-21	49.71	25.19	123.23	48.9	2.521	2863		49.76	25.30	124.85	49.2	2.538	2433
GB22-22	49.72	24.90	121.83	48.4	2.520	2394	45	49.80	25.02	123.32	48.7	2.531	2120
GB22-23	49.74	25.07	121.93	48.7	2.504	2507		49.67	25.14	123.14	48.7	2.528	2095
GB22-26	49.69	25.07	121.63	48.6	2.502	2725		49.77	25.18	123.44	49.0	2.520	2421
GB22-27	49.73	25.08	122.16	48.7	2.507	2986	50	49.88	25.21	123.30	49.2	2.504	2424
GB22-28	49.68	25.06	122.16	48.6	2.515	2848		49.74	25.12	123.50	48.8	2.530	2400
GB22-31	49.71	24.83	121.56	48.2	2.523	2956		49.74	24.97	123.23	48.5	2.540	2416
GB22-32	49.69	24.96	121.20	48.4	2.505	2713	55	49.68	25.05	122.45	48.5	2.522	2456
GB22-33	49.74	24.93	122.40	48.4	2.527	2968		49.79	25.01	123.57	48.7	2.538	2452
GB22-36	49.63	24.77	118.90	47.9	2.482	2477		49.65	24.87	120.64	48.1	2.506	2220
GB22-37	49.77	25.04	124.03	48.7	2.547	2981	60	49.80	25.18	125.17	49.0	2.553	2518
GB22-38	49.69	24.88	120.38	48.2	2.495	2704		49.72	25.01	121.76	48.6	2.507	2233
GB22-41	49.64	24.80	119.69	48.0	2.494	2696		49.66	24.96	121.38	48.3	2.511	2311
GB22-42	49.77	25.09	123.94	48.8	2.539	2987	65	49.79	25.22	125.17	49.1	2.550	2425
GB22-43	49.59	25.06	122.01	48.4	2.522	2847		49.64	25.11	123.18	48.6	2.535	2415
GB22-46	49.70	25.13	122.05	48.7	2.504	2991		49.83	25.19	124.73	49.1	2.539	2519
GB22-47	49.70	24.86	120.31	48.2	2.495	2390	70	49.73	24.99	121.59	48.5	2.505	2231
GB22-48	49.61	25.11	122.46	48.5	2.523	2854		49.70	25.14	123.55	48.8	2.534	2514
GB22-51	49.73	24.84	121.11	48.2	2.511	2957	75	49.78	24.90	124.80	48.5	2.576	2490
GB22-52	49.73	24.95	121.49	48.5	2.507	2712		49.75	25.04	122.69	48.7	2.521	2608
GB22-53	49.59	25.04	121.30	48.4	2.509	2722		49.66	25.18	122.65	48.8	2.515	2569
GB22-56	49.71	25.09	122.11	48.7	2.508	2727	80	49.85	25.13	124.82	49.0	2.546	2416
GB22-57	49.72	24.99	122.46	48.5	2.524	2717		49.76	25.12	123.81	48.8	2.535	2415
GB22-58	59.65	25.00	120.73	69.8	1.729	2404		49.80	25.04	122.13	48.8	2.504	2236
GB22-62	49.66	25.09	123.40	48.6	2.540	2851	85	49.68	25.24	124.51	48.9	2.545	2629
GB22-63	49.63	24.93	121.44	48.2	2.518	2493		49.70	25.10	122.93	48.7	2.524	2510
GB22-64	49.74	25.03	123.48	48.6	2.539	2979		49.87	25.08	126.21	49.0	2.576	2508
GB22-66	49.64	25.06	121.39	48.5	2.504	2983	90	49.58	25.21	124.37	48.7	2.556	2626
GB22-67	49.74	24.96	120.76	48.5	2.491	2496		49.79	25.12	122.02	48.9	2.495	2325
GB22-68	49.71	24.99	122.63	48.5	2.529	2716		49.80	25.09	124.11	48.9	2.540	2412
GB22-70	49.73	25.03	122.06	48.6	2.511	2317	95	49.75	25.15	125.80	48.9	2.573	2372
GB22-71	49.69	25.04	122.57	48.5	2.525	2721		49.77	25.15	123.63	48.9	2.527	2418
GB22-72	49.65	24.98	121.20	48.4	2.506	2402		49.77	25.03	122.25	48.7	2.511	2318

rapidly. When the water bath temperature was increased to 95°C, the volume expansion rate of the specimen reached the maximum of 0.94%.

The volume expansion rate of the sandstone specimen increases with the water bath temperature in a quadratic function relationship, as shown in equation (1), and the fitting curve is shown in Figure 4:

$$\begin{cases} V_{T1}' = 9 \times 10^{-5}T^2 - 0.003T + 0.4117, & 25^\circ\text{C} \sim 45^\circ\text{C}, & R^2 = 0.9975, \\ V_{T1}' = 9 \times 10^{-5}T^2 - 0.003T + 0.4117, & 45^\circ\text{C} \sim 95^\circ\text{C}, & R^2 = 0.9843, \end{cases} \quad (1)$$

where  $V_{T1}'$  and  $V_{T2}'$  are the volume expansion rate of sandstone specimen after water bath action, %.

The variation of the water absorption rate of sandstone specimens with the rise of water bath temperature after water bath action is shown in Figure 5.

As can be seen from Figure 5, the water absorption rate of specimens with different water bath temperatures increased with the increase of water bath temperature. With the increase of water bath temperature, the water absorption

capacity of sandstone becomes stronger. Sandstone is mainly cemented by sand grains, which have more sand content, thus showing a temperature effect. The higher the temperature is, the easier the water will enter the interior of the sandstone. The relationship between water absorption of sandstone specimens and water temperature increases with a strong quadratic function after different water bath temperatures. As shown in equation (2), the fitting curve is shown in Figure 5:

$$\begin{cases} M_{T1} = 4 \times 10^{-4}T^2 - 0.0224T + 1.514, & 25^\circ\text{C} \sim 45^\circ\text{C}, & R^2 = 0.9830, \\ M_{T2} = 5 \times 10^{-5}T^2 + 0.0176T + 0.4376, & 45^\circ\text{C} \sim 95^\circ\text{C}, & R^2 = 0.9820, \end{cases} \quad (2)$$

where  $M_{T1}$  and  $M_{T2}$  are the water absorption rate of sandstone specimen after water bath action, %.

After the water bath, the density of sandstone specimen changes with the rise of water bath temperature, as shown in Figure 6.

It can be seen from Figure 6 that the density of the specimen increases with the increase of water bath temperature after the action of different water bath temperatures. When the water bath temperature was in the range of 25°C~45°C, the increase rate of the specimen density was less affected by the change of the water bath temperature, and the amplitude of the increase rate of the specimen density was

0.51%~0.68%. When the water bath temperature was in the range of 45°C to 95°C, the density of the specimen was greatly affected by the water bath temperature. The density increase rate at 45°C was 0.68%, and the density increase rate at 95°C was the largest (2.47%), which was about 3.6 times that at 45°C. The basic reason for the increase of density of sandstone specimen is that the volume expansion and mass increase of sandstone specimen after water bath.

The density increase rate of sandstone specimen increases in a quadratic function between 25°C and 95°C, and the growth rate is different before and after 45°C, as shown in equation (3). The fitting curve is shown in Figure 6:

$$\begin{cases} \rho_{T1} = -6 \times 10^{-5}T^2 + 0.012T + 0.2489, & 25^\circ\text{C} \sim 45^\circ\text{C}, & R^2 = 0.9703, \\ \rho_{T2} = 4 \times 10^{-4}T^2 - 0.0288T + 1.0747, & 45^\circ\text{C} \sim 95^\circ\text{C}, & R^2 = 0.9693, \end{cases} \quad (3)$$

where  $\rho_{T1}$  and  $\rho_{T2}$  are the density increase rate of sandstone specimen after water bath action, %.

#### 4. Test Results and Analysis of Sandstone with Different Water Bath Temperatures

*4.1. Analysis of the Relationship between Different Water Bath Temperatures and Peak Stress Strength.* The variation of peak stress strength of sandstone specimens after water bath is shown in Figure 7.

It can be seen from Figure 7 that the dynamic peak stresses of sandstone specimen quadratic increase with the increase of water bath temperature between 25°C and 45°C.

The absorb water ratio of sandstone specimen increases with increasing bath temperature, which resists the extension of cracks. Therefore, the peak stress increases accordingly. The peak stress strength increases rapidly between 45°C and 95°C. It can be inferred that, with the increase of temperature, a certain amount of moisture and thermal stress accumulates inside the sandstone, and under the action of temperature-water coupling, the internal pores of the sandstone are filled, thus improving the compressive strength of the sandstone.

The peak stress strength of sandstone specimens increases as a quadratic function with the water bath temperature, as shown in equation (4), and the fitting curve is shown in Figure 7:

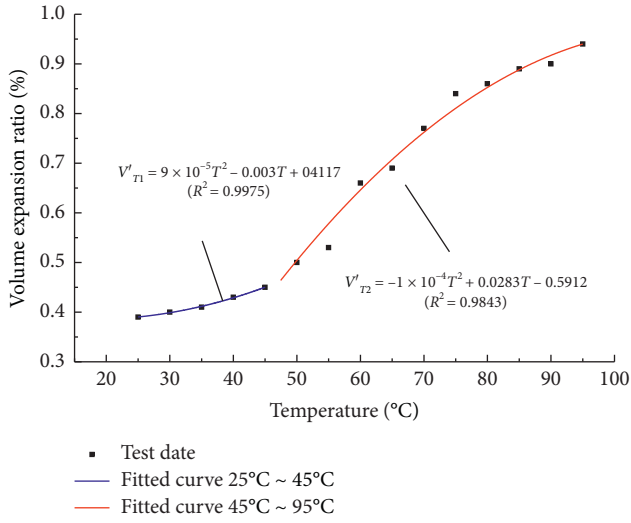


FIGURE 4: Volume changes with water bath temperature.

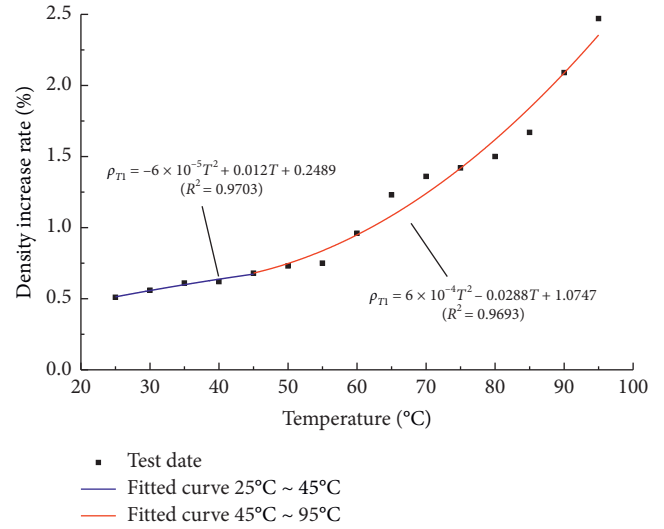


FIGURE 6: Density changes with water bath temperature.

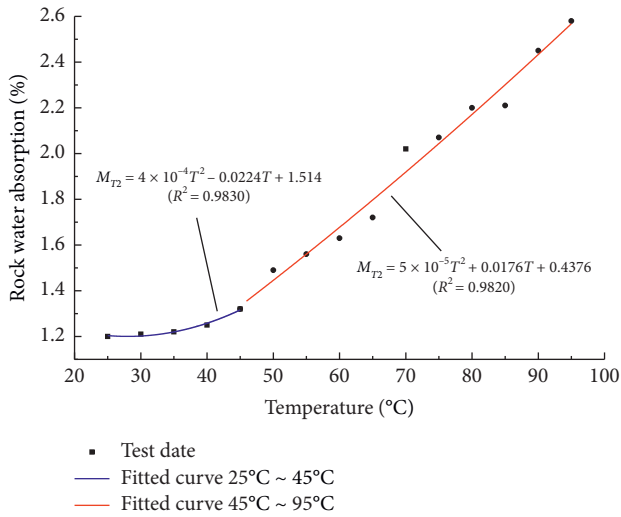


FIGURE 5: Relationship between water absorption of sandstone and water bath temperature.

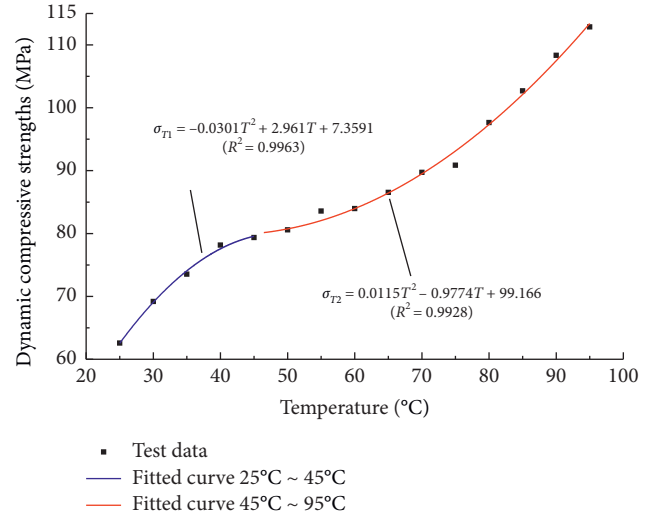


FIGURE 7: Fitting curve between water bath temperature and peak stress strength.

$$\begin{cases} \sigma_{T1} = -0.0301T^2 + 2.961T + 7.3591, & 25^\circ\text{C} \sim 45^\circ\text{C}, & R^2 = 0.9963, \\ \sigma_{T2} = 0.0115T^2 - 0.9774T + 99.166, & 45^\circ\text{C} \sim 95^\circ\text{C}, & R^2 = 0.9928, \end{cases} \quad (4)$$

where  $\sigma_{T1}$  and  $\sigma_{T2}$  are the peak stress strength of sandstone specimen after water bath action, MPa.

**4.2. Analysis of the Relationship between Different Water Bath Temperatures and Peak Strain.** The variation of peak strain of sandstone specimen with water bath temperature after water bath is shown in Figure 8.

It can be seen from the Figure 8, The peak strain of sandstone specimen decreases at,  $25^\circ\text{C} \sim 45^\circ\text{C}$ . The sandstone

specimen move the peak strain decreases with water bath temperature, and can be speculated that with the increase of bath temperature, sandstone specimens gathered a certain amount of internal thermal stress and water, and water under the action of thermal stress in these, the internal microcracks, filled with rock to produce thermal damage, the sandstone specimen of peak strain showed a trend of decrease. In the temperature range of  $45^\circ\text{C}$  water bath, the dynamic peak strain has little change, and the strain amplitude is  $1.35 \times 10^{-3} \sim 2.27 \times 10^{-3}$ . When the water bath



temperature exceeds 45°C, the dynamic peak strain obviously increases with the increase of the water bath temperature. When the temperature of the water bath reaches 95°C, the dynamic peak strain is  $5.23 \times 10^{-3}$ , which is about 3.9 times compared with that at 45°C.

$$\begin{cases} \varepsilon_{T1} = 0.0026T^2 - 0.2238T + 6.198, & 25^\circ\text{C} \sim 45^\circ\text{C}, & R^2 = 0.9657, \\ \varepsilon_{T2} = 0.0015T^2 - 0.1445T + 4.9419, & 45^\circ\text{C} \sim 95^\circ\text{C}, & R^2 = 0.9803, \end{cases} \quad (5)$$

where  $\varepsilon_{T1}$  and  $\varepsilon_{T2}$  are the dynamic peak strain of sandstone specimen after water bath action.

**4.3. Analysis of the Relationship between Different Water Bath Temperatures and Dynamic Elastic Modulus.** After the water bath, the dynamic elastic modulus of sandstone specimen changes with water bath temperature, as shown in Figure 9.

It can be seen from Figure 9 that the dynamic modulus of elasticity increases with the increase of water bath temperature between 25°C and 45°C. The dynamic modulus of elasticity is 27.61 GPa at 25°C and 79.36 GPa at 45°C, which is 187% higher than that at 25°C. It reaches the peak value at 45°C and then decreases with the increase of water bath temperature. This is because when the water bath

$$\begin{cases} E_{T1} = -0.0397T^2 + 4.284T - 54.141, & 25^\circ\text{C} \sim 45^\circ\text{C}, & R^2 = 0.9938, \\ E_{T2} = 0.0025T^2 - 1.0393T + 99.292, & 45^\circ\text{C} \sim 95^\circ\text{C}, & R^2 = 0.9869, \end{cases} \quad (6)$$

where  $E_{T1}$  and  $E_{T2}$  are the dynamic elastic modulus (GPa) of sandstone specimen after water bath.

**4.4. Analysis of the Relationship between Different Water Bath Temperatures and Average Strain Rates.** After the water bath, the average strain rate of sandstone varies with water bath temperature, as shown in Figure 10.

$$\begin{cases} \dot{\varepsilon}_{T1} = 0.0233T^2 - 2.1702T + 74.905, & 25^\circ\text{C} \sim 45^\circ\text{C}, & R^2 = 0.9959, \\ \dot{\varepsilon}_{T2} = -0.0004T^2 + 0.5051T + 3.5677, & 45^\circ\text{C} \sim 95^\circ\text{C}, & R^2 = 0.9935, \end{cases} \quad (7)$$

where  $\dot{\varepsilon}_{T1}$  and  $\dot{\varepsilon}_{T2}$  are the mean strain rate of sandstone specimen after water bath action, s<sup>-1</sup>.

**4.5. Failure Mode Analysis of Specimens.** After experiencing different water bath temperatures, the failure modes of sandstone specimens SHPB under impact compression are shown in Figure 11.

As can be seen from Figure 11, under the same impact pressure, with the increase of water bath temperature, the damage degree of the specimen gradually decreases. When

The relationship between the dynamic peak strain of sandstone specimen and the water bath temperature is a quadratic function, as shown in equation (5), and the fitting curve is shown in Figure 8:

temperature is lower than 45°C, the damage of sandstone is mainly affected by water. Due to the Stefan effect of water [48], water exerts resistance to rock cracks, impedes the expansion of cracks, and thus improves rock strength. After reaching the peak value, with the increase of water bath temperature, the failure of sandstone is mainly affected by the temperature, and the microcracks in sandstone specimens gradually expand, which leads to the decrease of deformation resistance and elastic modulus of the specimens. The elastic modulus of the specimen has a quadratic function relationship with the water bath temperature, as shown in equation (6), and the fitting curve is shown in Figure 9:

As can be seen from Figure 10, the average strain rate decreases in a quadratic parabola with the temperature increasing from 25°C to 45°C. From 45°C to 95°C, the average strain rate increases in a quadratic parabola with the increase of temperature. As shown in equation (7), the fitting curve is shown in Figure 10:

the temperature of the water bath was 25°C~45°C, the failure modes of specimens were large-scale flaking failure and axial splitting failure. When the water bath temperature was between 50°C and 95°C, the failure mode of the specimen was side spalling failure. When the temperature reaches 95°C, the damage degree of the specimen is small, and only a crack is formed on the side. To analyze the reasons, before the water bath temperature was 45°C, the specimen expanded slightly under the joint action of temperature and water. Under the action of the microexpansion force, the internal microcracks of the specimen were closed, thus



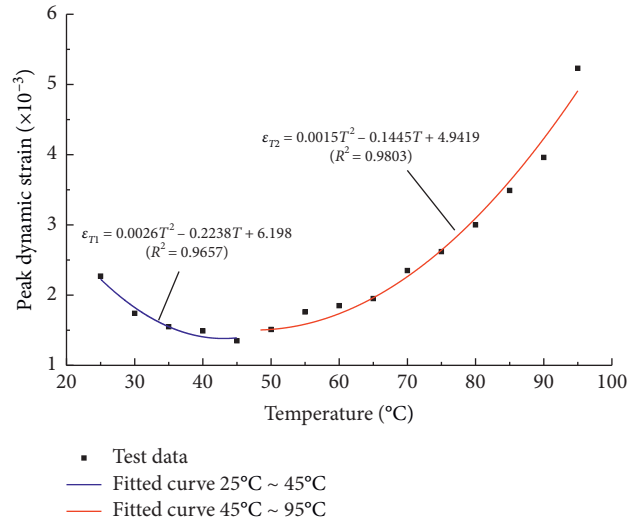


FIGURE 8: Fitting curve between water bath temperature and dynamic peak strain.

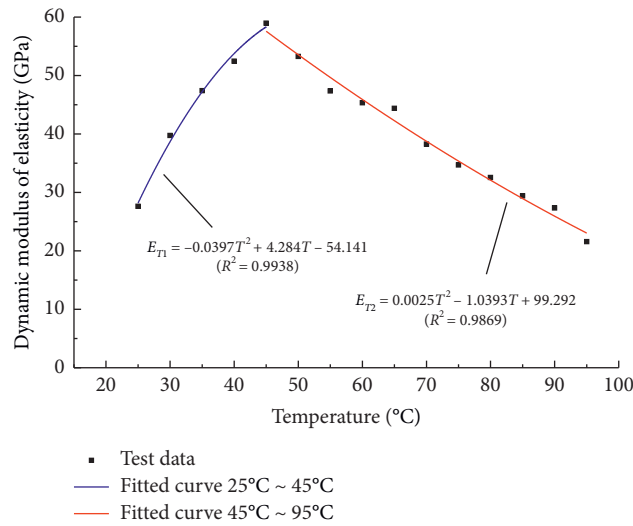


FIGURE 9: Fitting curve of water bath temperature and dynamic elastic modulus change law.

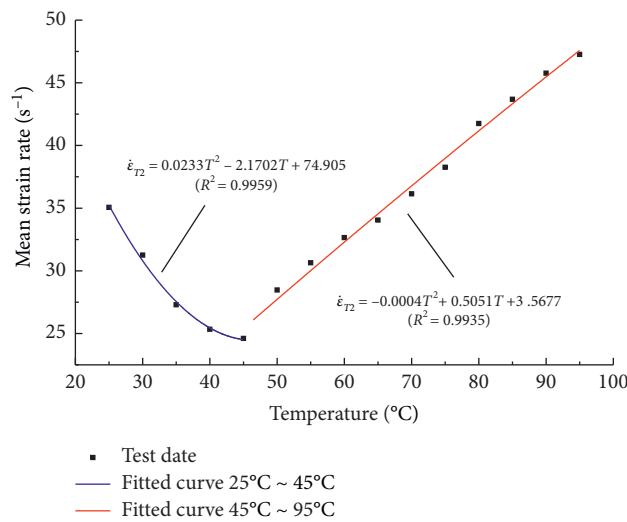


FIGURE 10: Fitting curve of change law between peak stress and average strain rate.

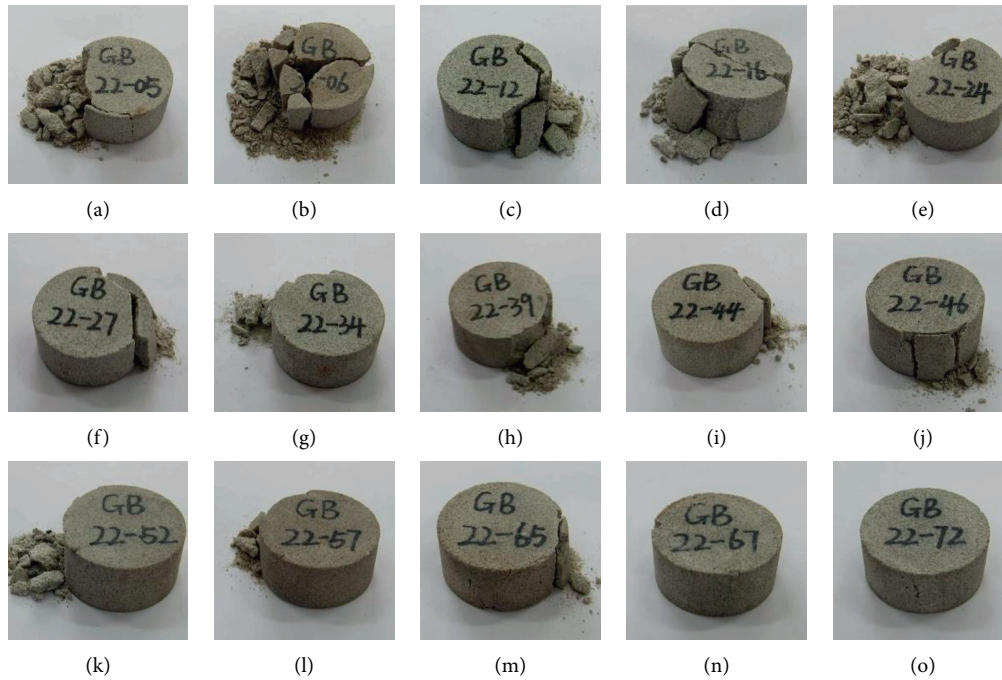


FIGURE 11: Dynamic compression failure modes of sandstone specimens with different water bath temperatures. (a) 25°C. (b) 30°C. (c) 35°C. (d) 40°C. (e) 45°C. (f) 50°C. (g) 55°C. (h) 60°C. (i) 65°C. (j) 70°C. (k) 75°C. (l) 80°C. (m) 85°C. (n) 90°C. (o) 95°C.

making the specimen compact, the compressive strength of the specimen also increased, and the damage degree of the specimen gradually decreased. When the bath temperature was larger than 45°C, more water was absorbed by sandstone specimen with the increase of temperature, resulting in the increase of Stefan effects. Therefore, it was more different for crack propagation of specimen under dynamic loading, and the specimen damage decreased gradually. In summary, the dynamic failure characteristics of water bath sandstone correspond to the strength characteristics.

## 5. Conclusion

- (1) The sandstone at 25°C~95°C is basically grayish-white, and the surface particles of the specimen at 25°C~45°C are compact. After 45°C, the surface particle gap of the specimen is obvious, and the water absorption rate of the sandstone also gradually increases. The volumetric expansion rate, water absorption rate, and density increase rate of the specimens increased in a quadratic function relationship with the water bath temperature and increased slowly from 25°C to 45°C, but rapidly from 45°C to 95°C. After a 95°C water bath, the maximum increase rates of specimen volume and density were 0.94% and 2.47%, respectively.
- (2) The peak stress strength of the specimen increases in a quadratic function with the increase of water bath temperature. The rate of increase is small from 25°C to 45°C but large from 45°C to 95°C. The dynamic peak strain of the specimen decreases first and then increases with the increase of water bath temperature,

which is a quadratic function with the water bath temperature. The dynamic peak strain of the specimen is the minimum when the water bath temperature is 45°C. The dynamic modulus of the specimen first increased and then decreased with the increase of the water bath temperature, which showed a quadratic function relationship with the water bath temperature. When the water bath temperature was 45°C, the dynamic modulus reached the maximum. The average strain rate of the specimen decreases first and then increases with the increase of water bath temperature.

- (3) The change of dynamic failure characteristics of the specimen corresponds to its strength characteristics. The fracture degree of the specimen under impact compression gradually decreases with the increase of water bath temperature. Because of the Stefan effect of water, the crack propagation of sandstone is hindered and the dynamic mechanical properties of sandstone are changed. When the temperature is 95°C, the fracture degree of the specimen is the least, which appears as a crack on the side.

## Data Availability

The data used to support the findings of this study are available from the corresponding author upon request.

## Conflicts of Interest

The authors declare that there are no conflicts of interest regarding the publication of this paper.

## Acknowledgments

This research received financial supports from the National Natural Science Foundation of China (nos. 52074005, 52074006, and 51674008), Anhui Provincial Natural Science Foundation (no. 1808085ME134), and Anhui Postdoctoral Science Foundation (no. 2015B058). Thanks are due to the State Key Laboratory of Mining Response and Disaster Prevention and Control in Deep Coal Mine, Engineering Research Center of Underground Mine Construction, Ministry of Education, and Anhui University of Science and Technology, for providing the experiment conditions.

## References

- [1] M. C. He and P. Y. Guo, "Deep rock mass thermodynamic effect and temperature control measures," *Chinese Journal of Rock Mechanics and Engineering*, vol. 32, no. 12, pp. 2377–2393, 2013, in Chinese.
- [2] M. C. He, H. P. Xie, and S. P. Peng, "Research on rock mechanics of deep mining," *Chinese Journal of Rock Mechanics and Engineering*, vol. 16, pp. 2803–2813, 2005, in Chinese.
- [3] N. Qin, Q. Ge, Z. H. Liang, J. Sun, and Y. Wang, "Experimental study on macro/micro damage of sandstone caused by high temperature and prediction of uniaxial strength by BP neural network," *Journal of Experimental Mechanics*, vol. 36, no. 1, pp. 105–113, 2021, in Chinese.
- [4] X. X. Yu, X. Z. Li, Y. Wu, M. Liu, and L. Deng, "Experimental study on change of physical and mechanical properties of limestone after high temperature," *Yangtze River*, vol. 51, no. 11, pp. 192–202, 2020, in Chinese.
- [5] A. B. Jin, S. L. Wang, Y. D. Wei, H. Sun, and L.-c. Wei, "Effect of different cooling conditions on physical and mechanical properties of high-temperature sandstone," *Rock and Soil Mechanics*, vol. 41, no. 11, pp. 3531–3539, 2020, in Chinese.
- [6] Y. C. Wu and L. Wang, "Experimental study on physico-mechanical properties of granite after high temperature," *Journal of Central South University*, vol. 51, no. 1, pp. 193–203, 2020, in Chinese.
- [7] B. Rohan, K. P. Sathis, and K. P. Samir, "Effects of high-temperature heating and cryogenic quenching on the physico-mechanical properties of limestone," *SN Applied Sciences*, vol. 2, no. 10, pp. 478–483, 2020.
- [8] X. Yu, G. Li, and Z. Chen, "Variation of uniaxial compressive strength for tight sandstone heating," *Science Technology and Engineering*, vol. 19, no. 32, pp. 133–138, 2019.
- [9] C. D. Su, C. S. Song, and F. Q. Su, "Deformation intensity and acoustic emission characteristics of hard coal sample under uniaxial compression after high temperature," *Journal of China Coal Society*, vol. 45, no. 2, pp. 613–625, 2020, in Chinese.
- [10] L. Y. Wei, G. L. Li, H. J. Su, H. Jing, and T. Zhang, "Experimental study on static and dynamic mechanical properties of anthracite after high temperature heating," *Chinese Journal of Rock Mechanics and Engineering*, vol. 36, no. 11, pp. 2712–2719, 2017, in Chinese.
- [11] L. Chen, X. L. Xu, and Y. H. Xu, "Effect of temperature and loading rate on mechanical properties of rock," *Journal of Guangxi University*, vol. 41, no. 1, pp. 170–177, 2016, in Chinese.
- [12] Q. Ping, M. J. Wu, and P. Yuan, "Experimental study on dynamic mechanical properties of high temperature sandstone under impact loads," *Chinese Journal of Rock Mechanics and Engineering*, vol. 38, no. 4, pp. 782–792, 2019, in Chinese.
- [13] Q. Ping, C. L. Zhang, H. J. Sun, and X. Han, "Dynamic mechanical properties and energy dissipation analysis of sandstone after high temperature cycling," *Shock and Vibration*, vol. 2020, Article ID 8848595, 11 pages, 2020.
- [14] Q. Ping, C. L. Zhang, H. P. Su, and H. Zhang, "Experimental study on dynamic mechanical properties and energy evolution characteristics of limestone specimens subjected to high temperature," *Advances in Civil Engineering*, vol. 2020, Article ID 8875568, 12 pages, 2020.
- [15] Q. Ping, H. P. Su, and D. D. Ma, "Experimental study on physical and dynamic mechanical properties of limestone after different high temperature treatment," *Rock and Soil Mechanics*, vol. 42, no. 4, pp. 1–12, 2021, in Chinese.
- [16] Y. Xu, K. Wang, and B. B. Shao, "Effect of temperature and load on dynamic mechanical properties and cracks of sandstone," *Engineering Blasting*, vol. 26, no. 4, pp. 17–22, 2020.
- [17] R. R. Zhang, "Test and analysis of dynamic mechanics and damage characteristics of deep sandstone after different temperatures," *Chinese Journal of Rock Mechanics and Engineering*, vol. 37, no. S2, pp. 3879–3890, 2018, in Chinese.
- [18] T. F. Chen, J. Y. Xu, S. Liu, P. Wang, and X.-Y. Fang, "Experimental study on dynamic mechanical properties of post-high-temperature sandstone," *Explosion and Shock Waves*, vol. 34, no. 2, pp. 195–201, 2014.
- [19] S. Liu and J. Y. Xu, "Effect of high temperature on dynamic compressive mechanical properties of granite," *Journal of Vibration and Shock*, vol. 33, no. 4, pp. 195–198, 2014.
- [20] S. Q. Yang, W. L. Tian, and J. P. Dong, "Experimental study on failure mechanical properties of two grain granites subjected to high temperature," *Chinese Journal of Geotechnical Engineering*, vol. 43, no. 2, pp. 281–289, 2021, in Chinese.
- [21] X. S. Xie, H. S. Chen, X. H. Xiao et al., "Microstructural characteristics and softening mechanism of red-bed soft rock under water-rock coupling," *Journal of Engineering Geology*, vol. 27, no. 5, pp. 966–972, 2019.
- [22] G. Liu, Y. M. Li, and F. K. Xiao, "Study on failure mechanics behavior and damage evolution law of yellow sandstone under uniaxial triaxial and pore water action," *Chinese Journal of Rock Mechanics and Engineering*, vol. 38, no. S2, pp. 3532–3544, 2019, in Chinese.
- [23] T. Z. Duan and Y. P. Ren, "Study on uniaxial compression mechanical properties of sandstone with different moisture content and wave velocity method," *Coal Geology & Exploration*, vol. 47, no. 4, pp. 153–158, 2019.
- [24] Y. B. Zhang, P. Liang, L. Sun et al., "Spectral characteristics of AE in the process of saturated granite fracture under uniaxial compression," *Rock and Soil Mechanics*, vol. 40, no. 7, pp. 2497–2506, 2019, in Chinese.
- [25] J. Fang, Q. L. Yao, and W. N. Wang, "Experimental study on damage characteristics of siltstone under water action," *Journal of China Coal Society*, vol. 43, no. S2, pp. 412–419, 2018.
- [26] J. Y. Teng, J. X. Tang, and Y. N. Zhang, "Damage process and characteristics of layered water-bearing shale under uniaxial compression," *Rock and Soil Mechanics*, vol. 38, no. 6, pp. 1629–1638, 2017, in Chinese.
- [27] C. D. Su, Y. N. Sun, Z. H. Zhang et al., "On the effect of water-saturated state on failure energy of sandstone from coal seam roof subjected to uniaxial compression," *Experimental Mechanics*, vol. 32, no. 2, pp. 223–231, 2017, in Chinese.

- [28] Y. Y. Zhang, *Microscopic Dynamics Mechanism of Deep Shale under Water-Rock Interaction*, China University of Petroleum, Beijing, China, 2019.
- [29] J. J. Fu, Z. D. Dong, Y. S. Yang, and H. Yi, "Evolution characteristics of mechanical parameters for sandstone under different water-rock interaction," *Journal of Shenyang University of Technology*, vol. 42, no. 3, pp. 350–354, 2020, in Chinese.
- [30] Y. Yang, L. Mei, H. Liu et al., "Study on infrared radiation characteristics of siltstone after process of different temperature soaking," *China Mining Industry*, vol. 26, no. 6, pp. 149–153, 2017, in Chinese.
- [31] L. S. Gao, Y. Xu, B. B. Wu, and S. Wang, "Dynamic compression strength of thermal damaged Fangshan marble on dry and saturated conditions," *Chinese Journal of Rock Mechanics and Engineering*, vol. 37, no. S2, pp. 3826–3833, 2018, in Chinese.
- [32] G. Y. Wang, R. Yu, D. F. Ma et al., "Comparative study on dynamic tensile and compressive strength of the saturated fine sandstone," *Chinese Journal of High Pressure Physics*, vol. 34, no. 4, pp. 49–58, 2020, in Chinese.
- [33] J. P. Zhao, M. H. Wang, and Y. H. Zhao, "Influence of moisture content on dynamic tensile strength of sandstone," *Gold Science and Technology*, vol. 27, no. 2, pp. 216–222, 2019.
- [34] Z. L. Zhou, X. Cai, J. Zhou, and R. Cheng, "Mechanical properties of saturated sandstone under different loading rates," *Chinese Journal of Rock Mechanics and Engineering*, vol. 37, no. S2, pp. 4069–4075, 2018, in Chinese.
- [35] F. J. Chu, D. W. Liu, M. Tao, and H.-D. Peng, "Dynamic response of sandstones with different water contents based on SHPB," *Journal of Engineering Science*, vol. 39, no. 12, pp. 1783–1790, 2017.
- [36] H. Y. Wang, J. X. Xu, P. Wang et al., "A study of dynamic compressive strength and microscopic mechanism on water-bearing rock," *Journal of Air Force Engineering University (Natural Science Edition)*, vol. 17, no. 4, pp. 107–111, 2016.
- [37] P. Y. Guo, B. H. Bai, S. Chen, C. Shi, and H. Du, "Effect of temperature and moisture content on thermal properties of sandstone," *Chinese Journal of Rock Mechanics and Engineering*, vol. 36, no. S2, pp. 3910–3914, 2017, in Chinese.
- [38] L. Yu, H. W. Peng, Y. Zhang et al., "Effects of the number of water-heat cycles on the physical and mechanical properties of granite," *Science Technology and Engineering*, vol. 21, no. 2, pp. 703–713, 2021.
- [39] K. Hashiba and K. Fukui, "Effect of water on the deformation and failure of rock in uniaxial tension," *Rock Mechanics and Rock Engineering*, vol. 48, no. 5, pp. 1751–1761, 2015.
- [40] L. N. Y. Wong and M. C. Jong, "Water saturation effects on the Brazilian tensile strength of gypsum and assessment of cracking processes using high-speed video," *Rock Mechanics and Rock Engineering*, vol. 47, no. 4, pp. 1103–1115, 2014.
- [41] H. Karakul and R. Ulusay, "Empirical correlations for predicting strength properties of rocks from P-wave velocity under different degrees of saturation," *Rock Mechanics and Rock Engineering*, vol. 46, no. 5, pp. 981–999, 2013.
- [42] H. M. An, T. S. Zeng, Z. H. Zhang, and L. Lei, "Experimental study of the rock mechanism under coupled high temperatures and dynamic loads," *Advances in Civil Engineering*, vol. 2020, Article ID 8866621, 19 pages, 2020.
- [43] M. Wen, J. Y. Xu, H. Y. Wang, X. Y. Fang, and G. H. Zheng, "Fractography analysis of sandstone failure under low temperature-dynamic loading coupling effects," *Rock Mechanics and Rock Engineering*, vol. 36, no. 2, 2017.
- [44] Z. L. Wang, H. Shi, and J. G. Wang, "Mechanical behavior and damage constitutive model of granite under coupling of temperature and dynamic loading," *Rock Mechanics and Rock Engineering*, vol. 51, no. 10, pp. 3045–3059, 2018.
- [45] National Standards Compilation Group of the People's Republic of China, *Method for Determination of Physical and Mechanical Properties of Coal and Rock*, Standards Press of China, Beijing, China, 2010.
- [46] Chinese Society for Rock Mechanics & Engineering, "T/CSRME 001-2019 technical specification for testing method of rock dynamic properties [EB/OL]," 2019, <http://www.ttbz.org.cn/Home/Show/10253>.
- [47] L. L. Wang, *Stress Wave Foundation*, National Defense Industry Press, Beijing, China, 2010.
- [48] Z. Dan and Q. B. Li, "An explanation for rate effect of concrete strength based on fracture toughness including free water viscosity," *Engineering Fracture Mechanics*, vol. 71, no. 16-17, pp. 2319–2327, 2004.

## Research Article

# Random Dynamic Response Characteristics of Pipeline Subjected to Blasting Cylindrical SH Waves

Shiwei Lu <sup>1</sup>, Heng Zhang <sup>1</sup> and Ling Ji <sup>2</sup>

<sup>1</sup>School of Urban Construction, Yangtze University, Jingzhou 434023, China

<sup>2</sup>Faculty of Engineering, China University of Geosciences, Wuhan 430074, China

Correspondence should be addressed to Heng Zhang; [hengzhang@yangtzeu.edu.cn](mailto:hengzhang@yangtzeu.edu.cn)

Received 5 February 2021; Revised 10 May 2021; Accepted 8 July 2021; Published 19 July 2021

Academic Editor: Bangbiao Wu

Copyright © 2021 Shiwei Lu et al. This is an open access article distributed under the Creative Commons Attribution License, which permits unrestricted use, distribution, and reproduction in any medium, provided the original work is properly cited.

It is essential to investigate the influence of blasting vibrations on pipelines, and the dynamic response is the crux in the safety issues. At present, the blasting seismic wave is usually regarded as a plane wave. However, there is little research about the dynamic response characteristics of underground structures subjected to nonplane waves. The analytical solution to dynamic stress concentration factor (DSCF) of pipelines subjected to cylindrical SH wave was derived. Besides, the randomness of the shear modulus of soil was considered, and the statistical analysis of DSCF was carried out by the Monte Carlo simulation method. Results show that the variability of the shear modulus of soil has a significant influence on the probability distribution of DSCF. The larger the variation coefficient of the shear modulus is, the more obvious the skewness of DSCF is. The influence of low-frequency wave on pipeline increases with the reducing normalized distance  $r^*$ , while the influence of high-frequency wave reduces and the variation amplitude of DSCF increases. Compared with the DSCF of pipe subjected to a plane wave, a lower dominant frequency or larger normalized distance for the cylindrical SH wave will generate a more similar statistical characteristic of DSCF.

## 1. Introduction

With the rapid development of transportation construction, the drilling and blasting method has been widely used in the excavation of underground space due to its efficiency and economy. However, blasting seismic waves induced by the structures excavation will undermine the safety of nearby pipelines which are important channels for energy transmission and even cause serious economic losses and successive disasters.

A large number of research studies have been implemented to study the dynamic response characteristics of underground structures subjected to blasting seismic waves. Pao and Mow [1] investigated the dynamic stress concentration factors (DSCFs) of a cavity in an unbounded elastic space under the incident plane P, SH, and SV waves. Lee and Trifunac [2–4] studied the dynamic response of tunnels and cavities induced by plane P, SH, and SV waves. Thambirajah et al. [5] considered the effect of DSCF and studied the

scattering of SH waves by two caverns. Liu and Wang [6] revealed the dynamic response law of cavities subjected to plane waves. Wang et al. [7] used the wave function expansion method to give an analytical solution to the dynamic response of a deep-buried soft rock circular tunnel under the incident plane SH wave. Fu et al. [8] studied the interaction between the soil and the tunnel when the blasting plane SH wave was considered. Yi et al. [9] proposed an analytical solution to the dynamic response of a circular tunnel when the imperfect contact exists between surrounding rock and lining subjected to incident plane P waves. Liu et al. [10] used the complex functions and multilevel coordinate method to analyze the influence of P wave on pipelines in saturated soil. He et al. [11] studied the scattering of plane SH waves by underground caverns with arbitrary cross-sectional shapes. Zhang et al. [12] derived the analytical solution to the dynamic responses of deep-water foundation sites when both incident plane P and SV waves were considered. Liang et al. [13] studied the diffraction of plane SH waves by a

semicircular cavity in half-space by using the wave function expansion method. Xu et al. [14] deduced a series solution of dynamic stress for a circular lining tunnel subjected to incident plane P waves in an elastic half-space. Xu [15] derived the blasting safety criterion of an unlined circular tunnel subjected to plane P waves. Qi et al. [16, 17] carried out the dynamic analysis for circular inclusions near interface impacted by SH waves using the complex method and Green's function method. Fan et al. [18] predicted the dynamic response of a circular lined tunnel with an imperfect interface to plane SV waves based on the wave function expansion method and the linear spring model. Lu et al. [19] studied the dynamic stress concentration and vibration velocity scaling factors of an unlined circular tunnel subjected to a triangular P wave. Xia et al. [20] calculated the vibration response of buried flexible HDPE pipes under impact loads based on the Winkler model and the Timoshenko beam theory. Recently, Jiang et al. [21–23] studied the dynamic failure behavior of buried cast iron gas pipeline subjected to blasting vibration. In order to simplify the analysis, most of these studies approximately regard blasting seismic waves as plane waves. However, the assumption is not reliable when the explosion source is close to the underground structure because the curvature of incident blasting waves cannot be ignored. Although some research studies about cylindrical waves have been carried out, the random dynamic response of underground structures under cylindrical waves is still rare in literature [24–26].

At present, He and Liang [27] used the Monte Carlo simulation method to study the influence of the shape variability of the outer wall on the peak value of DSCF around the inner wall. However, due to the effects of multiple factors, such as sedimentation, weathering, chemical action, transportation processes, and different loading history, the physical and mechanical properties of rock and soil vary spatially. Therefore, it is more suitable to study the DSCF of pipelines under cylindrical SH waves when the shear modulus of soil is considered as random parameter.

## 2. Random Dynamic Responses of Pipeline Subjected to Cylindrical SH Waves

**2.1. Simplified Model.** A linear wave source is assumed to locate at  $O_1$ , and the axis of a circular pipe whose inner and outer radius are  $a$  and  $b$ , respectively, coincides with  $O_2$ . The distance between  $O_1$  and  $O_2$  is  $r_0$ , and the coordinate systems  $O_1x_1y_1$  and  $O_2x_2y_2$  are established on  $O_1$  and  $O_2$ , respectively, as shown in Figure 1.  $P$  is an arbitrary point in the soil, and the distances away from  $O_1$  and  $O_2$  are  $r_1$  and  $r_2$ , respectively. The displacement function of the cylindrical SH wave generated at  $O_1$  can be expressed in the following form [28, 29]:

$$W^{(i)} = H_0^{(1)}(\beta_1 r_1) \exp(-i\omega t), \quad (1)$$

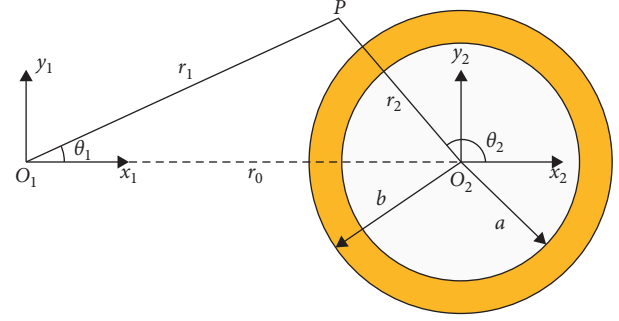


FIGURE 1: Incident cylindrical SH wave.

where  $H_0^{(1)}$  is the 0th-order Hankel function,  $i$  is the imaginary unit,  $\beta_1$  is the wave number of SH wave in the soil, and  $\beta_1 = \omega/c_{s1}$ , in which  $\omega$  is the frequency of the incident wave and  $c_{s1} = \sqrt{G/\rho}$  is the speed of SH wave in the soil.  $\rho$  is the density of the soil. The shear modulus  $G$  of the soil is considered as a random parameter, which can be described as

$$G(\xi) = \bar{G}(1 + \alpha\xi), \quad (2)$$

where  $\bar{G}$  is the mean value of the shear modulus of soil and  $\xi$  is a random variable with standard normal distribution  $N(0,1)$ . As a result, the shear modulus of the soil  $G$  and the SH wave-number  $\beta_1$  will be a function of the random variable  $\xi$ . Then, the coefficient of variation (Cov) of the shear modulus  $\delta_G$  of the soil can be calculated as

$$\delta_G = \frac{\sqrt{\mathbf{D}[G(\xi)]}}{\mathbf{E}[G(\xi)]} = \alpha. \quad (3)$$

Generally, when a cylindrical SH wave reaches the pipe, it will generate a reflected SH wave ( $W^{(r)}$ ) propagating outward in the soil and a refracted SH wave ( $W^{(f)}$ ) propagating outward and inward in the pipe. Their displacement can be expressed as follows:

$$\begin{cases} W^{(r)} = \sum_{n=0}^{\infty} H_n^{(1)}(\beta_1(\xi)r_2) [B_n \cos n\theta_2 + E_n \sin n\theta_2] \exp(-i\omega t), \\ W^{(f)} = \sum_{n=0}^{\infty} H_n^{(1)}(\beta_2 r_2) [C_n \cos n\theta_2 + F_n \sin n\theta_2] \exp(-i\omega t) \\ + \sum_{n=0}^{\infty} H_n^{(2)}(\beta_2 r_2) [D_n \cos n\theta_2 + G_n \sin n\theta_2] \exp(-i\omega t), \end{cases} \quad (4)$$

where  $\beta_2 = \omega/c_{s2}$  is the wave number of SH waves in the pipe and  $c_{s2} = \sqrt{G_2/\rho_2}$  is the speed of SH wave in the pipe, in which  $G_2$  is the shear modulus of the pipe and  $\rho_2$  is the density of the pipe.

In order to obtain the displacement function of the incident wave, the reflected wave, and the refracted wave, the incident wave potential function in the  $O_1x_1y_1$  coordinate system must be converted to the expression form in the  $O_2x_2y_2$  coordinate system. The conversion formula is expressed as follows [30, 31]:



$$H_n^{(1)}[\beta_1(\xi)r_1]\cos n\theta_1 = \sum_{m=-\infty}^{\infty} (-1)^m H_m^{(1)}[\beta_1(\xi)r_0]J_{m+n}[\beta_1(\xi)r_2]\cos(m+n)\theta_2, \quad (5)$$

where  $H_n^{(1)}$  is the  $n$ th-order Hankel function and  $J_n$  is the  $n$ th-order Bessel function.

Substituting equation (5) into equation (1), we can express the displacement function of the cylindrical SH wave as follows:

$$W^{(i)} = \sum_{n=0}^{\infty} A_{0n} J_n[\beta_1(\xi)r_2] \cos n\theta_2 \exp(-i\omega t), \quad (6)$$

where  $A_{0n} = (-1)^n \epsilon_n H_n^{(1)}[\beta_1(\xi)r_0]$ ; if  $n=0$ ,  $\epsilon_0 = 1$ ; when  $n > 0$ ,  $\epsilon_0 = 2$ .

**2.2. Boundary Conditions.** Let  $W_1 = W^{(i)} + W^{(r)}$  and  $W_2 = W^{(f)}$ ; considering the interface between the pipe and the soil as an ideal contact interface, the boundary conditions can be expressed as follows:

$$\begin{cases} \tau_{rz1} = \tau_{rz2}, W_1 = W_2, & \text{if } r_2 = b, \\ \tau_{rz2} = 0, & \text{if } r_2 = a. \end{cases} \quad (7)$$

The relationship between the displacement and the stress of a cylindrical SH wave can be expressed as follows:

$$\begin{aligned} \tau_{rz} &= \frac{\mu}{r} \frac{\partial W}{\partial r}, \\ \tau_{\theta z} &= \frac{\mu}{r} \cdot \frac{\partial W}{\partial \theta}. \end{aligned} \quad (8)$$

According to equations (5) and (8), the value of  $B_n$ ,  $C_n$ ,  $D_n$ ,  $E_n$ ,  $F_n$ , and  $G_n$  can be obtained.

**2.3. Solution of Random DSCF Based on the Monte Carlo Simulation Method.** In order to obtain general results, the dimensionless parameters of DSCF and normalized distance  $r^*$  are defined as follows:

$$\text{DSCF} = \max \left| \frac{\tau_{\theta z 2}}{\tau_{r z 1}^{(i)}} \right|, \quad (9)$$

$$r^* = \frac{r_0}{b}, \quad (10)$$

where  $\tau_{r z 1}^{(i)} = -\mu_1 \beta_1(\xi) H_1^{(1)}[\beta_1(\xi)r_1]$ .

When the randomness of structural parameters is considered, the dynamic response of the structure will also be random. In order to obtain the random response of the structure, a series of various strategies such as the Monte Carlo simulation method [32], stochastic finite element method [33], and the probability density evolution method [34] are proposed. The Monte Carlo simulation method has a high calculation accuracy in solving complex functions. Besides, the calculation accuracy is not affected by the variability of random parameters. Therefore, it is widely used in theoretical research studies. Owing to the given explicit formula of DSCF, the Monte Carlo simulation method is

adopted to obtain the statistical results of DSCF. The main steps are as follows:

*Step 1.* Use equation (2) to describe the randomness of the shear modulus of the soil and generate a sufficient number of samples  $\xi$  which obeys the standard normal distribution

*Step 2.* According to the derivation process of DSCF, substitute each sample into the expression of the shear modulus of soil and obtain the corresponding result of DSCF

*Step 3.* Perform statistical analysis on the samples of DSCF obtained in Step 2

### 3. Engineering Background

The underground passage of Baotong Temple passes through the concrete sewage pipe at a short distance and is excavated by drilling and blasting. The top of the passage is only 0.69 m away from the sewage pipe. The density and shear modulus of the pipeline are 2400 kg/m<sup>3</sup> and 12.61 GPa, respectively. The inner radius  $a$  and the outer radius  $b$  are 400 mm and 465 mm, respectively. The density of the surrounding soil is 1980 kg/m<sup>3</sup>, and the average shear modulus of the soil  $\bar{G}$  is 150 MPa. According to the construction information, the dominant frequency of blasting seismic waves is below 200 Hz. Consequently, the dominant frequency  $f$  and  $r_0$  are considered as 10~200 Hz and  $2b \sim 10b$ , respectively.  $\delta_G$  is selected as 0.1 and 0.2, respectively, in the following analysis.

### 4. Results and Discussion

**4.1. Convergence Analysis.** The Monte Carlo simulation method is employed to obtain the statistical results of the DSCF. First, a certain number of samples which obey the standard normal distribution are generated, then the random shear modulus is expressed using equation (2), and finally the sample values of the DSCF are calculated through equations (4)–(9).

Before the implementation of the Monte Carlo simulation progress, it is necessary to study the influence of the number of the samples on the convergence of the solution. Figure 2 exhibits the first four statistic moments (mean, standard deviation, skewness, and kurtosis) of DSCF generated by the Monte Carlo simulation method with the number of the samples increasing from  $1 \times 10^3$  to  $5 \times 10^5$  when the four dominant frequencies are 10 Hz, 50 Hz, 100 Hz, and 200 Hz, respectively. It is found that in the aspects of mean and standard deviation, only a small number of samples is needed to obtain stable results regardless of  $f$ . However, in the aspects of skewness and kurtosis, a large number of samples are required. It indicates that a sufficient large number of samples are necessary to obtain stable high-order statistical moments of DSCF to ensure the convergence. For example, the calculation results of the first four

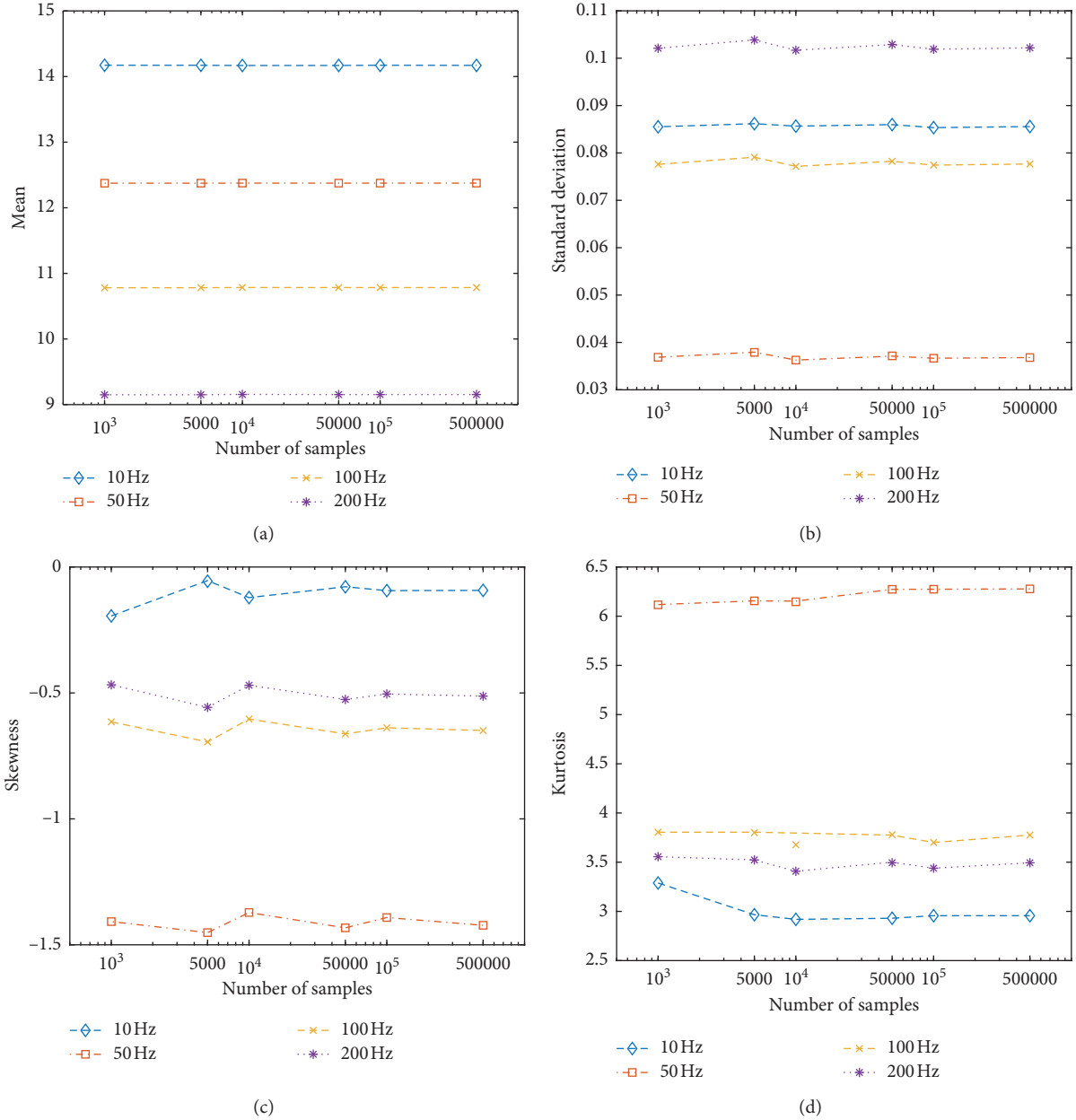


FIGURE 2: First four statistic moments of DSCF obtained with different numbers of samples: (a) mean; (b) standard deviation; (c) skewness; (d) kurtosis.

statistic moments tend to be stable when more than 100,000 samples are selected, and thus 100,000 samples should be used in the subsequent analysis.

Figure 3 shows the mean and standard deviation of the DSCF when different values of  $r^*$  are considered. It is observed from Figure 3 that when  $\delta_G$  is equal to 0.1 and 0.2, the mean of the DSCF decreases significantly when the dominant frequency increases. When the dominant frequency is equal to 50 Hz, 100 Hz, and 200 Hz, the standard deviation of DSCF decreases with the increasing  $r^*$ , especially when  $2 \leq r^* \leq 5$ . However, the standard deviation of DSCF is almost unchanged when  $f = 10$  Hz.

**4.2. Analysis of the Pipeline Dynamic Response Characteristics.** Figures 4 and 5 show the probability density function (PDF) curve and cumulative distribution function (CDF) curve of DSCF when  $\delta_G = 0.1$  and 0.2, respectively. DSCF of the pipeline under the plane wave is also provided for comparison.

It can be seen from Figure 4 that when  $\delta_G$  is small (i.e.,  $\delta_G = 0.1$ ), the PDF of DSCF approximately obeys the Gaussian distribution when  $f = 10$  Hz. With the increase in  $r^*$ , the PDF curve integrally shifts to the left, which suggests that the mean of the DSCF reduces. However, the mean of DSCF increases with the increase in  $r^*$  when  $f$  is equal to

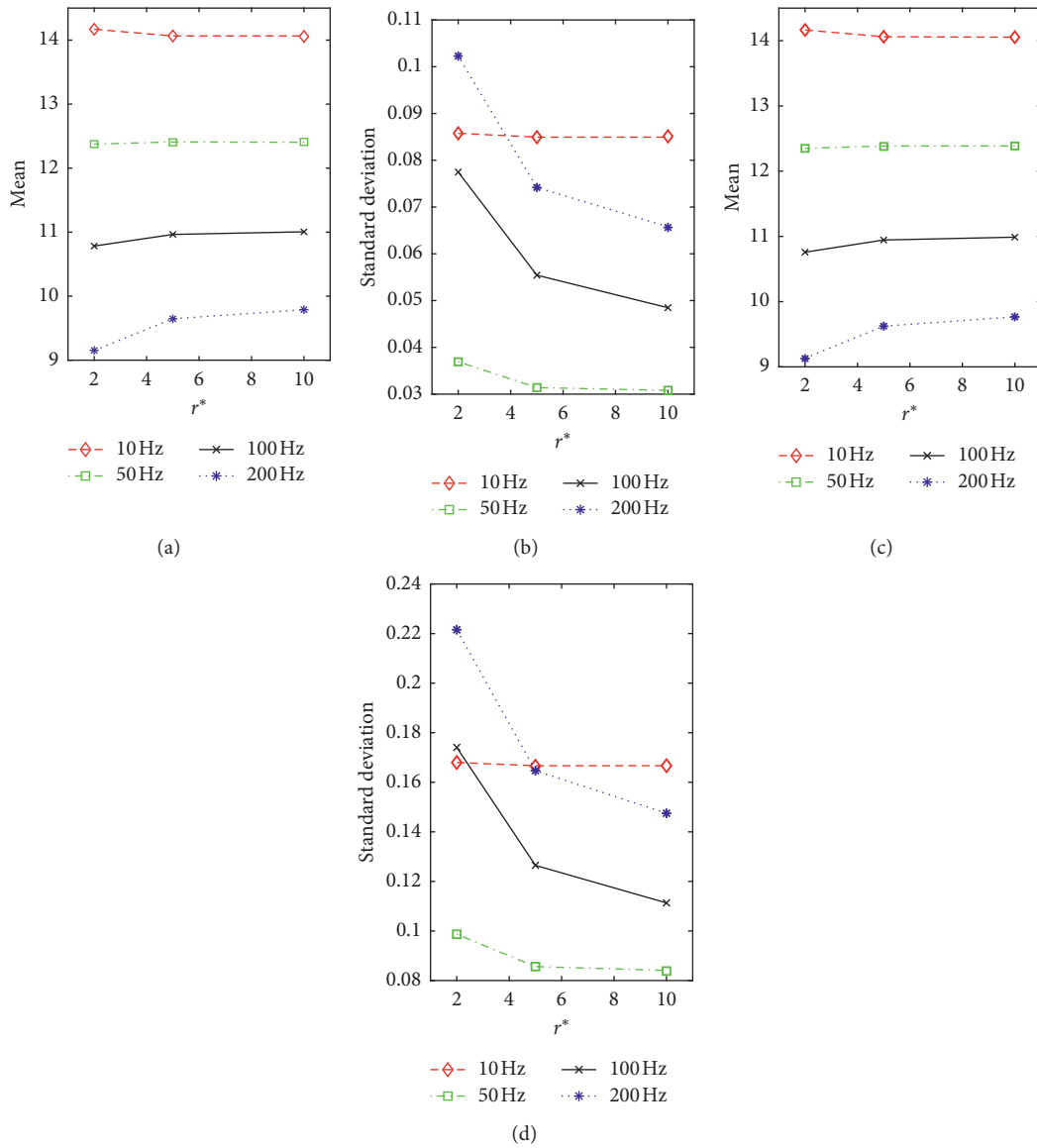


FIGURE 3: Mean and standard deviation of DSCF for different values of  $r^*$ : (a) mean ( $\delta_G = 0.1$ ); (b) standard deviation ( $\delta_G = 0.1$ ); (c) mean ( $\delta_G = 0.2$ ); (d) standard deviation ( $\delta_G = 0.2$ ).

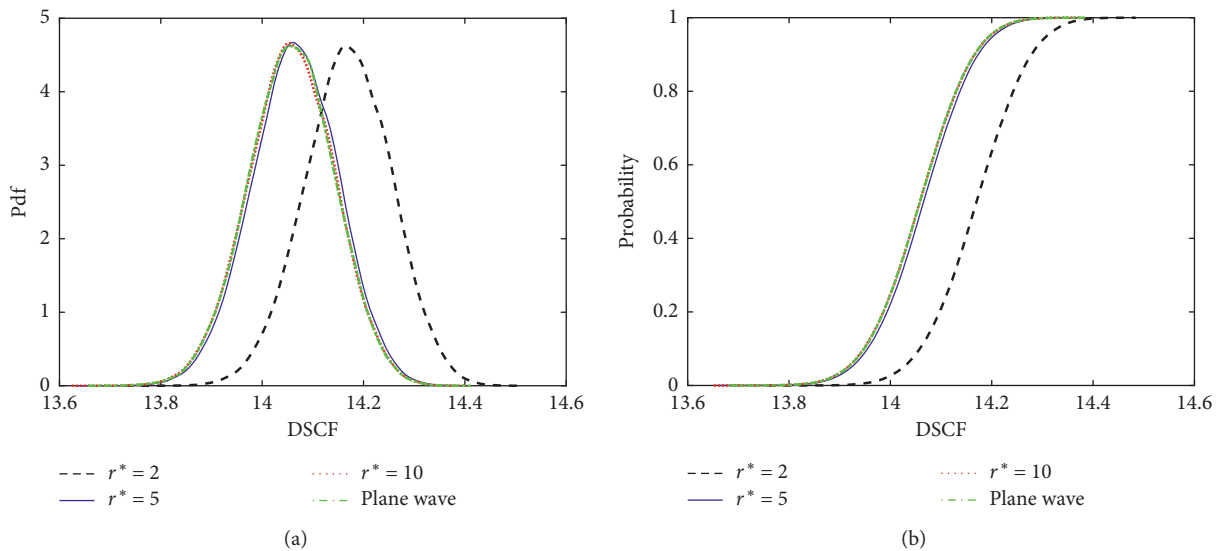


FIGURE 4: Continued.

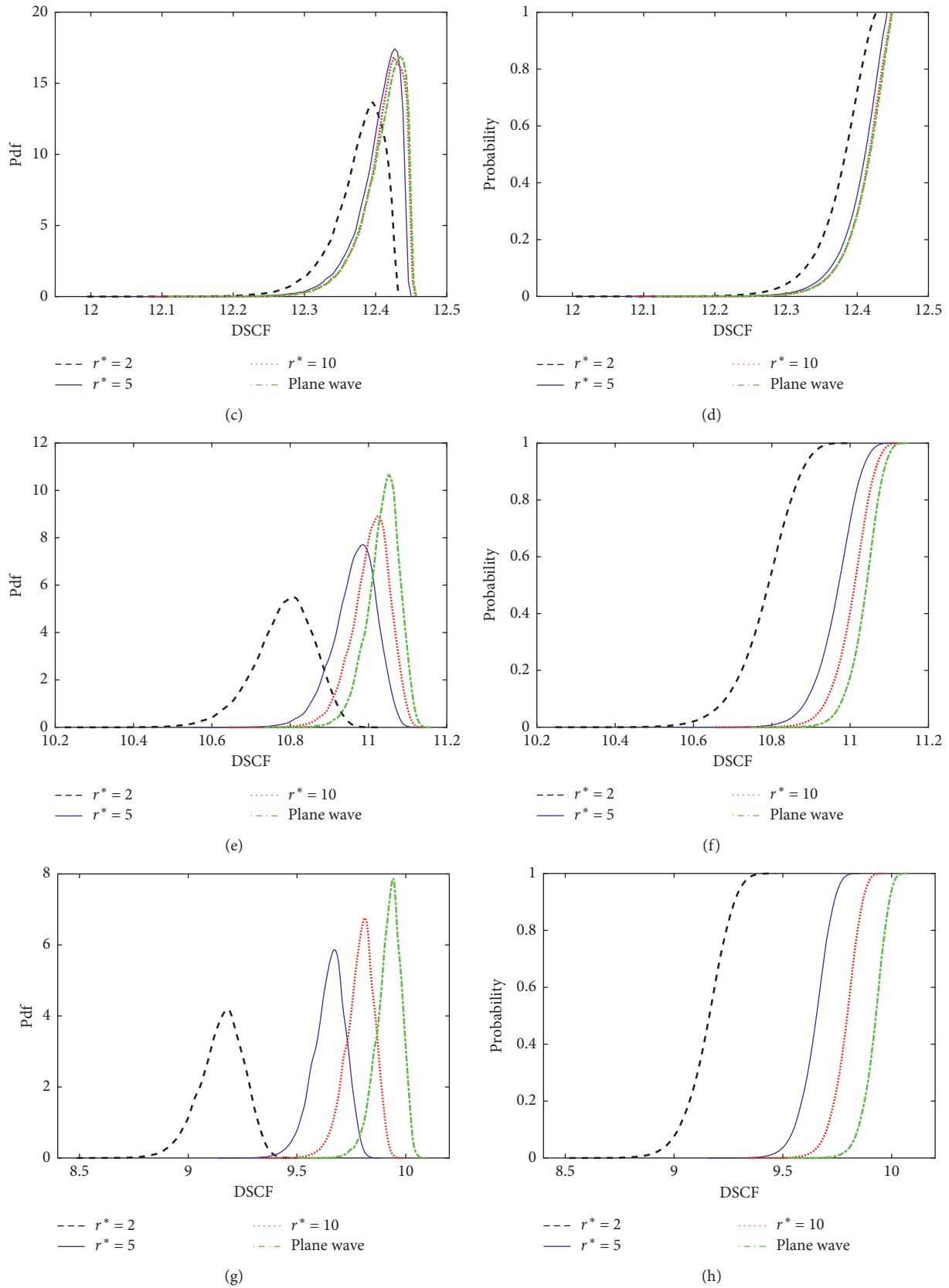


FIGURE 4: PDF curves (left) and CDF curves (right) of DSCF when  $\delta_G = 0.1$ : (a) PDF  $f = 10$  Hz; (b) CDF  $f = 10$  Hz; (c) PDF  $f = 50$  Hz; (d) CDF  $f = 50$  Hz; (e) PDF  $f = 100$  Hz; (f) CDF  $f = 100$  Hz; (g) PDF  $f = 200$  Hz; (h) CDF  $f = 200$  Hz.

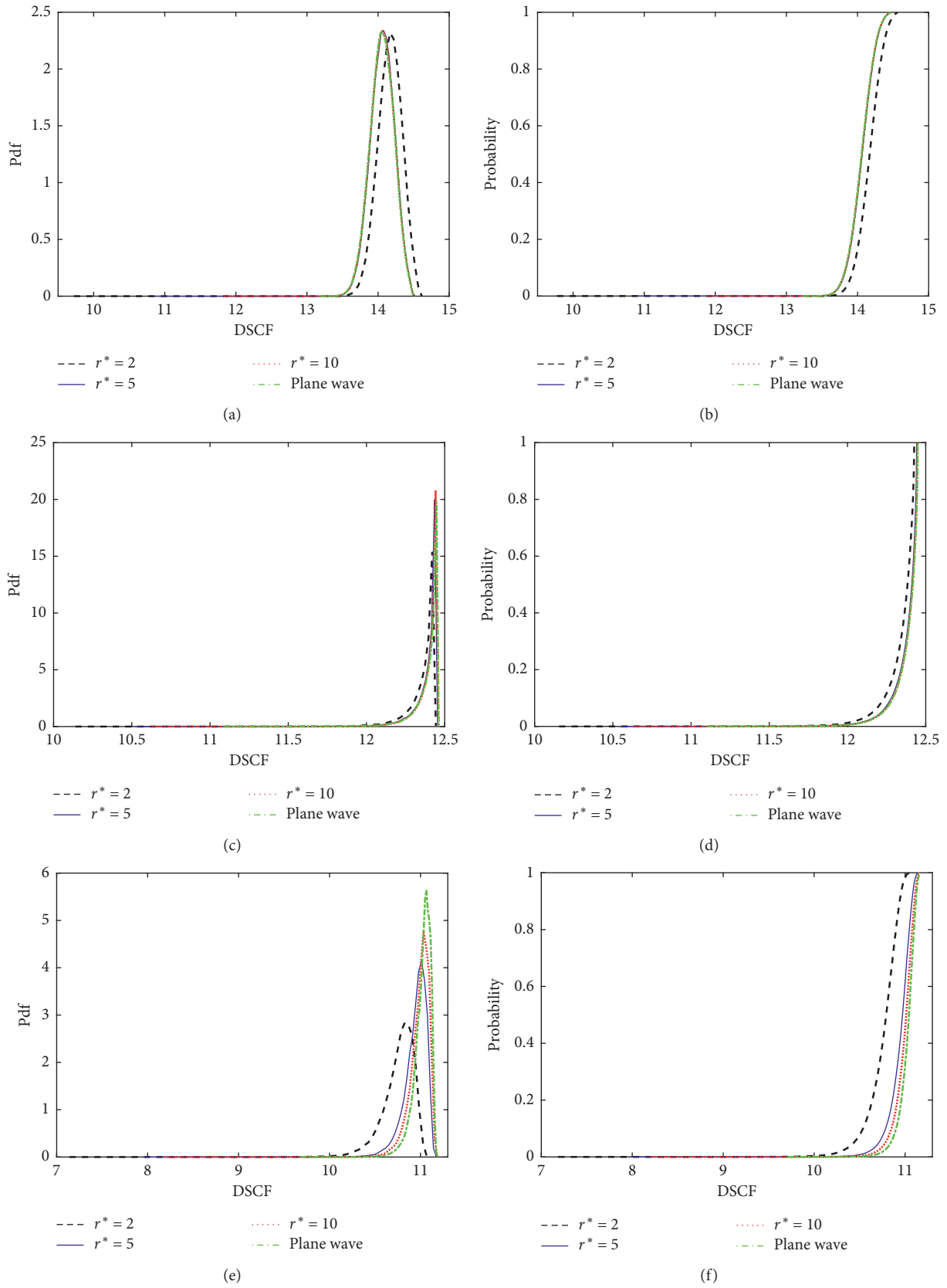


FIGURE 5: Continued.

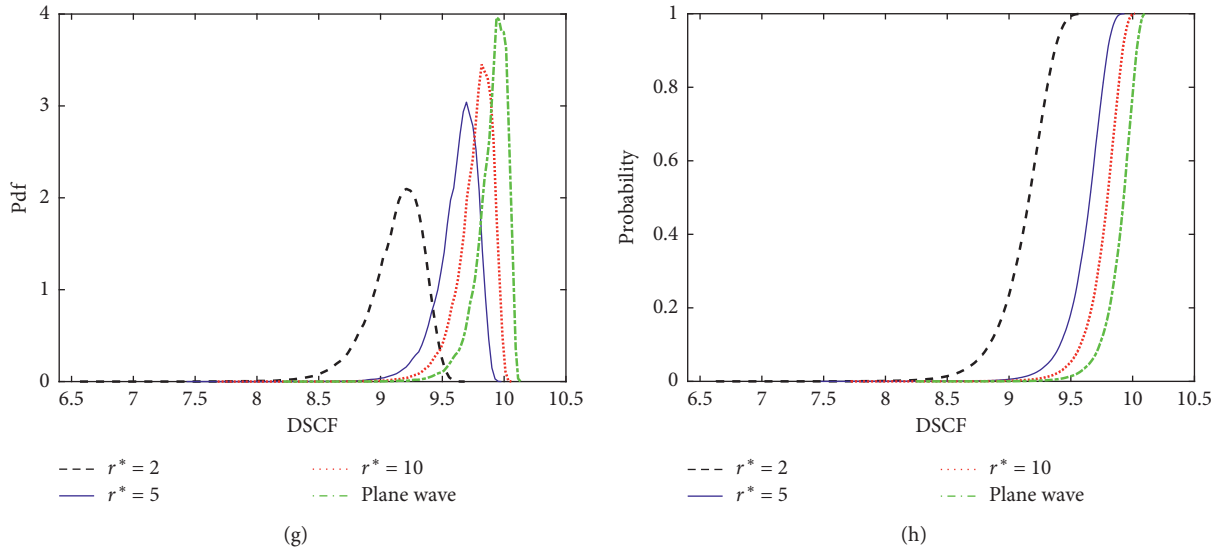


FIGURE 5: PDF curves (left) and CDF curves (right) of DSCF when  $\delta_G = 0.2$ : (a) PDF  $f = 10$  Hz; (b) CDF  $f = 10$  Hz; (c) PDF  $f = 50$  Hz; (d) CDF  $f = 50$  Hz; (e) PDF  $f = 100$  Hz; (f) CDF  $f = 100$  Hz; (g) PDF  $f = 200$  Hz; (h) CDF  $f = 200$  Hz.

50 Hz, 100 Hz, and 200 Hz. The PDF curve when  $f = 50$  Hz is obviously different from that of other cases. When the dominant frequency is relatively small (10 Hz or 50 Hz), the PDF and CDF of DSCF generated by the cylindrical SH wave are very similar to the results of the plane wave. As the dominant frequency increases, the distinctions between the cylindrical SH wave and plane wave will appear; however, the PDF and CDF of DSCF are getting close to the results of the plane wave as  $r^*$  increases.

It is found from Figure 5 that the variation of the mean of DSCF with  $r^*$  is similar when  $\delta_G$  is equal to 0.1 and 0.2, respectively. However, all the PDF curves of DSCF become leftward, and they do not obey the normal distribution any more, especially in the case of  $f = 50$  Hz. A comparison between Figures 4 and 5 shows that the larger  $\delta_G$  is, the more obvious the skewness of PDF is, which indicates that the relationship of DSCF and shear modulus of soil is significantly nonlinear. Compared with the DSCF under the plane wave, it has a same trend as  $\delta_G = 0.1$ ; a lower dominant frequency or larger normalized distance under the cylindrical SH wave will obtain a closer result.

## 5. Conclusions

- (1) The shear modulus of soil is defined as a random parameter, and the analytical expression of the maximum DSCF of pipe subjected to an incident cylindrical SH wave is established based on the Fourier–Bessel expansion and the Monte Carlo simulation method.
- (2) When the dominant frequency is 10 Hz, the mean and median of DSCF decrease as the normalized distance increases. However, this is contrary to those when the frequency of incident wave is 50 Hz, 100 Hz, and 200 Hz, which indicates that when the normalized distance is small, the lower-frequency

wave has a greater impact on the pipeline than the higher-frequency wave.

- (3) With the increase in normalized distance, the PDF of DSCF gradually becomes narrow, indicating that the variability of DSCF decreases with the increase in normalized distance.
- (4) Compared with the DSCF of pipe subjected to a plane wave, a lower dominant frequency or larger normalized distance for the cylindrical SH wave will generate much closer PDF and CDF of DSCF.

## Data Availability

The data used to support the findings of this study are included within the article.

## Conflicts of Interest

The authors declare that they have no conflicts of interest.

## Acknowledgments

The study was sponsored by Hubei Provincial Natural Science Foundation (Grant no. 2019CFB224), Hubei Provincial Department of Education (Grant no. Q20191308), and Open Research Fund of Hubei Key Laboratory of Blasting Engineering (Grant no. HKLBEF202011).

## References

- [1] Y. H. Pao and C. C. Mow, *Diffraction of Elastic Waves and Dynamic Stress Concentrations*, Crane Russak, New York, NY, USA, 1973.
- [2] V. W. Lee and M. D. Trifunac, “Response of tunnels to incident SH-waves,” *Journal of the Engineering Mechanics Division*, vol. 105, no. 4, pp. 643–659, 1979.



- [3] V. W. Lee and J. Karl, "Diffraction of SV waves by underground, circular, cylindrical cavities," *Soil Dynamics and Earthquake Engineering*, vol. 11, no. 8, pp. 445–456, 1992.
- [4] V. W. Lee and J. Karl, "On deformation near a circular underground cavity subjected to incident plane P waves," *European Journal of Earthquake Engineering*, vol. 6, no. 1, pp. 29–35, 1993.
- [5] B. Thambirajah, P. T. David, G. K. Chan et al., "Dynamic response of twin circular tunnels due to incident SH-waves," *Earthquake Engineering & Structural Dynamics*, vol. 12, no. 2, pp. 181–201, 1984.
- [6] Z. X. Liu and D. Wang, "FMM-MFS solution to two-dimensional scattering of elastic waves," *Journal of Vibration and Shock*, vol. 34, no. 5, pp. 102–109, 2015.
- [7] S. S. Wang, B. Gao, Y. S. Shen et al., "Study on the mechanism of resistance and damping technology of deep soft rock tunnels subjected to incident plane SH waves," *China Civil Engineering Journal*, vol. 47, no. S1, pp. 280–286, 2014.
- [8] J. Fu, J. W. Liang, and J. J. Du, "Analytical solution of dynamic soil-tunnel interaction for incident plane SH wave," *Chinese Journal of Geotechnical Engineering*, vol. 38, no. 4, pp. 588–598, 2016.
- [9] C. P. Yi, W. B. Lu, P. Zhang et al., "Effect of imperfect interface on the dynamic response of a circular lined tunnel impacted by plane P-waves," *Tunnelling and Underground Space Technology incorporating Trenchless Technology Research*, vol. 51, pp. 68–74, 2016.
- [10] Y. P. Liu, L. Qiao, and B. Xu, "Dynamic response of liquid-filled pipe embedded in saturated soil due to P waves," *Rock and Soil Mechanics*, vol. 34, no. 11, pp. 3151–3158, 2013.
- [11] Y. He, J. W. Liang, and Y. X. Lin, "Effect of cross-section-shape randomness of underground cavity on scattering of plane SH waves," *Earthquake Engineering and Engineering Vibration*, vol. 34, no. 1, pp. 1–7, 2014.
- [12] K. Zhang, L. H. Wei, and C. G. Zhao, "Dynamic responses of an underwater site subjected to plane P-or SV-wave incidence," *Chinese Journal of Geotechnical Engineering*, vol. 40, no. 6, pp. 1066–1074, 2018.
- [13] J. W. Liang, H. Luo, and V. W. Lee, "Diffraction of plane SH waves by a semi-circular cavity in half-space," *Earthquake Science*, vol. 23, no. 1, pp. 5–12, 2010.
- [14] H. Xu, T. Li, J. Xu, and Y. Wang, "Dynamic response of underground circular lining tunnels subjected to incident P waves," *Mathematical Problems in Engineering*, vol. 2014, Article ID 297424, 11 pages, 2014.
- [15] T. Xu, "Blasting vibration safety criterion of surrounding rock of a circular tunnel," *Geotechnical & Geological Engineering*, vol. 37, no. 4, pp. 3077–3084, 2019.
- [16] H. Qi, J. Yang, and Y. Shi, "Scattering of sh-wave by cylindrical inclusion near interface in Bi-material half-space," *Journal of Mechanics*, vol. 27, no. 1, pp. 37–45, 2011.
- [17] H. Qi, J. Yang, Y. Shi, and J. Y. Tian, "Dynamic analysis for circular inclusion near interfacial crack impacted by SH-wave in half space," *Journal of Mechanics*, vol. 28, no. 1, pp. 143–151, 2012.
- [18] Z. Fan, J. Zhang, and H. Xu, "Theoretical study of the dynamic response of a circular lined tunnel with an imperfect interface subjected to incident SV-waves," *Computers and Geotechnics*, vol. 110, pp. 308–318, 2019.
- [19] S. W. Lu, C. B. Zhou, Z. Zhang et al., "Theoretical study on dynamic responses of an unlined circular tunnel subjected to blasting P-waves," *Journal of Mechanics*, vol. 37, no. 4, pp. 242–252, 2021.
- [20] Y. Xia, N. Jiang, C. Zhou, X. Meng, X. Luo, and T. Wu, "Theoretical solution of the vibration response of the buried flexible HDPE pipe under impact load induced by rock blasting," *Soil Dynamics and Earthquake Engineering*, vol. 146, Article ID 106743, 2021.
- [21] B. Zhu, N. Jiang, C. Zhou, X. Luo, Y. Yao, and T. Wu, "Dynamic failure behavior of buried cast iron gas pipeline with local external corrosion subjected to blasting vibration," *Journal of Natural Gas Science and Engineering*, vol. 88, Article ID 103803, 2021.
- [22] N. Jiang, B. Zhu, X. He, C. Zhou, X. Luo, and T. Wu, "Safety assessment of buried pressurized gas pipelines subject to blasting vibrations induced by metro foundation pit excavation," *Tunnelling and Underground Space Technology*, vol. 102, Article ID 103448, 2020.
- [23] Q. C. Tang, N. Jiang, Y. K. Yao, C. B. Zhou, and T. Y. Wu, "Experimental investigation on response characteristics of buried pipelines under surface explosion load," *International Journal of Pressure Vessels and Piping*, vol. 183, Article ID 104101, 2020.
- [24] J. W. Liang, M. Ding, and J. J. Du, "Diffraction of cylindrical SH waves around circular lined cavity: analytical solution," *Earthquake Engineering and Engineering Vibration*, no. 1, pp. 1–7, 2013.
- [25] S. B. Chai, J. H. Zhao, and H. Wang, "UDEC simulation on cylindrical wave propagation through jointed rock masses," *Chinese Journal of Rock Mechanics and Engineering*, vol. 38, no. S1, pp. 2848–2856, 2019.
- [26] S. W. Lu, C. B. Zhou, Z. Zhang et al., "Particle velocity response of surrounding rock of a circular tunnel subjected to cylindrical P-waves," *Tunnelling and Underground Space Technology*, vol. 83, pp. 393–400, 2019.
- [27] Y. He and J. W. Liang, "Effect of outer-wall shape variation of underground lined cavity on inner-wall dynamic stress concentration factors peak values," *Chinese Journal of Rock Mechanics and Engineering*, vol. 34, no. S1, pp. 3160–3168, 2015.
- [28] M. Abramowitz and I. A. Stegun, *Handbook of Mathematical Functions: With Formulas, Graphs, and Mathematical Tables*, Dover Publications Inc., NY, USA, 1964.
- [29] X. L. Chen and M. J. Wen, "Dynamic characteristics of a cylindrical tunnel considering interaction between saturated soil and lining," *Chinese Journal of Applied Mechanics*, vol. 30, no. 4, pp. 557–562, 2013.
- [30] C. P. Yi, P. Zhang, D. Johansson et al., "Dynamic response of a circular lined tunnel with an imperfect interface subjected to cylindrical P-waves," *Computers and Geotechnics*, vol. 55, pp. 165–171, 2014.
- [31] S. W. Lu, C. B. Zhou, Z. Zhang et al., "Dynamic stress concentration of surrounding rock of a circular tunnel subjected to blasting cylindrical P-waves," *Geotechnical & Geological Engineering*, vol. 37, pp. 2363–2371, 2019.
- [32] H. Niederreiter and J. Spanier, *Monte Carlo and Quasi-Monte Carlo Methods*, Springer, Berlin, Germany, 2000.
- [33] M. Kleiber and T. D. Hien, *The Stochastic Finite Element Method*, John Wiley, Chichester, England, 1992.
- [34] J. Li and J. B. Chen, "The probability density evolution method for analysis of dynamic nonlinear response of stochastic structures," *Chinese Journal of Applied Mechanics*, vol. 35, no. 6, pp. 716–722, 2003.

## Research Article

# Numerical and Experimental Approach for Failure Analysis of Soil Subjected to Surface Explosion Loading

Iau-Teh Wang 

*Department of Civil Engineering, R.O.C Military Academy, Kaohsiung 830, Taiwan*

Correspondence should be addressed to Iau-Teh Wang; [itwangroc@gmail.com](mailto:itwangroc@gmail.com)

Received 27 April 2021; Accepted 8 July 2021; Published 16 July 2021

Academic Editor: Nan Jiang

Copyright © 2021 Iau-Teh Wang. This is an open access article distributed under the Creative Commons Attribution License, which permits unrestricted use, distribution, and reproduction in any medium, provided the original work is properly cited.

Controlling the hazards to facilities caused by detonation waves is a high priority in engineering design. To protect an underground facility, soil can reduce the destructive effects of detonation waves. Soil dynamic characteristics and the area of the destructive zone are affected by shock wave energy. The material at ground zero is impacted by high-intensity stress and forms a crater. To ensure the safety of the facility, the protective soil layers must be sufficiently thick. Therefore, the purpose of this study was to analyze the destructive effects that caused the deformation and destruction of an external protective soil layer. The results of the explosion experiments and the numerical simulation analysis were compared to explore the dynamic characteristics of the soil affected by the shock wave and the crater effects of on-ground explosions. The analysis model adopted an 8-node hexahedral element to create a three-dimensional solid structure model of the fluid-solid interaction. The material failure analysis demonstrated that the detonation wave destabilized the interior of the soil body, and the nearby high-intensity stress was the key factor for material failure. The results can serve as a reference for the design of soil-covering layers that provide explosion hazard control.

## 1. Introduction

Structural protection engineering is the essential design principle for vital industries and national defense infrastructure. Burster layers can be used to reduce the damage caused by blast effects to protect essential engineering facilities. Before designing military and industrial pipelines, it is necessary to calculate the area and extent of the explosion destruction effect to calculate the thickness of the protective layer. The detonation wave is transmitted outward through the medium; the generated stress wave induces particle vibration in the medium and affects the internal stability of the material [1–4]. The explosion shock wave compresses the ground and pushes soil, forming a crater. The extent of destruction and the affected range are determined by the energy of the shock wave and the material characteristics of the transmission medium [5]. Schenker et al. [6] investigated the explosion pressure generated by indoor explosions. Their results showed that the relative error between the shock pressure obtained from experiments and numerical analysis was 15%, and the relative error of the impulse was

approximately 9%. Wang and Lu [7] explored the shock wave energy generated by an explosion. Their results indicated that the energy released near the explosion source was high and the effect of the compression wave on the soil was relatively high. Crandle [8] analyzed the transmission of detonation waves and the factors that affected the vibration intensity. The results indicated that the transmission process of detonation wave induced particle vibration and caused different degrees of destruction to the medium. Koga and Matsuo [9] studied an explosion caused by burying explosives in soil. Part of the energy of the detonation wave was converted into seismic waves in the transmission process; those seismic waves induced particle vibration. Wang et al. [10] studied the seismic waves of a low-altitude explosion that were primarily generated by a shock wave in the air; the seismic waves were transmitted in the form of shock waves and then converted into elastic seismic waves, inducing particle vibration on the surface. Soil compression waves were generated by the ground compression induced by the air shock wave generated during an on-ground explosion. The compression wave eventually transformed into an elastic

seismic wave. Wang [11] applied a numerical analysis model of explosion pressure verification to an explosion experiment to prove that the LS-DYNA finite element program could effectively analyze the transmission behavior of a detonation wave during an on-ground explosion.

Soil strength impedes soil failure or sliding along any plane in the soil body. If soil has strength, then that soil maintains a certain shape. Soil strength provides stability in ultimate stress states, including stresses from soil weight or external loading. The principal reason for material failure is that the combination of normal and shear stresses reaches a critical state. If the shear stress exceeds the ultimate strength, the soil equilibrium state is upset and causes soil failure [12]. The process of soil loading and unloading during detonation wave transmission is an irreversible stress-strain relationship. When the detonation wave reaches the ground, the pressure increases rapidly and passes down to the interior of the soil. This state is referred to as overstress. The transmission of overstress in soil is a complicated topic. Under explosion dynamics, the yield criterion of a soil body can be defined as the amount of excessive deformation. On-ground explosions are converted into mechanical energy and thermal energy and cause medium deformation and crater [1].

According to the impact caused by a shock wave, compression, fracture, and vibration zones can be identified outside the explosion center. An on-ground explosion induces high temperature, high pressure, and detonation waves on the soil and causes soil compression, deformation, and the throwing phenomenon, resulting in crater [13]. Ambrosini and Luccioni [14] analyzed the energy released by the explosion of a unit volume of explosives through the crater effect. Bazant and Belytschko [15] analyzed the transmission of transient dynamic waves in strain-softening media and verified the phenomenon of localized strain softening in materials. The phenomenon of strain softening causes the stress to decrease with the increase in strain. Clough and Woodward [16] applied deformation analysis to geological engineering research; they analyzed the stress, strain, deformation, and displacement of an object under the effects of its weight or external forces. Based on the constitutive law, the equilibrium equation, and the deformation geometry law of continuum mechanics, the deformation analysis method was used to analyze the stresses and strains of different material compositions and the deformation geometries of different combinations of strain and displacement. A previously published study considered the characteristics of heterogeneous materials and explored material composition including linear elastic and nonlinear stress-strain relationships. The same study also investigated plastic behavior models to explore material behaviors induced by external forces such as stress, strain, deformation, and displacement.

On the ground, the explosion shock wave affects the stability of the material and causes different degrees of crater destruction on target objects [17]. This study analyzed the extent of destruction and impact of on-ground explosions on protective soil layers. In the context of the yield strength and

failure criteria of the material, this study analyzed the destruction radius, diameter, and destruction depth of craters to evaluate the extent of destruction caused by the crater effect of explosions.

The shock analysis was completed within a few milliseconds, and the discussion of destructive effects was focused on the dynamic soil response and the level of damage by shock waves. Given the spatial limitations of the experimental site and legal restrictions on the amount of explosive use, a large-scale explosion experiment is not feasible. According to the nature of the research questions, to enhance the accuracy of numerical analysis, this study employed a fluid-solid coupling finite element approach in conjunction with an explosion experiment that resulted in craters was used to verify the accuracy of the element erosion estimation. Exploring the transmission of shock waves in the soil, this study determined the optimal benefits of the parameters of soil element failure caused by contact explosions to establish the foundation of a dynamic numerical model.

## 2. Experimental Configuration

This study adopted on-site experiments and numerical simulation analyses to explore the deformation and destruction effects of explosions. The amount of trinitrotoluene (TNT) explosives in each of the three crater explosion experiments was the same. The effects of explosions on the crater effect of the soil were tested with explosives positioned upright on the ground.

Figure 1 shows the configuration of the experiment site for measuring the ground acceleration and apparent crater of explosion. This study used explosions to obtain experimental coefficients of ground acceleration to verify the accuracy of the numerical analysis model. In the on-ground explosion testing, 226.796 g (0.5 lb) TNT explosive was placed upright on the ground. Three-axis accelerometers were arranged at 350 and 500 cm from the explosion center to quantitatively analyze the ground accelerations on X, Y, and Z directions. The accelerometers measured the ground accelerations of explosion vibration. The signals went through an oscilloscope and to a signal conditioner for data transmission and storage. The experimental instrument included three-axis accelerometers, power supply systems, oscilloscopes, signal conditioners, and data acquisition systems.

## 3. Numerical Analysis Approach

The crater effect of explosions is highly nonlinear. Most related studies have focused on analyzing the characteristics of transmission medium failure caused by the shock wave. Explosion experiments are costly, the experimental sites are restricted, and the experiments can be dangerous. Using computer-aided engineering analysis can avoid the hazards of the explosion process. This study verified the results of explosion experiments by using numerical simulation. Numerical analysis based on the finite element method was conducted using hydrodynamic code in LS-DYNA. The Multi-Material Arbitrary Lagrangian-Eulerian (MMALE)

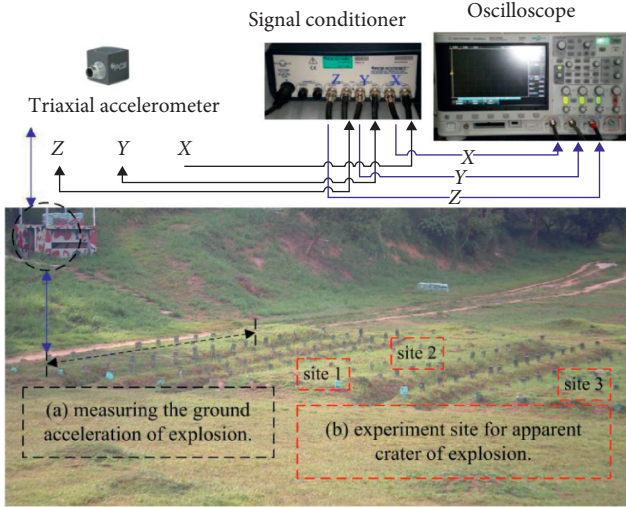


FIGURE 1: Configuration of the explosives in the field experiment. (a) For the ground acceleration measurement. (b) For testing the apparent crater effect of explosions.

algorithm was integrated with the 8-node solid element to establish a three-dimensional (3D) solid structure model of the fluid-solid interaction.

**3.1. Control of Time Stop and Element Type.** The numerical analysis tool for exploring explosion effects must satisfy the coupling between the hydrodynamic state and the solid. The LS-DYNA nonlinear finite element analysis program is based on the mechanics of the continuous medium and employs the explicit time integration method to calculate dynamic mechanical characteristics. Using explicit time integration analysis to investigate the instantaneous dynamics of explosions is conditionally a stable calculation method that requires time step ( $\Delta t$ ) control.

The conditional stability of explicit time integration is affected by the time step. However, when using explicit time integration, the time step must be less than the critical time interval, which is affected by its control factor (TSSFAC) (1). The program automatically divides time ( $T$ ) into  $T/\Delta t$  cycles, and the LS-DYNA program manual suggests that the time step control factor should be set in the range 0.1~0.9 and that for the explosion analysis should be lower than 0.67 [18, 19].

$$\Delta t = \text{TSSFAC} \cdot \frac{l_{\text{mesh}}}{C_l}, \quad (1)$$

where  $l_{\text{mesh}}$  is the minimum mesh size, and  $C_l$  is the wavelength.

The operations of finite element analysis require algorithms and element types that are appropriate for the material characteristics. The numerical calculation of motion in this study used the MMALE algorithm, which adopted 8-node hexahedral elements for analysis. The element is a 3D solid structure model and the shape function is expressed as in (2); the coordinates ( $\xi_j$ ,  $\eta_j$ , and  $\zeta_j$ ) are associated with different node positions and the values are  $\pm 1$ . Eight nodes were defined in the element; each node had degrees of

freedom for translation, velocity, and acceleration in the X, Y, and Z directions. This element was suitable for explicit dynamic analysis [18, 19].

$$\phi_j = \frac{1}{8} (1 + \xi \xi_j) (1 + \eta \eta_j) (1 + \zeta \zeta_j). \quad (2)$$

The MMALE algorithm exhibits the advantages of the Eulerian and Lagrangian algorithms. The Eulerian algorithm is used to arrange the element meshing to separate the mesh from the analyzed object, overcoming the negative volume caused by the severe mesh distortion. The Lagrangian algorithm is used for the material boundary analysis, which can effectively track the displacement and deformation of structural boundaries. For the dynamic analysis of the fluid-solid interaction, fluid is analyzed using the Eulerian algorithm to fix the nodes of the element mesh in the structure space. Only the material particles flow in the space. The solid is analyzed using the Lagrangian algorithm, and the material particles move with the deformation of the continuum, which is helpful for the deformation analysis of the movement of the fluid-solid interaction [20–22].

**3.2. Element Erosion Criterion.** Soil is a three-phase system composed of solid, liquid, and gas phases. For models of soil composition, yield criterion, stress, and strain analysis, the applicable conditions and material characteristics must be considered and the dynamic response of the pore material induced by the explosion force must be effectively analyzed. The Krieg yield criterion is based on isotropic plasticity theory, and the yield function is presented as in (3). The yield planes,  $J_2$  and  $\sigma_y$ , are presented as in (4) and (5), where  $a_0 = c^2$ ,  $a_1 = 2c \tan \phi$ , and  $a_2 = \tan^2 \phi$ . Before the material yields, a linear elastic relationship exists between the stress and strain. The relationship between the stress and strain of the plastic state conforms to the rule of plastic flow, and the material failure is determined according to the shear stress. Based on the strain after yielding, the stress zone of pore materials (e.g. soil, rock, concrete, foam, and honeycomb materials) can be divided into hydrostatic pressure and shear stress zones, which can be used to analyze the effect of pressure on the compaction and destruction of the material. It can be applied to numerical analysis programs such as LS-DYNA, ANSYS, and MSC/DYTRAN.

$$\phi_{\text{yield}} = J_2 - (a_0 + a_1 p + a_2 p^2), \quad (3)$$

$$J_2 = \frac{1}{3} \sigma_y^2, \quad (4)$$

$$\sigma_y = [3(a_0 + a_1 p + a_2 p^2)]^{1/2}, \quad (5)$$

where  $J_2$  is the second invariant of the deviatoric stress,  $p$  is the pressure,  $a_0, a_1, a_2$  are the shear force yield plane coefficients, and  $\sigma_y$  is the axial yield stress.

The shear stress of the octahedral stresses is a function of  $J_2$ . The normal stress of the octahedral stresses is equivalent to the average value of the principal stress as in (6). The relationship between the maximum shear stress is given in



equation (7), and the second invariant of the deviatoric stress is presented as in (8). For the pure shear stress,  $\sigma_1 = \tau > 0$ ,  $\sigma_2 = 0$ ,  $\sigma_3 = -\tau$ , and the shear stress ( $\tau$ ) is defined as  $\sqrt{J_2}$ ,  $\tau_{\text{oct}} = \sqrt{J_2} = \tau$ .

$$\sigma_{\text{oct}} = \frac{1}{3}(\sigma_1 + \sigma_2 + \sigma_3), \quad (6)$$

$$\tau_{\text{oct}} = \frac{\sqrt{2}}{3} \sqrt{\sigma_1^2 + \sigma_2^2 + \sigma_3^2 - \sigma_1\sigma_2 - \sigma_1\sigma_3 - \sigma_2\sigma_3}, \quad (7)$$

$$\tau_{\text{oct}} = \frac{\sqrt{2}}{3} J_2, \quad (8)$$

where  $\sigma_{\text{oct}}$  is the octahedral normal stress,  $\tau_{\text{oct}}$  is the octahedral shear stress, and  $\sigma_1, \sigma_2, \sigma_3$  are the maximum principal stress, middle principal stress, and minimum principal stress.

The soil constitutive law used in this study must consider the stress and strain behaviors of the pore material caused by pressure. Schwer [23] proposed that the shear failure criterion of the soil/rock model in LS-DYNA reveals a relationship between the mean stress and failure strength. The Krieg yield criterion can calculate the dynamic response in the soil and is also suitable for the analysis of 3D models. Therefore, this study used the Krieg yield criterion as its constitutive law for analyzing the characteristics of soil.

The overstress transmitted by a detonation wave in soil is an irreversible stress-strain relationship. The energy transmission and conversion process of the explosion causes destruction to soil and forms a crater. The finite element erosion algorithm is conducted based on the pressure, stress, and strain of the material. The high strain rate generated by the explosion shock wave affects the internal stress variation of the soil, resulting in strain in the soil. The soil yield criterion can be defined as the amount of excess deformation. LS-DYNA defines element failure and erosion criteria by MAT\_ADD\_EROSION. The failure element is thus removed from the material model. On the basis of the relationship between stress and strain of material, this study used the failure shear strain as the elemental erosion failure criterion and for soil destruction area analysis. If the material failure criterion  $\gamma_1 \geq \gamma_{\text{max}}$  is met, the element in the model is deleted, as presented in [19], where  $\gamma_1$  is the maximum shear strain,  $\gamma_1 = (\varepsilon_1 - \varepsilon_3)/2$ ,  $\varepsilon_1$  is the maximum principal strain,  $\varepsilon_3$  is the minimum principal strain, and  $\gamma_{\text{max}}$  is the shear strain at failure.

**3.3. Nonlinear Dynamic Models.** To verify the numerical model, the 1/4 symmetric numerical analysis model was established according to the experimental conditions of ground acceleration in the experiment. The fluid and the solid meshes were independent from each other. The solid mesh size was twice that of the fluid mesh. The fluid mesh adopted the common point mode and the solid mesh adopted the contact mode. The fluid-solid coupling was established using the mesh overlap method [24]. The size of the mesh was determined based on the minimum width of the TNT explosive. The application of finite element analysis

requires consideration of the complexity of an analysis model and the mesh size. To enhance the calculation accuracy, adopt a fluid dynamic analysis program LS-DYNA, finite element analysis software, to conduct the fluid-solid interaction. A TNT free-field explosion simulation is analyzed for mesh size convergence under an explosive load. The analysis results reveal the optimal mesh size is 0.5 times that of the side length of the TNT. The time step control parameter was set to 0.3 [25]. The fluid-solid interaction numerical analysis model of the MMALE algorithm was established through the use of the definition of LS-DYNA CONstrained\_Lagrange\_in\_Solid and the 3D solid elements. The explosives and air mesh were defined by the Eulerian algorithm, and the soil mesh was defined by the Lagrangian algorithm.

Figure 2 shows a 1/4 symmetry model for numerical simulation analysis of explosion-induced ground acceleration. The dimensions of the air model were  $550 \times 500 \times 200$  cm. The density of the TNT explosive was  $1.63 \text{ g/cm}^3$ , the weight was 226.796 g (0.5 lb), and the dimensions of the model were  $3.28 \times 3.28 \times 9.3$  cm. The explosive was placed in the center of the model and was on the ground. The dimensions of the soil model were  $550 \times 350 \times 200$  cm. The dimensions of the finite element mesh of air, explosives, and soil were  $1.64 \times 1.64 \times 3.28$  cm.

Figure 3 shows a 1/4 symmetry model for numerical analysis of crater failure effects. The dimensions of the air model were  $120 \times 150 \times 120$  cm. The dimensions of the soil model were  $120 \times 120 \times 120$  cm. The cuboidal TNT explosive sample was placed on the ground at the center of the model and the density was  $1.63 \text{ g/cm}^3$ . The amounts of TNT explosive were 113.389 g (0.25 lb), 226.796 g (0.5 lb), and 453.592 g (1.0 lb), which were selected to analyze the crater effect of placing dynamite samples upright on the ground. The dimensions of the 113.389 g, 226.796 g, and 453.592 g TNT models were  $1.64 \times 1.64 \times 9.3$  cm,  $3.28 \times 3.28 \times 9.3$  cm, and  $6.56 \times 6.56 \times 9.3$  cm. The dimensions of the finite element mesh of air, explosive, and soil were 0.82, 0.82, and 1.64 cm, respectively.

**3.4. Material Constitutive Laws.** The internal constitutive law of the material is presented by the relationship between the stress tensor and strain tensor. The equation of state (EOS) describes the relationship between pressure, temperature, density, internal energy, and change in volume after a material has been impacted by external force. The analysis of explosion phenomena must be paired with the corresponding equations of state to satisfy the dynamic response and volume change of the analyzed material after the material has been affected by the explosion force.

Soil from the explosion site was sampled for analyzing the physical and mechanical characteristics, and the Unified Soil Classification System (USCS) was applied for the categorization. According to the results of laboratory analysis, the soil moisture content of the explosion site was 12.8%, density was  $2.6 \text{ g/cm}^3$ , cohesive  $c = 8.43 \text{ kg/cm}^2$ , and friction angle  $\phi = 14^\circ$ . The classification symbol was SP-SM, which referred to poorly graded sand with silt.

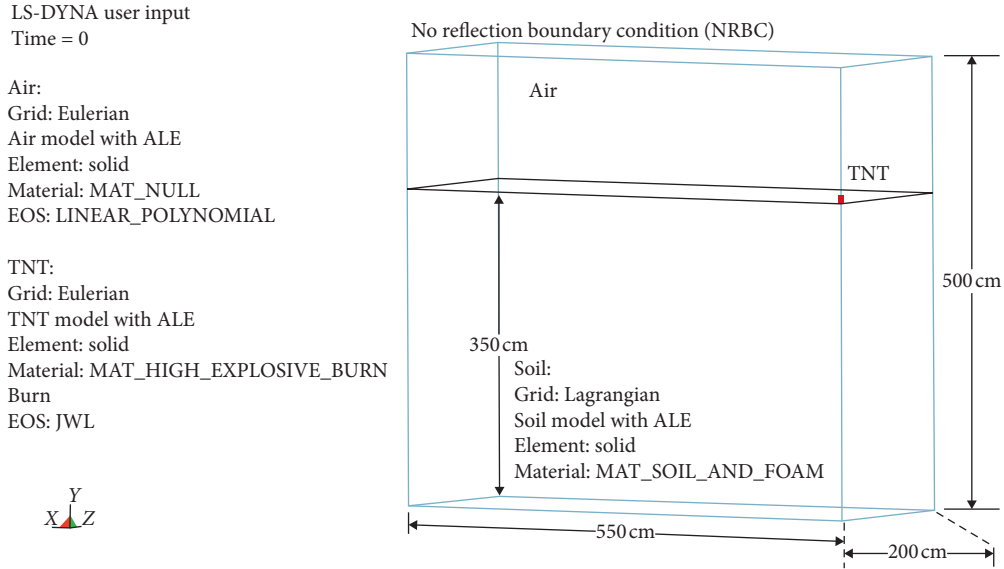


FIGURE 2: Numerical analysis of the 1/4 symmetry model of the ground acceleration induced by explosion.

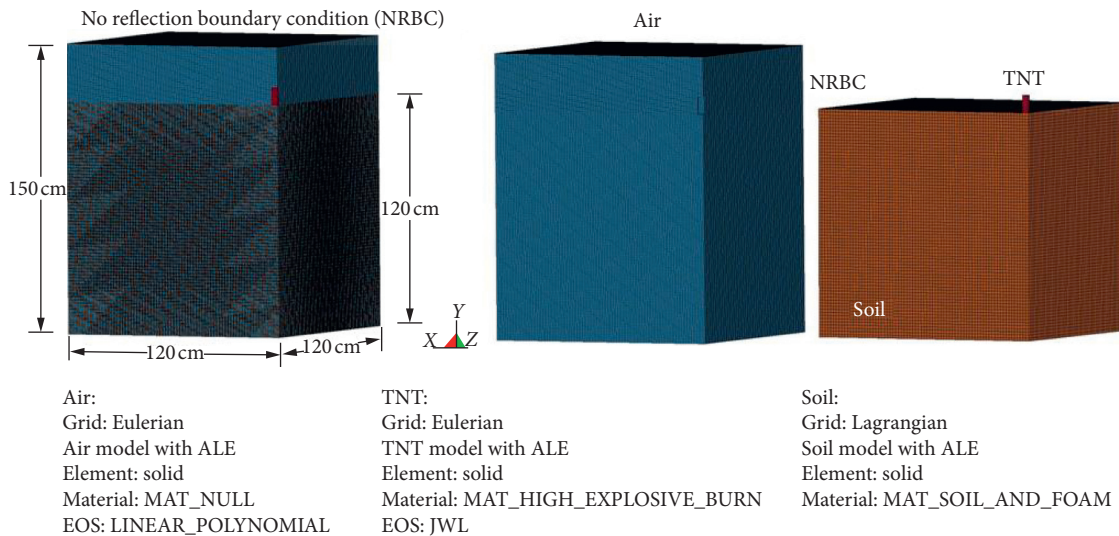


FIGURE 3: Numerical analysis of the 1/4 symmetry model of the explosion crater effect caused by material failure.

The soil constitutive law must be able to effectively simulate the crushing or compacting behavior of the pore material and the dynamic response after the material has been affected by the explosion. According to the material characteristics, this study selected the MAT\_SOIL\_AND\_FOAM material model to analyze the dynamic response characteristics of the soil. The soil parameters are, respectively, elastic modulus  $E = 43.75$  MPa, shear modulus  $G = 14.68$  MPa, bulk modulus  $K_v = 729$  MPa, and shear-yield surface parameters  $a_0 = 7.105 \times 10^{-7}$ ,  $a_1 = 4.198 \times 10^{-8}$ , and  $a_2 = 6.215 \times 10^{-10}$ .

The TNT explosive model used the MAT\_HIGH\_EXPLOSIVE\_BURN material model. Combined with the Jones–Wilkins–Lee (JWL) equation of state analysis in (9), the phenomena of the high speed, high temperature, high pressure, and rapid energy-releasing high explosives were

simulated. The parameters are, respectively,  $A = 3.712 \times 10^{11}$  Pa,  $B = 3.231 \times 10^9$  Pa,  $R_1 = 4.15$ ,  $R_2 = 0.95$ ,  $\omega = 0.30$ ,  $V = 1.0$ ,  $E_0 = 4.29 \times 10^6$  J/kg, initial density is  $1630$  kg/cm<sup>3</sup>, and its detonation velocity is  $6930$  m/s [19, 26, 27].

$$p = A \left( 1 - \frac{\omega}{R_1 V} \right) e^{-R_1 V} + B \left( 1 - \frac{\omega}{R_2 V} \right) e^{-R_2 V} + \frac{\omega E_0}{V}, \quad (9)$$

where  $p$  is the pressure,  $V$  is the relative volume,  $E_0$  is the initial internal energy per unit reference specific volume, and  $A$ ,  $B$ ,  $R_1$ ,  $R_2$ , and  $\omega$  are the constants representing characteristics of the explosive.

The air model used the MAT\_NULL material model and was analyzed using the EOS\_LINEAR\_POLYNOMIAL in (10). The coefficients in the LINEAR\_POLYNOMIAL are



$C_0 = C_1 = C_2 = C_3 = C_6 = 0$  and  $C_4 = C_5 = \gamma - 1$ . The EOS can be simplified as gamma law, which is expressed in (11). According to the gamma law calculation,  $\gamma = 1.4$ ,  $C_4 = C_5 = 0.4$ , and  $E_0 = 2.53 \times 10^6 \text{ J/kg}$  [19, 28].

$$p = C_0 + C_1 + C_2\mu^2 + C_3\mu^3 + (C_4 + C_5\mu + C_6\mu^2)E_0, \quad (10)$$

with  $\mu = (\rho/\rho_0) - 1$ ,

$$p = (\gamma - 1) \frac{\rho}{\rho_0} E_0, \quad (11)$$

where  $p$  is the pressure,  $C_0$ – $C_6$  are the constants,  $\gamma$  represents the rate of change to the specific air temperature,  $\mu$  is the dynamic viscosity coefficient,  $E_0$  denotes the initial internal energy per unit reference specific volume,  $\rho$  represents the current air density,  $\rho_0$  is the initial air density value, and  $\rho/\rho_0$  denotes the relative density.

## 4. Results and Discussion

**4.1. Validation of Numerical Modelling by the Experimental Results.** The numerical algorithms, material parameters, and numerical models were integrated with experimental data to verify the correctness of the analytical models. This study conducted on-ground explosion experiments to measure the physical quantity of ground acceleration and verify the numerical analysis results, providing numerical models for analyzing the crater. Figures 4 and 5 show the curves for the experimental and numerical ground acceleration for the points 350 and 500 cm from the explosion center. Relative error (%) of peak ground acceleration (PGA) was defined as follows: (numerical analysis value – experimental measurement value)/experimental measurement value  $\times$  100%.

The PGAs of the vertical ( $Y$ ) direction for points 350 and 500 cm from the explosion center in the experiment were 1.1932 and 0.9977  $\text{m/s}^2$ , respectively, and those in the numerical analysis ( $Y$ ) direction were 1.077 and 0.901  $\text{m/s}^2$ , respectively. The relative errors were  $-9.71\%$  and  $-9.73\%$ , respectively, lower than 10%. The PGAs in the horizontal ( $X$ ) direction for points 350 and 500 cm from the explosion center in the experiment were 0.9096 and 0.7371  $\text{m/s}^2$ , respectively, and the vertical PGAs of the numerical analysis were 0.824 and 0.671  $\text{m/s}^2$ , respectively. The relative errors were  $-9.39\%$  and  $-9.00\%$ , respectively, lower than 10%. The PGAs in the horizontal ( $Z$ ) direction of the experiment were 0.8493 and 0.6118  $\text{m/s}^2$ , respectively, and the vertical PGAs of numerical analysis were 0.766 and 0.557  $\text{m/s}^2$ , respectively. The relative errors were  $-9.84\%$  and  $-8.96\%$ , respectively. The relative error value is in the range of 10%.

In the experiment of placing the same amount of explosives and measuring waves at 350 and 500 cm from the explosion center, the results showed that high ground acceleration energy was induced near the explosion center. Specifically, the vertical ground acceleration was higher than the horizontal ground acceleration, and the transmission speed in vertical direction declined faster than that in the horizontal direction, which was consistent with the attenuation characteristics of detonation wave energy. The errors of experimental and numerical analysis results were in a

reasonable range, which were consistent with related studies [6]. The results also verified that using the MMAL algorithm to establish the numerical model of the fluid-solid interaction could effectively analyze the dynamic characteristics of the explosion phenomenon [17, 20, 21, 28].

The analytical results shown in Figures 4 and 5 reveal a short loading time and high vibration frequency in the dynamic process of the points. Although the ground acceleration yielded by the numerical analysis was not precisely consistent with signals measured in the experiment on-site, the overall dynamic temporal variation curves were consistent with the attenuation characteristics of the shock wave energy. The discrepancy between experimental and numerical analysis results was mainly attributable to the nonuniform, nonlinear dynamic variability in the materials, geometries, conditions, and contact characteristics involved in the shock effect analysis. In addition, the material parameters used in the finite element analysis of instantaneous dynamics must correspond to the dynamic responses obtained from the EOS—namely, changes in the internal energy, temperature, pressure, and volume of the material—and the numerical calculations were affected by the meshed model. According to the analysis results of shock wave transmission in the soil, the temporal variation curves of the ground acceleration produced by the experiment and the numerical analysis were consistent temporally and spatially, and the relative error was within 10%. Therefore, the numerical analysis was satisfactorily effective in estimating the dynamic response of the explosion effects and the material's changes in stress, strain, and volume after receiving external forces.

**4.2. Analysis of Control Parameters for Element Failure.** The LS-DYNA program mainly defines elemental erosion as destruction of material by pressure, stress, and strain parameters and provides settings for material model element failure and the erosion criteria as the basis for evaluating the failed element unit. The simulated material element fails according to the element erosion setting of the MAT\_ADD\_EROSION model. When element failure and erosion criteria are met, the element is removed from the calculation model. Considering the constitutive law and yield criteria of soil, the material destructive zone is affected by principal strain and shear strain. Therefore, this study examined the parameters of principal strain of failure and shear strain of failure as the main conditions for soil elemental erosion. The crater diameter and depth calculations for the numerical analysis of elemental erosion were based on the position of an eroded element on the axis of symmetry. The relative error percentage (%) of the crater diameter and depth was defined as follows: (numerical analysis value – experimental average value)/experimental average value  $\times$  100%.

Figure 6 shows the actual apparent craters of the three explosion experiments. The crater effect caused by the on-ground explosion by placing 226.796 g TNT explosive upright was analyzed. The experimental results indicated that the diameter and depth of the crater of experiment site 1 were 28.00 and 14.89 cm, respectively, experiment site 2 were

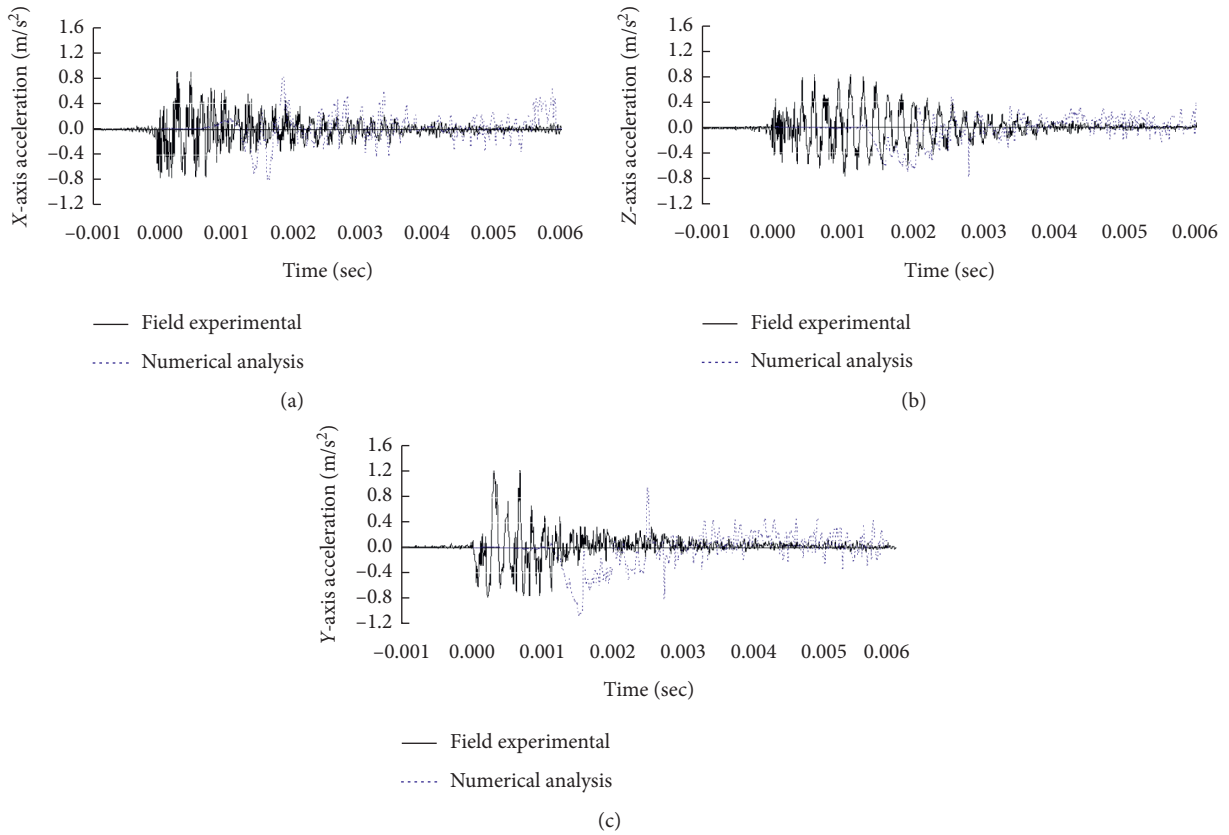


FIGURE 4: Temporal variation curves of the ground acceleration for a point 350 cm from the explosion center.

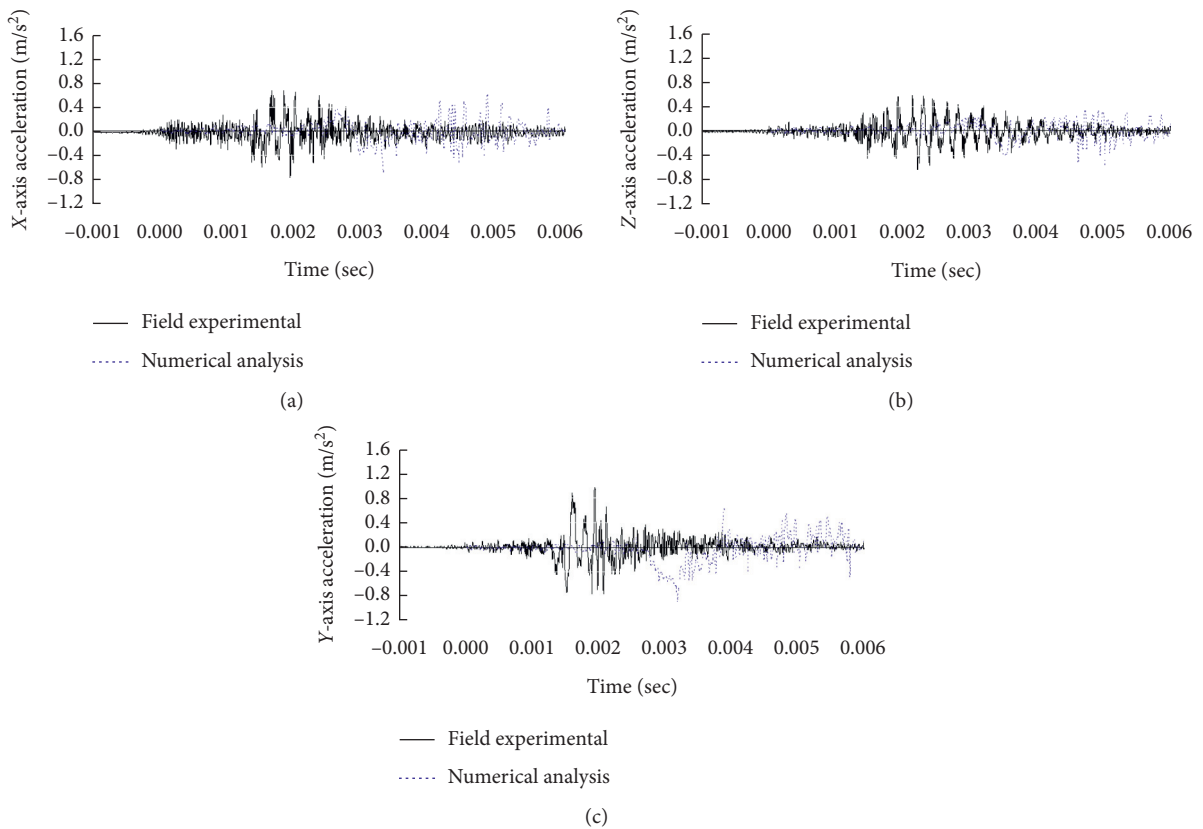


FIGURE 5: Temporal variation curves of the ground acceleration for a point 500 cm from the explosion center.

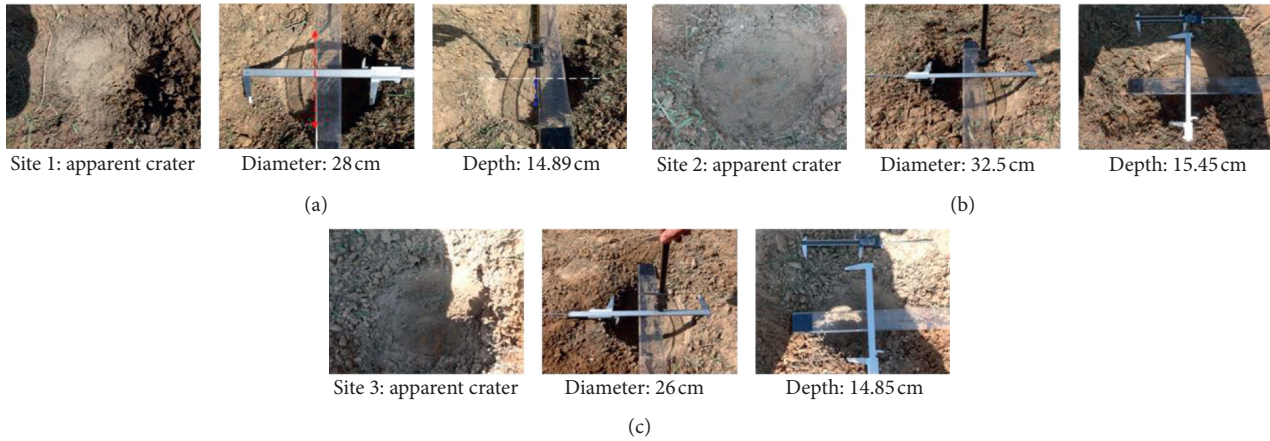


FIGURE 6: Apparent craters in explosion experiments.

32.50 and 15.45 cm, respectively, and experiment site 3 were 26.00 and 14.85 cm, respectively. The average crater diameter and depth were 28.83 and 15.06 cm, respectively.

Table 1 presents the relative error of principal strain control between the results of numerical simulation and explosion experiment caused by using 226.796 g TNT. The parameter range was between 0.006 and 0.016. The analysis results revealed that the relative error of the crater diameter and depth was  $-20.36\sim 70.66\%$  and  $-1.99\sim 63.35\%$ , respectively. The simulation result was most favorable when the failure principal strain value was 0.012. With the increase of the failure principal strain value, crater diameter and element erosion volume became increasingly irregular, mainly due to the material kinematic hardening associated with the high strain rate of explosion.

Table 2 presents a comparison of relative errors between shear strain control of the numerical simulation and experiment caused by using 226.796 g TNT. The analysis results revealed that with the increase in the failure shear strain value, the diameter and depth of the element erosion zone (the crater) decreased. Furthermore, the relative errors of the shear strain control analysis with respect to crater diameter and depth were within the range of  $-20.36\sim 36.53\%$  and  $-12.88\sim 52.46\%$ , respectively. Shear strain control resulted in a satisfactory numerical convergence trend. The convergence effect was most favorable when soil failure shear strain was 0.012, and the relative errors between crater diameter and depth were both within 10%.

The results revealed that shear strain and principal strain erosion conditions were the primary control parameters affecting soil element failure. When the failure shear strain value was 0.012, the numerical model exhibited a satisfactory convergence effect. Figure 7 shows the numerical analysis of the explosion caused by 226.796 g TNT. The element erosion condition was set that if the shear strain parameter of the soil reached the critical value of 0.012, the element would be deleted. The results indicated that the relative errors of the experiment were  $-8.98\%$  and  $-1.99\%$ , respectively. Using the numerical model established using the shear strain parameters to verify the element erosion algorithm in this study could effectively simulate the element failure of the explosion.

**4.3. Explosion Response and Failure Analysis of Soil.** This study explored the effects of ground explosions on soil deformation and crater effects from the perspective of explosion hazard control. This study conducted on-site explosion experiments and the finite element numerical analysis to analyze the yielding and failure of the protective soil material in the crater effect. This study focused on the destructive effects of high-energy external force, such as instant impact and vibration, caused by contact explosions on the ground medium and the craters created by explosions.

Figure 8 shows the temporal variation of soil plastic strain caused by an explosion of 226.796 g TNT. The figure shows that the detonation pressure was transmitted outward in soil in a spherical shape, and an explosion cavity was formed centering on the explosion source. The energy transmission process was divided into elastic seismic waves and plastic shock waves. The center of the explosion cavity was divided into broken, plastic-elastic, and elastic zones. In addition, the shock wave energy near the explosion center was high, and the compression wave intensity of the soil was relatively high. Figure 9 shows the crater effects caused by on-ground explosions of 113.389 g and 453.592 g TNT samples. For the 113.389 g dynamite sample, the crater diameter was 22.96 cm, and the depth was 13.12 cm. For the 453.592 g TNT sample, the crater diameter was 59.04 cm, and the depth was 22.96 cm.

The analysis results of Figures 7 and 9 show that the shape of the craters was irregular, which was caused by the material displacement, deformation, and failure induced by the shock wave. The primary cause was that the impedance of the shock wave in soil varied with pressure. When the pressure wave reached the free surface and was reflected in the form of a tensile wave, the effects of the expansion wave, pressure wave, and the pressure of the explosive gas caused the tensile wave and shear wave on the ground. The high pressure generated by the nearby explosion resulted in the concentrated and nonuniform distribution that caused local penetrative damage to the elements. Among them, some structural elements increased the dynamic strength because of the rapid rates of strain of the material under dynamic loading.

TABLE 1: Comparison of principal strain control.

Failure principal strain	Crater					
	Numerical simulation (cm)	Diameter Explosion experiment (cm)	Relative error (%)	Numerical simulation (cm)	Depth Explosion experiment (cm)	Relative error (%)
0.006	49.20		70.66	22.96		52.46
0.008	49.20		70.66	22.96		52.46
0.010	49.20	28.83	70.66	24.60	15.06	63.35
0.012	32.80		13.77	16.40		8.90
0.014	32.80		13.77	16.40		8.90
0.016	22.96		-20.36	14.76		-1.99

TABLE 2: Comparison of relative errors for shear strain control.

Failure shear strain	Crater					
	Numerical simulation (cm)	Diameter Explosion experiment (cm)	Relative error (%)	Numerical simulation (cm)	Depth Explosion experiment (cm)	Relative error (%)
0.006	39.36		36.53	22.96		52.46
0.008	32.80		13.77	21.32		41.57
0.010	32.80	28.83	13.77	16.40	15.06	8.89
0.012	26.24		-8.98	14.76		-1.99
0.014	26.24		-8.98	14.76		-1.99
0.016	22.96		-20.36	13.12		-12.88

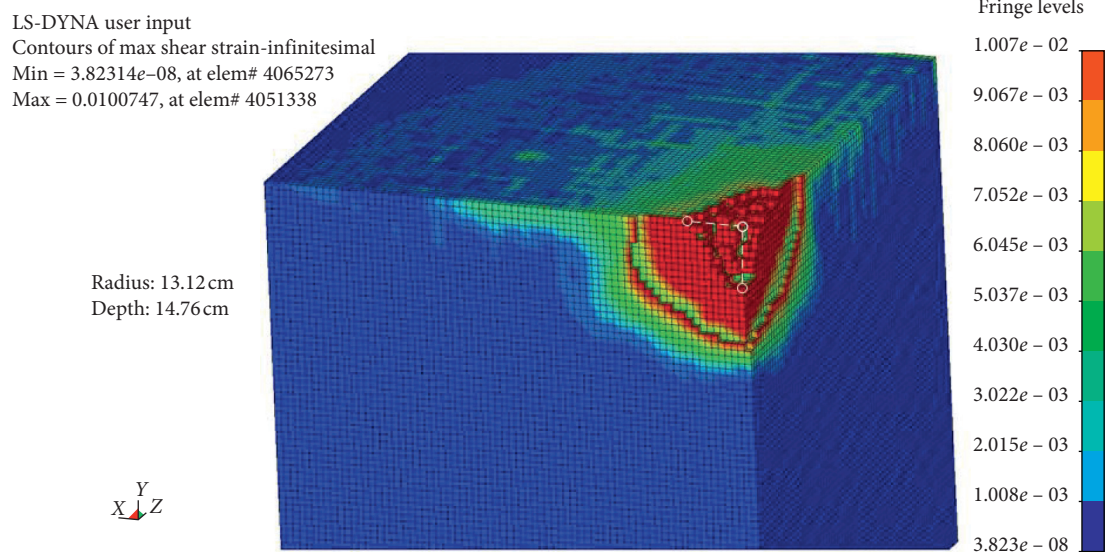


FIGURE 7: Numerical analysis of the element erosion of the crater caused by the on-ground explosion by using a 226.796 g (0.5lb) TNT.

The results indicated that if the amount of the explosive was increased multiple times, the radius and depth of the crater would increase, and the radius of the failure area would also increase multiple times. The radius of the crater was approximately 10~12 times the width of the rectangular dynamite samples, and the depth of the plastic zone was approximately 1.8~2.2 times the radius of the crater; the area was the affected range of the plastic shock wave. The energy outside the region was converted into elastic seismic waves, which induced surface particle vibration.

In addition, soil was a low-tensile material. Under the impact of the explosion shock wave, the acceleration of the particle motion increased the shear stress in the soil body. The soil structure was subjected to stress concentration because of the uneven distribution of stress, resulting in a decrease in shear strength. The compression wave caused particle displacement, and the failure started from local plastic deformation. The analysis results showed that under the effect of shock wave, the shear stress failure zone would appear in the periphery of the crater. The primary feature



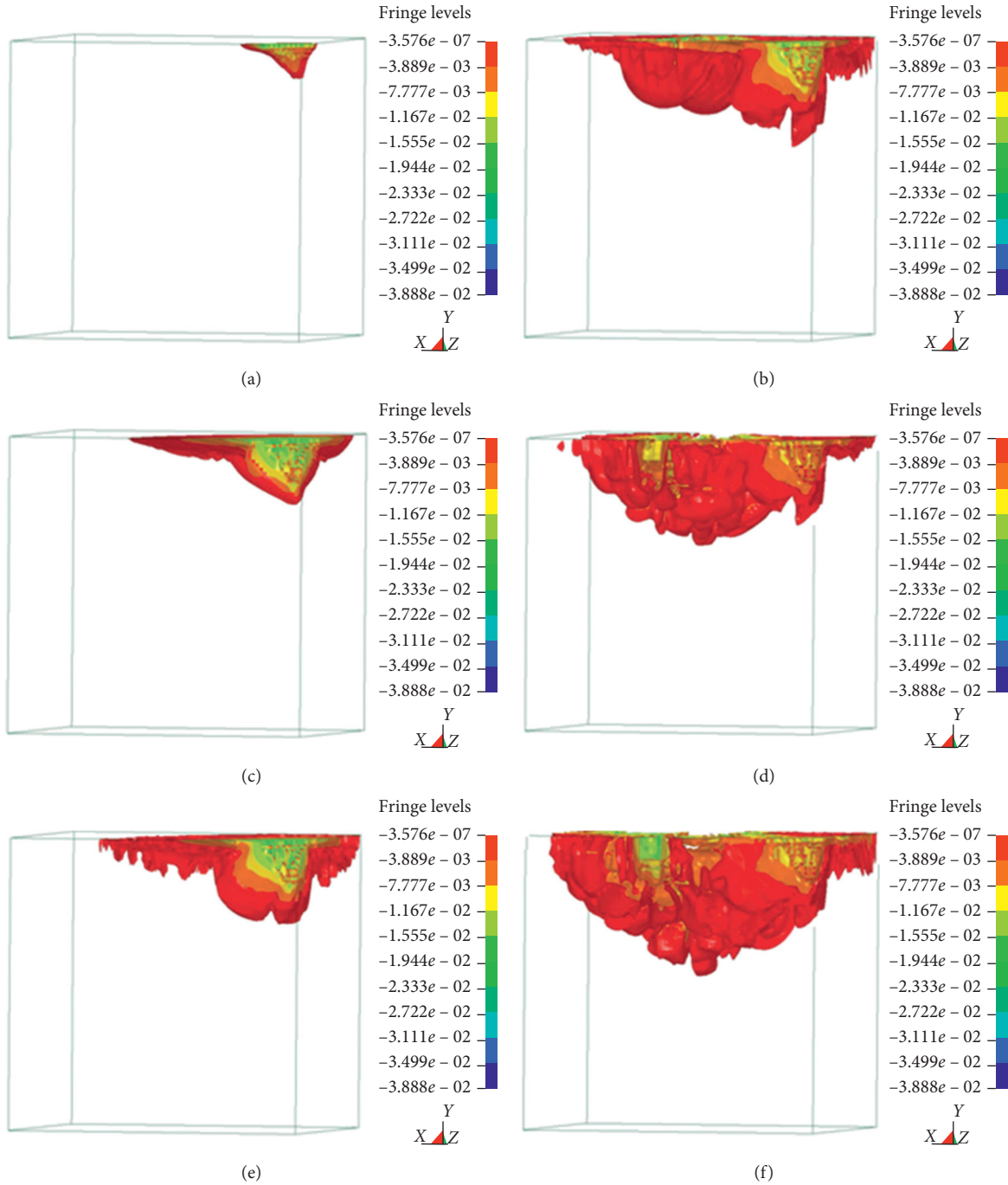


FIGURE 8: Temporal variation of soil plastic strain induced by an explosion. (a)  $t = 99.89 \mu\text{s}$ . (b)  $t = 1,499.90 \mu\text{s}$ . (c)  $t = 499.88 \mu\text{s}$ . (d)  $t = 2,000.00 \mu\text{s}$ . (e)  $t = 999.84 \mu\text{s}$ . (f)  $t = 2,499.90 \mu\text{s}$ .

was that the soil medium was plastically deformed. As the stress wave passed, if the second invariant ( $J_2$ ) of the stress deviation of the particle was higher than the yield strength of the material, plastic shearing would be generated in the region, resulting in permanent deformation and destruction.

Based on the aforementioned results, the sudden change in pressure caused by the explosion resulted in substantial deformation and destruction of the material. Shock wave was a strong compression wave. The shock wave generated by explosions was transmitted in the soil medium. The

energy was mostly depleted by the deformation, destruction, and pushing of the surrounding medium. Soil was a three-phase material composed of solid, liquid, and gas. The plasticity of soil was high, the strength was low, and compressive strength was higher than the tensile and shear strength. In addition, the explosion effect changed the stress state of the material, and if the stress exceeded the material yield strength, the internal structural stability would be affected, leading to soil deformation, local failure, and the affected range of stress.

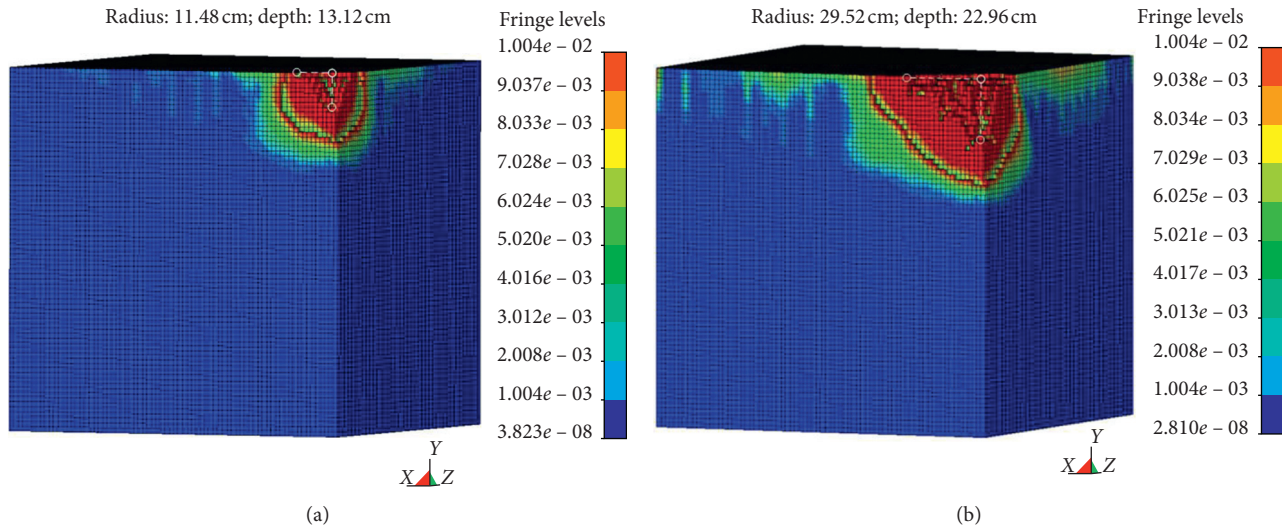


FIGURE 9: Numerical analysis of element erosion of the crater created by (a) 0.25 lb TNT (113.389 g) and (b) 1.0 lb TNT (453.592 g).

The explosion caused points on the ground surface to vibrate. The dynamic material response analysis was conducted according to the pressure applied to, stress of, and strain of the material. Shock waves were transmitted through mediums. A high strain rate changed the stress state of the material; when the stress exceeded the material's yield strength, plastic deformation occurred, and displacement increased, which in turn undermined the material stability. The transmission of shock waves was affected by the material properties of the transmission medium and terrain at the experimental site. From the perspective of controlling shock effects and minimizing damage, this study estimated the intensity and spatial range of damage caused by shock waves through the analysis of material deformation, temporal variation of plastic strain, displacement, and shear strain. The results could be conducive to determining the soil-covering layer material and the protective soil layer thickness to produce effective strength, thus preventing the transmission of shock wave energy. Additionally, the analysis of the ground surface vibration effect and a vibration isolation design could effectively block the transmission of shock waves, in turn reducing vibrations and minimizing the damage.

## 5. Conclusions

This study analyzed the failure characteristics of transmission medium caused by the shock wave. By using explosion-induced ground acceleration, this study verified the numerical model to establish an effective numerical analysis model for explosion. The hazards caused by craters created by explosions were explored. The material failure criterion and the finite element erosion algorithm were used to analyze the plastic deformation and destruction area of the soil. The results of this study can serve as a reference for the control of explosion vibration hazards, explosion at the exterior of protective soil, and disaster prevention. The results of the study are summarized as follows:

- (1) The numerical analysis of this study used an 8-node hexahedral element to establish a solid structural model of the fluid-solid interaction using the MMALE algorithm. A 3D numerical model was established by combining the shear strain parameters of the element erosion algorithm to analyze the crater effect of the explosion. The experimental results showed that the numerical model could effectively analyze the dynamic response of nonlinear materials, the hydrodynamic behavior generated by explosions, and the temporal pressure change of explosions.
- (2) A typical explosion is characterized by a sudden change in pressure at the explosion site. For the destruction phenomena in this study, the transmission of high-intensity shock waves affected material stability. The soil was affected by uneven stress, and the failure conditions of the material were affected by the stress and shear strain. The transmission of shock wave in soil was primarily caused by the increase of the inertial force that led to the decrease in shear strength; and the secondary cause was the continuous vibration effect that induced the increase in shear stress of the soil body and affected the stability of the material.
- (3) The stress state of the material that has been affected by explosive vibration changes tends to influence the structure and strength of the soil body. In this study, during the shock wave transmission process, the essential condition of failure was the plastic deformation and shear strain increment caused by the exceeded material yield strength. The ground surface was strongly compressed, destroying its original material structure. The soil was compressed by shock waves and crater was formed. The plasticity of the soil body varied with the pressure of shock wave and the extent of destruction varied. The area encompassing the crater radius and the depth of 1.8~2.2



times the crater radius was the plastic concentration zone of shear failure. In this region, the material was affected by compression, crushing, deformation, and destruction.

## Data Availability

The data used to support the findings of this study are available from the corresponding author upon request.

## Conflicts of Interest

The author declares that there are no conflicts of interest.

## Acknowledgments

The author thanks the engineering advisory group of the Ministry of National Defense in Southern Taiwan R.O.C. for assisting in this study.

## References

- [1] I. T. Wang, "Field experiments and numerical analysis of the ground vibration isolation of shock wave propagation under explosion shock loading," *Vibrations*, vol. 2, no. 4, pp. 300–310, 2019.
- [2] K. Balakrishnan, F. Genin, D. V. Nance, and S. Menon, "Numerical study of blast characteristics from detonation of homogeneous explosives," *Shock Waves*, vol. 20, no. 2, pp. 147–162, 2010.
- [3] E. Wang and A. Shukla, "Analytical and experimental evaluation of energies during shock wave loading," *International Journal of Impact Engineering*, vol. 37, no. 12, pp. 1188–1196, 2010.
- [4] S. E. Rigby, S. D. Fay, A. Tyas et al., "Influence of particle size distribution on the blast pressure profile from explosives buried in saturated soils," *Shock Waves*, vol. 28, no. 3, pp. 613–626, 2017.
- [5] L. B. Jayasinghe, D. P. Thambiratnam, N. Perera, and J. H. A. R. Jayasooriya, "Blast response and failure analysis of pile foundations subjected to surface explosion," *Engineering Failure Analysis*, vol. 39, pp. 41–54, 2014.
- [6] A. Schenker, I. Anteby, E. Gal et al., "Full-scale field tests of concrete slabs subjected to blast loads," *International Journal of Impact Engineering*, vol. 35, no. 3, pp. 184–198, 2008.
- [7] Z. Wang and Y. Lu, "Numerical analysis on dynamic deformation mechanism of soils under blast loading," *Soil Dynamics and Earthquake Engineering*, vol. 23, no. 8, pp. 705–714, 2003.
- [8] F. J. Crandle, "Ground vibration due to blasting and its effect upon structures," *Journal of Boston Society of Civil Engineers*, vol. 36, pp. 222–245, 1949.
- [9] Y. Koga and O. Matsuo, "Shaking table tests of embankments resting on liquefiable sandy ground," *Soils and Foundations*, vol. 30, no. 4, pp. 162–174, 1990.
- [10] Z. Wang, H. Hao, and Y. Lu, "A three-phase soil model for simulating stress wave propagation due to blast loading," *International Journal for Numerical and Analytical Methods in Geomechanics*, vol. 28, no. 1, pp. 33–56, 2004.
- [11] J. Wang, "Simulation of landmine explosion using LS-DYNA 3D software: benchmark work of simulation in soil and air," pp. 1–30, DSTO Aeronautical and Maritime Research Laboratory, Fishermans Bend, Australia, 2001, DSTO-TR-1168.
- [12] J. M. Duncan and C.-Y. Chang, "Nonlinear analysis of stress and strain in soils," *Journal of the Soil Mechanics and Foundations Division*, vol. 96, no. 5, pp. 1629–1653, 1970.
- [13] G. W. Ma, H. Hao, and Y. X. Zhou, "Modeling of wave propagation induced by underground explosion," *Computers and Geotechnics*, vol. 22, no. 3-4, pp. 283–303, 1998.
- [14] R. D. Ambrosini and B. M. Luccioni, "Craters produced by explosions on the soil surface," *Journal of Applied Mechanics*, vol. 73, no. 6, pp. 890–900, 2005.
- [15] Z. P. Bazant and T. B. Belytschko, "Wave propagation in a strain softening bar-exact solution," ASCE, *Journal of Engineering Mechanics*, vol. 3, pp. 381–389, 1985.
- [16] R. W. Clough and R. J. Woodward, "Analysis of embankment stresses and deformations," *Journal of the Soil Mechanics and Foundations Division*, vol. 93, no. 4, pp. 529–549, 1967.
- [17] C. Wu and H. Hao, "Modeling of simultaneous ground shock and airblast pressure on nearby structures from surface explosions," *International Journal of Impact Engineering*, vol. 31, no. 6, pp. 699–717, 2005.
- [18] LS-DYNA, *Theoretical Manual*, pp. 1–117, Livermore Software Technology Corporation, Finite Element Model Builder, Livermore, CA, USA, 2006.
- [19] LS-DYNA, *Keyword User's Manual*, vol. 1, pp. 37–2435, Livermore Software Technology Corporation, Livermore, CA, USA, 2010.
- [20] M. S. Chafi, G. Karami, and M. Ziejewski, "Numerical analysis of blast-induced wave propagation using FSI and ALE multi-material formulations," *International Journal of Impact Engineering*, vol. 36, no. 10, pp. 1269–1275, 2009.
- [21] Y.-T. Wang and J.-Z. Zhang, "An improved ALE and CBS-based finite element algorithm for analyzing flows around forced oscillating bodies," *Finite Elements in Analysis and Design*, vol. 47, no. 9, pp. 1058–1065, 2011.
- [22] M. A. Puso, J. Sanders, R. Settigast, and B. Liu, "An embedded mesh method in a multiple material ALE," *Computer Methods in Applied Mechanics and Engineering*, vol. 245–246, pp. 273–289, 2012.
- [23] L. Schwer, *Geomaterial Modeling with LS-DYNAU*, pp. 1–2, Livermore Software Technology Corporation, Livermore, CA, USA, 2001.
- [24] N. Gebbeken and M. Ruppert, "On the safety and reliability of high dynamic hydrocode simulations," *International Journal for Numerical Methods in Engineering*, vol. 46, no. 6, pp. 839–851, 1999.
- [25] I. T. Wang, "Numerical and experimental verification of finite element mesh convergence under explosion loading," *Journal of Vibroengineering*, vol. 16, no. 4, pp. 1786–1798, 2014.
- [26] B. M. Dobratz and P. C. Crawford, *LLNL Explosives Handbook: Properties of Chemical Explosives and Explosive Simulants*, Report UCRL-52997, pp. 208–230, Lawrence Livermore National Laboratory, Livermore, CA, USA, 1985.
- [27] A. Erdik, S. A. Kilic, N. Kilic, and S. Bedir, "Numerical simulation of armored vehicles subjected to undercarriage landmine blasts," *Shock Waves*, vol. 26, no. 4, pp. 449–464, 2016.
- [28] Y. S. Tai, T. L. Chu, H. T. Hu, and J. Y. Wu, "Dynamic response of a reinforced concrete slab subjected to air blast load," *Theoretical and Applied Fracture Mechanics*, vol. 56, no. 3, pp. 140–147, 2011.

## Research Article

# Study on Dynamic Evolution Law of Blasting Cracks in Elliptical Bipolar Linear Shaped Charge Blasting

Bo Wu <sup>1,2,3</sup>, Shixiang Xu <sup>1,4</sup>, Guowang Meng <sup>1,4</sup>, Junhua Cai <sup>5</sup>, Han Wei <sup>1,4</sup>,  
Hualong Li <sup>1,4</sup> and Jinglong Zhang <sup>1,4</sup>

<sup>1</sup>College of Civil Engineering and Architecture, Guangxi University, Nanning, Guangxi 530004, China

<sup>2</sup>School of Civil and Architectural Engineering, East China University of Technology, Nanchang, Jiangxi 330013, China

<sup>3</sup>School of Architectural Engineering, Guangzhou City Construction College, Guangzhou, Guangdong 510925, China

<sup>4</sup>The Key Laboratory of Disaster Prevention and Structural Safety of Ministry of Education, Guangxi University, Nanning, Guangxi 530004, China

<sup>5</sup>Sanming Puyan Expressway Co. Ltd., Sanming, Fujian 365000, China

Correspondence should be addressed to Shixiang Xu; 603559081@qq.com

Received 13 April 2021; Revised 21 May 2021; Accepted 11 June 2021; Published 28 June 2021

Academic Editor: Bangbiao Wu

Copyright © 2021 Bo Wu et al. This is an open access article distributed under the Creative Commons Attribution License, which permits unrestricted use, distribution, and reproduction in any medium, provided the original work is properly cited.

Based on LS-DYNA numerical simulation analysis and comparison with laboratory tests, the blasting crack development dynamic evolution mechanism of elliptical bipolar linear shaped charge is analyzed. The development law of rock crack and optimal radial decoupling coefficient under different blast hole diameters were studied. The results revealed that the blasting with elliptical bipolar linear shaped charge had a remarkable effect on the directional crack formation, and the maximum effective stress of rock close to the position of shaped charge in the direction of concentrating energy is about 2.3 times of that in the direction of nonconcentrated energy. Moreover, the directional crack could be formed by blasting with elliptical bipolar linear shaped charge with different hole diameters, whilst the length of the main crack was related to the radial decoupling coefficient. Particularly, the main crack reached the longest when the radial decoupling coefficient was 3.36.

## 1. Introduction

China has become the country with the largest scale, the largest number, and the highest difficulty of tunnel construction in the world [1]. According to statistics, by the end of 2020, China's railway operating mileage had reached 145000 km, of which 16798 railway tunnels had been put into operation, with a total length of about 19630 km [2]. In addition to the tunnel boring machine, the drilling and blasting method is still widely utilized in rock tunnel construction. Improper control of traditional drilling and blasting methods would easily lead to engineering and social problems such as vibration hazard, environmental pollution, instability of surrounding rock, and serious overbreak and underbreak, which seriously restrict the construction process of tunnel engineering [3].

In order to solve the above problems, directional fracture controlled blasting technology is often used at present. Many scholars have conducted in-depth research around the rock failure mechanism and directional fracture effect of directional fracture controlled blasting. For instance, Cho et al. [4] combined model test and numerical simulation method to study the influence of empty hole on crack propagation under different blasting and comprehensively analyzed the relationship between fracture energy and crack propagation. Yang et al. [5–8] adopted a testing system of digital laser dynamic caustics to study the influence of different cutting angle, depth, initial stress field, and other factors on the crack propagation of slotted cartridge blasting and then analyzed the mechanism of crack extension and penetration. Yue et al. [9–12] used a new testing system of digital laser dynamic caustics to carry out the experimental research on the

development of blasting crack under slotted cartridge blasting, whilst obtained the crack extension velocity, acceleration, dynamic stress intensity factor at the front end of the crack, and the law of dynamic energy release rate. Wang [13] explored the formation of detonation and initial crack of slotted cartridge blasting and the relationship between decoupling coefficient and blasting damage based on numerical simulation. Luo et al. [14, 15] made a preliminary study on the formation of guided crack, crack initiation, propagation, and penetration of shaped charge. In 2006, the Sinohydro Engineering Bureau 8 Co., Ltd. developed an elliptical bipolar linear shaped charge (EBLSC), which performed well in practical engineering applications [16]. Li et al. [17, 18] further conducted theoretical analysis, numerical simulation, and experimental research on the blasting of EBLSC, and the research showed that this charge structure has a good application effect and prospect in presplit blasting. Subsequently, the elliptical bipolar linear shaped charge blasting technology has been widely promoted and applied in engineering. Wu et al. [19–21] carried out a preliminary study on the blasting mechanism, influencing factors, and crack development of elliptical bipolar linear shaped charge blasting.

However, for the directional controlled blasting technology, most of the research studies are focused on the slotted cartridge blasting, while the research on the evolution law of shaped charge blasting crack is less. The rock breaking mechanism of elliptical bipolar shaped charge blasting excavation is not clear. In this paper, the rock failure mechanism, the temporal and spatial law of crack development, and decoupling coefficient of elliptical bipolar linear shaped charge blasting were studied. Moreover, the optimal decoupling coefficient was obtained via analyzing the crack development law of different blast hole diameters, which provide an important reference for practical engineering application.

## 2. Analysis of the Rock Failure Mechanism of Shaped Charge Blasting

The detonation products of conventional blasting scattered irregularly around the blast hole, and the cracks also expanded irregularly [22]. The shaped charge blasting uses a layer liner to change the structure of the explosive to make the detonation products accumulate in a specific direction and improve the destructive effect in a specific direction [23].

An energy cavity is set at the symmetrical position on both sides of the shaped charge. The detonation products generated by blasting will accumulate along the axis of the energy cavity to form a high-density, high-speed, and high-pressure air flow, which is called shaped charge jet [24]. The shaped charge jet penetrates the rock and produces the initial guide crack, which provides a directional effect for the subsequent explosion stress wave and blasting gas to further expand the crack. According to the rock fracture mechanics, a dynamic fracture mechanics model of shaped charge blasting is established, as shown in Figure 1.

During crack propagation, the stress intensity factor at the crack tip is as follows [25]:

$$K_1 = PF\sqrt{\pi(r_b + a)} + \sigma_\theta\sqrt{\pi a}. \quad (1)$$

Thereinto,  $P$  is the explosive gas pressure in the fracture;  $F$  is the correction factor of stress intensity factor;  $r_b$  is the blast hole radius;  $a$  is the fracture length; and  $\sigma_\theta$  is the tangential stress.

According to the theory of fracture mechanics,  $K_1 > K_{IC}$ , the crack initiates and propagates, where  $K_{IC}$  represents the fracture toughness of the rock. Therefore, to ensure that the crack continues to grow, the pressure of detonation gas should meet the following conditions:

$$P > \frac{K_{IC} - \sigma_\theta\sqrt{\pi a}}{F\sqrt{\pi(r_b + a)}}. \quad (2)$$

The guiding crack penetrated by the shaped energy jet is much larger than the other small cracks in the crushing zone. After blasting, a large amount of high-pressure explosive gas will be introduced, and the pressure of the explosive gas in the concentrating energy direction will increase; that is, the  $P$  will increase; according to the law of conservation of energy, the effect of explosive gas in the nonconcentrated energy direction will be weakened, and the  $P$  will decrease. Therefore, while the structure of the shaped charge leads to an increase in the evolution ability of cracks in the direction of concentrating energy, it also reduces the ability of evolution of cracks in the direction of nonconcentrated energy.

## 3. Validation of Numerical Solution

**3.1. Explosion Test of PMMA.** Polymethyl methacrylate (PMMA) is usually used as an ideal test material to study the crack propagation process of PMMA under laboratory conditions. Its main advantage is transparency, which makes the crack morphology easy to be observed directly by naked eyes. The fracture mechanical behavior of this material is similar to that of brittle rock [26, 27]. The test results of Rossmannith et al. [28] also suggested that the blasting cracks could be divided into the following three areas: crushing zone, radial microcrack zone, and radial crack zone. The crack morphology of PMMA is very similar to that of rock under dynamic loading. Hence, it can be considered that the blasting test results of PMMA are consistent with those of rock materials, which is suitable for exploring the mechanism of crack initiation and propagation near the blast hole and in the far-field area.

Chen [29] carried out the blasting test of a shaped charge with PMMA, wherein the outer diameter of the shaped charge was 7 mm, the inner diameter was 5 mm, the energy gathering tube was made of PVC material, and the thickness of the shell of the energy gathering tube was 1 mm. The structure design of the shaped charge is shown in Figure 2. The geometric size of the specimen was 300 mm × 200 mm × 100 mm. The blast hole was located in the center of the specimen, and the diameter of the blast hole was 12 mm. The specimen of PMMA is shown in Figure 3. The crack development was recorded by the digital laser dynamic caustics test system.

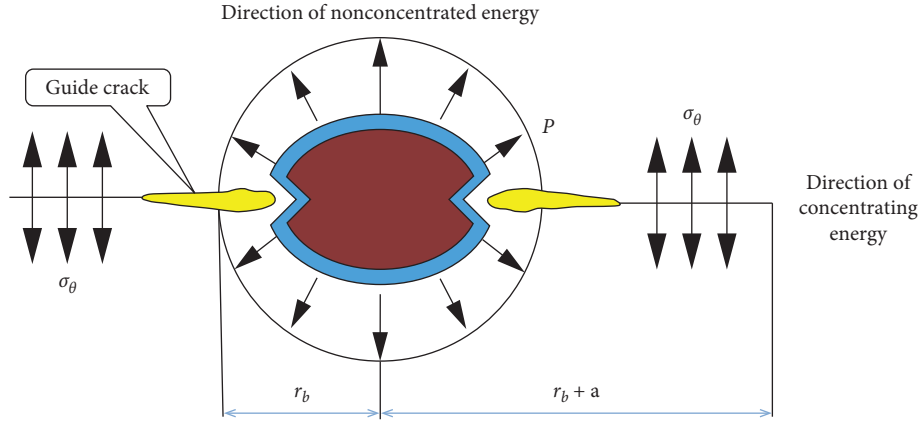


FIGURE 1: Mechanical model of cracking due to shaped charge blasting.

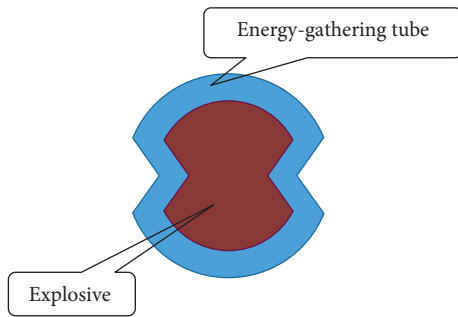


FIGURE 2: Structure design of shaped charge [29].



FIGURE 3: The specimen of PMMA [29].

The test results are shown in Figure 4. Next, numerical simulation analysis would be carried out for the blasting test to verify the effectiveness of the finite element solution.

**3.2. Numerical Model.** Using LS-DYNA nonlinear dynamic analysis software to carry out numerical simulation analysis, the geometric size of the model is the same as the above model test. A nonreflective boundary condition is added to simulate an infinite plane to eliminate the interference of reflected waves at the boundary. In the numerical model, the material model of the explosive is characterized by MAT\_HIGH\_EXPLOSIVE\_BURN, and the relationship

between the pressure and volume of the explosive after detonation is described by the JWL state equation.

$$p = A \left( 1 - \frac{\omega}{R_1 V} \right)^{-R_1 V} + B \left( 1 - \frac{\omega}{R_2 V} \right) + \frac{\omega E}{V}, \quad (3)$$

where  $p$  is the pressure,  $V$  is the volume,  $A$ ,  $B$ ,  $\omega$ ,  $R_1$ , and  $R_2$  are the basic parameters of the equation of state, and  $E$  is the initial internal energy per unit volume. Explosive and state equation parameters are shown in Table 1.

The PVC energy gathering tube material adopts the model MAT\_PLASTIC\_KINEMATIC, and the mechanical parameter of the PVC is shown in Table 2.

The MAT\_NULL model and the EOS\_LINEAR\_POLYNOMIAL state equation are used to simulate air, the HJC constitutive model is used for rock, and the failure mode is added to analyze crack development. The main rock parameter is shown in Table 3.

**3.3. Analysis of Numerical Simulation Results.** Figure 5 shows the development of blasting cracks at different times. The blasting cavity is formed after  $20 \mu\text{s}$  of detonation, and the length of the cracks in the concentrating energy direction is significantly greater than the length of the cracks in other directions. At  $80 \mu\text{s}$ , microcracks appear in other directions, and the crack in the concentrating energy direction keeps growing. At  $120 \mu\text{s}$ , the crack in the direction of energy accumulation and other directions keeps growing. At  $600 \mu\text{s}$ , the crack tends to stop and the crack in the concentrating energy direction is always larger than that of the other directions.

Compared with Figure 4, the results in Figure 5 indicate that the numerical simulation completely reproduces the crushing zone around the hole, the crack initiation, and development process in the concentrating energy direction and other directions of the PMMA under the shaped charge blasting. The final distribution of blasting cracks is in good agreement with the experimental results, thus proving the correctness of the established model and its numerical solution. Next, the numerical model will be used to study the evolution law of blasting cracks in elliptical bipolar linear shaped charge blasting.



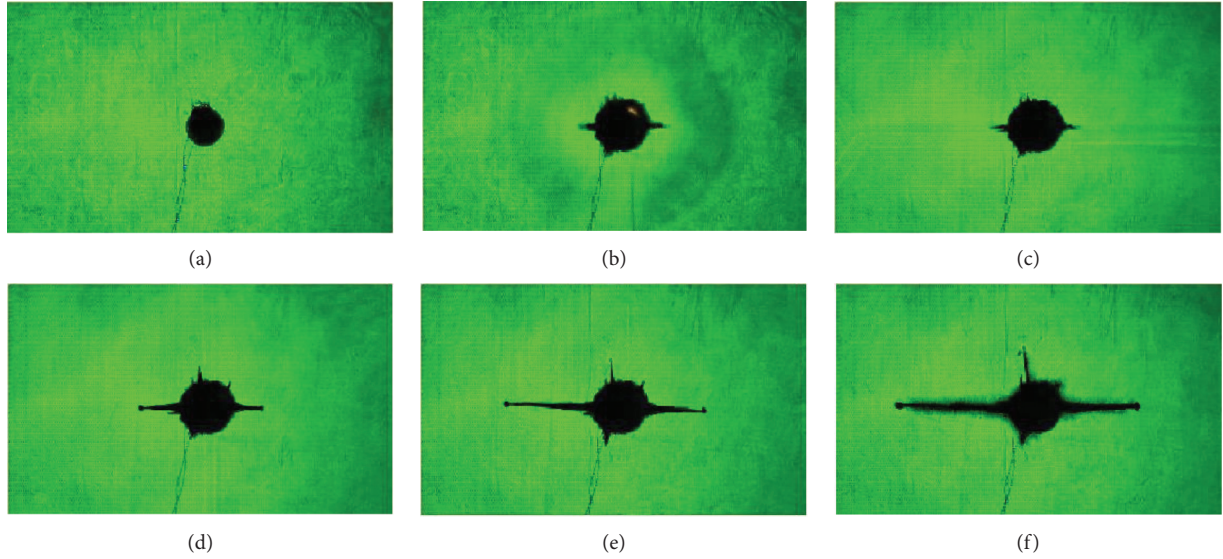


FIGURE 4: Test results of blasting crack of shaped charge [29]. (a)  $t = 0 \mu s$ , (b)  $t = 20 \mu s$ , (c)  $t = 80 \mu s$ , (d)  $t = 120 \mu s$ , (e)  $t = 400 \mu s$ , (f)  $t = 600 \mu s$ .

TABLE 1: Explosive and parameters of equation of state.

$\rho$ ( $g \cdot cm^{-3}$ )	$\nu_D$ ( $cm \cdot \mu s^{-1}$ )	$A$ (GPa)	$B$ (GPa)	$R_1$	$R_2$	$\omega$	$E$ (GPa)
1.3	0.4	214.4	0.182	4.2	0.9	0.15	4.192

TABLE 2: Mechanical parameter of PVC.

Material	Density ( $g \cdot cm^{-3}$ )	Elastic modulus (GPa)	Poisson's ratio ( $\mu$ )
PVC	1.3	3.0	0.38

TABLE 3: Material parameters of the HJC model.

Parameters	Property	Value
$\rho$ ( $g \cdot cm^{-3}$ )	Density	2.18
$G$ (GPa)	Shear modulus	14.86
$A$	Normalized cohesive strength	0.79
$B$	Normalized pressure hardening	1.60
$C$	Strain rate coefficient	0.007
$S_{fmax}$	Normalized maximum strength	7
$\epsilon_{fmin}$	Amount of plastic strain before fracture	0.01
$N$	Pressure hardening exponent	0.61
$T$ (MPa)	Maximum tensile hydrostatic pressure	4
$D_1$	Damage constant 1	0.04
$D_2$	Damage constant 2	1
$K_1$ (GPa)	Pressure constant 1	85
$K_2$ (GPa)	Pressure constant 2	-171
$K_3$ (GPa)	Pressure constant 3	200

## 4. Analysis on Crack Evolution of Elliptical Bipolar Linear Shaped Charge Blasting

**4.1. Geometric Model of Numerical Calculation.** In order to analyze the dynamic evolution law of blasting cracks with different blast hole diameters, the quasi two-dimensional calculation models with various blast hole diameters of

42 mm, 50 mm, 60 mm, 70 mm, 80 mm, 90 mm, and 100 mm were established, respectively. The shaped charge is an elliptical bipolar linear structure, the energy gathering tube is made of PVC material, the thickness of the shell of the energy gathering tube is 2 mm, the thickness of the layer liner is 1.4 mm, and the angle of the shaped charge groove is  $70^\circ$ . The calculation model is shown in Figure 6, and no reflective boundary condition is set around the model.

Select a measuring point every 10 mm along the blast hole radial in the concentrating energy direction and the non-concentrated energy direction. The concentrating energy direction is numbered as #G1 ~ #G5 from near to far, and the nonconcentrated energy direction is numbered as #N1 ~ #N5 from near to far. The layout of each measuring point is shown in Figure 7.

### 4.2. Analysis of Rock Crack Development with Blast Hole Diameter 42 mm

**4.2.1. Analysis of Initial Crack Formation.** After the shaped charge is detonated in the blast hole, the detonation wave acts on the shaped charge cover with huge pressure at  $5 \mu s$  to form a high-temperature, high-pressure, high-energy shaped charge jet. The jet first acts on the blast hole wall and forms a guide crack on the rock in this direction, as shown in Figure 8. In other directions of the blast hole, the shell of the shaped charge has instantaneous buffering and inhibiting effect on the detonation products and the air medium between the shell of the shaped charge and the blast hole wall has a buffering effect, which greatly reduces the direct effect and damage degree of the shock wave on the blast hole wall, thus inhibiting the development of cracks.

**4.2.2. Stress Time History Analysis.** The stress time history curves of each measuring point are shown in Figures 9 and 10.

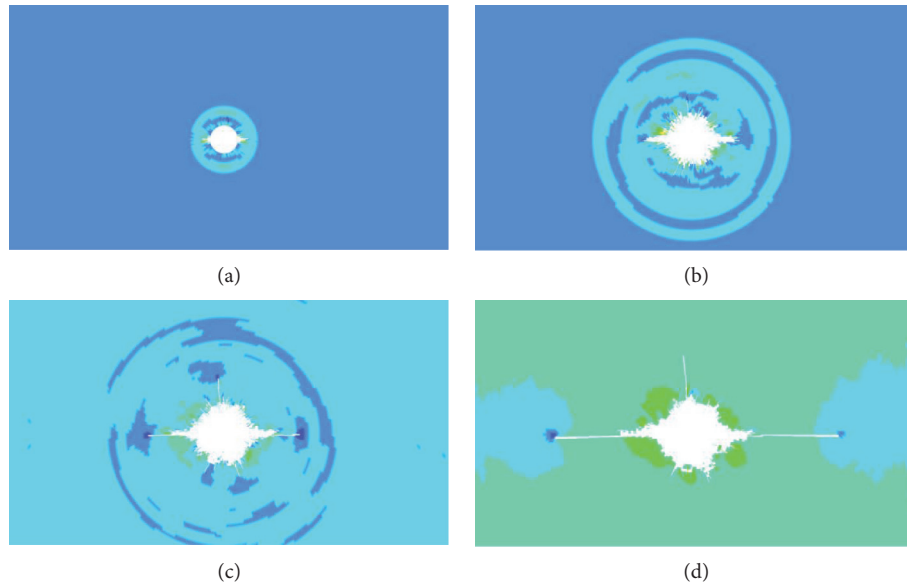


FIGURE 5: Numerical simulation results of blasting crack development of shaped charge. (a)  $t = 20 \mu s$ , (b)  $t = 80 \mu s$ , (c)  $t = 120 \mu s$ , (d)  $t = 600 \mu s$ .

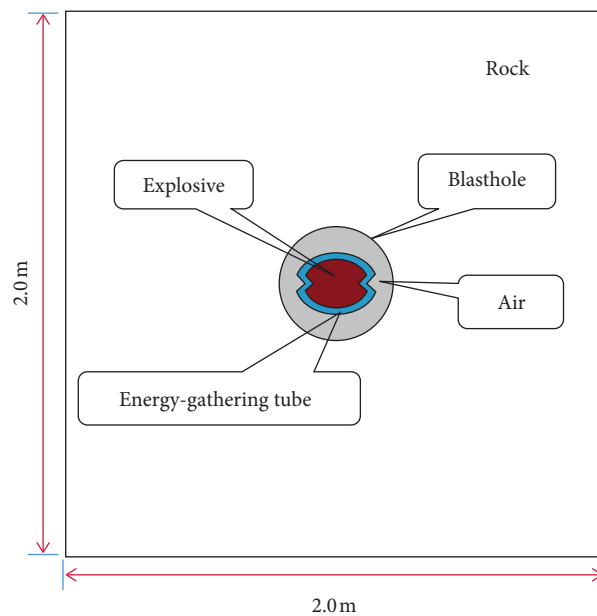


FIGURE 6: Schematic of the numerical calculation model.

The above curves suggested that the peak attenuation rate of rock equivalent stress is very fast along the center of the blast hole outward in both the concentrating energy and non-concentrated energy directions. Especially, the maximum equivalent stress in the direction of shaped charge is 39.25 MPa, the maximum equivalent stress in the direction of nonshaped charge is 17.33 MPa, and the maximum effective stress in the direction of concentrating energy is about 2.3 times of that in the direction of nonconcentrated energy. The results indicated that the ability of rock penetration in the direction of concentrating energy is much greater than that in the direction of nonconcentrated energy.

**4.2.3. Crack Propagation Analysis.** After the initial guide crack is formed, the explosive detonation product fills the whole blasting cavity, and the quasi-static load is applied to the rock on the blast hole wall. Under the quasi-static load and stress concentration, the tip of the guide crack forms a long crack and propagates.

Figure 11 shows the crack development of 42 mm blast hole in elliptical bipolar linear shaped charge blasting. At  $80 \mu s$ , microcracks begin to appear outside the direction of concentrating energy. At  $120 \mu s$ , both main cracks and microcracks keep growing. At  $300 \mu s$ , the cracks outside the direction of concentrating energy tend to stop growing. At



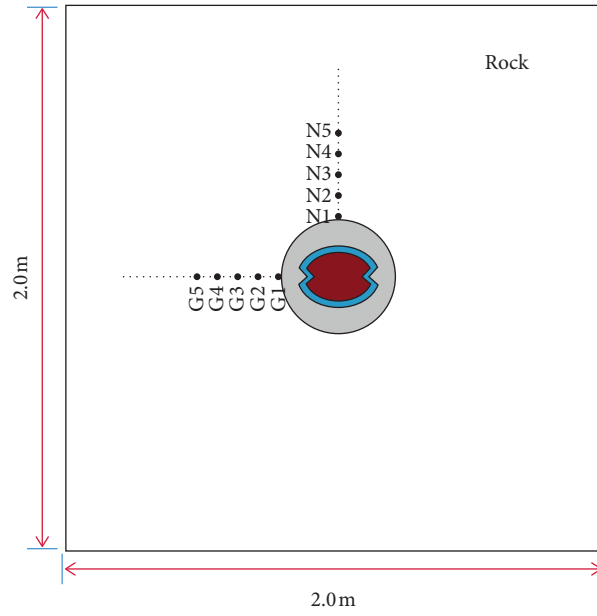


FIGURE 7: The layout of measuring points.

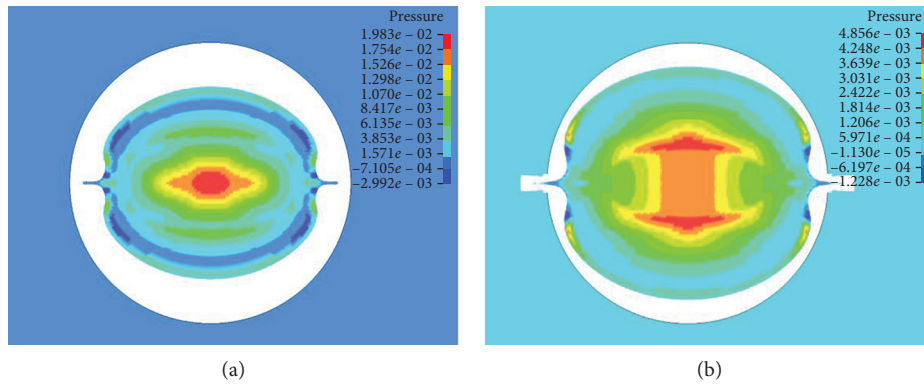


FIGURE 8: Initial crack formation. (a)  $t = 5 \mu s$ , (b)  $t = 8 \mu s$ .

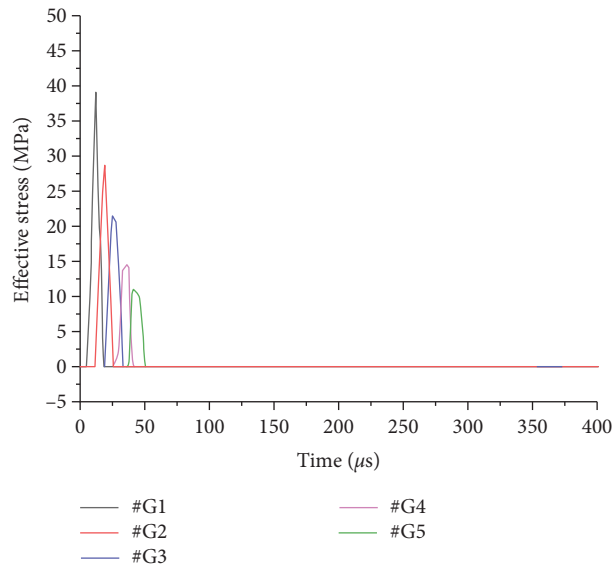


FIGURE 9: Effective stress time history curve in the concentrating energy direction.

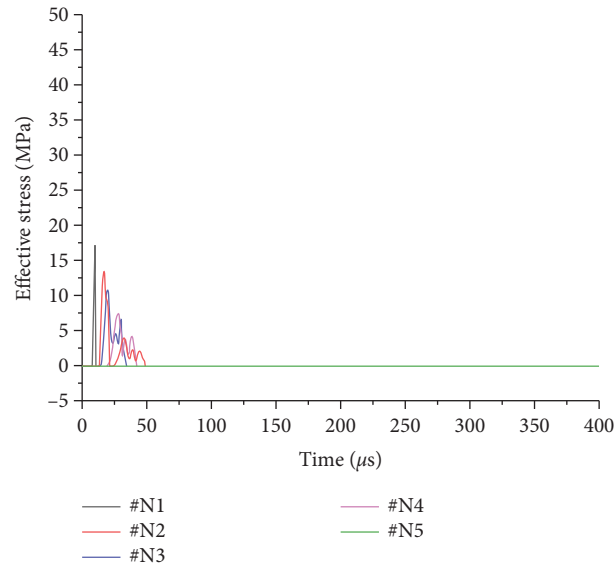


FIGURE 10: Effective stress time history curve in the nonconcentrated energy direction.

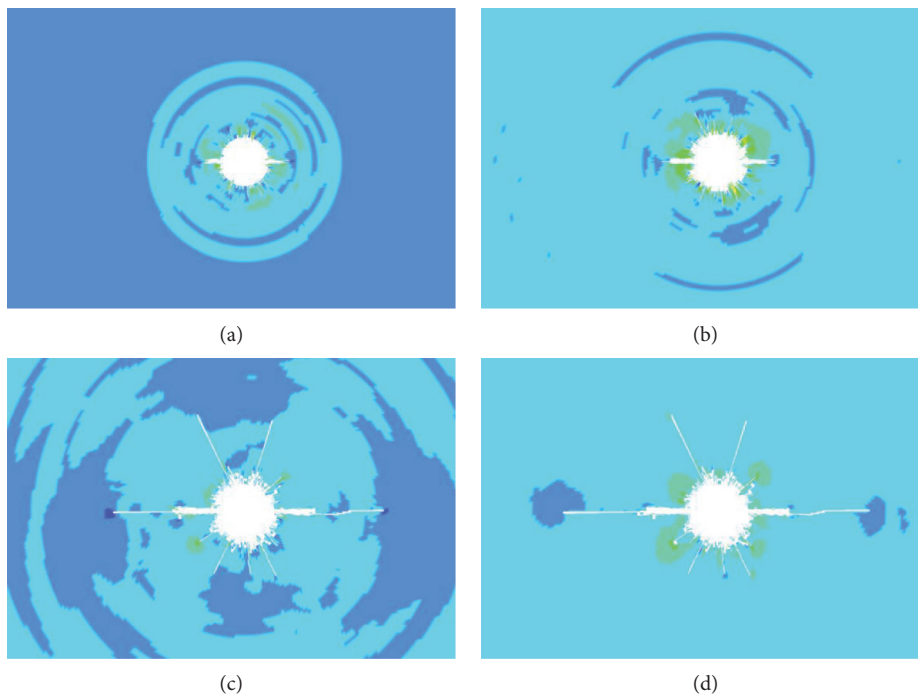


FIGURE 11: Crack development with blast hole diameter 42 mm. (a)  $t = 80 \mu s$ , (b)  $t = 120 \mu s$ . (c)  $t = 300 \mu s$ , (d)  $t = 600 \mu s$ .

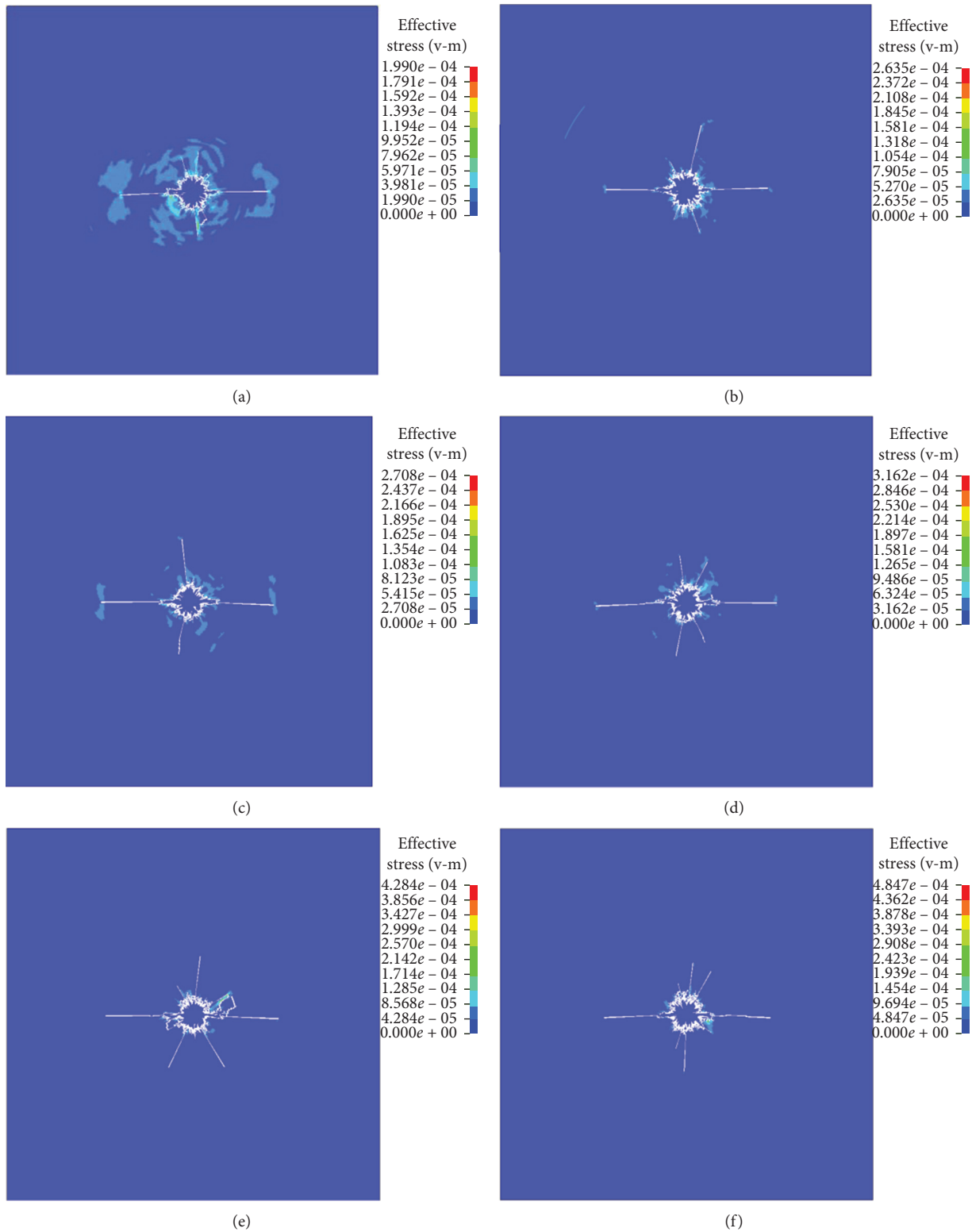


FIGURE 12: Crack development with different blast hole diameters. (a)  $D = 50$  mm, (b)  $D = 60$  mm, (c)  $D = 70$  mm, (d)  $D = 80$  mm, (e)  $D = 90$  mm, (f)  $D = 100$  mm.

TABLE 4: Main crack length of different hole diameter blasting.

Blast hole diameter	42 mm (cm)	50 mm (cm)	60 mm (cm)	70 mm (cm)	80 mm (cm)	90 mm (cm)	100 mm (cm)
Left main crack length	49.27	54.43	60.17	65.21	67.14	65.54	62.16
Right main crack length	49.27	57.40	62.16	65.32	67.44	65.64	63.16

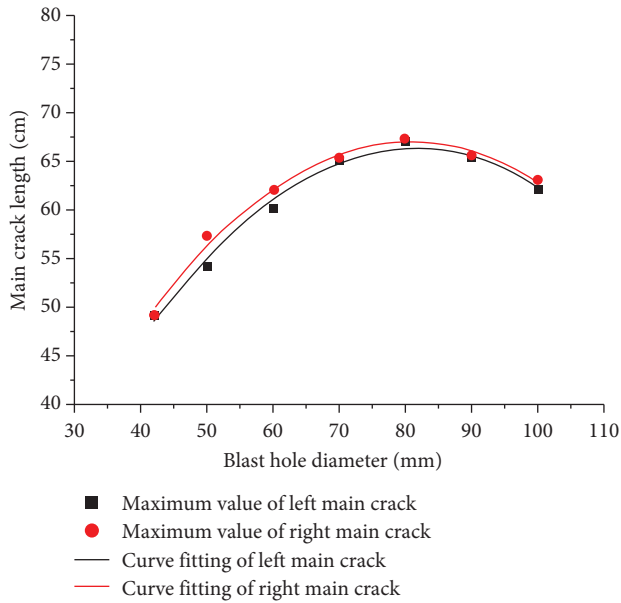


FIGURE 13: Relation curve between main crack length and blast hole diameter.

600  $\mu$ s, all cracks tend to stop growing. The cracks in the direction of concentrating energy are always much larger than those in other directions.

**4.3. Analysis of Rock Cracks Development with Different Blast Hole Diameter.** Based on the established numerical model, the crack development of rock with various diameters of 50 mm, 60 mm, 70 mm, 80 mm, 90 mm, and 100 mm is analyzed. The results of crack development are shown in Figure 12.

The results in Figure 12 indicate that under the blasting of an elliptical bipolar linear shaped charge with different blast hole diameters, two main cracks are formed in the left and right concentrating energy direction, and random secondary cracks are also formed in other directions. With the increase in blast hole diameter, the length of the main crack first increases and then decreases, indicating that there is an optimal blast hole diameter.

**4.4. Analysis of Radial Decoupling Coefficient.** The radial decoupling coefficient changes with the change of blast hole diameter. The main crack length of different blast hole diameter blasting is shown in Table 4.

The curve fitting between the length of the main crack and the diameter of the blast hole is shown in Figure 13. The correlation coefficients between the blast hole diameter and the length of the left and right main cracks have reached more than 0.98. The best blast hole diameter is 82 mm.

Moreover, the equivalent charge diameter of the elliptical bipolar linear shaped charge blasting is 24.4 mm based on the above established numerical simulation model, and thus the best radial decoupling coefficient calculated is 3.36.

## 5. Conclusions

- (1) Under the elliptical bipolar linear shaped charge blasting, the damage ability of rock penetrating in the concentrating energy direction is much greater than that in the nonconcentrated energy direction. The maximum effective stress of rock closed to the position of shaped charge in the concentrating energy direction is about 2.3 times of that in the direction of nonconcentrated energy.
- (2) Under the elliptical bipolar linear shaped charge blasting, the left and right main cracks can be formed in the concentrating energy direction with different hole diameters, and the random secondary cracks can be formed in other directions.
- (3) There is a certain relationship between the length of the main crack and the diameter of the blast hole under elliptical bipolar linear shaped charge blasting. The curve fitting shows that the main crack is the longest when the diameter of the blast hole is 82 mm; that is, the best decoupling coefficient is 3.36.

## Data Availability

The data supporting the results of this study can be obtained upon request to the corresponding author.

## Conflicts of Interest

The authors declare that they have no conflicts of interest regarding the publication of this paper.

## Acknowledgments

The authors would like to express the appreciation for the financial support from the National Natural Science Foundation of China (51678164 and 51478118), the Guangxi Natural Science Foundation Program (2018GXNSFDA138009), the Guangxi Science and Technology Plan Projects (AD18126011), and the GDHVPs (2019).

## References

- [1] M. S. Wang, "An overview of development of railways, tunnels and underground works in China," *Tunnel Construction*, vol. 30, no. 4, pp. 351–364, 2010.
- [2] S. M. Tian, W. Wang, and J. F. Gong, "Development and prospect of railway tunnels in China (including statistics of railway tunnels in China by the end of 2020)," *Tunnel Construction*, vol. 41, no. 2, pp. 308–325, 2021.
- [3] J. X. Wang, B. P. Zou, and L. S. Hu, "Advance and trend in smooth blasting technology for tunnel and underground engineering," *Chinese Journal of Underground Space and Engineering*, vol. 9, no. 4, pp. 800–807, 2013.
- [4] S. H. Cho, Y. Nakamura, B. Mohanty, H. S. Yang, and K. Kaneko, "Numerical study of fracture plane control in laboratory-scale blasting," *Engineering Fracture Mechanics*, vol. 75, no. 13, pp. 3966–3984, 2008.
- [5] R. S. Yang, Y. B. Wang, H. J. Xue et al., "Dynamic behavior analysis of perforated crack propagation in two-hole blasting,"

- Procedia Earth and Planetary Science*, vol. 5, pp. 254–261, 2012.
- [6] L. Yang, R. Yang, G. Qu, and Y. Zhang, “Caustic study on blast-induced wing crack behaviors in dynamic-static superimposed stress field,” *International Journal of Mining Science and Technology*, vol. 24, no. 4, pp. 417–423, 2014.
- [7] R. Yang, Y. Wang, and C. Ding, “Laboratory study of wave propagation due to explosion in a jointed medium,” *International Journal of Rock Mechanics and Mining Sciences*, vol. 81, pp. 70–78, 2016.
- [8] R. S. Yang, Y. B. Wang, D. M. Guo et al., “Experimental research of crack propagation in polymethyl methacrylate material containing flaws under explosive stress waves,” *Journal of Testing and Evaluation*, vol. 44, no. 1, pp. 56–60, 2016.
- [9] Z. W. Yue, L. Y. Yang, and Y. B. Wang, “Experimental study of crack propagation in polymethyl methacrylate material with double holes under the directional controlled blasting,” *Fatigue and Fracture of Engineering Materials and Structures*, vol. 36, no. 8, pp. 827–833, 2013.
- [10] Z. W. Yue, S. C. Zhang, P. Qiu et al., “Influence of charge structures on the slotted cartridge blasting effect,” *Journal of Vibration and Shock*, vol. 37, no. 10, pp. 27–34, 2018.
- [11] Z. W. Yue, S. Y. Tian, S. C. Zhang et al., “Expanding law of cracks formed by slotted cartridge blast under unidirectional confining pressure,” *Journal of Vibration and Shock*, vol. 38, no. 23, pp. 186–195, 2019.
- [12] Z. W. Yue, X. B. Hu, Z. Y. Chen et al., “Experimental study of effect of uncoupled charge on energy utilization efficiency of explosives,” *Blasting*, vol. 37, no. 3, pp. 34–39, 2020.
- [13] Y. Wang, “Study of the dynamic fracture effect using slotted cartridge decoupling charge blasting,” *International Journal of Rock Mechanics and Mining Sciences*, vol. 96, pp. 34–46, 2017.
- [14] Y. Luo, “Study on application of shaped charge in controlled rock mass blasting technology,” *Journal of Disaster Prevention and Mitigation Engineering*, vol. 27, no. 1, pp. 57–62, 2001.
- [15] Y. Luo, Z. W. Sheng, and X. R. Cui, “Application study on blasting with linear cumulative cutting charge in rock,” *Chinese Journal of Energetic Materials*, vol. 3, no. 14, pp. 236–241, 2006.
- [16] J. F. Qin, R. X. Qin, and B. H. Li, “Study and application of elliptical bipolar linear shaped charge,” *Engineering Blasting*, vol. 15, no. 3, pp. 70–74, 2009.
- [17] B. H. Li, W. F. Cui, S. L. Li et al., “Experimental investigation and numerical simulation of decouple coefficient of elliptic bipolar linear shaped charge,” *Blasting*, vol. 30, no. 2, pp. 54–58, 2013.
- [18] B. H. Li, *Research on Theory and Application Technology of Elliptic Bipolar Linear Shaped Charge’s Presplit blasting*, Central South University, Changsha, China, 2013.
- [19] B. Wu, H. Wei, S. Xu et al., “Analysis of the cracking mechanism of an elliptical bipolar linear-shaped charge blasting,” *Advances in Civil Engineering*, vol. 2021, Article ID 6669704, 12 pages, 2021.
- [20] B. Wu, H. Wei, S. Xu et al., “Numerical study of two-way shaped charge blasting with different charge structures,” *Engineering Blasting*, vol. 27, no. 1, pp. 14–21, 2021.
- [21] B. Wu, H. Wei, S. Xu et al., “Research on numerical optimization of smooth blasting layer parameters of shaped energy smooth blasting,” *Nonferrous Metals Engineering*, vol. 10, no. 12, pp. 113–121, 2020.
- [22] B. W. Xia, C. W. Liu, Y. Y. Lu et al., “Experimental study of propagation of directional fracture with slotting hydraulic blasting,” *Journal of China Coal Society*, vol. 41, no. 2, pp. 432–438, 2016.
- [23] D. Y. Guo, H. B. Pei, J. C. Song et al., “Study on splitting mechanism of coal bed deep-hole cumulative blasting to improve permeability,” *Journal of China Coal Society*, vol. 33, no. 12, pp. 1381–1385, 2008.
- [24] M. C. He, W. F. Cao, R. L. Shan et al., “New blasting technology-bilateral cumulative tensile explosion,” *Chinese Journal of Rock Mechanics and Engineering*, vol. 22, no. 12, pp. 2047–2051, 2003.
- [25] D. Y. Guo, D. Y. Shang, P. F. Lu et al., “Experimental research of deep-hole cumulative blasting in hard roof weakening,” *Journal of China Coal Society*, vol. 38, no. 7, pp. 1149–1153, 2013.
- [26] Q. Li, Y. Liang, K. K. Ren et al., “Experimental study of propagation of directional cracks with shaped charge under blasting load,” *Chinese Journal of Rock Mechanics and Engineering*, vol. 29, no. 8, pp. 1684–1689, 2010.
- [27] N. Murphy, M. Ali, and A. Ivankovic, “Dynamic crack bifurcation in PMMA,” *Engineering Fracture Mechanics*, vol. 73, no. 16, pp. 2569–2587, 2006.
- [28] H. P. Rossmannith, A. Daehnke, R. E. K. Nasmillner, N. Kouzniak, M. Ohtsu, and K. Uenishi, “Fracture mechanics applications to drilling and blasting,” *Fatigue and Fracture of Engineering Materials and Structures*, vol. 20, no. 11, pp. 1617–1636, 1997.
- [29] Y. L. Che, *Study on the Mechanism of Irregular Cartridge and the Damage of Surrounding Rock*, China University of Mining and Technology, Xuzhou, China, 2015.

## Research Article

# Research on Energy Dissipation Laws of Coal Crushing under the Impact Loads

Dengke Xu <sup>1</sup>, Chaomin Mu <sup>2,3</sup>, Wenqing Zhang<sup>2,3</sup> and Zhongqing Li<sup>2,3</sup>

<sup>1</sup>School of Civil Engineering and Architecture, Anhui University of Science and Technology, Huainan, Anhui 232001, China

<sup>2</sup>School of Safety Science and Engineering, Anhui University of Science and Technology, Huainan, Anhui 232001, China

<sup>3</sup>Key Lab of Mining Coal Safety and Efficiently Constructed by Anhui Province and Ministry of Education, Huainan, Anhui 232001, China

Correspondence should be addressed to Chaomin Mu; [chmmu@mail.ustc.edu.cn](mailto:chmmu@mail.ustc.edu.cn)

Received 21 February 2021; Revised 1 June 2021; Accepted 9 June 2021; Published 21 June 2021

Academic Editor: Qi ZHAO

Copyright © 2021 Dengke Xu et al. This is an open access article distributed under the Creative Commons Attribution License, which permits unrestricted use, distribution, and reproduction in any medium, provided the original work is properly cited.

Dynamic crushing characteristics of coals are closely related with energy absorption and release of coals under certain strain rate. Hence, it is necessary to investigate energy dissipation laws of coal crushing under the impact loads with different strain rates. Based on the dynamic and static mechanical tests, crushing energy, total absorption energy, total releasable elastic latent energy, and relations between fractal feature of fragments, mean particle diameter and energy during crushing behaviors of outburst coal and nonoutburst coal were investigated. According to research results, crushing energy, total absorption energy, and releasable elastic latent energy of outburst coal and nonoutburst coal are related with strain rate, and they present exponential growths with the increase of the strain rate. However, the energy dissipation rate (ratio of crushing energy and incident energy) was basically constant at about 10%~20%, that is, energy dissipation rate is a variable unrelated with strain rate. There is a good logarithmic relationship between the dynamic compressive strength of coals and the absorption energy density and elastic latent energy density, and dynamic comprehensive strength of coals has important impacts on energy absorption. The fractal features of coal fragments were obvious under dynamic impacts. The higher fractal dimension of fragment and the smaller mean particle diameter of experimental fragments bring the greater energy needed.

## 1. Introduction

Coal resources have been occupying the dominant role in the world energy structure. With the increase of coal mining depth, the coal seams are exposed to increasingly complicated occurrence conditions. Coals might accumulate more energy, and coals might bear strong impact loads upon sudden loading disturbances during uncovering, explosion, and advancing processes of coals, thus resulting in coal and rock dynamic disasters represented by coal-gas outburst and rock burst, etc. [1–4]. To prevent and decrease occurrences of such dynamic disasters, it is necessary to understand mechanical properties of coal and rock materials under dynamic loads. In the past few decades, the mechanism of coal deformation and failure has been extensively investigated through laboratory tests, such as uniaxial [5], biaxial

[6], and triaxial [7] compression, dynamic tensile [8], and cyclic impact loading [9]. The split Hopkinson pressure bar (SHPB) is considered to be a commonly used experimental device for the study of rock dynamic fragmentation process [10, 11].

Recently, many studies focus on the relations of coal deformation and fractures with energy. The dynamic crushing characteristics of materials are closely related to the energy absorption and release at a certain strain rate. The mechanism of coal outburst can be understood by accurately calculating the crushing energy and surface energy of coal. The fractal theory relating the coal particle size was developed to calculate the crushing energy of coal. The fractal model and crushed coal particle size distribution data fitted, and a kinetic equation was formulated to describe the particle size distribution for two types of coal [12]. The effect



of impact speed on the crushing energy and particle size distribution was investigated, and we found that the degree of fragmentation increases exponentially with impact speed [13]. Luo et al. [14] evaluated the energy for crushing coal to various size fractions in coal and gas outbursts through theoretical and experimental investigation of the shape of fine coal particles and their equivalent diameter. Many foreign researches has also investigated the relationship between crushing energy and particle size distribution using different methods, such as numerical simulation [15, 16] and vertical impact [17, 18]. The model and law of crushing ratio were proposed to evaluate coal crushing efficiency [19, 20]. In the crushing process of materials under external loading, the surface energy is a component of the crushing energy. The surface area of fragment is often used to measure the surface energy during crushing [21–24].

Coal crushing involves energy release and dissipation, including energy absorption, transformation, and release. The releasable strain energy is the driving force for the failure of coal or rock mass structure, and the crushing energy is related to the damage degree of coal or rock mass structure in the plastic zone [25–27]. The effects of water contents and incident energy levels on coal dynamic behavior were studied. The results indicate that dynamic strength and elastic modulus positively correlated with the incident energy. The incident energy-dominated and energy-induced failures were analyzed based on dissipation energy and stress-strain curve types [28]. Feng et al. [29] proposed the energy dissipation rate as a novel indicator of coal deformation and failure under static and dynamic compressive loads. The relationship between stress-strain, uniaxial compressive strength, displacement, loading, and energy dissipation rates and fractal dimension was investigated. The results showed that the peak value of energy dissipation rate is associated with stress drop during coal deformation, as well as to the uniaxial compressive strength. Hao et al. [30] analyzed the energy accumulation, energy rate of release, and failure modes of hard coal under dynamic, static, and coupled dynamic-static loading. The results showed that the degree of destruction and fragmentation of coal samples increases with the increase of prepeak energy accumulation. The first attempt by numerical methods was made in investigating the energy release during the failure of pillar-scale coal mass samples with varying cleat densities. The results indicate that cleat spacing can have a significant impact on the compressive strength and energy release, in which both strength and energy release (magnitude and rate) decrease as the number of cleats increases [31]. An effective elastic strain energy release rate index was proposed to evaluate the coal bursting liability and fully integrate the energy evolution of coal samples being damaged by loading. Results show that the propagation and coalescence of cracks are accompanied by energy release [32]. A simple and novel analytical solution was developed to calculate the amount of released energy under varying joint density, and three-dimensional numerical simulation was conducted to understand the influence of coal's joint and cleat characters (directions and densities) on the possible energy release and/or dissipation [33]. To determine the relationship between

energy transformation and coal failure, we established the damage evolution model of the rigidity degeneration of coal before the peak strength based on the test results. The results reveal that failure energy ratio is approximately linearly related to the fractal dimension of the coal fragments, and a high failure energy ratio corresponds to a large fractal dimension and severe failure [34]. In conclusion, the energy consumption of dynamic failure and static failure differ under the same damage or breakage degree.

Previous associated studies mainly emphasize on mechanical properties, degree of fragmentation, and total energy of coals and rocks under different strain rates. Only few have discussed the energy absorption and releasing mechanism of coals and rocks under different strain rates as well as the relationship between mean particle diameter of crushing coal and energy density. Based on uniaxial static compression and SHPB dynamic impact experiment, crushing energy, total absorption energy, and total releasable latent energy of different coal samples (different strengths) under dynamic and static loads were gained. Moreover, energy characteristics under different strain rates were compared, and the energy dissipation laws of different strengths coals with crushing under the impact loads were gained.

## 2. Experimental Method

*2.1. Sample Preparation.* Outburst coal is the low strength coal formed after the raw coal is crushed and bonded under the ground stress because it is difficult to core on-site; therefore, imitating the formation process of outburst coal in nature, that is, the crushing and bonding method, is used to reconstruct the outburst coal in the laboratory. Nonoutburst coal is the raw coal with high strength. In this experiment, coal samples were collected from the 13-1 coal seam, Zhangji Coal Mine, Huainan Mining Group. Outburst coal specimen is made by grinding raw coal, sifting 40~80 mesh coal powers, and then shaping with 100 MPa pressure on a large rigid press machine with a self-made coal pressure tank. The nonoutburst coal specimen is made by drilling on the raw coal by a rock drill, and then grinding and cutting into the cylindrical coal mass with a diameter of 50 mm. The cylinder specimens with a height of 100 mm and a diameter of 50 mm were used in the static uniaxial compression experiment, in which the nonoutburst coal specimens were numbered S1~S3 and the outburst coal specimens were numbered S4 and S5. The cylinder specimens with a height of 30 mm and a diameter of 50 mm were chosen in the dynamic impact experiment, in which the outburst coal specimens were numbered D1~D14 and the nonoutburst specimens were numbered D15~D20.

*2.2. Experimental System.* Failure characteristics of coals under static loads were concluded from the static uniaxial compression experiment of coal specimens on the RMT-350 rock mechanical testing system in the Mining Engineering Laboratory of the Anhui University of Science and Technology. Mechanical properties of coals under dynamic loads

were gained through a dynamic impact experiment based on the  $\Phi$  75 mm SHPB in the Impact Laboratory of the Anhui University of Science and Technology. Diameters of the trip rod (bullet), incidence rod, and output rod of the SHPB system were determined to be 75 mm, whereas lengths were 0.4 m, 4 m and 2.5 m, respectively. They were all made of high-strength alloy steel, and the elasticity modulus was 195 GPa. Physical picture of experimental system is shown in Figure 1.

**2.3. Experimental Procedures.** The static uniaxial compression loading rate of outburst coal and nonburst coal specimens was 0.02 mm/s. A dynamic impact test was carried out to test dynamic characteristics of outburst coal and nonburst coal specimens under different impact loads. In the impact experiment of nonoutburst coals, the pneumatic control of driving device was controlled at 0.2~0.6 MPa, and the corresponding impact speed of the bullet was 4.36~6.15 m/s. A total of 6 groups of effective data were gained successfully. In the impact experiments of outburst coals, the pneumatic control of driving device was controlled at 0.2~0.7 MPa, and the corresponding impact speed of the bullet was 3.21~10.81 m/s. A total of 14 groups of effective data were gained.

### 3. Energy Composition in the SHPB Compression Experiment

**3.1. Energy Carried by the Stress Wave.** The Hopkinson bar (SHPB) technology is based on the one-dimensional elastic stress wave theory and the hypothesis of uniformity. The energy carried by the stress wave  $\sigma(t)$  is expressed as

$$\begin{aligned} W &= \frac{A_e C_e}{E_e} \int_0^t \sigma^2(t) dt = \frac{A_e C_e}{E_e} \int_0^t [E_e \sigma(t)]^2 dt \\ &= A_e E_e C_e \int_0^t \varepsilon^2(t) dt, \end{aligned} \quad (1)$$

where  $A_e$  is the cross sectional areas of the input and output bars ( $m^2$ ).  $E_e$  is the elasticity modulus of the input and output bar materials (GPa).  $C_e$  is the speed of one-dimensional stress wave and speed of stress wave ( $C_e$ ) in the elasticity stage can be expressed by the mass density ( $\rho_e$ ) and elasticity modulus ( $E_e$ ) of the compression bar:  $C_e = \sqrt{E_e/\rho_e}$ . For this SHPB test system,  $C_e = 4984$  m/s.  $\varepsilon(t)$  is the strain corresponding to the stress wave.

The incident energy ( $W_I$ ), transmitted energy ( $W_T$ ), and reflected energy ( $W_R$ ) on the compression bar from loading to unloading could be expressed as the following equations:

$$W_I = A_e C_e E_e \int_0^t \varepsilon_I^2(t) dt, \quad (2)$$

$$W_R = A_e C_e E_e \int_0^t \varepsilon_R^2(t) dt, \quad (3)$$

$$W_T = A_e C_e E_e \int_0^t \varepsilon_T^2(t) dt, \quad (4)$$

where  $\varepsilon_I(t)$ ,  $\varepsilon_R(t)$ , and  $\varepsilon_T(t)$  are strains corresponding to the incident wave, reflected wave, and transmitted wave on the compression bar.

**3.2. Crushing Energy and Crushing Energy Density.** Because the two end surfaces of specimens were coated with lubricant, energy consumed by the frictional force between contact surfaces was ignored in the analysis. As a result, the energy carried by the incident wave minus the sum of energy carried by the reflected wave and the transmitted wave is equal to the energy consumed by failure of specimens under dynamic impacts. This is called the crushing energy of specimens, and it can be calculated as follows [35]:

$$W_D = W_I - (W_R + W_T) = A_e C_e E_e \int_0^t [\varepsilon_I^2(t) - \varepsilon_T^2(t) - \varepsilon_R^2(t)] dt. \quad (5)$$

Dissipated energy in unit volume was used to measure the energy consumption during impact-induced failure, which is known as the crushing energy density ( $w_D$ ):

$$w_D = \frac{W_D}{V}, \quad (6)$$

where  $V$  is the volume of specimens ( $m^3$ ).

**3.3. Energy Dissipation Rate.** The ratio of crushing energy and incident energy was defined as the energy dissipation rate ( $N$ ) to measure energy dissipation strength of coals and rocks under varying strain rates:

$$N = \frac{W_D}{W_I} \times 100\%. \quad (7)$$

**3.4. Total Absorption Energy and Releasable Elastic Latent Energy.** According to the theory of rock mechanics, the area enclosed by the stress-strain curves gained from the static loading experiment and dynamic experiments was the failure-induced absorption energy density ( $u$ ) of specimens during the loading process:

$$u = \int \sigma d\varepsilon, \quad (8)$$

where  $u$  is the failure-induced absorption energy density of specimens ( $J/m^3$ ) and  $\sigma$  is the coal-rock stress (MPa).

Then, the total absorption energy ( $U$ ) of specimens during the failure process is

$$U = uV, \quad (9)$$

where  $V$  is the volume of specimens ( $m^3$ ).

When coal-rock specimens are exposed to external loads, it is hypothesized that the deformation formation has no heat exchange with the external world. The total energy ( $U$ ) that is applied by the external force on the specimens can be expressed as

$$U = U^d + U^e, \quad (10)$$

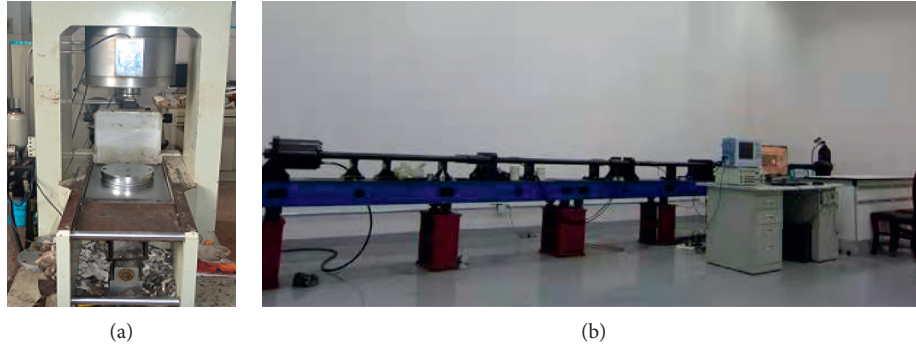


FIGURE 1: Physical picture of experimental system. (a) RMT-350; (b)  $\Phi$  75 mm SHPB.

where  $U^d$  is the dissipated energy of specimens during crushing, which is mainly to form internal damages and plastic deformation of specimens.  $U^e$  is the releasable elastic latent energy of specimens, and it is directly related with unloading elasticity modulus and unloading Poisson's ratio. Obviously, energy dissipation is one-way and irreversible, whereas releasable elastic latent energy is reversible. The relationship between energy dissipation and releasable elastic latent energy is reflected on the stress-strain curves (Figure 2).

## 4. Results and Discussion

### 4.1. Macroscopic Analysis of Impact Failure of Coals.

Failure modes of nonoutburst coal and outburst coal under different strain rates are shown in Figure 3. According to comparison, the nonoutburst coal fragments are uniform when the strain rate is  $81 \text{ s}^{-1}$ , and there is no significant block. With the increase of strain rate, the energy carried by the stress wave is enough to generate longitudinal run-through cracks on specimens, thus intensifying the degree of crushing. From the perspective of energy, both crack initiation and expansion in materials requires energy dissipation, whereas the energy needed for the formation of new cracks is significantly higher compared with that for crack expansion. Hence, fractures of coal materials is mainly attributed to expansion and running through of the original microcracks under a low strain rate. With the increase of strain rate, the material absorbs a high level of energies before running through of microcracks, which are expandable, so that more microcracks can expand and thereby attend in the crushing process. Furthermore, more new cracks are generated, which requires higher-energy dissipation and decreases the particle diameter of crushed materials. Consequently, the critical stress for the material crushing is the higher. This interprets that the material strength increases with the increase of strain rate.

**4.2. Relations of Crushing Energy Density, Energy Dissipation Rate, and Strain Rate.** According to the stress-strain experimental results under varying dynamic loads and equations (1)–(7), the crushing energy density and energy dissipation rate of coal samples could be calculated (Table 1).

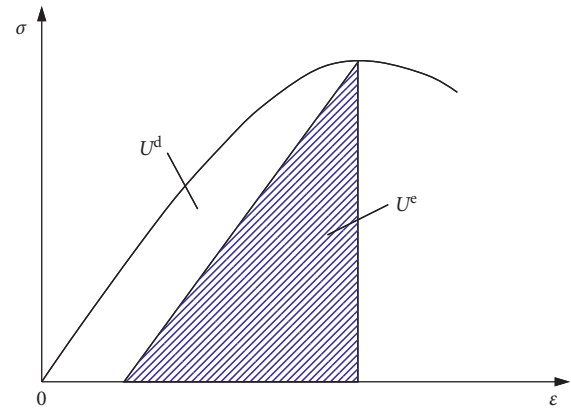


FIGURE 2: Relationship between dissipation energy and releasable elastic latent energy [36].

The relations of crushing energy density and strain rate are shown in Figure 4.

Seen from Figure 4, the crushing energy density of two types of coal specimens shows the relatively consistent variation laws (exponential growth) with strain rate. Crushing energy density of nonoutburst coal is the higher under the same strain rate. When the strain rate is low, the difference of crushing energy between outburst coal and nonoutburst coal is not very large, which is related with the preparation of nonoutburst coal specimens. The internal cracks of the drilled nonoutburst coal are kept well and can influence energy absorption to some extent. This is basically consistent with the energy dissipation laws of porous man-made rocks in the study of Xie [36]. When the strain rate is high, the difference of crushing energy between outburst and nonoutburst coal increases. This is because the nonoutburst coal has relatively high strength, and they have to consume more energy to generate the same crack. As seen from Table 1, the energy dissipation rate of both outburst coal and nonoutburst coal is basically consistent with the changes of strain rate. In other words, the energy dissipation rate is kept constant at about 10%~20%, and it is a variable unrelated with strain rate.

**4.3. Relations of Total Absorption Energy Density, Elastic Latent Density, and Strain Rate.** In order to compare and

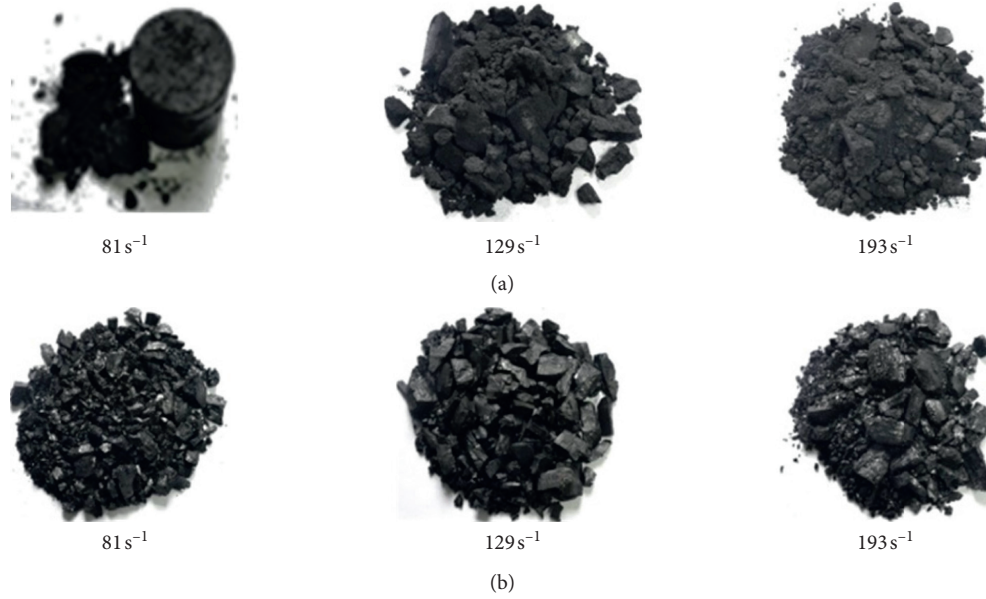


FIGURE 3: Specimens after impacting. (a) Outburst coal. (b) Nonoutburst coal.

TABLE 1: Energy of coal specimens under dynamic impact.

Type	Specimen no.	Strain rate ( $s^{-1}$ )	Incident energy (J)	Reflected energy (J)	Transmitted energy (J)	Crushing energy (J)	Crushing energy density ( $J \cdot m^{-3}$ )	Energy dissipation rate
Outburst coal	D1	73	32.98	27.04	0.17	5.78	81563	0.175
	D2	78	57.21	48.58	0.12	8.51	128991	0.149
	D3	81	63.19	56.64	0.10	6.46	90996	0.102
	D4	101	166.70	130.64	0.15	35.91	156918	0.215
	D5	115	226.65	183.42	0.65	42.59	188245	0.188
	D6	129	268.20	218.20	0.52	49.48	219607	0.184
	D7	160	424.55	344.91	0.50	79.14	345802	0.186
	D8	174	254.14	222.23	0.15	31.76	475742	0.206
	D9	193	609.29	494.99	0.79	113.51	499874	0.186
	D10	214	349.36	279.52	0.26	69.58	795067	0.149
	D11	219	391.21	328.17	0.29	62.75	951140	0.160
	D12	221	663.94	520.78	0.94	142.22	853109	0.173
	D13	268	497.17	400.90	0.67	95.61	1585950	0.192
	D14	279	518.02	430.40	0.55	87.07	1628234	0.187
Nonoutburst coal	D15	96	85.70	75.15	0.82	9.72	159767	0.113
	D16	120	111.73	87.44	0.77	23.52	315228	0.211
	D17	125	117.27	90.56	0.80	25.91	435503	0.221
	D18	145	152.78	113.10	0.51	39.17	651923	0.256
	D19	177	242.73	184.94	0.70	57.09	944028	0.235
	D20	186	304.03	232.57	1.23	70.23	1391585	0.231

analyze the energy absorption law of coal specimen under impact loading and quasi-static loading, the elastic latent energy density and total absorption energy density of two types of coal specimen are calculated according to the stress-strain curves under quasi-static loading, as shown in Table 2. According to stress-strain experimental results under varying dynamic loads and equations (8)–(10), the total absorption energy density and elastic latent energy density are calculated, as shown in Table 3. The ratio of absorption energy (Table 3) is defined as the ratio of absorption energy of specimens under varying strain rates and absorption

energy under static failure. The ratio of elastic latent energy (Table 3) is defined as elastic latent energy of specimens under varying strain rates and elastic latent energy under static failure.

The relations of total absorption energy density and ratio of absorption energy of two types of coal specimens with strain rate under different impact loads are shown in Figure 5. The total absorption energy density of nonburst coal is higher compared with that of outburst coal, indicating that the total absorption energy density of nonburst coal is more sensitive to strain rate. Because outburst coal is relatively



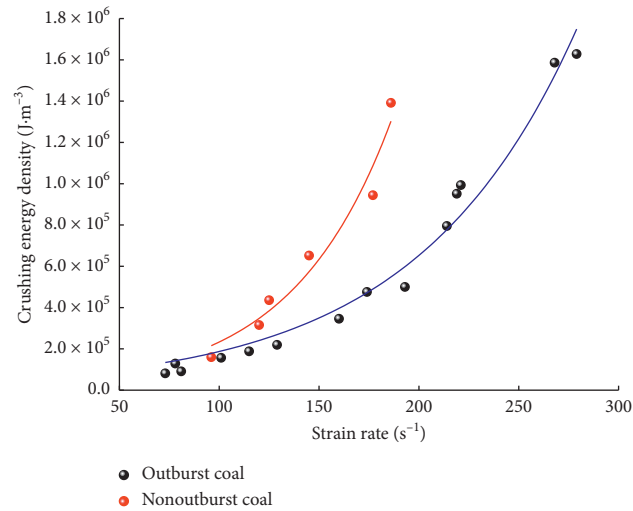


FIGURE 4: Relations of crushing energy density and strain rate.

TABLE 2: Elastic latent energy density and total absorption energy density of static test.

Type	Specimen no.	Peak strain ( $10^{-4}$ )	Elastic latent energy density ( $J \cdot m^{-3}$ )	Total absorption energy density ( $J \cdot m^{-3}$ )
Nonoutburst coal	S1	66.63	53736.92	58314.13
	S2	72.88	47401.89	56662.66
	S3	65.23	53058.81	61283.68
	Average	63.94	51399.21	58753.49
Outburst coal	S4	193.2	14383.48	22659.44
	S5	214.4	14104.76	23644.62
	Average	203.80	14244.12	23152.03

TABLE 3: Absorption energy density and elastic latent energy density of coal specimens under impact loads.

Type	Specimen no.	Strain rate ( $s^{-1}$ )	Elastic latent energy density ( $J \cdot m^{-3}$ )	Total absorption energy density ( $J \cdot m^{-3}$ )	Ratio of elastic latent energy	Ratio of total absorption energy
Outburst coal	D1	73	7514.4	15164.3	0.53	0.65
	D2	78	10462.4	20737.6	0.73	0.90
	D3	81	10924.5	18650.5	0.77	0.81
	D4	101	5820.8	15484.3	0.35	0.67
	D5	115	28707.9	53413.8	2.02	2.31
	D6	129	21715.6	43215.1	1.52	1.87
	D7	160	24476.2	45100.0	1.72	1.95
	D8	174	36180.2	74123.9	2.54	3.20
	D9	193	43826.1	80153.5	3.08	3.46
	D10	214	40665.1	76023.1	2.85	3.28
	D11	219	51529.5	94275.0	3.62	4.07
	D12	221	47259.1	84470.3	3.32	3.65
	D13	268	96275.4	175133.1	6.76	7.56
	D14	279	107619.6	207698.7	7.56	8.97
Nonoutburst coal	D15	96	12354.2	30345.0	0.24	0.52
	D16	120	22291.0	45932.7	0.43	0.78
	D17	125	21409.3	46927.4	0.42	0.66
	D18	145	33695.8	59910.0	0.66	1.02
	D19	177	47037.3	90295.5	0.92	1.54
	D20	186	66647.1	123949.5	1.30	2.11

soft, they can absorb less energy and experience the hardening effect with the increase of strain rate under static failure mode. The outburst coal shows the higher ratio of absorption energy under impact load-induced failures than nonburst coal, which explains why soft coals are easier to be damaged upon energy accumulation under disturbance loads like rock burst.

As seen from Figure 5(a), the absorption energy density with crushing of two types of coal specimens achieves an exponential growth with the increase of strain rate ( $\dot{\epsilon}$ ) in the experiment. The fitting relations can be expressed as

$$\text{nonoutburst coal : } u = 7076e^{0.015\dot{\epsilon}}, \quad (11)$$

$$\text{nonoutburst coal : } u = 3304e^{0.015\dot{\epsilon}}. \quad (12)$$

According to the fitting expressions, two types of coal specimens show the same growth trend of total absorption energy density, indicating that the outburst coal and non-outburst coal show consistent responses to the impact loading.

Relations of releasable elastic latent energy density and ratio of elastic latent energy of two types of coal specimens with strain rate under the impact loads are shown in Figure 6. Obviously, releasable elastic latent energy density of two types of coal specimens grows quickly with the increase of strain rate. They both show significant correlations with strain rate. The relevant relations can be expressed in the (13) and (14). The elastic latent density of nonoutburst coal is higher compared with that of outburst coal under different strain rates. In other words, nonoutburst coal can release more energy for damages. Seen from Figure 6(b), the ratio of elastic latent energy of outburst coal is higher under the same strain rate, and the outburst coal can release more times of energy compared with that under static failure. Moreover, outburst coal requires less energy to be fractured. As a result, energy released by the outburst coal is easier to cause failure damages of coals. This also explains the easier occurrence of dynamic phenomenon in the soft seams (there is a layer of soft seam in hard coals) of coals.

$$\text{Nonoutburst coal : } U^e = 2644e^{0.017\dot{\epsilon}}, \quad (13)$$

$$\text{outburst coal : } U^e = 3827e^{0.012\dot{\epsilon}}. \quad (14)$$

Based on fitting results, the nonoutburst coal can absorb more energy and contain more releasable elastic latent energy than outburst coal before failure under the same intensity of impact loads.

**4.4. Relations of Total Absorption Energy Density and Elastic Latent Density with Dynamic Strength.** Relations total absorption energy density and elastic latent energy density with dynamic strength of coal is shown in Figures 7 and 8, respectively. It can be seen from Figures 7(a) and 8(a) that dynamic strength of coal is the major influencing factor of absorption energy of different coals. The energy absorption of both outburst coal and nonoutburst coal under the same peak strength is almost the same. However, the

nonoutburst coal has the higher peak strength under the same strain rate due to the relatively higher hardness, thus showing the higher energy absorption and storage. Because ductile materials have a process of transforming from ductility to brittleness under the high strain rate (which is known as the strain rate-induced hardening effect) and the static crushing energy of outburst coal is relatively low, the outburst coal can absorb and store more times of energy for crushing than the nonoutburst coal under statistic test (Figures 7(b) and 8(b)).

**4.5. Relations of Energy Density and Fractal Dimension with Mean Particle Diameter.** Generally, the mass-frequency distribution of fragments observes the following laws [11, 37]:

$$\frac{M(R)}{M} = 1 - \exp\left[-\left(\frac{R}{R_0}\right)^b\right], \quad (15)$$

where  $M(R)$  is the cumulative mass of fragments with diameter smaller than  $R$  (kg),  $M$  is the total mass of fragments (kg), and  $R_0$  is scale parameter of the fragment distribution and related to the mean size. According to relevant studies [37, 38],  $D = 3 - b$ , where  $D$  is the fractal dimension of fragments. The screening statistics and fractal computing results of fragments of outburst and non-outburst coal are listed in Table 4.

As seen from Table 4, with the increase of strain rate (impact loading energy) in the experiment, the proportions of small fragments of outburst and nonoutburst coal show an increasing trend after the failure, and the degree of impact crushing of coal specimen increases, the fractal dimension of fragments increases. As coal is geologic material, part of the experimental data in Table 4 is discrete, but the overall trend is consistent with the above conclusion. The relations of crushing energy density, absorption energy density, and fractal dimension are shown in Figure 9. The fractal dimension ( $D$ ) of outburst and nonoutburst coal presents an evident logarithmic growth with the increase of crushing energy density and absorption energy density, indicating that the higher degree of crushing requires a larger impact energy to the specimens. This is basically consistent with other studies on fractal behaviors of rock [39], anthracite [40], and other materials under in impact experiments. Moreover, the proportion of small fragment of outburst coal is the higher when the energy absorption and storage are the same. This conforms to the previous analyses that the proportion of energy to damage the outburst coal is the higher given the same energy condition.

For quantitative description of degree of crushing after the impact test, the mean particle diameter of the certain coal specimen all fragments was defined as

$$\bar{d} = \frac{\sum \bar{d}_i \eta_i}{\sum \eta_i}, \quad (16)$$

where  $\bar{d}$  is the mean particle diameter of the certain coal specimen all fragments (mm),  $\bar{d}_i$  is the mean particle diameter of fragments retained in sieves with certain pore



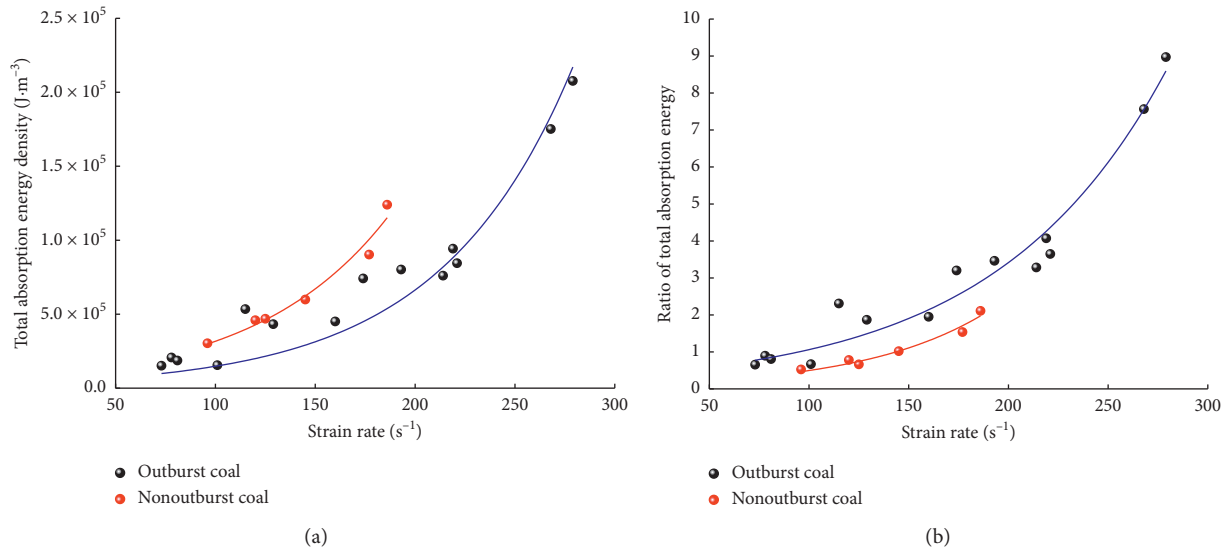


FIGURE 5: Relations of total absorption energy density, ratio of absorption energy, and strain rate. (a) Total absorption energy density; (b) ratio of absorption energy.

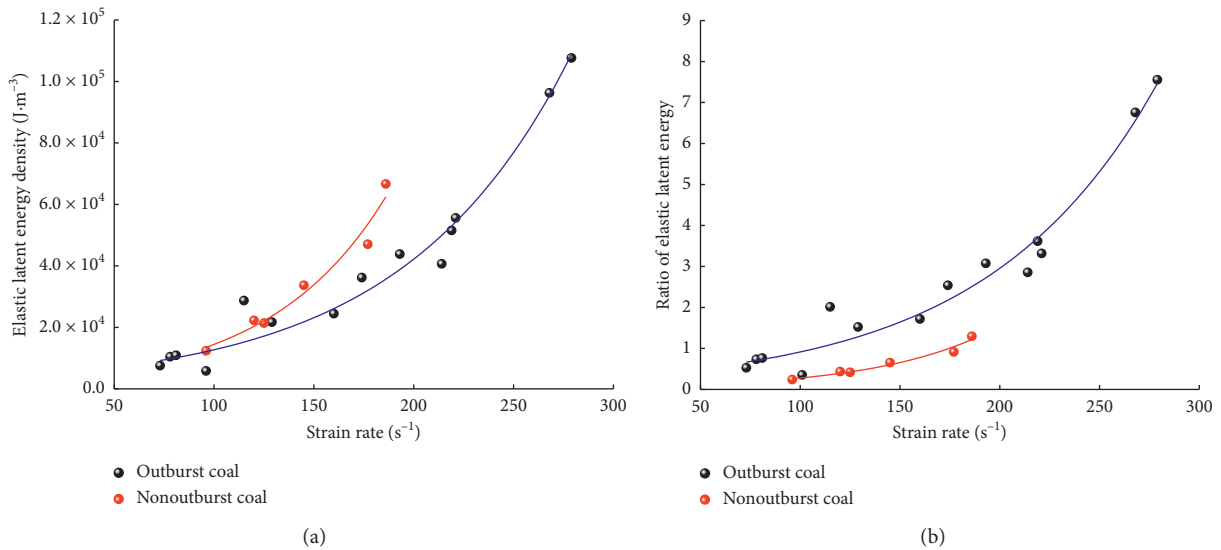


FIGURE 6: Relations of elastic latent energy density, ratio of elastic latent energy, and strain rate. (a) Elastic latent energy density; (b) ratio of elastic latent energy.

diameter during the screening process (mm), and  $\eta_i$  is the mass percentage of fragments intercepted by a certain diameter of pores (%).

The relationship between mean particle diameter of fragments and energy is shown in Figure 10. With the increase of energy absorption and storage, the mean particle diameter of fragments decreases exponentially, and such reduction is quicker in outburst coal. Due to various natural fractures and defects, the mean particle diameter of fragments of

nonoutburst coal is smaller than that of outburst coal (compacted into internally uniform) when there is less impact energy under the low strain rate. A lot of new cracks will be formed before running through of original cracks and defects. Because nonoutburst coal consume plenty of energy for form new cracks because of the high strength, the mean particle diameter of fragments of outburst coal begins to be smaller than that of nonoutburst coal under the relatively high impact energy.

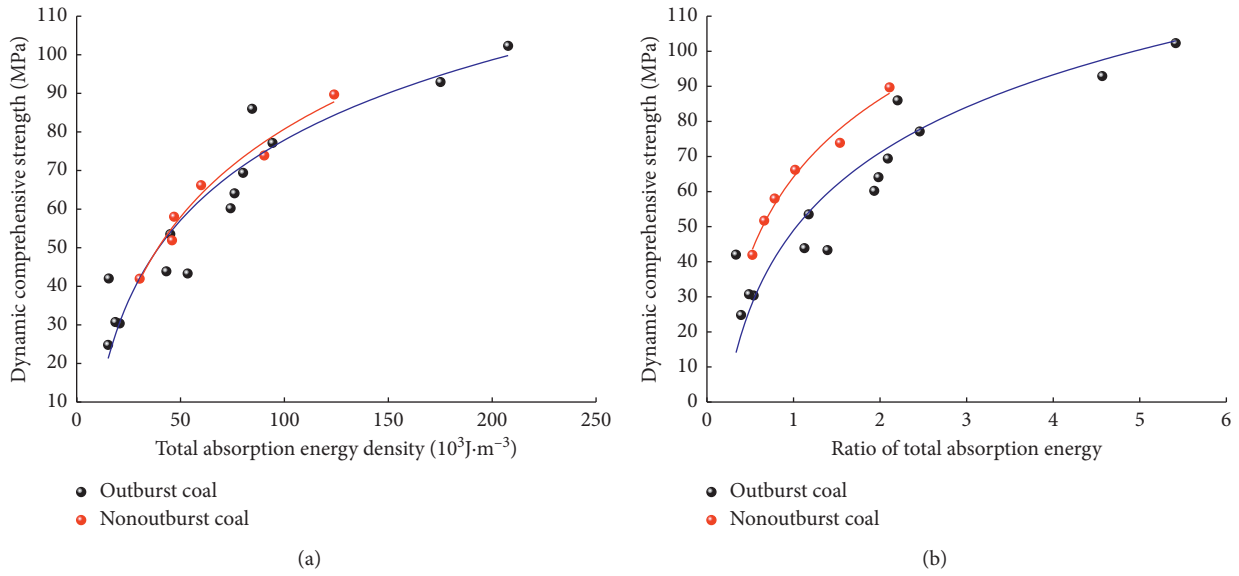


FIGURE 7: Relations of total absorption energy density, ratio of absorption energy, and dynamic strength. (a) Total absorption energy density; (b) ratio of total absorption energy.

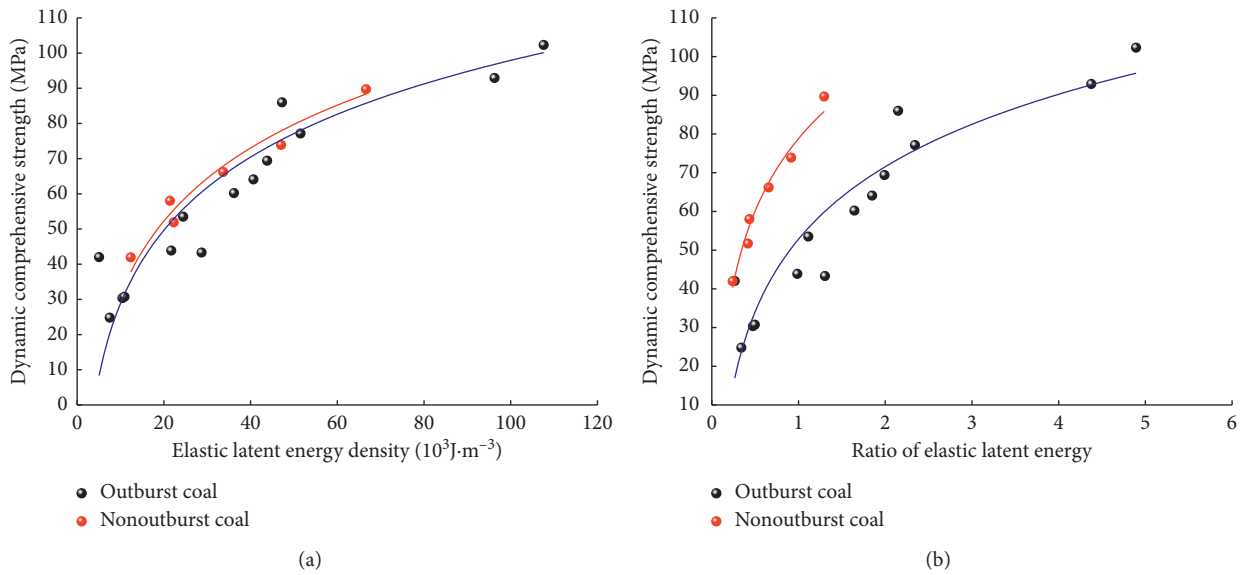


FIGURE 8: Relations of elastic latent energy density, ratio of elastic latent, and dynamic strength. (a) Elastic latent energy density; (b) ratio of elastic latent energy.

TABLE 4: The screening statistics and fractal computing results of fragments of outburst and nonoutburst coal.

Type	Specimen no.	Strain rate (s <sup>-1</sup> )	The cumulative mass under the sieve/g					Total mass of fragments (g)	Specimen mass (g)	<i>b</i>	Fractal dimension <i>D</i>
			<0.5 mm	<1 mm	<10 mm	<20 mm	<30 mm				
Outburst coal	D1	73	0.2	0.5	2.2	3.5	3.5	77.8	78.6	0.63	2.37
	D2	78	0.8	0.9	5.3	6.7	6.7	79.0	79.2	0.59	2.41
	D3	81	0.8	1.1	3.8	6.9	8.5	85.3	85.5	0.58	2.42
	D4	102	11	14.7	47.5	67.5	78.3	78.3	79.9	0.49	2.51
	D5	115	12.2	16.6	49.6	66.8	76.4	76.4	78.8	0.42	2.58
	D6	129	13.2	18.2	52.6	68.5	77.2	77.2	79.7	0.70	2.30
	D7	160	14.5	19.3	57.4	69.3	75.9	75.9	78.2	0.44	2.56
	D8	174	15.6	20.6	59.7	72.2	75.3	75.3	79.8	0.40	2.60
	D9	193	17.1	22.1	60.3	70.5	74.8	74.8	76.9	0.46	2.54
	D10	214	19.4	25.1	65.5	69.9	69.9	69.9	77.5	0.34	2.66
	D11	219	17.4	22.6	58.9	71.6	71.6	71.6	79.3	0.37	2.63
	D12	221	17.5	23.4	63.5	68.3	68.3	68.3	73.6	0.52	2.48
	D13	268	17.3	22.3	62.9	66.5	66.5	66.5	74.6	0.36	2.64
	D14	279	16.6	21.3	58.3	64.2	64.2	64.2	72.7	0.36	2.64
Nonoutburst coal	D15	96	0.1	1.3	38.5	87.1	87.1	87.1	89.2	1.61	1.39
	D16	120	0.3	2.0	39.2	75.4	76.8	76.8	79.4	1.46	1.54
	D17	125	0.4	2.5	50.5	71.5	75.6	75.6	83.0	1.27	1.73
	D18	145	2.5	5.7	48	80	90.1	90.1	86.9	0.89	2.11
	D19	177	2.2	6.3	54.6	75	77	77	82.5	0.80	2.20
	D20	186	1.4	5	59.4	76	76	76	83.7	0.69	2.31

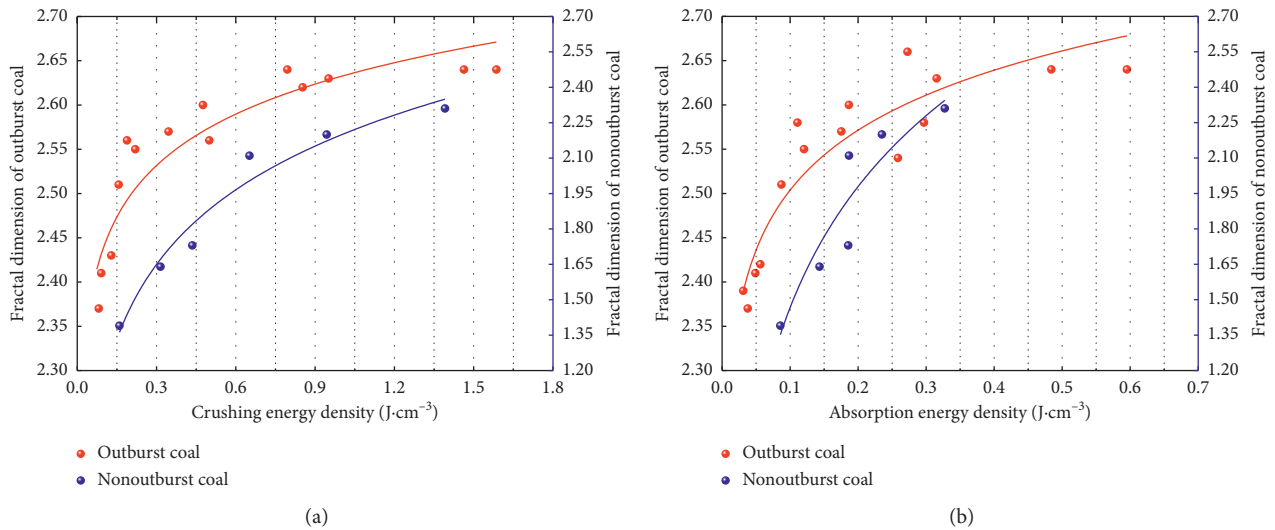


FIGURE 9: Relations of crushing energy density, absorption energy density and dynamic strength. (a) Crushing energy density; (b) absorption energy density.

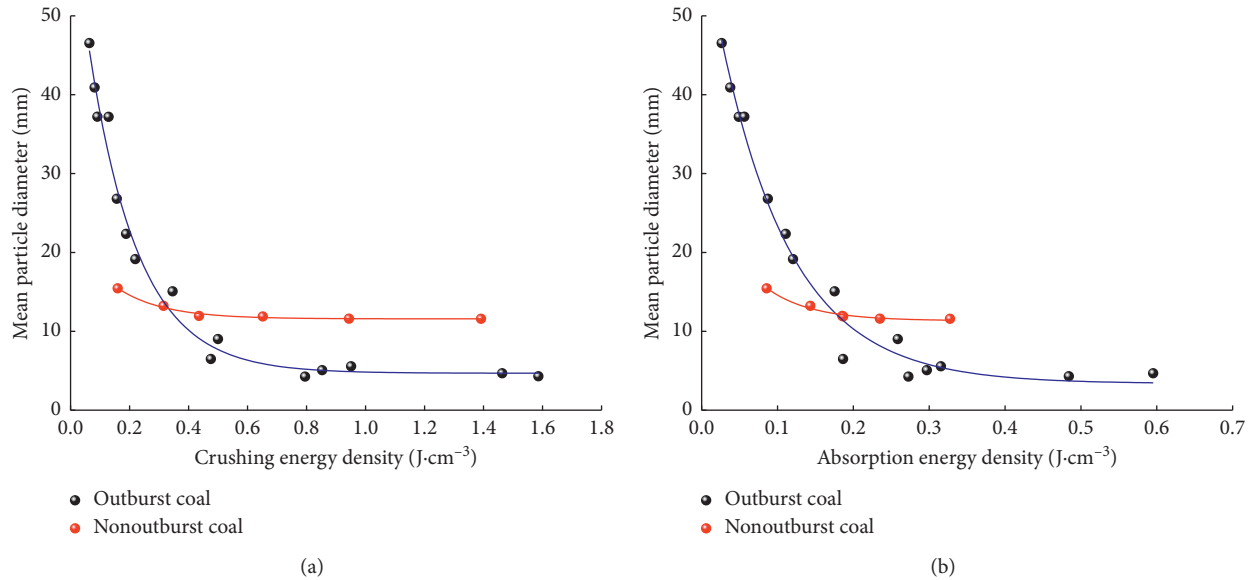


FIGURE 10: Relations of crushing energy density, absorption energy density, and mean particle diameter. (a) Crushing energy density; (b) absorption energy density.

## 5. Conclusions

- (1) Given the impact loads, crushing energy of coal is closely related with strain rate. Crushing energy shows an exponential growth with the increase of strain rate, indicating that more energy is used to damage the specimens. However, the energy dissipation rate of both outburst coal and non-outburst coal is basically constant. In other words, energy dissipation rate is kept constant at about 10%~20%, and it is a variable unrelated with strain rate.
- (2) With the increase of experimental strain rate, the absorption energy for the damage of coal and rock achieves an exponential growth, indicating that more energy is used to promote crack expansion and damage of specimens with the increase of loading strength. Moreover, outburst coal and nonoutburst coal show consistent responses to loads.
- (3) There is a good logarithmic relation between the dynamic compressive strength of coal and absorption energy density and elastic latent energy density. Both nonoutburst coal and outburst coal show almost the same energy adsorption under the same peak strength. Due to the higher hardness, the non-outburst coal has the higher peak strength given the same strain rate, so they have to absorb and store more energy. However, the outburst coal can absorb and store more times of energy for breakage than nonoutburst coals under the static test.
- (4) Fractal features of coal fragments under dynamic impacts are significantly. Moreover, fractal dimension and degree of fracture of specimens are positively related with strain rate, whereas mean particle diameter of fragment is negatively related. There is a

logarithmic growth relationship between the fractal dimension and strain rate. Moreover, the mean particle diameter of experimental fragment basically meets the negative exponential relationship with strain rate, indicating that coals need more energy to be broken into smaller pieces.

## Data Availability

All data included in this study are available upon request by contacting the corresponding author.

## Conflicts of Interest

The authors declare that there are no conflicts of interest regarding the publication of this article.

## Acknowledgments

This work was supported by the University Natural Science Foundation of Anhui Province (KJ2019A0098, KJ2017A091, and 1808085ME160).

## References

- [1] H. Lawson, A. Weakley, and A. Miller, "Dynamic failure in coal seams: implications of coal composition for bump susceptibility," *International Journal of Mining Science and Technology*, vol. 26, no. 1, pp. 3–8, 2016.
- [2] B. B. Beamish and P. J. Crosdale, "Instantaneous outbursts in underground coal mines: an overview and association with coal type," *International Journal of Coal Geology*, vol. 35, no. 1–4, pp. 27–55, 1998.
- [3] C. Mark and M. Gauna, "Evaluating the risk of coal bursts in underground coal mines," *International Journal of Mining Science and Technology*, vol. 26, no. 1, pp. 47–52, 2016.

- [4] H. Q. Zhu, S. H. Fang, Y. L. Zhang et al., "Study on the dynamic response characteristics of cylindrical coal-rock samples under dynamic loads," *Shock and Vibration*, vol. 2020, Article ID 8820316, 12 pages, 2020.
- [5] Z. T. Bieniawski and M. J. Bernede, "Suggested methods for determining the uniaxial compressive strength and deformability of rock materials," *International Journal of Rock Mechanics and Mining Science & Geomechanics Abstracts*, vol. 16, no. 2, pp. 137–140, 1979.
- [6] H. Zhang, Z. Wan, D. Ma, Y. Zhang, J. Cheng, and Q. Zhang, "Experimental investigation on the strength and failure behavior of coal and synthetic materials under plane-strain biaxial compression," *Energies*, vol. 10, no. 4, pp. 500–514, 2017.
- [7] F. Gao and H. Kang, "Experimental study on the residual strength of coal under low confinement," *Rock Mechanics and Rock Engineering*, vol. 50, no. 2, pp. 285–296, 2017.
- [8] B. B. Wu, R. Chen, and K. Xia, "Dynamic tensile failure of rocks under static pre-tension," *International Journal of Rock Mechanics and Mining Sciences*, vol. 80, pp. 12–18, 2015.
- [9] S. Gong, Z. Wang, L. Zhou et al., "Influence of cyclic impact loading and axial stress on dynamic mechanical properties of burst-prone coal," *Shock and Vibration*, vol. 2021, Article ID 6649308, 10 pages, 2021.
- [10] M. H. Ju, X. F. Li, and J. C. Li, "Large-scale asymmetric pulverization of fault zone: insights from rock axial strain in static and dynamic loading conditions," *International Journal of Rock Mechanics and Mining Sciences*, vol. 137, 2020.
- [11] X. F. Li, H. B. Li, Q. B. Zhang, J. L. Jiang, and J. Zhao, "Dynamic fragmentation of rock material: characteristic size, fragment distribution and pulverization law," *Engineering Fracture Mechanics*, vol. 199, pp. 739–759, 2018.
- [12] F. G. Zeng, "Grinding kinetic equation of coal characterized by particle size," *Journal of China Coal Society*, vol. 25, pp. 303–306, 2000.
- [13] H. X. Jiang, C. L. Du, and S. Y. Liu, "The effects of impact velocity on energy and size distribution of rock crushing," *Journal of China Coal Society*, vol. 38, pp. 604–610, 2013.
- [14] J. Luo, G. Huang, L. Zhang, F. Huang, and J. Zheng, "Micro shape of coal particle and crushing energy," *International Journal of Mining Science and Technology*, vol. 28, no. 6, pp. 1009–1014, 2018.
- [15] D. N. Whittles, S. Kingman, I. Lowndes, and K. Jackson, "Laboratory and numerical investigation into the characteristics of rock fragmentation," *Minerals Engineering*, vol. 19, no. 14, pp. 1418–1429, 2006.
- [16] D. J. Reddish, L. R. Stace, P. Vanichkobchinda, and D. N. Whittles, "Numerical simulation of the dynamic impact breakage testing of rock," *International Journal of Rock Mechanics and Mining Sciences*, vol. 42, no. 2, pp. 167–176, 2005.
- [17] L. M. Tavares, "Energy absorbed in breakage of single particles in drop weight testing," *Minerals Engineering*, vol. 12, no. 1, pp. 43–50, 1999.
- [18] B. Magnus and E. C. Magnus, "Measuring characteristics of aggregate material from vertical shaft impact crushers," *Minerals Engineering*, vol. 19, pp. 1479–1486, 2006.
- [19] T. Yan, W. Li, X. L. Bi et al., "A new evaluation method for rock-crushing efficiency based on crushing work ratio," *Acta Petrologica Sinica*, vol. 30, pp. 291–294, 2009.
- [20] A. Carpinteri and N. Pugno, "One, two, and three-dimensional universal laws for fragmentation due to impact and explosion," *Journal of Applied Mechanics*, vol. 69, no. 6, pp. 854–856, 2002.
- [21] C. Wang, Y. Cheng, M. Yi, B. Hu, and Z. Jiang, "Surface energy of coal particles under quasi-static compression and dynamic impact based on fractal theory," *Fuel*, vol. 264, Article ID 116835, 2020.
- [22] D. Maugis, "Subcritical crack growth, surface energy, fracture toughness, stick-slip and embrittlement," *Journal of Materials Science*, vol. 20, no. 9, pp. 3041–3073, 1985.
- [23] S. Takaomi and O. Masayuki, "Specific surface free energy and the morphology of synthesized ruby single crystals," *Journal of Crystal Growth*, vol. 318, pp. 76–78, 2011.
- [24] E. T. Stamboliadis, "The energy distribution theory of comminution specific surface energy, mill efficiency and distribution mode," *Minerals Engineering*, vol. 20, no. 2, pp. 140–145, 2007.
- [25] E. Gaziev, "Rupture energy evaluation for brittle materials," *International Journal of Solids and Structures*, vol. 38, no. 42–43, pp. 7681–7690, 2001.
- [26] E. G. Gaziev, "Strength and deformability of brittle polycrystalline materials in multiaxial stress-strain state: rupture energy evaluation for brittle materials," *Geomechanics and Geodynamics of Rock Masses*, vol. 1, pp. 31–40, 2018.
- [27] A. Sainoki, H. S. Mitri, D. Chinnasane, and A. K. Schwartzkopff, "Quantitative energy-based evaluation of the intensity of mining-induced seismic activity in a fractured rock mass," *Rock Mechanics and Rock Engineering*, vol. 52, no. 11, pp. 4651–4667, 2019.
- [28] H. L. Gu, M. Tao, X. B. Li et al., "The effects of water content and external incident energy on coal dynamic behaviour," *International Journal of Rock Mechanics and Mining Sciences*, vol. 123, Article ID 104088, 2019.
- [29] J. Feng, E. Wang, X. Chen, and H. Ding, "Energy dissipation rate: an indicator of coal deformation and failure under static and dynamic compressive loads," *International Journal of Mining Science and Technology*, vol. 28, no. 3, pp. 397–406, 2018.
- [30] X. J. Hao, G. Y. Pan, C. X. Ma et al., "Failure behavior and energy storage and release of hard coal under different static and dynamic loading states," *Advances in Civil Engineering*, vol. 2020, Article ID 8837289, 14 pages, 2020.
- [31] O. Vardar, C. Zhang, I. Canbulat, and B. Hebblewhite, "Numerical modelling of strength and energy release characteristics of pillar-scale coal mass," *Journal of Rock Mechanics and Geotechnical Engineering*, vol. 11, no. 5, pp. 935–943, 2019.
- [32] Z. Lu, W. Ju, F. Gao et al., "A new bursting liability evaluation index for coal -the effective elastic strain energy release rate," *Energies*, vol. 12, no. 19, p. 3734, 2019.
- [33] C. G. Zhang, F. Tahmasebinia, I. Canbulat et al., "Analytical determination of energy release in a coal mass," *Energies*, vol. 11, no. 2, p. 285, 2018.
- [34] R. Peng, Y. Ju, J. G. Wang, H. Xie, F. Gao, and L. Mao, "Energy dissipation and release during coal failure under conventional triaxial compression," *Rock Mechanics and Rock Engineering*, vol. 48, no. 2, pp. 509–526, 2015.
- [35] B. Lundberg, "A split Hopkinson bar study of energy absorption in dynamic rock fragmentation," *International Journal of Rock Mechanics and Mining Science & Geomechanics Abstracts*, vol. 13, no. 6, pp. 187–197, 1976.
- [36] H. P. Xie, Y. Ju, L. Y. Li et al., "Energy mechanism of deformation and failure of rock masses," *Chinese Journal of Rock Mechanics and Engineering*, vol. 27, pp. 1729–1740, 2008.
- [37] M. C. He, G. X. Yang, J. L. Miao et al., "Classification and research methods of rockburst experimental fragments," *Chinese Journal of Rock Mechanics and Engineering*, vol. 28, pp. 1521–1529, 2009.

- [38] Y. Liu, J. W. Zhou, and C. L. Du, "Fractal character of impact crushing granularity of coal lumps," *Journal of Vibration and Shock*, vol. 32, no. 3, pp. 18–21, 2013.
- [39] W. X. Gao and Y. T. Liu, "Energy dissipation rock damage under impact loading," *Chinese Journal of Rock Mechanics and Engineering*, vol. 28, pp. 1777–1780, 2003.
- [40] H. B. Zhao, Z. H. Li, S. H. Zhong et al., "Experimental study of mechanical properties of coal rock containing gas under uniaxial compression," *Journal of Mining and Safety Engineering*, vol. 27, pp. 131–134, 2010.



## Research Article

# Energy Action Mechanism of Coal and Gas Outburst Induced by Rockburst

Wenqing Zhang <sup>1</sup>, Chaomin Mu <sup>1</sup>, Dengke Xu,<sup>2</sup> and Zhongqing Li<sup>1</sup>

<sup>1</sup>School of Safety Science and Engineering, Anhui University of Science and Technology, Huainan 232001, Anhui, China

<sup>2</sup>School of Civil Engineering and Architecture, Anhui University of Science and Technology, Huainan 232001, Anhui, China

Correspondence should be addressed to Chaomin Mu; [chmmu@mail.ustc.edu.cn](mailto:chmmu@mail.ustc.edu.cn)

Received 21 February 2021; Revised 14 April 2021; Accepted 6 June 2021; Published 14 June 2021

Academic Editor: Bangbiao Wu

Copyright © 2021 Wenqing Zhang et al. This is an open access article distributed under the Creative Commons Attribution License, which permits unrestricted use, distribution, and reproduction in any medium, provided the original work is properly cited.

The essence of both rockburst and coal and gas outburst lies in fast energy release. In order to explore the energy action mechanism of coal and gas outburst induced by rockburst in rockburst and coal and gas outburst combined mines, the split Hopkinson pressure bar (SHPB) experimental device was firstly used to conduct uniaxial impact failure test of coal specimens prone to outburst under different strain rates, and their energy dissipation laws under impact loading were obtained. Next, under the engineering background of coal and gas dynamic phenomena induced by rockburst with different intensities in Xinyi Coal Mine and Pingdingshan Coal Group No. 12 Colliery in Henan Province and Dingji Coal Mine of Huainan Mining Group in Anhui Province, experimental study results were combined with numerical simulation analysis to discuss the energy mechanism of coal and gas outburst induced by rockburst. The study results show that the outburst can be divided into two different processes—critical outburst and outburst—according to the evolution law of outburst energy, and the critical energy conditions for coal and gas outburst are proposed. The minimum destructive energy range for the critical outburst of coal mass is obtained as  $(5-10) \times 10^4 \text{ J/m}^3$ . Under some low gas, high stress, or strong disturbance conditions, applied loads can become the main energy sources causing critical failure and even crushing and throwing of coal mass. The coal mass will present an interval splitting structure under dynamic loading, which is obviously different from the failure mode of coal mass under static actions.

## 1. Introduction

The coal and gas outburst and rockburst are the most serious dynamic disasters in the underground coal mining activities in various countries across the globe [1–6]. In shallow mining, the dynamic disaster is mostly manifested by the single appearance of coal and gas outburst or rockburst, while their interaction is not that prominent, and their prediction and prevention and control are usually separately implemented.

Rockburst usually happens in mining operation and civil engineering. There are diversified rockburst mechanisms, and the main factors are generally related to underground geometrical shape and geological conditions [7–9]. Rockburst in itself is the sudden release of elastic strain energy stored in the rock mass under the excavation unloading

effect, and it is an energy-driven dynamic instability phenomenon. Many scholars have investigated the dynamic mechanical behaviors of rockburst based on the energy theory and achieved prominent results. Cook [10] pointed out that energy release was one of the most important factors inducing rockburst and put forward the concept of energy release rate. Mitri et al. [11] proposed the burst potential index, expressing that rockburst would probably happen when the energy storage rate in the rock reached the energy storage limit. As indicated by Wiles [12], local energy release density (LERD) should be combined with the stress conditions to evaluate rockburst; namely, it could be used to predict rockburst only when approaching the stress conditions of rock mass strength. In order to understand rockburst from the angle of energy release, Jiang et al. [13] developed local energy release rate (LERR), which could be

used to predict the rockburst intensity very well. Xu et al. [14] combined LERR and limiting energy storage rate (LESR) to put forward a new energy index—rockburst energy release rate (RBERR).

Coal and gas outburst refers to the outburst phenomenon of mass coal or gas during the coal mining process. In recent hundred years, many scholars have explored this phenomenon, expecting to better understand its formation mechanism. A current viewpoint is that outburst means the intense dynamic instability of coal mass when the interaction of coals with abnormal ground stress, high gas pressure, and “inclination to outburst” reaches the critical conditions. The divergence among different theories lies in the different reasons for reaching the critical conditions of outburst. Many models such as pocket model, dynamic model, and multifactor model have been raised to explain the outburst mechanism [15, 16]. Hodot [17] and Zhao et al. [18] thought that the outburst could be divided into four phases: preparation, trigger, development, and termination. Díaz Aguado and González Nicieza [2] and Guan et al. [19] pointed out that the outburst conditions could be quantified through outburst thresholds such as gas pressure, gas content, and stress. However, it is difficult to estimate the energy participating in the outburst, not to mention to quantify it, because of the complexity of coal and gas outburst.

As the mining depth is increased, the interaction between two disasters—coal and gas outburst and rockburst—has started appearing, and therefore, they tend to coexist and combine each other. Especially in deep high-ground-stress zone, their interaction will be aggravated, which has gradually aroused high attention among domestic (Chinese) and foreign scholars. In rockburst and coal and gas outburst combined mine, the rockburst has induced coal and gas outburst, and the coal and gas outburst induced under low gas pressure has become more and more frequent. The gas concentrations in German Rhein-Westphal Mine, Ruhr Mine, and Husk Mine are elevated abnormally before and after the rockburst [20, 21]. The rockburst and mine earthquake-induced coal and gas outburst or abnormal gas emission have occurred in Laohutai Mine and Beipiao Taiji Mine in Liaoning Province, Hegang Coalfield in Heilongjiang, Huainan Dingji Mine, and Pingdingshan Coal Group No. 12 Colliery, China [22–25].

The former Soviet scholar Petukhov [26] put forward studying the two phenomena—rockburst and outburst—as a whole at the earliest; according to the increasing volume fraction of gas before and after rockburst, Айруни [27] proposed a doubt over whether it was rockburst that induced the increasing volume fraction of gas or it was the increasing volume fraction that induced rockburst or the two coexisted; Ogieglo et al. stated [28] that the gas emission quantity would be elevated when the working face was under vibration. In China, Zhang et al. [29] took the lead in proposing and establishing the theory of unified instability of rockburst and coal and gas outburst and deemed that rockburst was outburst without gas action while outburst was rockburst with nonnegligible gas action. Pan et al. [30] proposed the concept of coal and gas outburst and rockburst

combined dynamic disaster, put forward their integrated prediction and control, revealed the unification mechanism for the occurrence of this combined dynamic disaster, and established the judgment criteria for the uniform instability. Li et al. [31], Li et al. [32] and Wang et al. [33] expounded the internal relation, difference, induction and transformation mechanism, and transformation conditions of two disasters—rockburst and outburst at coal seam.

Materials usually show different failure modes and mechanical characteristics under static load and dynamic load conditions [34–36]. The quasistatic characteristics of coal and rock have been widely investigated, but its dynamic failure characteristics have not been fully recognized. Split Hopkinson pressure bar (SHPB) system has been generally used in dynamic tests at high loading rate, in order to determine the dynamic properties of brittle materials like concrete [37], glass [38] and rock [39, 40] under different strain rates. Shan et al. [41] and Liu et al. [42] used the SHPB device to perform impact tests of coal under different strain rates and obtained the failure deformation characteristics of coking coal and anthracite, etc. Mu and Gong [43] and Rong et al. [44] established a dynamic constitutive equation of coal mass and simulated its two damage forms—fast jumping type and slow stepping type—under impact load. Kong et al. [45, 46] studied the dynamic characteristics of gas-containing coal and established the dynamic constitutive equation of the gas-containing coal under impact load.

Both rockburst and coal and gas outburst refer to the fast energy release in essence, so they can be studied together from the aspect of dynamic energy. Under the engineering background of coal and gas dynamic phenomena induced by rockburst with different intensities in Xinyi Coal Mine and Pingdingshan Coal Group No. 12 Colliery in Henan Province and Dingji Coal Mine of Huainan Mining Group in Anhui Province, the SHPB experiment was combined to obtain the coal energy dissipation laws and investigate the energy mechanism for rockburst-induced coal and gas outburst. The judgment criteria for critical energy conditions and critical crushing energy of coal and gas outburst were proposed, thus providing a reference for recognizing and controlling the rockburst-induced coal and gas outburst.

## 2. Energy Analysis of Coal and Gas Outburst

The final energy condition for the coal seam to experience outburst-type crushing is as below [31]:

$$W_G + W_C + W_\Delta \geq W_P + W_D + W_V + W_B + \Delta K, \quad (1)$$

where  $W_G$  is total dilation energy of gas;  $W_C$  is elastic energy of coal;  $W_\Delta$  is energy entering the coal mass from surrounding rocks;  $W_P$  is energy consumed to crush coal mass into blocks;  $W_D$  is energy absorbed by surrounding rocks nearby the occurrence site of dynamic phenomenon;  $W_V$  is energy consumed by the coal vibration in the nearby region (smaller than 10%);  $W_B$  is energy consumed by the formation of air blast wave; and  $\Delta K$  is kinetic energy increased by the blocks.

The outburst process is divided into two different phases—critical outburst and outburst—and the critical energy condition for the coal and gas outburst is presented as follows:

$$W_{G1} + W_C + W_{\Delta} \geq W_{P1}, \quad (2)$$

where  $W_{G1}$  is total dilation energy of free gas;  $W_C$  is elastic energy of coal mass;  $W_{P1}$  is energy of coal crushing under the critical coal and gas outburst. The conditions for coal and gas outburst can be satisfied and the outburst will occur only when the sum of the energies applied by gas, surrounding rock, or other sudden loads to the coal mass is approximate to or exceeds the energy of coal crushing under critical outburst.

### 3. Energy Analysis of Coal Crushing under Impact Load

**3.1. Impact Test Results.** Soft coal extracted from soft layer was crushed; coal powders were sieved via 40-80-mesh screen, placed into a self-made coal compression tank, and finally made into cylindrical coal specimens (draw ratio: about 0.5) on a large rigid press.

This experiment was completed on the  $\Phi 75$  mm SHPB experimental system, and the device diagram is shown in Figure 1. The diameters of the impact bar, the incident bar, and the output bar are all 75 mm, and the lengths are 0.4 m, 4 m, and 2.5 m, respectively. The bar is made of high strength alloy steel with an elastic modulus of 195 GPa.

The basic parameters and experimental conditions of the specimen are shown in Table 1.

The crushing forms of coal specimens after the impact are shown in Figure 2.

According to the energy theory of stress wave, the size effect of different specimens was eliminated, and the relationship between coal crushing energy density and strain rate was calculated as seen in Figure 3.

It can be seen that the crushing energy density of each coal specimen presented an exponential increase with the strain rate, and their fitting relation could be expressed by.

$$w_d = 0.05e^{0.012\dot{\epsilon}}. \quad (3)$$

In general, the mass-frequency distribution in crushed coal follows the following law:

$$\frac{M(R)}{M} = 1 - \exp\left[-\left(\frac{R}{R_0}\right)^b\right], \quad (4)$$

$$b = \frac{\lg(M(R)/M)}{\lg R}, \quad (5)$$

where  $M(R)$  is accumulative mass of crushed coal with diameter of smaller than  $R$ , kg;  $M$  is total mass of crushed coal, kg;  $R_0$  is average size, mm. According to literature [47],  $D = 3 - b$ , and  $D$  is fractal dimension of crushed coal, while  $b$  is the slope of the line drawn by  $M(R)/M - R$ .

Standard screen was used to screen the experimental fragments, and the mesh diameters were 0.5, 1, 10, 20, and

30 mm, respectively. According to (4) and (5), the fractal dimension of experimental fragments is calculated, as shown in Table 2.

The relationship between fractal dimension and crushing energy density of crushed coal specimens is seen in Figure 4.

With the increase in the impact load intensity, the degree of crushing was elevated after the coal failure, the proportion occupied by tiny fragments was significantly enlarged, and the fractal dimension presented a logarithm growth relation with the crushing energy density, indicating that the higher the degree of specimen crushing, the higher the intensity of impact load needed. This is basically identical with the conclusions drawn in other literatures with respect to fractal characteristics of rock and anthracite, etc. under impact failure.

The average particle size of crushed specimens can be expressed by.

$$\bar{d} = \frac{\sum \bar{d}_i \eta_i}{\sum \eta_i}, \quad (6)$$

where  $\bar{d}_i$  is average size of crushed blocks retained in a sieve with some specifications during the sieving process, mm;  $\eta_i$  is mass percentage of crushed blocks intercepted in the sieve with the corresponding pore diameter, %.

As the sudden load energy was increased, the average size of crushed blocks was rapidly reduced, and there was a turning point. It could be seen from Figure 5 that when the experimental strain rate exceeded 200 s and the crushing energy density of sudden load reached  $6.5 \times 10^5$  J/m<sup>3</sup>, the average particle size of crushed blocks was approximately unchanged; at the time, the specimen was completely crushed into powders with extremely uniform distribution, and the energy required by the further crushing presented an exponential growth. This coincides with appearance and separation of coal powders following the coal and gas outburst in soft coal.

**3.2. Critical Crushing Energy.** According to the study of Hu [48] regarding the crushing energy of coal mass, the following can be obtained:

$$W_p = 46914 \rho f^{1.437} Y^{1.679}, \quad (7)$$

where  $f$  is firmness coefficient of coal mass;  $Y$  is mass percentage occupied by coal specimens with particle size of below 0.2 mm after crushing in the total mass of coal specimens. In consideration that the coal mass will be further crushed after the outburst, the  $Y$  value under critical outburst should be much smaller than that after the outburst. The relationship between crushing energy of Tolsti coal seam and particle size of coal specimen is listed in literature [49]. When the crushing energy is  $7 \times 10^4$  J/m<sup>3</sup>, the mass percentage occupied by coal specimens with particle size of below 0.375 mm in the total mass of coal specimens is 1.28%, 1.57% under crushing energy of  $12 \times 10^4$  J/m<sup>3</sup>, and 2.2% under crushing energy of  $16 \times 10^4$  J/m<sup>3</sup>. Therefore,  $Y$  value is taken as 2.0 under critical outburst, and  $W_p$  is  $5.6 \times 10^4$  J/m<sup>3</sup> when the firmness coefficient  $f$  is 0.4.

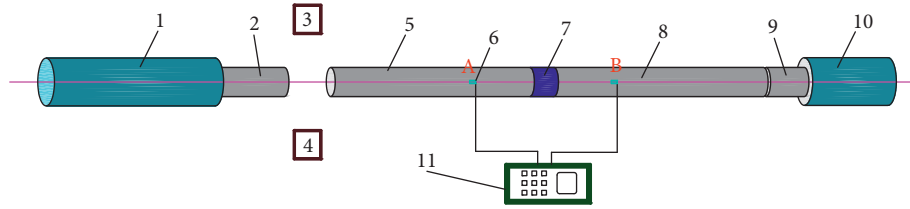


FIGURE 1: Sketch map of split Hopkinson pressure bar testing system. 1: air cannon; 2: drop bar; 3: laser unit; 4: laser receiver; 5: incident bar; 6: resistance strain gage; 7: test specimen; 8: transmission bar; 9: absorbing bar; 10: bumper; 11: superdynamic strain gage.

TABLE 1: The basic parameters and experimental conditions of the specimen.

Serial number	Quality (g)	Height (cm)	Diameter (cm)	Draw ratio	Bullet velocity (m·s <sup>-1</sup> )	Strain rate (s <sup>-1</sup> )
1	85.5	3.61	5	0.72	1.877	73
2	80.4	3.39	5	0.68	4.108	78
3	79.9	3.37	5	0.67	4.032	81
4	79.2	3.36	5	0.67	6.203	101
5	79.6	3.38	5	0.68	6.416	115
6	79.8	3.4	5	0.68	7.175	129
7	79.4	3.34	5	0.67	8.903	160
8	78.9	3.36	5	0.67	7.417	174
9	79.3	3.36	5	0.67	10.36	193
10	77.5	3.24	5	0.65	8.523	214
11	69	2.84	5	0.57	8.602	219
12	80.9	3.49	5	0.70	10.81	221
13	72.7	3.03	5	0.61	9.723	268
14	74.6	3.07	5	0.61	9.79	279

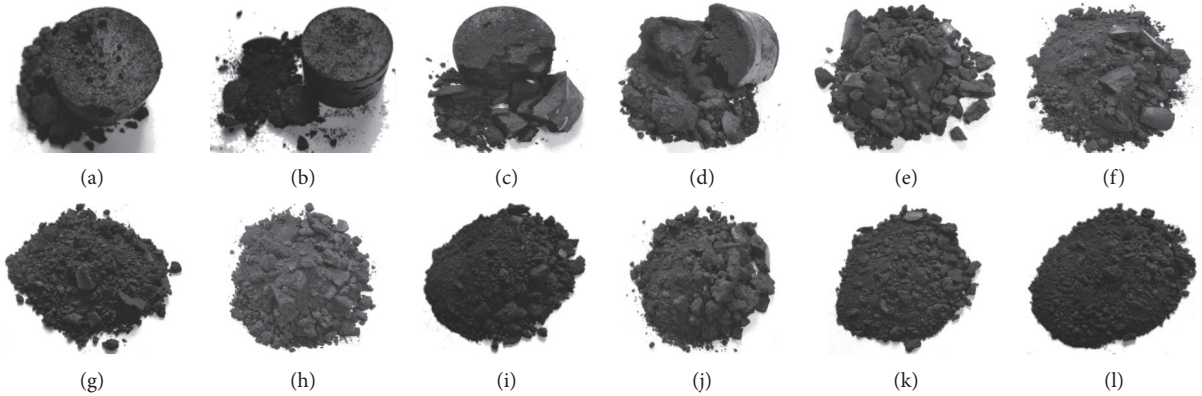


FIGURE 2: Specimens after impact. (a) 78 s. (b) 81 s. (c) 102 s. (d) 115 s. (e) 129 s. (f) 160 s. (g) 174 s. (h) 193 s. (i) 214 s. (j) 219 s. (k) 268 s. (l) 279 s.

As shown in Figure 1, the experimental strain rate corresponding to the critical state (crushed but not dispersed) of coal mass was about 80/s, and its actual crushing energy was about  $9 \times 10^4 \text{ J/m}^3$ . Based on the fractal results of impact lumpiness,  $Y \approx 2$ ,  $f = 0.6$ , and  $\rho = 1.4 \text{ kg/m}^3$ , which were substituted into (6) to obtain the critical crushing energy of coal mass as  $1.01 \times 10^5 \text{ J/m}^3$ , which was very approximate to the experimentally measured crushing energy. Therefore, the critical crushing energy of coal with  $f = 0.6$  was about  $1 \times 10^5 \text{ J/m}^3$ . However, the coal masses from different sources with different coal qualities have different hardness values and  $f$  values, so their critical

crushing energies will also be different. Hence, no unified judgment criteria for critical crushing energy have been proposed. Nevertheless, outburst coals are generally soft, their  $f$  values will not be that different, so a standard scope of critical crushing energy can be given as about  $(5-10) \times 10^4 \text{ J/m}^3$ .

#### 4. Numerical Simulation and Field Analysis of Rockburst-Induced Coal and Gas Outburst

4.1. Modeling. LS-DYNA software was used in this numerical simulation. LS-DYNA software is a general explicit

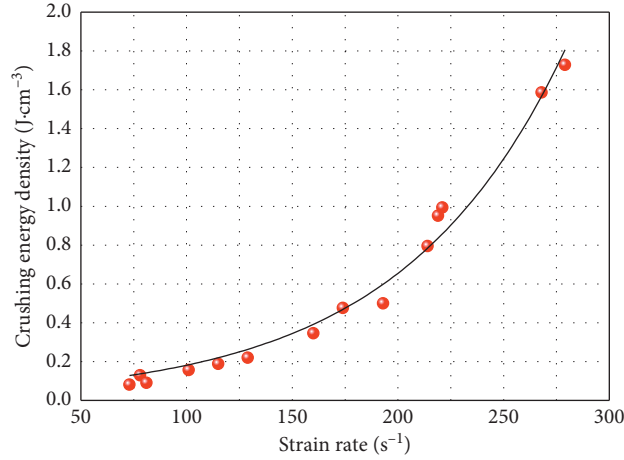


FIGURE 3: Relationship between crushing energy density and strain rate.

TABLE 2: Fractal dimension of fragment after impacting outburst coal.

Serial number	Strain rate ( $s^{-1}$ )	$b$	Fractal dimension $D$	Correlation coefficient $R$
1	73	0.63	2.37	0.990
2	78	0.59	2.41	0.962
3	81	0.58	2.42	0.992
4	102	0.49	2.51	0.999
5	115	0.44	2.56	0.996
6	129	0.45	2.55	0.995
7	160	0.43	2.57	0.991
8	174	0.40	2.60	0.986
9	193	0.44	2.56	0.996
10	214	0.36	2.64	0.959
11	219	0.37	2.63	0.983
12	221	0.38	2.62	0.992
13	268	0.36	2.64	0.955
14	279	0.36	2.64	0.966

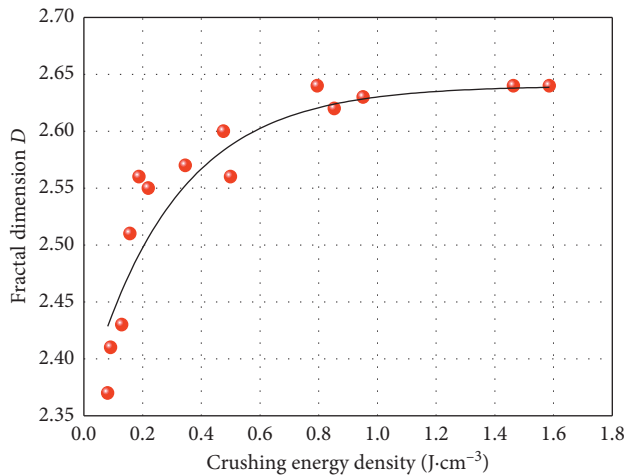


FIGURE 4: Relationship between fractal dimension and crushing energy density.

dynamic analysis program, especially suitable for solving a variety of two-dimensional and three-dimensional nonlinear structure of high-speed collision, explosion, and other nonlinear dynamic impact problems.

The driving working face was taken as the study object to investigate the failure characteristics of coal mass under the action of external sudden load. The model specification was  $15\text{ m} \times 10\text{ m}$ , where the thickness of both roof and floor was  $3\text{ m}$ , the thickness of coal seam was  $4\text{ m}$ , and the concrete geometric dimensions are shown in Figure 6.

The basic physical and mechanical parameters of the model are listed in Table 3.

According to related studies [50], the stress wave caused by impact load can be simplified into a triangular pulse load through the propagation for a certain time as shown in Figure 7.

The dynamic constitutive equation of coal mass constructed in literature [42] was embedded into the large-scale finite element analysis software to numerically simulate the coal damage under sudden loading action with peak intensities of  $P_{\max} = 30\text{ MPa}$ ,  $50\text{ MPa}$ , and  $70\text{ MPa}$ . Meanwhile, the cases of coal and gas outburst occurring in domestic coal mines in recent years are sorted out, and the three most similar cases are selected (shown in Figure 8). By comparing the results of SHPB experiment and numerical simulation, the coal body fracture characteristics and energy dissipation laws in the process of coal and gas



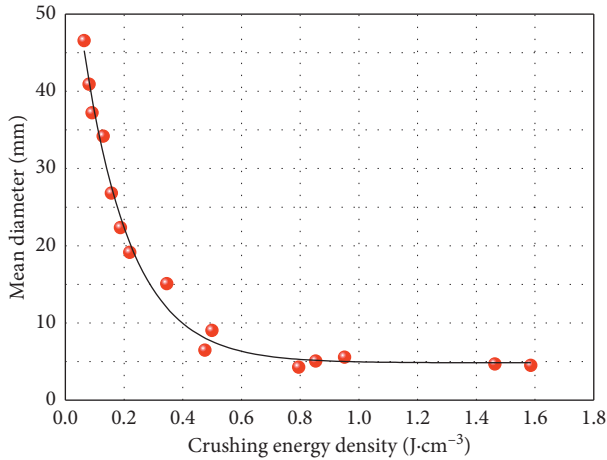


FIGURE 5: Relationship between mean diameter and crushing energy density.

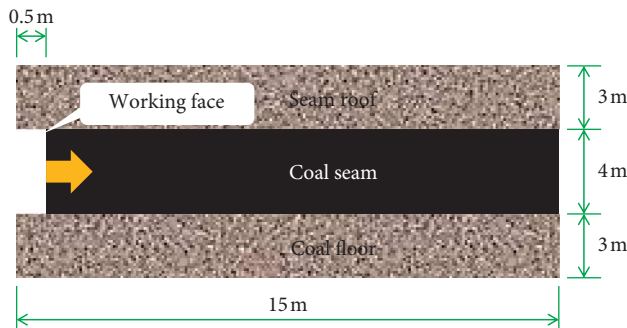


FIGURE 6: Dimensions of numerical model.

TABLE 3: Basic parameters of the model.

Parameter	Value
Elastic modulus of rock (GPa)	40
Poisson ratio of rock	0.25
Density of rock ( $\text{kg}\cdot\text{m}^{-3}$ )	2300
Cohesion of rock (MPa)	20
Internal frictional angle of rock ( $^{\circ}$ )	27
Elastic modulus of coal (GPa)	20
Poisson ratio of coal	0.4
Density of coal ( $\text{kg}\cdot\text{m}^{-3}$ )	1400
Cohesion of coal (MPa)	2.5
Internal frictional angle of coal ( $^{\circ}$ )	40

outburst caused by impact loads of different intensities were explored.

#### 4.2. Numerical Simulation and Case Analysis under Suddenly Applied Load of 30 MPa

4.2.1. Numerical Simulation. When the impact load of 30 MPa was applied to the coal mass at rate of 4 ms, it could be seen from the numerical simulation results that the first oblique crack appeared on the coal mass until 3.908 ms as shown in Figure 9(a), because of loading delay caused by the

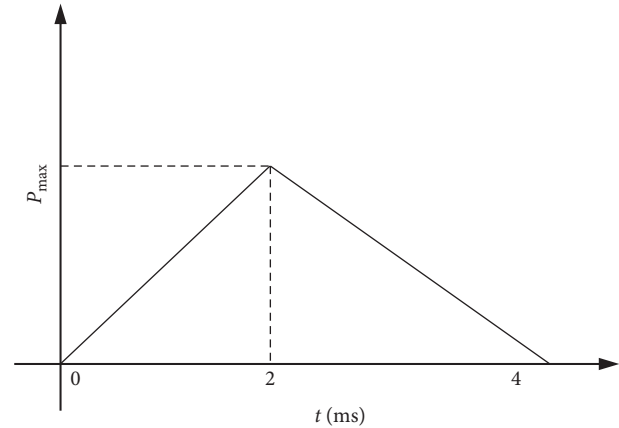


FIGURE 7: Load time-history curves.

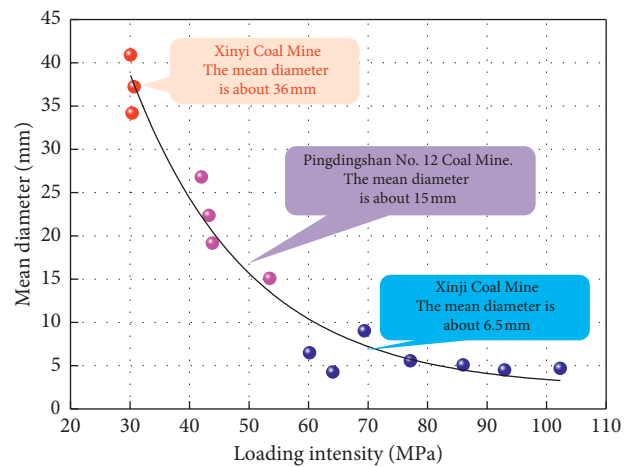


FIGURE 8: Relationship between mean diameter and loading intensity.

propagation of stress wave in the coal mass for a certain time. With the continuous loading of stress wave until 4.887 ms, the second oblique crack appeared and ran through the first crack, thus providing a channel for gas migration and desorption, and at the time, the coal permeability started increasing as shown in Figure 9(b). With the propagation of stress wave in coal mass, the compression wave would be transformed into tensile stress wave when encountering reflectors like cracks, thus causing further tensile failure of coal mass; new cracks were continuously formed until the energy of stress wave was exhausted at 14.66 ms; multilayered annular cracks were formed in the coal mass nearby the loading end, which damaged the remote coal mass to a certain extent; and microcracks were then formed as shown in Figure 9(f).

From the SHPB experiment, the experimental strain rate was about 80/s when the external load intensity was 30 MPa in the simulation, and the crushing energy input into the coal mass was about  $9 \times 10^4 \text{ J}/\text{m}^{-3}$ . According to the impact test results, the load intensity was not enough to cause the specimen failure, and only some crushed blocks were peeled off as shown in Figure 10. The coal mass could still keep intact, broken, but not dispersed, which was





FIGURE 9: Numerical simulation under rockburst of 30 MPa. (a) 3.908 ms; (b) 4.887 ms; (c) 5.865 ms; (d) 6.844 ms; (e) 7.822 ms; (f) 14.66 ms.

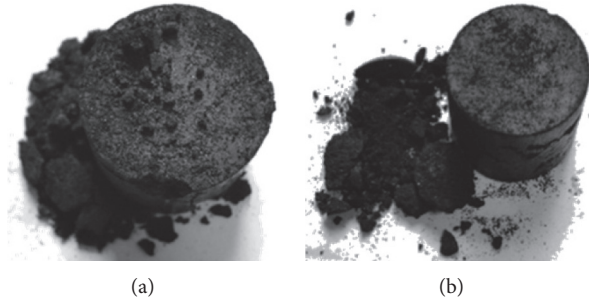


FIGURE 10: SHPB experimental results at strain rate of about 80 s. (a) 78 s. (b) 81 s.

embodied by dynamic phenomena like sound and slugging from a macroscopic perspective. Meanwhile, cracks were increased in the coal mass with enhanced gas permeability, but restricted by the gas desorption rate, and the emission amount presented a certain time delay and persistence.

**4.2.2. Outburst Case Analysis: Outburst Accident on Driving Working Face 12011 Belt Roadway in Xinyi Mine, Henan Province.** On July 11, 2009, when the blasting driving construction was implemented at about 21 m of 12011 belt roadway from the crossheading port in Xinyi Mine, Henan Province, coal blasting with loud sound took place continuously at 111 m of working face of this belt roadway from the crossheading port after the blasting continued for 130 min. After another 10 min, the abnormal gas emission exceeded the limit, the maximum concentrate reached about 11%, and the total gas emission was about  $700 \text{ m}^3$ , without significant coal falling or coal outburst. At 1 h, the gas concentration declined to below 1%.

It was found through the field reconnaissance that the head-on coal mass on the working face was shifted outside for about 50 cm, and a crack with length of about 8 m, width of about 6 cm, and detectable depth of about 1 m appeared on the floor 16 m away from the head-on place as shown in Figures 11 and 12.

The geodetic survey data of the coal mine showed that the gas content at this coal seam was  $8.38\text{--}12.84 \text{ m}^3/\text{t}$  (average content:  $9.86 \text{ m}^3/\text{t}$ ), the gas pressure was  $0.57\text{--}1.25 \text{ MPa}$  (average pressure:  $0.81 \text{ MPa}$ ), and the coal was soft with firmness coefficient of  $f=0.22\text{--}0.65$  (average value: 0.35). Before the coal blasting occurred, the gas concentrations in both head-on place and return air of the belt roadway were lower than 0.5%. In addition, no large rupture and fold structures existed in the scope of the mine, and no apparent geological structures were seen nearby the occurrence site of dynamic phenomenon. It could be

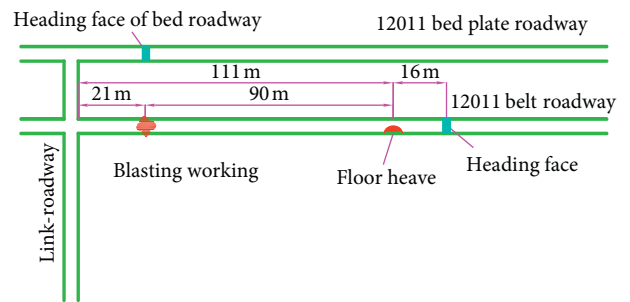


FIGURE 11: Location of coal and gas dynamic phenomenon in Xinyi Mine, Henan Province.

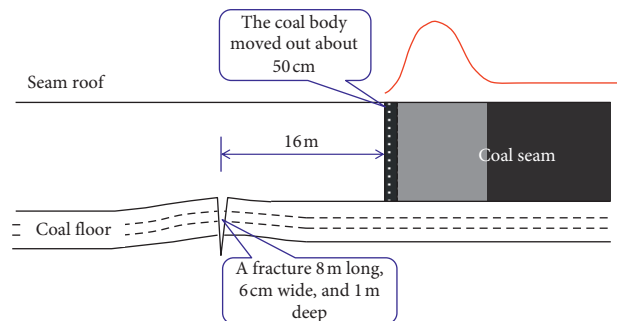


FIGURE 12: Profile map of working face outburst.

inferred that the gas dynamic phenomenon was triggered by floor fracture-type rockburst.

According to the field microearthquake observation results, the energy generated by the rockburst triggered by this floor fracture was about  $1 \times 10^5 \text{ J}$ . The existing studies have shown that the energy used to generate vibration and received by the monitoring equipment in the formation of primary rockburst accounts for about 5%–10% in the total energy. If calculated by 10%, here the energy generated by this rockburst was about  $1 \times 10^6 \text{ J}$ . In addition, the

occurrence source of floor fracture was only 16 m from the location of gas dynamic phenomenon, and it could be approximately deemed that the impact energy generated by the vibration was totally input into the nearby coal mass without attenuation.

Furthermore, the outward shift of head-on coal mass triggered by rockburst was about 0.5 m, while the sectional area of working face was  $18.9 \text{ m}^2$ , and then the total volume of coal mass experiencing outward shift was about  $9.5 \text{ m}^3$ . Hence, the energy density input by rockburst into the coal mass could be estimated as  $1.05 \times 10^5 \text{ J/m}^3$ . By combining the field gas data, the gas content and gas pressure in the coal seam were  $Q = 9.86 \text{ m}^3/\text{t}$  and  $P_0 = 0.74 \text{ MPa}$ , respectively. According to literature [47], the dilation energy of gas participating in the coal failure could be calculated as  $2.3 \times 10^4 \text{ J/m}^3$ .

To sum up, in this dynamic phenomenon, the total energy of gas and external rockburst acting upon the coal mass was about  $1.28 \times 10^5 \text{ J/m}^3$ , which was slightly greater than the minimum energy intensity criterion needed by the critical failure of coal mass as given in the previous part. Therefore, it was just enough to trigger the failure, but the coal mass was crushed but not dispersed, and internal cracks were generated, which provided a channel for the gas migration and desorption. By a comparison between the two input energies, the dilation energy of gas was only 1/5 of the impact vibration energy, so the main energy source triggering this dynamic phenomenon was rockburst caused by the floor fracture. Meanwhile, as the gas pressure was low at the coal seam, the generated minimum dilation energy of gas was not enough to trigger the coal outburst, no coal mass was thrown out, but only abnormal gas emission took place.

As the desorption of adsorbed gas is a slow process while the free gas only accounts for about 10% of total gas, the gas emission on the site showed a certain time delay and continuity, the gas concentration exceeded the limit after 10 min, reaching about 11%, and after about 1-2 h, about over 90% of the gas inside the coal mass was desorbed and released, and the field gas concentration was gradually recovered to below 1%.

### 4.3. Numerical Simulation and Case Analysis under Suddenly Applied Load of 50 MPa

**4.3.1. Numerical Simulation.** When the simulated load intensity reached 50 MPa, the crack propagation was obviously aggravated in the coal mass. Multilayer annular spalling occurred in the coal mass at near loading end at 5.862 ms as shown in Figure 13(c). The coal mass started crushing since 6.841 ms, and the crushing was continuously aggravated and extended till the roof of coal seam as shown in Figure 13(f). Apparent cracks appeared at the far end of coal mass.

From the SHPB experiment, the experimental strain rate was about 160/s when the intensity of external applied load reached 50 MPa, and the crushing energy input into the coal mass reached about  $3.5 \times 10^5 \text{ J/m}^3$ . The energy input into

the coal mass was enough to trigger the coal failure and instability, and the coal was crushed into large blocks as shown in Figure 14. After the coal mass was crushed, the crushed coal mass was damaged and peeled off the coal wall and even thrown out for a certain distance under the releasable elastic latent energy accumulated in the coal mass and internal energy of gas.

**4.3.2. Outburst Case Analysis: Outburst Accident during the Driving Process on the Working Face of 17310 Conveyor Lane in Pingdingshan Coal Group No. 12 Colliery.** At 17:00 on March 19, 2006, the coal and gas dynamic phenomenon triggered by the rockburst occurred after the blasting operation on the working face of 17310 conveyor lane in Pingdingshan Coal Group No. 12 Colliery as shown in Figure 15.

Through the field reconnaissance, the coal and gas dynamic phenomenon presented the following characteristics: (1) about 46 t of coal mass was thrown out, without separation phenomenon; the throwing angle of coal mass was close to the natural angle of repose, the stacking length along the roadway was 5.6 m, where the first 4.0 m showed complete-roadway stacking, and the remaining 1.6 m presented half-roadway stacking. (2) Above the stacked coal and rock was a layer of crushed coal blocks, and there was a small quantity of crushed coal inside the coal and rock, without separability. (3) From the thrown crock and rock and stacking status, there was no gas channel. (4) No floating dust was stacked on the surface or at rear part of the thrown surface. (5) The total gas emission was  $1,280 \text{ m}^3$ , which was converted into gas emission per ton of coal of  $28 \text{ m}^3/\text{t}$ , approaching the gas content at the coal seam. (6) The coal wall at left of the roadway bulged for 0.9 m; obvious deformation of trapezoid beam and reinforcing mesh triggered by outward impact force could be observed at the roadway roof, the tapered end of anchor rope was loosened, and obvious nonuniform subsidence took place at the immediate roof. The upper-wall trapezoid beam was deformed; the scraper conveyor on the floor deviated towards the right wall of roadway for  $5^\circ$ , and the maximum displacement reached 0.9 m. The overall outward shift of coal wall was observed at the lower wall of the head-on roadway and outward head-on roadway, the displacement and thickness of the lower wall were 10 m and 0.8 m, respectively, the floor bulged for 0.5 m, and the head-on place was shifted out of the wall mass for 3 m. Therefore, the power source for this dynamic phenomenon mainly came from the left side of the roadway.

The elevation of the working face in 17310 conveyor lane where the coal and gas dynamic phenomenon happened was  $-1,100 \text{ m}$ , and it was located at the lower segment of Likou large syncline under serious influence of tectonic stress. The immediate roof of this coal seam consisted of sandstone and mudstone with an average thickness of 0.8 m, while the upper roof was composed of sandstone and fine sandstone with average thickness of 8.0 m. The coal seam was dry and brittle, the coal failure types were II-III, and the firmness coefficient of coal was  $f = 0.4-1.5$ . Influenced by the mining-induced stress like roadway blasting excavation and

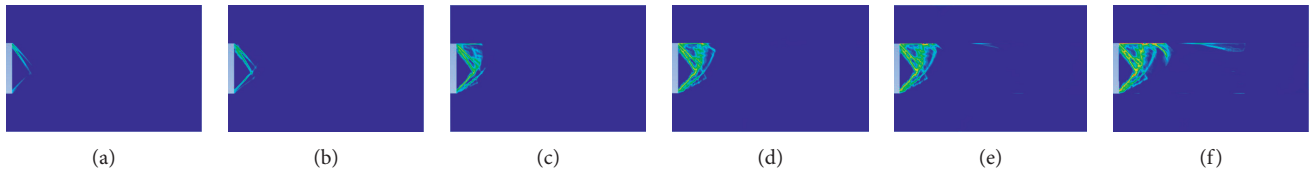


FIGURE 13: Numerical simulation of rockburst under load of 50 MPa. (a) 3.907 ms; (b) 4.884 ms; (c) 5.862 ms; (d) 6.841 ms; (e) 7.819 ms; (f) 14.66 ms.

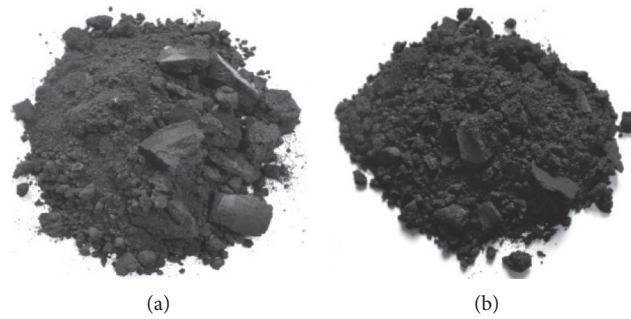


FIGURE 14: SHPB experimental results under strain rate of about 160 s. (a) 160 s. (b) 174 s.

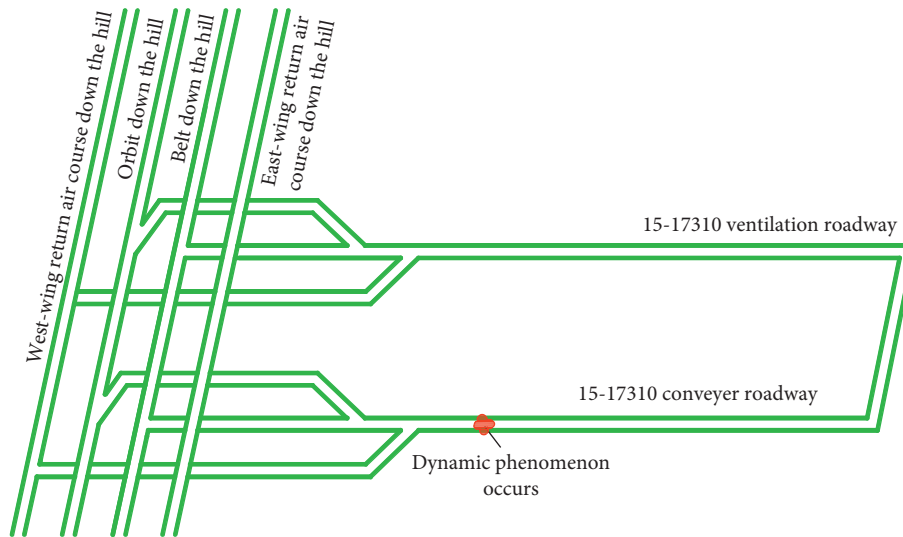


FIGURE 15: Location of dynamic phenomenon in 17310 conveyor lane of Pingdingshan Coal Group No. 12 Colliery.

tectonic stress, stress concentration could be easily formed in the coal mass behind the working face, and thus a large quantity of elastic latent energy was accumulated. When the coal and rock mass reached or exceeded the ultimate strength, the coal mass would experience a failure. The gas occurring in the coal mass released gas energy with the fracture of coal mass, and the energy superposition at the time created conditions for the coal and gas dynamic phenomenon.

Given this, this was a gas dynamic phenomenon induced by the rockburst in the zone with high ground stress, concentrated stress, and gas pressure.

From the gas data, the gas pressure in the coal seam was 0.74 MPa (after the antioutburst measures were taken), and the dilation energy of gas participating in the coal failure

could be calculated as about  $4.68 \times 10^4 \text{ J/m}^3$ , which was approximate to the lower limit of the standard scope  $((5 \sim 10) \times 10^4 \text{ J/m}^3)$  of critical crushing energy as given in the previous part, indicating that this outburst is the product of joint action of gas and external applied load. Moreover, due to high gas content in the coal seam, a large quantity of gas was released after the critical failure, the coal mass was further crushed and thrown out, and thus a large quantity of coal mass was extruded out.

#### 4.4. Numerical Simulation and Case Analysis of Rockburst under Suddenly Applied Load of 70 MPa

4.4.1. Numerical Simulation. From the numerical simulation results, the coal crushing speed was significantly

accelerated when the intensity of applied load reached 70 MPa in comparison with the previous two circumstances. The coal mass at loading end presented multiple layered cracks at 3.906 ms, the cracks basically ran through each other at 5.863 ms, and multilayer annular spalling was generated as shown in Figures 16(a)–16(c). With the continuous and reciprocal propagation of stress wave, the original cracks were further stretched, and meanwhile, the surrounding coal mass experienced continuous tensile failure, and the cracks were extended to deep parts. Since 6.842 ms, as a large quantity of elastic latent energy was stored in the coal mass within the stress concentration zone in front of the working face, the coal mass was crushed when the energy storage limit (namely, ultimate strength) of the coal mass was exceeded. Moreover, the elastic latent energy was continuously released outward, thus damaging the surrounding coal mass as shown in Figures 16(d) and 16(e). The surplus elastic latent energy and released internal energy of gas further acted upon the crushed coal mass, so the crushed coal mass in the pressure relief zone was continuously peeled off the coal wall and even thrown towards the exterior space. Moreover, a wedge-shaped hole with large mouth and small cavity might be formed on the coal mass. In the later loading phase as shown in Figure 16(f), the coal failure was aggravated with the continuous energy release, the supporting stress was reduced and the roof and floor nearby the coal mass started experiencing failures, along with dynamic phenomena like roof caving or floor bulging deformation. As the releasable elastic latent energy stored in the coal mass was gradually released and exhausted, the coal and rock continuously stacked in the hole formed greater and greater supporting force on the hole wall, so the coal mass around the hole wall was not further fractured, and the outburst process became unsustainable and was even terminated.

From the SHPB experimental results, the strain rate was about 200/s and the crushing energy input into the coal mass reached about  $6.5 \times 10^5 \text{ J/m}^{-3}$  when the intensity of external applied load reached 70 MPa. At the time, the energy input could trigger the intense coal failure, and the coal might be even crushed into powders as shown in Figure 17.

#### 4.4.2. Outburst Case Analysis: Outburst Accident on the Working Face of 1331 (1) Conveyor Lane in Dingji Mine.

The working face of 1331 (1) conveyor lane where the accident occurred was located in east No. 2 mining area of Dingji Mine, and the burial depth and coal thickness were 870 m and 2.1–2.2 m, respectively. At the roof was sandy mudstone with a thickness of 6.0 m, and at the immediate floor was mudstone with thickness of 3.6 m. The excavation team was on the scene of this accident, and the pattern of two rows per cycle was adopted. The one-cycle construction and anchor bolt supporting were already completed at about 18:40, and the second-cycle drivage was started. At 19:40, the coal mass was thrown out in right front of the working face. The roof wall zone at right of the roadway presented irregular hemiellipsoidal collapse, the top steel belts in the first row at the left wall of the driving working face were exposed

forward on the roof for 1.6 m (there were cutting nicks of roadheader at the roof of the working face), the right wall caved forward for 4.6 m, and the maximum caving height was 1.7 m. An irregular hole appeared above the coal mass at the interface between right wall and working face on the field, with diameter of 0.65 m and depth of about 3 m, and the horizontal distance from the center line of hole to the extension cord of the right wall of the roadway was 1.5 m as shown in Figure 18. The gas concentration in the hole was about 0.8%.

The disaster triggered by gas dynamic phenomenon showed the following characteristics.

The maximum value of gas concentration sensor T2 on the working face was 2.02% after the dynamic phenomenon. Through the calculation, the total gas emission and coal quantity were  $235.4 \text{ m}^3$  and 35 t, respectively; due to this dynamic phenomenon, the average gas emission per ton of coal was  $6.7 \text{ m}^3/\text{t}$ , which was smaller than the standard; namely, the gas emission per ton of coal in the coal and gas outburst was greater than  $30 \text{ m}^3/\text{t}$  or twice the gas content in the coal seam. Moreover, except for the deaths caused by coal burying, other deaths on the accident scene had no sign of asphyxia, and the gas concentration at the bottom of cavity formed by the dynamic phenomenon was about 0.8% after the accident took place for 135 h.

Before the accident took place, there was no coal blasting sound during the working shift, and the gas concentration in the return air did not experience any abnormal change. The right wall of the roadway and the coal wall on the working face were caving, where the right wall caving width of the roadway was about 1.6 m, and the maximum depth was 0.5–0.6 m. The coal wall caving width and depth in right front of the working face were about 2 m and 0.9 m, respectively.

The driver of roadheader heard a sound of “bang,” just like blasting sound when the accident occurred. The field staffs felt vibration and blast, the air duct was obviously agitated, the well-connected metal net was not torn open, and the air duct and existing supporting facilities were not obviously damaged.

Partial coal mass was thrown out, and the distance from stacked coal to the working face was 4–6 m. The cavity formed after the coal mass was thrown out was located the interfacial zone (wedge shape) between right wall and coal wall of the working face, with width of about 3–4 m and depth of 6–7 m, and it presented pinching-out towards the deep part. After the coal and gangues were cleared away from the field, the residual cavity was about 0.65 m in width and 3 m in depth, and there was a split fissure surface at the coal seam inside the cavity with clear stratification as shown in Figure 19. The coal stacked on the field had no obvious separation phenomenon, which was obviously different from the traditional coal fracture form induced by coal and gas outburst.

By comparing Figures 16 and 19, it could be found that the coal mass generated vertical split cracks under the impact load, and the cracks were under interbed interval distribution. With the increase in the impact load, the through cracks (red region in the figure) were wedge-shaped, seriously damaged wedge-shaped through cracks were



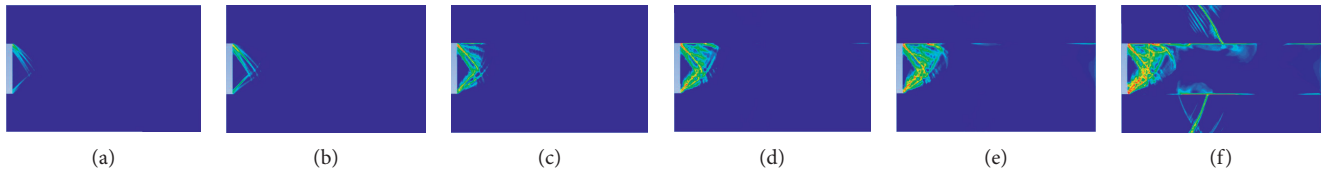


FIGURE 16: Numerical simulation of rockburst under load of 70 MPa. (a) 3.906 ms; (b) 4.884 ms; (c) 5.863 ms; (d) 6.842 ms; (e) 7.82 ms; (f) 15 ms.

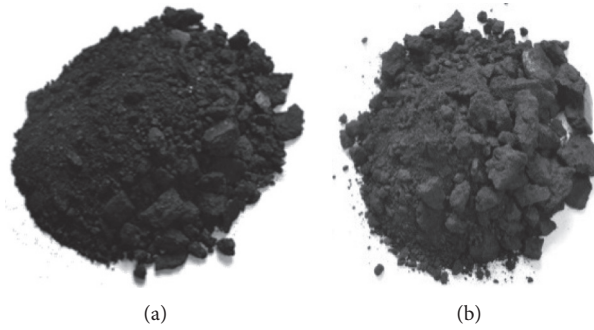


FIGURE 17: SHPB experimental results under strain rate of about 210 s. (a) 214 s. (b) 219 s.

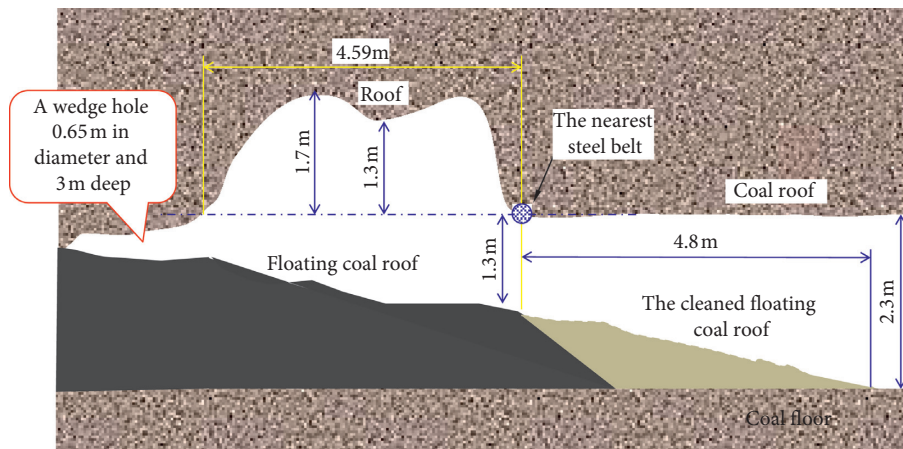


FIGURE 18: Profile map of outburst accident scene.

generated at 2-3 m from the free face of the coal mass, and these cracks were basically identical with the shape and location of wedge-shaped holes found on the field. The coal and rock crushing under the impact load generated larger particle size than the traditional gas-dominated outburst coal and rock crushing did, and the outburst holes were not traditional “pyriform” holes with small mouth and large belly, but instead, they were wedge-shaped.

There was a normal fault with drop height of 0.9 m at 16.7 m away behind the working face, and the working face was located at its footwall but still in the tectonically affected zone. As predicted by the geodetic survey department, the coal seam was thinned at 3-4 m in front of the working face where the accident took place, and minor structures were quite developed.

To sum up, this was a dynamic disaster of coal outburst caused by local rockburst during the excavation process of

the working face under large burial depth and high ground stress of coal seam in the tectonically affected zone. According to the field gas data, the gas content and gas pressure in the coal seam were  $Q=5.2\text{ m}^3/\text{t}$  and  $P_0=0.74\text{ MPa}$ , respectively, and the dilation energy of gas participating in the coal failure was only  $1.13\times 10^4\text{ J/m}^3$ , which was different from the previously given critical coal crushing energy of  $(5-10)\times 10^4\text{ J/m}^3$  by orders of magnitude. Hence, the main energy leading to the critical coal failure in the coal and gas outburst was not dilation energy of gas but the energy applied by the intense external load on the coal mass. By combining the above numerical simulation, it could be known that when the impact load was large (like 70 MPa), the coal mass would not only present stratiform splitting until being extruded out. Moreover, the surplus elastic latent energy could also cause the roof and floor failure, so the dynamic phenomena like roof caving or floor



FIGURE 19: Coal fracture form under impact load. (a) Roadway; (b) coal body.

bulging deformation would take place, which was very identical with this case.

Based on the above numerical simulation of coal damage under the loading action with intensities of 30 MPa, 50 MPa, and 70 MPa and combining the corresponding field cases and energy calculation, it can be found that the coal and gas outburst is caused by the coaction of dilation energy of gas and external applied load (like excavation, blasting, tectonic stress, surrounding rock stress, etc.). Under low gas content, high stress, or strong disturbance, the external applied load can become the main energy source for the critical coal failure, and even crushing and throwing. Meanwhile, it is verified through the field measured data that the proposed standard scope  $((5-10) \times 10^4 \text{ J/m}^3)$  of the minimum coal crushing energy needed by the critical outburst is reasonable.

It can be seen that, in different geological conditions and mining conditions, the risk of coal mine disaster is very different. The influence of geological conditions on rockburst and gas outburst is mainly shown in the following. (1) Normal fault is formed by tensile stress, there is no energy accumulation in the layer, and it has little influence on rockburst and gas outburst. The mechanism of rockburst and gas outburst induced by normal faults is mainly stress superposition. (2) Since the reverse fault is formed by compression, the rock layer accumulates a lot of elastic energy in the process of compression. Therefore, the release of elastic energy is easy to induce rockburst and gas outburst. (3) Because the fold is formed by horizontal stress extrusion, there will be residual stress and elastic energy in the rock mass in the fold area. The further release of elastic energy is an important factor causing rockburst and gas outburst. (4) When the hardness, thickness, and dip angle of the coal seam changed, the stress concentration of the surrounding rock mass is easy to appear. When the mining face is close to these areas, it is prone to cause stress superposition, which may lead to the occurrence of rockburst and gas outburst.

In order to ensure mining safety, commonly used goaf gas extraction methods include (1) buried tube extraction; (2) high drilling extraction; (3) high lane extraction; (4) surface borehole extraction.

When the sealing of the roof and floor is good, and in the stress concentration area, it is more likely to lead to the

occurrence of rockburst and gas outburst. With the increase of mining depth, the coupled disaster of stress and gas will increase, which is the focus of the next research.

## 5. Conclusions

- (1) Through the energy analysis of outburst process, the outburst process can be divided into two different processes: critical outburst and outburst, and the critical energy condition for the coal and gas outburst is proposed as  $W_{G1} + W_C + W_{\Delta} \geq W_{P1}$ . In other words, the initiating conditions for the coal and gas outburst can be met and the outburst can occur only when the sum of energies applied by gas, surrounding rock, or other suddenly applied loads to the coal mass is approximate to or exceeds the coal crushing energy in the critical outburst. By combining the experimental results of coal mass under the impact load and predecessors' study results, the scope of minimum coal crushing energy for the critical outburst is proposed, namely,  $(5-10) \times 10^4 \text{ J/m}^3$ .
- (2) Based on a comparative analysis of numerical simulation and field cases, the coal and gas outburst is caused jointly by the dilation energy of gas and external applied load (such as excavation, blasting, tectonic stress, and surrounding rock stress). Under low gas content, high stress, or strong disturbance, the external applied loads can become the main energy source for the critical coal failure and even crushing and throwing.
- (3) The evolution process of split cracks under different impact loads is effectively investigated through the numerical analysis of coal impact failure caused by the stress waves with different peak intensities. The study results show that an interval split structure appears in the coal mass under the dynamic loading action, which is evidently different from the failure form of coal mass under static action. With the increase in the peak intensity of stress wave, all the interval splitting damage in different zones presents an enhancement trend, but the enhancement amplitude is varied.



## Data Availability

All data included in this study are available upon request by contacting the corresponding author.

## Conflicts of Interest

The authors declare that there are no conflicts of interest regarding the publication of this paper.

## Acknowledgments

This work was supported by the University Natural Science Foundation of Anhui Province (KJ2017A091, KJ2019A0098, and 1808085ME160).

## References

- [1] D. J. Black, "Review of coal and gas outburst in Australian underground coal mines," *International Journal of Mining Science and Technology*, vol. 29, no. 6, pp. 815–824, 2019.
- [2] M. B. Diaz Aguado and C. González Nicieza, "Control and prevention of gas outbursts in coal mines, Riosa-Olloniego coalfield, Spain," *International Journal of Coal Geology*, vol. 69, no. 4, pp. 253–266, 2007.
- [3] L. Yuan, "Control of coal and gas outbursts in Huainan mines in China: a review," *Journal of Rock Mechanics and Geotechnical Engineering*, vol. 8, no. 4, pp. 559–567, 2016.
- [4] A. Keneti and B. A. Sainsbury, "Review of published rockburst events and their contributing factors," *Engineering Geology*, vol. 246, pp. 361–373, 2018.
- [5] P. Konicek, M. R. Saharan, and H. Mitri, "Destress blasting in coal mining—state-of-the-art review," *Procedia Engineering*, vol. 26, pp. 179–194, 2011.
- [6] J. Ptáček, "Rockburst in Ostrava-Karvina coalfield," *Procedia Engineering*, vol. 191, pp. 1144–1151, 2017.
- [7] W. D. Ortlepp and T. R. Stacey, "Rockburst mechanisms in tunnels and shafts," *Tunnelling and Underground Space Technology*, vol. 9, no. 1, pp. 59–65, 1994.
- [8] W. L. Zhang, N. J. Ma, and J. Ma, "Mechanism of rock burst revealed by numerical simulation and energy calculation," *Shock and Vibration*, vol. 2020, Article ID 8862849, 15 pages, 2020.
- [9] M. T. Gao, Z. Q. Song, and H. Q. Duan, "Mechanical properties and control rockburst mechanism of coal and rock mass with bursting liability in deep mining," *Shock and Vibration*, vol. 2020, Article ID 8833863, 15 pages, 2020.
- [10] N. G. W. Cook, "The design of underground excavations," in *Proceedings of Eighth Rock Mechanics Symposium*, pp. 45–52, American Rock Mechanics Association, Minneapolis, MN, USA, September 1966.
- [11] H. S. Mitri, B. Tang, and R. Simon, "FE modelling of mining-induced energy release and storage rates," *Journal of the South African Institute of Mining and Metallurgy*, vol. 99, pp. 103–110, 1999.
- [12] T. D. Wiles, "Correlation between local energy release density observed bursting conditions at Creighton mine," *Sudbury*, vol. 20, pp. 101–115, 1998.
- [13] Q. Jiang, X. T. Feng, T. B. Xiang, and G. S. Su, "Rockburst characteristics and numerical simulation based on a new energy index: a case study of a tunnel at 2,500 m depth," *Bulletin of Engineering Geology and the Environment*, vol. 69, no. 3, pp. 381–388, 2010.
- [14] J. Xu, J. Jiang, N. Xu, Q. Liu, and Y. Gao, "A new energy index for evaluating the tendency of rockburst and its engineering application," *Engineering Geology*, vol. 230, pp. 46–54, 2017.
- [15] N. I. Aziz and W. Ming-Li, "The effect of sorbed gas on the strength of coal—an experimental study," *Geotechnical and Geological Engineering*, vol. 17, no. 3/4, pp. 387–402, 1999.
- [16] B. B. Beamish and P. J. Crosdale, "Instantaneous outbursts in underground coal mines: an overview and association with coal type," *International Journal of Coal Geology*, vol. 35, no. 1–4, pp. 27–55, 1998.
- [17] B. Hodot, *Coal and Gas Outbursts*, Coal Industry Press, Beijing, China, 1966.
- [18] W. Zhao, Y. Cheng, H. Jiang, K. Jin, H. Wang, and L. Wang, "Role of the rapid gas desorption of coal powders in the development stage of outbursts," *Journal of Natural Gas Science and Engineering*, vol. 28, pp. 491–501, 2016.
- [19] P. Guan, H. Wang, and Y. Zhang, "Mechanism of instantaneous coal outbursts," *Geology*, vol. 37, no. 10, pp. 915–918, 2009.
- [20] С. Г. Авершин, *Rockburst*, China Coal Industry Publishing House, Beijing, China, 1959.
- [21] G. Bräuner, *Mine Pressure and Rockburst*, China Coal Industry Publishing House, Beijing, China, 1985.
- [22] T. Li, M. F. Cai, J. A. Wang et al., "Discussion on relativity between rockburst and gas in deep exploitation," *Journal of China Coal Society*, vol. 30, pp. 562–567, 2005.
- [23] F. M. Zhang, Z. Y. Yu, X. Y. Xu et al., "Research on induced earthquakes by coal mining in Hegang," *Journal of Natural Disasters*, vol. 14, pp. 139–143, 2005.
- [24] F. W. Zhang and T. Li, "Cognizance on compound dynamic disaster of coal and gas in deep mining," *Zhongzhou Coal*, vol. 106, pp. 73–76, 2009.
- [25] Y. C. Lu, "Technology of bumping prevention and control for gateway driving in seam with outburst in potential," *Coal Science and Technology*, vol. 36, pp. 43–46, 2008.
- [26] Petukhov, *Coal Mine Rock Burst*, China Coal Industry Publishing House, Beijing, China, 1992.
- [27] А. Т. Айруни, *Prediction and Prevention of Gas Dynamic Phenomena in Mines*, China Coal Industry Publishing House, Beijing, China, 1992.
- [28] K. Ogieglo, M. Lubryka, J. Kutkowski et al., "Influence of mine shock to gas emission rate," *Ground Pressure and Strata Control*, vol. 22, pp. 109–111, 2005.
- [29] M. T. Zhang, Z. H. Xu, Y. S. Pan et al., "A united instability theory on coal (rock) burst and outburst," *Journal of China Coal Society*, vol. 16, pp. 48–53, 1991.
- [30] Y. S. Pan, Z. H. Li, and M. T. Zhang, "Distribution type mechanism and prevention of rockburst in China," *Chinese Journal of Rock Mechanics and Engineering*, vol. 22, pp. 1844–1851, 2003.
- [31] S. Y. Li, X. S. He, K. Pan et al., "Relationship between mining seismicity and gas outburst in coal mine," *Journal of China Coal Society*, vol. 31, pp. 11–18, 2006.
- [32] T. Li, T. T. Mei, G. Q. Li et al., "Mechanism study of coal and gas outburst induced by rockburst in "three-soft" coal seam," *Chinese Journal of Rock Mechanics and Engineering*, vol. 30, pp. 1283–1288, 2011.
- [33] Z. Wang, G. Z. Yin, Q. T. Hu et al., "Inducing and transforming conditions from rockburst to coal-gas outburst in a high gassy coal seam," *Journal of Mining & Safety Engineering*, vol. 27, pp. 572–575, 2010.
- [34] B. Wu, W. Yao, and K. Xia, "An experimental study of dynamic tensile failure of rocks subjected to hydrostatic confinement," *Rock Mechanics and Rock Engineering*, vol. 49, no. 10, pp. 3855–3864, 2016.

- [35] Y. Xue, P. G. Ranjith, F. Gao et al., "Mechanical behaviour and permeability evolution of gas-containing coal from unloading confining pressure tests," *Journal of Natural Gas Science and Engineering*, vol. 40, pp. 336–346, 2017.
- [36] Y. Xue, F. Gao, and X. Liu, "Effect of damage evolution of coal on permeability variation and analysis of gas outburst hazard with coal mining," *Natural Hazards*, vol. 79, no. 2, pp. 999–1013, 2015.
- [37] Y. Al-Salloum, T. Almusallam, S. M. Ibrahim, H. Abbas, and S. Alsayed, "Rate dependent behavior and modeling of concrete based on SHPB experiments," *Cement and Concrete Composites*, vol. 55, pp. 34–44, 2015.
- [38] S. S. Daryadel, P. R. Mantena, K. Kim, D. Stoddard, and A. M. Rajendran, "Dynamic response of glass under low-velocity impact and high strain-rate SHPB compression loading," *Journal of Non-crystalline Solids*, vol. 432, pp. 432–439, 2016.
- [39] S. Mishra, T. Chakraborty, and V. Matsagar, "Dynamic characterization of Himalayan quartzite using SHPB," *Procedia Engineering*, vol. 191, pp. 2–9, 2017.
- [40] E. Kim and H. Changani, "Effect of water saturation and loading rate on the mechanical properties of red and buff sandstones," *International Journal of Rock Mechanics and Mining Sciences*, vol. 88, pp. 23–28, 2016.
- [41] R. L. Shan, R. Q. Cheng, and W. J. Gao, "Study on dynamic constitutive model of anthracite of Yunjialing coal mine," *Chinese Journal of Rock Mechanics and Engineering*, vol. 25, pp. 2258–2263, 2006.
- [42] X. H. Liu, R. Zhang, and J. F. Liu, "Dynamic test study of coal rock under different strain rates," *Journal of China Coal Society*, vol. 37, pp. 1528–1534, 2012.
- [43] C. M. Mu and N. P. Gong, "Damage mechanism of coal under impact loads," *Journal of China Coal Society*, vol. 42, pp. 2011–2018, 2017.
- [44] L. F. Rong, C. M. Mu, and W. Q. Zhang, "Mechanical properties and establishment of constitutive relation of coal rock in 13-1 coal seam from Panxie coalfield under impact load," *Journal of China Coal Society*, vol. 40, pp. 40–46, 2015.
- [45] X. G. Kong, S. G. Li, E. Y. Wang et al., "Dynamics behaviour of gas-bearing coal subjected to SHPB tests," *Composite Structures*, vol. 256, Article ID 113088, 2021.
- [46] X. G. Kong, E. Y. Wang, S. G. Li, H. Lin, Z. Zhang, and Y. Ju, "Dynamic mechanical characteristics and fracture mechanism of gas-bearing coal based on SHPB experiments," *Theoretical and Applied Fracture Mechanics*, vol. 105, Article ID 102395, 2020.
- [47] M. C. He, G. X. Yang, J. L. Miao et al., "Classification and research methods of rockburst experimental fragments," *Chinese Journal of Rock Mechanics and Engineering*, vol. 28, pp. 1521–1529, 2009.
- [48] Q. T. Hu, *Study on the Mechanical Mechanism of Coal and Gas Outburst and Its Application*, China University of Mining and Technology, Beijing, China, 2007.
- [49] B. B. Ходот, *Coal and Gas Outburst*, China Industry Press, Beijing, China, 1966.
- [50] X. C. Zhang and X. X. Miao, "Numerical simulation of layer-c rack and failure of laminated rock masses," *Chinese Journal of Rock Mechanics and Engineering*, vol. 21, pp. 1645–1650, 2002.

## Research Article

# Blasting Vibration Control Using an Improved Artificial Neural Network in the Ashele Copper Mine

Shida Xu , Tianxiao Chen , Jiaqi Liu , Chenrui Zhang , and Zhiyang Chen 

Key Laboratory of Ministry of Education on Safe Mining of Deep Metal Mines, Northeastern University, Shenyang, Liaoning 110819, China

Correspondence should be addressed to Shida Xu; xushida@mail.neu.edu.cn

Received 5 March 2021; Revised 17 April 2021; Accepted 29 May 2021; Published 11 June 2021

Academic Editor: Qi ZHAO

Copyright © 2021 Shida Xu et al. This is an open access article distributed under the Creative Commons Attribution License, which permits unrestricted use, distribution, and reproduction in any medium, provided the original work is properly cited.

Blasting is currently the most important method for rock fragmentation in metal mines. However, blast-induced ground vibration causes many negative effects, including great damage to surrounding rock masses and projects and even casualties in severe cases. Therefore, prediction of the peak particle velocity (PPV) caused by blasting plays an important role in reducing safety threats. In this paper, a genetic algorithm (GA) and an artificial neural network (ANN) algorithm were jointly used to construct a neural network model with a 4-5-1 topology to predict the PPV. For this model, the ANN parameters were optimized using the GA, and the deviating direction, horizontal distance, vertical distance, Euclidean distance, explosive type, burden, hole spacing, and maximum charge per delay were used as input information. Moreover, principal component analysis (PCA) was used to extract the first four principal components from the eight input factors as the four inputs of the ANN model. The model was successfully applied to protect an underground crushing cave from blasting vibration damage by adjusting the blasting parameters. Compared with several widely used empirical equations, the GA-ANN PPV prediction model produced significantly better results, while the Ambraseys-Hedron method was the best of the empirical methods. Therefore, the improved GA-ANN model can be used to predict the PPV on site and provide a reference for the control of blasting vibration in field production.

## 1. Introduction

Blasting is currently the most economical and widely used method for artificial caving in underground mines. However, the utilization efficiency of the energy released by explosive charges is very low. According to statistics, only 20–30% of the explosive energy is used for rock fragmentation, and the rest of the energy is lost in other forms, resulting in some negative effects, such as surrounding rock vibration, flyrock, shock waves, tremendous noise, and a large amount of released heat [1–4]. The negative effects result in a large amount of energy loss and cause severe damage to the surrounding rock masses, which easily leads to rock bursts, large-scale collapses, and other disasters, further threatening the safety of underground personnel and equipment [5–8]. In particular, as the mining depth increases, the geostatic stress also gradually increases, and the issue of blast-induced rock bursts becomes increasingly

prominent. According to statistics, approximately two-thirds of rock bursts in mines occur as a result of blast-induced disturbances [9]. The roadway of the –647 m middle section of the Hongtoushan copper mine experienced severe damage over a distance of tens of meters. According to the literature, the peak particle velocity (PPV) is the most commonly used predictor to evaluate blasting vibration [10]. Therefore, conducting studies on PPV prediction would help control the blasting vibration and reduce the corresponding hazards.

According to the literature, the PPV is influenced by many factors, including the maximum charge per delay, burden, hole spacing, total charge, number of delays, rock mass quality, and stress [11, 12]. Many scholars have studied the relationship between these influencing factors and the PPV. Based on these relationships, empirical methods, numerical simulation methods, linear regression methods, and other methods have been used to predict the PPV, and

many meaningful achievements have been obtained [4]. To date, there is still no widely accepted method. In recent decades, with the development of computer technology, neural networks have been increasingly applied in PPV prediction due to the advantages of self-adaptivity and nonlinearity [13, 14].

In a study on the blasting parameter-based prediction of blasting vibration using a neural network approach, Singh and Singh [15] found that the neural network approach accurately predicted ground vibration, and the error did not increase as the number of inputs and nonlinearity increased. Khandelwal and Singh [16] used an artificial neural network (ANN) approach to predict the blast-induced ground vibration of a surface coal mine and compared it with the conventional statistical analysis method. Khandelwal and Singh [17] established an ANN model to predict blast-induced ground vibration. The model contained 10 input parameters, 15 hidden neurons, and two output parameters. A comparative analysis demonstrated that the model has a higher prediction accuracy than conventional predictors and multivariate regression analysis. Monjezi et al. [18] established a four-layer neural network model with a 4-1085-1 topology to predict the PPV and determined the distance from the blasting face to be the parameter that had the greatest impact on the PPV by sensitivity analysis. Amnieh et al. [19] used an ANN to establish the relationship between the PPV, block volume, explosive types, and blasting parameters and used this relationship to determine the appropriate burden, hole spacing, and maximum charge corresponding to the PPV values for a safe blasting pattern. Álvarez-Vigil et al. [20] divided the influencing factors into two categories, viz., environmental conditions and waveform parameters, proposed an ANN model for the prediction of ground vibration caused by blasting in an open-pit mine, and verified the effectiveness of this method by comparing it with multiple linear regression. Jayawardana et al. [21] used a neural network to study the relationship between the vibration mitigation effects of dual in-filled trenches under different conditions and the control parameters and established a vibration prediction model based on the relationship.

Some scholars combined the neural network method with other methods for the prediction of blasting vibration. Verma and Singh [22] established a PPV predictor using a genetic algorithm (GA) based on 127 data sets. They compared its predictors with traditional vibration predictors, multivariate regression analysis, and ANNs and discussed the superiority of the GA network. Mohamed [23] separately used an ANN and fuzzy logic analysis to predict the PPV and found that the fuzzy model had a slightly higher prediction accuracy than the ANN model. Armaghani et al. [24] proposed a flyrock and PPV prediction model based on the particle swarm optimization (PSO) algorithm and an ANN and input the top 10 influential blasting parameters to estimate the flyrock and PPV. They found that the maximum charge per delay was the blasting parameter that influenced the flyrock distance and PPV the most. Hajihassani et al. [25] used a hybrid ANN and PSO algorithm to predict the air blast overpressure and obtained a training correlation

coefficient of 0.94, indicating that the PSO-based ANN model has a high prediction accuracy. Hajihassani et al. [26] established a hybrid algorithm model for PPV prediction (an ANN algorithm and an imperialist competitive algorithm (ICA)), the ICA-ANN model, based on the blasting data of a granite quarry in Malaya, and the application results showed that the ICA-ANN model has a high prediction accuracy. Azimi et al. [27] used the monitoring data of blast-induced ground vibration from the Sungun copper mine to establish a GA-ANN prediction model and found that the prediction accuracy was higher when the horizontal and radial distances were replaced with the modified radial distance. Nguyen et al. [28] analyzed and affirmed the prediction accuracy of blast-induced PPV using a hybrid model based on the hierarchical  $k$ -means (HKM) clustering algorithm and an ANN (an HKM-ANN model) and a hybrid model based on fuzzy  $c$ -means clustering (FCM) and support vector regression (SVR) and concluded that the HKM algorithm could effectively improve the prediction accuracy of ANN models.

Based on the monitoring data of ground vibration caused by underground blasting in the Ashele copper mine, the present study established a PPV prediction model by combining the GA with the ANN. In this model, the ANN parameters were optimized by the GA, and the optimal number of nodes and connection weights of the hidden layers in the neural network were obtained. The model was applied to provide guidance for optimizing the blasting parameters and controlling blasting vibration.

## 2. Combined Method Based on a Neural Network and GA

The backpropagation (BP) network is currently one of the most widely used neural network models. The BP network generally consists of an input layer, hidden layers, and an output layer. The learning algorithm of the BP network can be summarized as the process of iteratively performing forward computation, reverse computation, and weight and threshold updating according to a given sample set. The training weight coefficient is reversed. The error of the middle layer is obtained based on the error of the output, and then the weight coefficient of the input is obtained. This process is repeated until the correct output is obtained. The BP network is essentially the input-output mapping and does not require any precise mathematical expression between the input and the output. As long as a known model is used to train the BP network, the network has the capability of mapping between input and output pairs. It actually transforms the input/output problems of a sample set into a nonlinear optimization problem and uses the most common gradient descent optimization method and iterative operation to solve for the weights.

The neural network uses a gradient descent-based BP algorithm and its variants, and its dependence on the initial weight selection inevitably leads to the problem of a local optimum, resulting in a decrease in the reliability of the neural network approach. In view of the shortcomings of the BP neural network, this paper adopts an improved GA-BP



neural network to overcome the shortcomings of the BP neural network. The GA simulates the evolutionary phenomena of biological inheritance, genetic variation to adapt to the environment, and survival of the fittest in nature [29]. It treats each solution as a chromosome, each element of the solution as a gene, and all chromosomes as a population. The chromosomes are evaluated using a predetermined objective function to calculate the fitness. The algorithm initially randomly generates some chromosomes, performs genetic operations such as genetic inheritance and variation on the chromosomes based on the fitness, selects chromosomes with a high fitness, and conducts the next generation of genetic operations to obtain new populations. Because each iteration selects the elites from the population of the previous generation, the new generation inherits the superior genes of the previous generation and reorganizes in time to produce better chromosomes and eliminate defective new individuals. Therefore, through repeated iterations, the solution evolves toward the optimal solution until the termination condition is met. Due to the high level of parallelism, the GA has been widely applied in neural networks.

### 3. Background of the Ashele Copper Mine

*3.1. Production and Monitoring of the Ashele Copper Mine.* The Ashele copper mine, located in Xinjiang Province in China, has a copper reserve of 920,000 tons, with an average grade of 2.4%. The main ore body has a strike length of 700 m, an average thickness of 20 m to 45 m, and an inclination of 55° to 85°. The deposit is mainly formed by volcanic ejection and deposition and is then remolded by hydrotherm fluids. The average rock quality designation (RQD) of the surrounding rock in the hanging wall is 81.2%, with 41.5% of the surrounding rock in the footwall and 70.9% of the ore body. The current mining depth exceeds 1000 m, with 1243 m of the shaft length. The hanging wall of the ore body is mainly composed of dacite porphyry, and the footwall of the ore body is mainly basalt, with chalcopyrite as the main mineral. The results of an in situ stress test showed that the maximum horizontal principal stress at the maximum mining depth was close to 45 MPa, with an inclination of 18°, which was almost perpendicular to the strike of the ore body, and the minimum principal stress was approximately 20 MPa, with an inclination of 64°. The Ashele copper mine mainly employs the large-diameter deep-hole mining method, which allows a high production capacity. Ores were gathered from the bottom using trenches. After the formation of the trenches, the vertical crater retreat (VCR) method was adopted to form cutting grooves at the mining face, and then large-hole lateral caving was used for mining. The Ashele copper mine produces 6,000 tons of ore daily; the charge for a single blast is as high as 4 tons, and the maximum charge per delay reaches 400 kg. Frequent blast and stress transfers due to excavation disturb the surrounding rock mass of roadways, in some cases causing severe damage and requiring significant effort to maintain and rehabilitate the secondary support. Stope collapses have occurred at two different levels of the Ashele copper mine,

which were attributed to the blasting disturbance of adjacent stopes after microseismic activity analysis [30].

The NUBOX-6016 intelligent vibration monitor and the NUBOX-6016 portable data acquisition device used in this study were designed based on optimization tests for blasting, vibration, shock, and noise on site (see Figure 1). The instruments can digitally convert and store the dynamic and static analog signals generated by sensors (including the acceleration, pressure, strain, and temperature) and have a triggering mechanism to ensure the correct recording of signals only for the features concerned. They allow data acquisition for up to 2048 segments to achieve continuous automatic recording of multisegment vibration signals. The maximum sampling frequency is 200 kHz. The signal-to-noise ratio (SNR) is  $\geq 62$  dB. The minimum sampling frequency is 5 Hz. This equipment is equipped with a TP3V-4.5 sensor, which has the advantages of easy installation, high robustness, reliability, compactness, high measurement precision, and strong anti-interference. The stope of the Ashele copper mine adopted retreats mining from the hanging wall to the footwall, and during the blasting vibration field test, the monitoring points were placed in the footwall of the ore body to avoid measuring the blasting vibration waves that propagated through the goaf.

Every two or three levels are used as a mining combination in the Ashele copper mine. The mining sequence is from bottom to top in the mining combination. At present, the first stope at a depth of 1012 m is to be mined according to the production plan. Unfortunately, a crushing chamber is located near the stope, which is used to crush the ore produced below 600 m depth. Apparently, it has a long service cycle. Therefore, it is necessary to control the PPV of the stope blast to protect the crushing chamber.

*3.2. Factors Controlling the PPV.* Samples of the inputs and outputs should be offered to train and test the blasting vibration prediction model based on the neural network. The related factors concerning the blasting vibration should be selected carefully. Then, the inputs of the ANN model, including blasting parameters and field conditions, were determined after investigation. Field conditions mainly include the buried depth, maximum principal stress, deviating direction, horizontal distance, vertical distance, and Euclidean distance. The blasting parameter mainly contains the explosive type, burden, hole spacing, delay number, total charge, and maximum charge per delay.

*3.2.1. Weak Effect of Burial Depth and Maximum Stress.* There are few studies considering the impact of the buried depth and the maximum stress on blasting vibration. Little correlation between the buried depth, the maximum stress, and the PPV was found before. In this paper, the blasting vibration at a deeper level was studied based on the shallow level, so the two impactors were taken to analyze the impact on the PPV. The blasting vibration data were all collected at 562 m depth, 762 m depth, and 912 m depth, which were the main mining levels in the Ashele copper mine. The PPV values of different depths and maximum principal stresses

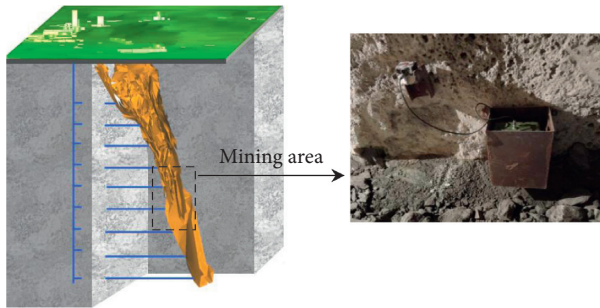


FIGURE 1: Field test of blasting vibration in mining area.

are shown in Figure 2. The PPV tends to increase with increasing burial depth. It can be predicted that the influence of burial depth on PPV will become increasingly prominent with increasing mining depth. According to the results of the in situ stress test of the Ashele copper mine, the maximum principal stress of the in situ stress is near horizontal and approximately perpendicular to the ore body. In addition, there is little change in the direction of the maximum principal stress. Hence, only the value of maximum principal stress is considered for the model. The PPV grows with increasing maximum horizontal principal stress. However, the correlation coefficients between the buried depth, maximum stress, and PPV are small. It can be concluded that there is no significant correlation between them. Therefore, the buried depth and the maximum stress are not taken as the inputs of the PPV prediction. At the same time, the correlation coefficients between the delay number, total charge, and PPV are small, illustrating that the two factors have little impact on the PPV. Therefore, the delay number and the maximum stress are eliminated.

**3.2.2. Deviating Direction.** The scatterplot matrix of the PPV database with correlation is shown in Figure 3. The deviating direction is the angle between the stope centerline and the line linking the blasting center and the monitoring point. The deviating direction is a positive number when the stope centerline rotates clockwise. Otherwise, the deviating direction is a negative number. Apparently, the PPV is the smallest when the deviating direction is 0. With the increase in the absolute value of the deviating direction, the PPV rises gradually. The correlation coefficient between the deviating direction and PPV is 0.307, and a significance test finds significance at the level of 0.05. It can be concluded that the deviating direction has some influence on the blasting vibration.

**3.2.3. Horizontal Distance, Vertical Distance, and Euclidean Distance between the Blasting Source and Monitoring Point.** Most empirical formulas incorporate the influence of propagation distance on blasting vibration. The horizontal distance is the horizontal projection of the distance between the blasting center and the monitoring point. Clearly, there is a high correlation between the horizontal distance and PPV. As we thought, the PPV decreases as the horizontal distance increases. Similar to the horizontal distance, the

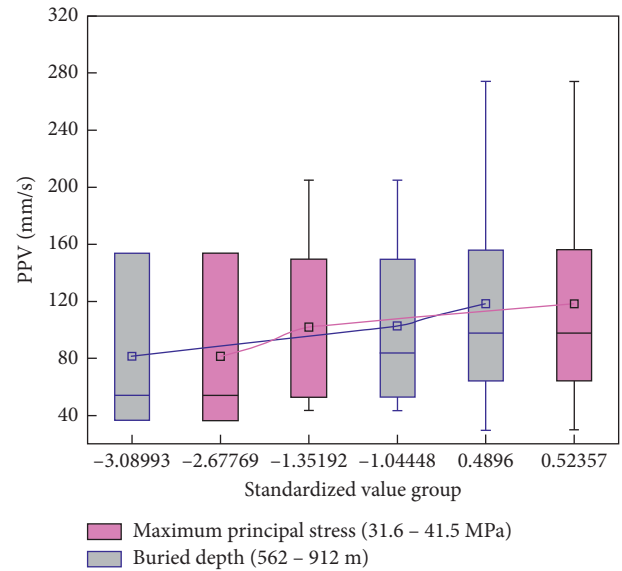


FIGURE 2: Range of the PPV with different burial depths and the maximum principal stress.

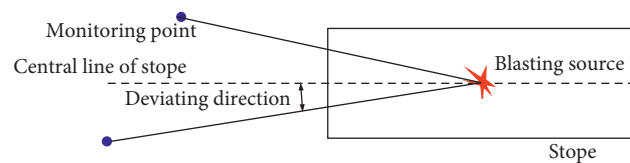


FIGURE 3: Deviating direction schematic diagram.

vertical distance, which is the vertical projection of the distance between the blasting center and the monitoring point, has an obvious influence on blasting vibration. However, there are some differences between the influences of horizontal distance and vertical distance on blasting vibration. The vertical propagation distance should be considered when studying the propagation of blasting vibration at different levels. With the increase in the Euclidean distance between the blasting center and monitoring point, the PPV decays gradually. In other words, with increasing horizontal distance, vertical distance, and Euclidean distance, the PPV decreases gradually. The correlation coefficients of the horizontal distance, vertical distance, and Euclidean distance are 0.607,  $-0.587$ , and  $-0.73$ , respectively. They are significantly correlated with the PPV at the 99% confidence level. Therefore, they are all incorporated into the PPV prediction model.

**3.2.4. Factor of Explosive Type.** The blasting speed, power and other parameters vary greatly for different explosive types. In this paper, two types of explosives are mainly used to break the rock. They are emulsion explosive and ammonium oil explosive, which are represented by 1 and 2, respectively. The blasting vibration generated by blasting with emulsion explosive is significantly greater than that of blasting with ammonium oil explosive. The correlation coefficient between the explosive type and PPV is  $-0.392$ ,



which is significant at the 0.01 level. According to the theory proposed by Cohen [31], an absolute value of coefficient greater than 0.3 can be regarded as moderate correlation. Consequently, the explosive type is taken as one of the inputs of the model.

**3.2.5. Burden.** The burden is the distance from the explosive cartridges to the free surface. When the burden is less than 2.5 m, the PPV increases with decreasing burden. Moreover, the PPV increases with the growth of the burden when the burden is more than 2.5 m. The correlation coefficient between the burden and PPV is 0.324, which is relatively small. However, a significance test identifies significance at the level of 0.05. Therefore, the burden can be considered to have an impact on the PPV and can be used to predict PPV.

**3.2.6. Hole Spacing.** With increasing hole spacing, the mean values and the minimum values of the PPV present an increasing trend. When the hole spacing is 2.0 m, the PPV values were relatively concentrated. The value range of the PPV is large at most hole spacings. The correlation coefficient between the hole spacing and PPV is 0.350, which is significant at the 0.05 level. As a result, the hole spacing is selected as the input of the model.

**3.2.7. Maximum Charge per Delay.** Similar to the distance, the maximum charge per delay often appears in empirical formulas. When the maximum charge per delay equals 220 kg, the PPV is the smallest according to the fitting curve. The PPV increases gradually with the increase in the maximum charge per delay after exceeding 220 kg. The PPV also increases with the decrease in the maximum charge per delay when it is less than 220 kg. The correlation coefficient between the maximum charge per delay is 0.381, which is significant at the level of 0.01 (see Figure 4). Hence, the maximum charge per delay is selected for model input.

As a result, the deviating direction, horizontal distance, vertical distance, Euclidean distance, explosive type, burden, hole spacing, and maximum charge per delay are selected to predict the PPV.

**3.3. Standardization of the Data.** The values of all kinds of information vary greatly. The ratio of the largest to the smallest is more than 1000. It is necessary to standardize the input data to eliminate the influence of dimension and variation size. In this paper, the Z-score method, which is the most widely used standardized method at present, is used to standardize the input data of the model. The Z-score method is shown in equation (1). After establishment of the standardized model, all the prediction sample data need to be standardized according to the same model of the training samples.

$$x_{ij}^* = \frac{(x_{ij} - x_j)}{\sigma_j}. \quad (1)$$

## 4. Prediction and Control of the PPV

**4.1. Principal Component Analysis (PCA) of Input Information.** The input data of the ANN model contain eight kinds of variables according to Section 3.1. The input data contain considerable repetitive and redundant information, and an obvious correlation is found between each factor and PPV. For example, the layout characteristics of PPVs with different horizontal distances and Euclidean distances are similar. The reason for this phenomenon is that the horizontal distance has a high correlation with the Euclidean distance in the Ashele copper mine. The correlation coefficient between them is 0.930. In other words, some information overlap exists. There are no apparent direct connections between the blasting parameters, such as the hole spacing and burden. If the explosive consumption is constant, the hole spacing is restricted by the burden. The hole spacing and burden are not completely independent. The existence of this repetitive and redundant information directly affects the prediction accuracy of PPV, which requires some data processing before use for the ANN model. The method of PCA extracts the key information to establish new variables that are unrelated to each other. At the same time, it deletes redundant information while making the best effort to preserve the original information. In this paper, PCA is used to eliminate the influence of the repetitive and redundant information included in the data of eight factors after standardization.

The error contribution of PCA is shown in Figure 5. The larger the variance percentage is, the greater the contribution of the principal component to the output. The variance contributions of the first four principal components are 39.20%, 31.75%, 14.43%, and 7.78%. The cumulative variance contribution of the first four principal components accounts for 93.16%. In this paper, the first four principal components are selected to predict PPV. The eigenvalues of the four principal components are 3.136, 2.540, 1.154, and 0.622.

**4.2. Establishment of the PPV Prediction Model.** Generally, the training error decreases rapidly in the training process, while the testing error sometimes decreases with relatively narrow fluctuations. Referring to the early stopping method, the maximum number of learning sessions was 200,000. Then, the best number of learning steps was determined to reduce the overfitting problem according to the error of learning and testing. In addition, a simple structure of the neural network model is helpful to avoid overfitting problems. Consequently, a topology with one hidden layer was used. The hidden layer had a node search range of 5–15. The neural network model had four inputs and one output. The population size was 200, the total number of generations was 30, the code string length was 15, the crossover probability was 0.8, the mutation probability was 0.2, the inversion operator was 0.3, and the initial weight was from  $-0.5$  to  $0.5$ . The individual error and test target error were controlled at  $10^{-6}$  and  $10^{-5}$ , respectively. The inertia coefficient was set to 0.5, and the generation with a stable fitness

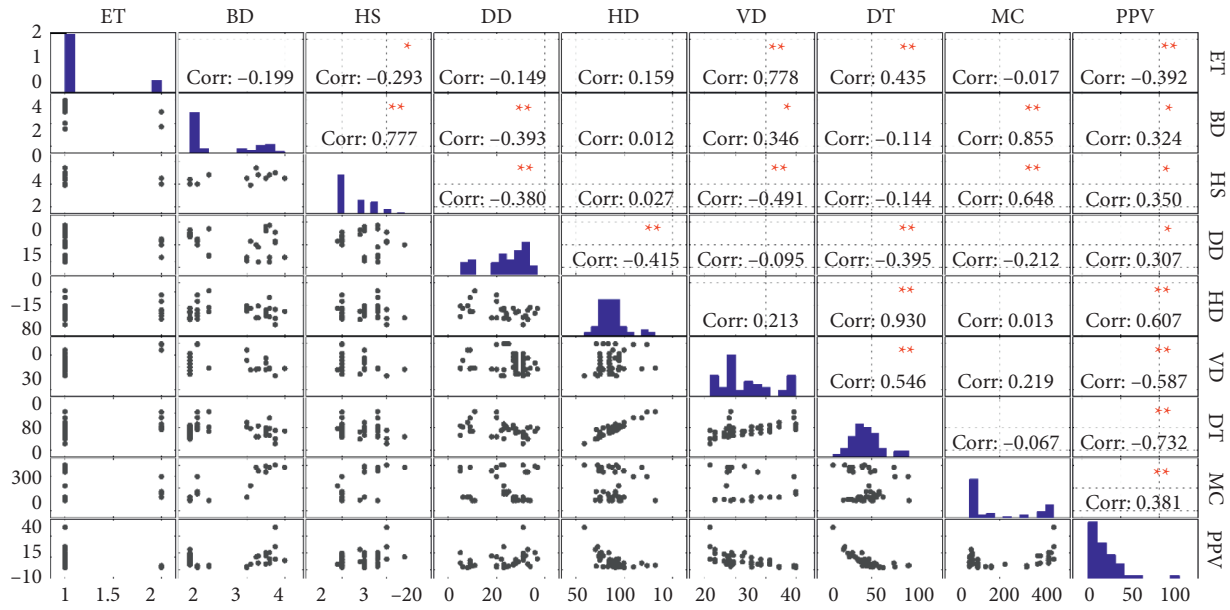


FIGURE 4: Scatterplot matrix of the PPV database with correlation. \* indicates that the correlation is significant at the 0.05 level, and \*\* indicates that the correlation is significant at the 0.01 level.

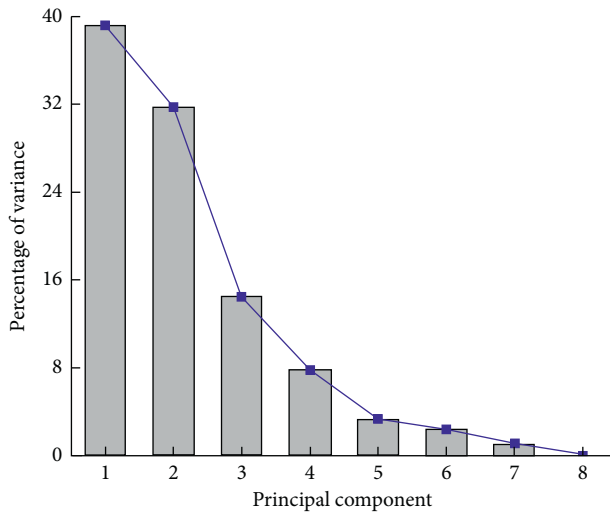


FIGURE 5: Variance contribution of each principal component.

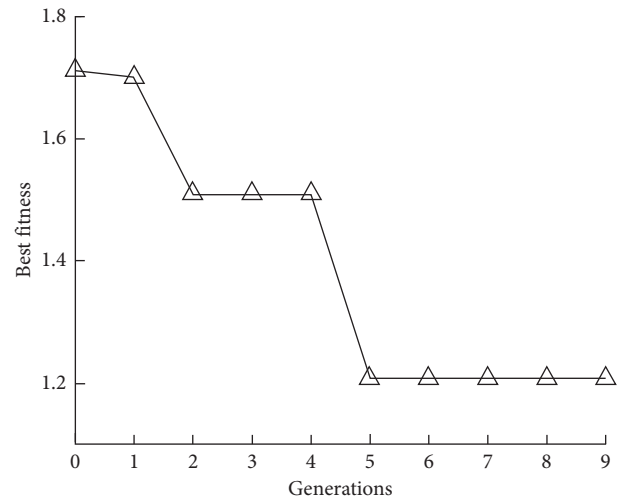


FIGURE 6: Best fitness values of different generations.

value was set to 5. In this paper, the mean squared error of the outputs from the measured results was chosen to calculate the fitness value.

The above parameter setting was used for the nine generations of genetic evolution. The best fitness value for each generation is shown in Figure 6. The optimal fitness value of the initial population was 1.711. The best fitness value of the first-generation population was 1.700, indicating a significant decrease. Then, a slight decrease in the best fitness value was found in the second generation. There was no significant change in the third and fourth generations, indicating that in the current genetic operation process, no chromosomes were better than those of the second generation. Afterwards, the best fitness value of the fifth generation was 1.207, showing a significant decrease and

indicating that during the evolution from the fourth generation to the fifth generation, a better chromosome was generated, so the best fitness value was greatly reduced. Until the ninth generation, none of the individuals were better than those of the fifth generation. At this point, the generation with the stable best fitness value was set to 5, and the genetic evolution was terminated. In this case, the best fitness values for the second to fourth generations were the same, as were the corresponding weights and topological parameters of the neural network. Therefore, the best fitness value and the corresponding weights and topological parameters of the neural network of any generation from the fifth generation to the ninth generation can be applied to the PPV neural network. The fitness values of each individual in the ninth generation and their corresponding topological parameters in the neural network are shown in Figure 7.

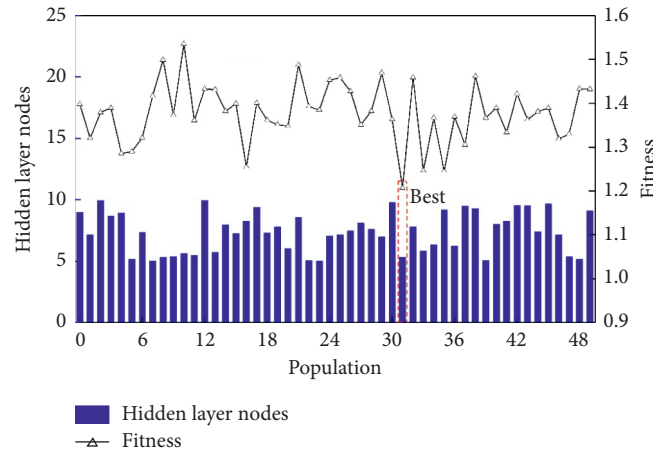


FIGURE 7: Hidden layer nodes of different generations.

There were 50 individuals in the population. The best fitness value of the ninth generation corresponded to individual no. 31, and the topological parameter of its neural network was 5. Finally, the number of nodes in the hidden layer of the neural network was 5. Based on this, a PPV prediction model with a 4-5-1 topology was established. This model had one input layer, one hidden layer, and one output layer. The input layer contained four inputs, the hidden layer contained 5 nodes, and the output layer contained one output. In addition, there were 31 initial weights. The frame diagram of the three-layer neural network is shown in Figure 8.

The outputs of this model during learning and testing are shown in Figure 9. During learning and testing, the output values of the GA-ANN model were very close to the measured values. The errors of all learning and testing cases were within an acceptable range.

#### 4.3. Blasting Vibration Control for Crushing Cave Protection.

There is a crushing cave near the blasting stope at the 1012 m mining depth of the Ashele copper mine, which is shown in Figure 10. Two blasting vibration monitoring points were arranged near the stope to collect the PPV generated by the blasts. The blasting parameters and field conditions are shown in Table 1. The PPV values at points 1 and 2 induced by large-hole blast were 116.1 mm/s and 166.2 mm/s according to the PPV prediction model and blasting design, respectively. The PPV at monitoring point 2 caused by a large-hole blast is close to the minimum safety value recommended in the blasting safety regulation. The blasting parameters were adjusted to control the blasting vibration to avoid damage to the crushing cave caused by blasts near the stope. The burden and hole spacing were changed to 3.5 m and 2.5 m from 3.3 m and 3.4 m, respectively. Moreover, the maximum charge per delay was reduced from 400 kg to 300 kg, while the delay number increased from 10 to 13. The corresponding delay times were 0, 50 ms, 110 ms, 150 ms, 200 ms, 250 ms, 310 ms, 380 ms, 460 ms, 550 ms, 650 ms, 760 ms, and 880 ms. After the adjustment of the blasting parameters, the predicted PPVs at monitoring points 1 and 2 were 55.60 mm/s and 87.80 mm/s, respectively. Finally, the blast of the near stope did not cause apparent damage to the

crushing cave. The measured PPVs at points 1 and 2 caused by the large-hole blast and medium-deep hole blast were 56.28 mm/s and 96.99 mm/s, respectively.

## 5. Discussion

According to previous studies, the PPV is influenced by many factors, including environmental parameters such as the stress and rock mass quality and blasting parameters such as the maximum charge per delay, total charge, Euclidean distance, and number of delays. Most previous studies have considered the maximum charge per delay and the Euclidean distance to be the two most important parameters affecting the PPV. For example, empirical PPV predictors, such as those of the United States Bureau of Mines [32], Langefors and Kihlstrom [33], the Bureau of Indian Standards criteria [34], Ambraseys and Hendron [35], and the Central Mining Research Institute (CMRI) predictors [36], consider only the influences of the maximum charge per delay and the Euclidean distance on the PPV. These empirical formulas are shown in Table 2.

Using the learning and testing samples, the above five empirical models were used to establish the PPV prediction equations to predict the PPV values at different sites during the two blasts. The results predicted by the empirical equations were relatively poor (see Table 3). There is no significant difference between the PPV values predicted by the five empirical equations. This is because the same factors are taken into account by the five empirical equations with different expressions. The Ambraseys–Hendron equation was the best among these empirical equations for PPV prediction, and its prediction errors were approximately 13.36% and 87.81%. As a result, the PPV values predicted by the GA-ANN algorithm were the closest to the measured values, and the prediction errors were less than 10%, indicating that the prediction accuracy of the GA-ANN algorithm was the highest (see Figure 11). It is believed that the PPV prediction accuracy will be further improved with the accumulation of data. In general, the PPV should be predicted according to the actual factors rather than simply using empirical equations.

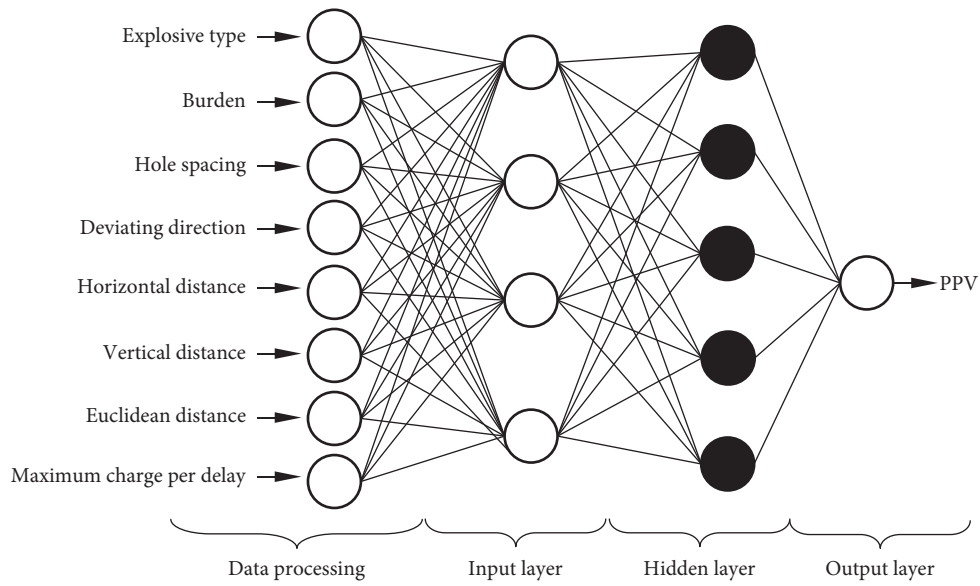


FIGURE 8: Frame diagram of the three-layer neural network.

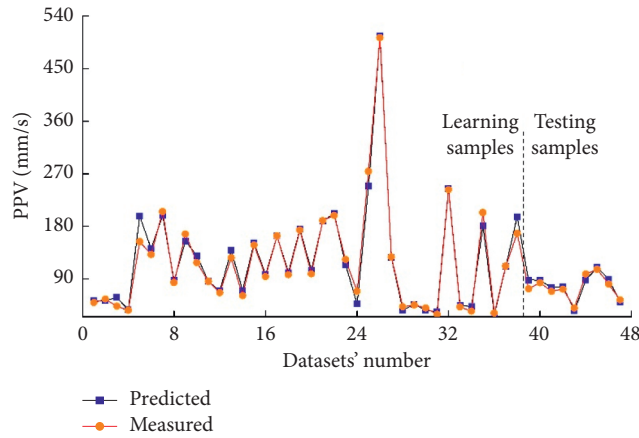


FIGURE 9: Relative errors of the training cases.

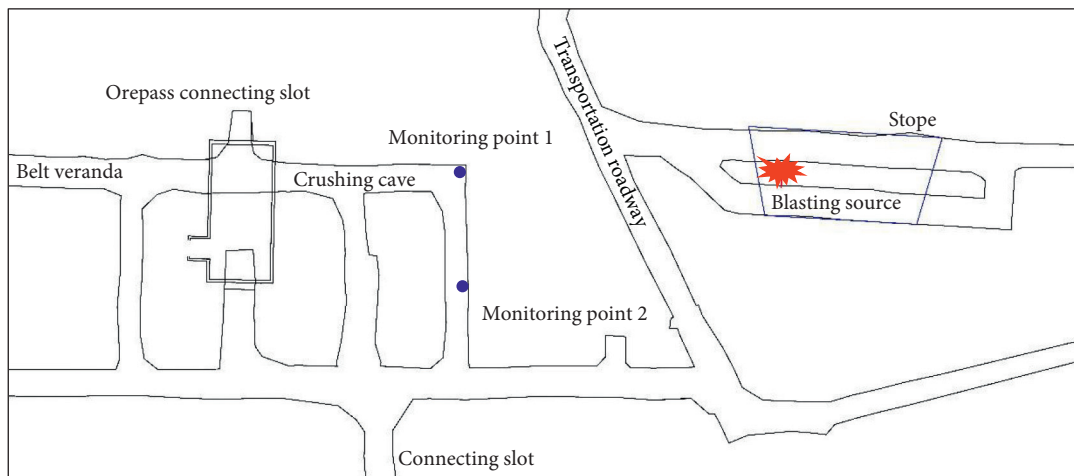


FIGURE 10: Location of the blasting source and crushing cave at a depth of 1012 m in the Ashele copper mine.

The traditional empirical formula considers only the blasting vibration Euclidean distance and the maximum charge per delay. In this paper, the Euclidean distances

between the monitoring points and blasting source are close, while the maximum charges per delay are the same. Therefore, the predicted PPVs based on empirical formulas

TABLE 1: Parameters used to predict the PPV.

Explosive type	Burden (m)	Hole spacing (m)	Deviating direction (°)	Horizontal distance (m)	Vertical distance (m)	Euclidean distance (m)	Maximum charge per delay (kg)
1	3.3	3.4	-2	46.02	17.5	49.24	400
1	3.3	3.4	-20	47.85	17.5	50.95	400
1	3.5	2.5	-2	46.02	17.5	49.24	300
1	3.5	2.5	-20	47.85	17.5	50.95	300

TABLE 2: Different conventional predictors.

Name	Equation
USBM	$v = K [R/\sqrt{Q_{\max}}]^{-B}$
Langefors–Kihlstrom	$v = K [\sqrt{Q_{\max}}/R^{2/3}]^B$
Ambraseys–Hendron	$v = K [R/(Q_{\max})^{1/3}]^{-B}$
Bureau of Indian Standards	$v = K [Q_{\max}/R^{2/3}]^B$
CMRI predictor	$v = n + K [R/Q_{\max}]^{-1}$

TABLE 3: Measured and predicted PPV values for different models.

Predictor	Site constant			PPV (mm/s)	
	$K$	$B$	$n$	1	2
USBM	345.38	1.02		119.37	115.30
Langefors–Kihlstrom	13.31	1.54		146.94	144.37
Bureau of Indian Standards	13.31	0.77		146.94	144.37
Ambraseys–Hendron	1100.46	1.15		109.95	105.70
CMRI predictor	13.86		46.29	130.71	127.88
GA-ANN				55.60	87.80
Measured				56.28	96.99

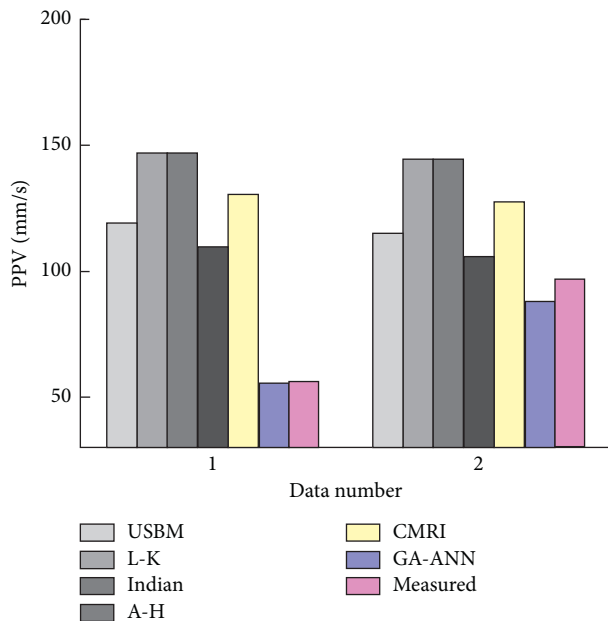


FIGURE 11: PPV values predicted by the GA-ANN model and the empirical models.

at two different monitoring points are very similar. In addition, the maximum charge per delay and Euclidean distance are found to significantly influence the PPV through

correlation analysis. In fact, the influence of deviating direction, hole spacing, burden, and explosive type on the PPV cannot be ignored according to the data in this paper. Coupled with the advantages of neural networks in solving nonlinear problems, these reasons make the predicted PPV using the model in this paper more accurate than the empirical formulas. This can also be seen from the PPV prediction results of the two monitoring points. Compared with the traditional empirical formula, the predicted PPV values of the neural network at the two monitoring points with different deviating directions have marked differences.

## 6. Conclusion

This paper proposed a GA-ANN PPV prediction method. The input information of the PPV prediction method contains field conditions and blasting parameters, such as the deviating direction, horizontal distance, vertical distance, Euclidean distance, explosive type, burden, hole spacing, and maximum charge per delay. PCA was used to eliminate redundant and repetitive information of the field conditions and blasting parameters. The mean squared error of the outputs from the measured results was chosen as the fitting function to search for the best node number of the hidden layer. In this way, the GA-ANN PPV prediction model with a 4-5-1 topology was established for the Ashele copper mine. In the learning and testing data, the predicted results were in good agreement with the measured values. This model was used to predict and control the blasting vibration of a deep stope located at a 1012 m buried depth in the Ashele copper mine. Through the adjustment of blasting parameters, such as the maximum charge per delay, delay number, burden, and hole spacing, the blasting vibration was successfully reduced, and the crushing cave was protected from damage. By comparing the prediction results of the GA-ANN PPV prediction model with those of traditional empirical PPV prediction models, the superiority of the GA-ANN PPV prediction model was verified. Among the traditional PPV prediction methods, the Ambraseys–Hendron method was the best. The proposed GA-ANN PPV model can be used to guide the design of blasting parameters for field production.

## Data Availability

The datasets used in the present study are available from the corresponding author upon reasonable request.



## Conflicts of Interest

The authors declare that they have no conflicts of interest regarding the publication of this paper.

## Acknowledgments

This work was financially supported by project nos. 51704056 and 51974059 of the National Natural Science Foundation of China, project nos. 2017YFC0602904 and 2016YFC0801605 of the National Key Research and Development Plan of China, project no. 2017 M621152 of the Postdoctoral Science Foundation of China, and project nos. N160103006 and N180115010 of the Fundamental Research Funds for the Central University of China.

## References

- [1] E. Ghasemi, M. Ataei, and H. Hashemolhosseini, "Development of a fuzzy model for predicting ground vibration caused by rock blasting in surface mining," *Journal of Vibration and Control*, vol. 19, no. 5, pp. 755–770, 2013.
- [2] N. Jiang, C.B. Zhou, X.D. Luo, and S.W. Lu, "Damage characteristics of surrounding rock subjected to VCR mining blasting shock," *Shock and Vibration*, vol. 2015, Article ID 373021, 2015.
- [3] M. Monjezi, M. Hasanipanah, and M. Khandelwal, "Evaluation and prediction of blast-induced ground vibration at Shur River Dam, Iran, by artificial neural network," *Neural Computing and Applications*, vol. 22, no. 7–8, pp. 1637–1643, 2013.
- [4] M. Wang, X. Shi, and J. Zhou, "Charge design scheme optimization for ring blasting based on the developed Scaled Heelan model," *International Journal of Rock Mechanics and Mining Sciences*, vol. 110, pp. 199–209, 2018.
- [5] Y.-h. Li, S.-d. Xu, and J.-p. Liu, "A new convergence monitoring system for tunnel or drift based on draw-wire displacement sensors," *Tunnelling and Underground Space Technology*, vol. 49, pp. 92–97, 2015.
- [6] R.J. Durrheim, M.K.C. Roberts, A.T. Haile et al., "Factors influencing the severity of rock burst damage in South African gold mines," *The Journal of South African Institute of Mining and Metallurgy*, vol. 98, no. 2, pp. 53–57, 1998.
- [7] Q. Jiang, X.-T. Feng, T.-B. Xiang, and G.-S. Su, "Rockburst characteristics and numerical simulation based on a new energy index: a case study of a tunnel at 2,500 m depth," *Bulletin of Engineering Geology and the Environment*, vol. 69, no. 3, pp. 381–388, 2010.
- [8] G.A. Donald, T. Shahram, A. Keith, B. Patrice, and N.D. Stephen, "Ground vibrations produced by surface and near-surface explosions," *Applied Acoustics*, vol. 74, pp. 1279–1296, 2013.
- [9] R. Guo, C.L. Pan, and R.C. Yu, *Theory and Technology of Hard Rock Deposit with Rock Burst Tendency*, Metallurgical Industry Press, Beijing, China, 2003.
- [10] C. H. Dowding, "Suggested method for blast vibration monitoring," *International Journal of Rock Mechanics and Mining Sciences & Geomechanics Abstracts*, vol. 29, no. 2, pp. 145–156, 1992.
- [11] J. Zhou, X. Shi, and X. Li, "Utilizing gradient boosted machine for the prediction of damage to residential structures owing to blasting vibrations of open pit mining," *Journal of Vibration and Control*, vol. 22, no. 19, pp. 3986–3997, 2016.
- [12] A. Kahrman, "Analysis of parameters of ground vibration produced from bench blasting at a limestone quarry," *Soil Dynamics and Earthquake Engineering*, vol. 24, no. 11, pp. 887–892, 2004.
- [13] S. Xu, Y. Li, J. Liu, and F. Zhang, "Optimization of blasting parameters for an underground mine through prediction of blasting vibration," *Journal of Vibration and Control*, vol. 25, no. 9, pp. 1585–1595, 2019.
- [14] S. Xu, C. Zhang, Z. Chen, Y. Li, and J. Liu, "Accurate identification of microseismic waveforms based on an improved neural network model," *Journal of Applied Geophysics*, vol. 190, Article ID 104343, 2021.
- [15] T. N. Singh and V. Singh, "An intelligent approach to prediction and control ground vibration in mines," *Geotechnical and Geological Engineering*, vol. 23, no. 3, pp. 249–262, 2005.
- [16] M. Khandelwal and T. N. Singh, "Prediction of blast induced ground vibrations and frequency in opencast mine: a neural network approach," *Journal of Sound and Vibration*, vol. 289, no. 4–5, pp. 711–725, 2006.
- [17] M. Khandelwal and T. N. Singh, "Prediction of blast-induced ground vibration using artificial neural network," *International Journal of Rock Mechanics and Mining Sciences*, vol. 46, no. 7, pp. 1214–1222, 2009.
- [18] M. Monjezi, M. Ghafurikalajahi, and A. Bahrami, "Prediction of blast-induced ground vibration using artificial neural networks," *Tunnelling and Underground Space Technology*, vol. 26, no. 1, pp. 46–50, 2011.
- [19] H. Bakhshandeh Amnieh, A. Siamaki, and S. Soltani, "Design of blasting pattern in proportion to the peak particle velocity (ppv): artificial neural networks approach," *Safety Science*, vol. 50, no. 9, pp. 1913–1916, 2012.
- [20] A. E. Álvarez-Vigil, C. González-Nicieza, F. López Gayarre, and M. I. Álvarez-Fernández, "Predicting blasting propagation velocity and vibration frequency using artificial neural networks," *International Journal of Rock Mechanics and Mining Sciences*, vol. 55, pp. 108–116, 2012.
- [21] P. Jayawardana, D. P. Thambiratnam, N. Perera, and T. Chan, "Dual in-filled trenches for vibration mitigation and their predictions using artificial neural network," *Soil Dynamics and Earthquake Engineering*, vol. 122, pp. 107–115, 2019.
- [22] A. K. Verma and T. N. Singh, "Intelligent systems for ground vibration measurement: a comparative study," *Engineering with Computers*, vol. 27, no. 3, pp. 225–233, 2011.
- [23] M. T. Mohamed, "Performance of fuzzy logic and artificial neural network in prediction of ground and air vibrations," *International Journal of Rock Mechanics and Mining Sciences*, vol. 48, no. 5, pp. 845–851, 2011.
- [24] D. J. Armaghani, M. Hajihassani, E. T. Mohamad, A. Marto, and S. A. Noorani, "Blasting-induced flyrock and ground vibration prediction through an expert artificial neural network based on particle swarm optimization," *Arabian Journal of Geosciences*, vol. 7, no. 12, pp. 5383–5396, 2014.
- [25] M. Hajihassani, D. Jahed Armaghani, H. Sohaei, E. Tonnizam Mohamad, and A. Marto, "Prediction of airblast-overpressure induced by blasting using a hybrid artificial neural network and particle swarm optimization," *Applied Acoustics*, vol. 80, pp. 57–67, 2014.
- [26] M. Hajihassani, D. Jahed Armaghani, A. Marto, and E. Tonnizam Mohamad, "Ground vibration prediction in quarry blasting through an artificial neural network optimized by imperialist competitive algorithm," *Bulletin of Engineering Geology and the Environment*, vol. 74, no. 3, pp. 873–886, 2015.

- [27] Y. Azimi, S. H. Khoshrou, and M. Osanloo, "Prediction of blast induced ground vibration (BIGV) of quarry mining using hybrid genetic algorithm optimized artificial neural network," *Measurement*, vol. 147, Article ID 106874, 2019.
- [28] H. Nguyen, C. Drebenstedt, X.-N. Bui, and D. T. Bui, "Prediction of blast-induced ground vibration in an open-pit mine by a novel hybrid model based on clustering and artificial neural network," *Natural Resources Research*, vol. 29, no. 2, pp. 691–709, 2020.
- [29] J. N. D. Gupta and R. S. Sexton, "Comparing backpropagation with a genetic algorithm for neural network training," *Omega*, vol. 27, no. 6, pp. 679–684, 1999.
- [30] J.-p. Liu, R. Wang, G. Lei, Y.-t. Si, S.-d. Xu, and Y.-h. Li, "Studies of stress and displacement distribution and the evolution law during rock failure process based on acoustic emission and microseismic monitoring," *International Journal of Rock Mechanics and Mining Sciences*, vol. 132, Article ID 104384, 2020.
- [31] J. Cohen, *Statistical Power Analysis for the Behavioral Sciences*, Lawrence Erlbaum Associates, Publishers, Hillsdale, NJ, USA, 2nd edition, 1988.
- [32] W.I. Duvall and B. Petkof, *Spherical propagation of explosion of generated strain pulses in rocks*, pp. 21-22, US Bureau of Mines, Washington, DC, USA, 1958.
- [33] U. Langefors and B. Kihlstrom, *The Modern Technique of Rock Blasting, seconded*, p. 405, Wiley Publisher, New York, NY, USA, 1973.
- [34] Bureau of Indian Standards, *Criteria for safety and design of structures subjected to underground blast*, Bureau of Indian Standards, Manek Bhawan, New Delhi, India, 1973.
- [35] N.R. Ambraseys and A.J. Hendron, "Dynamic behaviour of rock masses," *Rock Mechanics in Engineering Practices*, pp. 203–207, Wiley, London, UK, 1968.
- [36] P. Roy, "Putting ground vibration predictors into practice," *Colliery Guardian*, vol. 241, pp. 63–67, 1993.

## Research Article

# Testing Method for the Range of Fracture Zone of Rock Slope under Blasting Load

Zhide Wang,<sup>1</sup> Zuyao Ma,<sup>1</sup> Yuanyou Xia,<sup>1</sup> Xiong Zhou,<sup>1</sup> Manqing Lin,<sup>2</sup> Jie Li,<sup>1</sup>  
and Jinyuan Wang<sup>1,3</sup> 

<sup>1</sup>School of Civil Engineering and Architecture, Wuhan University of Technology, Wuhan 430070, China

<sup>2</sup>Engineering Research Center of Phosphorus Resources Development and Utilization of Ministry of Education, Wuhan Institute of Technology, Wuhan 430205, China

<sup>3</sup>State Key Laboratory of Water Resources and Hydropower Engineering Science, Wuhan University, Wuhan 430072, China

Correspondence should be addressed to Jinyuan Wang; [jinyuan.wang521@whut.edu.cn](mailto:jinyuan.wang521@whut.edu.cn)

Received 12 January 2021; Accepted 27 May 2021; Published 7 June 2021

Academic Editor: Qi ZHAO

Copyright © 2021 Zhide Wang et al. This is an open access article distributed under the Creative Commons Attribution License, which permits unrestricted use, distribution, and reproduction in any medium, provided the original work is properly cited.

In engineering blasting, the determination of the range of rock blasting fracture zone has important guiding significance for blasting construction. This paper proposes a method that can accurately and directly obtain the range of rock blasting fracture zone. Based on the theory of elastic wave propagation, test rods which are made of appropriate material are selected and prepared. A certain number of boreholes are drilled for subsequent insertion of the test rods along the direction perpendicular to the free surface of the excavation at a certain distance from the blast hole. Based on the field blasting test results, the deepest fracture position of the test rod is used as the boundary of the blasting fracture zone, and the range of the rock blasting fracture zone is obtained. A numerical analysis model is established according to the Mohr–Coulomb constitutive relationship and the Von Mises yield criterion. Then, the range of the fracture zone and the maximum horizontal radius of the fracture zone are analyzed and obtained. The numerical analysis results are compared with the field measured data. It is demonstrated that the range of the fracture zone obtained by the numerical simulation is in good agreement with the blasting test results of the pre-embedded test rods. The research results can provide references for the safety control of blasting and excavation of rock slopes.

## 1. Introduction

Because blasting has the merits of fast excavation speed, high efficiency, and low cost, it has been widely used in the process of rock slope excavation and open-air pit mining. However, blasting inevitably affects and damages the slope. The study of the maximum horizontal radius and range of the slope fracture zone can guide on-site blasting excavation and is of great significance to retain the integrity of the bedrock and ensure the engineering safety. It is also a problem that the engineering community is generally concerned about. When the explosive is buried adjacent to the ground free surface, the phenomenon of rupture, bulging, and throwing will occur according to the distance between the explosion center and the free surface. Livingston [1] divided the explosive depth into four zones. When the

explosive depth is in the impact damage zone, the surface rocks exhibit bulging and throwing, forming a blasting funnel. According to different blasting action indexes, the blasting funnel can be divided into four forms, i.e., standard throwing blasting funnel, strengthened throwing blasting funnel, weakened throwing blasting funnel, and loosened blasting funnel. When the explosive explodes in the blast hole, a high-strength dynamic stress wave will be formed on the surface of the rock outside the blast hole, and then the stress wave will propagate as an elastic wave in the surrounding rocks, producing crushing zones, fracture zones, and vibration zones [2]. Research [3, 4] showed that the radius of the crushed circle is about 2~3 times the charging radius, but the results of the research on the relationship between the radius of the fracture zone and the charging radius are controversial.

Regarding the theoretical description of the damage caused by explosive loads to rock masses, it is currently mainly quantified by damage variables. Researchers have made certain progress in this regard. For example, Taylor et al. [5, 6] have defined damage variables of rock by describing the statistical distribution characteristics of fractures and established the corresponding damage model. Chen et al. [7–10] further customized the damage variables, established a damage model that considers the integrity of the rock mass, and conducted a research on the range of blasting damage. At present, the widely used damage models include Taylor–Chen–Kuzmaul (TCK) model and YANG model [11, 12]. The research on the range of blasting damage is often carried out by a combination of field test and numerical analysis [13]. In the aspect of field testing, testing methods such as rock drilling acoustic wave testing and borehole television are widely used to determine the range of damage and tend to be convenient and efficient [14–18]. However, the acoustic wave test method requires water as a coupling agent, while the accuracy of the borehole television method needs to be further improved. Both methods need to reserve holes in advance, which is not necessarily required in actual blasting shock wave propagation. In terms of numerical analysis, numerical software such as ANSYS/LS-DYNA and FLAC3D is generally used. Based on the Von Mises yield criterion, tensile stress failure criterion, or compressive stress failure criterion in the rock, the range of blasting damage is determined by adopting equivalent explosive load, appropriate blasting geometric model, and constitutive model, combined with actual boundary conditions and initial conditions [19, 20]. Pan et al. [21] believed that there is a free-surface blasting, and the failure mode of the rock is mainly tensile failure. The Von Mises yield criterion is used as the basis for rock failure under blasting load, and the optimal hole bottom distance and minimum resistance line are obtained. Li et al. [19] determined the range of blasting damage according to the effective stress in the rock, which turns out relatively accurate. Although the related research is much, due to the complicated generation mechanism and evolution law of the blasting fracture zone, there are visible differences in the range of the fracture zone obtained. Moreover, there are relatively few studies on the practical application of the theory that describes stress wave propagation through the interface between different media.

On the basis of previous research results, this paper attempts to propose a more accurate and intuitive test method to determine the range of rock blasting fracture zone. In the area near the blast hole, the pre-embedded test rod was drilled along the direction perpendicular to the free surface of the excavation. The rupture depth of each test rod at different positions from the blast hole was obtained through the field blasting test, and the range of the rock fracture zone under the blasting load was obtained. The results will provide construction references for safe blasting excavation of rock slopes.

## 2. Test Method and Principle

**2.1. Test Method.** According to the wave impedance, compressive strength, and dynamic compressive strength of the rock at the test site, the appropriate test rod material is selected and test rods with similar materials are prepared in the laboratory. The ratio of the dynamic compressive strength of the test rod to the dynamic tensile strength of the rock is required to be close to the transmission coefficient of the stress wave at the interface between the test rod and rock. The transmission coefficient is determined by the ratio of the wave impedance of the test rod material to the rock.

At a certain distance from the blast hole, each test hole is drilled along the direction perpendicular to the free surface of the excavation. The test holes have the same depth as that of the blast hole and are numbered in an increasing order with the distance from the blast hole. The prepared test rods are numbered accordingly based on their respective test holes. The diameter of the test hole and blast hole drilled by the field drill is slightly larger than the diameter of the test rod. After each test rod is placed into the test hole separately, the gap between them is filled with gravel so that the test rod is in close contact with the original rock. After blasting, the maximum rupture range of the test rod is taken as the range of blasting fracture zone of the rock.

**2.2. Test Principle.** The rock is in a three-dimensional stress state of tension and compression. Due to the impact load, the surrounding rock is in a strongly compressed state. The explosive stress is much greater than the dynamic compressive strength of the rock. Subjected to the great explosive stress and the action of the high temperature and high pressure produced by the explosive gas, the rock is crushed. Outside the crushing zone, the explosive stress in the rock is less than the dynamic compressive strength of the rock and the tensile stress generated in the rock is greater than the dynamic tensile strength of the rock. As a result, the rock is subjected to tensile failure [4]. The Von Mises yield criterion is used to approximately judge whether the rock is damaged [21]. Radial stress  $\sigma_r$  and tangential stress  $\sigma_\theta$  at any point in the rock are as shown in Figure 1 [22]. The sign rule is according to the convention which considers the tension positive. The stress at any point in the rock can be expressed as follows:

$$|\sigma_i| = \sqrt{\frac{(\sigma_r - \sigma_\theta)^2 + (\sigma_\theta - \sigma_z)^2 + (\sigma_z - \sigma_r)^2}{2}}, \quad (1)$$

where  $\sigma_i$  is Von Mises stress (MPa);  $\sigma_r$  is the radial stress in the rock (MPa);  $\sigma_\theta$  is the tangential stress in the rock (MPa); and  $\sigma_z$  is the normal stress along the longitudinal axis of the blast hole (MPa).

According to the Von Mises criterion, there are inequalities expressed by equation (2). When the stress at any



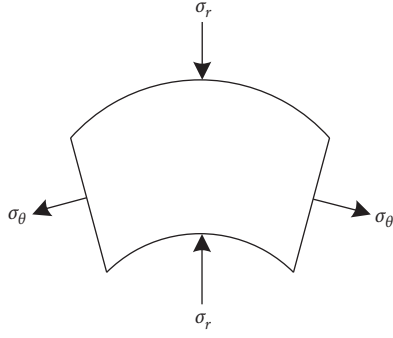


FIGURE 1: Stress state at any point in the rock mass.

point in the rock satisfies equation (2), the rock will be damaged [4].

$$|\sigma_i| \geq \begin{cases} \sigma_{td} \text{ (fractured circle),} \\ \sigma_{cd} \text{ (crushed circle),} \end{cases} \quad (2)$$

where  $\sigma_{td}$  is the dynamic tensile strength of the rock (MPa) and  $\sigma_{cd}$  is the dynamic compressive strength of the rock (MPa). The dynamic tensile strength of the rock is generally determined by  $\sigma_{td} = (4 \sim 8)\sigma_t$ , where  $\sigma_t$  is the static tensile strength of the rock. The dynamic compressive strength of rock increases with the increase in the loading strain rate [4]:

$$\sigma_{cd} = \sigma_c \dot{\epsilon}^{(1/3)}, \quad (3)$$

where  $\sigma_c$  is the static compressive strength of the rock (MPa) and  $\dot{\epsilon}$  is the loading strain rate of the rock ( $s^{-1}$ ).

As shown in Figure 2, when the explosive stress wave passes through the interface between the test rod and the rock, reflection and transmission occur. When an elastic stress wave is transmitted from one medium to another medium, the reflection and transmission of the stress wave will occur at the interface of the two media. According to Newton's third law [4],

$$\begin{cases} \sigma_R = F\sigma_I, \\ \sigma_T = T\sigma_I, \end{cases} \quad (4)$$

where  $\sigma_R$  and  $\sigma_T$  are the reflected wave stress and the transmitted wave stress of the particles on both sides of the interface, respectively, and  $\sigma_I$  is the incident wave stress of the particle (MPa).

$$\begin{cases} n = \frac{\rho_1 c_1}{\rho_2 c_2}, \\ F = \frac{1-n}{1+n}, \\ T = \frac{2}{1+n}, \end{cases} \quad (5)$$

where  $F$  and  $T$  are the reflection coefficient and transmission coefficient, respectively;  $\rho_1$  and  $\rho_2$  are the densities of the original medium and the other medium ( $kg/m^3$ ), respectively;  $c_1$  and  $c_2$  are the longitudinal wave velocities of the

original medium and the other medium (m/s), respectively; and  $n$  is the ratio of the wave impedance of the two media.

Since the compressive strength of the test rod is much smaller than that of the rock on-site, the intensity of the transmitted stress wave after the explosion stress wave passes through the interface between the test rod and the rock is much greater than the dynamic compressive strength of the test rod. Therefore, the test rod will be mainly subjected to compressive failure. When the original on-site rock is at the position of the test rod, the intensity of the stress wave passed is smaller than the dynamic compressive strength of the rock. It thus cannot directly crush the rock. However, it can still damage the rock. The relatively large radial compression results in radial compressive strains and tangential tensile strains in the rock layer surrounding the crushing zone. Once the generated tangential tensile stress is greater than the dynamic tensile strength of the rock, radial cracks will be generated, which form the fracture zone. Therefore, the original rock corresponding to the rod position is mainly subjected to tensile failure.

When the ratio of the dynamic compressive strength of the test rod to the dynamic tensile strength of the rock and the ratio of the transmitted wave stress to the incident wave stress (i.e., transmission coefficient) are close, it can be considered that the fracture position of the test rod under the blasting load and its corresponding field rock is the same, so the fracture position and fracture range of the test rod can be used to judge the fracture range of the rock on-site.

### 3. Field Blasting Test

**3.1. Project Overview.** A limestone mine in Bazhong, Sichuan, is a hillside open-pit mine. The mine mainly yields limestone and flint limestone. The rock mass in the mining area has a steeply dipping layered structure. The fractures are generally developed, but the connectivity is poor, and no secondary folds and faults are seen. The integrity of the rock formation is good, and the geological structure is relatively simple. The blasting scheme adopts a top-down open-pit mining method with horizontal steps, following the principle of simultaneous mining and stripping with stripping first. The on-site blasting test was selected on a platform with an elevation of 1278 m, and the test location is shown in Figure 3. There was a certain thickness (around 5 cm) of fine gravel muck on the surface (see Figure 4), but the thickness of the top soil of the platform is negligible relative to the hole depth.

**3.2. Drilling and Blasting Parameters.** The field blasting test uses 2# rock emulsion explosive, and the drilling and blasting parameters are shown in Table 1. The physical and mechanical parameters of the limestone rock obtained by laboratory tests are shown in Table 2. The values of  $c_1$  and  $\varphi_1$  listed in Table 2 were obtained by triaxial compression tests on the limestone rock in natural state. The natural rock samples were tested at five confining pressures (i.e., 2 MPa, 4 MPa, 6 MPa, 8 MPa, and 10 MPa). Mohr's circles and obtained strength parameters are shown in Figure 5.



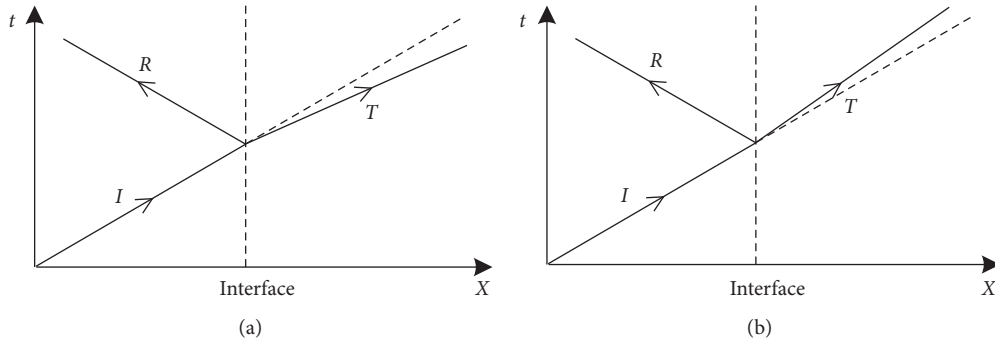


FIGURE 2: Reflection and transmission of elastic waves: (a)  $\rho_1 c_1 < \rho_2 c_2$ ; (b)  $\rho_1 c_1 > \rho_2 c_2$ .



FIGURE 3: Mine test site: (a) test platform; (b) test position.

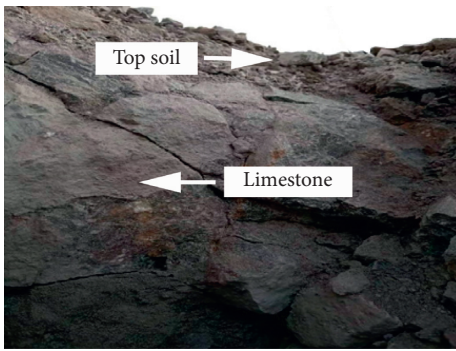


FIGURE 4: Photograph of the blast hole taken upward from the inside.

**3.3. Parameter Determination of Test Rod.** In the field blasting test, the gypsum rod was used as the test rod. The gypsum rods are prepared by mixing gypsum and water with a certain gravimetric ratio. Three kinds of gypsum rods are made by adopting water-gypsum ratios of 0.7, 1.0, and 1.3, respectively. The physical parameters of the gypsum rods with the three water-gypsum ratios are shown in Table 3.

The longitudinal wave velocity of the stress wave in the elastic medium is as follows:

$$c_0 = \sqrt{\frac{E}{\rho_0}}, \quad (6)$$

where  $c_0$  is the longitudinal wave velocity in the medium (m/s);  $E$  is the elastic modulus of the medium (Pa); and  $\rho_0$  is the density of the medium ( $\text{kg}/\text{m}^3$ ).

In engineering blasting, the loading rate in crushed zone is high, which is taken as  $\dot{\epsilon} = 10^0 \sim 10^4 \text{ s}^{-1}$ . When the gypsum rod is located outside the crushed zone, the loading rate decreases further. According to the condition of the field testing, the load rate is taken as  $\dot{\epsilon} = 10^2 \text{ s}^{-1}$ . The dynamic compressive strength of the gypsum rod can be obtained by equation (3). From equation (6), it can be derived that the longitudinal wave velocities of the gypsum rods with water-gypsum ratios of 0.7, 1.0, and 1.3 are  $c_{p0.7} = 1277.7 \text{ m/s}$ ,  $c_{p1.0} = 1149.8 \text{ m/s}$ , and  $c_{p1.3} = 1100.6 \text{ m/s}$ , respectively.

The longitudinal wave velocity in the rock measured by sonic tester on-site is  $c_p = 3430 \text{ m/s}$ . The dynamic tensile strength of the on-site rock is determined as  $\sigma_{td1} = 6\sigma_t = 33.42 \text{ MPa}$ , in which the value of the static tensile strength  $\sigma_t$  is from the laboratory tensile strength test result listed in Table 2. Using equation (5), the wave impedance ratio,  $n$ , and the transmission coefficient,  $T$ , of gypsum rods with different water-gypsum ratios and the

TABLE 1: Drilling and blasting parameters of the field blasting test.

Blast hole diameter (cm)	Blast hole depth (m)	Dose (kg)	Blockage length (cm)
14	2	10	40

TABLE 2: Physical and mechanical parameters of the limestone rock.

Elastic modulus $E_1$ (GPa)	Poisson's ration $\mu_1$	Density $\rho_1$ ( $\text{kg} \cdot \text{m}^{-3}$ )	Internal friction angle $\varphi_1$ ( $^\circ$ )	Cohesion $c_1$ (MPa)	Tensile strength $\sigma_t$ (MPa)
38.5	0.296	2680	55	16.25	5.57

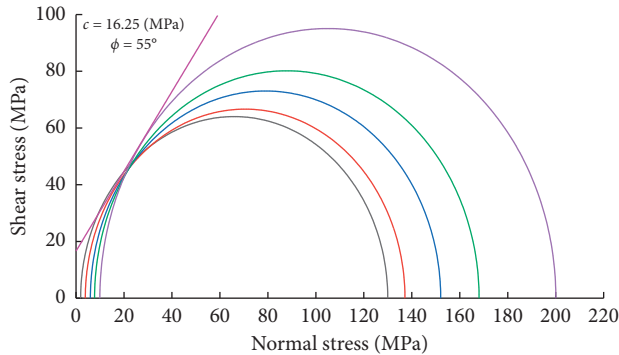


FIGURE 5: Compressive strength parameters of limestone rock samples in natural state.

original rock at the contact surface can be obtained. The ratio of the dynamic compressive strength of the gypsum rod to the dynamic tensile strength of the rock can be then calculated. The calculation results are tabulated in Table 4.

It can be seen from Table 4 that when the ratio of water to gypsum is 1.0, the transmission coefficient  $T$  is 0.247, which is close to the ratio of the dynamic compressive strength of the gypsum rod to the dynamic tensile strength of the rock  $\sigma_{cd2}/\sigma_{td1} = 0.229$ . Therefore, the gypsum rod with a water-gypsum ratio of 1.0 is selected for field testing.

The preparation procedure of the test rod is as follows.

- (1) A PVC pipe with a length of 1.0 m and an inner diameter of 0.14 m was cut and split into two halves along the center line. After brushing a layer of oil on the inner side of the pipe, it was then wounded with adhesive tape for bonding.
- (2) One end of the PVC pipe was sealed, and an iron wire was fastened at the center of sealed end.
- (3) Gypsum slurry was then poured into the PVC pipe. When grouting, the iron wire was kept in a centered and tensed state, while vibrating and stirring until the gypsum was uniformly formed.
- (4) The gypsum rods were taken out and cured naturally for 7 days. Two 1.0 m length gypsum rods are connected to a 2.0 m long gypsum rod through the embedded iron wire.

**3.4. Blasting Test.** At a distance of 1.0 m from the blast hole, test holes were drilled along the direction perpendicular to the free surface near the excavation. In the field blasting test, the orientation angle of the connection line between the blast hole and the nearest test hole is  $60^\circ$ . The test hole spacing is 0.6 m. Before the test, the prepared gypsum rods were numbered 1~4 according to their distances from blast hole

from the near to the distant. The diameter of the gypsum rod was 0.14 m, and the test holes and blast hole were all 2.0 m deep. The layout of the on-site shallow hole blasting test is shown in Figure 6, and the gypsum rods before the blasting test are shown in Figure 7.

**3.5. Result Analysis.** After the field blasting test, the free-surface fracture zone on the top of the blast hole is shown in Figure 8, and the rupture range of the gypsum rod is shown in Figure 9.

It can be seen from Figure 8 that the explosive center with a burial depth of 1.2 m is in the impact damage zone, forming a loose blasting funnel [1], and bulging occurs on the slope surface. The longest radial fracture length measured on-site is 3.16 m, which is about 20 times the radius of the blast hole. The distance from the circumferential fracture closest to the blast hole to the circumference of the blast hole measured on-site is 0.224 m, which is about 3 times the radius of the blast hole. Therefore, the field test results conform to the general blasting law.

In Figure 9(a), the gypsum rods are No. 1~4 in order from right to left. Since the No. 1 and No. 2 gypsum rods are very close to the blast hole and most affected by the blasting, the lower half parts stuck in the test hole and were not extracted. The measurements of rupture position are shown in Figure 9(b). It can be seen from Figure 9 that the fracture depth of No. 3 gypsum rod is 1.445 m, and the upper part is broken; the fracture depth of No. 4 gypsum rod is 0.3 m. Because there is a fracture in the lower part of No. 3 gypsum rod and the No. 1 and No. 2 gypsum rods are closer to the blast hole, it can be inferred that there are fractures in both upper and lower parts for No. 1 and No. 2 gypsum rods. According to the fracture depth of each gypsum rod, it can be concluded that the fracture depth of the gypsum rod decreases with the increase in the distance from the explosion center during the blasting process, and the rock fracture range is funnel-shaped.

## 4. Numerical Simulation

The combination of field test and numerical analysis can more accurately reproduce the damage range of the rock under the blasting load. Therefore, the numerical analysis is conducted to further validate the accuracy of using test rod to obtain the fracture range of the original rock on-site under the blasting load.

TABLE 3: The physical parameters of the gypsum rods with different water-gypsum ratios.

Water-gypsum ratio	Elastic modulus $E_2$ (GPa)	Poisson's ratio $\mu_2$	Density $\rho_2$ ( $\text{kg} \cdot \text{m}^{-3}$ )	Compressive strength $\sigma_c$ (MPa)
0.7	2.31	0.250	1408.8	4.08
1.0	1.49	0.198	1127.1	1.65
1.3	1.23	0.169	1015.4	1.25

TABLE 4: Calculated parameters of the original rock and test rods with different water-gypsum ratios.

Water-gypsum ratio	Wave impedance ratio $n$	Transmission coefficient $T$	Dynamic compressive strength $\sigma_{cd2}$ (MPa)	$\sigma_{cd2}/\sigma_{td1}$
0.7	5.10	0.327	18.930	0.566
1.0	7.09	0.247	7.656	0.229
1.3	8.20	0.217	5.800	0.173

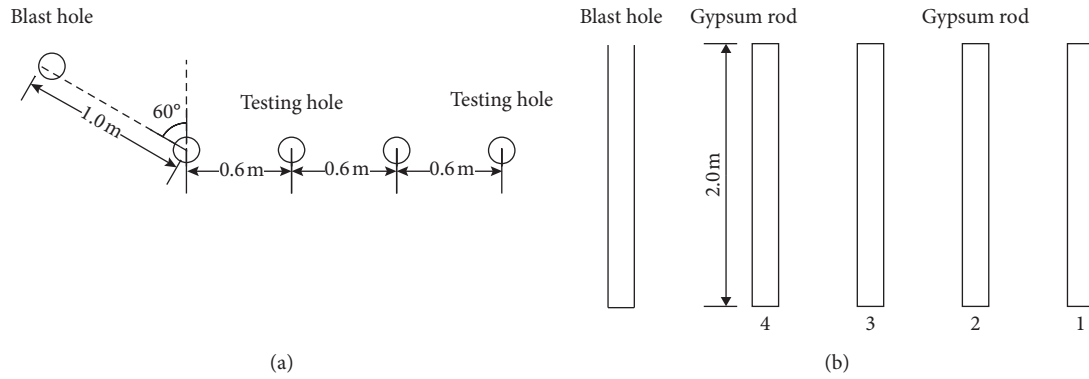


FIGURE 6: Schematic diagram of the field blasting test: (a) plan view; (b) sectional view.



FIGURE 7: Gypsum rod before the blasting test.

**4.1. Blasting Load.** The Chapmam–Jouguet (C-J) theory can qualitatively explain the physical phenomenon of explosive detonation. The C-J model of detonation regards the detonation surface as a sudden interface [4] between the explosive without thickness and the reactant. Under C-J conditions, the average instantaneous detonation pressure of condensed explosive,  $P_0$ , is expressed as follows:

$$P_0 = \frac{\rho_0 D_0^2}{\gamma + 1}, \quad (7)$$

where  $\rho_0$  is the explosive density;  $D_0$  is the explosive velocity;  $\gamma$  is a constant related to the properties of condensed explosives and charge density, and the value is 2~3. For 2# rock emulsion explosive, take  $\rho_0 = 1200 \text{ kg/m}^3$ ,  $D_0 = 3600 \text{ m/s}$ , and  $\gamma = 3$ .

The peak shock pressure,  $P_b$ , is expressed as follows:

$$P_b = \frac{2\rho c_p}{\rho c_p + \rho_0 D_0} P_0, \quad (8)$$

where  $\rho$  is the rock density ( $\text{kg/m}^3$ ) and  $c_p$  is the measured longitudinal wave velocity in the rock,  $c_p = 3430 \text{ m/s}$ .

The field blasting test adopts a coupled charge structure and uses a triangular load to approximate the blasting load. The impact pressure loading curve on the blast hole wall can be simplified to a triangular loading curve, as shown in Figure 10.

The explosion load increases rapidly at the moment of blasting, assuming the rise time of the explosion load  $t_r$  equals to the propagation time of the detonation wave [23], namely:

$$t_r = \frac{L_1}{D_0}, \quad (9)$$

where  $L_1$  is the length of the charge.



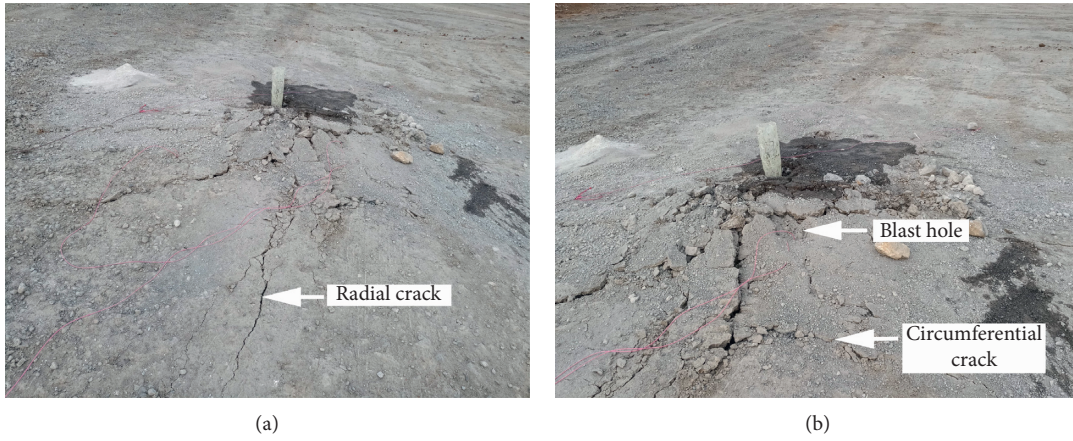


FIGURE 8: Fracture diagram after the blasting test: (a) radial crack; (b) circumferential crack.

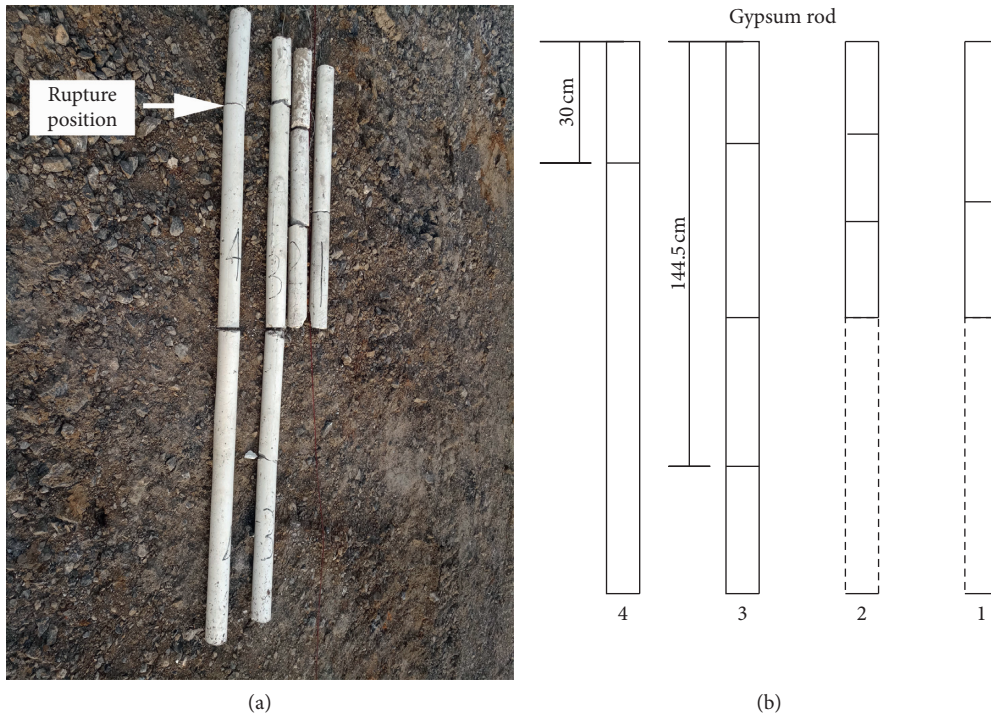


FIGURE 9: Gypsum rod after the blasting test: (a) field observation; (b) measured data.

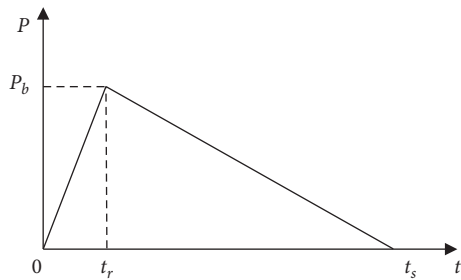


FIGURE 10: Equivalent diagram of blasting load.

The ratio of the rise time to the total action time of the commonly used triangular explosion load [23] is  $1: 7Q^{0.15}$  ( $Q$  is the charge dosage; see Table 1). The total action time of the explosion load  $t_s$  can be obtained by the following equation:

$$t_s = 7Q^{0.15}t_r. \tag{10}$$

Calculated by equations (9) and (10), the rise time of the on-site gypsum rod test load is  $t_r = 0.5$  ms. The total load time is  $t_s = 5.0$  ms.

## 4.2. Calculation Model

**4.2.1. Constitutive Model.** Assuming that the rock is an isotropic material, the Mohr–Coulomb constitutive model is adopted in this work to analyze the constitutive stress-strain relationship of rock materials.

**4.2.2. Model Size and Boundary Conditions.** In order to simplify the calculation, a 1/4 cylinder is taken as the calculation model based on the symmetry. In order to reduce the influence of the model boundary, based on the size of the crushing zone and the fracture zone produced by rock blasting, the 1/4 cylinder with the radius of 8.0 m and the height of 8.0 m is used as the model for simulating the field blasting. The blast hole radius is set to be 0.07 m according to the actual on-site geometry. The vertical boundary of the model restricts the horizontal displacement. The lower boundary restricts the vertical displacement. The circumferential boundary adopts a static viscous boundary to reduce the influence of boundary reflection waves on the calculation results. The top horizontal plane is set as the free surface, and the particle velocity on each boundary in the initial state is set to be 0.

**4.2.3. Damping.** In the dynamic analysis with large strain, simply setting a very small damping ratio can meet the requirements. Rayleigh damping [3] is selected in this work, and its value is set to be 0.005.

**4.2.4. Meshing.** The size of the grid element has a great effect on the numerical simulation results. To reach decent accuracy, the following relationship [3] must be satisfied:

$$\Delta l \leq \left( \frac{1}{8} \sim \frac{1}{10} \right) \lambda, \quad (11)$$

where  $\Delta l$  is the grid size and  $\lambda$  is the wavelength corresponding to the highest frequency  $f$  that signifies appreciable energy,  $\lambda = c/f$ , where  $c$  is the corresponding wave velocity.

Blasting vibration velocity waveforms and dominant frequencies were obtained by employing the blasting vibration tester (UBOX-5016; see Figure 11). The on-site blasting vibration velocity waveforms in horizontal radial, horizontal tangential, and vertical directions are shown in Figure 12.

It can be seen from Figure 12 that the maximum dominant frequency in three directions is  $f_m = 29.907$  Hz, which approximately represents the highest frequency  $f$ . The corresponding wave velocity  $c$  is approximately represented by the longitudinal wave velocity  $c_p$  of the rock, which is  $c_p = 3430$  m/s as measured. The wavelength is then obtained,  $\lambda \approx c_p/f_m = 114.7$  m. According to equation (11),  $\Delta l \leq (1/8 \sim 1/10)$  and  $\lambda = (11 \sim 14)$  m.

The cylindrical shell modeling method is adopted. The inner and outer radii of the shell are 0.07 m and 8.0 m, respectively. The number of grid elements in the radial direction is 20, and the size of the individual grid is increased

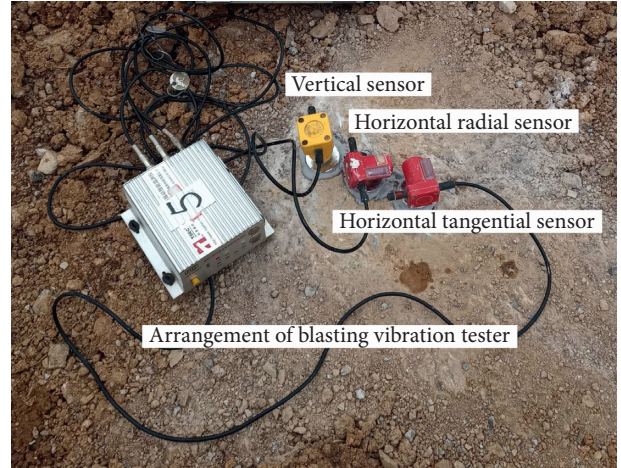


FIGURE 11: The arrangement of on-site blasting vibration tester.

by a ratio of 1.1 from center outward. The vertical plane is evenly divided into 10 grid elements within a depth of 2 m. In the depth range below 2 m, the size of the individual grid is increased downward by the ratio of 1.05. The centripetal part of the shell below the depth of 2 m is filled. The counterpart within the depth of 2 m is not filled to reserve the blast hole. The radius of the filling part is 0.07 m. The number of grids in the radial direction is 2, and the mesh division method is the same as that of the shell below the depth of 2 m. At the same time, the annulus sector is equally divided into 30 parts. The portions closer to the blast hole are divided more densely so as to ensure the accuracy of the calculation results and reduce the calculation convergence time. The minimum size of the model mesh is 0.03 m, and the maximum mesh size is 0.85 m. The numerical analysis model is shown in Figure 13. The red part is the blast hole.

**4.3. Result Analysis.** The Von Mises yield criterion is used as the rock failure criterion to depict the rock fracture zone in the numerical analysis. Figures 14 and 15 show the evolution process with time of the rock fracture zone in the horizontal and vertical planes, respectively.

It can be seen from Figures 14 and 15 that the fracture range of the rock under the blasting load increases with time. After 3.0 ms, the fracture range is basically unchanged, and the stress generated by blasting gradually attenuates. Therefore, the numerical analysis result at 3.0 ms is taken as the range of the rock fracture zone. The comparison of the numerical analysis and the measured results is shown in Figure 16.

It can be seen from Figure 16 that the fracture depths of No. 1~4 gypsum rods are 2.353 m, 2.161 m, 1.572 m, and 0.354 m, respectively. The measured fracture depths of No. 3 and No. 4 gypsum rods are close to the numerical analysis results, and the relative error between the numerical analysis results and the measured results of the gypsum rods is not more than 18%, which meets the requirements of engineering accuracy. At the same time, the fracture depths corresponding to No. 1 and No. 2 gypsum rods from the numerical analysis are both greater than 2.0 m, indicating



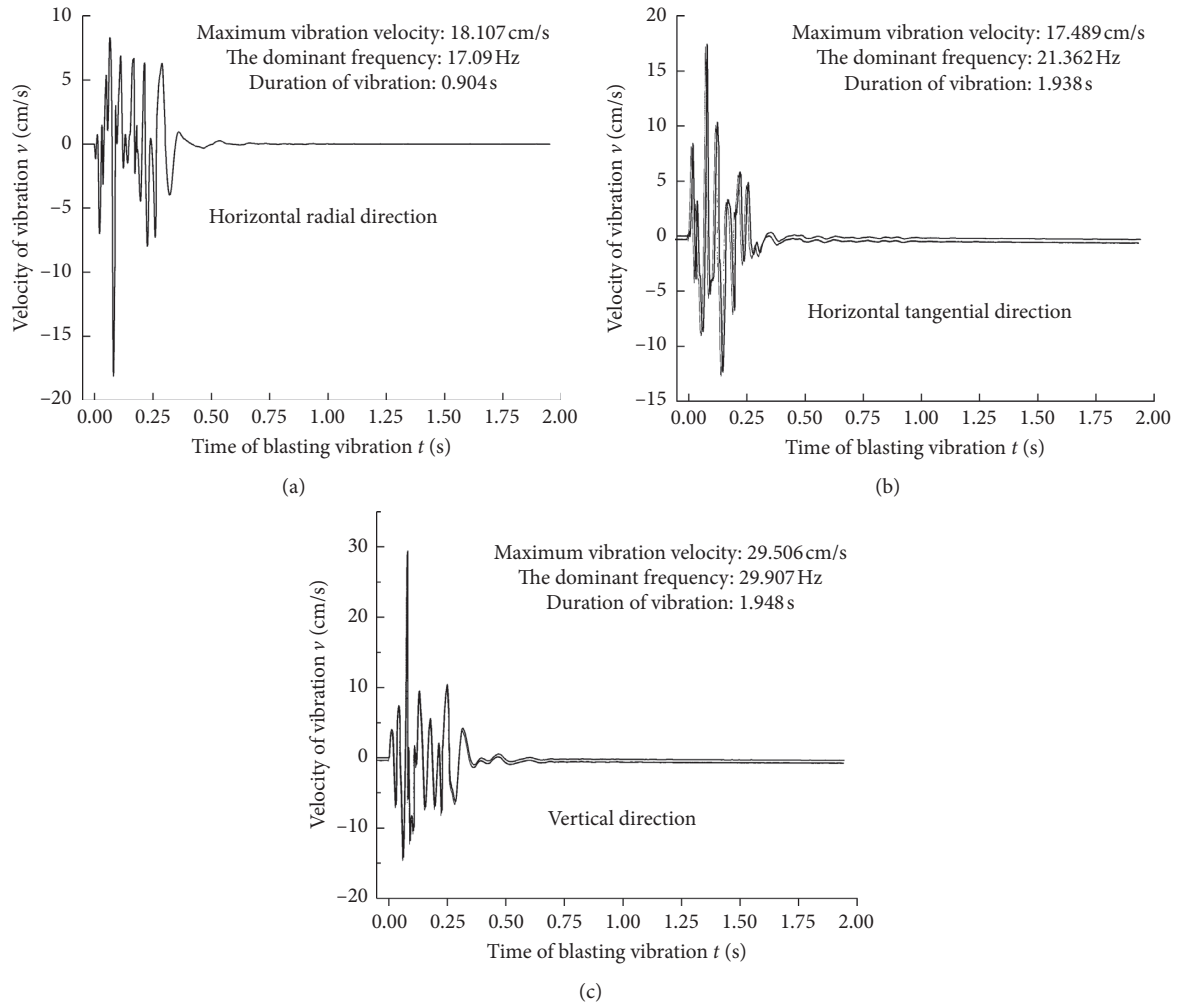


FIGURE 12: Field blasting vibration test results: (a) horizontal radial vibration of the particle; (b) horizontal tangential vibration of the particle; (c) vertical vibration of the particle.

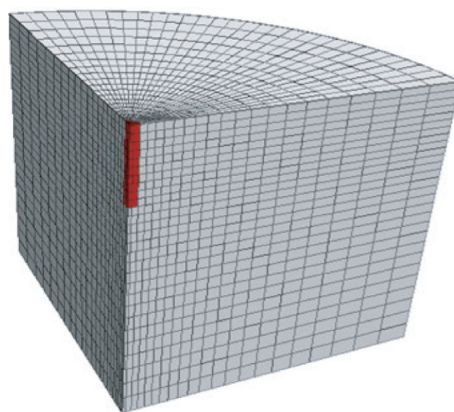


FIGURE 13: The meshing diagram of the numerical model.

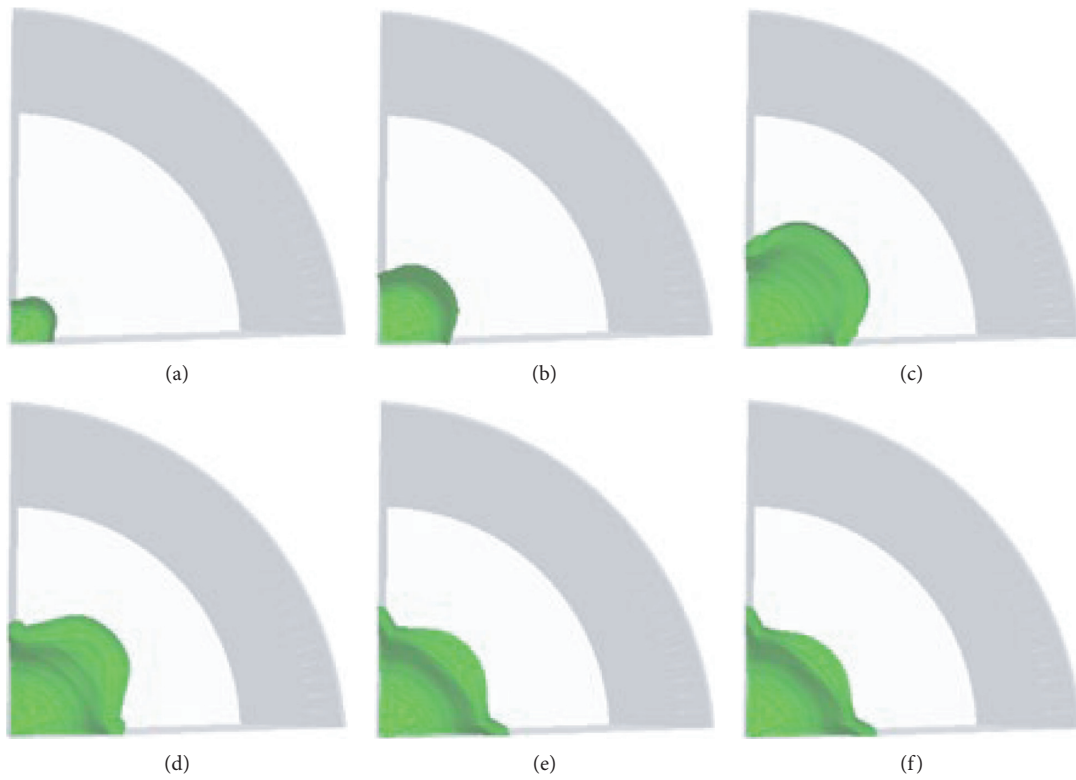


FIGURE 14: The development of rock mass fracture zone in bird's-eye view: (a) 0.5 ms; (b) 0.8 ms; (c) 1.5 ms; (d) 2.0 ms; (e) 2.5 ms; (f) 3.0 ms.

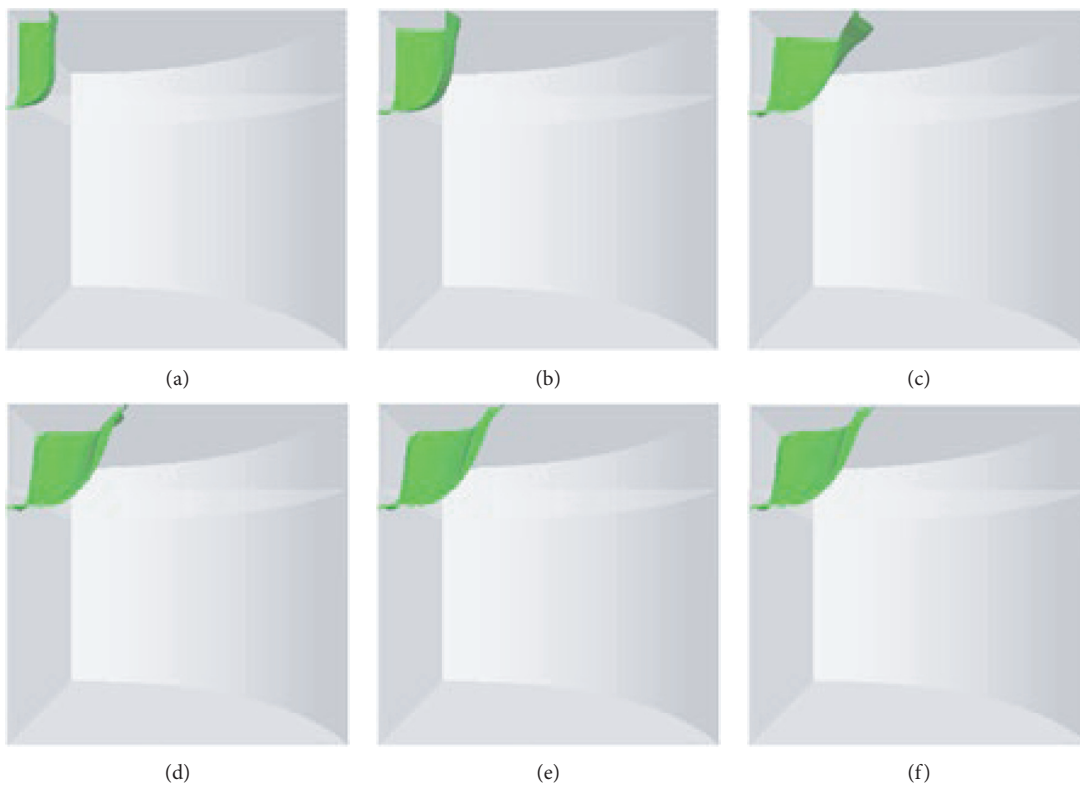


FIGURE 15: The development of rock mass fracture zone in head-up view: (a) 0.5 ms; (b) 0.8 ms; (c) 1.5 ms; (d) 2.0 ms; (e) 2.5 ms; (f) 3.0 ms.

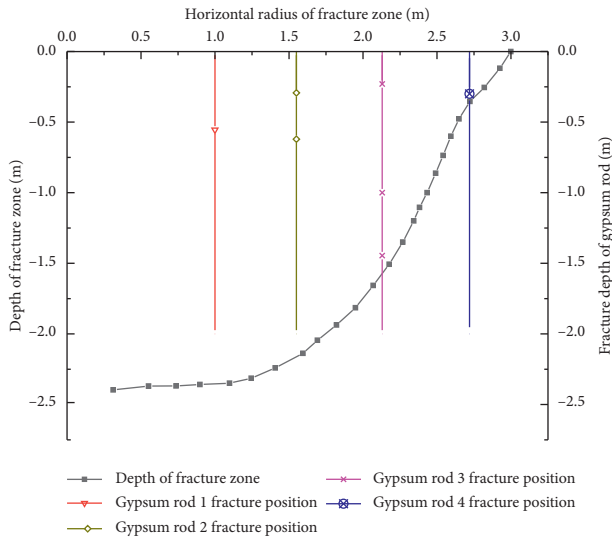


FIGURE 16: Comparison of the range of fracture zones in the blasting test.

that both the upper and lower parts of the No. 1 and No. 2 gypsum rods are broken, and the measured fracture depths of the lower parts of the gypsum rods are both greater than 2.0 m. Therefore, the borehole pre-embedded gypsum rod test can relatively accurately and intuitively reflect the critical fracture depth of the rock under the blasting load and thus obtain the range of the rock fracture zone.

## 5. Conclusions

This paper proposes a method that can accurately and directly obtain the range of the fracture zone of the rock slope under the blasting load. The basic principle of the method in which embedded test rods are drilled around the blast hole and subjected to blasting load is based on the reflection and transmission theory of the stress wave of different media interface. Based on the field blasting test and the numerical simulation presented in this study, the following conclusions can be drawn:

- (1) Based on the closeness between the transmission coefficient of the stress wave through the test rod-rock interface and the ratio of the dynamic compressive strength of the test rod to the dynamic tensile strength of the rock, the fracture range of the test rod after blasting can be used as the range of the surrounding rock fracture zone after the slope blasting.
- (2) In the field blasting test, the range of the surrounding rock blasting fracture zone conforms to the general distribution pattern of the surrounding rock fracture zone under blasting load.
- (3) The relative error between the field blasting test results and the numerical analysis results in this paper is less than 18%, indicating that the proposed test method has a good accuracy. The test method

described in this paper adopts shallow hole blasting, and this method is also applicable to deep hole blasting.

## Data Availability

The data sets used to support the findings of this study are included within the article.

## Conflicts of Interest

The authors declare that they have no conflicts of interest.

## Acknowledgments

This work was supported by the National Natural Science Foundation of China (no. 51909192) and the Open Project of Engineering Research Center of Phosphorus Resources Development and Utilization of Ministry of Education (no. LKF202004).

## References

- [1] C. W. Livingston, "Fundamental concepts of rock failure," *Quarterly of the Colorado School of Mines*, vol. 51, no. 3, pp. 1–11, 1956.
- [2] H. P. Rossmannith, K. Uenishi, and N. Kouzniak, "Blast wave propagation in rock mass-part I: monolithic medium," *Fragblast*, vol. 1, no. 3, pp. 317–359, 1997, in Chinese.
- [3] X. Xia, *Study on damage characteristics and safety threshold of rock vibration by blast*, Ph.D. thesis, Institute of Rock and Soil Mechanics, Chinese Academic of Sciences, Wuhan, China, 2000, in Chinese.
- [4] J. Dai, *Dynamic Behaviors and Blasting Theory of Rock*, Metallurgical Industry Press, Beijing, China, 2013, in Chinese.
- [5] L. M. Taylor, E.-P. Chen, and J. S. Kuzsmaul, "Microcrack-induced damage accumulation in brittle rock under dynamic loading," *Computer Methods in Applied Mechanics and Engineering*, vol. 55, no. 3, pp. 301–320, 1986.
- [6] R. Yang, W. F. Bawden, and P. D. Katsabanis, "A new constitutive model for blast damage," *International Journal of Rock Mechanics and Mining Sciences & Geomechanics Abstracts*, vol. 33, no. 3, pp. 245–254, 1996.
- [7] J. Chen, J. Zhang, and X. Li, "Rock blasting-induced damage zone under blasting excavation in a large underground chamber," *Journal of Central South University (Science and Technology)*, vol. 47, no. 11, pp. 3808–3817, 2016.
- [8] B. J. Thorne, P. J. Hommert, and B. Brown, "Experimental and computational investigation of the fundamental," in *Mechanisms of Cratering* Sandia National Labs, Albuquerque, NM, USA, 1990.
- [9] J. Lemaitre, "How to use damage mechanics," *Nuclear Engineering and Design*, vol. 80, no. 2, pp. 233–245, 1984.
- [10] Y. Yang, Z. Shao, J. Mi, and X. Xiong, "Effect of adjacent hole on the blast-induced stress concentration in rock blasting," *Advances in Civil Engineering*, vol. 2018, Article ID 5172878, 13 pages, 2018.
- [11] Z. L. Wang, Y. C. Li, and R. F. Shen, "Numerical simulation of tensile damage and blast crater in brittle rock due to underground explosion," *International Journal of Rock Mechanics and Mining Sciences*, vol. 44, no. 5, pp. 730–738, 2007.
- [12] L. Liu and P. D. Katsabanis, "Development of a continuum damage model for blasting analysis," *International Journal of*

- Rock Mechanics and Mining Sciences*, vol. 34, no. 2, pp. 217–231, 1997.
- [13] B. Mobaraki and M. Vaghefi, “Numerical study of the depth and cross-sectional shape of tunnel under surface explosion,” *Tunnelling and Underground Space Technology*, vol. 47, pp. 114–122, 2015.
- [14] J. H. Williams and C. D. Johnson, “Acoustic and optical borehole-wall imaging for fractured-rock aquifer studies,” *Journal of Applied Geophysics*, vol. 55, no. 1, pp. 151–159, 2004.
- [15] Y. Kanaori, “The observation of crack development around an underground rock chamber by borehole television system,” *Rock Mechanics and Rock Engineering*, vol. 16, no. 2, pp. 133–142, 1983.
- [16] K. J. Cunningham, “Application of ground-penetrating radar, digital optical borehole images, and cores for characterization of porosity hydraulic conductivity and paleokarst in the biscayne aquifer, Southeastern Florida, USA,” *Journal of Applied Geophysics*, vol. 55, no. 1-2, pp. 61–76, 2004.
- [17] S. Ray and S. Dauji, “Ground vibration attenuation relationship for underground blast: a case study,” *Journal of the Institution of Engineers (India): Series A: Series A*, vol. 100, no. 4, pp. 763–775, 2019.
- [18] Y. Fang, Z. Yao, and W. Gabriel, “Evaluating the impact of blast-induced damage on the rock load supported by liner in construction of a deep shaft: a case study of ventilation shaft of micangshan road tunnel project,” *Advances in Civil Engineering*, vol. 2020, Article ID 9068345, 19 pages, 2020.
- [19] X. Li, J. Chen, and Y. Li, “Research on blasting damage range and criterion of underground powerhouse in Xiluodu power stati,” *Chinese Journal of Rock Mechanics and Engineering*, vol. 29, no. 10, pp. 2042–2049, 2010, in Chinese.
- [20] Y. Hu, R. Li, X. Wu, G. Zhao, and Q. Zhang, “Blasting damage depth in layered jointed basalt before and after grouting,” *Journal of Geotechnical and Geoenvironmental Engineering*, vol. 145, no. 3, Article ID 04018113, 2019.
- [21] M. Pan, Y. Wu, and X. Shi, “Numerical simulation of deep hole blasting parameters in Fankou lead and zinc mine,” *Mining Technology*, vol. 13, no. 5, pp. 87–89, 2013, in Chinese.
- [22] X. Wang, “Study on damage range of rock mass under blasting impact,” *Journal Engineering Geology*, vol. 22, no. 2, pp. 233–237, 2014.
- [23] J. Yang, W. Lu, and M. Chen, “Determination of explosive load variation course of gun hole,” in *Proceedings of the 2nd National Engineering Safety and Protection Academic Conference*, pp. 773–777, Beijing, China, August 2010, in Chinese.

## Research Article

# Strength Weakening Effect of High Prestatically Loaded Marble Subjected to Low-Frequency Dynamic Disturbance under Point Load

Wuxing Wu <sup>1,2</sup> and Fengqiang Gong <sup>1,2</sup>

<sup>1</sup>Engineering Research Center of Safety and Protection of Explosion & Impact of Ministry of Education (ERCSPIME), Southeast University, Nanjing 211189, China

<sup>2</sup>School of Civil Engineering, Southeast University, Nanjing 211189, China

Correspondence should be addressed to Fengqiang Gong; [fengqiangg@126.com](mailto:fengqiangg@126.com)

Received 1 March 2021; Accepted 19 May 2021; Published 28 May 2021

Academic Editor: Nan Jiang

Copyright © 2021 Wuxing Wu and Fengqiang Gong. This is an open access article distributed under the Creative Commons Attribution License, which permits unrestricted use, distribution, and reproduction in any medium, provided the original work is properly cited.

The deep high prestatically loaded rock is often subjected to low-frequency dynamic disturbance and exhibits unusual strength characteristics, and thus, it is important to investigate the strength characteristics under the coupling effect of prestatic load and low-frequency dynamic disturbance loading conditions. In this study, a series of point load tests were conducted on the high prestatically loaded marble subjected to low-frequency disturbance by the MTS system, focusing on exploring the role of prestatic load level and low-frequency disturbance frequency in the process of rock strength change. Based on the average static failure load ( $F_{\max}$ ) of samples under the static point loading, the high prestatic load levels ( $F_p$ ) were selected as 70%, 80%, and 90% of  $F_{\max}$ , the corresponding low-frequency dynamic disturbance was loaded by sinusoidal waves with amplitudes of 60%, 40%, and 20% of  $F_{\max}$ , and the low-frequency dynamic disturbance frequencies ( $f$ ) are 1, 2, 5, and 10 Hz. The change curve of the point load strength with the prestatic load level or the disturbance frequency was analyzed, which indicates that the point load strength under the coupled high prestatic load and low-frequency dynamic disturbance load was significantly lower than that under the pure static loading, presenting a significant point load strength weakening effect. Only when  $F_p$  or  $f$  reaches a certain level, the point load strength decreases significantly as  $f$  or  $F_p$  increases. Moreover, the point load strength weakening rate was proposed to characterize the degree of strength weakening. The comprehensive analysis demonstrates that  $F_p$  has a greater effect on the point load strength weakening effect than  $f$ , which is mainly reflected in the point load strength weakening level dominated by the  $F_p$ , and the weakening degree is affected by  $f$ .

## 1. Introduction

With the decrease of shallow mineral resources and the increasing demand for underground space, more and more underground projects extend to great depth. The deep surrounding rock has been subjected to high static stress before excavation [1–3] and then undergoes various forms of dynamic disturbance during the excavation process [4, 5], resulting in the high static load surrounding rock in a stress state coupled with high static load and dynamic disturbance load. For instance, Li et al. [2, 6] pointed out the deep high prestatically loaded rock often affected by the dynamic

disturbance and developed the split Hopkinson pressure bar (SHPB) test device to deeply study the mechanical characteristics and failure mechanism of rock under static and dynamic combined loading. Zhang and Zhao [7] summarized the research of rock dynamic mechanics in detail and reported that the high prestatic rocks are often affected by dynamic disturbances during, before, and after the excavation process. Liu et al. [8] pointed out in detail that the high prestressed rock is in the coupled static-dynamic stress state during deep rock engineering excavation. Ernesto et al. [9] analyzed the deep high prestatic rock failure under deep engineering excavation and estimated the probability of



static and dynamic demand for rock mass stable in underground excavation. These studies have clearly pointed out that the deep high prestatically loaded surrounding rock is often subjected to dynamic disturbance, under the coupling stress state of the high prestatic load and dynamic disturbance. Moreover, compared with pure static or pure dynamic stress state, the failure characteristics of the deep high prestatically loaded surrounding rock under the dynamic disturbance are obviously different, which cannot be explained reasonably by traditional rock mechanics theory [2, 6]. Therefore, knowledge of the high prestatically loaded rock subjected to dynamic disturbance on deep rock fracture characteristics and mechanical behaviors has significance for the construction of deep underground rock engineering.

To date, researchers have conducted a lot of experimental and theoretical studies to understand the fracture behavior and mechanism of high prestatically loaded rock. Gao et al. [10] studied the effect of dynamic loading rate on the development of cracks in the process of deep rock failure and obtained the fractal dimension change characteristics of the dynamic fracture of the sample under impact load with different loading rates. Vaneghi et al. [11, 12] carried out a large number of uniaxial cyclic loading-unloading tests on deep rocks and investigated the influence of different loading and unloading conditions on the failure characteristics of deep rocks. Moreover, in order to better fit the stress state of deep rock failure, a large number of impact tests under high prestatic rock were also carried out. Li et al. [2] concluded that the dynamic compressive strength of siltstone firstly increased and reached a maximum constant value under the constant axial precompression stress and increased impact load. Gong et al. [13] conducted a one-dimensional coupled static-dynamic loading test on red sandstone and obtained that the impact compression strength of the rock reached the maximum value if the axial precompressive stress ratio was 0.6 to 0.7. Zhou et al. [14] used the modified SHPB to carry out impact tests of sandstone with the axial static prestresses of 0~75 MPa, and the results showed that the dynamic compressive strength increases with the prestress until it reaches 75 MPa. Zhu et al. [15] used the numerical simulation methods to discuss in detail the effect of the coupled static-dynamic loads on the compression failure characteristics of rocks. These results enrich the failure characteristics of the one-dimensional high prestatic rock subjected to the strong impact dynamic disturbance. Additionally, the deep rock subjected to the impact dynamic disturbance under different confining pressures on deep rock compressive failure was also carried out. Peng et al. [16] used the SHPB to carry out dynamic impact tests under different confining pressures and reported that the rock only shows shear failure as the confining pressure limits the lateral deformation. Yin et al. [17] and Ma et al. [18] investigated the failure characteristic under the rock was in a state of confining pressure after excavation and conducted a dynamic compressive test of the rock under confining pressure by the SHPB. Liu et al. [19] used the triaxial Hopkinson bar and investigated the dynamic compressive characteristics of sandstone under biaxial compression. Yuan et al. [20] conducted a numerical simulation to study the dynamic

failure characteristics of rock under confining pressure. Hu et al. [21] used the finite element to simulate dynamic impact tests under different multiaxial static loads on rocks and explored the influence of prestatic load and dynamic impact on rock failure. With the improvement of the understanding of rock failure, people not only carry out the above compression tests but also deeply explore the characteristics of rock failure such as tension and fracture. Zhu and Tang [22] and Wu et al. [23] explored the tensile failure characteristics of rocks subjected to the coupled high prestatic load and impact dynamic loads. Moreover, Yao et al. [24], Chen et al. [25], and Shi and Chen [26] investigated the fracture failure characteristics of the prestatically loaded rock subjected to dynamic loads.

However, the above research on rock fracture failure subjected to coupled high prestatic load and dynamic load is mainly based on strong impact dynamic disturbance load, rarely involving low-frequency dynamic disturbance. Su et al. [27] reported that, in the process of deep rock engineering excavation, the surrounding rock was often affected by low-frequency dynamic disturbance, which poses a threat to underground engineering construction. However, these studies have not focused on the rock strength variation characteristics under the low-frequency disturbance, especially the strength characteristics of high prestatically loaded rock under low-frequency disturbance. Therefore, it is necessary to research the prestatically loaded rock subjected to the low-frequency dynamic disturbance, especially for point load on the deep rock fracture subjected to coupled high prestatic load and low-frequency dynamic load. In essence, the deep rock is always under high prestatic load, and then it is affected by various dynamic disturbances, which induces the deep rock failure. From this point of view, this paper carried out a point load test in which the high prestatic rock was subjected to low-frequency dynamic disturbance to study the strength characteristics of the rock under this stress state, that is, the corresponding prestatic load is applied to the rock first, and then the low-frequency dynamic disturbance is applied until failure.

To further study the rock fracture characteristics of high preloaded rock subjected to low-frequency dynamic disturbance, a series of point load tests under these coupled load conditions were designed. In our study, the sum of all prestatic load levels and the corresponding one-half of the dynamic disturbance amplitude is equal to the average failure load ( $F_{max}$ ) under the static point load tests (i.e., the  $F_p + 0.5F_d = F_{max}$ ). Therefore, the prestatic load levels ( $F_p$ ) were set to 70%, 80%, and 90% of  $F_{max}$ , while the corresponding low-frequency dynamic disturbance amplitudes ( $F_d$ ) were set as 60%, 40%, and 20% of  $F_{max}$ . Moreover, a sinusoidal disturbance wave at low-frequency dynamic disturbance frequencies ( $f$ ) of 1, 2, 5, and 10 Hz was selected. It is hoped that these coupled static and dynamic loading tests can be designed to study the failure characteristics of rock under low-frequency dynamic disturbance rather than the existing strong impact disturbance. The resulting variations in point load strength were obtained, and the obvious weakening effect of point load strength was found. Furthermore, through the load-deformation curve, the variation

of the point load strength with  $F_p$  and  $f$ , the rock failure mechanism in the point load test under coupled static-dynamic loading was obtained.

## 2. Experimental Plans

**2.1. Sample Preparation.** The rock samples selected in the all point load tests were obtained from the marble blocks in Hezhou City (Guangxi Province, China) as it has good homogeneity. Petrographic thin section analysis indicates that the marble is fine-grained and well sorted, which is mainly composed of quartz (99%), and the matrix material composed of clay is about 1% of the sample [28]. The micrograph from the marble samples and the composition content are illustrated in Figure 1.

For the marble preparation for the point load tests, the whole marble rock block was made into cylindrical samples of  $50 \times 50 \text{ mm}^2$  (i.e., the ratio of the diameter ( $D$ ) to the length ( $L$ ) of the sample is 1). A series of screening and polishing procedures (such as measuring scale, weighing, measuring wave velocity, and sandpaper grinding) were conducted on cylindrical samples to make the sample size accuracy meet the requirements suggested by ISRM (International Society of Rock Mechanics) [29], thereby reducing the test errors (as shown in Figure 2). The prepared marble samples have the following physical and mechanical properties: density was  $4272 \text{ kg/m}^3$ ,  $P$ -wave velocity was  $2.69 \text{ km/s}$ , and the UCS (average uniaxial compressive strength) was  $54.84 \text{ MPa}$  [28].

**2.2. Test Equipment.** The axial point load tests of the prestatically loaded marble subjected to low-frequency dynamic disturbance were conducted on the MTS Landmark servocontrolled testing system, as illustrated in Figure 3. This MTS Landmark test system is mainly composed of hydraulic test equipment and control software, which can perform static, dynamic, or coupled static-dynamic loading tests. The equipment can withstand the maximum dynamic load of  $\pm 100 \text{ kN}$  and provide sine waves, triangle waves, and ramp waves with the disturbance frequency between 0 and  $100 \text{ Hz}$  as dynamic disturbance loads. The control software automatically collects the axial load and displacement changes during the whole process of loading the sample. Moreover, two special loading cones were machined according to the ISRM recommendations on the point load strength measurement method [29].

### 2.3. Experimental Procedures

**2.3.1. Point Load Test under Static Loading.** To obtain the relevant parameters of the point load test under the prestatically loaded marble subjected to low-frequency dynamic disturbance, the point load test under the static load was first carried out. The specific test process is as follows: (1) the cylindrical end of the loading cone was put into the clamping groove of MTS Landmark and the clamping force was adjusted to fix it; (2) the test piece was placed between the two pressure cones, and the loading cone was aligned at the

center of the sample section; (3) after the sample was placed, a load of  $0.5 \text{ kN}$  was preapplied to fix it. In the static loading process, the sample was loaded at  $5 \text{ kN/min}$  until the sample was damaged. The calculation formula of the point load strength is given by [29]

$$I_s = \frac{F}{D_e^2}, \quad (1)$$

where  $I_s$  is the point load strength (MPa),  $F$  is the failure load (N), and  $D_e$  is the "equivalent core diameter" (mm) [29]. For the axial point load test,  $D_e^2 = (4A/\pi)$ , and  $A = WD =$  minimum cross-sectional area of a plane through the platen contact points [29].

Table 1 shows the static point load test results. The failure load under static loading of the sample is  $6.44$ ,  $6.48$ , and  $6.61 \text{ kN}$ , the average failure load is  $6.51 \text{ kN}$  (i.e.,  $F_{\max} = 6.51 \text{ kN}$ ,  $F_{\max}$  represents the maximum failure load), and the standard deviation is 2%, indicating that the sample has good homogeneity. Based on equation (1), the point load strength of the marble sample is  $2.03 \text{ MPa}$  (i.e.,  $I_s = 2.03 \text{ MPa}$  represents the average point load strength under static loading). Figure 4 represents the load-displacement curves and the typical point load failure mode of the samples under the static point load. The variation characteristics of the load-displacement curves of the three marble samples are basically the same, and the curve S-3 may be deviated due to the difference in the homogeneity of the sample. Moreover, the sample fractures into two approximately symmetrical halves at the axial centerline under the static point load loading.

**2.3.2. Point Load Test on Prestatically Loaded Marble Subjected to Low-Frequency Dynamic Disturbance.** In the prestatically loaded marble subjected to dynamic disturbance test, the marble samples were first loaded to the prestatic load level ( $F_p$ ) at the loading speed of  $5 \text{ kN/min}$  under the static loading, and then the sine-wave load with a specific low-frequency disturbance frequency ( $f$ ) and disturbance amplitude ( $F_d$ ) was applied, as represented in Figure 5. Based on the static point load test, the corresponding dynamic disturbance parameters are determined. The prestatic load levels are set to 70%, 80%, and 90% of  $F_{\max}$  (i.e.,  $4.65$ ,  $5.21$ , and  $5.86 \text{ kN}$ ), the corresponding low-frequency dynamic disturbance amplitudes are 60%, 40%, and 20% of  $F_{\max}$  ( $F_d = F_{\max} - F_{\min}$ , where  $F_{\max}$  and  $F_{\min}$  are the maximum and minimum disturbance loads), and the low-frequency dynamic disturbance frequency is 1, 2, 5, and  $10 \text{ Hz}$ .

## 3. Results and Discussion

**3.1. Overall Load-Deformation Behavior.** After processing the load and displacement data of all prestatically loaded marbles subjected to low-frequency dynamic disturbance, some typical load-displacement curves are obtained as illustrated in Figure 6. Compared with the static point load tests, the load-displacement curve of the prestatically loaded sample subjected to the low-frequency dynamic disturbance

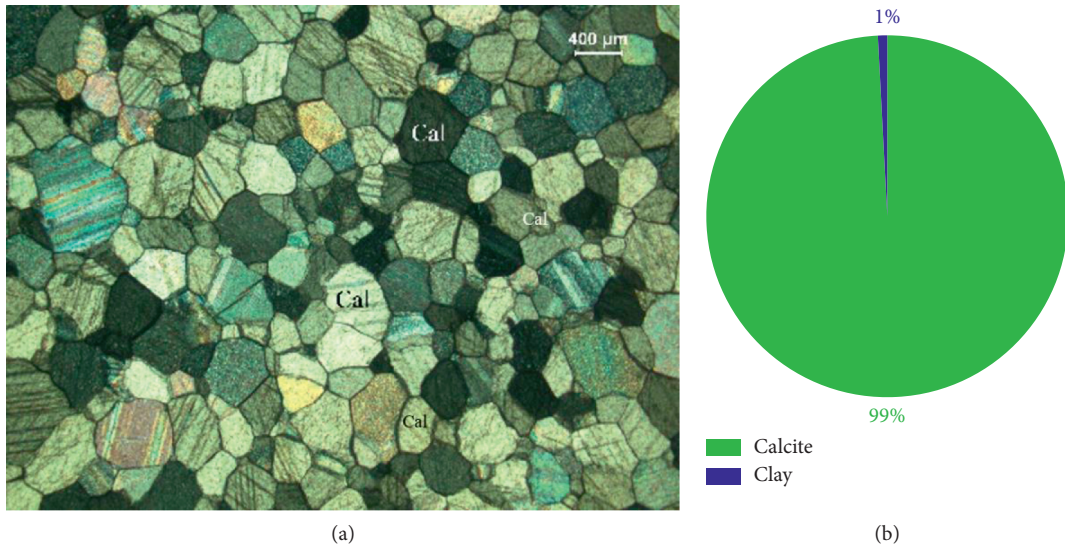


FIGURE 1: Photomicrographs of marble samples. (a) Single polarization (Cal = calcite) [28]. (b) Composition content.

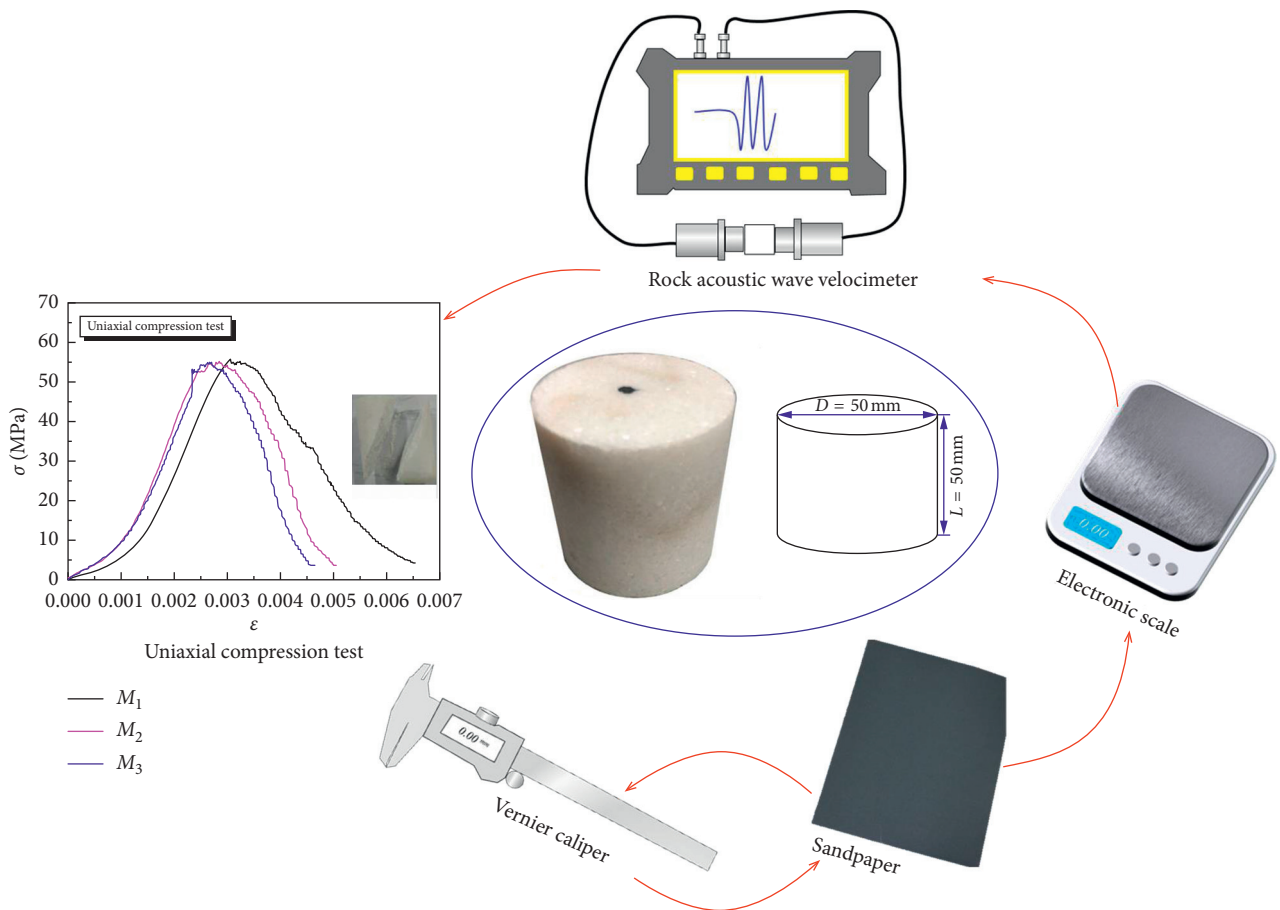


FIGURE 2: Marble sample processing process.

presents an obvious hysteretic loop and even an obvious sparse density-sparse evolution law. Additionally, when the sample was subjected to disturbance loading to the maximum failure load for the first time from the prestatic load level, the axial deformation develops faster, indicating that

the rock has large deformation and generated initial cracks. Subsequently, the deformation curve develops as a dense hysteretic loop with the development of the dynamic disturbance process, indicating that the internal cracks continued to develop and penetrate until the rock failure. Table 2



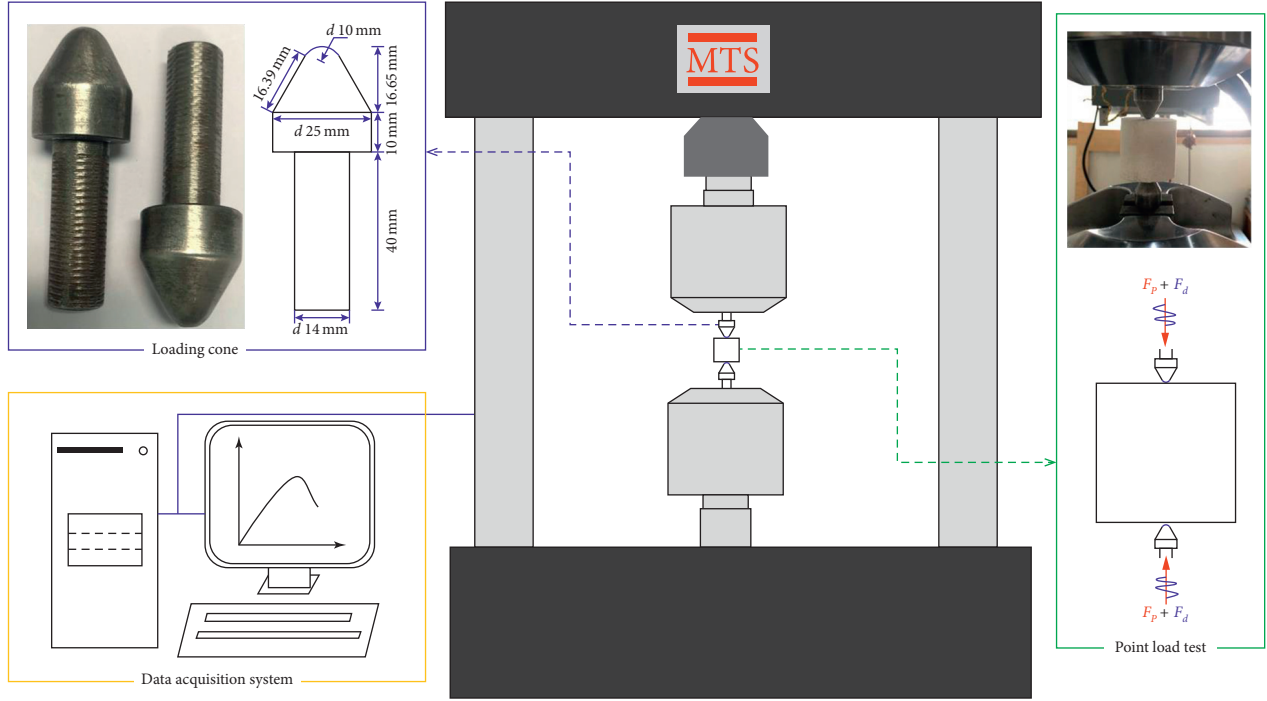


FIGURE 3: Test equipment.

TABLE 1: Point load test results under static load.

Sample	$F$ (kN)	$I_s$ (MPa)
S-1	6.44	2.01
S-2	6.48	2.03
S-3	6.61	2.07
Average	6.51	2.03

and Figure 7 summarize the failure loads of all prestatically loaded marble samples subjected to low-frequency dynamic disturbance. Obviously, the failure loads of all marble under the prestatic load and low-frequency dynamic coupling are significantly lower than that under static point load tests. For instance, if  $F_p$  is 80% of  $F_{max}$ , the maximum failure load that the sample can withstand at  $f=5$  Hz is 6.21 kN, which is lower than the maximum failure load of 6.51 kN under the static loading, and similar trends can be found in other load conditions. Furthermore, the failure load continuously decreases with the increase of  $f$ , indicating a significant strength weakening trend (Figure 7). As a result, the corresponding point load strength will inevitably gradually decrease as the failure load decreases. Therefore, the influences of  $F_p$  and  $f$  on the point load strength weakening are discussed hereafter.

**3.2. The Influence of  $F_p$  on the Point Load Strength Weakening Effect.** The failure loads in the point load test of the prestatically loaded marble subjected to low-frequency dynamic disturbance are significantly lower than that under the static point load test (Figure 7), and the corresponding point load strength will also change. Therefore, the corresponding point load strength is calculated based on equation (1), as

presented in Table 3. Clearly, the point load strength of the prestatically loaded marble under low-frequency dynamic disturbance is lower than that under static loading, and it also shows obvious strength weakening. For instance, if  $F_p$  is 70% of  $F_{max}$ , the point load strength of the sample at  $f=10$  Hz is 1.91 MPa, which is lower than 2.03 MPa under the static loading. Similarly, when  $F_p$  is 90% of  $F_{max}$ , the point load strength of the sample is 1.87 MPa at  $f=10$  Hz, which is also significantly lower than  $I_s^s$ , and similar trends can be found in other load conditions. This comparison suggests that the prestatically loaded marble subjected to low-frequency dynamic disturbance significantly weakens the point load strength, showing obvious strength weakening effect.

Therefore, to quantitatively analyze the point load strength weakening effect, the point load strength weakening rate (PSWR) is proposed as follows:

$$PSWR = \frac{I_s^s - I_s^d}{I_s^s} \times 100\%, \quad (2)$$

where  $I_s^s$  is the average static point load strength under the static loading test and  $I_s^d$  is the point load strength of prestatically loaded marble samples subjected to low-frequency dynamic disturbances.

Figure 8 presents the change in point load strength and the PSWR of the prestatically loaded marble samples as the disturbance frequency increases. Clearly, no matter what  $F_p$  and  $f$  are, the point load strength of the prestatically loaded marble subjected to low-frequency dynamic disturbance is obviously lower than that under the static loading. Moreover, the point load strength gradually decreases with the increase of  $f$  under the same  $F_p$ , which indicates that the

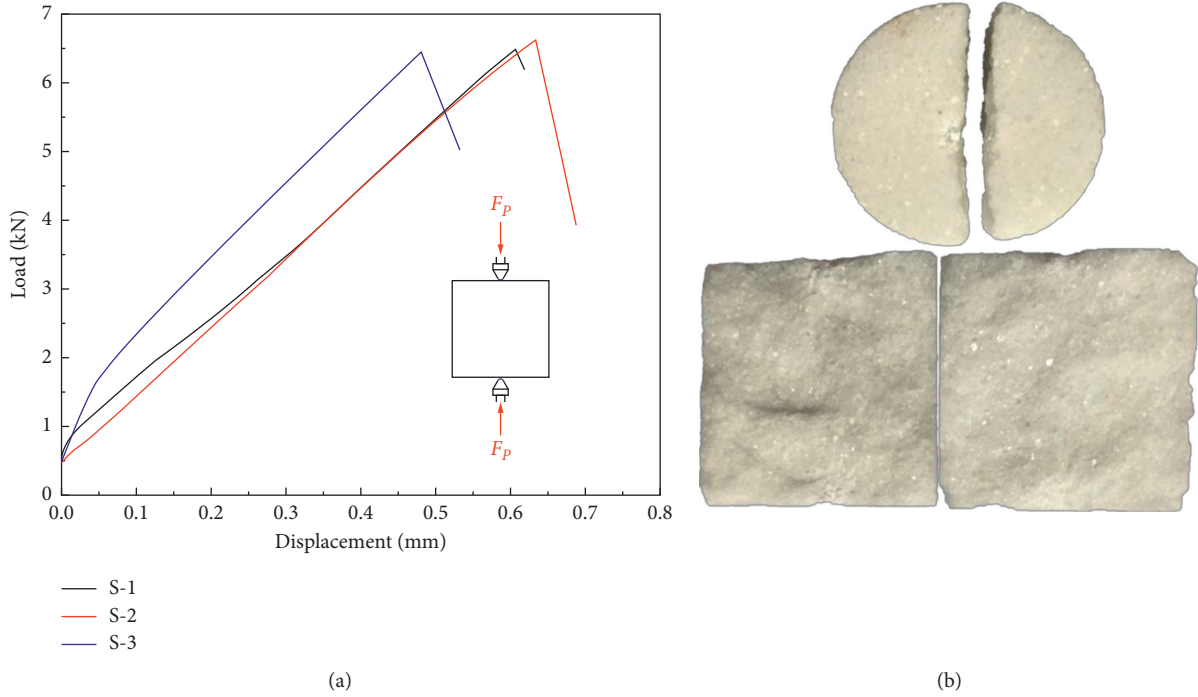


FIGURE 4: Point load test under static load. (a) Load-displacement curve. (b) Failure mode.

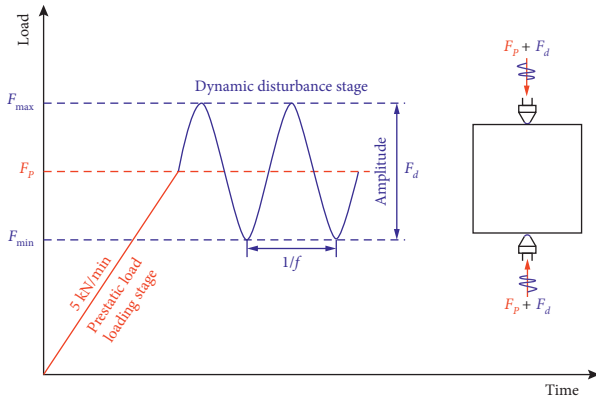


FIGURE 5: Point load test loading path of prestatically loaded marble subjected to low-frequency dynamic disturbance.

point load strength has obvious strength weakening effect. As shown, if  $F_P$  is 70% of  $F_{max}$ , the point load strength gradually decreases from 2.03 MPa under static loading to 1.99 MPa at  $f=1$  Hz, and the lowest is as low as 1.91 MPa under  $f=10$  Hz, with a maximum reduction of 6.20%. Similar trends can also be found at other prestatic load levels, for example, the reduction range of point load strength is 1.96~1.90 MPa at 80% of  $F_{max}$  and 1.95~1.87 MPa at 90% of  $F_{max}$ . These results imply that increasing  $f$  can promote the point load strength weakening and affect the strength weakening degree. Furthermore, the higher the  $F_P$ , the point load strength weakening effect is more significant at the high frequencies. For instance, when  $F_P$  is 80% of  $F_{max}$ , the PSWR is between 3.57% and 6.51%, while if  $F_P$  is 90% of  $F_{max}$ , the PSWR is between 4.32% and 8.00%, which is much larger than that of other prestatic load levels. These results strongly

demonstrate that  $F_P$  is dominant in the point load strength weakening process, that is, the  $F_P$  determines its strength weakening level.

**3.3. The Influence of  $f$  on Weakening Point Load Strength.** Figure 9 presents the change in point load strength and the PSWR of prestatically loaded marble samples as the prestatic load level increases. Clearly, the point load strength gradually decreases due to the increase in  $F_P$  under the same  $f$ . Obviously, if  $f=1$  Hz, the point load strength decreases from 1.99 MPa at the 70% of  $F_{max}$  to 1.96 MPa at the 80% of  $F_{max}$  as the  $F_P$  increases, until the maximum decreases to 1.95 MPa at 90% of  $F_{max}$ , and similar trends can also be observed at other disturbance frequencies. Moreover,  $F_P$  promotes the point load strength weakening more significantly at high disturbance frequencies. As shown, when  $f=2$  Hz, the point load strength decreases from 2.03 MPa under the static load to 1.94 MPa at 90% of  $F_{max}$ , and the PSWR can reach up to 4.71%. However, if  $f$  increases to 10 Hz, the point load strength maximum decreases to 1.87 MPa with the increase of the  $F_P$ , and the PSWR is as high as 8.00%, which is much higher than the decrease at other disturbance frequencies. Furthermore, the interval between the disturbance frequency between 5 Hz and 10 Hz is much larger than the interval between other disturbance frequencies, which implies that increasing  $F_P$  can obviously promote the point load strength weakening if  $f$  reaches a value.

**3.4. Point Load Strength Weakening Mechanism Analysis.** These experiments indicated that, in the point load tests of the kind of high preloaded rock subjected to low-frequency



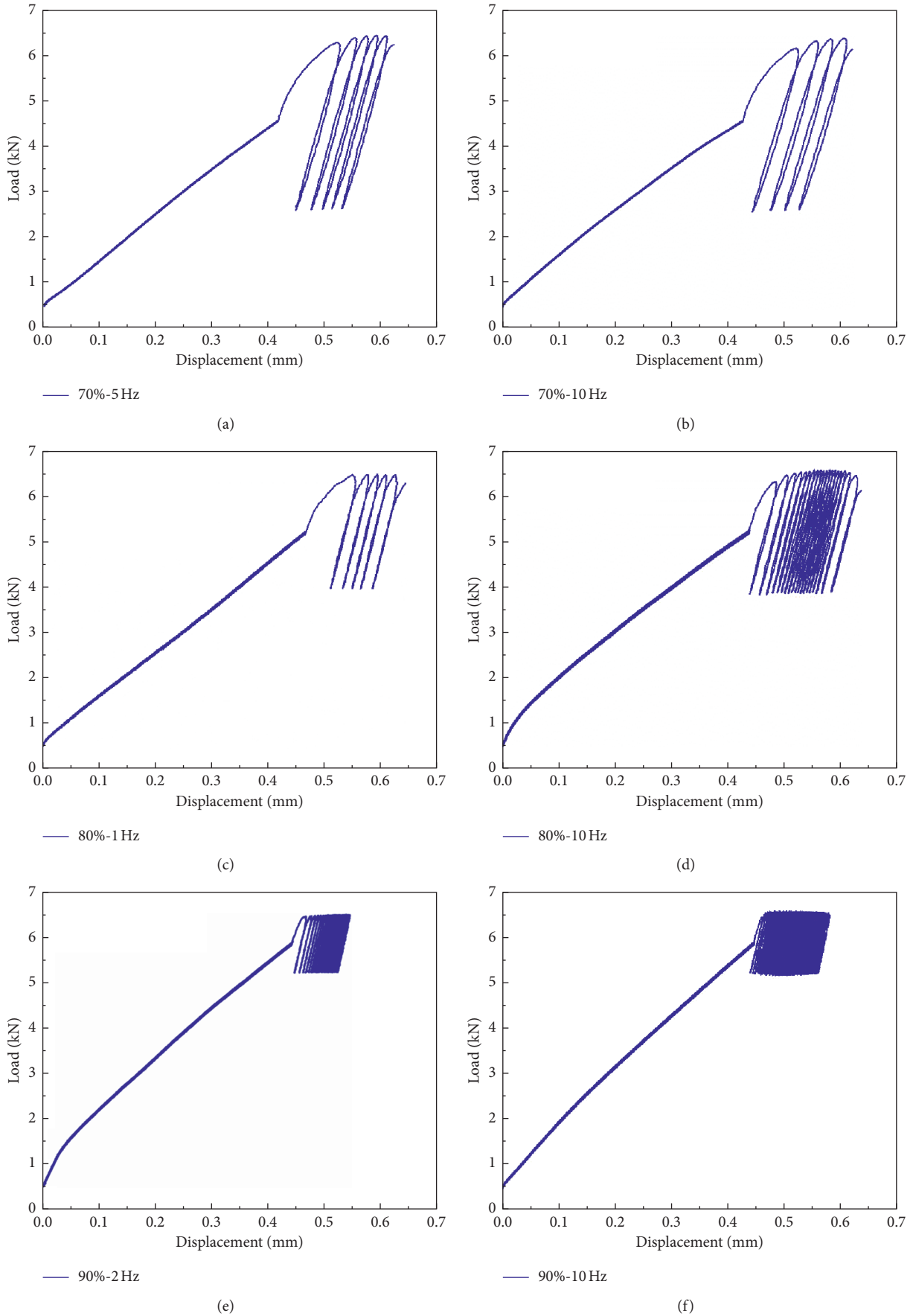


FIGURE 6: Typical load-displacement curves under the point load test. (a) 70%-1 Hz; (b) 70%-10 Hz; (c) 80%-1 Hz; (d) 80%-10 Hz; (e) 90%-2 Hz; (f) 90%-10 Hz.

TABLE 2: The results under different prestatic loads and dynamic disturbances.

Sample	$F_p$ (kN) ( $F_p/F_{max}$ )	$F_{min}$ (kN)	$F_{max}$ (kN)	$f$ (Hz)	$F$ (kN)
70%-1 Hz				1	6.38
70%-2 Hz				2	6.30
70%-5 Hz	4.56 (70%)	2.60	6.51	5	6.23
70%-10 Hz				10	6.14
80%-1 Hz				1	6.29
80%-2 Hz				2	6.27
80%-5 Hz	5.21 (80%)	3.91	6.51	5	6.21
80%-10 Hz				10	6.11
90%-1 Hz				1	6.26
90%-2 Hz				2	6.23
90%-5 Hz	5.86 (90%)	5.21	6.51	5	6.18
90%-10 Hz				10	6.03

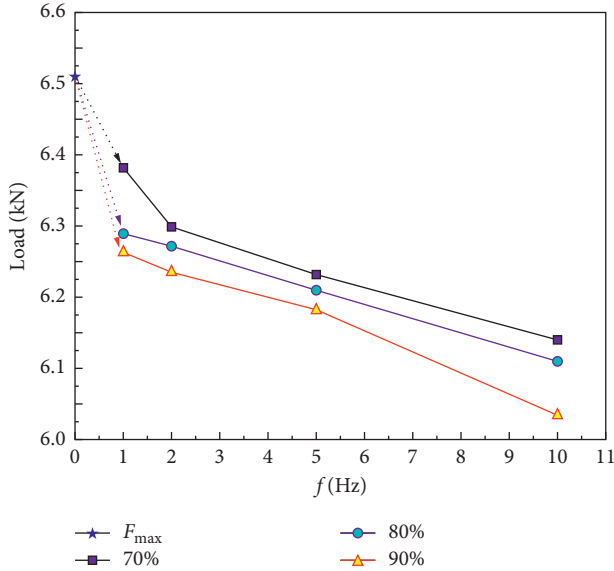


FIGURE 7: Failure load under the point load test.

TABLE 3: The point load strength of prestatically loaded marble subjected to dynamic disturbance.

Sample	$F$ (kN)	$I_s^d$ (MPa)	PSWR (%)
70%-1 Hz	6.38	1.99	2.39
70%-2 Hz	6.30	1.96	3.65
70%-5 Hz	6.23	1.95	4.30
70%-10 Hz	6.14	1.91	6.20
80%-1 Hz	6.29	1.96	3.57
80%-2 Hz	6.27	1.95	4.07
80%-5 Hz	6.21	1.93	4.98
80%-10 Hz	6.11	1.90	6.51
90%-1 Hz	6.26	1.95	4.32
90%-2 Hz	6.23	1.94	4.71
90%-5 Hz	6.18	1.92	5.71
90%-10 Hz	6.03	1.87	8.00

dynamic disturbance load, the point load strength has a significant strength weakening effect, which is attributed to the corresponding  $F_p$  and  $f$  (as illustrated in Figures 8 and 9). Moreover, this point load strength is obviously different from the mechanical properties of pure static point load strength. Obviously, the point load strength weakening degree depends on  $F_p$  and  $f$ . Furthermore, within the same  $f$ , the greater the  $F_p$ , the more significant the point load strength weakening effect (as illustrated in Figure 8). Similarly, the test results further prove that, in the process of strength weakening,  $F_p$  is dominant and determines its weakening level. At the same time, the test results also demonstrate that  $f$  can promote the strength weakening process based on  $F_p$ , and  $f$  also affects the weakening degree. In summary, the point load strength weakening process occurs under the combined action of  $F_p$  and  $f$ . Only when  $F_p$  reaches a certain degree,  $f$  can induce obvious strength weakening (Figure 8). Similarly, only when  $f$  reaches a certain degree,  $F_p$  can promote the weakening process (Figure 9). However, in the whole strength weakening mechanism, the  $F_p$  dominates and determines the weakening level, while the dynamic disturbance further induces the weakening process and  $f$  affects the degree of weakening.

In this paper, the influence of the unloading process on rock strength is not considered. Our previous research shows that unloading can also weaken the rock strength [30, 31]. In the future, we will study the failure characteristics of rock subjected to dynamic disturbance after unloading, and we have started to study the rock subjected to low-frequency or impact dynamic disturbance after unloading.

**3.5. Discussion on the Strength Weakening Mechanism under Tension Failure.** After the deep rock engineering excavation, the surrounding rock has obvious strength weakening effects [30, 31]. Moreover, the sidewall of the tunnel often has obvious tensile failure [32], and the point load test is a typical tensile failure process. The point load failure mode of the sample subjected to the coupled static-dynamic loading conditions is basically similar to the static load, and both are obvious tensile failure modes (as shown in Figure 10). Comparison of the point load strength under the traditional static loading and the point load test under the coupled static-dynamic loading shows that the point load strength has obvious strength weakening effect. The existing literature has also confirmed that the tensile strength of rock shows obvious strength weakening effect under the coupled static-dynamic loading [32]. Gong et al. [32] carried out a Brazilian disk (BD) test on prestatically loaded BD samples subjected to low-frequency dynamic disturbance, and systematically analyzed the characteristics and mechanism of tensile strength changes, and the main conclusions are shown in Figure 11. The tensile strength of the BD sample under the pure static state is 4.89 MPa, but when  $F_p$  is 90% under the coupled static-dynamic loading, the tensile strength decreases with  $f$  until it reaches 4.32 MPa at  $f=50$  Hz, showing obvious strength weakening effect. A similar trend can also be observed when  $F_p$  is 80%. In the process of tensile strength weakening,  $F_p$  still dominates the weakening level,

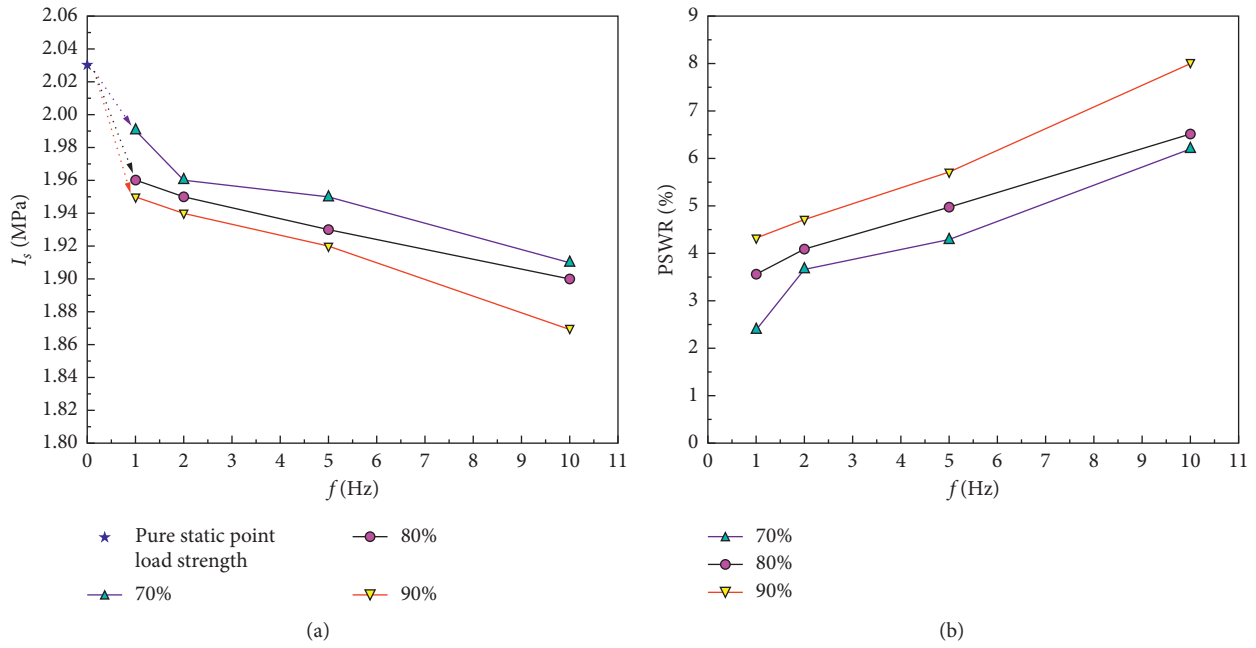


FIGURE 8: The point load strength and the corresponding weakening rate change trend with the disturbance frequency. (a) Point load strength. (b) PSWR.

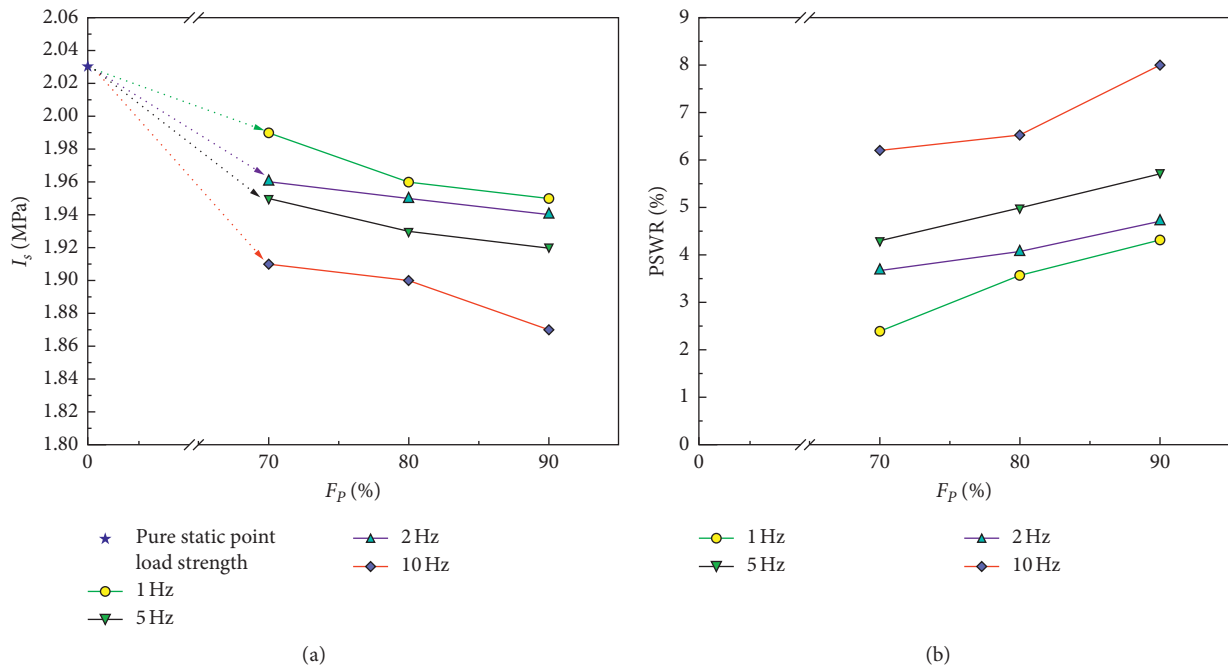


FIGURE 9: The point load strength and the corresponding weakening rate change trend with the prestatic load level. (a) Point load strength. (b) PSWR.

while the dynamic disturbance induces strength weakening and  $f$  determines the weakening degree. This is consistent with the point load strength weakening mechanism.

In light of the comparison indicated above, the prestatic load rock subjected to low-frequency dynamic disturbance under the point load test or Brazilian disc test shows that the

rock strength (point load strength and tensile strength) shows obvious strength weakening effect during the rock failure process. Moreover, in the process of rock strength weakening,  $F_p$  dominates the strength weakening level and  $f$  affects the degree of weakening. This conclusion also shows that the strength weakening mechanism is the same whether

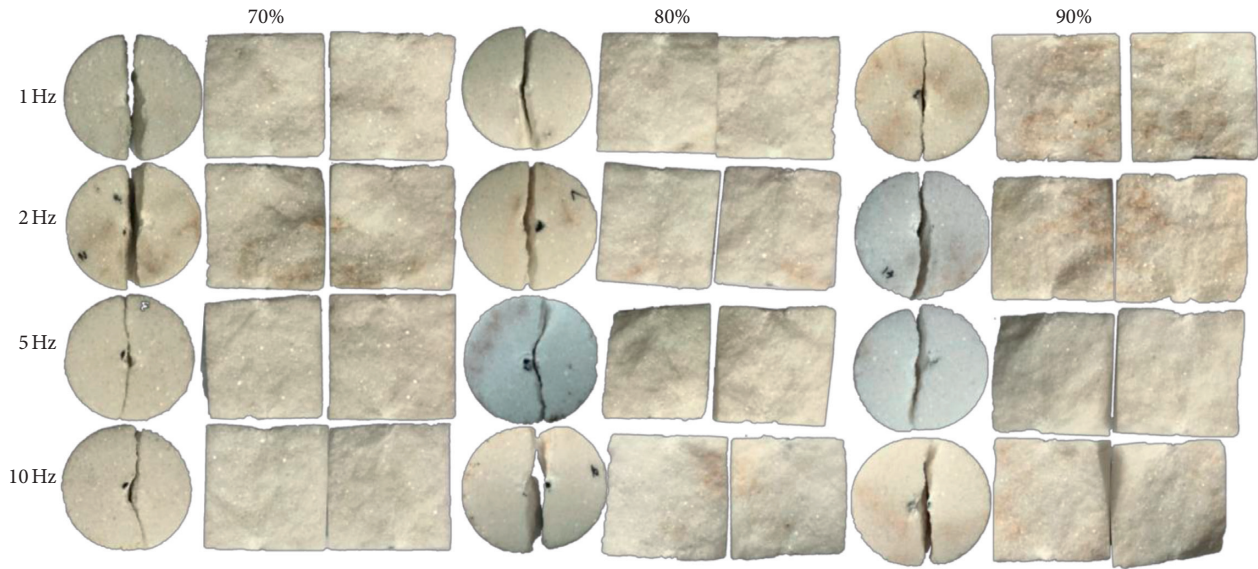


FIGURE 10: Failure mode of prestatically loaded marble subjected to dynamic disturbance.

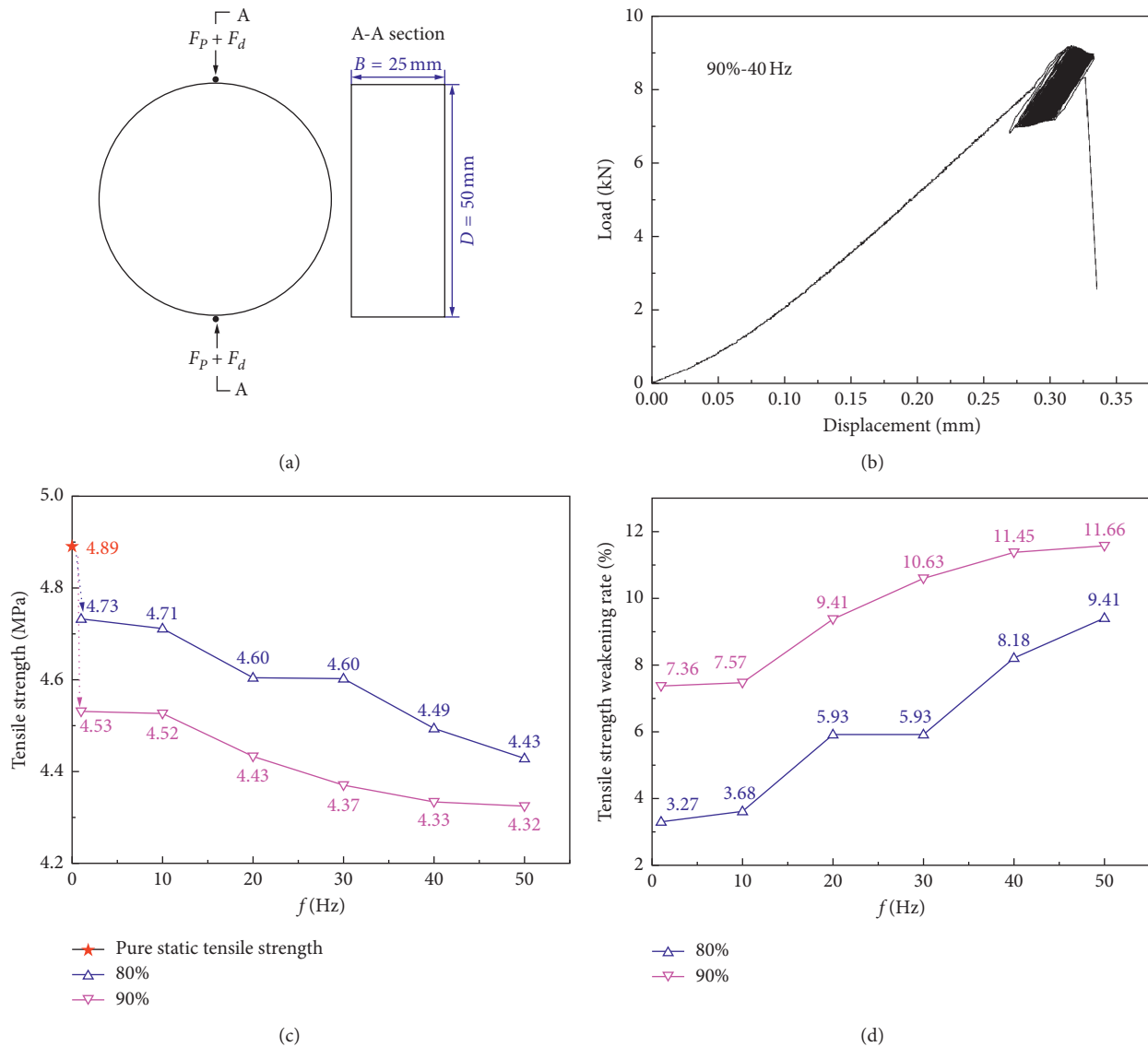


FIGURE 11: Test results of BD samples. (a) Sample size. (b) Typical load-displacement curve [32]. (c) Variation characteristics of tensile strength with disturbance frequency. (d) Variation characteristics of tensile strength weakening rate with disturbance frequency.

the loading mode is the point load test or the Brazilian disc test during the tensile failure process, that is, the strength weakening process is not necessarily related to the loading mode, only related to  $F_p$  and  $f$ .

#### 4. Conclusions

A series of point load tests were conducted on the prestatically loaded marble sample subjected to low-frequency dynamic disturbance, and several important conclusions were obtained as follows:

- (1) The point strength of the point load test under the prestatically loaded marble sample subjected to low-frequency dynamic disturbance loading tests is significantly lower than that under pure static loading, showing a significant strength weakening effect.
- (2) As long as  $F_p$  and  $f$  exceed a certain value, the strength weakening effect decreases significantly with the increase of  $f$  and  $F_p$ .
- (3) During the whole point load strength weakening process,  $F_p$  dominates and determines the weakening level, while  $f$  affects the weakening degree.
- (4) Both the point load test and the Brazilian disc test of the deep high prestatically loaded rock subjected to low-frequency dynamic disturbance show obvious strength weakening effects, and it is strongly proved that the strength weakening process is only related to  $F_p$  and  $f$ , while the loading mode is basically irrelevant.

#### Data Availability

All data used to support the findings of this study are included within the article.

#### Conflicts of Interest

The authors declare that there are no conflicts of interest regarding the publication of this article.

#### Acknowledgments

This work was supported by the National Natural Science Foundation of China (grant no. 42077244) and the Fundamental Research Funds for the Central Universities of Southeast University (grant no. 2242021R10080).

#### References

- [1] W. D. Ortlepp, "The behaviour of tunnels at great depth under large static and dynamic pressures," *Tunnelling and Underground Space Technology*, vol. 16, no. 1, pp. 41–48, 2001.
- [2] X. B. Li, Z. L. Zhou, T. S. Lok, L. Hong, and T. B. Yin, "Innovative testing technique of rock subjected to coupled static and dynamic loads," *International Journal of Rock Mechanics and Mining Sciences*, vol. 45, no. 5, pp. 739–748, 2008.
- [3] S. Zhong, Q. Jiang, C. Liu et al., "In-site core disk testing phenomenon and break mechanism of hard marble: investigation in 2400 m deep-buried underground laboratory," *Journal of Central South University of Technology*, vol. 27, pp. 2899–2913, 2020.
- [4] J. Zhao, Y. X. Zhou, A. M. Hefny et al., "Rock dynamics research related to cavern development for ammunition storage," *Tunnelling and Underground Space Technology*, vol. 14, no. 4, pp. 513–526, 2001.
- [5] R. Q. Huang and X. N. Wang, "Analysis of dynamic disturbance on rock burst," *Bulletin of Engineering Geology and the Environment*, vol. 57, no. 3, pp. 281–284, 1999.
- [6] X. B. Li, F. Q. Gong, M. Tao et al., "Failure mechanism and coupled static-dynamic loading theory in deep hard rock mining: a review," *Journal of Rock Mechanics and Geotechnical Engineering*, vol. 9, no. 4, pp. 767–782, 2017.
- [7] Q. B. Zhang and J. Zhao, "A review of dynamic experimental techniques and mechanical behaviour of rock materials," *Rock Mechanics and Rock Engineering*, vol. 47, no. 4, pp. 1411–1478, 2014.
- [8] K. Liu, Q. B. Zhang, G. Wu, J. C. Li, and J. Zhao, "Dynamic mechanical and fracture behaviour of sandstone under multiaxial loads using a triaxial hopkinson bar," *Rock Mechanics and Rock Engineering*, vol. 52, no. 7, pp. 2175–2195, 2019.
- [9] V. Ernesto, T. Alan, and W. Christopher, "Probabilistic estimate of rock mass static and dynamic demands for underground excavation stabilization," *Journal of Rock Mechanics and Geotechnical Engineering*, vol. 11, no. 3, pp. 45–57, 2019.
- [10] M. Z. Gao, J. G. Zhang, S. W. Li, M. Wang, Y. W. Wang, and P. F. Cui, "Calculating changes in fractal dimension of surface cracks to quantify how the dynamic loading rate affects rock failure in deep mining," *Journal of Central South University*, vol. 27, no. 10, pp. 3013–3024, 2020.
- [11] R. G. Vaneghi, B. Ferdosi, A. D. Okoth et al., "Strength degradation of sandstone and granodiorite under uniaxial cyclic loading," *Journal of Rock Mechanics and Geotechnical Engineering*, vol. 10, no. 1, pp. 117–126, 2018.
- [12] R. G. Vaneghi, K. Thoeni, A. V. Dyskin et al., "Strength and damage response of sandstone and granodiorite under different loading conditions of multistage uniaxial cyclic compression," *International Journal of Geomechanics*, vol. 20, no. 9, Article ID 04020159, 2020.
- [13] F. Q. Gong, X. B. Li, X. L. Liu et al., "Experimental study of dynamic characteristics of sandstone under one-dimensional coupled static and dynamic loads," *Chinese Journal of Rock Mechanics and Engineering*, vol. 29, no. 10, pp. 2076–2085, 2010.
- [14] Z. L. Zhou, X. Cai, X. B. Li, W. Z. Cao, and X. M. Du, "Dynamic response and energy evolution of sandstone under coupled static-dynamic compression: insights from experimental study into deep rock engineering applications," *Rock Mechanics and Rock Engineering*, vol. 53, no. 3, pp. 1305–1331, 2020.
- [15] W. C. Zhu, Y. Bai, X. B. Li, and L. L. Niu, "Numerical simulation on rock failure under combined static and dynamic loading during SHPB tests," *International Journal of Impact Engineering*, vol. 49, pp. 142–157, 2012.
- [16] K. Peng, Z. P. Liu, Q. L. Zou et al., "Static and dynamic mechanical properties of granite from various burial depths," *Rock Mechanics and Rock Engineering*, vol. 52, pp. 3545–3566, 2019.
- [17] Z. Q. Yin, X. B. Li, J. F. Jin, X. Q. He, and K. Du, "Failure characteristics of high stress rock induced by impact disturbance under confining pressure unloading," *Transactions of Nonferrous Metals Society of China*, vol. 22, no. 1, pp. 175–184, 2012.



- [18] S. S. Ma, W. Z. Chen, and W. S. Zhao, "Effects of axial static stress and confining pressure on the dynamic compressive behaviours of granite," *European Journal of Environmental and Civil Engineering*, vol. 25, no. 5, 2019.
- [19] K. Liu, J. Zhao, G. Wu, A. Maksimenko, A. Haque, and Q. B. Zhang, "Dynamic strength and failure modes of sandstone under biaxial compression," *International Journal of Rock Mechanics and Mining Sciences*, vol. 128, Article ID 104260, 2020.
- [20] W. Yuan, X. Wang, and X. B. Wang, "Numerical investigation on effect of confining pressure on the dynamic deformation of sandstone," *European Journal of Environmental and Civil Engineering*, 2020.
- [21] W. R. Hu, K. Liu, D. O. Potyondy, and Q. B. Zhang, "3D continuum-discrete coupled modelling of triaxial Hopkinson bar tests on rock under multiaxial static-dynamic loads," *International Journal of Rock Mechanics and Mining Sciences*, vol. 134, Article ID 104448, 2020.
- [22] W. C. Zhu and C. A. Tang, "Numerical simulation of Brazilian disk rock failure under static and dynamic loading," *International Journal of Rock Mechanics and Mining Sciences*, vol. 43, no. 2, pp. 236–252, 2006.
- [23] B. B. Wu, R. Chen, and K. W. Xia, "Dynamic tensile failure of rocks under static pre-tension," *International Journal of Rock Mechanics and Mining Sciences*, vol. 80, pp. 12–18, 2015.
- [24] W. Yao, K. W. Xia, and A. K. Jha, "Experimental study of dynamic bending failure of Laurentian granite: loading rate and pre-load effects," *Canadian Geotechnical Journal*, vol. 56, pp. 228–235, 2018.
- [25] R. Chen, K. Li, K. Xia, Y. Lin, W. Yao, and F. Lu, "Dynamic fracture properties of rocks subjected to static pre-load using notched semi-circular bend method," *Rock Mechanics and Rock Engineering*, vol. 49, no. 10, pp. 3865–3872, 2016.
- [26] D. D. Shi and X. D. Chen, "Flexural tensile fracture behavior of pervious concrete under static preloading," *Journal of Materials in Civil Engineering*, vol. 30, no. 11, Article ID 06018015, 2018.
- [27] G. S. Su, L. H. Hu, X. T. Feng et al., "True triaxial experimental study of rockburst process under low frequency cyclic disturbance load combined with static load," *Chinese Journal of Rock Mechanics and Engineering*, vol. 35, no. 7, pp. 1309–1322, 2016.
- [28] W. X. Wu, F. Q. Gong, and W. M. Yang, "Experimental simulation study of spalling in deep rectangular tunnel with plastic fine grain marble," *Tunnelling and Underground Space Technology*, vol. 98, Article ID 103319, 2020.
- [29] International Society for Rock Mechanics (ISRM), "Suggested method for determining point load strength: ISRM common testing methods," *International Journal of Rock Mechanics and Mining Sciences & Geomechanics Abstracts*, vol. 22, no. 4, p. 112, 1985.
- [30] X. F. Si and F. Q. Gong, "Strength-weakening effect and shear-tension failure mode transformation mechanism of rockburst for fine-grained granite under triaxial unloading compression," *International journal of rock mechanics and mining sciences*, vol. 131, Article ID 104347, 2020.
- [31] X. F. Si and F. Q. Gong, "Study on rockburst simulation tests and strength-weakening effect of circular tunnels under deep high stress and internal unloading conditions," *Chinese Journal of Rock Mechanics and Engineering*, vol. 40, pp. 1–14, 2021.
- [32] F. Q. Gong, W. X. Wu, and L. Zhang, "Brazilian disc test study on tensile strength-weakening effect of high pre-loaded red sandstone under dynamic disturbance," *Journal of Central South University*, vol. 27, no. 10, pp. 2899–2913, 2020.

## Research Article

# Study on the Propagation Law of Water Hammer Wave in Underwater Blasting and the Reducing Effect of Air Curtain on Water Hammer Wave

Chao Qi <sup>1</sup>, Zuxiang Hu <sup>1</sup>, Suihong Wang,<sup>2</sup> Zhixiong Jiang <sup>1</sup>, Haoyuan Wu <sup>1</sup>,  
and Zhiqiang Yin <sup>3</sup>

<sup>1</sup>School of Mining Engineering, Anhui University of Science and Technology, Huainan 232001, Anhui, China

<sup>2</sup>Nuclear Industry Jingxiang Construction Group Co., Ltd., Huzhou 313000, Zhejiang, China

<sup>3</sup>The Provincial Key Laboratory of Mining Effects and Disasters Preventing Under Deep Mining in Anhui, Anhui University of Science and Technology, Huainan 232001, Anhui, China

Correspondence should be addressed to Zuxiang Hu; [zxhu@aust.edu.cn](mailto:zxhu@aust.edu.cn) and Zhiqiang Yin; [zhqyin@aust.edu.cn](mailto:zhqyin@aust.edu.cn)

Received 4 March 2021; Revised 14 April 2021; Accepted 6 May 2021; Published 13 May 2021

Academic Editor: Bangbiao Wu

Copyright © 2021 Chao Qi et al. This is an open access article distributed under the Creative Commons Attribution License, which permits unrestricted use, distribution, and reproduction in any medium, provided the original work is properly cited.

The harmful effects (water hammer wave, flying stone, and broken quality of concrete) produced in the process of underwater drilling and blasting are the key factors affecting the safety of underwater drilling and blasting. In fact, the harm caused by the water hammer wave is the most significant. As a consequence, it is of great significance to study the propagation law of water hammer waves. Based on the background of the cofferdam demolition project at the inlet section of Shibishan Central Canal in Ningguo City, China, a three-dimensional numerical model was established based on Coupled Eulerian-Lagrangian (CEL) method. Besides, the propagation law of water hammer waves at different water depths with different millisecond times was studied. Meanwhile, the reduction effect of the water hammer wave at different positions of the bubble curtain was analyzed. The results showed that, in the direction of the minimum resistance line of the charge, the attenuation law of the water hammer wave is accorded with the Cole formula and attenuated exponentially. The attenuation speed of the water hammer wave increased at first and then decreased with the increase of the millisecond time. In addition, the attenuation rate of the peak pressure was the fastest when the millisecond interval 30 ms was used. The attenuation of the water hammer wave at different water depths decreased at first and then decreased with the increase of water depth. The attenuation law of the water hammer wave decreased linearly with the increase of the distance between the bubble curtain and the charge. The research results can provide particular guiding significance for similar on-site construction.

## 1. Introduction

The tunnel intake cofferdam needs to be demolished after the tunnel inlet construction is completed to generate electricity from the tunnel inlet as scheduled. One-time demolition of the cofferdam by underwater millisecond blasting is the most commonly used method at present. Underwater millisecond blasting technology has been used in major civil projects in recent years, such as the blasting of the cofferdam of the Three Gorges Dam, the underwater blasting of the impenetrable wall of the upstream cofferdam of Gezhouba Hydropower Station, and the demolition of the intake cofferdam of the Qiandao Lake

Water Distribution Project. A series of harmful effects caused by underwater blasting technology (concrete crushing quality, water hammer wave and flying stone, etc.) have attracted the attention of many scholars with the popularization of underwater blasting technology. Water hammer wave is the most harmful.

In the past, many researchers have focused on the blasting parameters and initiation mode [1, 2], and the influence of porous fixed interval time and blockage length on adjacent structures in blasting aiming at the research on the propagation law of water hammer wave [3, 4]. It mainly focuses on reducing regular air curtain layer position on water hammer wave in the

aspect of air curtain [5, 6]. However, the interval time of millisecond blasting affects the peak pressure of the water hammer wave in the process of underwater drilling millisecond blasting [7]. On the other hand, the reduction effect of bubble curtain is different at different distances from the charge [8]. It is of obvious practical significance to study the propagation law of water hammer waves according to the interval time of millisecond blasting and the different positions of the air curtain wall.

## 2. State of the Art

Many scholars have carried out numerical simulation and field measurement in order to explore the propagation law of underwater blasting water hammer waves and the influence of bubble curtain on the reduction effect of water hammer waves. The types of explosives and blasting parameters are studied by using different numerical simulation software, such as AUTODYN and ANSYS/LS-DYNA. It is concluded that the magnitude of the water hammer wave is related to the type of explosive in the case of the same amount of charge, TNT explosive > high energy emulsion explosive > ordinary emulsion explosive [9]. However, there are few research studies on the interval time of underwater millisecond blasting and the shape of air wall curtain. On the other hand, the attenuation effect of the air curtain on the peak value and impulse of the shock wave increases with the increase of the number of bubbles in the fixed air curtain area. However, when the number of bubbles in the air curtain area reaches a specific number, the attenuation rate tends to be stable [10]. It can be seen that the influence of the shape of the bubble curtain on the subsequent structure is also apparent. Consequently, based on the actual engineering background and the three-dimensional millisecond blasting model, which is more in line with the actual state, the influence of millisecond blasting interval on the propagation law of water hammer wave is studied. In addition, the reduction effect of bubble curtain on the water hammer wave in different positions is analyzed. This will help to solve the harmful effects of water hammer waves in practical engineering.

In the aspect of the propagation law of water hammer wave, Peng [11] derives the vibration frequency prediction formula considering the altitude effect. In addition, Ma et al. [12] analyze the peak velocity (PPV) of surface blasting of the same structure and predict the peak velocity of underwater blasting (PPV). Besides, Huang [13] establishes the numerical model of multimaterial arbitrary Lagrangian–Eulerian (MMALE) technique and studies the peak pressure of the explosive underwater explosion. Moreover, using the multiphase interface captured by the fluid volume (VOF) method, Liu [14] establishes the Eulerian finite element method (EFEM) for an underwater explosion. The underwater explosion at different depths is simulated, and the characteristics of near-field pressure are analyzed. Based on the finite element dynamic program LS-DYNA, according to the explosive rupture principle, Zhai [15] designs different explosive experimental conditions, the reserved hole parameters such as blasting parameters are

designed, and the influence of stress wave is analyzed. Based on the blasting vibration data of underwater lighthouse from Ningbo to Shipu Port of Zhoushan Port, Gu [16] establishes a linear fitting model, and the vibration correction formula based on water depth is derived. Besides, Xin [17] monitors the underwater hammer wave through the first phase of the main channel project of Ningbo-Zhoushan Port Shipu Port. The characteristics of underwater hammer wave are obtained through the analysis of a typical measured pressure-time history curve. Gu [18] develops an underwater vibration monitor. The actual underwater vibration caused by underwater drilling blasting is measured and the vibration frequency band is analyzed with the help of this equipment. The above scholars have deduced the vibration prediction formula of water hammer wave, predicted the peak velocity, and studied the peak pressure of water hammer wave, the propagation characteristics of shock wave, and so on. However, there is no research on the propagation characteristics of water hammer waves based on different millisecond times.

In the aspect of the air curtain, Liu et al. [8] realize that a certain number of bubbles of different diameters were randomly placed in the set air curtain area to simulate the distribution of bubbles in the natural air curtain by programming with the APDL language of LS-DYNA finite element software during single-hole blasting. In addition, the air curtain effect under different pressure conditions was simulated by changing the number of air bubbles in the fixed area. Zhao et al. [9] carry out numerical simulation of underwater drilling and blasting with LS-DYNA software. Moreover, they study the propagation law of water hammer waves and the reduction effect of regular bubble curtain on water hammer waves. At present, many scholars mainly focus on the regular bubble wall and a small number of bubble combinations, but few on the real bubble wall.

The above researchers focused on single-hole blasting or fixed interval millisecond blasting. However, they did not systematically analyze the influence of millisecond blasting at a different time and using a real bubble curtain wall on the propagation law of water hammer wave. Combined with the specific engineering practice, how to determine the reasonable millisecond blasting time and the design of the actual bubble curtain wall, so that the adjacent structures behind the bubble curtain can be better protected, and ensure the safe operation of the project and improve the economic benefits of the project still needs to carry out in-depth research work. As a consequence, this paper used the large-scale finite element simulation software ABAQUS to establish the three-dimensional model of underwater millisecond blasting based on the engineering background of cofferdam blasting at the inlet of Shibishan main canal tunnel in Ningguo City, Anhui Province, in view of the deficiency of the existing research. The concrete cutoff wall of cofferdam was simulated by ABAQUS built-in subroutine JH-2 (dynamic constitutive model with damage), and the blasting process is simulated by CEL, which is a coupling method of Eulerian and Lagrangian. Based on Python, a script was written to generate a three-dimensional real bubble curtain wall from large to small in the water depth

direction by setting the maximum and minimum radius of bubbles and the difference interval between the minimum particle sizes. The study of millisecond time on the propagation law of water hammer wave caused by different water depths and bubble curtain was carried out to provide some reference for controlling the harmful effect of underwater blasting.

### 3. Methodology

**3.1. Project Overview.** The entrance of the Shibishan trunk canal diversion tunnel is located on the left bank upstream of Gangkouwan Reservoir in Ningguo City, Anhui Province, China, under the highway from Qinglong Township to Fangtang Town, X061 County Road. The surface below the highway is mainly abandoned residue during highway construction, and the topographic slope is about  $35^{\circ}$ – $40^{\circ}$ . The excavation area and geological conditions of the project are shown in Figure 1. The side of the cofferdam cutoff wall is covered with slag filling and steel plate supporting structure. Besides, the blasting holes are arranged in a single row in the middle line of the concrete cutoff wall and detonated hole by hole. The excavated part and the gate chamber are all filled with water, so that the same water pressure is maintained inside and outside the cofferdam before blasting. The depth of the water level is about 20 m, and the nearest distance between the intake building and the cofferdam is 20 m, as shown in Figure 1.

**3.2. Numerical Simulation Model.** The underwater drilling and blasting model was established by coupling the Euler–Lagrange method aiming at the cofferdam structure of the entrance section of the Shibishan main canal tunnel. The numerical methods based on grid Eulerian body and the Lagrangian body cannot simulate the blasting process very well, so it is difficult to use these two methods. Coupled Lagrangian method (CEL) can separate the structure from the fluid, calculate the coupling on the contact surface, and solve the problems of mesh distortion. In the Lagrangian algorithm, the material is attached to the mesh, and the mesh will move and deform with the flow of the material. In the Eulerian algorithm, the mesh is fixed and does not move, while the material transfers between the meshes. Eulerian elements contain different substances, and the Eulerian volume fraction is used to describe the initial state and position of materials. The coupling algorithm completely separates the two kinds of calculation and transforms the material mesh into a fixed space mesh through the state variables of the Lagrange element, and the Lagrange body and Euler body are boundary conditions at the interface. In this numerical simulation, the Lagrange method solved the structure, and the fluid was solved by the Euler method. Two kinds of elements (Eulerian body and Lagrangian body) were included in the model. Water, air, and charge were modeled by the Eulerian body and the cofferdam and lock chamber were modeled by the Lagrangian body, both of which were divided by hexahedron mesh, and the contact was set as general contact. The calculation model is shown in Figure 2.

The calculation domain of the model was  $30\text{ m} \times 10\text{ m} \times 30\text{ m}$ , the water depth was 20 m, the wall thickness was 0.8 m, the pore diameter was 0.09 m, the hole depth was 2 m according to the wall height removed, the minimum resistance line  $W$  was 0.4 m, the distance between the holes was 0.8 m, the plugging length was 0.8 m, and the charge quantity per hole was 14 kg. The nonreflection boundary condition was established to simulate the water boundary. The propagation laws of water hammer waves at different depths during prompt blasting and millisecond interval 10 ms, 20 ms, 30 ms, and 40 ms blasting were studied, and the above five working conditions were studied under the condition that the charge was uncoupled and the total charge was constant.

The study of cylindrical charge by Hammond [19] shows that the shape of the charge has a significant influence on the shock wave performance of underwater explosion in a close range. The shock wave produced by the cylindrical charge can be approximated by a spherical charge with the same mass when the distance between the center of the explosion is more than half of the length of the charge. As a consequence, the cylindrical charge was equivalent to a regular spherical charge to simplify the calculation process.

**3.3. Material Parameters.** The equation of the state of the detonation products of the charge is based on the parameters of the JWL equation [20]. The equation of state is as follows:

$$P = A \left( 1 - \frac{\omega\eta}{R_1} \right) e^{-(R_1/\eta)} + B \left( 1 - \frac{\omega\eta}{R_2} \right) e^{-(R_2/\eta)} + \omega\eta\rho_0 e. \quad (1)$$

In the formula,  $\eta$  is the ratio of the detonation product density to the initial explosive density, that is,  $\eta = \rho/\rho_0$ ,  $A$ ,  $B$ ,  $R_1$ ,  $R_2$ , and  $\omega$  are the constants related to the explosive state, and  $e$  is the internal energy per unit mass of high explosives. The parameters are shown in Table 1.

By using ABAQUS built-in subroutine JH2 concrete material [21], the parameters are shown in Table 2.

The  $U_s - U_p$  equation of state is used to simulate the water area, as shown in Table 3, and the equation of state is presented as follows:

$$P + P_0 = (\gamma - 1)\rho E_m, \quad (2)$$

$$E_m = c_v(\theta - \theta^z).$$

In the formula,  $P_0$  is the external pressure,  $\gamma$  is the adiabatic index,  $E_m$  is the internal energy per unit mass,  $\rho$  is the density of air,  $\theta$  is the current temperature,  $\theta^z$  is absolute zero, and  $c_v$  is the specific heat capacity.

The ideal gas (Ideal Gas) equation of state is used for air. The equation of state is as follows (Table 4):

$$P = P_H \left( 1 - \frac{\Gamma_0\eta}{2} \right) + \Gamma_0\rho_0 E_m. \quad (3)$$

In the formula,  $E_m$  is the unit mass internal energy,  $\Gamma_0$  is the material constant,  $\rho_0$  is the reference density, Grüneisen ratio  $\Gamma$  can be expressed as  $\Gamma = \Gamma_0 (\rho_0/\rho)$ ,  $\eta$  is the nominal

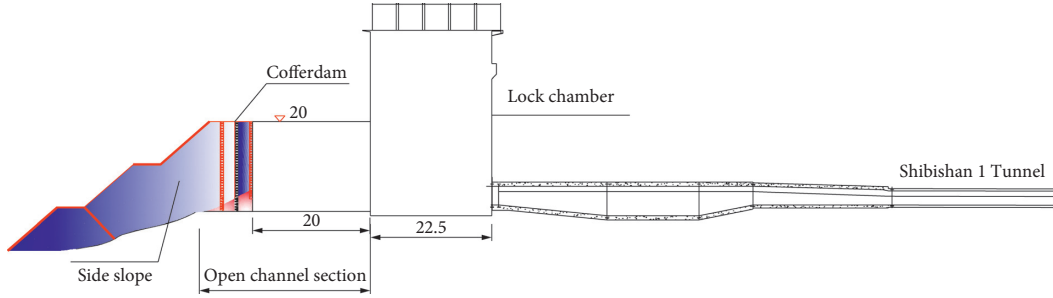


FIGURE 1: Project site map.

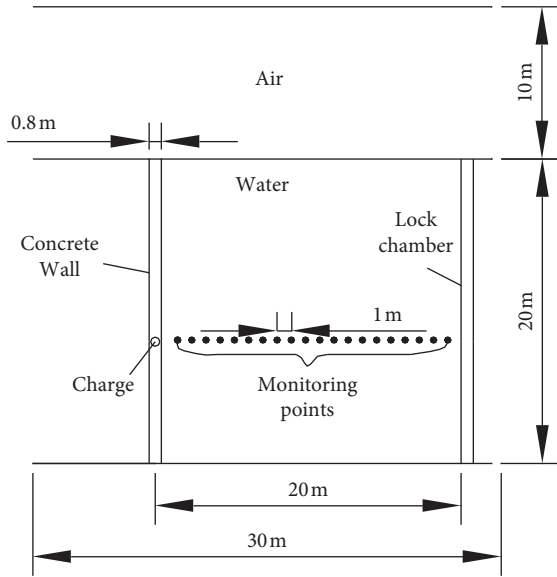


FIGURE 2: Schematic diagram of the calculation model.

volume compression strain, its expression is  $\eta = 1 - \rho_0/\rho$ , and  $P_H$  is the Hugoniot pressure. By using the commonly used Hugoniot data, the expression is as follows:

$$P_H = \frac{\rho_0 c_0^2 \eta}{(1 - s\eta)^2}. \quad (4)$$

The linear equation of state in  $U_s$ - $U_p$  Hugoniot can be obtained as follows:

$$P = \frac{\rho_0 c_0^2 \eta}{(1 - s\eta)^2} \left( 1 - \frac{\Gamma_0 \eta}{2} \right) + \Gamma_0 \rho_0 E_m. \quad (5)$$

In addition,  $c_0$  and  $s$  define linear impact velocity  $U_s$  and particle velocity  $U_p$  as follows:

$$U_s = c_0 + sU_p. \quad (6)$$

The lock chamber adopts the ductile-damage failure criterion, and the parameters are shown in Table 5.

#### 4. Result Analysis and Discussion

The propagation law of water hammer waves under different water depths with different millisecond times and the reduction effect of bubble curtain on water hammer wave at

different positions were studied. The pressure cloud images of the water hammer wave in the explosion process are intercepted and analyzed. In addition, the typical unit was selected to extract the curve in the direction of the charge axis. Besides, the propagation law of the water hammer wave was analyzed at different water depths. In the meanwhile, the pressure-time history curve of the left and right measuring points of the bubble curtain was analyzed to quantify the reduction effect of the water hammer wave in different positions of the bubble curtain.

**4.1. Pressure Nephogram.** The charge adopts the uncoupled charge mode, which is equivalent to a regular sphere and is placed in the center of the borehole. The total time of wave propagation to the right boundary of a single charge explosion is 0.014 s, the empirical propagation velocity of the wave in the solid is 6930 m/s, and the propagation velocity in water is 1435 m/s. The explosion delay time of charge is 10 ms, 20 ms, 30 ms, and 40 ms in order to study the propagation law of water hammer wave in different millisecond times. The total time of millisecond blasting is 0.04 s, 0.06 s, 0.08 s, and 0.1 s in order to ensure the integrity of wave propagation. Figure 3 shows the stress cloud diagram of water hammer waves at different times when delaying 10 ms.

As shown in Figure 3(a), the first charge explodes first, and the water hammer wave caused by the explosion spreads in a spherical direction. As shown in Figure 3(b), the second charge explodes immediately after the first one in 12 ms. As shown in Figure 3(c), the third charge explodes after the second one in 22 ms. However, the water hammer wave pressure caused by the explosion of the first two charges reaches the third charge, and the water hammer waves caused by the explosion of the three charges influence each other. In addition, the pressure cloud diagram shows a "gourd" shape. As shown in Figure 3(d), the water hammer waves produced by the explosion of the three charges continue to spread outward in strips, and the stratification is evident after the water hammer waves are superimposed on each other.

**4.2. Propagation Law of Water Hammer Wave in Different Millisecond Times.** The pressure-time history curves of typical units at the distance of 3 m from prompt blasting and millisecond blasting (10 ms–40 ms) (unit number 54013) in the



TABLE 1: JWL parameters for TNT charge.

$\rho$ (kg/m <sup>3</sup> )	$D$ (m/s)	$G_1$ (GPa)	$G_2$ (GPa)	$R_1$	$R_2$	$\omega$	$e_0$
1630	6930	373.8	3.747	4.15	0.9	0.35	6.0e6

TABLE 2: JH2 parameters (Holmquist and Johnson 1993).

Variable	Numerical value	Variable	Numerical value	Variable	Numerical value
$\rho$ (kg/m <sup>3</sup> )	2440	$A$	0.79	$c$	0.007
$G$ (GPa)	14.86	$B$	1.6	$m$	0.61
$\varepsilon_0$	1	$T$ (GPa)	0.00354	$\varepsilon_{fmax}$	1
$S_{max}$	7	$\varepsilon_{fmin}$	0.001	$P_{hel}$ (MPa)	48
$D_1$	0.04	$K_1$ (GPa)	85	$K_3$ (GPa)	208
$D_2$	1	$K_2$ (GPa)	-171	$HEL$	80

TABLE 3: Water model and state equation parameters.

$\rho$ (kg/m <sup>3</sup> )	$c_0$	$s$	$\Gamma$	Viscosity
983	1435	1.75	0.28	0.00094

TABLE 4: Air model and state equation parameters.

$\rho$ (kg/m <sup>3</sup> )	Gas constant	Ambient pressure (Pa)	Specific heat	Viscosity
1.2	287	101325	717.7	$8.25e-5$

direction of the minimum resistance line of charge were extracted under the condition that the total charge quantity was constant in order to quantitatively study the pressure attenuation law of water hammer wave with different millisecond times, as shown in Figure 4.

Figure 4 shows the pressure-time history curve at 3 m in the direction of the axis of the blasting charge with different millisecond times. It can be seen that the attenuation trend of the curve of different millisecond times is similar. It will produce enormous energy in a concise when the charge begins to detonate. It is characterized by the rapid rise of the water hammer wave curve. Because the propagation velocity of the seismic wave is more significant than that of the water hammer wave, there is a precursor wave in the pressure-time history curve [8]. There are multiple peaks in the peak pressure curve of the water hammer wave at the typical unit in the case of different millisecond times, which was caused by the successive explosion of the charge. The stress waves of the three charge delay explosions cancel each other. The vibration waves and the central frequency generated by each blast hole are staggered with each other. Each segment reaches the peak value independently and then decays. The second peak pressure is higher and the third peak pressure is significantly lower in the image.

A typical unit with a distance of one meter from  $r$  was taken in the direction of the minimum resistance line of the intermediate charge in order to further study the attenuation law of the water hammer wave, and the monitoring point is shown in Figure 2. The variation of the peak pressure of the typical unit with the explosion center distance is extracted in the case of each millisecond time, as shown in Figure 5.

As shown in Figure 5, the peak pressure of the water hammer wave shows an exponential attenuation trend with the

increase of the explosion center distance in the direction of the minimum line of resistance. In the range of explosion center distance from 1 m to 5 m, the attenuation of the water hammer wave is the most obvious. Besides, the attenuation velocity of the water hammer wave is different in different millisecond times.

At the same distance from the charge, the peak pressure of the water hammer wave is different in different millisecond times in the direction of the center of the charge. The peak pressure of the water hammer wave is 86 MPa at millisecond interval 10 ms, 85 MPa at millisecond interval 20 ms, 74 MPa at millisecond interval 30 ms, and 80 MPa at millisecond interval 40 ms. It can be concluded that the peak pressure of the water hammer wave is the lowest at millisecond interval 30 ms.

Cole proposed that the attenuation formula of the water hammer wave is presented as follows:

$$p = a \left( \frac{\sqrt[3]{Q}}{r} \right)^b. \quad (7)$$

In the formula,  $p$  is the pressure of the water hammer wave,  $Q$  is the amount of charge in a single hole,  $Q = 14$  kg, and  $r$  is the distance between the explosion source and the measuring point.

Based on equation (7), the peak pressure of the water hammer wave is fitted by nonlinear exponential fitting, and the fitting curve is shown in Figure 6.

The fitting parameter  $a = 16.43$ ,  $b = 1.09$ , and  $s = 0.98$ .  $s$  is the relevant parameter of fitting, the nearer  $s$  is, the better the fitting effect is in the case of prompt blasting. The attenuation formula of water hammer wave in prompt blasting is as follows:

$$p = 16.43 \left( \frac{\sqrt[3]{Q}}{r} \right)^{1.09}. \quad (8)$$

The  $a$ ,  $b$ , and  $s$  parameters of delay 10 ms, 20 ms, 30 ms, and 40 ms are shown in Table 6.

It can be obtained from Table 6 that the fitting parameter  $a$  fluctuates slightly, the  $b$  value changes little, and the fitting effect is better when blasting with different millisecond times. The relevant results can provide a reference for predicting the peak attenuation of water hammer pressure under similar working conditions. At the millisecond interval of 0 ms, the peak

TABLE 5: Steel parameters.

$\rho$ (kg/m <sup>3</sup> )	Young's modulus (GPa)	Poissonby	Ductile damage	
			Fracture strain	Stress triaxiality
7800	206	0.2	2.193828 0.314962024	0 0.7

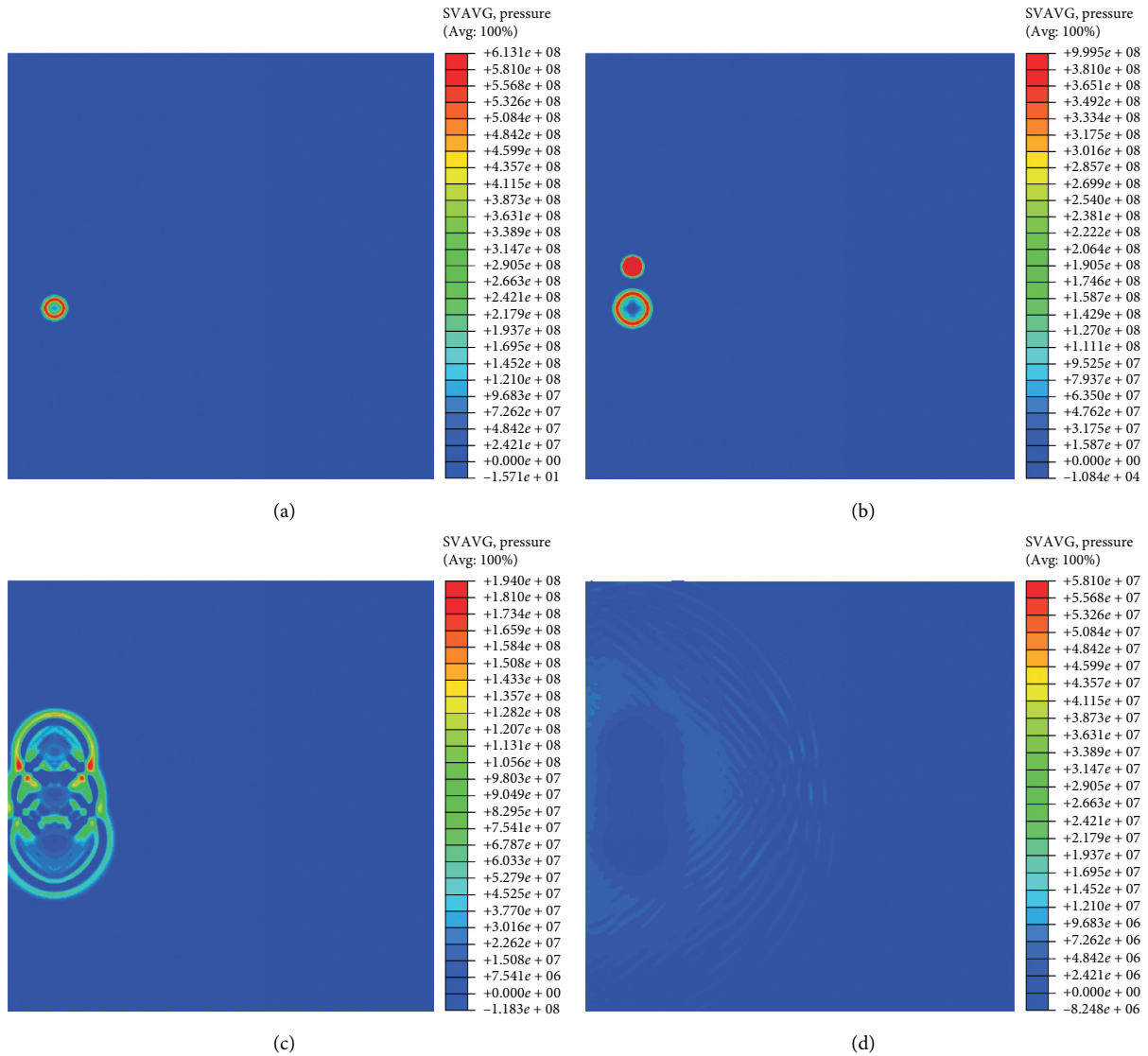


FIGURE 3: Stress nephogram of 10 ms delayed SVAG pressure. (a) 8 ms. (b) 12 ms. (c) 22 ms. (d) 25 ms.

pressure of the water hammer wave attenuates from 90 MPa to 4.5 MPa, by 95.0%. At the millisecond interval 10 ms, the peak pressure attenuates from 86 MPa to 2.1 MPa, which is 95.2% lower. At millisecond interval 20 ms, the peak pressure attenuates from 85 MPa to 2.5 MPa, decreasing by 97.1%. At the millisecond interval of 30 ms, the peak pressure attenuates from 74 MPa to 1.8 MPa, which decreases by 97.6%. At the millisecond interval of 40 ms, the peak pressure attenuates from

80 MPa to 2.2 MPa, an attenuation of 97.2%. Peak pressure attenuation is shown in Figure 7.

With the increase of millisecond time, the attenuation velocity of peak pressure of water hammer wave increases first and then decreases. It can be concluded that the attenuation rate of peak pressure of water hammer wave was the fastest and the peak pressure of water hammer wave was the smallest in the case of millisecond interval 30 ms through

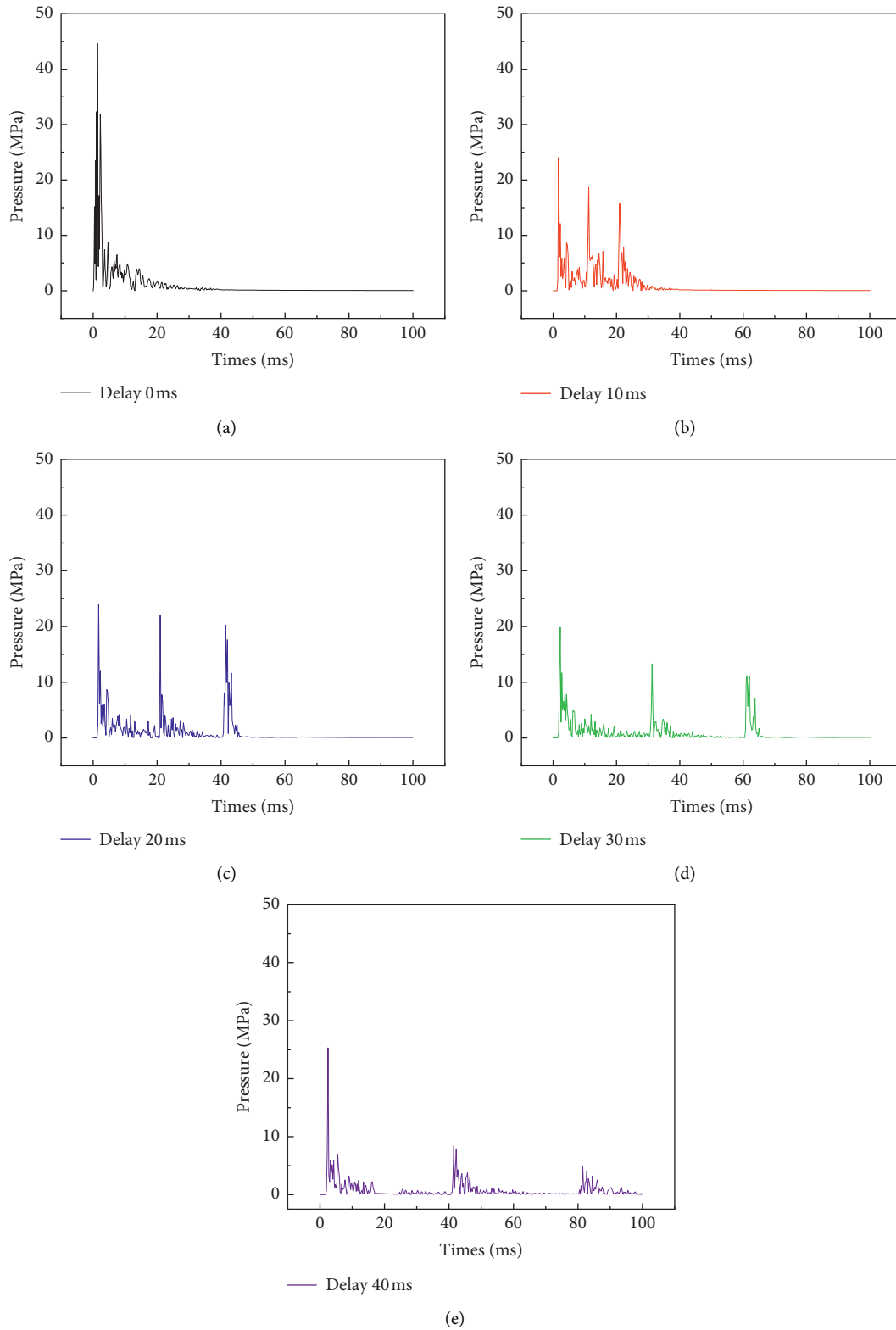


FIGURE 4: Typical unit pressure-time history curve. (a) Delay 0 ms. (b) Delay 10 ms. (c) Delay 20 ms. (d) Delay 30 ms. (e) Delay 40 ms.

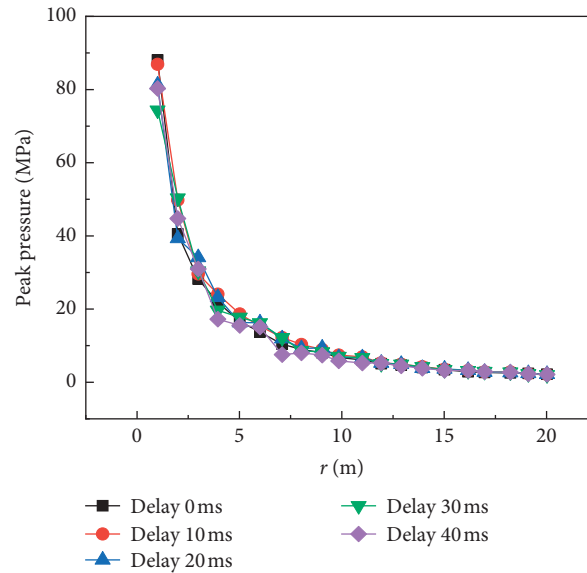


FIGURE 5: The change of the peak pressure in the direction of the minimum resistance line with the burst center distance.

the analysis of the propagation law of water hammer wave with different millisecond times.

**4.3. Influence of Different Millisecond Times and Water Depths on Propagation Law of Water Hammer Wave.** The attenuation velocity of water hammer waves in different water depths is different. The curve of the peak pressure along the direction of the minimum line of resistance with the center of the explosion at the water depth of 5 m and 20 m was extracted in order to study the influence of different millisecond times on the pressure propagation law of the water hammer wave at different water depths, as shown in Figure 8.

As shown in Figure 8, the peak pressure attenuation with the explosion center distance also attenuates exponentially in different water depths. In addition, the peak pressure of the water hammer wave is the highest when the 0 ms is delayed. The peak pressure of the water hammer wave is 12.0 MPa at the depth of 5 m and 4.9 MPa at the depth of 20 m.

As shown in Figure 8(a), the peak pressure of the water hammer wave attenuates from 12.0 MPa to 2.7 MPa, attenuating by 77.5%, and the peak pressure of the water hammer attenuates from 8.12 MPa to 1.8 MPa, attenuating by 77.8% when millisecond blasting is 0 ms and millisecond blasting is 10 ms. When millisecond blasting is 20 ms, the peak pressure of water hammer attenuates from 8.02 MPa to 1.7 MPa, by 78.9%. When millisecond blasting is 30 ms, the peak pressure of water hammer attenuates from 7.56 MPa to 1.4 MPa, by 81.4%. When millisecond blasting is 40 ms, the peak pressure of water hammer attenuates from 7.78 MPa to 1.7 MPa, attenuating by 78.1%.

As shown in Figure 8(b), when millisecond blasting is 0 ms, the peak pressure of water hammer wave decays from 4.9 MPa to 1.2 MPa, and the attenuation rate is 75.5%. The peak pressure of the water hammer decreases from 3.96 MPa to 0.95 MPa, which is 76.0% when the millisecond blasting is

10 ms. The peak pressure of the water hammer decreased from 3.63 MPa to 0.82 MPa, 77.4%, when millisecond blasting was 20 ms. The peak pressure of the water hammer decreased from 3.38 MPa to 0.8 MPa, which decreased by 79.1%, when the millisecond blasting time was 30 ms. When the millisecond blasting time is 40 ms, the peak pressure of the water hammer decreases from 3.49 MPa to 0.9 MPa, which is 74.2%. It can be seen that the peak pressure of the water hammer wave in millisecond blasting 30 ms was the smallest and the attenuation was the fastest. In addition, when the water depth was changed, this conclusion was still valid. The attenuation velocity of the water hammer wave was different in different water depths. The attenuation velocity of the water hammer wave increased at first and then decreased with the increase of water depth. The peak pressure of the water hammer wave was the highest and the attenuation speed was the fastest at the water depth of 10 m.

**4.4. Reducing Effect of Bubble Curtain Wall on Water Hammer Wave.** Measures need to be taken to buffer the water hammer wave to ensure the safety of the lock chamber and further reduce the impact of the water hammer wave. The bubble curtain wall is a new method to reduce the shock wave of underwater blasting, which has been widely used because of its good effect of blocking water hammer wave [1].

Python generated the bubble curtain generated by random bubbles based on the maximum and minimum radius and the minimum interparticle radius to simulate the real bubble curtain wall. In addition, the peak value of the water hammer wave before and after the bubble curtain was studied, which provides a sure basis for protecting the safety of adjacent structures. The schematic diagram of the model is shown in Figure 9. The stress nephogram is shown in Figure 10.

Figure 10 is a schematic diagram of the stress of water hammer wave weakened by bubble curtain during 30 ms millisecond blasting. It can be seen that the bubble curtain

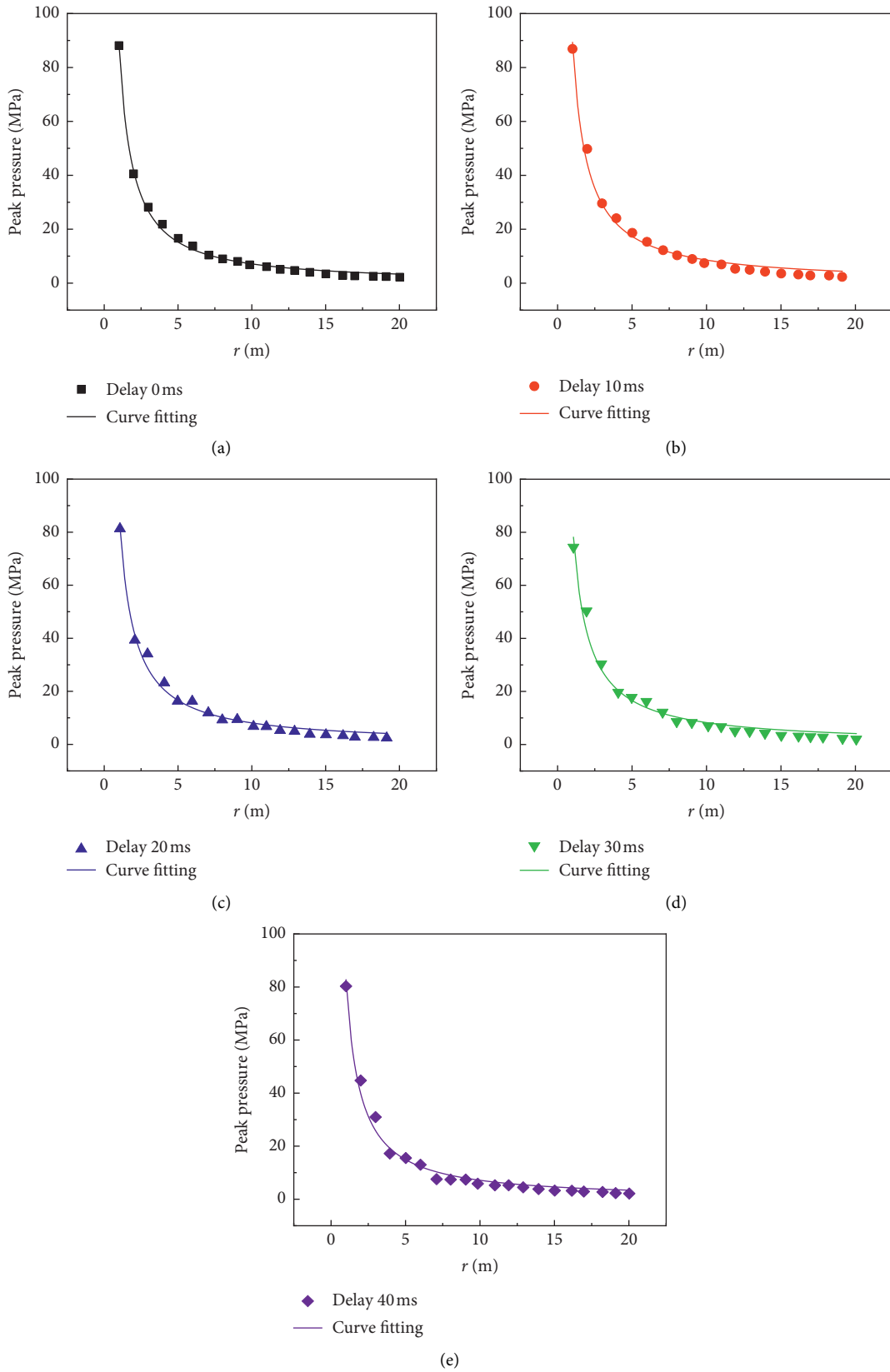


FIGURE 6: The attenuation curve of water hammer wave on the minimum resistance line. (a) Delay 0 ms fitting curve. (b) Delay 10 ms hole blasting fitting curve. (c) Delay 20 ms fitting curve. (d) Delay 30 ms hole blasting fitting curve. (e) Delay 40 ms hole blasting fitting curve.



TABLE 6: Fitting parameters.

Delay time (ms)	$a$	$b$	$s$
0	16.43	1.09	0.98
10	18.55	1.02	0.90
20	17.76	1.03	0.95
30	17.76	1.00	0.97
40	16.38	1.05	0.98

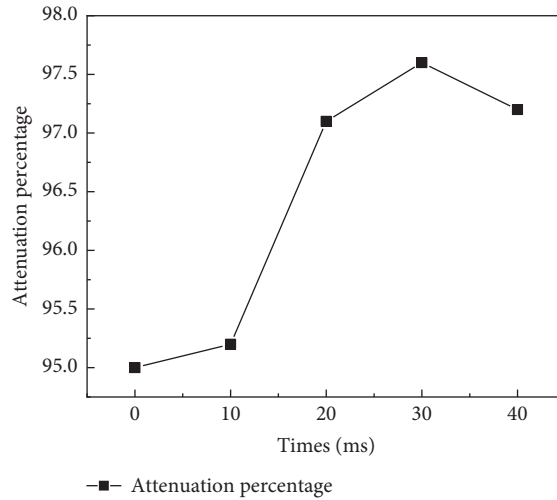


FIGURE 7: Attenuation ratio of peak pressure at 10 m water depth.

wall has a good effect on reducing the water hammer wave. When the water hammer wave passes through the bubble curtain wall, the peak pressure of the water hammer wave is significantly weakened behind the wall due to the refraction and reflection of the air in the bubble and the diffuse reflection of the bubble surface. As shown in Figure 10(a), the charge explodes in the concrete wall quickly, forming a circular water hammer wave. The water hammer wave continues to propagate to the bubble curtain. As shown in Figure 10(b), the water hammer wave is flattened near one end of the bubble curtain, which is due to the difference between the left and correct medium impedance of the bubble curtain. In 8 ms, when the water hammer wave is transferred to the bubble curtain wall, cavitation will occur near the free surface where the air and water contact, which shows that the pressure of water hammer wave in the cavitation area behind the wall decreases, the difference between the water hammer pressure and the far away from water hammer pressure in cavitation area is not significant, as shown in Figure 10(c), most of the incident waves are reflected by the bubble curtain, and the reflected water hammer waves propagate to the concrete impervious wall. The secondary reflected incident waves continue to propagate along the direction of the bubble curtain. The superimposed coincidence of the light waves reflects several times propagates to the bubble curtain. In addition, the sparse incident waves continue to diverge outward through the gap between the bubble curtains, as shown in Figure 10(d).

The measuring points were set up on the explosion face and back explosion surface of the bubble curtain in order to quantitatively study the reduction effect of the water hammer wave, centering on the position elevation of the charge (the face mark of the forward explosion is 1 and that of the back explosion is 2). The pressure-time history curves of the measuring points on the left and right sides of the bubble curtain at the distance of 3 m, 5 m, 8 m, 10 m, and 15 m from the charge are extracted, respectively, the pressure-time history curves of each measuring point are shown in Figure 11, and the peak pressure of each point is shown in Table 7.

As shown in Figure 11, with the increase of the distance between the bubble curtain and the charge, the effect of water hammer wave reduction becomes worse and worse. The percentage reduction is shown in Table 7.

Figure 12 shows the attenuation effect of bubble curtain at different distances from the charge.

As shown in Figure 12 and Table 7, the pressure-time history curves are 15 m, 10 m, 8 m, 5 m, and 3 m away from the center of the charge, respectively. Figure 11 shows the attenuation percentage curve at different distances from the bubble curtain to the charge. It can be seen from Table 7 that when the bubble curtain is 15 m away from the center of the charge, the peak pressure attenuates by 75.0%. When the distance is 10 m, the peak pressure attenuates by 80.0%, when the distance is 8 m from the center of the charge, the attenuation of the peak pressure is 82.3%, when the distance is 5 m, the peak

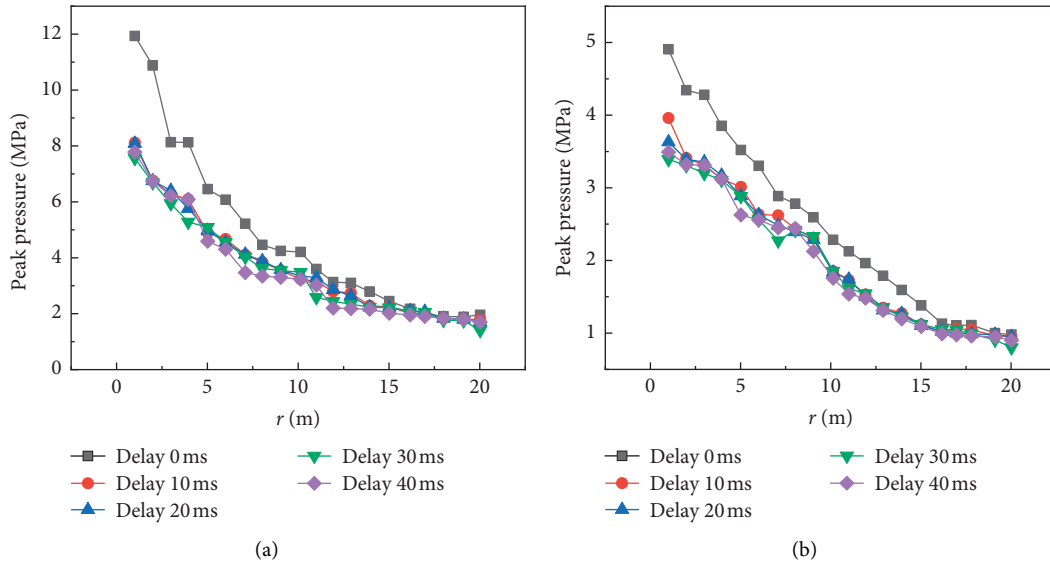


FIGURE 8: The attenuation curve of water hammer wave on the minimum resistance line. (a) 5 m. (b) 20 m.

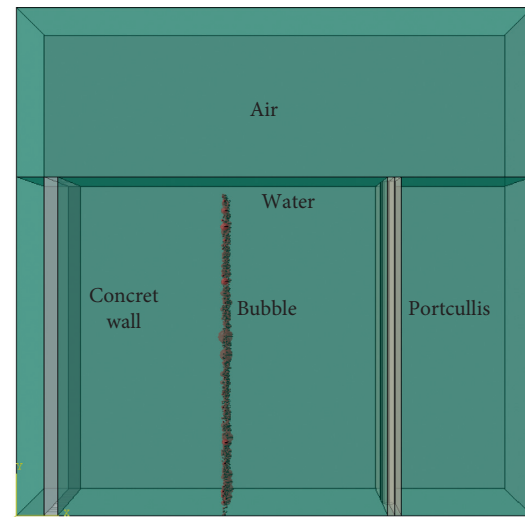


FIGURE 9: Schematic diagram of numerical simulation.

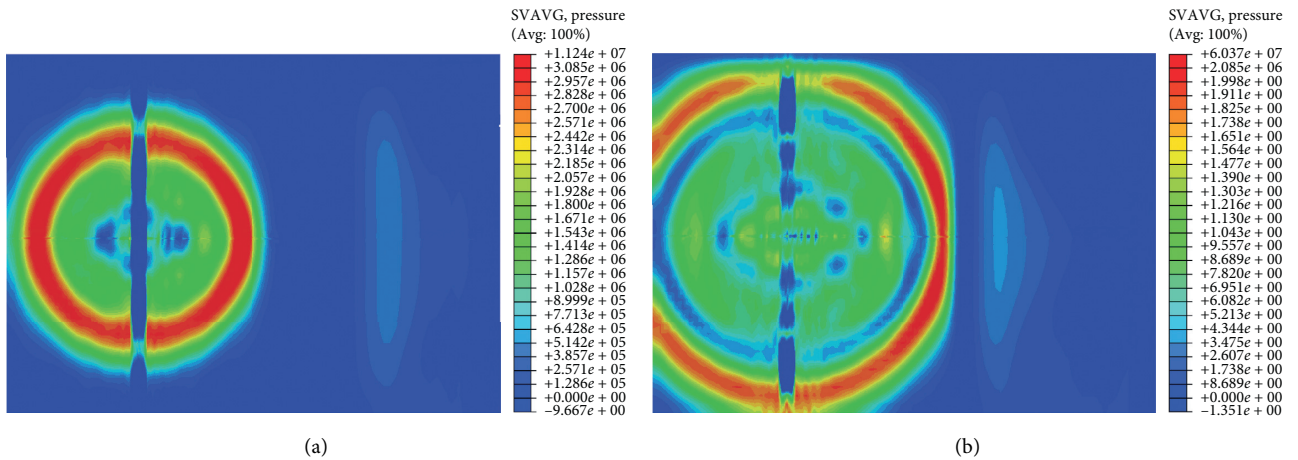


FIGURE 10: Continued.

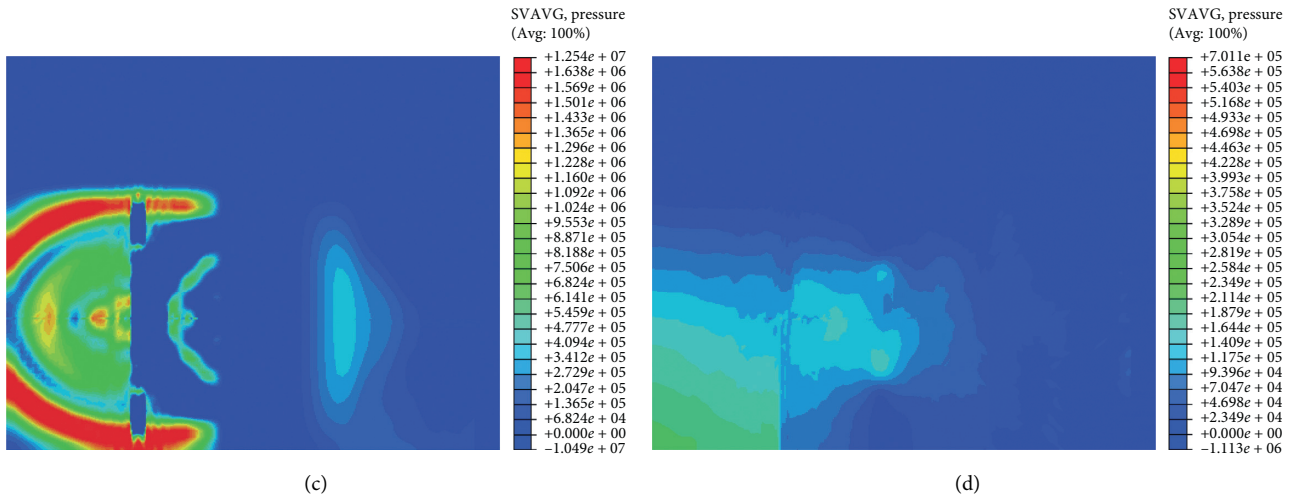


FIGURE 10: Stress nephogram of bubble wall weakening water hammer wave. (a) 0.05 ms. (b) 4 ms. (c) 8 ms. (d) 20 ms.

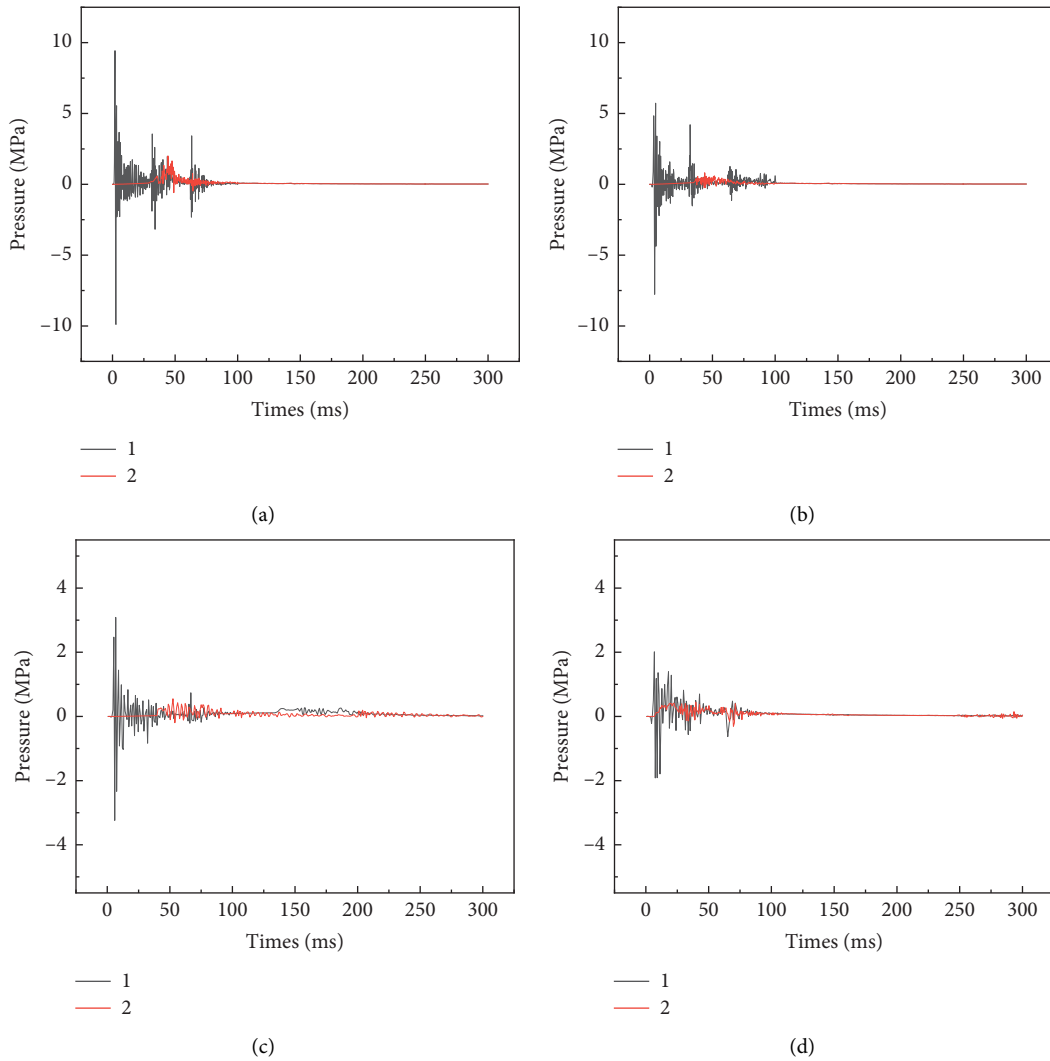


FIGURE 11: Continued.

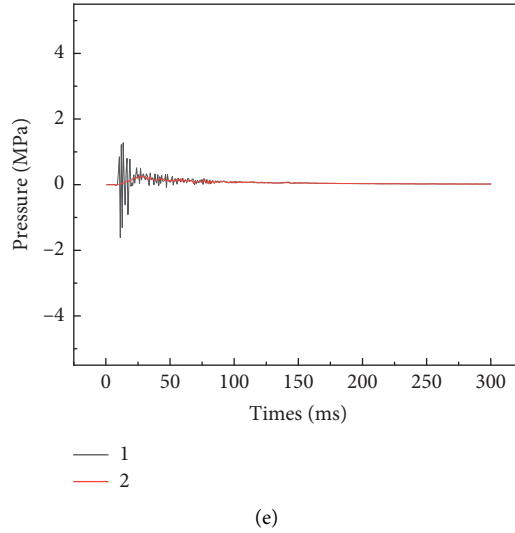


FIGURE 11: Pressure-time curve at different distance from charge. (a) 3 m. (b) 5 m. (c) 8 m. (d) 10 m. (e) 15 m.

TABLE 7: Statistical table of peak values of measuring points.

Distance from bomb (m)	Direction of explosion	Peak pressure (MPa)	Attenuation ratio (%)
15	1	1.20	75.0
	2	0.30	
10	1	2.00	80.0
	2	0.40	
8	1	3.10	82.3
	2	0.55	
5	1	5.90	86.1
	2	0.82	
3	1	9.43	88.3
	2	1.10	

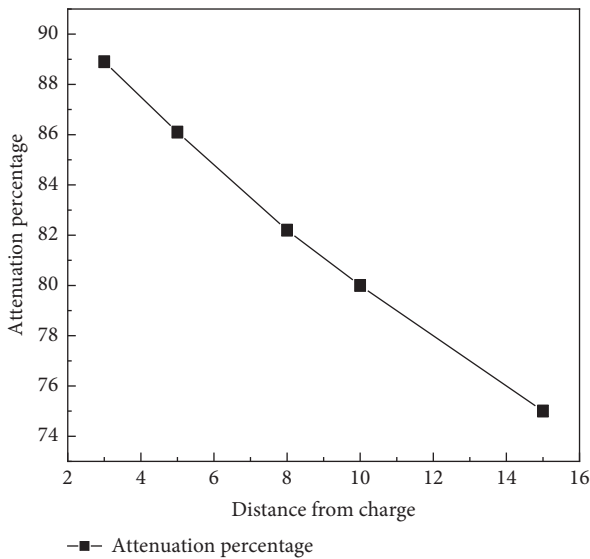


FIGURE 12: Attenuation percentage diagram of different distance between bubble curtain and charge.

pressure attenuates by 86.1%, and when the distance is 3 m from the center of the charge, the peak pressure attenuates by 88.3%. As a consequence, it can be seen that

the closer the bubble curtain was to the charge, the better the attenuation effect was, and it showed a linear attenuation trend.

### 5. Conclusion

A three-dimensional model was established based on CEL, a coupling method of Eulerian and Lagrangian, and a script was written based on Python to generate natural bubble curtain in order to study the influence of millisecond blasting with different millisecond times and bubble curtain on the propagation law of water hammer wave. In the process of postprocessing, the pressure-time history curve of the typical unit at the distance of 3 m in the direction of the minimum resistance line of charge was extracted. The peak pressure curves of water hammer waves with different millisecond times in different water depths were extracted. In addition, the reduction effect of bubble curtain at different positions was analyzed, and the following conclusions were obtained:

- (1) The peak pressure of the water hammer wave attenuates exponentially with the increase of explosion center distance under different millisecond times. When the millisecond interval was 0 ms, 10 ms, 20 ms, 30 ms, and 40 ms, the peak

pressure of the water hammer wave was 4.5 MPa, 2.1 MPa, 2.5 MPa, 1.8 MPa, and 2.2 MPa, respectively, in the direction of the minimum resistance line (water depth 10 m) and 20 m away from the charge. With the increase of millisecond time, the attenuation velocity of the water hammer wave increased at first and then decreased, the peak pressure of the water hammer wave in 30 ms was the smallest, and the attenuation was the fastest.

- (2) The peak pressure of water hammer wave in different water depths also showed an exponential attenuation law with the increase of explosion center distance, but the attenuation rate was different. Besides, with the increase of water depth, the attenuation velocity increased at first and then decreased. Taking millisecond blasting 30 ms as an example, the peak pressure of water hammer wave at the depth of 5 m, 10 m, and 20 m was 1.4 MPa, 1.8 MPa, and 0.8 MPa, respectively. The peak pressure of the water hammer wave was the highest and the attenuation speed was the fastest at the water depth of 10 m.
- (3) The closer the bubble curtain was to the center of the charge, the better the peak pressure attenuation of the water hammer wave behind the bubble curtain was. In addition, it showed a linear attenuation trend. At the distance of 15 m, 10 m, 8 m, 5 m, and 3 m from the bubble wall, the peak pressure attenuation rate behind the bubble curtain was 75.0%, 80.0%, 82.3%, 86.1%, and 88.3%, respectively.

The nonreflection boundary condition was established, but in practice, the amount of concrete impervious wall is located on the bank, and the site is affected by river banks and dams. As a consequence, its boundary conditions may need to be further optimized. Consequently, it is necessary to further study the influence of boundary conditions closer to the field on the attenuation of water hammer pressure, which will contribute to understanding the propagation characteristics of underwater drilling millisecond blasting in more detail.

### Data Availability

The data used to support the findings of this study are available from the corresponding author upon request.

### Conflicts of Interest

The authors declare that there are no conflicts of interest regarding the publication of this article.

### Acknowledgments

This work was supported by the National Natural Science Foundation of China (51874006) and the Anhui Provincial Natural Science Foundation (1808085ME159).

### References

- [1] J. Pang, "Numerical simulation of TNT charge explosion in water," *Journal of Explosives and Explosives*, vol. 32, no. 5, pp. 37–40, 2009, Chinese.
- [2] K. Li, X. L. Dong, X. J. Li, Y. G. Wang, and W. Wang, "Determination of JWL parameters from underwater explosion test of spherical explosives by continuous velocity probe," *Journal of Energetic Materials*, vol. 7, no. 12, pp. 5383–5396, 2014.
- [3] C. H. Chen, L. Wu, J. W. Zhao, B. Li, H. Y. Li, and C. J. Li, "Study on the influence of underwater drilling and blasting on the safety of adjacent buildings," *Blasting*, vol. 33, no. 2, pp. 117–122, 2016, Chinese.
- [4] S. F. Qi, X. B. Liu, and Y. C. Li, "Numerical simulation of underwater drilling and blasting," *Engineering Blasting*, vol. 16, no. 4, pp. 13–17, 2010, Chinese.
- [5] D. J. Xie, L. Wu, J. Hong, L. Yuan, M. Cao, and X. H. Luo, "Study on weakening effect of bubble curtain on underwater blasting shock wave," *Renmin Changjiang River*, vol. 49, no. 8, pp. 72–77, 2018, Chinese.
- [6] X. Liu, W. B. Gu, and X. P. Chen, "Numerical simulation study on attenuation characteristics of shock wave in water by bubble curtain," *Blasting*, vol. 32, no. 3, pp. 79–84, 2015, Chinese.
- [7] Z. J. Fan, "Application of millisecond blasting method in underwater reef blasting," *Water Transport Engineering*, vol. 6, pp. 38–40, 2002, Chinese.
- [8] T. Y. Liu, S. T. Gong, W. C. Hu, Y. W. Zhong, and L. Wu, "Propagation law of water hammer wave in underwater drilling blasting and reduction effect of bubble curtain on water hammer wave," *Blasting Equipment*, vol. 49, no. 2, pp. 16–22, 2020, Chinese.
- [9] G. Zhao, R. Ji, X. N. Zheng, W. H. Wang, and C. Q. Wu, "Experimental study on shock wave propagation law of underwater explosion of emulsion explosive," *Blasting*, vol. 28, no. 2, pp. 1–4, 2011, Chinese.
- [10] J. F. Si, D. W. Zhong, and L. B. Li, "Analysis of attenuation effect of underwater gas curtain on shock wave based on bubble shape," *Explosion and Shock*, pp. 1–9, 2021, Chinese.
- [11] Y. X. Peng, L. Wu, Y. Su, and C. H. Chen, "Study on the effect of elevation on the prediction of underwater drill and blasting vibration frequency," *Geosystem Engineering*, vol. 19, no. 4, pp. 170–176, 2016.
- [12] Y. Ma, C. Liu, P. Wang, J. Zhu, and X. Zhou, "Blast vibration control in A hydropower station for the safety of adjacent structure," *Applied Sciences*, vol. 10, no. 18, p. 6195, 2020.
- [13] C. Huang, M. Liu, B. Wang, and Y. Zhang, "Underwater explosion of slender explosives: directional effects of shock waves and structure responses," *International Journal of Impact Engineering*, vol. 130, pp. 266–280, 2019.
- [14] Y. Liu, A.-M. Zhang, Z. Tian, and S. Wang, "Investigation of free-field underwater explosion with Eulerian finite element method," *Ocean Engineering*, vol. 166, pp. 182–190, 2018.
- [15] X. Zhai, S. Wu, H. Li, K. Wang, W. Wang, and X. Song, "Experimental and numerical investigation on dynamic behaviors of the concrete wall in underground coal mine with hydraulic blasting demolition," *Journal of Vibroengineering*, vol. 19, no. 3, pp. 2043–2062, 2017.
- [16] W. Gu, Z. Wang, J. Liu et al., "Water-depth-based prediction formula for the blasting vibration velocity of lighthouse caused by underwater drilling blasting," *Shock and Vibration*, vol. 2017, Article ID 7340845, 9 pages, 2017.



- [17] L. Xin, W. B. Gu, J. Q. Liu, J. L. Xu, T. Cao, M. Filippi et al., "Investigation of the propagation characteristics of underwater shock waves in underwater drilling blasting," *Shock and Vibration*, vol. 2018, Article ID 9483756, 10 pages, 2018.
- [18] W. B. Gu, J. H. Chen, Z. X. Wang, J. Q. Liu, M. Lu, M. Lallart et al., "Experimental study on the measurement of water bottom vibration induced by underwater drilling blasting," *Shock and Vibration*, vol. 2015, Article ID 496120, 8 pages, 2015.
- [19] L. Hammond, *Underwater Shock Wave Characteristics of Cylindrical Charges*, Defence Science and Technology Organisation, AMRL, DSTO-GD-0029, Australia, 1995.
- [20] C. Oucif and L. Muhammad Mauludin, "Numerical modeling of high velocity impact applied to reinforced concrete panel," *Underground Space*, vol. 4, no. 1, pp. 1-9, 2018.
- [21] M. Mokhtari and A. Alavi Nia, "The application of CFRP to strengthen buried steel pipelines against subsurface explosion," *Soil Dynamics and Earthquake Engineering*, vol. 87, pp. 52-62, 2016.

## Research Article

# Sabot Discard Characteristics under Different Spin Rates of the Rifled Barrel Launching APFSDS

Chengqing Zhang,<sup>1,2</sup> Huiyuan Wang ,<sup>1</sup> Ting Liu,<sup>2</sup> and Yingxian Duo<sup>1</sup>

<sup>1</sup>College of Mechatronics Engineering, North University of China, Taiyuan 030051, China

<sup>2</sup>Key Laboratory of Information Detection and Processing, North University of China, Taiyuan 030051, China

Correspondence should be addressed to Huiyuan Wang; wanghuiyuan@nuc.edu.cn

Received 1 April 2021; Accepted 29 April 2021; Published 10 May 2021

Academic Editor: Qi ZHAO

Copyright © 2021 Chengqing Zhang et al. This is an open access article distributed under the Creative Commons Attribution License, which permits unrestricted use, distribution, and reproduction in any medium, provided the original work is properly cited.

The sabot discard asymmetry caused by spinning affects the exterior ballistic characteristics and shooting accuracy of a gun with the rifled barrel. To gain a deeper understanding of the complex sabot discard performance for the armor-piercing, fin-stabilized discarding sabot (APFSDS), a numerical investigation is performed to assess the effects of the spin rate on the sabot discard characteristics. We obtain the calculation boundary by the interior ballistics and the firing conditions and carry out a numerical simulation under different spin rates using computational fluid dynamics (CFD) and a dynamic mesh technique. We analyze four aspects of sabot discard characteristics, namely, sabot separation, rod surface pressure, rod aerodynamic parameters, and discarding quantization parameters. Computational results show that the sabot separation nearly presents perfect symmetry at 0 rad/s, and when the initial rate of the sabot increases, there is more obvious separation asymmetry, and it contributes to the relative position variation among the sabots and the rod. The distinction of rod surface pressure indicates that the choked flow is the strongest flow source, and the spin rate has almost no effect on the pressure of the rod front part. When the monitoring point moves towards the fins, the pressure distribution and intensity change more dramatically. The initial spin rate and separation asymmetry produce a variation in the surface pressure, which further influences the rod aerodynamic characteristics. The discarding quantization parameters exhibit a certain variation rule with its spin rate. 2,000 rad/s has a significant influence on the rod aerodynamic coefficients during the weak coupling phase. When the spin rate is in the range of 0–900 rad/s, the discarding characteristics remain the same. However, when the spin rate exceeds 900 rad/s, the separation time and aerodynamic impulse have a quadratic polynomial relationship with the rate. Additionally, a spin rate of 1,000 rad/s is the optimal value for a rifled barrel gun.

## 1. Introduction

The ultimate challenge of conventional weapons is the achievement of a longer firing range, higher muzzle velocity, and higher firing accuracy; therefore, the armor-piercing projectile comes into being and has a broad array of applications in tube-launched weapons [1]. An APFSDS is a kinetic energy projectile with high velocity, excellent ballistic performance, high energy density, and other advantages. Generally, APFSDS comprises several sabots, a slim long rod, an obturator, and other parts. The function of sabots is to transfer the axial load and support the projectile. As a kind of low-density and high-strength metal material, aluminum

alloy is widely used in automobile, aerospace, machinery manufacturing, shipbuilding, and other industries [2, 3]. Thus, aluminum alloy is the preferred material for sabots to meet the high overload requirements of launching. A slipping obturator is essential to provide the rifled barrel of Gatling gun, and it can seal gunpowder gas and give the rod a low spin rate [4]. When the APFSDS is ejected from the gun tube, the separation of sabots from the rod is called as the sabot discarding process (SDP), and it is accompanied by mechanical and aerodynamic interference [5]. In particular, the sabot spin rate and tangential velocity of the APFSDS affect the aerodynamic interference of the SDP, which results in the loss of stability and a sacrifice of accuracy [6, 7].

We use high-speed photography to capture the APFSDS projectile attitude and provide a photo of the launching phenomenon in Figure 1, which is a millisecond-level process. The schematics in Figures 2(a) and 2(b) illustrate the aerodynamic interaction of the SDP. When the APFSDS is out of the barrel constraint, the gunpowder gas quickly coats the projectile. Then, it escapes from the muzzle flow field, and the high-velocity airstream impinges on the front scoop of the sabots, and the back of the sabot is hardly affected by the gunpowder gas. Aerodynamic forces and moments cut a nylon ring into small pieces, and the APFSDS begins to separate dynamically without the obturator restriction. Generally, as shown in Figure 2(a), the incoming flow is divided into three parts: one flows from the surface of the rod and sabots, another passes through the gaps among the sabots or between the sabots and the rod, and the rest mostly hit the sabot scoop. A series of shocks, including attached waves, detached shock waves, choked flows, reflected waves, and expansion waves, as shown in Figure 2(b), accompany the SDP. Therefore, this separation is a complex process that involves various shock wave interactions [6].

Previous investigations have demonstrated that multiplex interference factors can result in a ballistic disturbance during the SDP [7], and the aerodynamic interference remains a major disturbance that affects the projectile flight stability, and it ultimately influences the exterior ballistic and shooting accuracy [7, 8]. Hence, some scholars have achieved initial results with the APFSDS SDP. Original studies involved shooting tests and engineering practices to study the basic phenomena [7–9]. Scholars have analyzed several sticking points of the SDP at different periods. In the 1980s, Schmidt and Shear [6, 7] conducted several important and fundamental investigations in shooting tests and measurement. Consequently, Schmidt and Shear [6] showed that aerodynamic interference affected the rod characteristics, and Schmidt [7] revealed the effects of multiple shock and boundary layer interactions. In the 1990s, Dick and Dolling [9] conducted tests at 5 Ma for two fixed SDP stages, and the results showed that the interference of splitter plates mainly affected the bow shock generated by the projectile. However, shooting tests and wind tunnels have disadvantages, including time consumption, high risk, motion uncertainty, and testing difficulty. Nonetheless, the above critical results provide a foundation for sabot design.

Advances in computer technology and numerical algorithms have promoted the rapid development of CFD, which can be used to solve complex flow problems with supersonic characteristics [10]. The implantation of multi-body dynamics, dynamic mesh, and even turbulence models has led to many improvements to aerodynamic calculations [11] and dynamic separation results [12–14]. Lee and Wu [12, 13] used CFD to research the SDP in a fixed attitude case, concluding that the pressure distribution of the spring was more consistent with the test results [14, 15]. Snyder et al. [16] adopted unstructured dynamic grids to settle store separation simulations, which are built upon a foundation for unsteady SDP. Cayzac et al. [17, 18] applied the two-dimensional Euler algorithm to predict the sabot trajectory,

and the computational result was in good agreement with experimental data. Huang et al. [19] claimed a combination of the unstructured dynamic mesh technology to solve the unsteady SDP problem, revealing the basic phenomenon of the SDP and the symmetrical separation. Li et al. [20] established a coupled model to explore the SDP under different angles of attack (AOA) and induced that the greater the AOA, the more intense the disturbance for the SDP. Reck et al. [21] confirmed the conclusion that the asymmetric disturbance, acting by an angular rate of the armature, affects the sabot separation process to a minor extent using the wind tunnel and numerical calculations. Additionally, Li [5] proposed a basic standard that the weaker aerodynamic interference and shorter separation time of the SDP would be more logical for sabot design.

Numerous scholars have conducted detailed studies on the SDP, but the impact of the sabot spin rate is a factor that cannot be ignored. The spin rate can affect the variation in sabot motion and rod aerodynamic, which further result in the difference of sabot discard characteristics. Against this background, a small-caliber APFSDS was chosen as a sub-caliber representative configuration with three sabots in the simulation of a rifled barrel gun. We consider the Gatling gun launching peculiarity and the interior ballistic model to establish a simulation model under different spin rate cases. We then adopt the dynamic unstructured grid technology to solve the APFSDS separation and flow field. Subsequently, these analyses of sabot discard characteristics are conducted by sabot separation, rod surface pressure, rod aerodynamic forces, and discarding quantization parameters.

## 2. Simulation Model

*2.1. Model Assumption.* For the spin rate effect on the SDP, we make the following assumptions:

- (1) The influence of the propellant gas on the projectile is so small that the propellant gas action is not considered [19].
- (2) The total separation time of the SDP is in the millisecond scale; thus, we can neglect the velocity attenuation of the APFSDS.
- (3) The rod spin rate is very low; thus, its rotational motion is not considered.
- (4) There are several positioning grooves between the sabots and the rod, and the relative displacement between them is extremely small during cutting an obturator. Thus, we set the initial axial clearance as 1 mm between the rod and sabots.
- (5) We assumed that the inlet flow is a perfect gas.

*2.2. Interior Ballistic Model.* The propellant type of the APFSDS is a single charge used to solve the simulation initial boundary, and the interior ballistic model can be written as follows [22].

State equation of the propellant gas:



FIGURE 1: Launching phenomenon of a rifled barrel APFSDS.

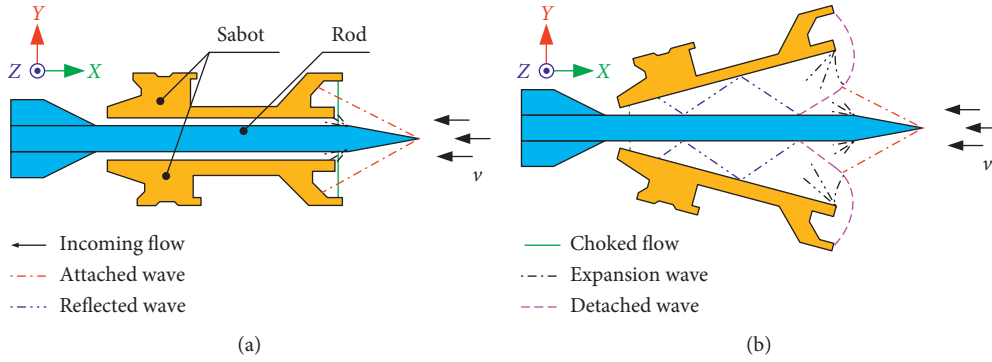


FIGURE 2: Schematic diagram of the SDP. (a) Initial status of sabot separation. (b) Aerodynamic interference model.

$$S_p p_p (l + l_A) = m_g \text{ART}. \quad (1)$$

Equation of energy conservation:

$$m_g \text{ART} = f m_g A - 0.5(k-1) B m_p v_p^2. \quad (2)$$

Kinetic equation of the projectile:

$$B m_p \frac{dv_p}{dt} = S_p p_p, \quad (3)$$

$$v_p = \frac{dl}{dt},$$

$$a_p = \frac{dv_p}{dt},$$

$$v_\tau = \omega_b r_b.$$

The numerical parameters (i.e., distance, time, velocity, and average pressure) are processed as dimensionless, and the fourth-order Runge–Kutta scheme is adopted to solve the internal ballistic equations.

**2.3. Solution Method.** For dynamic grids of cases, the general form of the control equation is obtained as follows:

$$\frac{\partial(\rho\phi)}{\partial t} + \text{div}(\rho\phi(\mathbf{u} - \mathbf{u}_D)) = \text{div}(\Gamma \text{grad}\phi) + \mathbf{S}. \quad (4)$$

Regarding equation (4), the first item on the left side is the transient term, and the second is the convection term.

Moreover, the first on the right is the diffusion term, and the second is the source term.

Finite volume method [15, 16] implicit time integration scheme [18–20], and advection upstream splitting method (AUSM) form were adopted to discretize the governing equation. The implicit time scheme has an absolute advantage in terms of simulation stability and time consumption reduction. The discretization in the convective fluxes can be written by the three-point scheme in the conservation form as in [23]:

$$(\rho\phi_1)_j^{n+1} = (\rho\phi_1)_j^n - \left(\frac{\Delta t}{\Delta x}\right) \cdot (\mathbf{f}_{(j+1/2)}^n - \mathbf{f}_{(j-1/2)}^n). \quad (5)$$

For the interface  $j + 1/2$  straddling the  $j$ th and  $(j + 1)$ th cells, the numerical flux is the sum of the numerical convective flux and numerical pressure flux and the subscripts, and “L” and “R” are the left-side and right-side states of the cell interface.

The turbulence model plays a key role in supersonic behavior, especially in dynamic separation with complex shock interactions. Chen et al. [24] concluded that the two-equation turbulence model performed much better than the one-equation version with up to 20% discrepancy, and the  $k-\omega$  model had approximately 5% accuracy relative to the  $k-\varepsilon$  model for the wind tunnel [25]. Not only is the influence of turbulent fluctuations in the projectile boundary layer considered but the effect of the far field is also not ignored. The SST  $k-\omega$  model can effectively ameliorate the reverse pressure gradient flow compared with the standard  $k-\varepsilon$  model. Therefore, the SST  $k-\omega$  model is an ideal turbulence model for SDP simulation.

The dynamic equations and kinematics can describe the sabot separation motion and are derived using a Newtonian approach with inertial and flat earth assumptions. Therefore, the center of gravity (CG) translational motion and the rotational motion of CG are associated with the resulting forces and moments as follows:

$$\begin{cases} m_i \dot{\mathbf{V}}_i + m_i \boldsymbol{\omega}_i \times \mathbf{V}_i = \mathbf{F}_i, \\ \mathbf{I}_i \cdot \dot{\boldsymbol{\omega}}_i + \boldsymbol{\omega}_i \times (\mathbf{I}_i \cdot \boldsymbol{\omega}_i) = \mathbf{M}_i \end{cases}, \quad i = 1, 2, 3, \quad (6)$$

where  $\mathbf{V} = (u, v, w)$ ,  $\boldsymbol{\omega} = (p, q, r)$ ,  $\mathbf{F} = (F_x, F_y, F_z)$ ,  $\mathbf{M} = (M_x, M_y, M_z)$ , and  $\mathbf{I} = (I_{xx}, I_{yy}, I_{zz})$ .

The inertial position kinematics and Euler angle kinematics are then determined:

$$\begin{aligned} \dot{P}_i &= \mathbf{C} \mathbf{V}_i, \\ \dot{S}_i &= \mathbf{E} \boldsymbol{\omega}_i, \end{aligned}$$

$$\mathbf{C} = \begin{bmatrix} C_\theta C_\psi & C_\theta S_\psi & -S_\theta \\ S_\theta C_\psi S_\varphi - S_\psi C_\varphi & S_\theta S_\psi S_\varphi + C_\psi C_\varphi & C_\theta S_\varphi \\ S_\theta C_\psi C_\varphi + S_\psi S_\varphi & S_\theta S_\psi C_\varphi - C_\psi S_\varphi & C_\theta C_\varphi \end{bmatrix}, \quad (7)$$

$$\mathbf{E} = \begin{bmatrix} 1 & \frac{S_\varphi S_\theta}{C_\theta} & \frac{C_\varphi S_\theta}{C_\theta} \\ 0 & C_\varphi & -S_\varphi \\ 0 & \frac{S_\varphi}{C_\theta} & \frac{C_\varphi}{C_\theta} \end{bmatrix},$$

where  $\varphi$ ,  $\theta$ , and  $\psi$  are the roll, yaw, and pitch Euler angles representing rotation on  $X$ ,  $Y$ , and  $Z$ , respectively. For the shorthand notation,  $S_\chi = \sin(\chi)$  and  $C_\chi = \cos(\chi)$  were used in the transformation matrices of  $\mathbf{C}$  and  $\mathbf{E}$ .

Figure 3 presents the numerical process of the unsteady APFSDS SDP using ANSYS Corp.'s FLUENT system. Based on the interior ballistics, firing conditions, and projectile structure, we obtained the initial conditions and established a numerical grid to implement discretization in space. User-defined functions (UDFs) were used to endow these sabot parameters and the APFSDS initial state, and the diameter and length of the rod were set to initial reference parameters. After initializing the simulation condition, we adopted the AUSM+ scheme and the SST  $k-\omega$  turbulence model to solve the fluid parameters and to check their convergence. Then, by combining the initial state of the APFSDS, the rigid body equations were used to account for every sabot motion and to update the mesh. The following step repeats this process until it reaches the set of calculation steps. Then, we monitored the specific point pressures, the APFSDS aerodynamic parameter, and the sabot motion history. Finally, we processed the flow field characteristics using post-processing software.

### 3. Numerical Verification

The Army-Navy Basic Finned Missile (ANF) model discussed in Army Ballistic Research Lab Report 539 is usually utilized to verify the projectile aerodynamic, and we created its physical model with a 20 mm diameter [26]. As shown in Figure 4(a), the ANF model is configured with a cylinder body, a cone, and four fins, and we provided these values as 200 mm full length, 20° cone angle, 1.6 mm maximum thickness, 20 mm length, and the width of the fins. Additionally, the refined zone had a nine-caliber diameter and length, and the boundary layer had a prism mesh of  $H_{\text{first}} = 0.001$  mm and  $N_L = 10$ . The computed grid is shown in Figure 4(b). Free-stream conditions and properties from [26] were used to obtain the aerodynamic parameters, and Figure 5 presents a comparison of the ANF drag coefficient (DC) between the calculated (Cal.) and experimental (Exp.) conditions. The Cal. results are very close to the measured data in [26], and the maximum error is 3.4% for the 1.5 Ma case, and the average error is 1.39% at others. The fitted curve of the simulation is in good agreement with [27].

### 4. Physical Model

Based on the SDP mechanism, APFSDS structure, and assumptions (1)–(4), we simplified the projectile as a model having a five-fin rod and three sabots [19], and we describe its parameters using  $D$  in Figure 6(a). As shown in Figure 6(b), these sabots are marked as S1, S2, and S3 in the counterclockwise rotation. The nose points forward on the  $X$ -axis to coincide with the rod axis, the  $Y$ -axis extends in the negative direction of gravity, and the  $Z$ -axis is determined by the right-hand rule. The coordinates of the sabots are set as 0 mm on the  $X$ -axis so that the origin of the coordinates is the intersection of the plane created by the sabot CG point and the rod axis.

Based on the APFSDS parameters and the estimated sabot motions, we established the outer flow zone with a hemisphere in the front and a cylinder in the back, and we optimized the outer field with  $D_O = 46.3D$  and  $L_O = 88.7D$ . The origin point of the zone is the hemisphere center. Subsequently, we performed a subtraction operation between the outer flow zone and the APFSDS to produce the simulation model, and we adopted the T-grid method to generate the unstructured tetrahedral mesh with ANSYS Corp.'s ICEM-CFD software. First, the shell grid was generated on the APFSDS surface and far field. Then, the prism grid was generated on the shell grid of sabots and rod, and the volume mesh finally grew from the prism grid to the shell grid as shown in Figure 7(a). The refined zone with  $L_R = 39D$  and  $D_R = 22D$  covers the APFSDS in Figure 7(b). To ensure simulation accuracy, we created the  $H_{\text{first}} = 0.015$  mm and  $N_L = 10$  boundary layers, as shown in Figure 7(c).

After fulfilling the model discretization in space, we set the far field as the inlet pressure. Moreover, the wall of the APFSDS is assumed to be an adiabatic boundary. Considering the gravity effect and assumption (5), the incoming



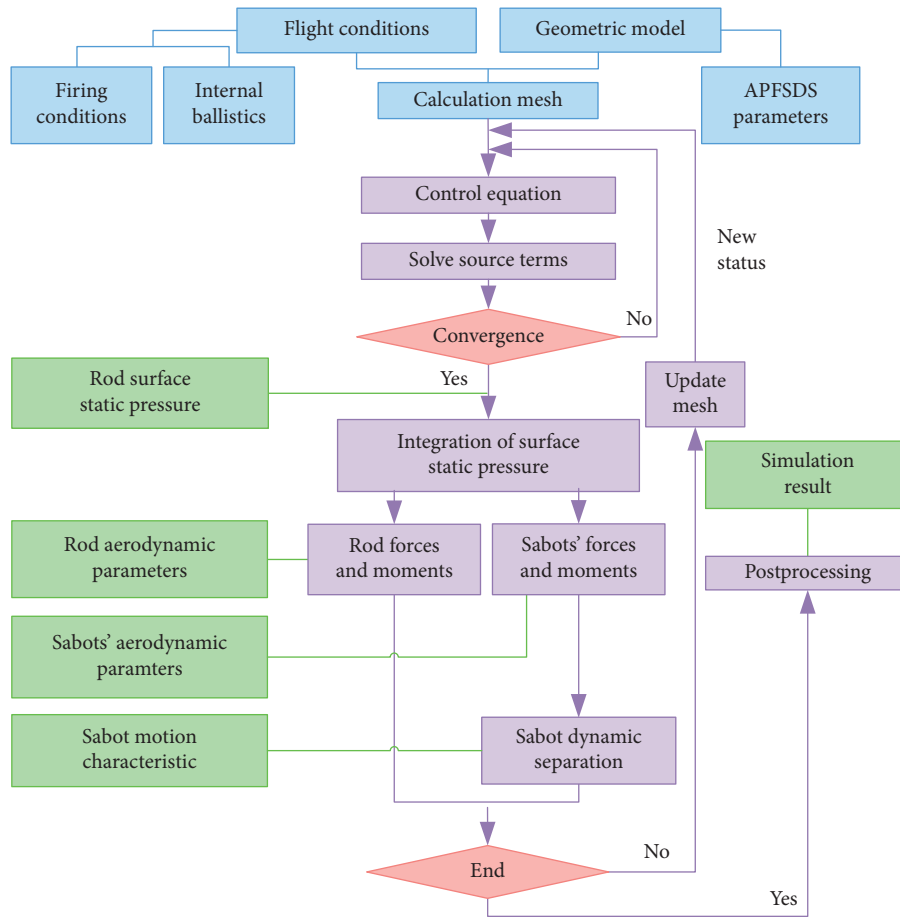


FIGURE 3: Schematic of calculation.

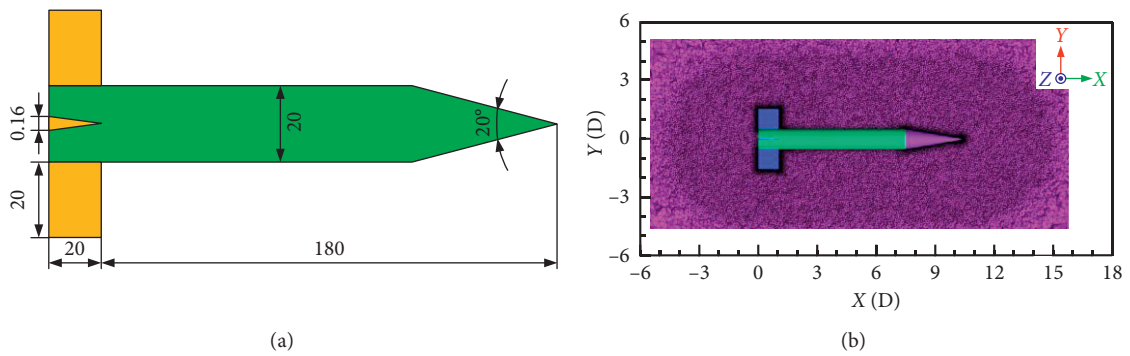


FIGURE 4: ANF verification model: (a) ANF parameters (mm) and (b) computed grid.

flow was a perfect gas with its parameter from state equations. Thus, the ambient conditions were 101325 Pa and 300 K. Combining assumptions (2) and (3) and the results from Section 2.2, the incoming Mach number was 3.6035 Ma, the attack angle was  $0.64^\circ$ , and the rod spin rate was 0 rad/s. For the given firing parameters of the rifled gun, this maximum value can reach approximately 2,000 rad/s. Hence, we determined the sabot spin rate for different cases as shown in Table 1. Next, we utilized the UDF code to endure the physical characteristics of all sabots' internal statuses, as shown in Table 2. We also performed the

optimization operation in the grid number and step time to content simulation requirements [28, 29]. Thus, the optimized parameters were 20.53 million and  $2.5 \times 10^{-4}$  ms, respectively. For the initialization of parameters to solve aerodynamic coefficient, the reference in area and length was  $91.61 \text{ mm}^2$  and 170 mm, respectively. After solution initialization using the above model and various parameters for different spin rate cases, we monitored the pressure variation with separation time at the rod surface points and obtained the aerodynamic parameters of the rod and sabots and the motion history of the three-sabot system.

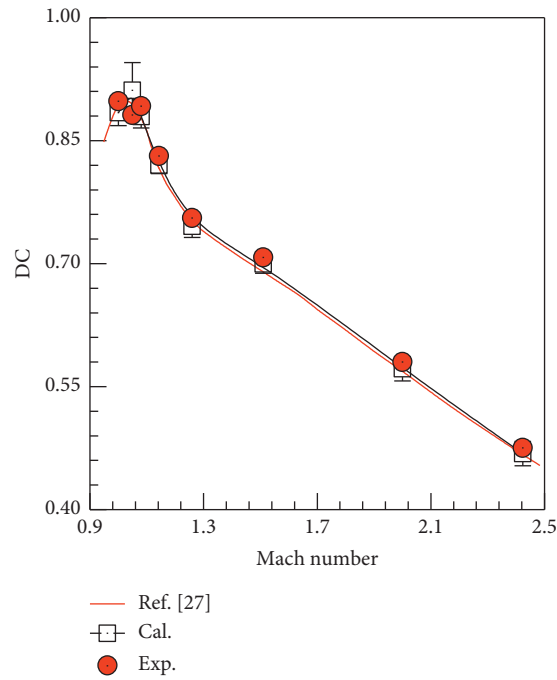


FIGURE 5: Comparison of DC between simulation and experiment.

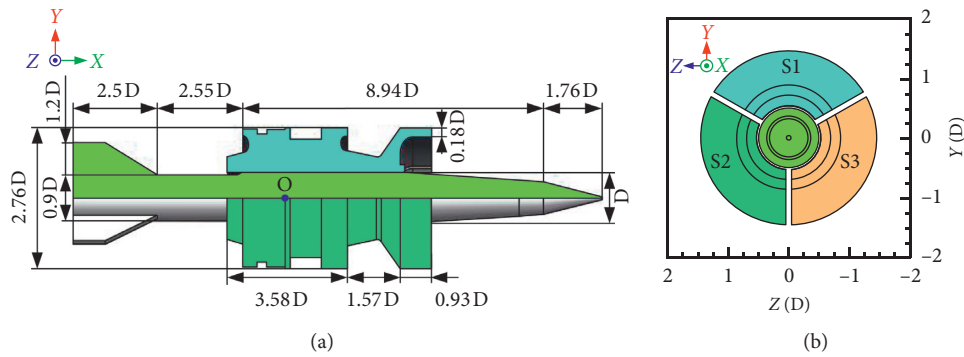


FIGURE 6: Model definition. (a) Model configuration and dimension ( $D$ ) and  $D = 10.8$  mm. (b) Sabot number.

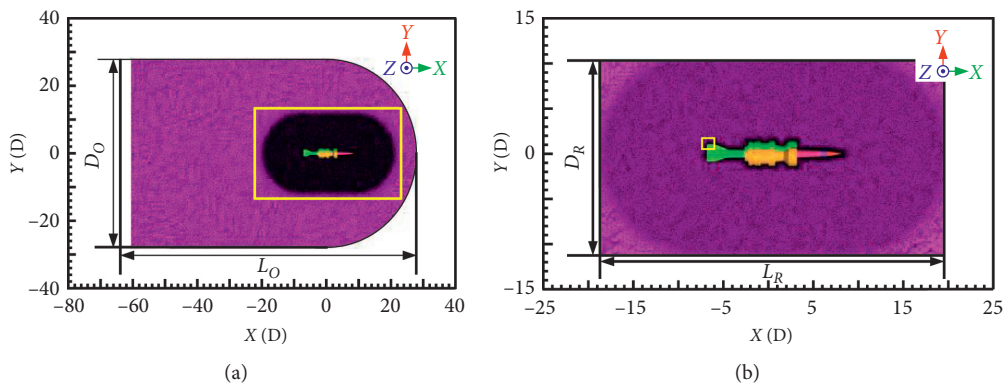
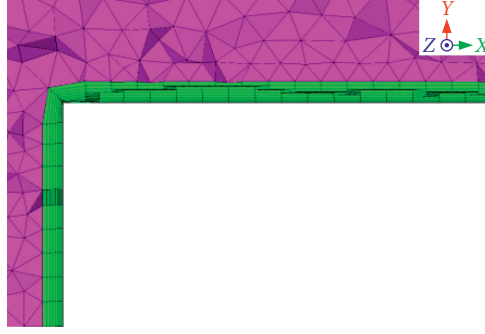


FIGURE 7: Continued.



(c)

FIGURE 7: Computed grid. (a) Computational domain grid. (b) Refined zone grid. (c) Boundary layer grid.

TABLE 1: Spin rate of the sabot.

Case	Case 1	Case 2	Case 3	Case 4	Case 5	Case 6
Spin rate (rad/s)	0	750	900	1,050	1,500	2,000

TABLE 2: Main properties of sabots.

Parameters	Expression	S1	S2	S3
CG coordinate (mm)	$(x, y, z)$	(0, 8.6, 0)	(0, -4.3, -7.7)	(0, -4.3, 7.7)
Euler angle (degree)	$(x, y, z)$	(0, 0, 0)	(0, -120, 0)	(0, 120, 0)
Inertia moment ( $\text{g}\cdot\text{mm}^2$ )	$(I_{xx}, I_{yy}, I_{zz})$	(2305, 6852, 6359)	(2305, 6852, 6359)	(2305, 6852, 6359)
Inertia product ( $\text{g}\cdot\text{mm}^2$ )	$(I_{xy}, I_{xz}, I_{yz})$	(60, 0, 0)	(-30, -51.9, 42.8)	(-30, 51.9, -42.8)
Mass (g)		20.3	20.3	20.3

## 5. Result Analysis

As described in [5], SDP is a complex interaction process between sabots and rods, namely, aerodynamic interference and mechanical interference. For the case of 0 rad/s, the APFSDS separation of the Gatling gun is consistent with that of a tank gun [19]. However, the intensity and interaction position of the rod change with an increase in the spin rate, and the shift in the aerodynamic characteristics is affected by the rod surface pressure. Therefore, we conducted an analysis in four aspects of discarding characteristics described below.

**5.1. Sabot Asymmetry Separation.** The dynamic characteristics of sabots are affected by the interaction of their initial states, the aerodynamic parameters, and gravity. Therefore, we investigated the boundary condition, aerodynamic characteristics, and kinematic parameters of the SDP under different spin rates. First, the initial state of the sabots is shown in Figure 6(b), and the three sabots are evenly distributed on the YOZ-plane. S2 and S3 are symmetrical about the XOY-plane. Each sabot has a gravity effect in the negative direction of the Y-axis. Concerning lift, the direction of S1 is positive, whereas that of S2 and S3 is negative. The lateral forces of S2 and S3 are in opposite directions. Furthermore, the 14 m/s inflow simulates the APFSDS tangential velocity in the positive direction of the Z-axis. The incoming flow in the Z-axis and the external force in the Y-axis express asymmetry.

Different spin rates can produce a difference in the movement and attitudes of sabots. Hence, we provide the sabots' separation on the YOZ-plane at different rates. As shown in Figure 8 (a1-d1), the initial rate of the sabots has little effect on the movement state at 0.025 ms, and the pressure distribution at the sabot front scoop is the same. Moreover, as shown in Figure 8 (a2-d2), regarding the separation time of 0.1 ms, the pressure distribution of S1 and S2 is obviously different on the sabots' front scoop, and the rate existence causes the sabots' sides to remain close to the rod. Still, the movement position slightly changes. Then, Figure 8 (a3-d3) shows the sabots' movement at 1.5 ms. For the 1,500 rad/s case, the sabots' rolling motion is on the Z-axis, and there is a different pressure distribution simultaneously at the outer surface. A similar phenomenon occurs at 2,000 rad/s. As shown in Figure 8 (a4-d4), when the separation time arrives at 1.95 ms, the sabot status has completely changed with the pressure distribution and strength. Overall, the 1,500 rad/s rate is the demarcation point, resulting in the interaction of the aerodynamic forces and CG motion.

We plotted the aerodynamic coefficient curve for different spin rates. Figures 9(a)-9(f) show the time history of the aerodynamic coefficients of the sabots in cases 1-6. When a sabot's windward side reaches the largest area in the YOZ-plane, the DC presents its maximum value. Like the DC, the lift coefficient (LIC) and lateral force coefficient (LAC) conform to this trend along the responding plane.

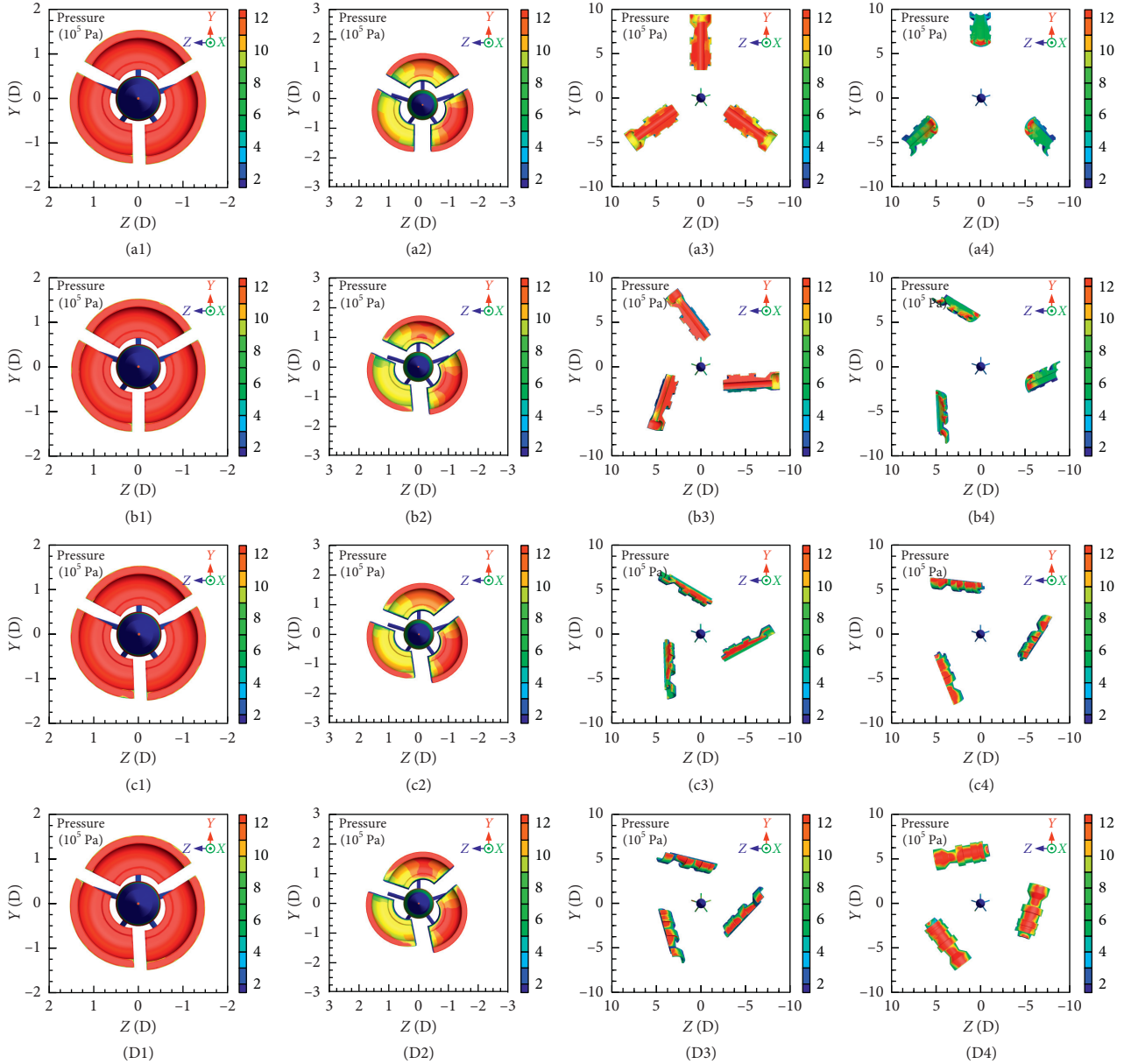


FIGURE 8: Sabots' motion of the YOZ-plane. Letters a, b, c, and d, respectively, stand for case 1, case 3, case 5, and case 6. Numbers 1, 2, 3, and 4 are the time of 0.025, 0.1, 1.5, and 1.95 ms, respectively.

The increase in the initial spin rate and the sabot rolling movement can be observed by comparing LIC and LAC in Figures 9(b)–9(d), which exhibit wave variations at the same amplitude. Comparing the sabot coefficients of a tank gun, the coefficients in Figure 9(a) are in good agreement with those of [19]. The DC of the sabots and the S2 and S3 LICs are symmetrical, and the S2 and S3 LACs show approximate symmetry. However, the S1 LAC nearly preserves zero. In summary, when the rate is equal to 0 rad/s, the sabot coefficients are nearly symmetrical.

As the spin rate increases, the aerodynamic coefficients exhibit asymmetry. When the rate reaches 750 rad/s as compared with all forces in Figure 9(b), the DC shows a slight asymmetry, but the LIC of S2 and S3 exhibits obvious asymmetry. As shown in Figure 9(e), the DCs of sabots are

only slightly convex at around 1.5 ms, which leads to insufficient drag. This is the main reason for the increase in separation time. As seen from Figure 9(f), when the spin rate reaches 2,000 rad/s, the LIC and LAC change periodically while maintaining asymmetry, but the DC reappears at near symmetry and produces a platform effect in 0.5–1.4 ms. Therefore, when the rate is in the range of 750–1,050 rad/s, all aerodynamic forces are asymmetrical. There is an initial spin rate of sabots, and the asymmetry of LIC and LAC becomes more obvious in contrast to the DC.

The following presents the CG motion in Figure 10, and Schmidt and Shear [6] found that the aerodynamic force was a primary source of external forces for sabot separation, which determines the relative movement between the sabots and the rod. As shown in Figure 10(a) at 0 rad/s, considering

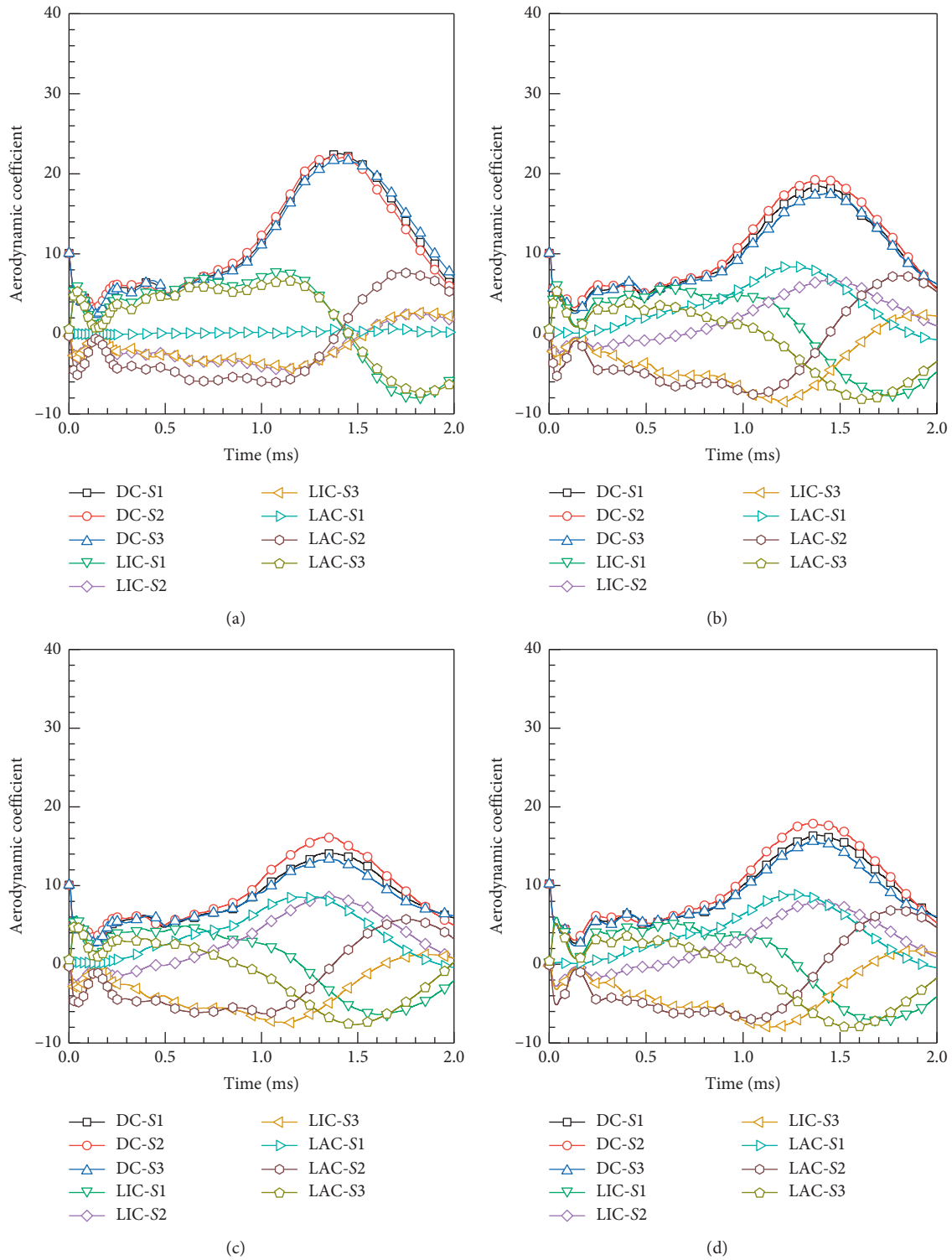


FIGURE 9: Continued.



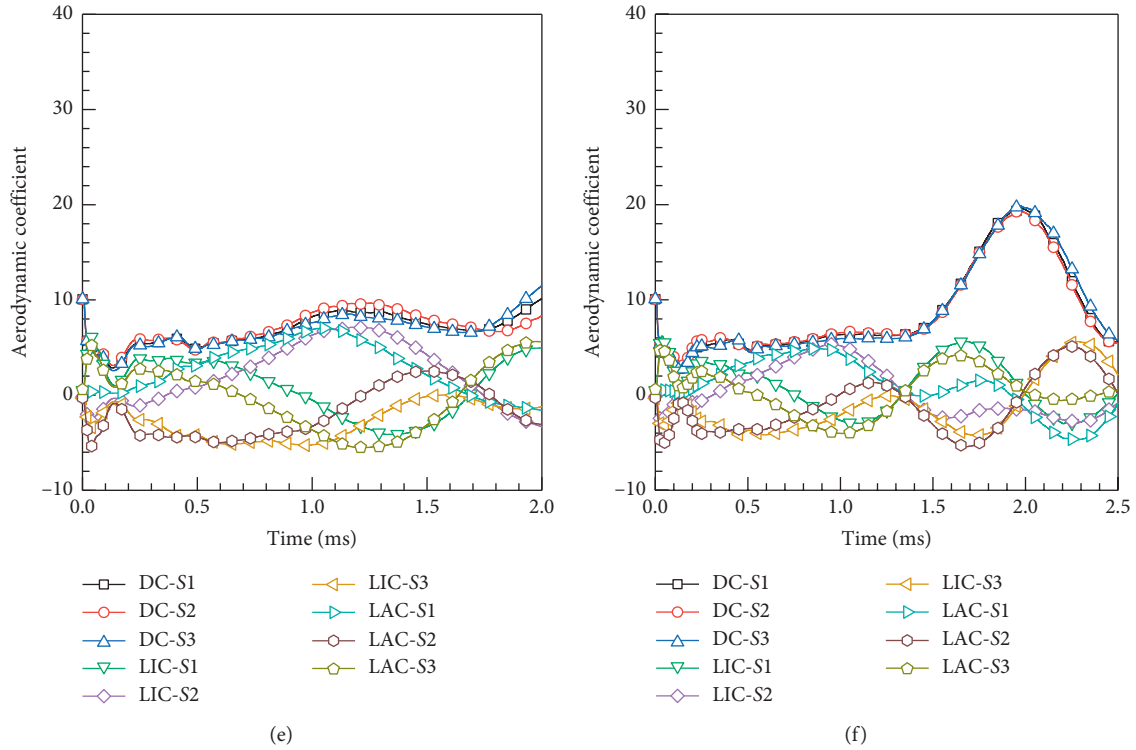


FIGURE 9: Aerodynamic force coefficients. Letters a–f stand for cases 1–6, respectively. DC is the drag coefficient, LIC is the lift coefficient, and LAC is the lateral force coefficient.

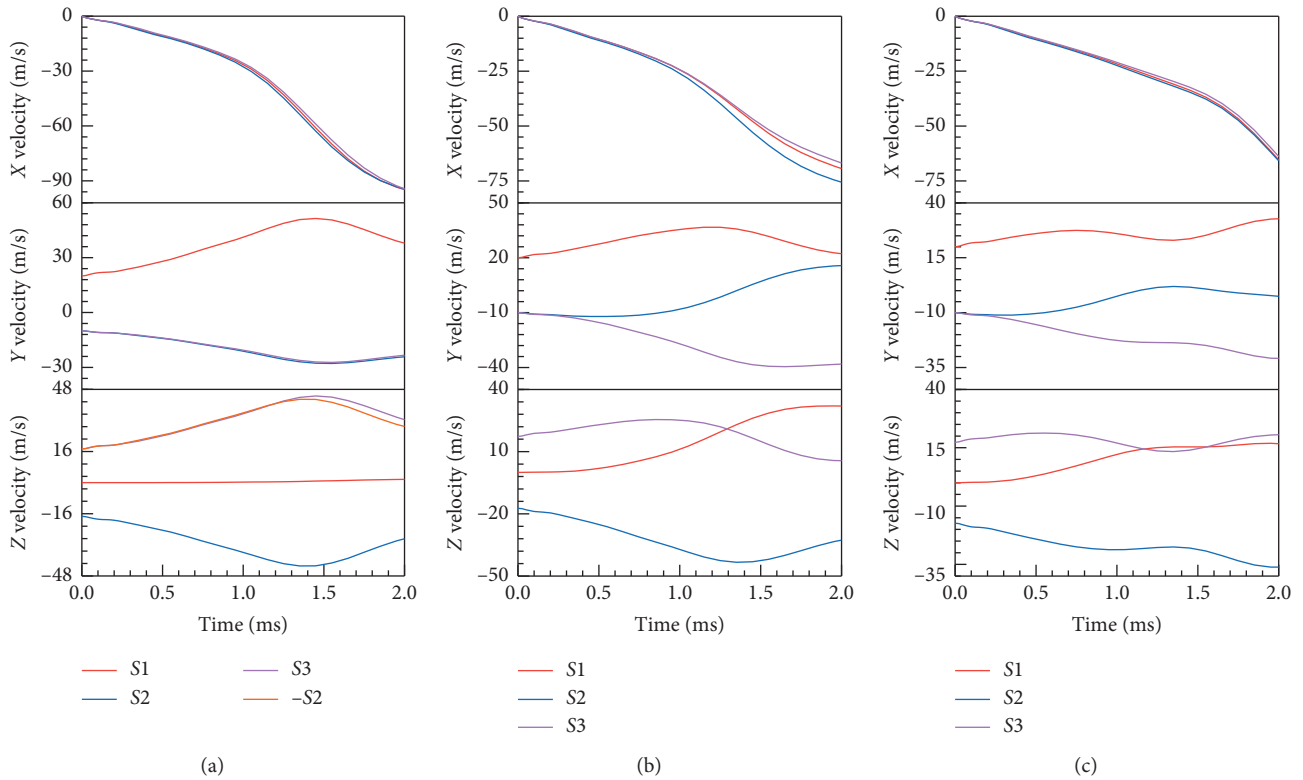


FIGURE 10: CG velocity of all sabots. Letters a, b, and c, respectively, stand for cases 1, 4, and 6. -S2 is the opposite value of S2.

the 1,250 m/s muzzle velocity, we can calculate the sabot velocity difference to be less than 1%, and the motion in the X-axis is nearly symmetrical. Those of the other axes present certain symmetry. Regarding the CG velocity of the Y- and Z-axes, Figures 10(a)–10(c) show that the higher the rate of the sabot, the more obvious the asymmetry. However, owing to the presence of the muzzle velocity, the impact of the spin rate can be negligible for symmetry along the X-axis. In summary, the initial sabot spin rate can result in a certain asymmetry in the YOZ-plane movement.

Therefore, the separation process shows near symmetry under 0 rad/s, which is the same conclusion about the tank gun in [19]. However, the asymmetry of the boundary condition has an almost negligible effect on separation. Owing to the presence of spin rate, LC, LAC, and the YOZ-plane movement still show a certain asymmetry.

**5.2. Rod Surface Pressure.** The separation asymmetry changes the relative position between the sabots and the rod, further affecting the intensity and action position of the shock wave. Therefore, the direct result is a variation in rod pressure and distribution. We established a series of monitoring points on the rod surface to explore the pressure intensity located at the rod axis section. As shown in Figure 11, these sectional planes are named A, B, C, and D, and the X-axis coordinates of the corresponding planes are described in Table 3. Arabic numerals mark these points, and their direction is counterclockwise along the section plane. The A-, B-, and C-planes are evenly arranged with six points, and the D-plane is evenly configured with five points on the fin surface.

As mentioned in [5], the main types of shock waves in the rod/sabot interaction are attached shock, detached shock, reflected shock wave, expansion waves, and others. Furthermore, when the flow rate of the incoming flow is much greater than that of the outgoing flow, the choked flow creates a high-pressure zone that emerges from multiple reflected shock waves. For a rate of 0 rad/s, we obtained the maximum pressure of the monitoring points in Table 4 and plotted their pressure changes over time, as shown in Figure 12(a). Regarding the pressure intensity, we can see that there are two pressure peaks in the A- and B-planes, and the C-plane has a wave peak. However, the D-plane is relatively gentle. During the initial phase [19], these sabots are located at the rod body, and the gap between all sabots and the rod is extremely narrow so that a choked flow is generated in the front part. However, the flow gradually stabilizes from the nose to the fins, and the pressure gradually decreases. In other words, the pressure intensity of the front part is significantly higher than that at the back. During the coupling phase [19], these sabots flip backward, and the reflected shock wave hits the front or middle of the rod body to form a high-pressure zone on the body. Then, the sabots continue to flip back and generate a narrow gap between their tail and the rod. Hence, a choked flow emerges at the back body. Subsequently, it is relative to the rearward movement of the rod. Only the detached shock acts on the fins to form a high pressure on the fin. Generally, the

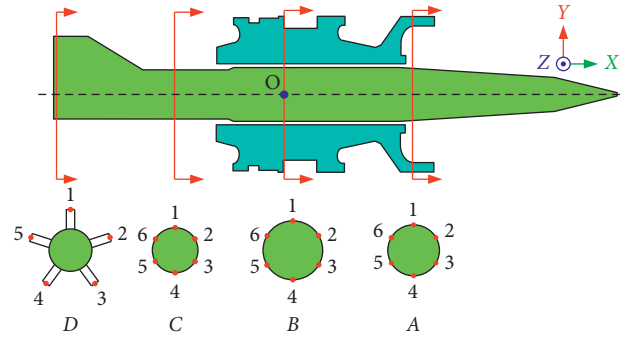


FIGURE 11: Schematic of monitoring points.

TABLE 3: Plane coordinates of the X-axis.

Plane	A	B	C	D
Value (mm)	27.9	0	-27.9	76.5

TABLE 4: Peak values of points at 0 rad/s, and the unit is MPa.

Plane	Peak value						Average
	1	2	3	4	5	6	
A	2.074	3.225	2.701	3.171	2.312	3.345	2.805
	1.398	1.262	1.592	1.033	1.336	1.19	1.302
B	0.631	0.189	0.635	0.190	0.636	0.187	0.411
	0.626	0.712	0.554	0.736	0.616	0.756	0.666
C	1.689	1.208	1.917	1.144	1.400	1.265	1.437
	0.060	0.067	0.065	0.255	0.060		0.102

pressure strength of the fins is weaker than that of the rod body. The above detailed separation description produces the pressure change tendency at 0 rad/s.

Figures 12(a)–12(d) show the pressure change at different rates. During the time range of 0–0.1 ms, the relative positions of the sabots/rod are the same, and the A- and B-planes are located in the front part of the rod so that their pressure intensities and distributions exhibit the same trend. Thus, the rate has almost no effect on the pressure. Moreover, owing to the C-plane location of the back part and the gap difference from various rates, the pressure intensity will be significantly reduced. However, the pressure on the D-plane of the fins remains nearly the same. The pressure intensity and the action time increase only at 2,000 rad/s.

For the pressure intensity at 0 rad/s in Table 4, the A-plane peaks are front-body choked flow and reflected shock, and the corresponding average values are 2.805 and 1.302 MPa. However, compared with the A-plane, the peak values of B are much weaker. As the gap increases and the relative motion varies between sabots and the rod, the C-plane peak, resulting from the choked flow action, still reaches 1.437 MPa. However, it is only half that of the A-plane. For the D-plane intensity, the pressure at D4 is approximately four times that of the others, and it results from the detached shock of the sabots and the increased gap between the sabots and the rod. Therefore, choked flow is the most intensive source during separation.

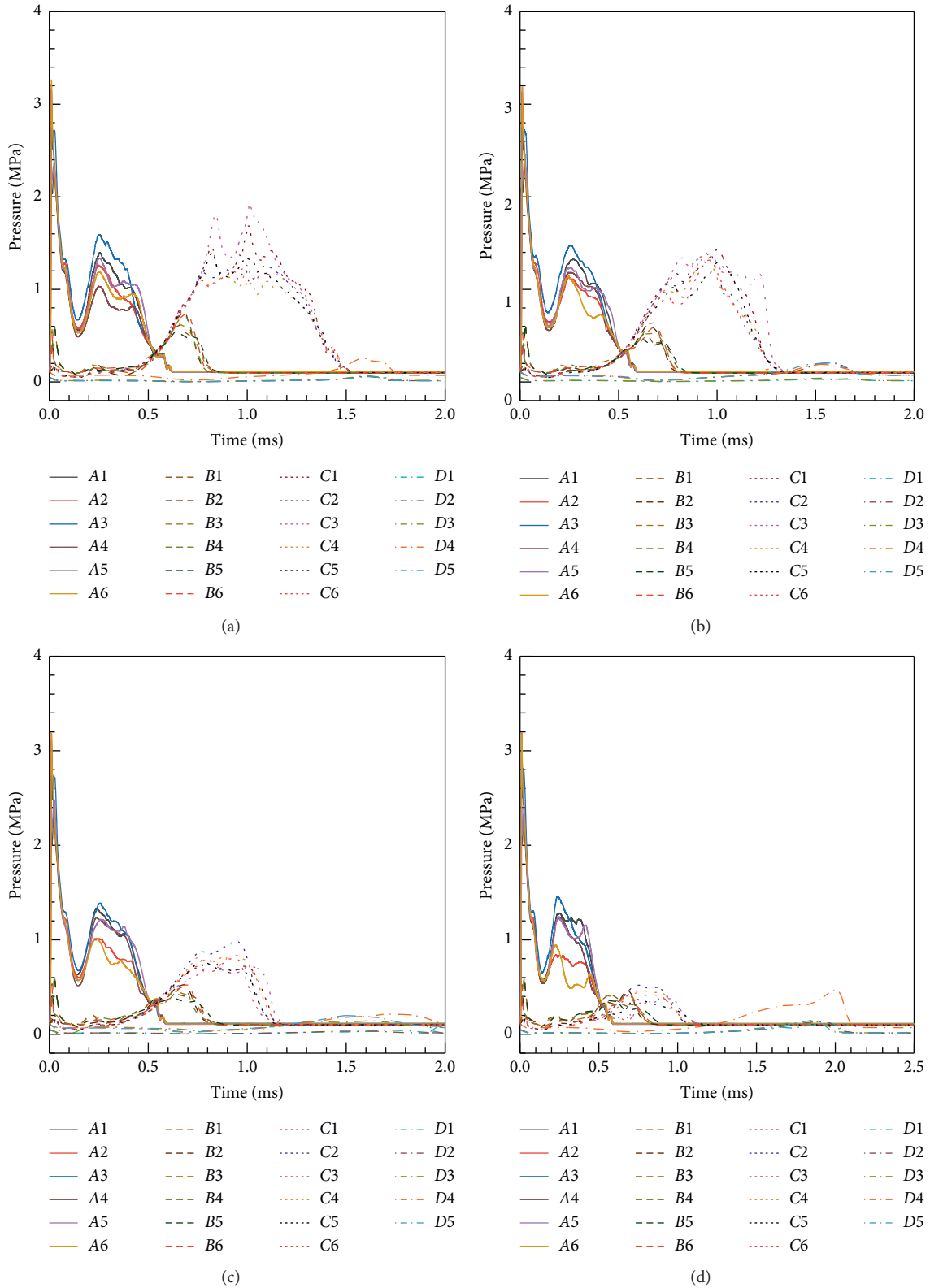


FIGURE 12: Pressure of different points under different cases: (a) case 1, (b) case 4, (c) case 5, and (d) case 6.

To further explore the pressure intensity at various rates, as shown in Figure 12, we see that A6, B6, C3, and D4 are the maximum intensities for their corresponding planes. Thus, we

analyze the pressure at these points in Figures 13(a)–13(d). The spin rate has little effect on A6, followed by B6. However, C3 and D4 have the maximum impact. With an increase in the spin

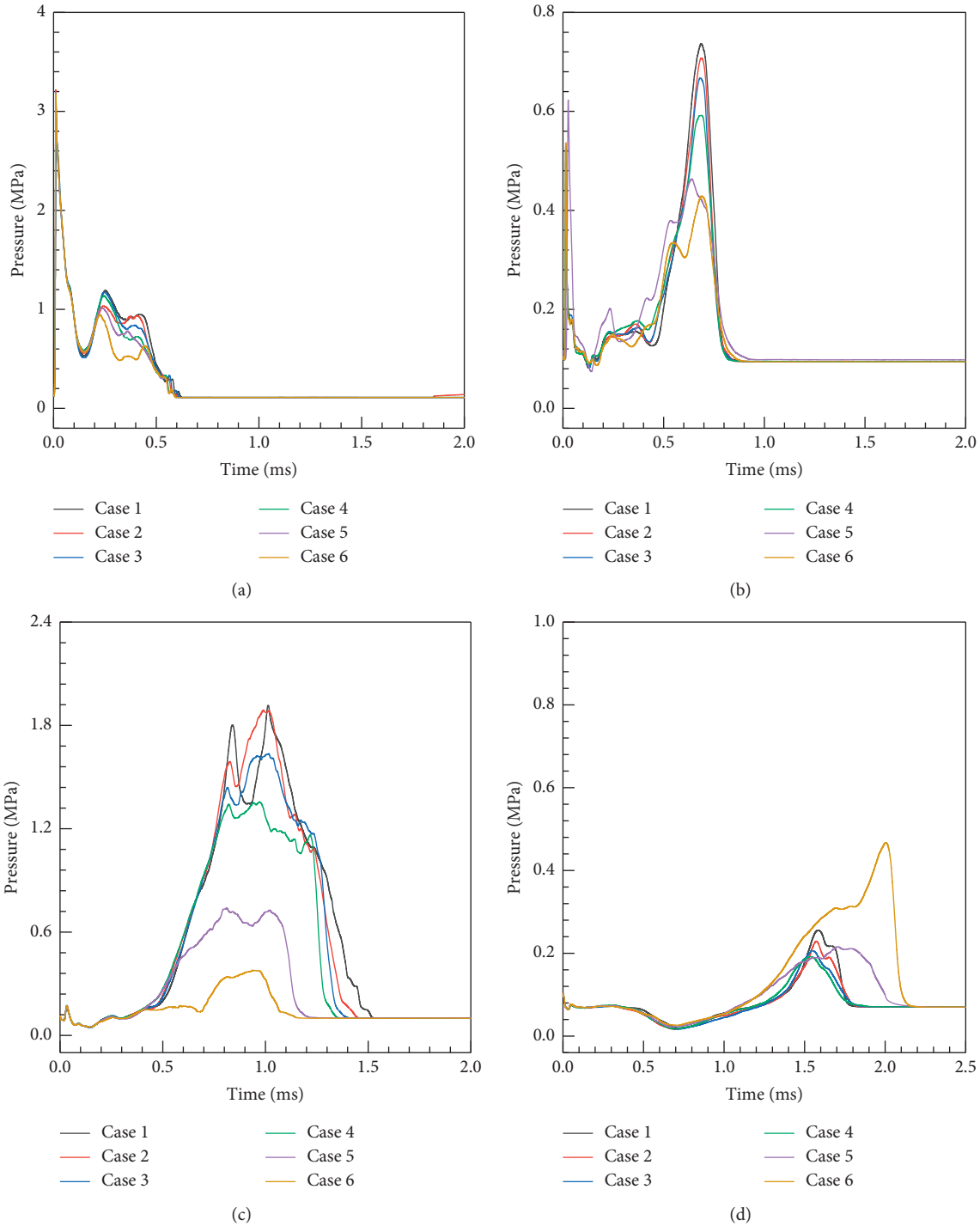


FIGURE 13: Pressure under different cases: (a) A6, (b) B6, (c) C3, and (d) D4.

rate, the second peaks of A6 and B6 and the C3 peak decrease obviously, as does the acting time of the C3 pressure. At the D4 point, the maximum pressure decreases gradually in the range of 0–1,050 rad/s, but the peak and the acting time remain the same. However, when the spin rate exceeds 1,500 rad/s, the peak value and acting time increase. This trend is caused by the relative position diversification of the sabots and the rod. In short, the pressure distribution and variation show similar liability. However, the spin rate has an influence on the pressure

intensity. Hence, the uneven pressure distribution is the reason for the variation in the aerodynamic characteristics.

**5.3. Rod Aerodynamic Characteristics.** The uneven pressure distribution mentioned in Section 5.2 causes the aerodynamic alteration in force and moment. Figures 14 and 15 present the aerodynamic force coefficients and moment coefficients under different cases.

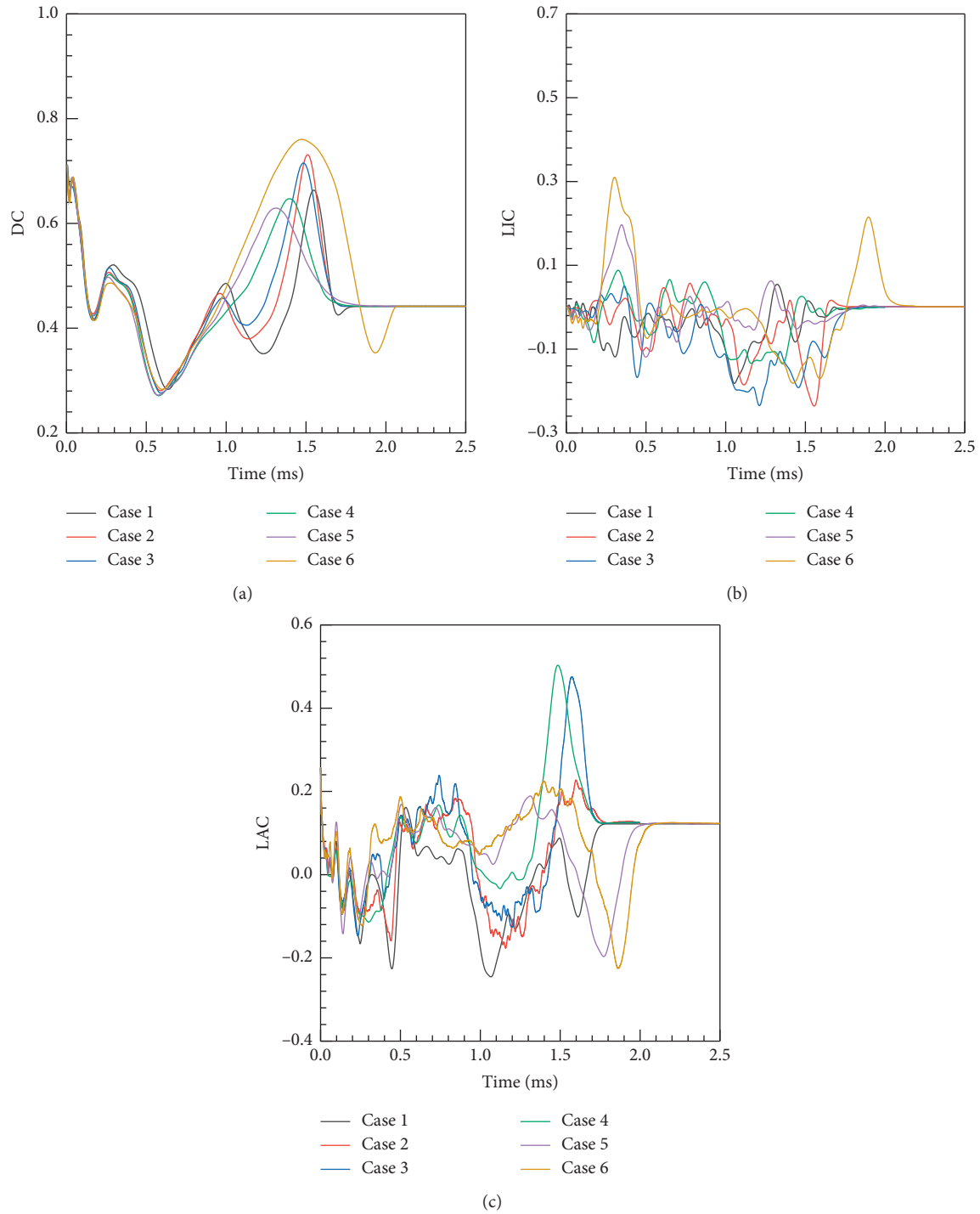


FIGURE 14: Force coefficient: (a) DC, (b) LIC, and (c) LAC.

During the time of 0-0.1 ms in Figure 14(a), the spin rate has almost no effect on the DC. Subsequently, the maximum value first increases, then decreases, and finally increases with the increase in the spin rate. Regarding the variation tendency and peak numbers, the important spin rate is 900 rad/s. Thus, two values, namely, that one is between 750 and 900 rad/s and the other is 1,500 rad/s, are the decomposition points. As shown in Figures 14(b) and 14(c), LIC and LAC fluctuate violently during the SDP. For the LIC, the

maximum value changes more obviously, but the minimum value is basically the same. Moreover, there are two peaks at 2,000 rad/s. Toward the LAC, the changes in cases 1 and 2 are similar, which also applies to groups of cases 3-4 and 5-6. Generally, the rate has a greater influence on the LIC, and the rate of 1,500 rad/s is the demarcation point of the aerodynamic force.

Figures 15(a)–15(c) display the RMC, YMC, and PMC. The minimum value of RMC increases gradually with the



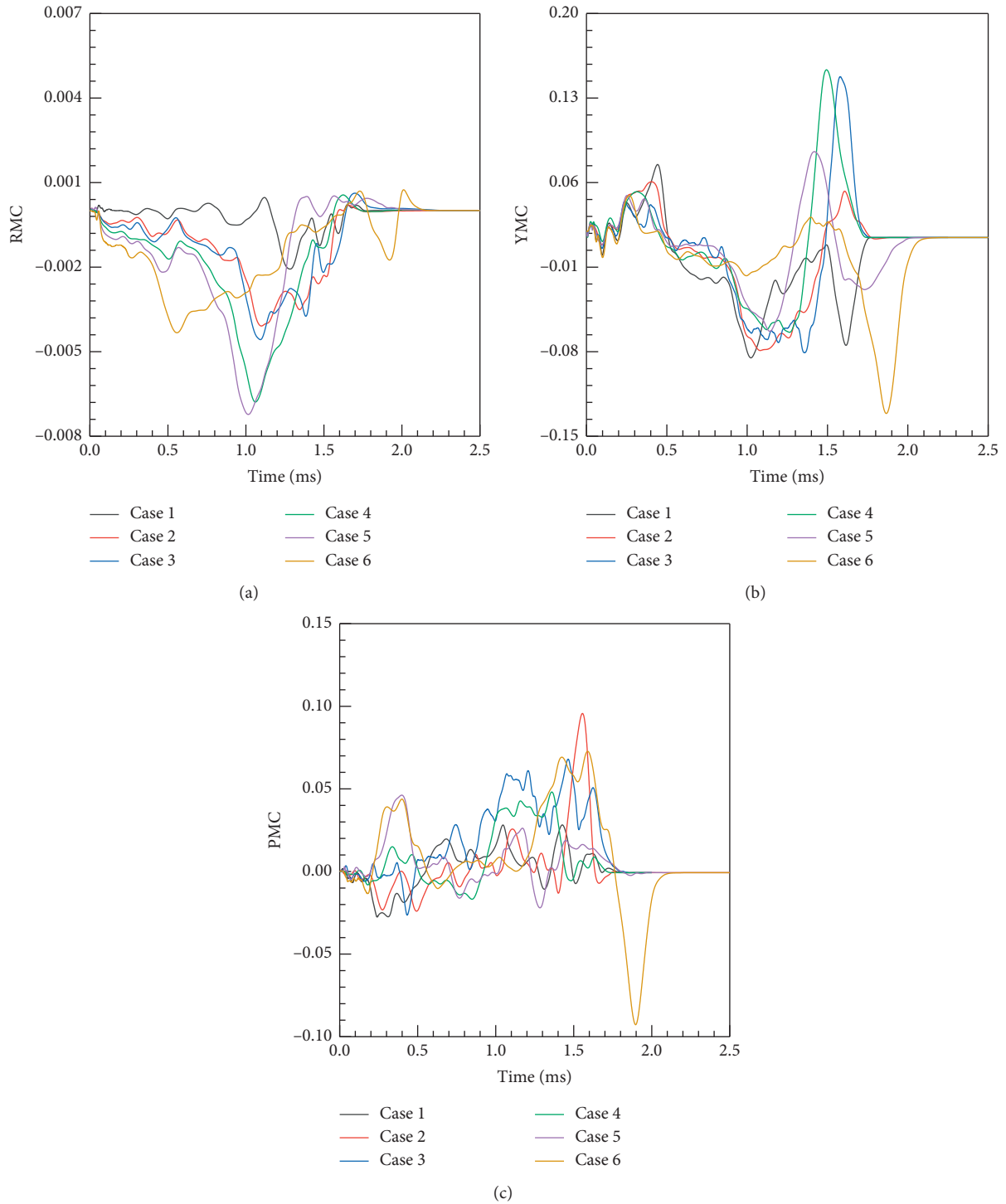


FIGURE 15: Moment coefficient: (a) RMC, (b) YMC, and (c) PMC.

increase in rotating speed, but the maximum value is the same. Additionally, that of the 2,000 rad/s case decreases significantly. The variation process of YMC is similar in the time range of 0–0.5 ms; subsequently, with the increase in the rate, the maximum value first increases and then decreases. However, the minimum value first remains unchanged, then it decreases, and finally increases. The maximum PMC gradually increases with the rate at a time of 0–0.5 ms; after

that, the maximum value first increases, then decreases, and finally increases. Then, the minimum value remains unchanged. Finally, in the 2,000 rad/s case, there is an extreme value at 1.9 ms caused by the detached shock hitting the fin surface. The pressure distribution of the fin surface is the reason for the aerodynamic change at that time.

Therefore, the 1,500 rad/s rate is the dividing point of the SDP. However, 2,000 rad/s has a significant influence on the

TABLE 5: Discarding characteristic under different spin rates.

Spin rate (rad/s)	0	500	750	900	1000	1050	1500	1750	2000
Discarding time (ms)	1.780	1.781	1.785	1.786	1.85	1.865	2.000	2.091	2.251
Aerodynamic impulse (N·s)	0.0743	0.0746	0.0751	0.0762	0.0794	0.0796	0.0855	0.0938	0.1049

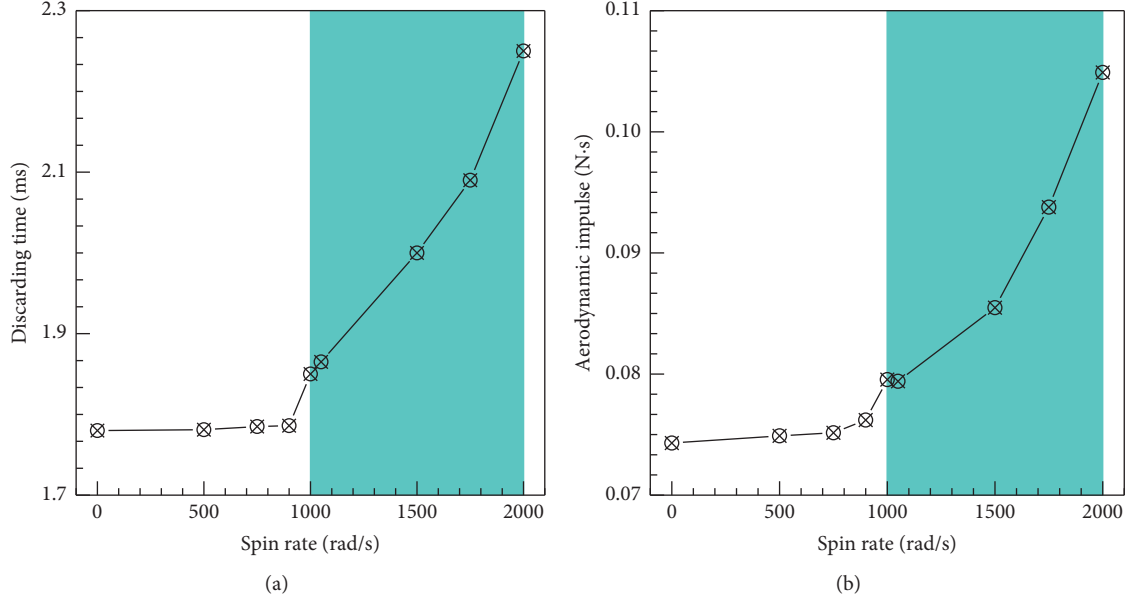


FIGURE 16: Discarding characteristic. (a) Discarding time. (b) Aerodynamic impulse.

rod aerodynamic coefficients during the weak coupling phase, which may result in the loss of flight stability.

**5.4. Discarding Quantization Parameters.** The fundamental requirement for the SDP is rapid separation and interference reduction [5], which can be evaluated using the discarding time and aerodynamic impulse. When a sabot's detached shock completely leaves the fins, there is no aerodynamic interference between the sabots and rod. Therefore, we defined the corresponding moment as the discarding time. The aerodynamic impulse is a physical quantity of the aerodynamic force accumulation effect during separation time, which results in impulse changes and muzzle disturbances of the rod. Aerodynamic interference generates the disturbance characteristics in the impulse form. The drag force can cause velocity attenuation, and lift and lateral forces produce velocity disturbances, which can directly affect external ballistic characteristics and shooting accuracy. According to the impulse definition, the aerodynamic impulse of the SDP is the integral of the aerodynamic force with respect to the discarding time, and it can be written as follows:

$$P_A = \frac{1}{2} \rho v^2 S \int_{t_D}^0 C dt, \quad (8)$$

$$C = DC \vec{i} + LIC \vec{j} + LAC \vec{k},$$

where  $C$  is the resultant aerodynamic coefficient.

Combining the aerodynamic parameters with the surface pressure to analyze the separation time, we calculate the aerodynamic impulse from the separation time and aerodynamic forces. Table 5 gives the separation times and aerodynamic impulses under different spin rates, and we plot the discarding characteristic curve against the spin rate.

As seen in Figures 16(a) and 16(b), the discarding characteristics show a definite trend with the spin rate. When the rate is no greater than 900 rad/s, the separation time and aerodynamic impulse basically maintain a constant value, and their average is 1.78 ms and 0.075 N·s, respectively. However, if it is over 900 rad/s, both time and aerodynamic impulse increase significantly, and these values have a quadratic function law with the spin rate. When the rate is equal to 2,000 rad/s, compared with the average values at below 900 rad/s, the time and impulse are increased by 26 and 39%, respectively. Hence, in case that the rate exceeds a certain value, the higher the spin rate of the sabot, the worse the discarding characteristic.

According to the interior ballistic parameters and launch conditions, the range of spin rate is approximately 1,000–2,000 rad/s, and the blue blocks of Figure 16 represent the spin rate range of sabots. Combined with the discarding characteristic parameters, it is concluded that a spin rate of 1,000 rad/s is the optimal value for the APFSDS launched from the rifled barrel.

## 6. Conclusions

In this paper, we investigated the effect of the initial spin rate on the dynamic separation of the APFSDS using CFD and dynamic mesh approaches. This study explored the separation process at various spin rates. We also quantitatively analyzed the discarding characteristics against separation time and aerodynamic impulse. Special attention was given to understanding the separation of sabots, rod surface pressure, rod aerodynamic parameters, and quantization parameters of complex discarding characteristics. The following conclusions were drawn:

- (1) When the spin rate was 0 rad/s, the SDP exhibited near symmetry. As the initial spin rate of the sabot increased, there was more obvious separation asymmetry, and it contributed to the relative position variation among the sabots and the rod.
- (2) The distinction of the rod surface pressure indicates that the choked flow was the strongest flow source of the SDP. The spin rate had almost no effect on the pressure distribution of the front part of the rod. When the monitoring point moved towards the fins, the pressure distribution and intensity changed more dramatically. The initial spin rate and separation asymmetry produced a variation in surface pressure, which further influenced the rod aerodynamic characteristics.
- (3) For the aerodynamic coefficients, the 1,500 rad/s rate is the dividing point. However, 2,000 rad/s has a significant influence on the rod aerodynamic coefficients during the weak coupling phase, which may result in the loss of flight stability.
- (4) When the spin rate is in the range of 0–900 rad/s, the discarding characteristics remain the same. However, when the spin rate exceeds 900 rad/s, the discarding time and aerodynamic impulse have a quadratic polynomial relationship with the rate. Furthermore, a spin rate of 1,000 rad/s was found to be the optimal value for the APFSDS of the rifled barrel.
- (5) The results give a design reference for the APFSDS from a rifled barrel. Our future work is to calculate the dynamic separation process of the APFSDS considering the influence of gunpowder gas, making the APFSDS initial boundary agree with the firing condition.

## Abbreviations

$\phi$ :	Flux variable
<b>S</b> :	General source term
$\mathbf{u}_D$ :	Velocity of the dynamic mesh
$\Delta t$ :	Time step
$\phi_1$ :	Velocity vector
$i$ :	Sabot number
<b>I</b> :	Inertia tensor
<b>M</b> :	External moments

$\omega$ :	Angular velocity
<b>S</b> :	Euler angles
<b>C</b> :	Transformation matrix from inertial to body coordinates
$p_p$ :	Projectile base pressure
$l_A$ :	Equivalent length of the chamber
$A$ :	Burned ratio of the propellant
$R$ :	Gas constant
$f$ :	Energy capacity of the propellant
$v_p$ :	Muzzle velocity
$v_\tau$ :	Tangential velocity
$D_p$ :	Diameter of the projectile
$H_{\text{First}}$ :	Height of the first layer
$D_O$ :	Diameter of outer flow
$D_R$ :	Diameter of the refined zone
$P_A$ :	Aerodynamic impulse
$S$ :	Rod reference area
$r$ :	General diffusion coefficient
$\mathbf{u}$ :	Flow velocity
$\rho$ :	Fluid density
$\Delta x$ :	Space step
$\mathbf{f}$ :	Pressure flux
$m$ :	Sabot mass
<b>F</b> :	External forces
<b>V</b> :	Translational velocity
<b>P</b> :	Absolute coordinates
$S_p$ :	Projectile base area
<b>E</b> :	Transformation matrix from sabot Euler to attitude angles
$l$ :	Projectile displacement
$m_g$ :	Propellant mass
$B$ :	Coefficient of secondary work
$T$ :	Burning temperature of the propellant
$m_p$ :	Projectile mass
$k$ :	Specific heat
$\omega_b$ :	Rotational velocity of the barrel group
$r_b$ :	Rotation radius of the barrel group
$N_L$ :	Number of layers
$L_O$ :	Length of outer flow
$L_R$ :	Length of the refined zone
$v$ :	Incoming flow velocity
$t_D$ :	Discarding time
APFSDS:	Armor-piercing fin-stabilized discarding sabot
AOA:	Angle of attack
AUSM:	Advection upstream splitting method
UDFs:	User-defined functions
DC:	Drag coefficient
LAC:	Lateral coefficient
YMC:	Yaw moment coefficient
Cal.:	Calculated
SDP:	Sabot discarding process
CFD:	Computational fluid dynamics
CG:	Center of gravity
ANF:	Army-navy basic finned missile
LIC:	Lift coefficient
RMC:	Roll moment coefficient
PMC:	Pitch moment coefficient
Exp.:	Experimental.

## Data Availability

The data used to support the findings of this study are included within this paper.

## Conflicts of Interest

The authors declare that they have no conflicts of interest.

## References

- [1] A. Aruna and R. Rene, "A diagnostic approach to weapon system lifecycle support: the phalanx close-in weapon system," *International Journal of Defense Acquisition Management*, vol. 2, pp. 1–16, 2009.
- [2] M. Blatnický and M. Sága, "Application of light metal alloy EN AW 6063 to vehicle frame construction with an innovated steering mechanism," *Materials*, vol. 13, no. 4, 2020.
- [3] M. Sága and M. Blatnický, "Experimental determination of the manson-coffin curves for an original unconventional vehicle frame," *Materials*, vol. 13, no. 20, pp. 1–20, 2020.
- [4] F. E. Thomas, J. P. Brendan, and F. H. Alan, "Dispersion analysis of the XM881 APFSDS projectile," *Shock & Vibration*, vol. 8, pp. 183–191, 2013.
- [5] H. Li, *Intermediate Ballistics*, Beijing Institute of Technology University Press, Beijing, China, 2015.
- [6] E. M. Schmidt and D. D. Shear, "Aerodynamic interference during sabot discard," *Journal of Spacecraft and Rockets*, vol. 15, no. 3, pp. 162–167, 1978.
- [7] E. M. Schmidt, "Wind tunnel measurements of sabot-discard aerodynamics," *Journal of Spacecraft and Rockets*, vol. 19, no. 1, pp. 235–240, 1982.
- [8] H. Conn, *The Influence of Sabot Separation on the Yawing Motion of a Cone*, Defense Research Establishment, Valcartier, Canada, 1970.
- [9] J. N. Dick and D. S. Dolling, "Pressure measurements on a Mach 5 sabot during discard," *Journal of Spacecraft and Rockets*, vol. 35, no. 1, pp. 23–29, 1998.
- [10] L. Zhao, Z. He, Q. Niu, X. Yang, and S. Dong, "Near-field-coupled lighting-rod effect for emissivity or absorptivity enhancement of 2-D (1, 2) magnetic plasmon mode by rotating the square resonators array," *Journal of Quantitative Spectroscopy and Radiative Transfer*, vol. 240, Article ID 106631, 2020.
- [11] J. Jia, D. Fu, Z. He, J. Yang, and L. Hu, "Hypersonic aerodynamic interference investigation for a two-stage-to-orbit model," *Acta Astronautica*, vol. 168, pp. 138–145, 2020.
- [12] Y. K. Lee, "High resolution Navier-Stokes computations of a sabot separating from a gun-launched projectile with turbulence model," in *Proceedings of the 14th International Symposium of Ballistics*, pp. 519–527, Quebec, Canada, September 1993.
- [13] P. Wu, "Three dimension numerical simulation for APFSDS sabots separating and discarding flow field," *ACTA Aerodynamica Sinica*, vol. 23, no. 1, pp. 1–4, 2005.
- [14] M. J. Guillot, R. Subramanian, and W. G. Reinecke, "A numerical and experimental investigation of sabot separation dynamics," in *Proceedings of the 34th Aerospace Sciences Meeting and Exhibit*, Reno, NV, USA, January 1996.
- [15] S. E. Kim, S. R. Mathur, and J. Y. Murthy, "A reynolds-averaged navier-stokes solver using unstructured mesh-based finite-volume scheme," in *Proceedings of the 36th Aerospace Sciences Meeting and Exhibit Reno*, Reno, NV, USA, January 1998.
- [16] D. O. Snyder, E. K. Koutsavdis, and J. S. R. Anttonen, "Transonic store separation using unstructured CFD with dynamic meshing," in *Proceedings of the 33rd AIAA Fluid Dynamics Conference and Exhibit*, pp. 23–26, Orlando, FA, USA, June 2003.
- [17] R. Cayzac, E. Carettean, and T. A. de Roquefort, "Intermediate ballistics unsteady sabot separation: first computations and validations," in *Proceedings of the 19th International Symposium of Ballistics*, pp. 297–305, Interlaken, Switzerland, May 2001.
- [18] R. Cayzac and E. Carette, "Computational fluid dynamics and experimental validations of the direct coupling between interior, intermediate and exterior ballistics using the euler equations," *Journal of Applied Mechanics*, vol. 78, no. 6, pp. 1–18, 2011.
- [19] Z.-G. Huang, M. E. Wessam, and Z.-H. Chen, "Numerical investigation of the three-dimensional dynamic process of sabot discard," *Journal of Mechanical Science and Technology*, vol. 28, no. 7, pp. 2637–2649, 2014.
- [20] X. Li, J. Lu, and J. Feng, "Simulation of sabot discard for electromagnetic launch integrated projectile," *IEEE Transactions on Plasma Science*, vol. 46, no. 7, pp. 2636–2641, 2018.
- [21] B. Reck, S. Hundertmark, D. Simicic et al., "Behavior of a railgun launch package at the muzzle and during sabot discard," *IEEE Transactions on Plasma Science*, vol. 47, no. 5, pp. 2545–2549, 2019.
- [22] M.-S. Liou, "A sequel to AUSM, part II: AUSM±up for all speeds," *Journal of Computational Physics*, vol. 214, no. 1, pp. 137–170, 2006.
- [23] G. Avital, Y. Cohen, L. Gamss et al., "Experimental and computational study of infrared emission from under-expanded rocket exhaust plumes," *Journal of Thermophysics and Heat Transfer*, vol. 15, no. 4, pp. 377–383, 2001.
- [24] Y.-C. Chen, X.-B. Gao, and M. Gao, "Investigation of the aerodynamic parameters simulation method of a guided rocket," *Simulation*, vol. 94, no. 6, pp. 477–491, 2018.
- [25] X. Zhang, *Interior Ballistics of Guns*, Beijing Institute of Technology University Press, Beijing, China, 2014.
- [26] L. C. MacAllister, "The aerodynamic properties of a simple non-rolling finned cone-cylinder configuration between Mach number 1.0 and 2.5," BRL Report No. 934, Defense Technical Information Center, Fort Belvoir, VA, USA, 1955.
- [27] R. L. McCoy, *Modern Exterior Ballistics: The Launch and Flight Dynamic of Symmetric Projectiles*, Schiffer Pub Ltd, Atglen, PA, USA, 2012.
- [28] S. Cloete, S. T. Johansen, and S. Amini, "Grid independence behaviour of fluidized bed reactor simulations using the two fluid model: effect of particle size," *Powder Technology*, vol. 269, pp. 153–165, 2015.
- [29] A. Kaabeche, M. Belhamel, and R. Ibtouen, "Sizing optimization of grid-independent hybrid photovoltaic/wind power generation system," *Energy*, vol. 36, no. 2, pp. 1214–1222, 2011.

## Research Article

# Rockburst Prediction on the Superimposed Effect of Excavation Accumulation Energy and Blasting Vibration Energy in Deep Roadway

Qingwen Li  and Ben Xiang

*Beijing Key Laboratory of Urban Underground Space Engineering, University of Science and Technology Beijing, Beijing 100083, China*

Correspondence should be addressed to Qingwen Li; [qingwenli@ustb.edu.cn](mailto:qingwenli@ustb.edu.cn)

Received 2 November 2020; Revised 7 February 2021; Accepted 27 April 2021; Published 7 May 2021

Academic Editor: Nan Jiang

Copyright © 2021 Qingwen Li and Ben Xiang. This is an open access article distributed under the Creative Commons Attribution License, which permits unrestricted use, distribution, and reproduction in any medium, provided the original work is properly cited.

In deep mining, much elastic energy is stored in rock mass due to the high geostress. Rockburst will be induced by accumulated energy during excavation. Meanwhile, because of blasting vibration energy in the host rock, there will be an obvious superimposed effect on the probability and intensity of rockburst. To explore the most reasonable and effective method for understanding rockburst problem under blasting, a deep roadway of Sanshandao gold mine was studied. On the basis of in situ geostress data, the accumulated energy of three-centered arch roadway after quasi-static excavation was derived. Then, a series of in situ blasting vibration were monitored, and the blasting vibration energy was calculated by employing the equivalent theory of elastic vibration boundary. Finally, the tendentiousness of rockburst was evaluated qualitatively with the superimposed energy. The results indicated that the disaster-driven energy was increased by 45.1% and 28.2% on different places of roadway. Also, the probability and intensity of rockburst would be raised.

## 1. Introduction

Nowadays, resource exploration has entered deep mining. Much elastic energy is stored in rock mass, and deeper buried depth leads to more energy. Many scholars have paid attention to energy storage characteristics of rocks [1–4]. Affected by excavation, the stress and strain will redistribute, resulting in rock damage and destruction. Kong et al. gave a new method to estimate the pressure arch formation above underground excavation in rock mass [5]. Also, the distribution characteristics of stored energy will change. Some energy will release to damage the host rock. Gao et al. studied the rock damage based on the energy principles [6]. Xiao et al. raised a new method for calculating energy release rate in tunnel excavation subjected to high in situ stress [7]. Sometimes, the intense energy releasing process will cause dynamic disasters, especially rockburst. Recently, energy theory has been regarded as the most effective approach to

explain the mechanism of deep dynamic disasters and has attracted attentions of scholars around the world. Chen et al. studied the rock burst intensity classification based on the radiated energy with damage intensity at Jinping II Hydropower Station, China [8]. Xu et al. established a new energy index for evaluating the tendency of rockburst and its engineering application also in Jinping II hydropower station [9]. Wang et al. did the research on the energy criterion for rockbursts induced by broken hard and thick rock strata [10]. Miao et al. predicted the rockburst based on in situ stress and energy accumulation theory [11].

Meanwhile, drill and blast is still the main excavation way for the rock mass tunneling [12–14]. Under the action of blasting wave, there are many negative effects, such as host rock damage [15–17], high initial stress release [18], intense stress and strain [19, 20], and blasting vibration of surrounding rock mass [21, 22], to name a few. Also, due to blasting effect, the energy accumulation degree is much



higher [23], so the possibility and intensity of rockburst and other dynamic disasters will increase accordingly. Also, some scholars have noticed the relationship between rockburst intensity and rock blasting. Fan et al. studied the influence of tunneling methods on the strainburst characteristics during the excavation of deep rock mass [24]. Liu et al. put forward a method for dynamic risk assessment and management of rockbursts in drill and blast tunnels [25]. However, these methods mentioned above are mainly based on theoretical derivations or numerical simulations. The superposition effect and degree cannot be quantitatively given. Hence, based on the in situ geostress data and energy calculation method of circular tunnels, the accumulated energy of three-centered arch roadway in Sanshandao gold mine after quasi-static excavation was derived. Then, a series of modified SHPB dynamic tests were conducted after employing the equivalent theory of elastic vibration boundary and the monitoring data of near field blasting impact velocity. So, the energy attenuation in the long granite specimens (400 mm in length and 50 mm in diameter) and blasting vibration energy dispersion with different incident bars were confirmed. Finally, according to the superimposed energy, the tendentiousness of rockburst was evaluated qualitatively. So, the effect of blasting vibration on rockburst intensity was quantified, which provides theoretical guidance and supporting data for dynamic disasters of deep rock under blasting vibration conditions.

## 2. Energy Accumulation Caused by Deep Roadway Excavation

**2.1. Engineering Cases and Geostress Measurement.** The largest exploitation depth in Sanshandao gold mine has already exceeded 1400 m. Rockburst and other dynamic disasters are becoming more and more serious. To study the rockburst tendency, a 1000 m depth roadway was selected as the research cases. The cross-section diagram of excavated roadway is displayed in Figure 1. The dimensions of the roadway are 4.2 m in height and 4.5 m in width. As shown, region I is the roof and the circular arc area of side wall, with the arc radius 2.25 m; region II is the transition region of side wall and the floor, with the arc radius 0.94 m; and region III is the circular arc area of floor, with the arc radius 4.6 m.

A large number of studies have shown that deep high geostress is the essential cause of dynamic disasters; to obtain accurate geostress measurement data, the stress relief method was employed to measure the in situ geostress, and the adopted in situ stress probe is shown in Figure 2.

In order to acquire the accurate distribution law of geostress, in situ geostress measurements of 11 groups were carried out. After measuring, it is found that all curves show similar stress characteristics. As relief length increases, the measured strain values increase constantly and finally become stable. Typical measuring data curves of geostress are shown in Figure 3. In the legend of Figure 3, A, B, and C are the three sets of strain rosette and 0, 45, 90, and 135 are the direction of strain gage in a strain rosette.

The stress relief method is to reverse the stress value according to the measured value of strain recovery value

with the basis of generalized Hooke's law, so the elastic modulus and Poisson's ratio of rock cores are necessary for data processing; they can be acquired by the confining pressure rating test (shown in Figure 4(a)), and the following formulas are obtained:

$$E = \frac{P_c}{\varepsilon_\theta} \cdot \frac{2L^2}{L^2 - l^2}, \quad (1)$$

$$\nu = \frac{\varepsilon_z}{\varepsilon_\theta}, \quad (2)$$

where  $E$  is the elastic modulus;  $\nu$  is the Poisson ratio;  $P_c$  is the confining pressure;  $\varepsilon_\theta$  and  $\varepsilon_z$  are radial and axial strain, respectively; and  $L$  and  $l$  are outer and inner diameter of the rock core, respectively.

Considering the influence of colloid, formula (1) can be modified as follows:

$$E = K_1 \cdot \frac{P_0}{\varepsilon_\theta} \cdot \frac{2L^2}{L^2 - l^2}, \quad (3)$$

where  $K_1$  is the compensation factor. When  $E \geq 50$  MPa,  $K_1$  is 1.12.

After in situ strain monitoring, confining pressure calibration tests were carried out on the drilled cores; typical confining pressure rating curves are displayed in Figure 4(b). After analyzing the measured data of 11 points, the value and direction of geostress of Sanshandao gold mine are listed in Table 1, and the fitted results are illustrated in Figure 5.

As listed in Table 1, for the geostresses in three directions, the dip angles of maximum principal stress ( $\sigma_1$ ) are between  $-10^\circ$  and  $4^\circ$ ; this principal stress is close to the horizontal direction; it is named as the maximum horizontal principal stress ( $\sigma_H$ ). For the intermediate principal stress ( $\sigma_2$ ) and minimum principal stress ( $\sigma_3$ ), one of them is in the near horizontal state and the other one is in the near vertical state by the dip angle analysis. The geostress with near horizontal state is named as the minimum horizontal principal stress ( $\sigma_h$ ), and the geostress with vertical dip angle is the vertical principal stress ( $\sigma_v$ ). These three principal stresses all increase linearly with depth, and the maximum horizontal principal stress increases much more rapidly. The relationships between three different principal stress and depth are as follows:

$$\begin{cases} \sigma_H = 0.035H + 7.434, \\ \sigma_h = 0.017H + 8.366, \\ \sigma_v = 0.026H + 1.072, \end{cases} \quad (4)$$

where  $H$  is the depth.

Based on the fitting formula (4), taking example of 1000 m depth geostress, the value of in situ stress values in three directions is as follows:  $\sigma_H = 42.4$  MPa,  $\sigma_h = 25.4$  MPa, and  $\sigma_v = 27.1$  MPa, and the three values are 35.4, 22.0, and 21.9 for 800 m depth, respectively. So, for the value of geostress, the minimum horizontal principal stress is almost equal to the vertical principal stress, and the maximum horizontal stress is about 1.6 times the minimum horizontal principal stress and vertical principal stress.

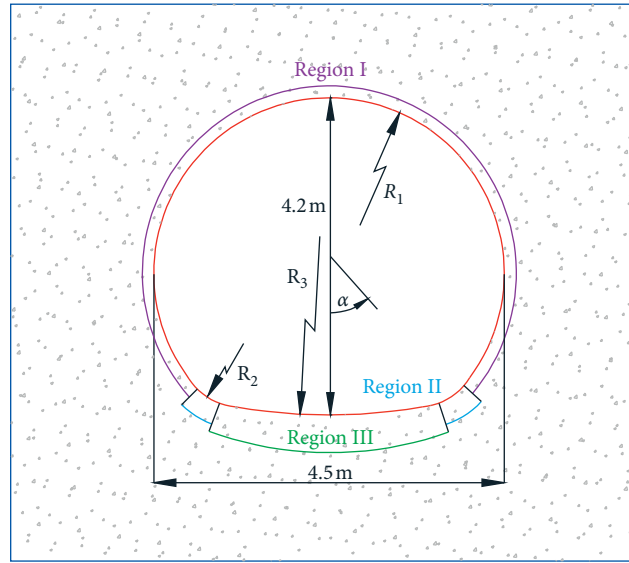


FIGURE 1: The cross-section diagram of excavated roadway and its partition.

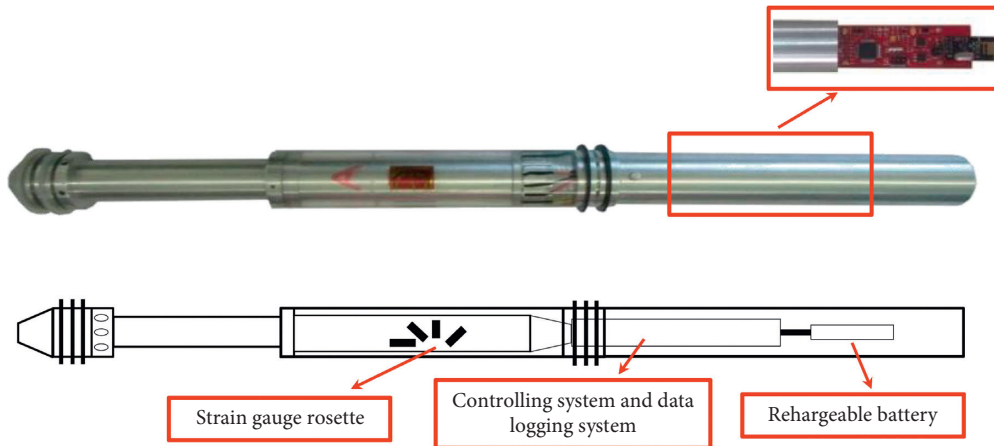


FIGURE 2: The used digital hollow inclusion strain gauge.

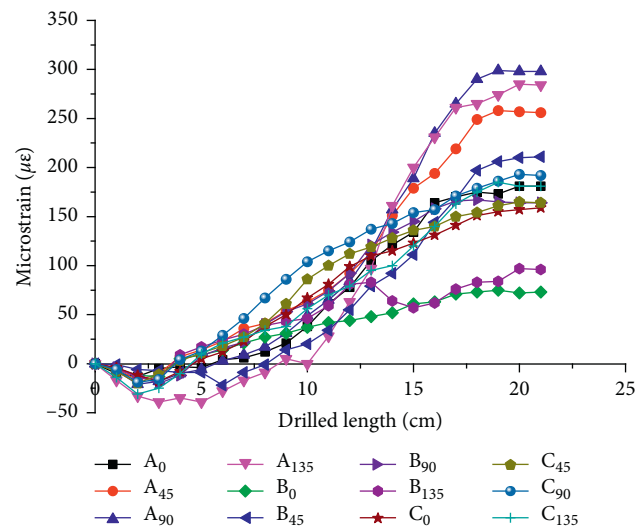


FIGURE 3: Typical measuring data curves of geostress.

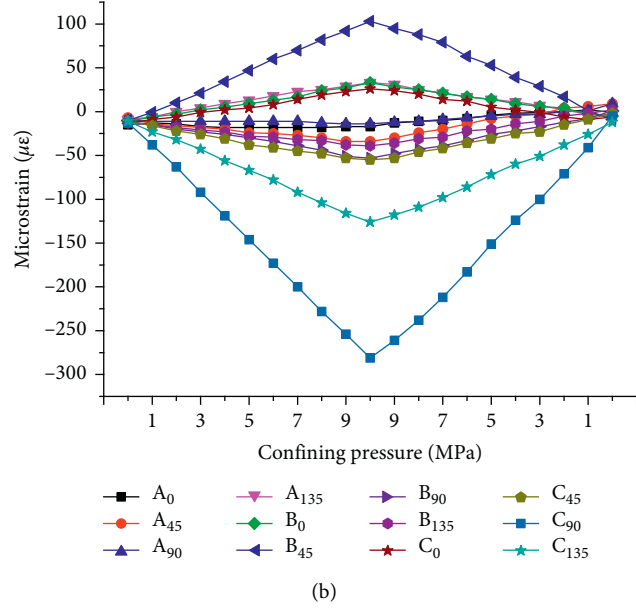
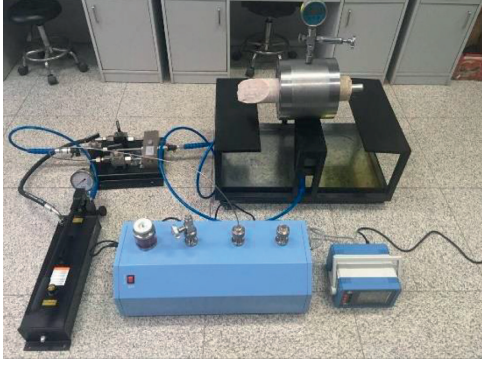


FIGURE 4: Confining pressure calibration test and its typical testing curves.

**2.2. Analysis of Energy Accumulation in Excavation.** To avoid the effect of tectonic stress, most of the underground mine main roadway will be designed and excavated along with the direction of the maximum horizontal stress. So, the maximum horizontal principal stress will be released during excavation. When the roadway is excavated along the maximum horizontal principal stress, the vertical principal stress is very close to the minimum horizontal principal stress based on the geostress monitoring results. So, the excavated roadway can be equivalent to an infinite three-centered arch roadway, and the far field geostress effect can be approximate to hydrostatic pressure, which means  $P_0 = \sigma_v \approx \sigma_h$ . Using the plane strain problem method, the confining pressure of circular roadway can be expressed as follows [26]:

$$\begin{cases} \sigma_1 = P_0 \left( 1 + \frac{R^2}{r^2} \right), \\ \sigma_2 = P_0, \\ \sigma_3 = P_0 \left( 1 - \frac{R^2}{r^2} \right), \end{cases} \quad (5)$$

where  $\sigma_1$ ,  $\sigma_2$ , and  $\sigma_3$  are the first, second, and third principal stress, respectively;  $R$  is the radius of roadway; and  $r$  is the distance between the surrounding rock to the roadway center.

Then, the strain energy density of surrounding rock is

$$U = \frac{[\sigma_1^2 + \sigma_2^2 + \sigma_3^2 - 2\nu(\sigma_1\sigma_2 + \sigma_2\sigma_3 + \sigma_1\sigma_3)]}{2E} \quad (6)$$

Under hydrostatic pressure conditions, the stresses in the far field have the rule as

$$\sigma_1 = \sigma_2 = \sigma_3 = P_0. \quad (7)$$

Substituting equations (5) and (7) into equation (6), the strain energy density of surrounding rock before and after excavation can be calculated as follows:

$$U_w = P_0^2 \frac{[3(1-2\nu) + 2(1+\nu)(R^4/r^4)]}{2E}, \quad (8)$$

$$U_0 = \frac{P_0^2 [3(1-2\nu)]}{2E},$$

where  $U_0$  and  $U_w$  are the strain energy density of surrounding rock before and after excavation, respectively.

For any point  $N(r, \theta)$  in the three-centered arch roadway, according to the region partition in Figure 4, when  $\theta \in (-\alpha, \alpha)$ , which means  $N(r, \theta)$  is in the region I, the strain energy density of surrounding rock after excavation is

$$U_{w1} = \frac{P_0^2 [3(1-2\nu) + 2(1+\nu)(R^4/r^4)]}{2E}. \quad (9)$$

When  $N(r, \theta)$  is in the region II,

TABLE 1: Geostress data from in situ monitoring.

No.	Depth (m)	Maximum principal stress $\sigma_1$			Intermediate principal stress $\sigma_2$			Minimum principal stress $\sigma_3$		
		Value (MPa)	Direction (°)	Dip angle (°)	Value (MPa)	Direction (°)	Dip angle (°)	Value (MPa)	Direction (°)	Dip angle (°)
1	510	24.55	129	4	16.35	-138	2	14.49	133	-85
2	510	24.64	-111	3	15.68	155	82	15.02	161	-10
3	555	25.71	-45	-13	14.00	14	73	13.00	50	-20
4	645	29.57	112	-3	19.56	-177	-80	15.48	-156	-9
5	600	28.88	103	1	16.54	10	76	14.77	13	-8
6	600	30.17	110	-6	18.83	24	-11	16.94	236	-70
7	690	31.50	-80	2	19.08	230	-79	17.54	10	-10
8	690	29.77	-83	4	20.84	-8	-74	19.63	8	15
9	750	33.22	119	-10	19.93	-89	-82	17.10	208	-8
10	795	48.93	164.09	3	23.15	74.41	-5.97	21.66	47.22	83.29
11	825	46.95	40.06	3.84	28.88	-49.55	-5.77	26.49	-83.43	83.06

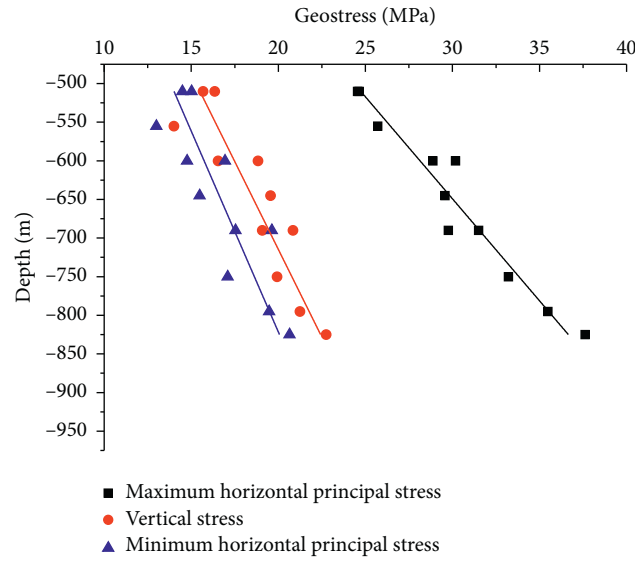


FIGURE 5: The relationship between geostress and depth.

$$r'^2 = (R_1 - R_2)^2 + r^2 - 2r(R_1 - R_2)\cos(\theta - \alpha_2), \quad (10)$$

$$U_{w2} = \frac{P_0^2 [3(1 - 2\nu) + 2(1 + \nu)(R_2^4/r'^4)]}{2E} = \frac{P_0^2}{2E} \frac{3(1 - 2\nu) + 2(1 + \nu)R_3^4}{[(R_1 - R_2)^2 + r^2 - 2r(R_1 - R_2)\cos(\theta - \alpha_2)]^2}. \quad (11)$$

When  $N(r, \theta)$  is in the region III,

$$O_1 O_2^2 = (R_3 - R_2)^2 + (R_1 - R_2)^2 - 2(R_3 - R_2)(R_1 - R_2)\cos \alpha_3, \quad (12)$$

$$r''^2 = O_1 O_2^2 + r^2 - 2r|O_1 O_2|\cos \theta, \quad (13)$$

$$U_{w3} = \frac{P_0^2}{2E_0} \frac{[3(1 - 2\nu) + 2(1 + \nu)]R_3^4}{O_1 O_2^2 + r^2 - 2r|O_1 O_2|\cos \theta} \quad (14)$$

Substituting in situ geostress data, elastic modulus, and Poisson's ratio into formulas (9)–(14), the quasi static energy distribution of host rock mass can be fitted, as shown in Figure 6.

It can be seen from Figure 6 that after excavation, the maximum accumulated energy on the top and both sides of the roadway is  $89.7 \text{ kJ/m}^3$ . For the bottom of the roadway, the value is  $143.6 \text{ kJ/m}^3$ . The maximum values all appear in the host rock at the location 5 m from the free face.

### 3. Energy Superposition Effect by Blasting Vibration

**3.1. Confirmation of Equivalent Elastic Vibration Zone.** Blasting in the rock mass is a very complicated process; the energy produced by the explosion of an explosive can be roughly divided into two parts: one is for the excavation of the target rock mass and the other can produce the rock mass vibration at a certain distance. Under these combination effects, different damage zones are formed. Based on the damage types and degrees, the recognized zones are blasting crushed zone, blasting fragmentation zone, and elastic vibration zone, as shown in Figure 7,

As seen in Figure 7, some of the energy of the explosion will be consumed in blasting crushed zone and blasting fragmentation zone to excavate target rock mass. The remaining energy will propagate outward in the form of a vibrational wave; this part energy will have a superimposed effect on the accumulated energy of rock mass. Therefore, for the analysis of energy superposition effect by blasting vibration, an equivalent elastic vibration boundary (region 4 in Figure 7) could be adopted. In this region, the blasting wave can be recognized as the elastic wave gradually decays along the radius [27]. When single-hole blasting is used for infinite rock, the failure mode of rocks in blasting crushed zone is mainly shearing failure. While for the rocks in blasting fragmentation zone, it is tensile failure. The radius can be calculated by the following equation [28]:

$$\begin{aligned} r_1 &= \left( \frac{\rho_r c_p^2}{5\sigma_c} \right)^{1/2} \left( \frac{P}{\sigma_*} \right)^{1/4} r_0, \\ r_2 &= \left[ \frac{vP}{(1-v)\sigma_t} \right]^{1/\alpha} r_0, \end{aligned} \quad (15)$$

where  $r_0$  is the radius of blasting drill hole;  $r_1$  is the radius of blasting crushed zone;  $r_2$  is the radius of blasting fragmentation zone;  $c_p$  is the velocity of  $P$  wave in the rock;  $\sigma_c$  is the dynamic compressive strength;  $\sigma_t$  is the dynamic tensile strength;  $\sigma_*$  is the static compressive strength;  $P$  is the blasting loading;  $\alpha$  is the attenuation coefficient of vibration wave; and  $\rho_r$  is the density of rock.

Here,  $c_p^2 = \lambda + 2G/\rho_r$ ,  $\lambda = 2G\nu/(1-2\nu)$ , and  $G$  is the shear modulus.

Calculations suggest that the radius of single-hole blasting crushed zone is 4 times the radius of blasting hole. For the blasting fragmentation zone, the value is ten times. Therefore, in this paper, 10 times of blasting hole radius can be equivalent to elastic vibration zone [29].

**3.2. In Situ Blasting Vibration Wave Monitoring.** For the in situ blasting, the drilled blasting hole is 40 mm; according to the equivalent elastic vibration zone model, the range of blasting crush zone in the rock mass is 160 mm around blasting hole and the range of blasting fragmentation zone is about 400 mm around blasting hole. It also means that the blasting energy will propagate outward in the form of vibration waves out of the range of 0.4 m. To acquire accurate velocity of blasting vibration wave, Ubox-5016 blasting vibration monitor (see Figure 8) was used in in situ blasting monitoring.

Because it is close to the roadway working face, it is difficult to conduct in situ monitoring. Here, 7 groups of near-field blasting vibration monitoring were applied, and the monitoring location and monitoring results are shown in Table 2.

After data analysis, the attenuation law of vibration velocity with blasting distance could be fitted as shown in Figure 9.

As shown in Figure 9, the peak velocity of blasting decreases gradually with the increase of the propagation distance in rock mass, and the total vibration velocity will attenuate by the formula in Figure 9.

### 4. Rockburst Tendentiousness Analysis

According to the value of elastic energy, the rockburst intensity can be divided into four degrees, as shown in Table 3.

As calculated in Section 2.2, without considering the explosion vibration effect, the maximum accumulated energy on the top and both sides of the roadway is  $89.7 \text{ kJ/m}^3$  after excavation. For the bottom of the roadway, the value is  $143.6 \text{ kJ/m}^3$ . These two values indicate that the rockburst intensity is slight and medium, respectively. The maximum values all appear at about 5 m from the free face.

At 5 m position in the host rock, the velocity caused by blasting is 3.86 m/s which is calculated by the formula in Figure 9. Taking the theorem of kinetic energy, the energy density per unit volume of rock mass could be calculated by considering the granite density  $2712 \text{ kg/m}^3$ , and the blasting vibration energy density is  $40.41 \text{ kJ/m}^3$ . Then, the accumulated energy has risen to  $130.11 \text{ kJ/m}^3$  on the top and both sides of the roadway and  $184.01 \text{ kJ/m}^3$  on the bottom of the roadway. The accumulated energy increase rates are 45.1% and 28.2%, respectively, and the rockburst intensity has risen to medium. It can be seen that blasting vibration obviously increases the probability and intensity of the rockburst, which increases the potential threat of dynamic disasters at a certain extent.



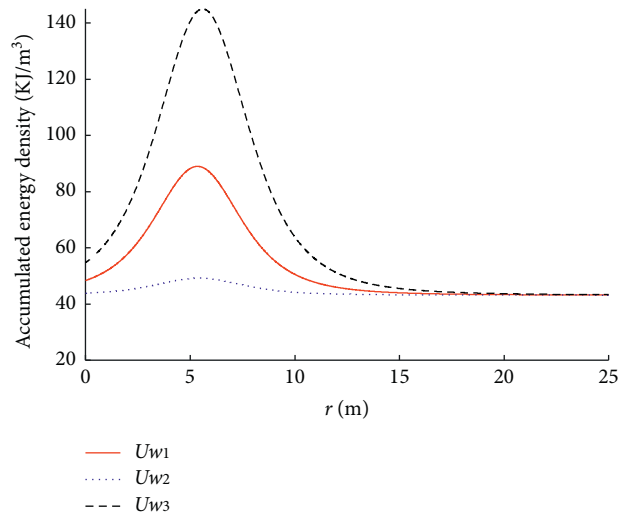
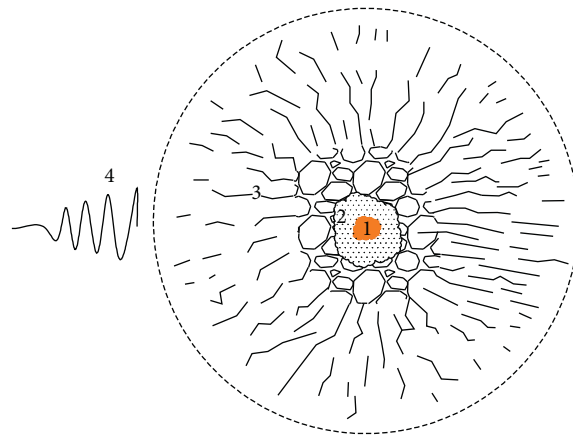


FIGURE 6: The quasi static energy distribution of surrounding rock mass.



- 1: blasting hole
- 2: blasting crushed zone
- 3: blasting fragmentation zone
- 4: elastic vibration zone

FIGURE 7: Sketch diagram of drilled hole blasting.



FIGURE 8: Ubox-5016 blasting vibration monitor.

TABLE 2: Monitoring location and results of near-field blasting vibration.

Blasting distance (m)	X-velocity (m/s)	Y-velocity (m/s)	Z-velocity (m/s)	Velocity (m/s)
4.2	1.82	1.23	1.91	2.91
3.6	2.12	2.04	1.79	3.44
2.4	3.52	3.36	3.51	6.00
4.4	2.01	1.95	1.83	3.49
3.8	2.35	2.24	2.23	3.94
3.2	2.57	2.16	1.96	3.86
2.6	3.18	2.79	2.89	5.12

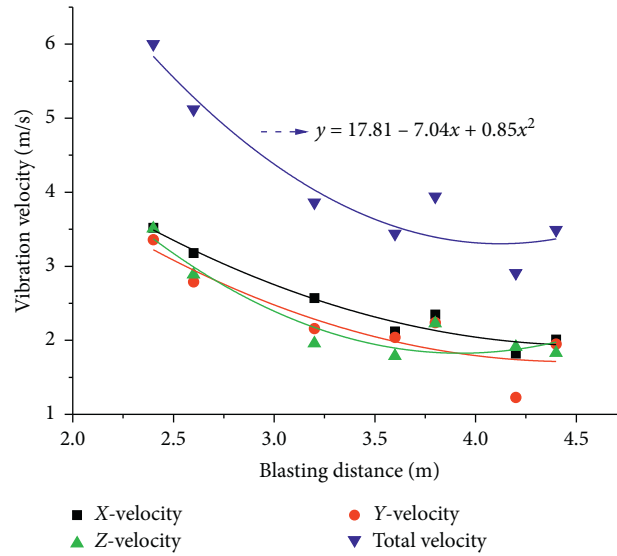


FIGURE 9: Blasting vibration velocity attenuation curve with distance.

TABLE 3: Grading value of rockburst tendentiousness.

Rockburst degree	None	Slight	Medium	Intensity
Energy density value ( $\text{kJ}/\text{m}^3$ )	$U_e < 40$	$40 \leq U_e < 100$	$100 \leq U_e < 200$	$200 < U_e$

## 5. Conclusions

Considering the superimposed effect of excavation accumulation energy and blasting vibration energy in deep roadway,

- (1) Based on the in situ geostress data and energy calculation method of circular tunnels, the accumulated energy of three-centered arch roadway after quasi-static excavation was derived. The maximum accumulated energy on the top and both sides of the roadway is  $89.7 \text{ kJ}/\text{m}^3$  after excavation. For the bottom of the roadway, the value is  $143.6 \text{ kJ}/\text{m}^3$ . The maximum values all appear at about 5 m from the free face.
- (2) Based on near-field monitored data, the attenuation law blasting vibration velocity could be fitted, and the

result shows that the peak velocity of blasting will decrease gradually with the increase of the propagation distance.

- (3) After considering blasting vibration, the accumulated energy has risen to  $130.11 \text{ kJ}/\text{m}^3$  on the top and both sides of the roadway and  $184.01 \text{ kJ}/\text{m}^3$  on the bottom of the roadway. There is an increase of 45.1% and 28.2%, respectively. It can be seen that blasting vibration obviously increases the probability and intensity of the rockburst, which increases the potential threat of dynamic disasters at a certain extent.

## Data Availability

The datasets used in the present study are available from the corresponding author upon reasonable request.

## Conflicts of Interest

The authors declare that they have no conflicts of interest.

## Acknowledgments

This work was supported by the National Natural Science Foundation of China (U1806209) and the Fundamental Research Funds for the Central Universities (FRF-TP-19-021A3 and FRF-IDRY-19-002).

## References

- [1] D. Li, Z. Sun, T. Xie, X. Li, and P. G. Ranjith, "Energy evolution characteristics of hard rock during triaxial failure with different loading and unloading paths," *Engineering Geology*, vol. 228, pp. 270–281, 2017.
- [2] M. Soleiman Dehkordi, K. Shahriar, P. Moarefvand, and M. Gharouninik, "Application of the strain energy to estimate the rock load in squeeze ground condition of eamzade hashem tunnel in Iran," *Arabian Journal of Geosciences*, vol. 6, no. 4, pp. 1241–1248, 2013.
- [3] I. C. Engin, F. Bayram, and N. E. Yasitli, "Experimental and statistical evaluation of cutting methods in relation to specific energy and rock properties," *Rock Mechanics and Rock Engineering*, vol. 46, no. 4, pp. 755–766, 2013.
- [4] M. Mirahmadi, M. Tabaie, and M. S. Dehkordi, "Estimation of the specific energy of TBM using the strain energy of rock mass, case study: amir-kabir water transferring tunnel of Iran," *Geotechnical and Geological Engineering*, vol. 35, no. 5, pp. 1991–2002, 2017.
- [5] X. X. Kong, Q. S. Liu, Q. B. Zhang, Y. X. Wu, and J. Zhao, "A method to estimate the pressure arch formation above underground excavation in rock mass," *Tunnelling and Underground Space Technology*, vol. 71, pp. 382–390, 2018.
- [6] W. Gao, L. Wang, and D. Y. Yang, "Rock damage research based on the energy principles," *Applied Mechanics and Materials*, vol. 87, pp. 238–242, 2011.
- [7] Q. H. Xiao, J. G. Liu, S. X. Lei, and B. Gao, "A new method for calculating energy release rate in tunnel excavation subjected to high in situ stress," *Perspectives in Science*, vol. 7, pp. 292–298, 2016.
- [8] B.-R. Chen, X.-T. Feng, Q.-P. Li, R.-Z. Luo, and S. Li, "Rock burst intensity classification based on the radiated energy with damage intensity at jinping II hydropower station, China," *Rock Mechanics and Rock Engineering*, vol. 48, no. 1, pp. 289–303, 2015.
- [9] J. Xu, J. Jiang, N. Xu, Q. Liu, and Y. Gao, "A new energy index for evaluating the tendency of rockburst and its engineering application," *Engineering Geology*, vol. 230, pp. 46–54, 2017.
- [10] J. Wang, J. Ning, J. Jiang, T. Bu, and X. Shi, "Research on the energy criterion for rockbursts induced by broken hard and thick rock strata and its application," *Geotechnical and Geological Engineering*, vol. 35, no. 2, pp. 731–746, 2017.
- [11] S.-J. Miao, M.-F. Cai, Q.-F. Guo, and Z.-J. Huang, "Rock burst prediction based on in-situ stress and energy accumulation theory," *International Journal of Rock Mechanics and Mining Sciences*, vol. 83, pp. 86–94, 2016.
- [12] J. Yang, W. Lu, M. Chen, P. Yan, and C. Zhou, "Microseism induced by transient release of in situ stress during deep rock mass excavation by blasting," *Rock Mechanics and Rock Engineering*, vol. 46, no. 4, pp. 859–875, 2013.
- [13] J. Yang, W. Lu, Y. Hu, M. Chen, and P. Yan, "Numerical simulation of rock mass damage evolution during deep-buried tunnel excavation by drill and blast," *Rock Mechanics and Rock Engineering*, vol. 48, no. 5, pp. 2045–2059, 2015.
- [14] J. Yang, W. Lu, Q. Jiang, C. Yao, S. Jiang, and L. Tian, "A study on the vibration frequency of blasting excavation in highly stressed rock masses," *Rock Mechanics and Rock Engineering*, vol. 49, no. 7, pp. 2825–2843, 2016.
- [15] L. X. Xie, W. B. Lu, Q. B. Zhang, Q. H. Jiang, G. H. Wang, and J. Zhao, "Damage evolution mechanisms of rock in deep tunnels induced by cut blasting," *Tunnelling and Underground Space Technology*, vol. 58, pp. 257–270, 2016.
- [16] H. K. Verma, N. K. Samadhiya, M. Singh, R. K. Goel, and P. K. Singh, "Blast induced rock mass damage around tunnels," *Tunnelling and Underground Space Technology*, vol. 71, pp. 149–158, 2018.
- [17] M. Chen, W. B. Lu, P. Yan, and Y. G. Hu, "Blasting excavation induced damage of surrounding rock masses in deep-buried tunnels," *KSCE Journal of Civil Engineering*, vol. 20, no. 2, pp. 933–942, 2016.
- [18] W. Cao, X. Li, M. Tao, and Z. Zhou, "Vibrations induced by high initial stress release during underground excavations," *Tunnelling and Underground Space Technology*, vol. 53, pp. 78–95, 2016.
- [19] J. González-Cao, L. R. Alejano, E. Alonso, and F. G. Bastante, "Convergence-confinement curve analysis of excavation stress and strain resulting from blast-induced damage," *Tunnelling and Underground Space Technology*, vol. 73, pp. 162–169, 2018.
- [20] J. H. Yang, Q. H. Jiang, Q. B. Zhang, and J. Zhao, "Dynamic stress adjustment and rock damage during blasting excavation in a deep-buried circular tunnel," *Tunnelling and Underground Space Technology*, vol. 71, pp. 591–604, 2018.
- [21] J. H. Yang, W. B. Lu, P. Li, and P. Yan, "Evaluation of rock vibration generated in blasting excavation of deep-buried tunnels," *KSCE Journal of Civil Engineering*, vol. 22, no. 3, pp. 1–16, 2017.
- [22] B. Duan, H. Xia, and X. Yang, "Impacts of bench blasting vibration on the stability of the surrounding rock masses of roadways," *Tunnelling and Underground Space Technology*, vol. 71, pp. 605–622, 2018.
- [23] Y. Fan, W. B. Lu, P. Yan, M. Chen, and Y. Z. Zhang, "Transient characters of energy changes induced by blasting excavation of deep-buried tunnels," *Tunnelling and Underground Space Technology*, vol. 49, pp. 9–17, 2015.
- [24] Y. Fan, W. Lu, Y. Zhou, P. Yan, Z. Leng, and M. Chen, "Influence of tunneling methods on the strainburst characteristics during the excavation of deep rock masses," *Engineering Geology*, vol. 201, pp. 85–95, 2016.
- [25] G.-F. Liu, X.-T. Feng, G.-L. Feng, B.-R. Chen, D.-F. Chen, and S.-Q. Duan, "A method for dynamic risk assessment and management of rockbursts in drill and blast tunnels," *Rock Mechanics and Rock Engineering*, vol. 49, no. 8, pp. 3257–3279, 2016.
- [26] Y. Fan, W. B. Lu, Y. H. Zhou, P. Yan, and M. Chen, "Study on energy release process of high energy storage rock mass induced by excavation unloading," *Chinese Journal of Rock Mechanics and Engineering*, vol. 35, no. S2, pp. 3706–3715, 2016, (in Chinese).
- [27] W. Lu, J. Yang, M. Chen, and C. Zhou, "An equivalent method for blasting vibration simulation," *Simulation Modelling Practice and Theory*, vol. 19, no. 9, pp. 2050–2062, 2011.
- [28] A. H. Xahykaeb, *Physical Process of Rock Blasting in Mining*, Mineral Press, Leningrad, Russia, 1974.

- [29] Q. Li, L. Qiao, G. Dasgupta, S. Ma, L. Wang, and J. Dong, "Blasting vibration safety criterion analysis with equivalent elastic boundary: based on accurate loading model," *Shock and Vibration*, vol. 2015, pp. 1-10, 2015.

## Research Article

# Dynamic Splitting Behavior and the Constitutive Relationship of Frozen Sandstone Containing a Single Fissure

Tao Zhao , Gengshe Yang , Lei Wang , Hailiang Jia , and Yuzhe Qiao 

College of Architecture and Civil Engineering, Xi'an University of Science and Technology, 58 Yanta Middle Road, Xi'an, Shaanxi Province, China

Correspondence should be addressed to Hailiang Jia; [hailiang.jia@xust.edu.cn](mailto:hailiang.jia@xust.edu.cn)

Received 3 December 2020; Revised 8 March 2021; Accepted 16 April 2021; Published 22 April 2021

Academic Editor: Bangbiao Wu

Copyright © 2021 Tao Zhao et al. This is an open access article distributed under the Creative Commons Attribution License, which permits unrestricted use, distribution, and reproduction in any medium, provided the original work is properly cited.

Fractured sandstone is widely distributed in mining areas throughout western China where the artificial freezing method is extensively adopted to construct vertical shafts. Blasting and excavation generate stress waves and break frozen fractured sandstone. Among the failure modes of frozen fractured rocks, tensile failure is very common. In this study, the dynamic tensile strength of fractured sandstone samples with four crack inclination angles ( $0^\circ$ ,  $30^\circ$ ,  $60^\circ$ , and  $90^\circ$ ) is tested by using a split Hopkinson pressure bar at four subzero temperatures ( $-5$ ,  $-10$ ,  $-15$ , and  $-20^\circ\text{C}$ ). Accordingly, a damage constitutive relationship that considers the effect of fissure angle and freezing temperature is established. The results show the following: (1) the fissure angle does not significantly affect the dynamic tensile strength of frozen fractured sandstone but mainly affects the failure mode of the sample. (2) The dynamic tensile strength of fractured sandstone has a negative linear correlation with the freezing temperature. (3) When the fissure angle is small, only tensile cracking occurs; when the fissure angle is large, tensile cracking occurs along both the loading direction and the fissure; and shear cracking occurs along the fissure as well. (4) Regardless of the fissure angle, tensile cracking is initiated at the stress-concentration zone and then propagates towards the loading end. Fissure ice provides both resistance to deformation and resistance to crack propagation which affects the crack propagation and coalescence mode. A dynamic constitutive relationship is established by considering the effects of fissure angle and freezing temperature on the dynamic properties of frozen fractured sandstone, which is proven to be highly reliable and provides a reference and basis to study the dynamic mechanical properties of similar rock types.

## 1. Introduction

A large number of mine shafts in western China pass through Cretaceous strata. These strata have a short sedimentation time, containing many macro- and mesoscale fissures, and are in a water-rich state [1, 2]. The artificial freezing method has become the best plan for vertical shaft construction in water-rich soft rock strata [3, 4]. The fractured rock mass is easily damaged in blasting and excavation by the action of stress waves [5, 6]. Due to the complex characteristics of rock mass structure, the dynamic mechanical behavior of frozen rock mass and the underlying mechanisms of crack propagation induced by impact loading are unclear [7].

Dynamic mechanical properties of fractured rock at room temperature have been investigated vastly primarily

through the split Hopkinson pressure bar test device [8, 9], which can determine the dynamic compressive strength [10], dynamic tensile strength [11], dynamic fracture toughness [12], and other mechanical properties of the material [13, 14]. Dong et al. [15] used a separate Hopkinson pressure bar system to study the fracture behaviors of rock plates containing a single fissure and an ultra-high-speed camera system combined with the digital image correlation (DIC) method was adopted to record the transient fracture process. Li [16] used an improved Hopkinson pressure bar device to test the dynamic mechanical properties of prismatic marble with a single defect, and the effects of different crack angles and lengths on the dynamic mechanical properties were analyzed. Yan [17] conducted a dynamic compression test on rock specimens with multiple parallel cracks; the effects of the strain rate and crack strength on the



dynamic response of the fractured specimen strength, deformability, progressive failure behavior, rock fragmentation characteristics, and energy dissipation were considered. Li [18] performed numerical simulations on the dynamic mixed mode I/II fracture behavior of fractured rock employing notched semicircular bending (NSCB) models.

A number of studies have been conducted on frozen intact rocks. Yang et al. [19] considered Cretaceous red sandstone and conducted the SHPB dynamic impact test to study its deformation, failure, and energy transfer laws under low-temperature conditions. The dynamic mechanical properties of weakly consolidated soft rock under different freezing temperatures were studied using the split Hopkinson pressure bar system, and a dynamic constitutive model considering the temperature effects was established [20, 21]. Weng et al. [22] studied the effects of strain rate on the dynamic mechanical properties of dry siltstone and saturated siltstone at low temperatures, and the associated mechanism of water/ice weakening and strengthening of the dynamic mechanical properties of siltstone was discussed. Shan et al. [23] studied the effect of strain rates on the damage distribution and broken shape of frozen red sandstone subjected to dynamic compression. The above studies reveal primary principles of the dynamic mechanical properties of frozen rocks and form the basis for understanding the dynamic mechanical properties of the frozen rock mass. However, the scarcity of systematic studies on the dynamic mechanical properties poses risk to blasting excavation of frozen rock mass.

In this study, the SHPB system was used to perform dynamic splitting tests on sandstone samples containing a single artificial fissure filled with ice at different freezing temperatures ( $-5$ ,  $-10$ ,  $-15$ ,  $-20$  °C) and with loading angles ( $0^\circ$ ,  $30^\circ$ ,  $60^\circ$ , and  $90^\circ$ ). The reason for adopting samples containing a single fissure is that it will make it easier to acquire the first-order rules of how predominant factors (e.g., loading angle and freezing temperature) affect the dynamic properties of frozen fractured rock. The dynamic mechanical properties and failure process of the sandstone samples were studied along with the associated morphological analysis. The crack propagation process was recorded using high-speed photography equipment. A dynamic constitutive relationship is established by considering the effects of initial multiscale damage and freezing temperature on the dynamic properties of frozen fractured sandstone.

## 2. Methodology

**2.1. Specimen Preparation.** The rock used in this study was medium-coarse-grained yellow sandstone commonly found in the mining areas of western China. An entire rock block with good uniformity was selected as the specimen. A core drill was used to extract a cylindrical specimen with a diameter of 50 mm. According to the standards of the International Society of Rock Mechanics, the height of the specimen was 25 mm. The artificial crack was cut across the center of a sample through a water jet scalpel; its length was 20–22 mm with an opening of 1–1.7 mm (Figure 1(a)). The

basic physical and mechanical parameters of the sandstone at 20 °C are shown in Table 1.

The sample with good integrity was selected as the test to ensure that the sample is in full contact with the end surface of the rod during loading based on the requirements of the dynamic splitting test. This test involves four freezing temperatures ( $-5$ ,  $-10$ ,  $-15$ , and  $-20$  °C) and four loading angles ( $0^\circ$ ,  $30^\circ$ ,  $60^\circ$ , and  $90^\circ$ ). Fissure angle, labeled by  $\theta$ , is defined as the angle between the loading direction and the artificial fissure. Considering the influence of material inhomogeneity on the dispersion of the test results, three specimens are carried out under the same test conditions with the test average selected for the analysis of the results. Therefore, a total of 48 fractured sandstone specimens were used in this test.

Heat treatment was conducted on specimens so that their dry mass was obtained; combining with their saturation mass, the porosity of these samples can be calculated. We used porosity as an index for selecting samples with similar values.

Before the dynamic split test, specimens were conditioned as follows: The specimen was placed in the oven for 24 h at a temperature of 105 °C before drying in a vacuum saturation instrument; the gauge pressure was at  $-0.1$  MPa and maintained for 2 h, and then, the specimen was placed in distilled water to continue pumping. After 3 h under vacuum, the rock specimen was placed in distilled water for 48 h. Afterwards, the artificial fissure was sealed with a thin layer of Vaseline at both sides; then, water was injected into it. The specimens were finally wrapped with plastic film and placed into an environmental chamber to freeze at testing temperatures for at least 24 h (Figure 1(b)).

**2.2. Dynamic Split Test.** The prepared specimens were taken out from the environmental chamber; afterwards, the dynamic split test was conducted immediately. Since the test duration was extremely short, the temperature of the samples was regarded as unchanged. To understand the influence of the fissure angle on the mechanical properties of fractured sandstone, dynamic splitting tests at  $0^\circ$ ,  $30^\circ$ ,  $60^\circ$ , and  $90^\circ$  were performed (Figure 2). The impact velocity was 2.2 m/s, and the crack growth process was recorded with high-speed photography equipment.

**2.3. Split Hopkinson Pressure Bar.** The SHPB test is based on two fundamental assumptions: one-dimensional stress wave in the elastic rod and the uniformity of stress in the specimen. During testing, the specimen is held between the incident and transmitted bar (Figure 2). A copper ring sheet is used to reshape the test stress waveform to eliminate the wave dispersion, and petroleum jelly is applied to reduce friction. The striker hits the incident bar at an initial speed, generates a stress wave in the incident bar, and propagates forward. After reaching the sample, a stress balance is achieved after multiple reflections. As the specimen deforms, it generates reflected and transmitted waves.

According to the one-dimensional elastic wave theory, the average applied load at both ends of the rod is



FIGURE 1: Fractured sandstone samples. (a) Sandstone specimens containing single fissure. (b) Sandstone specimens after freezing.

TABLE 1: Basic physical and mechanical parameters of the sandstone used.

Sample	Density (g/cm <sup>3</sup> )	Porosity (%)	P-wave velocity (m/s)	Uniaxial compressive strength (MPa)	Poisson's ratio
Saturation	2152–2198	19.56–20.12	2650–2695	19.65–20.18	0.21–0.24

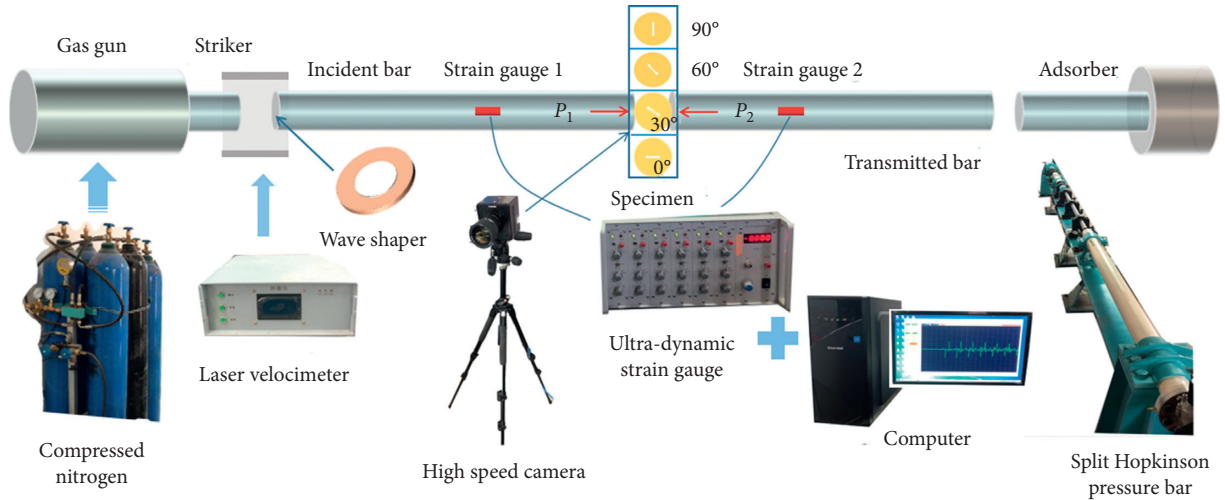


FIGURE 2: Diagram of the SHPB test system.

$$P(t) = \frac{P_1 + P_2}{2} = E_s A_b \frac{\varepsilon_I + \varepsilon_R + \varepsilon_T}{2}, \quad (1)$$

where  $P_1$  and  $P_2$  are the loads on both ends;  $E_s$  is the elastic modulus of the sample;  $A_b$  is the cross-sectional area of the pressure bar; and  $\varepsilon_I$ ,  $\varepsilon_R$ , and  $\varepsilon_T$  are the strain values of the incident wave, reflected wave, and transmitted wave as collected by the strain gauge.

The assumption of stress homogenization suggests that after the specimen reaches its internal stress balance, its stress distribution remains nearly the same as the stress distribution under static loads. Thus, the dynamic tensile stress at the center of the specimen is

$$\sigma(t) = \frac{P_1(t)}{\pi RB} = \frac{E_s A_b \varepsilon_T(t)}{\pi RB}, \quad (2)$$

where  $R$  and  $B$  are the radius and height of the specimen, respectively.

### 3. Results and Discussion

**3.1. Dynamic Equilibrium.** In the dynamic split tests, the load conditions of the constant strain rate must be satisfied so that the internal force of the specimen is uniform. According to the work of Liang et al. [24] on wave-shaping materials in the SHPB test system, a copper sheet with holes is selected as the shaper. The voltage signal obtained during testing is shown in Figure 3(a), where the reshaped waveform is a sine wave. When the wave propagates in the specimen, after four transmissions and reflections, it is considered that the internal stress balance of the specimen is reached. The sample wave speed is 2670 m/s, and the specimen diameter is 5 cm. Therefore, the specimen can attain the stress equilibrium state after 75  $\mu$ s. It is seen from Figure 3(a) that the rising edge time is 85  $\mu$ s, which can be considered as the specimen reaches a constant strain rate loading state.

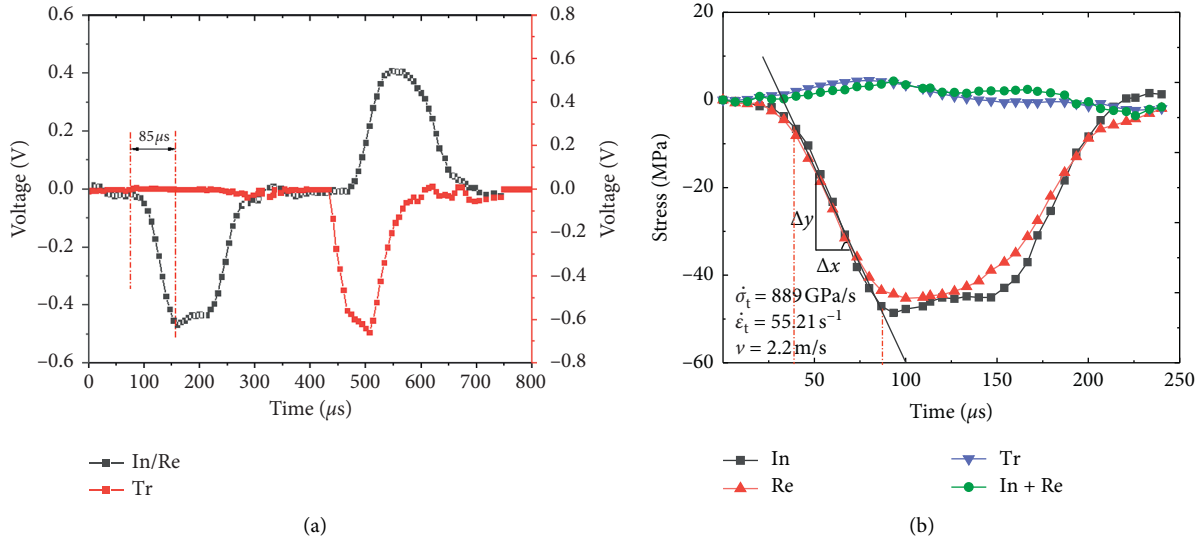


FIGURE 3: Evolution curves of the voltage (a) and stress (b) with time.

Figure 3(b) is the obtained stress time history curve. The rising edge of the incident stress and the reflected stress curve nearly overlapped, and the linear slope of the increasing incident stress can be considered as the loading rate. The impact speed is maintained equal during testing, which means that the same loading rate is applied to the specimen. However, the strain rate changes with variations in the temperature and loading angle. The incident stress wave + reflected stress waves and the transmitted stress wave nearly coincide, indicating that the sample has reached the stress equilibrium condition and the test data are highly accurate. According to the experimental results, the presence of ice will affect the propagation of stress wave. Since the longitudinal wave velocity of the two is different, they will be reflected and transmitted at the interface, but the dynamic stress equilibrium will not be affected.

**3.2. Stress-Strain Curve.** The mechanical properties of the material, such as peak strength and elastic modulus, can be obtained from the characteristics of the stress-strain curves. Figure 4 shows the stress-strain curves obtained from the dynamic splitting tests of fractured sandstone under different freezing temperatures and loading angles.

It is seen that the curve can be divided roughly into three stages. The first stage is the elastic stage where the stress linearly increases with the strain and the sample absorbs energy. Thus, elastic energy storage is achieved, which is used for the next stage of crack propagation and coalescence. The slope of this stage can be used as the tensile modulus of the sample. The second stage is the plastic development stage where the growth rates of the stress with strain slowdown, which shows the characteristics of strain hardening. As the temperature decreases, the proportion of this stage in the stress curve gradually decreases, and the internal microcracks in the sample expand rapidly and reach their tensile stress limit after absorbing energy. The third stage is the failure stage, where the stress decreases with the strain. As

the temperature decreases, the decline rate of the stress is enhanced, which may be caused by the shrinkage of the rock matrix and the enhancement of brittleness. This stage shows the obvious characteristics of plastic softening.

Under the same freezing temperature, the stress-strain curves of fractured sandstone with different fissure angles are different, mainly reflected in the slope of elastic stage and failure stage, and the length of the plastic stage, but none of them show a certain rule. With lower temperature, the slope of the elastic stage first decreases and then increases; the corresponding peak strain and the length of the plastic stage show a similar trend. This should be attributed to the coupling effects of frost damage-induced weakening and freezing-induced strengthening. As temperature decreases, pore water freezes and its volumetric expansion during freezing expands pores and microcracks; rock is thus damaged. On the other hand, ice in pores acts as both cement providing extra adhesive force and filling providing supporting force during rock failure; therefore, rock is strengthened.

**3.3. Peak Stress.** The peak stress is the ultimate bearing capacity of a material when it fails and is an important parameter to characterize rock strength. The maximum value on the stress-strain curve obtained from the dynamic splitting test of frozen sandstone is its tensile strength, and its change law is shown in Figure 5. It is seen that, under the test conditions, the dynamic tensile strength of the fractured sandstone varied with the loading angle within only  $\pm 0.5 \text{ MPa}$  when at the same temperature, which does not form a specific change rule. As the temperature decreases, the strength of the fractured sandstone gradually increases. The change rules of the cracks at each dip are nearly the same, and a linear relationship is fit. This may be due to the small impact speed of the test and the small influence of the fissure angle on the strength of the specimen. The strength of the fissure ice and rock matrix is the primary controlling factor for the strength of the fractured sandstone.

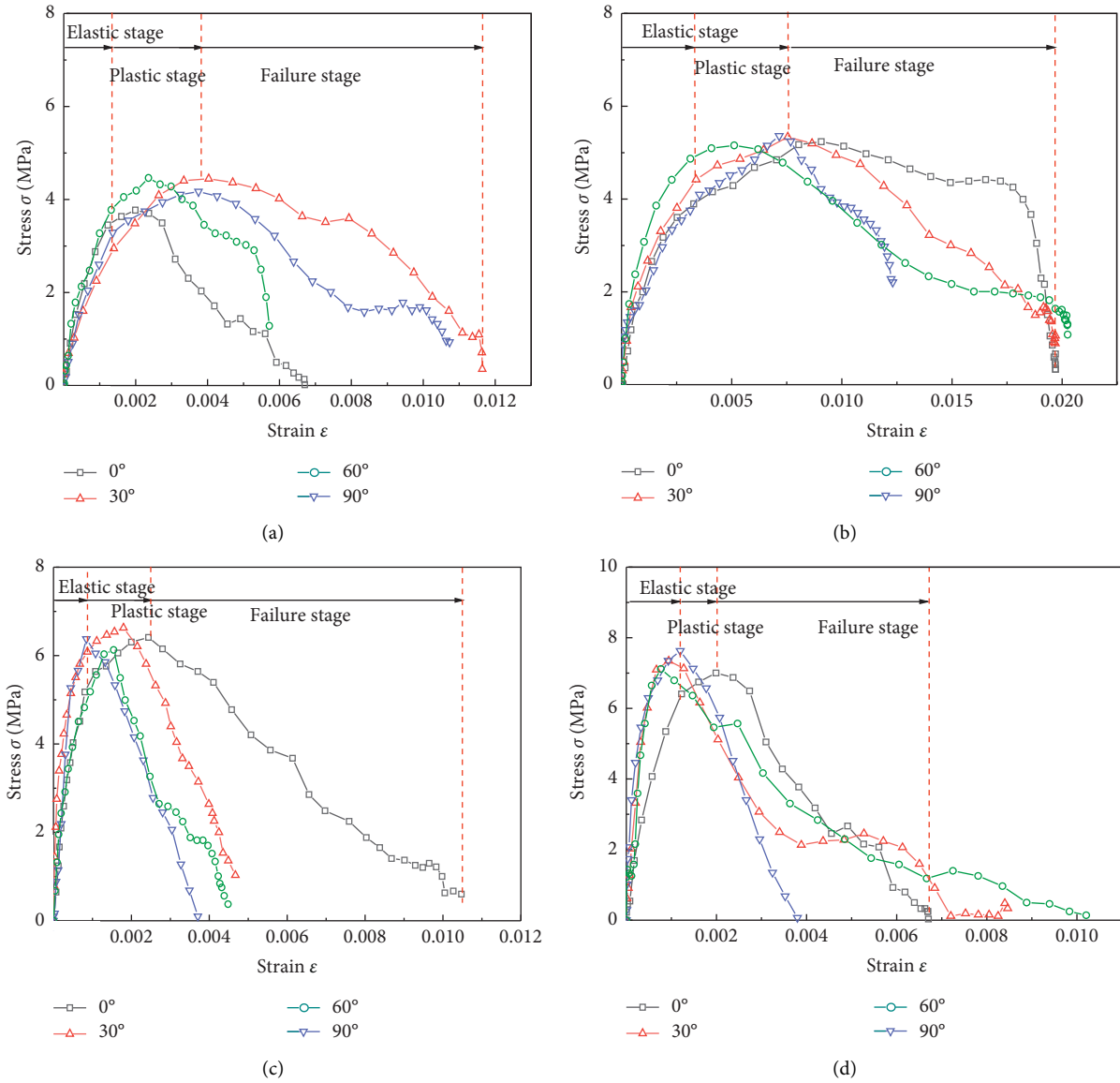


FIGURE 4: Dynamic splitting stress-strain curve of fractured sandstone at various fissure angles and subzero temperatures. (a)  $T = -5^{\circ}\text{C}$ . (b)  $T = -10^{\circ}\text{C}$ . (c)  $T = -15^{\circ}\text{C}$ . (d)  $T = -20^{\circ}\text{C}$ .

**3.4. Crack Propagation and Coalescence.** According to the dynamic splitting test process of fractured sandstone at different freezing temperatures, the failure mode of the sample under the same fissure angle is basically the same and does not change significantly with lower temperatures. The failure process of the specimen collected at  $-5^{\circ}\text{C}$  is analyzed as an example. Photos of the failure process at each loading angle collected with high-speed photography are shown in Figures 6 and the schematic diagram of the failure process is shown in Figure 7.

It is seen from Figure 6 that the loading angle significantly impacts the dynamic split failure model of fractured sandstone. When the impact loading direction is parallel to the fissure ( $\theta = 0^{\circ}$ ), tensile failure of the sample along the loading direction occurs when the fissure ice is detached from the fissure wall. The compression strength of the ice is much greater than the tensile strength at the interface, so

the specimen is stretched along the normal direction of the artificial fissure. Moreover, there is a stress concentration at the contact end of the incident rod and the test piece. Under the continuous action of the stress wave, the rock matrix in this area is crushed into small lumps (Figures 6(a) and 7(a)).

When the loading direction is not parallel to the artificial fissure (not perpendicular as well), tensile crack is initiated at the tip of the artificial fissure before it propagates to the contact surface between the sample and the pressure bar. At small fissure angles (for instance,  $\theta = 30^{\circ}$ ), the ice-rock interface in the fissure breaks under tension which is the final stage of failure; that is, the sample only exhibits tensile cracking (Figures 6(b) and 7(b)). While at large fissure angles (e.g.,  $\theta = 60^{\circ}$ ), the ice-rock interface in the fissure experiences shear failure before the final rupture of the sample (Figures 6(c) and 7(c)).

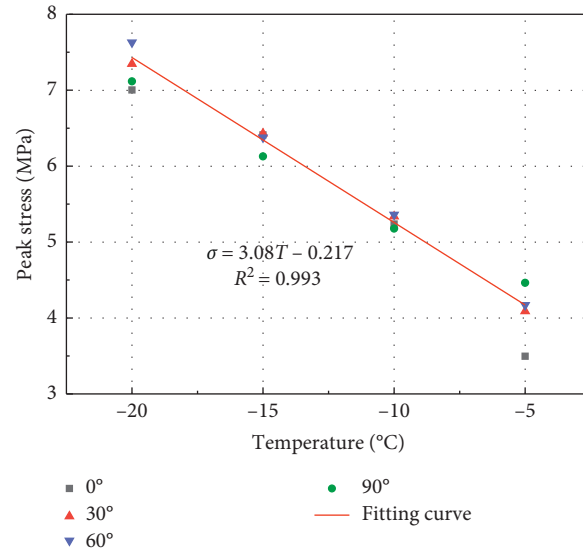


FIGURE 5: Peak stress change of frozen fractured sandstone with loading angle and freezing temperature.

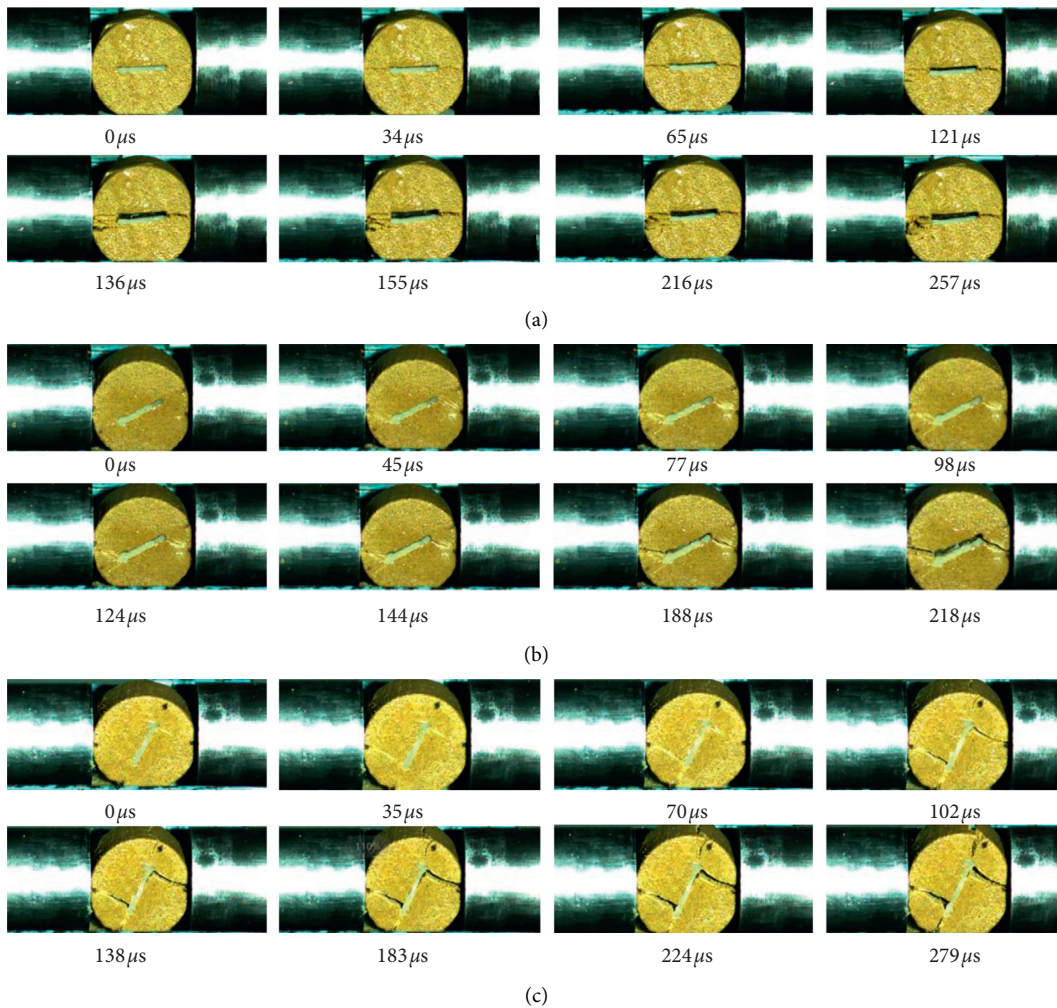


FIGURE 6: Continued.



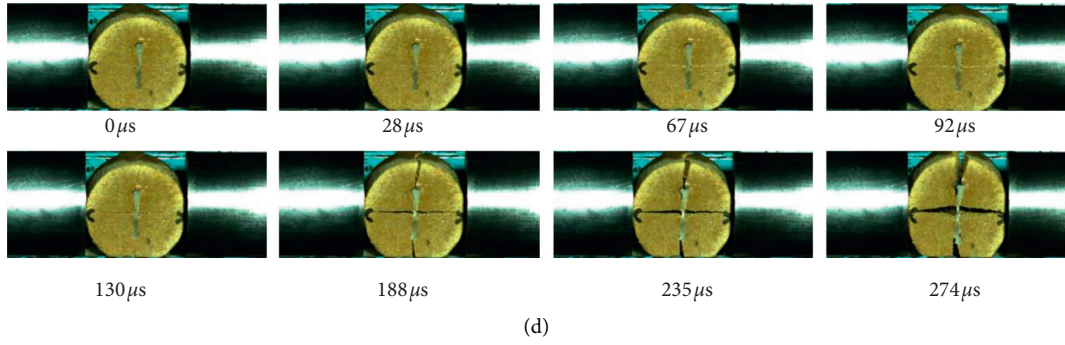


FIGURE 6: Failure process of samples with different fissure angles recorded by the high-speed photography at  $-5^{\circ}\text{C}$ . (a)  $T = -5^{\circ}\text{C}$ ,  $\theta = 0^{\circ}$ . (b)  $T = -5^{\circ}\text{C}$ ,  $\theta = 30^{\circ}$ . (c)  $T = -5^{\circ}\text{C}$ ,  $\theta = 60^{\circ}$ . (d)  $T = -5^{\circ}\text{C}$ ,  $\theta = 90^{\circ}$ .

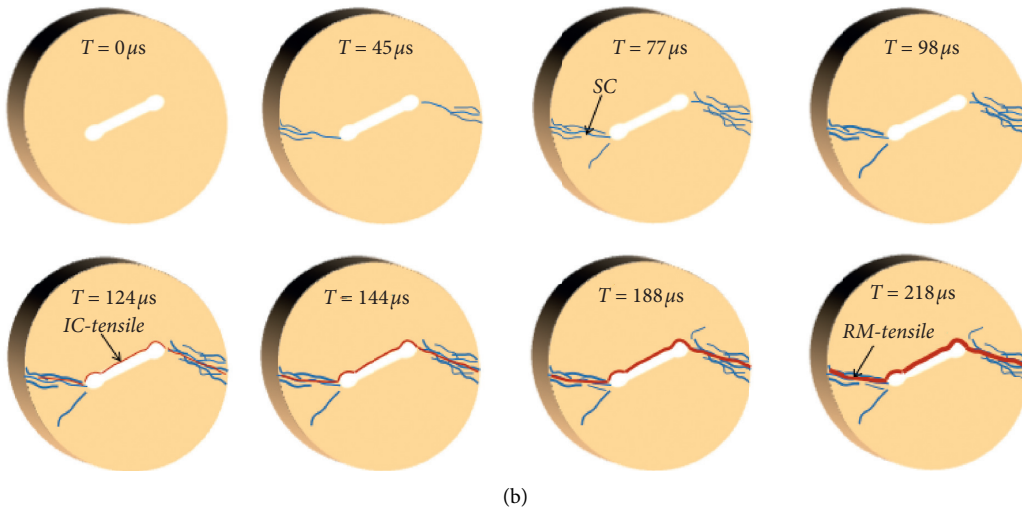
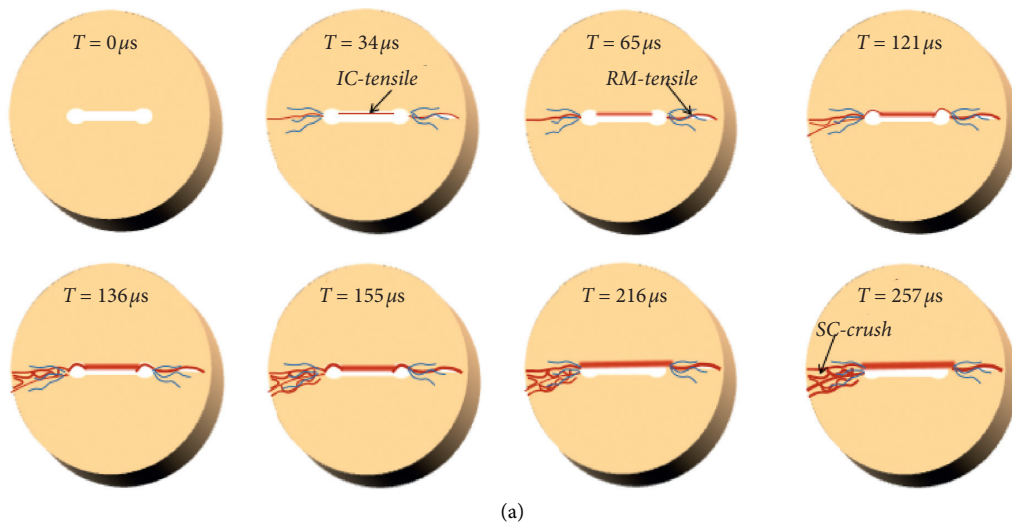


FIGURE 7: Continued.



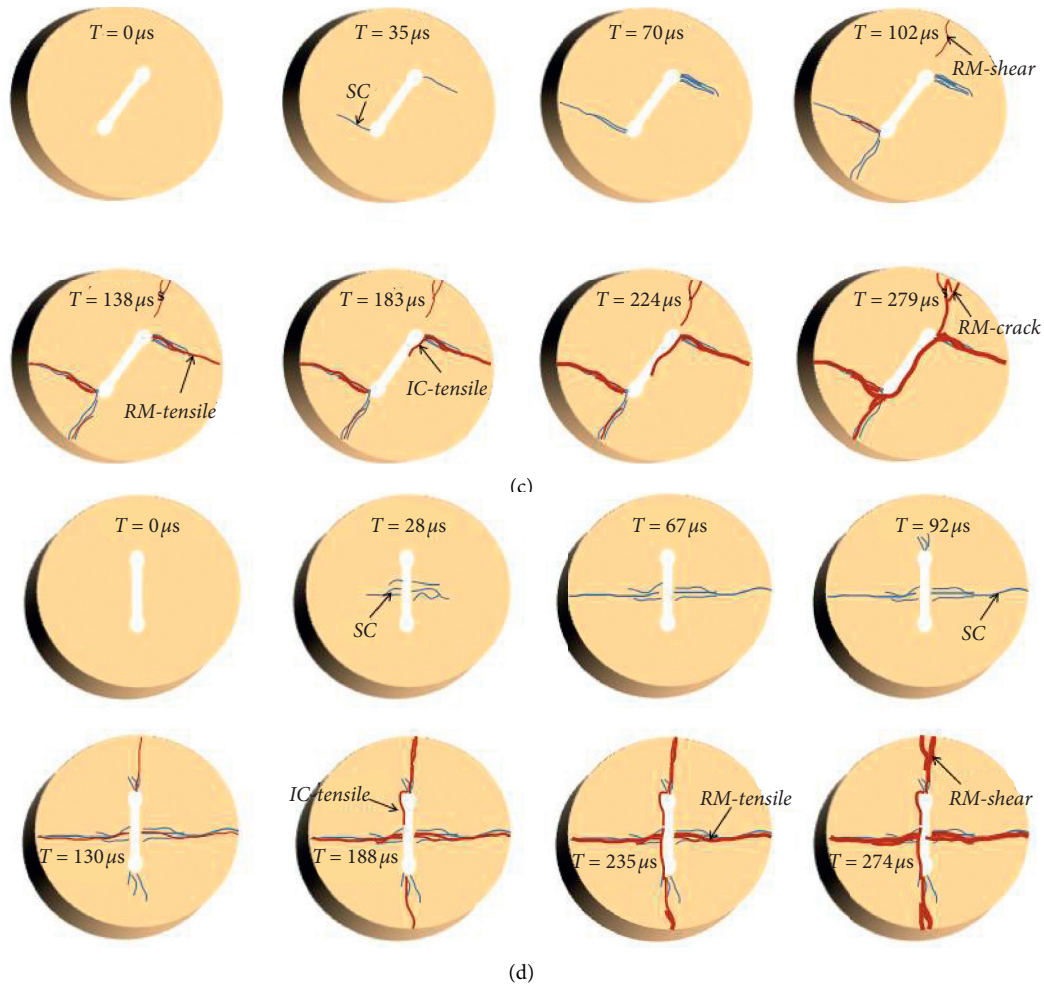


FIGURE 7: Schematic diagram of crack propagation in the fractured sandstone. (Note: IC is interface crack; RM is rock matrix; SC is stress-concentration) (a)  $T = -5^{\circ}\text{C}$ ,  $\theta = 0^{\circ}$ . (b)  $T = -5^{\circ}\text{C}$ ,  $\theta = 30^{\circ}$ . (c)  $T = -5^{\circ}\text{C}$ ,  $\theta = 60^{\circ}$ . (d)  $T = -5^{\circ}\text{C}$ ,  $\theta = 90^{\circ}$ .

In the case that the impact loading direction is perpendicular to the artificial fissure ( $\theta = 90^{\circ}$ ), tensile crack is initiated at the center of the specimen along the loading direction. With the propagation of the tensile crack towards the pressure bar, fissure ice is pulled apart in the middle. Afterwards, tensile cracking occurs at the top and bottom edge of the sample along the artificial fissure direction, which is caused by stretching waves formed after the reflection of the stress wave (Figures 6(d) and 7(d)).

The above experimental results show that the failure modes of specimens differ under different loading angles; the underlying mechanisms are embedded in the interaction between fissure ice and rock matrix. Under an impact load, stress-concentration first appears at the ice-rock interface in the artificial fissure. Regardless of the fissure angle, tensile cracking is initiated at the stress-concentration zone and then propagates towards the loading end. Fissure ice provides both resistance to deformation and resistance to crack propagation. When the fissure angle is 0, fissure ice is under tension, and due to its resistance to deformation, tensile cracking will not be initiated until the ice-rock interface is detached (Figure 8(a)). In the case of nonzero loading angles

(not  $90^{\circ}$  neither), tensile cracking is initiated close to the tip of the fissure and propagates towards the loading bar; afterwards, however, shear cracking dominates the failure process. The cohesion at the ice-rock interface provides resistance to shear cracking, after the shear failure of which final failure occurs (Figure 8(b)). When the impact loading direction is perpendicular to the artificial fissure ( $\theta = 90^{\circ}$ ), tensile cracking is initiated at the center of the sample along the loading direction. With the propagation of the tensile crack towards the pressure bar, fissure ice is pulled apart in the middle, suggesting that tensile strength of ice itself provides the resistance to failure in this case.

## 4. Constitutive Model

**4.1. Establishment of the Constitutive Relationship.** Combining the statistic damage model and viscoelastic model, Shan [24] built a time effect damage model of rock under dynamic loading. Based on this model, we considered the influence of fissure angle and freezing temperature on rock constitutive relation and then built a dynamic constitutive model for frozen fractured sandstone.

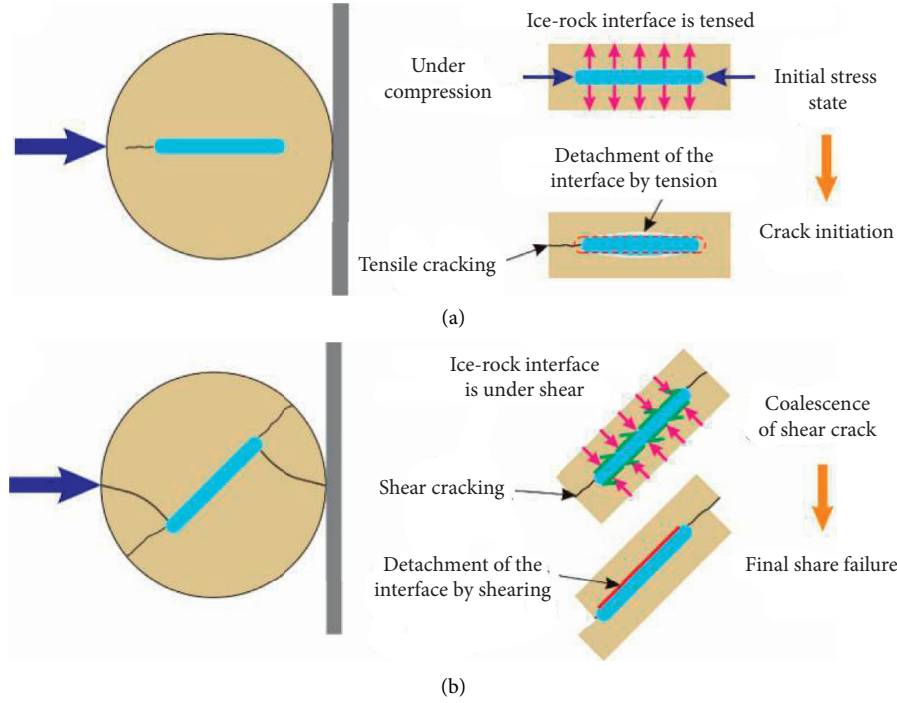


FIGURE 8: Schematic diagram of the mechanism of how ice alters the dynamic properties of frozen fractured sandstone.

The basic assumptions of this model are as follows:

- (1) The interior microelements of rock are regarded as the parallel combination of damage element and viscous element, which satisfies

$$\varepsilon = \varepsilon_a = \varepsilon_b, \quad (3)$$

$$\sigma = \sigma_a + \sigma_b, \quad (4)$$

where  $\varepsilon_a$  is the strain of damage element;  $\varepsilon_b$  is the strain of viscous element;  $\sigma_a$  is the stress of damage element; and  $\sigma_b$  is the stress of viscous element.

- (2) Under the static load, the viscous element does not work. It only works when the loading rate reaches a certain value; its constitutive relation is

$$\sigma = \eta \frac{d\varepsilon}{dt}, \quad (5)$$

where  $\eta$  is the viscosity coefficient.

- (3) Based on the heterogeneity and anisotropy of fractured rock mass, the physical properties of each element are in probability distribution. So, the mechanical properties of the element can be mathematically described by the statistical method. It is assumed that the strength of rock elements obeys Weibull distribution [25], and its probability density function is

$$P(\varepsilon) = \frac{m}{\alpha} \left(\frac{\varepsilon}{\alpha}\right)^{m-1} \exp\left[-\left(\frac{\varepsilon}{\alpha}\right)^m\right], \quad (6)$$

where  $P(\varepsilon)$  is the corresponding intensity probability and  $m$  and  $\alpha_0$  are Weibull distribution constants.

In the process of deformation and failure of fractured rock mass under load, the axial stress is mainly borne by four parts: intact rock, the damage caused by fissure, the damage caused by load, and the damage under the coupling action of fissure and load. In the axial direction, it is assumed that the total element area of fractured rock mass is  $A$ , the damage element area caused by prefabricated fissure is  $A_\beta$ , the damage element area caused by the load is  $A_s$ , and the damage element area caused by coupling of fissure and load is  $A_1$ .

The damage caused by fissure ( $D_\beta$ ) can be defined as the ratio of the damage element area caused by the prefabricated fissure to the total element area:

$$D_\beta = \frac{A_\beta}{A}. \quad (7)$$

The fractured rock mass is further damaged under the action of load, and the damage variable under load is defined as ( $D_s$ )

$$D_s = \frac{A_s - A_1}{A - A_\beta}. \quad (8)$$

As a whole, the microelement failure of rock mass is caused by the combined action of prefabricated fissure and load. Therefore, the total damage variable of fractured rock mass under load can be defined according to the final damage degree of rock mass:

$$D_t = \frac{A_s + A_\beta - A_1}{A}. \quad (9)$$

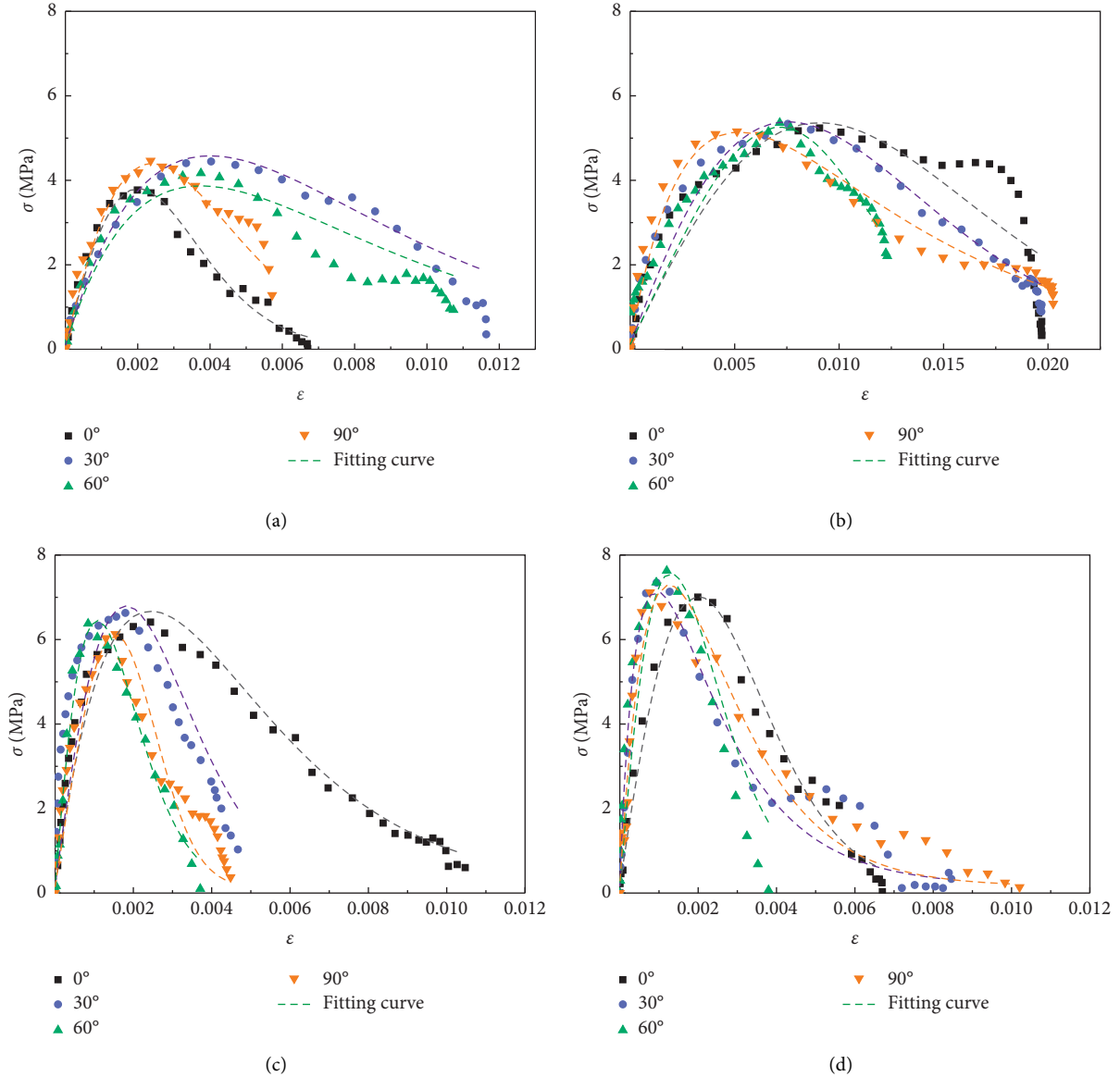


FIGURE 9: Fitting curve of the constitutive equation. (a)  $T = -5^{\circ}\text{C}$ . (b)  $T = -10^{\circ}\text{C}$ . (c)  $T = -15^{\circ}\text{C}$ . (d)  $T = -20^{\circ}\text{C}$ .

Substituting equations (7) and (8) into (9), the relationship among  $D_{\beta}$ ,  $D_s$ , and  $D_t$  can be obtained:

$$D_t = D_s + D_{\beta} - D_s D_{\beta}. \quad (10)$$

It can be seen from equation (10) that the combined action of fissure and load aggravates the total damage of rock, but the coupling action of the two weakens the total damage to some extent and shows obvious nonlinear characteristics.

According to the theory of macroscopic phenomenological damage mechanics, the degree of deterioration inside the material can be characterized by the response of macroscopic mechanical properties of the rock mass. Therefore, the elastic modulus was selected as the measurement benchmark of the initial damage of the fractured rock mass, and  $D_{\beta}$  was defined as

$$D_{\beta} = 1 - \frac{E_{\beta}}{E_0}, \quad (11)$$

where  $\beta$  is the fissure angle and  $E_{\beta}$  is the elastic modulus of fractured rock mass with different fissure angles.  $E_0$  is the elastic modulus of intact rock.

The deformation and failure of rock mass are a continuous process of continuous internal damage of material. By integrating equation (6), the damage accumulation effect of the destruction of the element can be obtained, and the damage variable under load can be expressed as

$$D_s = \int_0^{\varepsilon} P(\varepsilon) d\varepsilon = 1 - \exp\left[-\left(\frac{\varepsilon}{\alpha}\right)^m\right]. \quad (12)$$

Substituting equations (11) and (12) into (10), the total damage of fractured rock mass can be obtained as follows:

$$D_t = 1 - \frac{E_\beta}{E_0} \exp\left[-\left(\frac{\varepsilon}{\alpha}\right)^m\right]. \quad (13)$$

According to the Lemaitre strain equivalent hypothesis, the constitutive relation of fractured rock mass is

$$[\sigma] = [\sigma^*](1 - D_t) = [E][\varepsilon][1 - D], \quad (14)$$

where  $[\sigma]$  is the nominal stress matrix;  $[\sigma^*]$  is the effective stress matrix;  $D$  is the damage variable;  $[E]$  is the elastic matrix; and  $[\varepsilon]$  is the strain matrix.

According to (13) and (14), the constitutive relation of the damaged body under uniaxial condition can be written as

$$\sigma_a = E_0(1 - D_t)\varepsilon = E_\beta\varepsilon \exp\left[-\left(\frac{\varepsilon}{\alpha}\right)^m\right]. \quad (15)$$

According to the geometrical conditions of the stress-strain curve, we get

$$a = \frac{\varepsilon_{\max}}{(1/m)^{1/m}}, \quad (16)$$

$$m = \frac{1}{\ln(E\varepsilon_{\max}/\sigma_{\max})}, \quad (17)$$

where  $\sigma_{\max}$  is the peak stress and  $\varepsilon_{\max}$  is the strain at peak stress. Substituting equations (16) and (17) into equation (15) gives

$$\sigma_a = E_\beta\varepsilon \exp\left[-\frac{1}{m}\left(\frac{\varepsilon}{\varepsilon_{\max}}\right)^m\right]. \quad (18)$$

According to hypotheses (1) and (2), the dynamic damage constitutive relation of fractured rock mass under uniaxial condition can be obtained by combining equations (3)–(5) and (18):

$$\sigma = \sigma_a + \sigma_b = E_\beta\varepsilon \exp\left[-\frac{1}{m}\left(\frac{\varepsilon}{\varepsilon_{\max}}\right)^m\right] + \eta\dot{\varepsilon}. \quad (19)$$

Considering the influence of freezing temperature on dynamic constitutive properties of fractured sandstone, we add the temperature term to equation (19), so it becomes

$$\sigma = \left\{E_\beta\varepsilon \exp\left[-\frac{1}{m}\left(\frac{\varepsilon}{\varepsilon_{\max}}\right)^m\right] + \eta\dot{\varepsilon}\right\}T^{*n}, \quad (20)$$

where  $T^{*n}$  is the temperature influencing factor, which can be calculated by the following equation:

$$T^* = \frac{T}{T_n}, \quad (21)$$

where  $T$  is the freezing temperature of frozen fractured sandstone,  $T_n$  is the reduced temperature parameter of temperature, and the value of  $T_n$  is  $-5^\circ\text{C}$ .

So, the final dynamic constitutive model for frozen fractured sandstone is

$$\sigma = \left\{E_\beta\varepsilon \exp\left[-\frac{1}{m}\left(\frac{\varepsilon}{\varepsilon_{\max}}\right)^m\right] + \eta\dot{\varepsilon}\right\}\left(\frac{T}{T_n}\right)^n. \quad (22)$$

TABLE 2: Constitutive parameters.

Sample number	$E_\beta$ (GPa)	$\varepsilon_{\max}$ (%)	$m$	$\eta(10^{-3})$	$n$
$-5^\circ\text{C}/0^\circ$	3.307	0.201	1.7		
$-5^\circ\text{C}/30^\circ$	2.852	0.400	1.1		
$-5^\circ\text{C}/60^\circ$	2.742	0.374	1.0		
$-5^\circ\text{C}/90^\circ$	3.541	0.239	1.5	1.52	0.5
$-10^\circ\text{C}/0^\circ$	0.713	0.906	1.8		
$-10^\circ\text{C}/30^\circ$	0.922	0.755	1.6		
$-10^\circ\text{C}/60^\circ$	0.726	0.716	2.8		
$-10^\circ\text{C}/90^\circ$	2.022	0.521	0.9		
$-15^\circ\text{C}/0^\circ$	3.853	0.244	1.1		
$-15^\circ\text{C}/30^\circ$	3.968	0.181	1.6		
$-15^\circ\text{C}/60^\circ$	6.551	0.108	1.5		
$-15^\circ\text{C}/90^\circ$	3.396	0.154	2.4	1.52	0.5
$-20^\circ\text{C}/0^\circ$	3.105	0.199	1.7		
$-20^\circ\text{C}/30^\circ$	12.95	0.094	0.8		
$-20^\circ\text{C}/60^\circ$	5.553	0.130	1.5		
$-20^\circ\text{C}/90^\circ$	7.689	0.076	1.0		

**4.2. Parameter Determination.** In equation (22), there are 5 parameters unknown.  $\varepsilon_{\max}$  can be obtained directly from Figure 4. The other 4 parameters can be obtained by fitting with the experimental curves. The fitting results are shown in Figure 9. All the parameters of the dynamic constitutive model of frozen fractured sandstone are listed in Table 2.

It can be seen from Figure 9 that the experimental data agree well with the constitutive equation fitting curves, which can accurately reflect the stress-strain relationship at each stage. This indicates that the dynamic tensile mechanical properties of frozen fractured sandstone can be characterized by the above dynamic constitutive relationship considering the effect of fissure angle and freezing temperature.

## 5. Conclusions

This study investigates the dynamic properties of frozen fractured sandstone. By adopting specimens containing a single fissure filled with ice, we reveal the first-order rules of how predominant factors (e.g., fissure angle and freezing temperature) affect the dynamic properties of frozen fractured rock. Accordingly, a constitutive model considering the effect of fissure angle and freezing temperature is proposed. We draw the following conclusions:

- (1) In the dynamic splitting tests, the stress curves of the fractured sandstone are divided into three stages: elastic, plastic, and failure. Under different fissure angles, the dynamic tensile strength of the fractured sandstone has no obvious change rule at the same freezing temperature. As the temperature decreases, the dynamic tensile strength of fractured sandstone gradually increases following a linear relationship. With lower temperature, the slope of the elastic stage first decreases and then increases, and the corresponding peak strain and the length of the plastic stage show a similar trend. This should be attributed to the coupled effects of frost damage-induced weakening and freezing-induced strengthening.

- (2) The fissure angle significantly impacts the dynamic split failure model of fractured sandstone. When the impact loading direction is parallel to the fracture, tensile failure of the specimen along the loading direction occurs when the fissure ice is detached from the fissure wall. When the loading direction is not parallel to the artificial fissure (not perpendicular as well), tensile crack is initiated at the tip of the artificial fissure before it propagates to the contact surface between the specimen and the pressure bar. In the case that the impact loading direction is perpendicular to the artificial fissure, tensile crack is initiated at the center of the sample along the loading direction. With the propagation of the tensile crack towards the pressure bar, fissure ice is pulled apart in the middle. Afterwards, tensile cracking occurs at the top and bottom edge of the sample along the artificial fissure direction.
- (3) The failure modes of specimens differ under different fissure angles; the underlying mechanisms are embedded in the interaction between fissure ice and rock matrix. Fissure ice provides both resistance to deformation and resistance to crack propagation. When the fissure angle is zero, fissure ice is under tension and, due to its resistance to deformation, tensile cracking will not be initiated until the ice-rock interface is detached. In the case of nonzero fissure angles (not 90° neither), shear cracking dominates the failure process after the initiation of tensile cracking. The cohesion at the ice-rock interface provides resistance to shear cracking. When the fissure angle is 90°, with the propagation of the tensile crack towards the pressure bar, fissure ice is pulled apart in the middle, suggesting that the tensile strength of ice itself provides resistance to failure in this case.
- (4) Considering the effect of fissure angle and freezing temperature on dynamic mechanical properties of frozen fractured sandstone, a constitutive model describing the dynamic behavior of frozen fractured rocks is proposed employing the strain equivalence principle and time effect damage model. The test data agrees well with the constitutive equation curves, which can accurately reflect the stress-strain relationship at each stage.

### Data Availability

The data used to support the findings of this study are included within the article.

### Conflicts of Interest

The authors declared that there are no conflicts of interest.

### Acknowledgments

The study was funded by the National Natural Science Foundation of China (Grant nos. 41702334 and 41702339)

and the Key Research and Development Program in Shaanxi Province (2019SF-264).

### References

- [1] H. Jia, F. Zi, G. Yang et al., "Influence of pore water (ice) content on the strength and deformability of frozen argillaceous siltstone," *Rock Mechanics and Rock Engineering*, vol. 53, no. 2, pp. 967–974, 2020.
- [2] S. Huang, Y. Ye, X. Cui, A. Cheng, and G. Liu, "Theoretical and experimental study of the frost heaving characteristics of the saturated sandstone under low temperature," *Cold Regions Science and Technology*, vol. 174, Article ID 103036, 2020.
- [3] Y. Shen, H. Yang, J. Xi et al., "A novel shearing fracture morphology method to assess the influence of freeze–thaw actions on concrete–granite interface," *Cold Regions Science and Technology*, vol. 169, 2020.
- [4] H. Zhang, C. Yuan, G. Yang et al., "A novel constitutive modelling approach measured under simulated freeze–thaw cycles for the rock failure," *Engineering with Computers*, vol. 37, no. 1, pp. 779–792, 2019.
- [5] H. Jia, S. Ding, Y. Wang et al., "An NMR-based investigation of pore water freezing process in sandstone," *Cold Regions Science and Technology*, vol. 168, Article ID 102893, 2019.
- [6] L. Tang, Y. Du, L. Liu, L. Jin, L. Yang, and G. Li, "mechanism of unfrozen water on the frozen soil–structure interface during the freezing–thawing process," *Geomechanics and Engineering*, vol. 22, no. 3, pp. 245–254, 2020.
- [7] Q. Sun, Z. Dong, and H. Jia, "Decay of sandstone subjected to a combined action of repeated freezing–thawing and salt crystallization," *Bulletin of Engineering Geology and the Environment*, vol. 78, no. 8, pp. 5951–5964, 2019.
- [8] L. N. Y. Wong and H.-Q. Li, "Numerical study on coalescence of two pre-existing coplanar flaws in rock," *International Journal of Solids and Structures*, vol. 50, no. 22–23, pp. 3685–3706, 2013.
- [9] R. Yang, S. Fang, W. Li, Y. Yang, and Z. Yue, "Experimental study on the dynamic properties of three types of rock at negative temperature," *Geotechnical and Geological Engineering*, vol. 37, no. 1, pp. 455–464, 2019.
- [10] L. Weng, Z. Wu, and Q. Liu, "Dynamic mechanical properties of dry and water-saturated siltstones under sub-zero temperatures," *Rock Mechanics and Rock Engineering*, vol. 53, pp. 4381–4401, 2020.
- [11] A. Mardoukhi, Y. Mardoukhi, M. Hokka, and V. T. Kuokkala, "Effects of test temperature and low temperature thermal cycling on the dynamic tensile strength of granitic rocks," *Rock Mechanics and Rock Engineering*, vol. 21, pp. 1–12, 2020.
- [12] S. Nemat-Nasser and H. Horii, "Compression-induced nonplanar crack extension with application to splitting, exfoliation, and rockburst," *Journal of Geophysical Research: Solid Earth*, vol. 87, no. 8, pp. 6805–6821, 1982.
- [13] F. Dai, S. Huang, K. Xia, and Z. Tan, "Some fundamental issues in dynamic compression and tension tests of rocks using split hopkinson pressure bar," *Rock Mechanics and Rock Engineering*, vol. 43, no. 6, pp. 657–666, 2010.
- [14] T. De Kock, M. A. Boone, T. De Schryver et al., "A pore-scale study of fracture dynamics in rock using X-ray micro-CT under ambient freeze–thaw cycling," *Environmental Science & Technology*, vol. 49, no. 5, pp. 2867–2874, 2015.
- [15] P. Dong, B. Wu, K. Xia, and Q. Wang, "Fracture modes of single-flawed rock-like material plates subjected to dynamic compression," *International Journal of Geomechanics*, vol. 20, no. 9, Article ID 04020145, 2020.

- [16] X. Li, T. Zhou, and D. Li, "Dynamic strength and fracturing behavior of single-flawed prismatic marble Specimens under impact loading with a split-Hopkinson pressure bar," *Rock Mechanics and Rock Engineering*, vol. 50, no. 1, pp. 29–44, 2017.
- [17] Z. Yan, F. Dai, Y. Liu, and H. Du, "Experimental investigations of the dynamic mechanical properties and fracturing behavior of cracked rocks under dynamic loading," *Bulletin of Engineering Geology and the Environment*, vol. 79, no. 10, pp. 5535–5552, 2020.
- [18] Y. Li, F. Dai, M. Wei, and H. Du, "Numerical investigation on dynamic fracture behavior of cracked rocks under mixed mode I/II loading," *Engineering Fracture Mechanics*, vol. 235, Article ID 107176, 2020.
- [19] Y. Yang, J. Wang, S. Fang, and N. Zhang, "Experimental study on dynamic mechanical properties of red sandstone under low temperatures," *Journal of China Coal Society*, vol. 43, no. 4, pp. 967–975, 2018.
- [20] L. Wang, H. Su, Y. Qin, and S. Chen, "Study on dynamic constitutive model of weakly consolidated soft rock in western China," *Shock and Vibration*, vol. 2020, Article ID 8865013, 10 pages, 2020.
- [21] L. Wang, H. Su, S. Chen, and Y. Qin, "Nonlinear dynamic constitutive model of frozen sandstone based on Weibull distribution," *Advances in Civil Engineering*, vol. 2020, Article ID 6439207, 12 pages, 2020.
- [22] L. Weng, Z. Wu, Q. Liu, and Z. Wang, "Energy dissipation and dynamic fragmentation of dry and water-saturated siltstones under sub-zero temperatures," *Engineering Fracture Mechanics*, vol. 220, Article ID 106659, 2020.
- [23] R. Shan, Y. Song, L. Song, and Y. Bai, "Dynamic property tests of frozen red sandstone using a split hopkinson pressure bar," *Earthquake Engineering and Engineering Vibration*, vol. 18, no. 3, pp. 511–519, 2019.
- [24] S. Liang, "The study on damage evolution and constitutive model of the granite under constant strain rate impact", Ph.D dissertation, China University of Mining and Technology, Beijing, China, 2016.
- [25] C. Fan, S. Li, D. Elsworth, J. Han, and Z. Yang, "Experimental investigation on dynamic strength and energy dissipation characteristics of gas outburst prone coal," *Energy Science and Engineering*, vol. 8, no. 4, pp. 1015–1028, 2020.



## Research Article

# Experimental Study on Injuries to Animals Caused by a Gas Explosion in a Large Test Laneway

Runzhi Li <sup>1</sup>, Zhigang Zhang <sup>1</sup>, Rongjun Si <sup>1</sup>, Lei Wang <sup>1</sup>, Shengnan Li <sup>2</sup>,  
Weidong Wu <sup>3</sup>, Jia Cao <sup>4</sup> and Wenjie Ren <sup>3</sup>

<sup>1</sup>Fire and Explosion Prevention Research Branch, China Coal Technology and Engineering Group Chongqing Research Institute, Chongqing 400037, China

<sup>2</sup>School of Safety Science and Engineering, Liaoning Technical University, Huludao 125105, Liaoning, China

<sup>3</sup>School of Public Health, Xinxiang Medical University, Xinxiang 453003, Henan, China

<sup>4</sup>Army Medical University, Chongqing 400038, China

Correspondence should be addressed to Runzhi Li; [runzhi\\_li@126.com](mailto:runzhi_li@126.com)

Received 21 November 2020; Revised 11 February 2021; Accepted 20 March 2021; Published 16 April 2021

Academic Editor: Qi Zhao

Copyright © 2021 Runzhi Li et al. This is an open access article distributed under the Creative Commons Attribution License, which permits unrestricted use, distribution, and reproduction in any medium, provided the original work is properly cited.

Gas explosion accidents in underground coal mines caused a significant number of casualties. By using a large laneway test system, the damage to Sprague-Dawley (SD) rats at locations at different distances from the source of ignition along the direction of propagation of an explosion was investigated after 100 m<sup>3</sup> of the gas-air mixture was ignited and exploded. In this way, the data pertaining to explosion flames and explosion pressures at different propagation distances were obtained to investigate the propagation of explosion flames and explosion pressures along the laneway. Besides, the damage to SD rats at different propagation distances was statistically analyzed. Furthermore, the damage mechanism of explosion flames, explosion pressures, and hazardous gases on humans or animals was discussed. The results indicated that explosive blast injury induced by the gas explosion was the primary reason for the death of animals and SD rats at a distance equal to or greater than 80 m from the point of ignition under the effects of an explosive blast even though SD rats at a distance of 240 m were killed. During the explosion of 100 m<sup>3</sup> of mixed gas, the explosion flames propagated 40 m from the point of ignition, and the SD rats in the cage located some 40 m from the point of ignition were subjected to combined damage involving being burned at high temperature and suffering the effects of the explosive blast. These findings provide a theoretical basis for emergency rescue and salvage after gas explosion accidents in underground coal mines.

## 1. Introduction

China is one of the countries suffering the most serious coal mine gas explosion accidents in the world: not only are there numerous such accidents but also great harm is caused [1]. A gas explosion accident causes not only serious damage to the mine but often cause multiple casualties, with all the concomitant negative effects on society.

In recent years, the mechanism and propagation of gas explosions have been investigated experimentally or numerically [2–7]. Based on the available research, the factors influencing gas explosions in test pipelines, the propagation of explosion pressure, flames, etc., were investigated: this

result is expected to provide an important theoretical basis for effectively preventing and controlling gas explosion accidents in underground coal mines. Through research, the influencing factors, explosion pressure, and flame propagation trends in a gas explosion in a test pipeline were ascertained.

Some scholars demonstrated the damage of explosive blasts on humans. For example, Bowen et al. explored human injuries and overpressure endurance under the effect of blast waves by analyzing previous clinical data and experimental results [8]. Mayorga investigated the pathology of primary explosive blast injury by analyzing previous experiments on explosive blast-induced injury and clinical

data in the USA [9]. Owing to the data on injuries to the human bodies caused by explosions being hard to acquire, the relevant research was carried out by conducting animal experiments to reveal the damage mechanism of explosive blasts on various parts (including the brain [10–13], lung [14], and eyes [15, 16] of animals and the influences of an explosive blast on the animal nervous system [17], food intake, and exercise performance [18]). During the propagation of a gas explosion in an underground coal mine, overpressure induced by explosive blast waves is generated [19]. In addition to this, high-temperature flames induced by a gas explosion and hazardous gases generated by incomplete combustion of gas are also important factors causing mass death and injuries to personnel in underground coal mines. As the environmental conditions in underground coal mine are difficult to simulate, research into the damage caused by gas explosions to humans or animals in practical large test laneways has not been reported.

By using a large laneway test system and taking  $100\text{ m}^3$  of the gas-air mixture as the explosive source, the study explored the damage due to a gas explosion on Sprague-Dawley (SD) rats at different propagation distances based on the propagation laws governing explosion flames and pressures along the laneway. This research is expected to provide an important theoretical basis for emergency rescue and salvage after gas explosion accidents in the underground coal mines.

## 2. Experimental System and Methods

**2.1. Components of the Experimental System.** The experiment was conducted in a large laneway test system in Chongqing Research Institute of China Coal Technology and Engineering Group Corporation. The large laneway test system is mainly composed of a large test laneway, a comprehensive test system for explosion analysis, a gas-mixing and circulating system, and an ignition system. The system can be adopted to simulate explosion propagation experiments involving gas and coal dust at a certain scale under different conditions (Figure 1). The test laneway was 896 m long, and the main laneway available for the explosion experiment was about 700 m long. An inclined drift that was 300 m long at a dip angle of  $24^\circ$  was connected to the end of the roadway. The cross-section of the laneway appeared as a semicircular arch, with an area of  $7.2\text{ m}^2$ . The test laneway is the only large test laneway in China and also the largest in the Asia-Pacific region.

The niche box was arranged in the roadway, and the niche position was fixed relative to the roadway. Pressure and flame sensors could be installed in the niche box. Niches were arranged in the laneway and pressure and flame sensors installed therein. The presence of the niches could protect connecting cables and the sensors from the explosive blast. The sensors were connected to a monitoring system in an observation room by using data lines. From the end of the laneway where the explosion started (namely, the position of the explosion-proof door), niches were installed within 40 m at intervals of 10 m; beyond 40 m from the point of ignition, niches were arranged at intervals of 20 m. In this experiment, a GYG1401F high-frequency dynamic pressure sensor (with

a range of 0 to 0.5 MPa) was adopted; a GHZ5 (A) mine-safe ultraviolet flame sensor was used, which could quickly and accurately determine the presence of the flame, respectively, from 10 m to 140 m. The layout of the niche box in the roadway is shown in Figure 2.

**2.2. Experimental Methods.** The cages for SD rats were made by welding steel members, and each cage was enclosed all around by iron wire mesh. In the test laneway whose one end was closed while the other end was open, the explosion pressure varied with the propagation distance. To ensure that the explosion pressure can cause different degrees of injuries to SD rats, six cages were installed at intervals of 40 m from 40 m away from the point of ignition at distances (for cages 1 to 6) to the closed end of the laneway of 40 m, 80 m, 120 m, 160 m, 200 m, and 240 m, respectively. During the explosion experiment, 18 SD rats were put into each cage. To avoid overturning of the cages, the cages were fixed to the laneway floor using setscrews (Figure 3).

During the experiment, the gas (its composition includes methane, ethane, propane, butane, hydrogen sulfide, and carbon dioxide; the extracted gas was treated by gas branch to obtain pure methane gas with a purity of 99.9%) extracted from the local Zhongliangshan Coal Mine in Chongqing, China, was used as the explosive source and was injected into the explosion chamber in the test laneway, thus forming a gas-air mixture. The volume of the gas-air mixture was set to  $100\text{ m}^3$  with a gas concentration of 9.0%. Two fuse heads were used as ignition sources in which the energy of each forehead was 10 J. The experimental conditions are displayed in Table 1.

This experiment was carried out three times. During the three replicate experiments, although there are some differences in the experimental data, the overall trend therein is the same. Some omissions of measured data inevitably arose: through comparative analysis, the most representative group of data was selected for analysis and research. During the experiment, 18 SD rats were placed in each cage fixed in advance for preexperiment checks and tests on the arrangement of sensors in niches in the laneway before closing the niches. After sealing the laneway using plastic film, the hydraulic explosion-proof door was closed to form a sealed explosion chamber between the sealing film and the explosion-proof door. The volume of the sealed explosion chamber was  $100\text{ m}^3$  according to the requirements of the experiment. By using the gas-mixing and circulating system, a certain amount of gas was injected into the explosion chamber and stirred until the gas and air were uniformly mixed. After the gas and air were uniformly mixed, the concentration was accurately measured by a CJG10 optical interference gas detector. The gas mixture was ignited to make gas explode in the laneway. Additionally, the test system was triggered to collect the explosion pressures and flame front at various measurement points along the direction of propagation of the explosive blast waves in the laneway. After completing the experiment, the air in the test laneway was exhausted via the exhaust system. After 20 min, casualties among the SD rats in the laneway were checked.

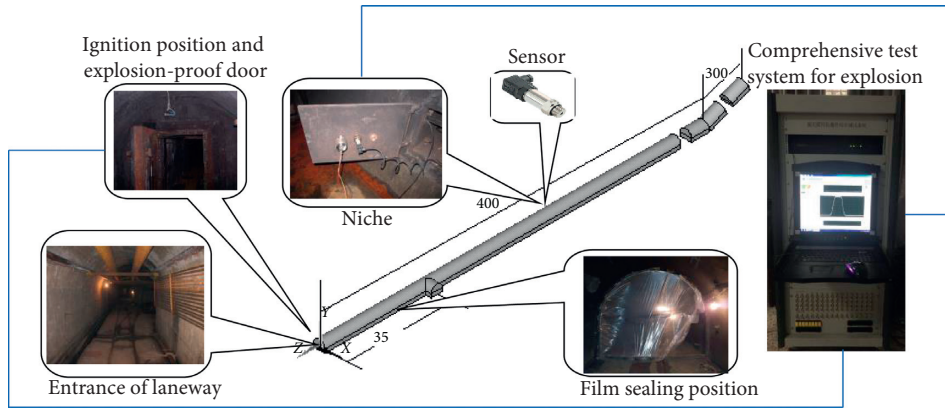


FIGURE 1: Layout of the large laneway test system.

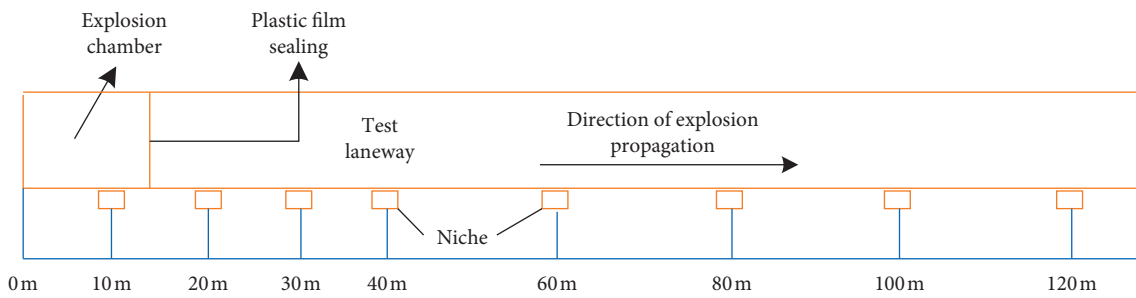


FIGURE 2: Layout of the niches.



FIGURE 3: Arrangement diagrams of SD rat cages in the laneway.

TABLE 1: Experimental conditions.

Ignition energy (J)	Volume of mixed gas (m <sup>3</sup> )	Volume of pure gas (m <sup>3</sup> )	Concentration of gas (%)
20	100	9.0	9.0

### 3. Analysis of the Propagation of a Gas Explosion

**3.1. Propagation of Explosion Flames.** After conducting the explosive test, the explosion flames spread to the location at 40 m from the source, while no explosion flame signals were detected in the area 60 m and more than 60 m from the point of ignition. The explosion flame signals at various measuring points within the area located within 40 m of the point of ignition are demonstrated in Figure 4. The cross-sectional area of the test laneway was 7.2 m<sup>2</sup>. Therefore, the length of the 100 m<sup>3</sup> of the gas-air mixture was calculated as 13.9 m. This implied that unreacted gas flew into the area without gas during the explosion to therefore expand the range of damage of the explosion flames. If the length of the original gas-air mixture area was  $L_{\text{gas}}$  and the propagation length of flames was set to  $L_{\text{flame}}$ , the ratio  $L_{\text{flame}}/L_{\text{gas}}$  of the propagation length of flames to the length of the gas-air mixture area was 2.88. The ratio was related to diverse factors, including the length of the gas-air mixture area, the gas concentration, and the cross-sectional area of the laneway.  $L_{\text{flame}}/L_{\text{gas}}$  is an important parameter. During the investigation of a gas explosion accident in a coal mine, the propagation length of flames could be judged based on burn marks of flames on structures and equipment in underground coal mines, and also the amount of gas during the gas explosion could be preliminarily estimated according to the ratio  $L_{\text{flame}}/L_{\text{gas}}$ .

The duration ( $T_a$  in Figure 4) of the explosion flames can reflect the duration during which humans or animals were burned by flames during the gas explosion. The longer the duration of flames at a certain point, the more seriously humans or animals would be burned. By conducting this experiment, it can be speculated that the durations of the flames within 10 to 40 m from the point of ignition were 583, 893, 874, and 634 ms, respectively. The duration of the explosion flames at a location 10 m from the ignition position was shown to be short. It was because the explosion chamber was located in a sealed section of the laneway. After the explosion occurred, the unreacted gas-air mixture broke through the sealing film and rapidly flew to the front of the laneway. As a result, the volume of gas in the original explosion chamber was rapidly decreased. At 20 m and 30 m from the point of ignition, the duration of flames was longer, which indicated that, as the explosion continued, most of the unreacted gas-air mixture in the initial stage flew into a zone 20 to 30 m from the point of ignition and was subjected to complete chemical reaction. As the explosion continued, gas was gradually consumed, and the explosive reaction was nearly completed when the explosion flames reached a point 40 m from the source. Therefore, the explosion flames there only lasted for 634 ms, which was shorter than the duration of the flames at the locations around 20 m and 30 m from the point of ignition.

The propagation velocity of flames could be calculated by dividing the distance between two measurement points by the difference ( $T_b$  in Figure 4) in times when the flames reached the two measurement points, as shown in the following formula:

$$V = \frac{L_2 - L_1}{T_b}, \quad (1)$$

where  $L_1$ ,  $L_2$ ,  $T_b$ , and  $V$  represent the distances of No. 1 and No. 2 measurement points from the point of ignition, the time interval between the flames that reach the two measurement points, and the average propagation velocity of flames between the two measuring points, respectively.

The average propagation velocity of flames at different locations could be derived, as shown in Figure 5. It can be seen from the figure that the propagation velocity of flames gradually increased during the gas explosion. In the initial stage of the explosion, the propagation velocity of flames was low, merely 74.5 m/s on average in the area 10 m to 20 m from the point of ignition. As the explosion continued, the explosion flames successively propagated forwards and suffered from the compressive effect of blast waves. Therefore, the speed of the explosive reaction increased, causing the corresponding acceleration of flame propagation. The average velocity of the flames reached 339 m/s when the flames propagated from 30 to 40 m. As shown in Figure 4, the duration of the flames was reduced when the flames propagated to 40 m. Moreover, no flames were detected at 60 m from the point of ignition, which indicated that gas had been consumed and also flames had been extinguished within 40 to 60 m from the point of ignition. During this process, the flame propagation velocity gradually decreased.

**3.2. Propagation of Explosion Pressures.** After many tests, the repeatability of the gas explosion propagation test in the large roadway was found to be relatively poor, and it would be affected by the weather conditions and the uniformity achieved in the mixing of the gases. The explosion pressures recorded at each measuring point would be different, but the trend therein was similar; that is, throughout the explosion and its propagation, the maximum explosion pressure at each measuring point would decay with increasing distance, but the explosion pressure was not subject to monotonic attenuation but fluctuated. Through this test, the maximum explosion pressure at each measuring point was obtained, as shown in Figure 6. By comparing and analyzing the fluctuations in the explosion pressure at each measuring point, it can be divided into three zones, namely, the pressure-relief zone after the initial breaking of the film, a zone with strengthened explosion pressure, and a zone with attenuated explosion pressure, corresponding to areas A, B, and C in Figure 6. Among them, the pressure-relief area after the initial film broke appeared within 60 m of the source of the explosion; the explosion pressure enhancement area appeared between 60 and 80 m; beyond 80 m, the explosion pressure gradually decayed, passing out of the test roadway.

The maximum explosion pressures at various points obtained through the experiment are shown in Figure 6: the maximum explosion pressures at various measuring points showed a certain fluctuation rather than successively decreasing along the laneway during propagation. They can be divided into three zones: a pressure-relief zone after breaking the film in the initial stage, a zone with strengthened explosion



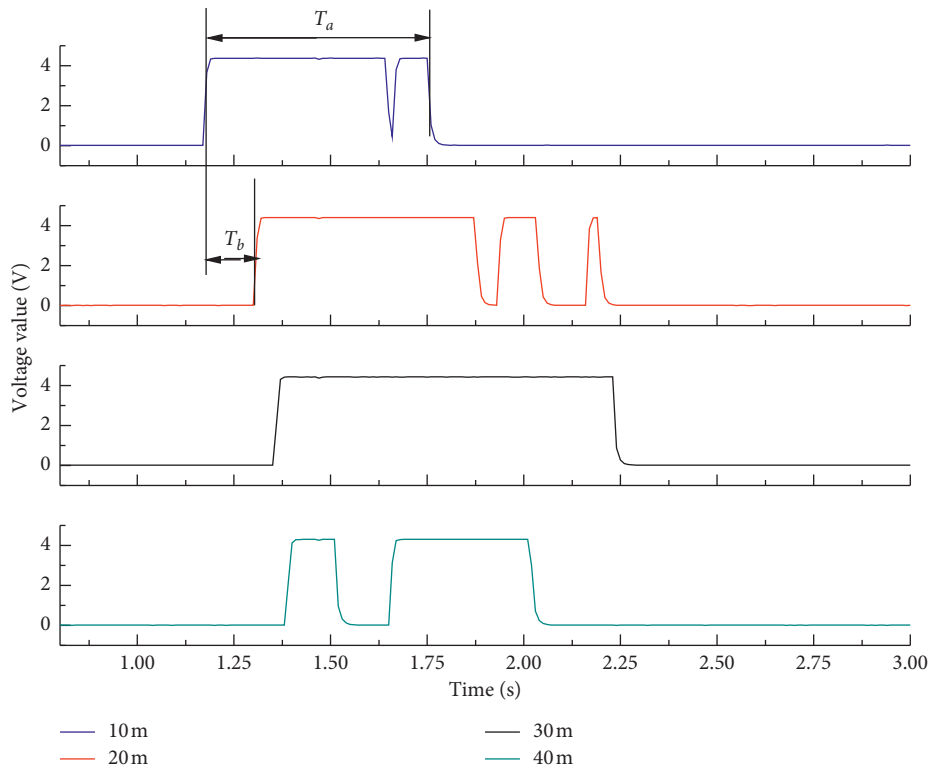


FIGURE 4: Flame signals at various measurement points.

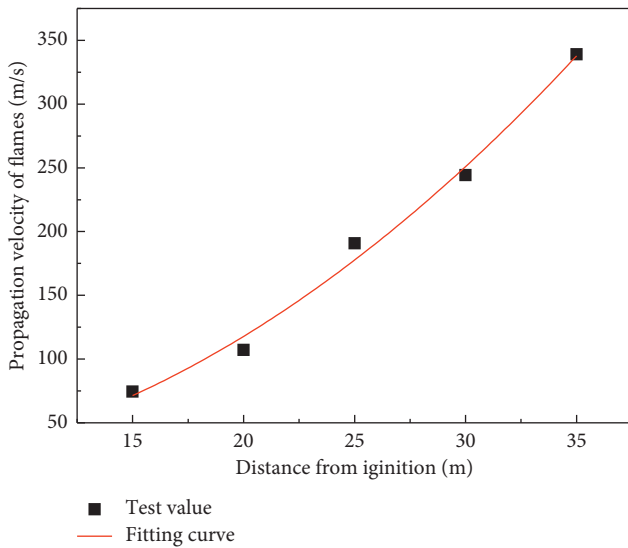


FIGURE 5: Average flame propagation velocities at different locations.

pressure, and a zone with attenuated explosion pressure, which, respectively, corresponded to zones A, B, and C in Figure 6. Zones A and B were separately 60 m and 60 to 80 m, from the point of ignition. After reaching a point about 80 m from the point of ignition, the explosion pressure gradually decreased until propagation went beyond the test laneway.

After the gas-air mixture was ignited, a spherical flame front was immediately formed to propagate towards the

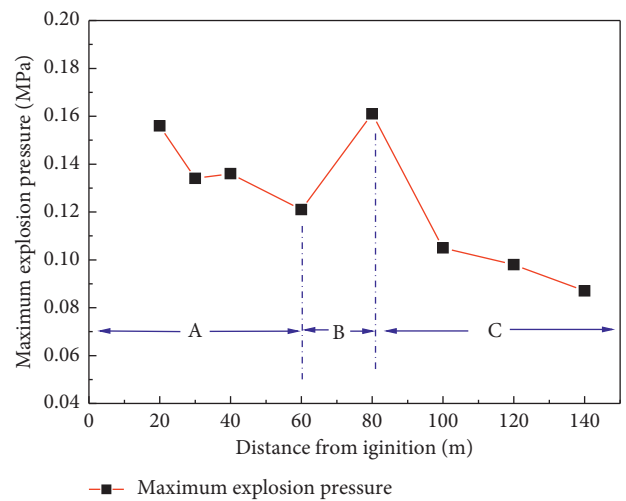


FIGURE 6: The maximum explosion pressures at various measurement points.

unburned gas. The flame front rapidly propagated to the whole cross-section of the laneway and therefore rapidly generated pressure waves in the narrow, confined space. The propagation velocity of the pressure wave was greater than that of the burning front; therefore, the pressure wave went ahead of the burning front, which was also called the precursor blast wave (or precursor pressure wave). The gas pressure behind the wave increased and the gas flew (generating a storm-force wind) to result in damage to the sealing film and further caused the release of a certain amount of

pressure. Thus, in the initial propagation stage of this gas explosion, the peak explosion pressure decreased slightly. As the propagation distance increased, the explosion pressure rose owing to it being restricted by the narrow space in the laneway, namely, a zone with strengthened explosion pressure developed. In these experimental conditions, the volume of the gas-air mixture was  $100\text{ m}^3$ . As the gas during the explosion reaction was gradually consumed, the explosion pressure gradually declined and therefore a zone with attenuated explosion pressure developed.

During the propagation of the explosion, the change in explosion pressure from 20 m from the point of ignition with time is shown in Figure 7. The explosion pressure at the location rapidly increased at first and then rapidly reduced and became negative after a certain time. After the gas explosion, the air in the vicinity of the explosive source was diffused as driven by high temperature and pressure, and thus, blast waves were generated along the diffusion path, resulting in the rapid increase in the explosion pressure. However, after the explosive blast waves passed through, the gas-air mixture rapidly flew forwards and therefore formed a certain negative pressure at that location. The negative pressure caused a backflow of air after the explosion. During a gas explosion in an underground coal mine, the positive and negative pressures triggered by the explosion can cause harm to personnel and damage to equipment.

By analyzing the explosion flames, it can be seen that the duration of the flames was longest, and the explosion reaction was mostly completed, at 20 m from the point of ignition. Additionally, explosion pressure at the location was large, reaching  $0.156\text{ MPa}$  at  $1,369\text{ ms}$ . For convenience of analysis and calculation, the time when flames reached the first sensor (10 m from the point of ignition) was considered as the initial time of the explosion. Namely, the time of ignition of the gas explosion was  $1,173\text{ ms}$ . Thus, the process from ignition to initiate the explosion to the moment when the maximum explosion pressure occurred at a location 20 m from the point of ignition took  $196\text{ ms}$ . At a location 20 m from the point of ignition, the durations of positive and negative explosion pressures were about  $600\text{ ms}$  and  $1,125\text{ ms}$ , respectively. If someone stood at the location of 20 m from the explosive source in an underground coal mine, he or she would be successively impacted by positive explosion pressure for  $600\text{ ms}$ , and then negative explosion pressure for  $1,125\text{ ms}$  after the gas explosion took place.

Figures 8–10 separately demonstrate the changes in explosion pressures with time at 40, 80, and  $120\text{ m}$  from the point of ignition. As shown in Figure 8, the maximum explosion pressure at a location  $40\text{ m}$  from the point of ignition was  $0.136\text{ MPa}$ , which was lower than that ( $0.156\text{ MPa}$ ) at  $20\text{ m}$  from the point of ignition. The durations of positive and negative explosion pressures also correspondingly decreased to  $375\text{ ms}$  and  $500\text{ ms}$ , respectively: this corresponded exactly to the analysis of the explosion flame. At  $40\text{ m}$  from the point of ignition, gas was gradually consumed, and therefore, the duration of explosion flames was correspondingly reduced. The explosion pressure also correspondingly decreased because of the interactive effect between the explosion flames and

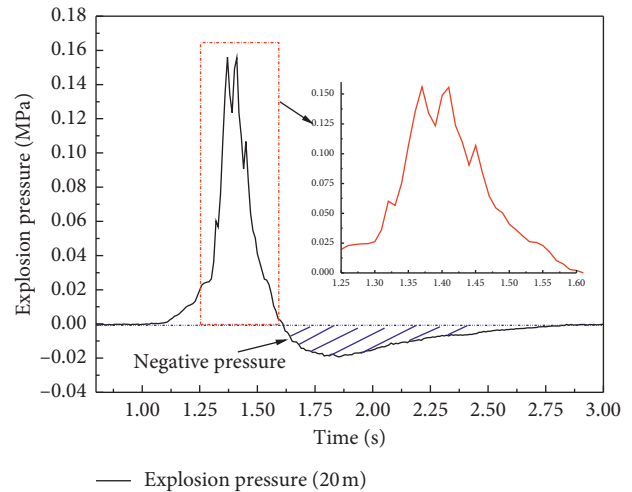


FIGURE 7: The explosion pressure-time curve at 20 m from the point of ignition.

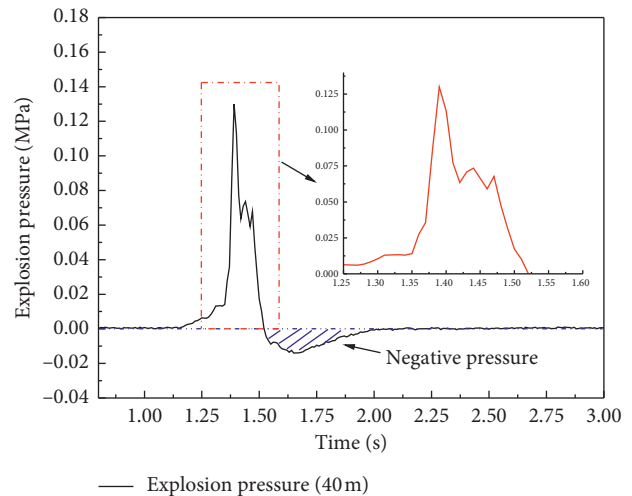


FIGURE 8: The explosion pressure-time curve at 40 m from the point of ignition.

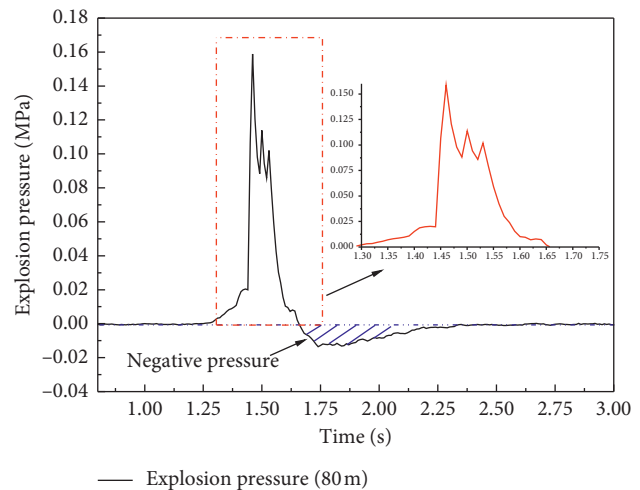


FIGURE 9: The explosion pressure-time curve at 80 m from the point of ignition position.



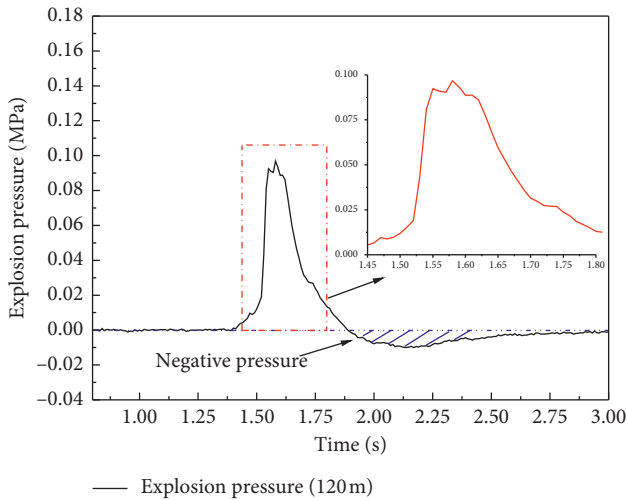


FIGURE 10: The explosion pressure-time curve at 120 m from the point of ignition.

pressures. In Figure 9, the explosion pressure at 80 m from the point of ignition increased to 0.161 MPa, which was the highest pressure recorded between 10 and 140 m from the point of ignition. By 120 m, the maximum explosion pressure had fallen to 0.098 MPa, and correspondingly, the absolute value of negative pressure also gradually decreased.

## 4. Harm to Animals

**4.1. Statistical Analysis of Casualties among SD Rats.** After completing the explosion experiment, the casualties among SD rats in each cage were assessed after ventilating the laneway for 20 min. The statistical results are displayed in Table 2. By comparing the explosion pressures at different locations, it can be speculated that there were more dead SD rats at the location with a higher explosion pressure. The explosion pressure (0.161 MPa) was the largest at 80 m from the point of ignition, at which there were 13 dead SD rats with five SD rats surviving. At 200 and 240 m, the explosion pressures were much smaller: only two or three SD rats were found dead. This also shows that the shock wave overpressure generated during the explosion was one of the main reasons for harm to the animals.

The survival rates of SD rats within 8 h after the explosion were calculated, as shown in Table 3: within 8 h after the gas explosion, the survival rates of SD rats in the No. 3, No. 5, and No. 6 cages did not decrease, while the survival rates of SD rats in the No. 1, No. 2, and No. 4 cages decreased to different extents. Some SD rats did not die instantly during the gas explosion but died after the explosion (mainly because the explosion blast caused visceral rupture among SD rats and burning damaged their respiratory system). It can be speculated that the No. 1, No. 2, and No. 4 cages were damaged by the explosion, such that SD rats were thrown out of the cages, and therefore, they were also injured. Some SD rats were drowned after falling in an area containing water between tracks in the laneway.

**4.2. Analysis of Gas Explosion-Induced Harm to Animals.** Figure 11 illustrates a comparison of SD rats before and after the gas explosion. It can be seen from the figure that, before the gas explosion, SD rats were all alive and had white coats. After the explosion, SD rats were injured to different extents. A majority of living SD rats exhibited the following symptoms: dyspnea, body tremble, fracture, and visceral rupture and bleeding. The SD rats in the No. 1 cage were burned all over, besides having the aforementioned symptoms.

The harm to animals is mainly demonstrated: high-temperature burn by explosion flames, overpressure damage caused by explosive blast waves, and toxicosis induced by incomplete combustion of gas.

High-temperature gas and flames were generated during the gas explosion. By analyzing the propagation, after the gas-air mixture exploded, flames spread to a location some 40 m from the point of ignition, and therefore, the SD rats in the No. 1 cage installed at that location were injured by the flames. After observing casualties among animals after a gas explosion, it was found only SD rats in the No. 1 cage were burned, while those in cages 2 to 6 were not burned. By carrying out the test, it was inferred that although the duration of the explosion flames was only 634 ms at 40 m from the point of ignition, the hair on the majority of these SD rats was still burnt owing to the high-temperature conditions generated. In underground coal mines, if the gas was accumulated over a large area and thus there was a large amount of gas, the duration for which personnel in the vicinity of the explosive source were burned by the explosion and its ensuing flames was longer. Within the whole range of propagation of the gas explosion, the explosion pressure near the explosive source was not the highest, while personnel at that location were subjected to injury from both the explosive blast and flame burns, resulting in a greater number of casualties.

The explosive blast waves were imposed on animal bodies, causing damage to multiple organs therein. Additionally, under the dynamic pressure induced by high-speed flows, the SD rats fell, causing further injury (even fracturing limbs). Therefore, blast damage caused by the explosion was the primary reason behind the instant deaths of these animals. The experimental research showed that the ability of SD rats to bear dynamic pressure was weak. Fan [20] pointed out that when the pressure induced by the gas explosion was 20% higher than normal atmospheric pressure, SD rats died instantly: the higher the explosion pressure, the more serious the injuries, and the higher the mortality. The analysis of the propagation of explosive pressures indicated that the pressure induced by the gas explosion passed through multiple zones (including a pressure-relief zone after breaking the sealing film in the initial stage, a zone with strengthened explosion pressures, and a zone with attenuated explosion pressures) during its propagation along the laneway. Different explosion pressures that were generated in different zones resulted in different injury degrees. The analysis of accident cases showed that, in gas explosion accidents in coal mines, the death rates are different due to the different regions in which personnel are located. The difference in explosion pressure in different regions is one of the main reasons for the different death rates.

TABLE 2: Casualty statistics: SD rat populations.

Cage	#1	#2	#3	#4	#5	#6
Distance to the point of ignition (m)	40	80	120	160	200	240
Population status	8 alive, 10 dead	5 alive, 13 dead	11 alive, 7 dead	7 alive, 11 dead	16 alive, 2 dead	15 alive, 3 dead

TABLE 3: Survival rates of SD rats within 8 h after the explosion.

Time (h)	Survival rate (%)					
	No. 1 cage	No. 2 cage	No. 3 cage	No. 4 cage	No. 5 cage	No. 6 cage
0	44.4	27.8	61.1	38.9	88.9	83.3
1	44.4	16.7	61.1	33.3	88.9	83.3
4	44.4	16.7	61.1	33.3	88.9	83.3
8	38.9	11.1	61.1	33.3	88.9	83.3

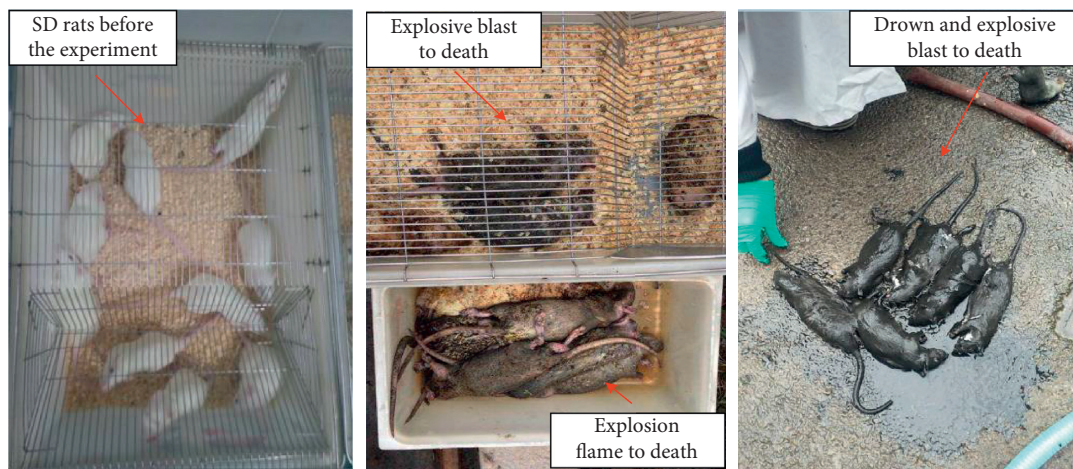


FIGURE 11: Comparison of SD rats before and after the gas explosion.

A significant amount of gas was involved in an explosion, while the incomplete reaction of the gas also occurred due to the lack of oxygen, thus generating a large amount of CO. Therefore, poisoning and asphyxiation are also important causes of death caused by gas explosions. Compared with the explosion flames, hazardous gas could result in larger-scale damage owing to it being diffused over a wider area. The gas concentration measured in the test was 9.0%. In this context, gas was reacted completely in the explosion and the test laneway was ventilated after the explosion. Therefore, toxic damage to SD rats occurred at a low rate.

## 5. Conclusion

The harm to animals caused by a gas explosion was investigated experimentally by using a large laneway test system. During the explosion of  $100 \text{ m}^3$  of gas at a concentration (in the air) of 9.0% in the test laneway, the maximum explosion pressure reached 0.161 MPa. The explosive blast injury induced by this gas explosion was the major reason for the deaths of SD rats far from the point of ignition (i.e., at a distance of 240 m). During the gas explosion, the explosive pressure could be described as occupying three zones (including a pressure-relief zone after breaking the film in the

initial stage, a zone with strengthened explosion pressure and a zone with attenuated explosion pressure therein). Different explosion pressures were generated in different zones, leading to different amounts and severities of damage. The durations of positive and negative explosion pressures could reach 600 and 1,125 ms, respectively, and the positive and negative pressures generated due to the explosion caused severe blast damage. The explosion flames could spread to a location 40 m from the point of ignition, and their duration could reach 893 ms. The SD rats in the cage located some 40 m from the point of ignition were also burned at high temperature as well as being damaged by the blast. Under the aforementioned experimental conditions, toxic damage to SD rats was low since the methane was fully reacted and the laneway was ventilated after the gas explosion.

## Data Availability

The data that support the findings of this study are available from the corresponding author upon reasonable request.

## Conflicts of Interest

The authors declare that there are no conflicts of interest.

## Acknowledgments

This work was supported by the National Key R&D Program of China (Grant no. 2018YFC0807900) and the National Natural Science Foundation of China (Grant no. 51504285).

## References

- [1] G. Ke, L. Zimeng, J. Jinzhang et al., "Study on flame spread characteristics of flame-retardant cables in mine," *Advances in Polymer Technology*, vol. 2020, Article ID 8765679, 7 pages, 2020.
- [2] K. Gao, S. Li, Y. Liu, J. Jia, and X. Wang, "Effect of flexible obstacles on gas explosion characteristic in underground coal mine," *Process Safety and Environmental Protection*, vol. 149, pp. 362–369, 2021.
- [3] K. Gao, Z. Qi, J. Jia et al., "Investigation of coupled control of gas accumulation and spontaneous combustion in the goaf of coal mine," *AIP Advances*, vol. 10, no. 4, 2020.
- [4] B. Nie, L. Yang, B. Ge, J. Wang, and X. Li, "Chemical kinetic characteristics of methane/air mixture explosion and its affecting factors," *Journal of Loss Prevention in the Process Industries*, vol. 49, pp. 675–682, 2017.
- [5] M. J. Ajrash, J. Zanganeh, and B. Moghtaderi, "Methane-coal dust hybrid fuel explosion properties in a large scale cylindrical explosion chamber," *Journal of Loss Prevention in the Process Industries*, vol. 40, pp. 317–328, 2016.
- [6] C. Wang, Y. Zhao, and E. K. Addai, "Investigation on propagation mechanism of large scale mine gas explosions," *Journal of Loss Prevention in the Process Industries*, vol. 49, pp. 342–347, 2017.
- [7] Q. Zhang and Q. J. Ma, "Dynamic pressure induced by a methane-air explosion in a coal mine," *Process Safety and Environmental Protection*, vol. 93, 2015.
- [8] I. G. Bowen, E. R. Fletcher, and D. R. Richmond, *Estimate of Mans Tolerance to the Direct Effects of Air Blast*, Lovelace Foundation for Medical Education and Research, Albuquerque, NM, USA, 1968.
- [9] M. A. Mayorga, "The pathology of primary blast overpressure injury," *Toxicology*, vol. 121, no. 1, pp. 17–28, 1997.
- [10] A. Knauf, "Blast injury causing extensive brain injury and elevated skull fracture," *Indian Journal of Neurotrauma*, vol. 11, no. 01, pp. 64–67, 2014.
- [11] V. Rubovitch, M. Ten-Bosch, O. Zohar et al., "A mouse model of blast-induced mild traumatic brain injury," *Experimental Neurology*, vol. 232, no. 2, pp. 280–289, 2011.
- [12] A. Saljo, M. Mayorga, H. Bolouri, B. Svensson, and A. Hamberger, "Mechanisms and pathophysiology of the low-level blast brain injury in animal models," *Neuroimage*, vol. 54, 2011.
- [13] H. Z. Toklu, Z. Yang, S. Oktay et al., "Overpressure blast injury-induced oxidative stress and neuroinflammation response in rat frontal cortex and cerebellum," *Behavioural Brain Research*, vol. 340, 2017.
- [14] A. J. Januszkiewicz, T. G. Mundie, and K. T. Dodd, "Maximal exercise performance-impairing effects of simulated blast overpressure in sheep," *Toxicology*, vol. 121, no. 1, pp. 51–63, 1997.
- [15] J. Hines-Beard, J. Marchetta, S. Gordon, E. Chaum, E. E. Geisert, and T. S. Rex, "A mouse model of ocular blast injury that induces closed globe anterior and posterior pole damage," *Experimental Eye Research*, vol. 99, pp. 63–70, 2012.
- [16] J. M. Petras, R. A. Bauman, and N. M. Elsayed, "Visual system degeneration induced by blast overpressure," *Toxicology*, vol. 121, no. 1, pp. 41–49, 1997.
- [17] I. Cernak, A. C. Merkle, V. E. Koliatsos et al., "The pathobiology of blast injuries and blast-induced neurotrauma as identified using a new experimental model of injury in mice," *Neurobiology of Disease*, vol. 41, no. 2, pp. 538–551, 2011.
- [18] R. A. Bauman, N. Elsayed, J. M. Petras, and J. Widholm, "Exposure to sublethal blast overpressure reduces the food intake and exercise performance of rats," *Toxicology*, vol. 121, no. 1, pp. 65–79, 1997.
- [19] K. Gao, "Study on the propagation law of gas explosion in the space based on the goaf characteristic of coal mine," *Safety Science*, vol. 127, 2020.
- [20] X. T. Fan, Z. Li, and C. Zhouquan, "Experimental study on harm of gas explosion to animals," *Mining Safety & Environmental Protection*, vol. 4, pp. 7-8+83, 2005.

## Research Article

# Investigation and Control of the Blasting-Induced Ground Vibration under Cold Condition

Yingguo Hu, Zhaowei Yang , Erlei Yao, Meishan Liu, and Yu Rao

Key Laboratory of Geotechnical Mechanics and Engineering of Ministry of Water Resources,  
Changjiang River Scientific Research Institute, Wuhan 430010, Hubei, China

Correspondence should be addressed to Zhaowei Yang; yangzw@whu.edu.cn

Received 29 December 2020; Revised 12 February 2021; Accepted 23 March 2021; Published 8 April 2021

Academic Editor: Nan Jiang

Copyright © 2021 Yingguo Hu et al. This is an open access article distributed under the Creative Commons Attribution License, which permits unrestricted use, distribution, and reproduction in any medium, provided the original work is properly cited.

This paper focuses on the investigation and control of the blasting-induced ground vibration under cold condition. The mechanical performance and wave propagation characteristics of the frozen rock mass are quite different from that of the conventional condition. Laboratory tests were implemented to investigate the wave impedance of rock mass in the frozen, saturated, normal, and drying states. Results reveal the longitudinal wave velocity could be enlarged by 40 percent in the frozen state. Then long-term monitoring of blasting vibration was implemented based on the blasting excavation of the Fengman hydropower station reconstruction project in the north of China. Results demonstrate the PPV and frequency both attenuate much slower when the rock mass is frozen, and the obvious turning points of PPV could be found between different temperatures, where the change of the PPV relationship happens. At last, numerical simulation of the blasting seismic wave attenuation and the response in the protected structure was implemented. The equivalent freezing simulation method was proposed and verified with the site experiment data. Results demonstrate that the attenuation coefficient decreases obviously as the frozen depth of the rock mass increases. The dynamic degree response in structure is much stronger and the maximum charge weight per delay was limited more strictly under the frozen condition. A most adverse frozen depth was determined when the charge weight per delay gets the minimum value. With the above control approaches, a total of 676 blasting was completed in Fengman hydropower station reconstruction and no case of excessive measurement could be found.

## 1. Introduction

Blasting is often a necessary part of mining and construction operations and is the most cost-effective way to break rock. When an explosive is detonated, a chemical reaction occurs very rapidly and a relatively small quantity of explosive is converted into gas of very high temperature. This reaction results in two types of loadings applied on the borehole wall, namely, a stress wave and a gas pressure with longer duration [1–4]. The detonation properties of the explosive consist of the explosion pressure, its time history, and the total energy delivered to the rock. The response of the rock mass to such time-varying high-amplitude stresses is even more complex, as all the relevant strain-rate-dependent properties of the subject rock are not known. For this case, it is essential to implement both experimental study and

numerical study. The experimental study could generate an experimental database, and the numerical study could simulate the processes of blasting and fragmentation through the use of numerical models so as to obtain a better understanding of the dominant parameters that control blast results [5–9].

In a properly designed blast, the major part of the explosion energy is used in crushing and breaking the rock. However, some energy also causes noise and ground vibration. The prediction of ground vibration components has great importance in the minimization of environmental complaints [10, 11]. Estimating the particle velocity and other components of ground vibration with reliable approaches will be very useful in blast design. The most widely used method is the so-called “scaled distance” method, based on the empirical principle that states peak particle velocity



(PPV) at a point is inversely proportional to the distance from the blast and shows a square root dependence on the maximum charge per delay [12–16]. There are many ground motion predictors proposed by different authors based on their own collection of data from different sites. But, due to the complexity of the geological and technological and other associated parameters in blasting, a prediction of PPV is difficult and sometimes confusing if these attenuation equations are not updated due to the movement of blasting places [17–20].

The existed literature studies demonstrate that blasting vibration attenuation law is quite related to the physical and mechanical parameters of the rock mass. Since the structures are surrounded by jointed rock mass, the blast wave propagation in the rock mass is significantly influenced by the joints [21, 22]. The vastly existed joints in rock mass not affect only the mechanical properties of the rock mass but also their dynamic response. The water usually exists in the joint, but it could turn into ice under the low temperature. The wave impedance of the ice is quite different from that of water, which significantly affects the vibration attenuation. This is a concern problem during the blasting excavation in the cold region which has a large temperature difference in summer and winter. However, there is still some lack of knowledge about the blasting vibration control for the rock blasting excavation under cold condition.

This paper focuses on the blasting earthquake response of reconstruction project under cold condition. Laboratory tests were implemented to investigate the change of mechanical performance for rock mass at the frozen, saturated, normal, and drying states. Then long-term monitoring of blasting vibration was implemented based on the blasting excavation of Fengman hydropower station reconstruction project in China to study the vibration attenuation law of the rock mass at different seasons. At last, numerical simulation of the blasting seismic wave attenuation and the response in the protected structure at different states was finished and suggestion of blasting earthquake control of rock mass excavation under cold condition was proposed.

## 2. Laboratory Study on Physical Properties of the Rock Mass under Freezing

When the rock is frozen, the propagation medium of the seismic wave is changed from the water-rock combination solid to the ice-rock combination solid. In general, the water density is  $1000 \text{ kg/m}^3$ , and the P-wave velocity is  $1500 \text{ m/s}$ , while the ice density is  $900 \text{ kg/m}^3$ , the P-wave velocity is about  $4500 \text{ m/s}$ . The wave impedance of the ice is about three times that of water. Therefore, the propagation of seismic waves in frozen rock could be quite different from that of the conventional condition. In the next section, the laboratory experiment was implemented to investigate the physical and mechanical properties of the rock mass under frozen state.

*2.1. Experiment Design.* In the present study, the laboratory experiment includes two important aspects: the first step is measuring the sonic wave velocity of different kinds of rock

medium in different states. By controlling the temperature and humidity of the air, the rock mass could be in the state of dry, natural, saturated, and frozen conditions. The rock medium of sandstone, mudstone, glutenite, limestone, marble, basalt, dolomite, and granite was selected. The second step is investigating the change of the density and sonic wave velocity in the sandstone of different porosities under frozen state. The porosity of 5%~30% was selected to be studied in the experiment. Figure 1 plots a photograph of the frozen sandstone specimen and equipment of the sonic wave test.

*2.2. Comparison of the Physical Properties of Rock Medium under Different States.* The waveform of the sonic wave test could reflect the damping characteristic of the rock mass according to the existed literature studies. When the rock mass is of better quality, the starting point of the longitudinal wave is more obvious and the frequency of the sonic waveform is higher. Figure 2 plots the comparison of the waveform of the sonic wave test for sandstone under conventional and frozen states.

It can be seen that the starting point of the longitudinal wave is much clearer in the frozen state than in the conventional state. The amplitude of the longitudinal wave in the frozen sandstone at the start point is about ten times that in the conventional rock mass. The frequency of frozen state for sandstone is also much larger than that of conventional state, while the former is about five times the latter. Results demonstrate that the waveform of the sonic wave test for the sandstone in the frozen state is more close to that of the rock mass of better quality, which reveals that the damping property of the rock is weakened after frozen. Figure 3 plots the comparison of longitudinal wave velocity of different kinds of rock medium in different states.

The longitudinal wave velocity of the rock mass in the frozen state is the biggest, and the wet saturated state takes the second place, while the natural state is third and the dry state is least. It can be explained that when the rock is frozen, the liquid water in the joint changes into solid ice, which could improve the propagation of the longitudinal wave. But for the rock medium in the dry state, the water was vaporized by the wind, and the air was filled with joints. It is known that the longitudinal wave velocity in the ice is larger than that in water, but the longitudinal wave velocity in water exceeds that in the air by 2 times. The difference between the longitudinal wave velocity in the frozen and natural states is about 30% in the sandstone, but in the granite that is only about 5%. That is because the granite is usually dense, and the porosity is less than that of sandstone, which weakens the change of physical properties when the rock mass is frozen. Figure 4 plots the comparison of longitudinal wave velocity of sandstone of different porosities in the frozen and natural states.

Results reveal that as the porosity increases, the longitudinal wave velocity decreases obviously, and the longitudinal wave velocity and the porosity obey the linear law. When the rock mass is frozen, the longitudinal wave velocity exceeds that of the natural state by about 10%~35%. The



FIGURE 1: Photograph of the (a) frozen sandstone specimen and (b) equipment of the sonic wave test.

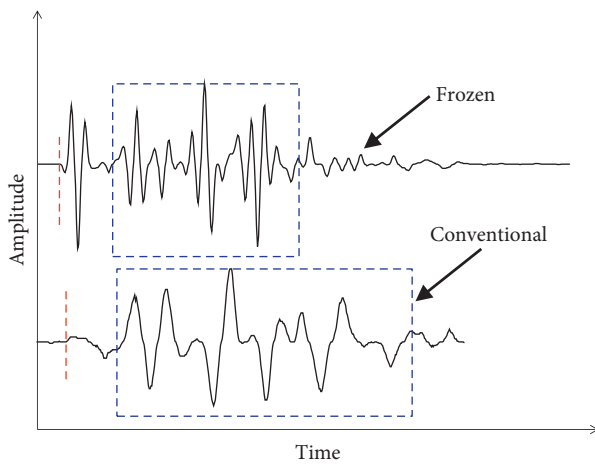


FIGURE 2: Comparison of the waveform of the sonic wave test under conventional and frozen states.

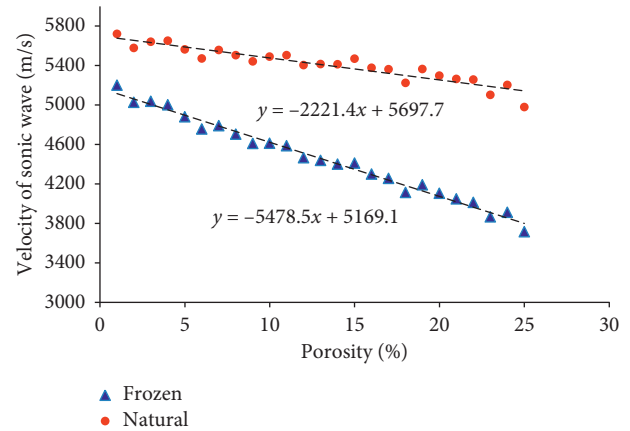


FIGURE 4: Comparison of longitudinal wave velocity of sandstone of different porosities in the frozen and natural states.

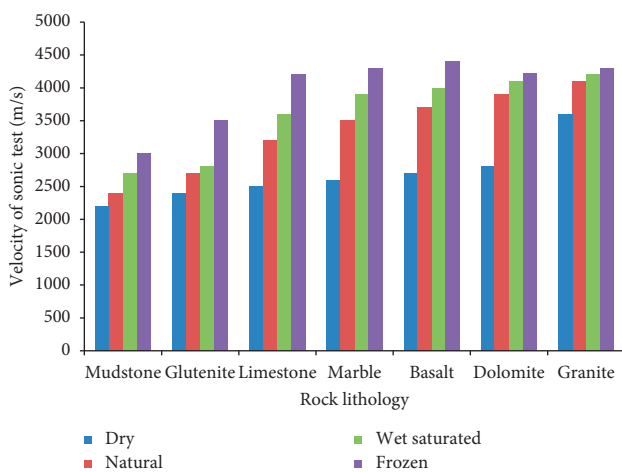


FIGURE 3: Comparison of longitudinal wave velocity of different kinds of rock medium in different states.

difference between the frozen state and the natural state increases with the porosity obviously. That is because as the porosity increases, the effect proportion of water changing

into ice is enlarged, which makes the longitudinal wave velocity in the frozen rock mass larger. It is known that wave impedance is a very important index in evaluating the propagation of stress wave in the rock mass. Figure 5 plots the curve of wave impedance increment versus the porosity when the sandstone is in the frozen state.

It can be seen that as the porosity increases, the enlargement of wave impedance increment could be found. The wave impedance increment and the porosity obey the exponential relationships obviously, while the coefficient of correlation reaches as much as 0.88. Results demonstrate that the ability to conduct the stress waves is enlarged when the rock mass is frozen, especially in the rock medium with high porosity. But it should be pointed that it is not a complete good change during the blasting vibration control process. Firstly, when the rock mass is frozen, and the physical properties of the rock mass become better, the attenuation of blasting stress wave is slower, which is not helpful for the safety of the protective structures in the far field. Secondly, the frozen depth is usually about 0.5~3 m in the engineering practice, the rock is layered in the frozen state, which makes the propagation of the stress wave more complex, and it is difficult to determine reasonable blasting parameters under this condition.



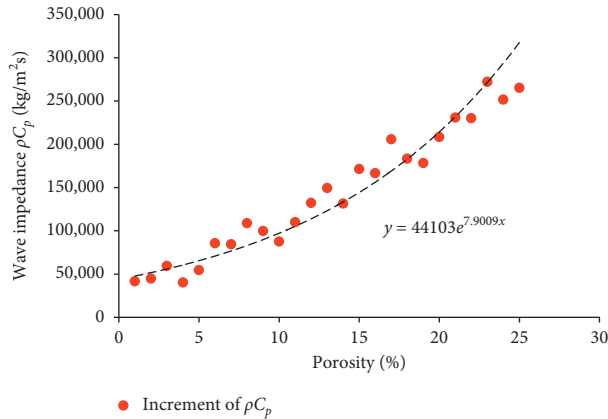


FIGURE 5: Wave impedance increment versus the porosity in the frozen sandstone.

### 3. Field Experiment of the Blasting Vibration Attenuation Law in Cold Condition

**3.1. Project Ground.** Field experiments were implemented to study the blasting vibration attenuation law in cold condition based on the foundation excavation of the Fengman hydropower station. Fengman hydropower station is one of the most famous hydropower projects in China. It was built in 1937 in the Songhua River in Jilin province. The Chinese government decides to implement the reconstruction to increase installed capacity in 2012, and the protection of the existing buildings in the hydropower station was one of the most concern problems during the blasting excavation of reconstruction. Another difficulty is that the temperature in the Fengman hydropower station is very low in autumn and winter. Figure 6 shows the photograph of the engineering site. The annual development curve of the temperature and frozen depth of the rock mass is plotted in Figure 7.

It can be seen that the temperature at the Fengman hydropower station in five months is under  $0^{\circ}\text{C}$ , which means the rock mass is in the frozen state for about a half year. According to meteorological data, the frozen depth of the rock mass is between 0.25 and 2.25 m. The rock lithology of the Fengman hydropower project foundation is sandstone. With the results of the laboratory test, the physical properties of sandstone in the frozen state are quite different from the natural state. So the field experiment is implemented in this section to study the blasting vibration attenuation law in cold condition. The design of the experiment is measuring the blasting vibration at different detonation distances, and the measurement was implemented at different season and temperature conditions. Figure 8 shows the typical layout of the vibration measurement points, the blasting vibration equipment (Minimate Plus), and the typically measured blasting vibration waveform. The measurement range of this instrument is  $0.001\sim 25.4\text{ cm/s}$ . The sampling rate was taken as  $125\ \mu\text{s}$ , i.e. recording 8000 samples per second.

**3.2. Comparison of Blasting Vibration in Cold and Conventional Conditions.** To investigate the blasting vibration characteristic under different temperatures, the comparison



FIGURE 6: Photograph of engineering site of Fengman hydropower station.

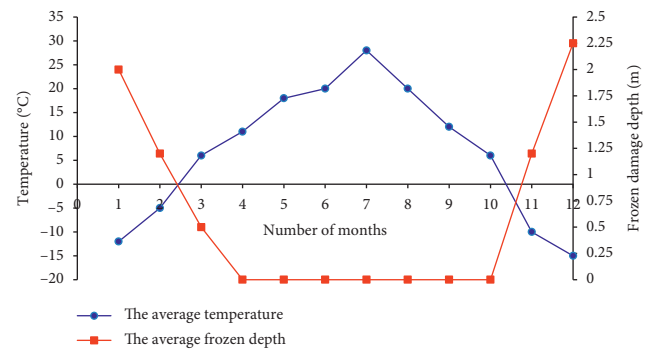


FIGURE 7: The annual development curve of the temperature in a year.

of the curve of blasting vibration and frequency was implemented. To ensure the effectiveness of the results, the charge weight, detonation distance, and blasting vibration equipment are all the same. Figure 9 plots two comparison examples of blasting vibration waveform in the conventional and frozen rock mass.

It can be seen that the PPV of the frozen rock mass is larger than that of the conventional rock mass. When the detonation distance is 15 m, the PPV in the frozen rock mass exceeds that under conventional condition by  $0.9\text{ cm/s}$ . But the difference of PPV increases when the detonation distance is 20 m, in which the PPV under frozen condition exceeds that of the conventional rock mass with  $2.2\text{ cm/s}$ . The frequency of the blasting vibration in the frozen rock mass is also larger than that in conventional condition. The dominant frequency of blasting vibration in the conventional condition is about  $110\text{ Hz}$ , while that is  $289\text{ Hz}$  after the rock mass is frozen. The increment rate of dominant frequency is about 171%. Results demonstrate that the PPV and the dominant frequency were both enlarged after the rock mass is frozen, which indicates that the attenuation speed of blasting seismic wave is slower. Figure 10 plots the distribution of PPV versus detonation distance at the temperature of  $-5^{\circ}\text{C}$  and  $-20^{\circ}\text{C}$ .

The turning point could be found obviously during the comparison of PPV at different detonation distances. When the detonation distance is less than the turning point, the PPV of the rock mass under  $20^{\circ}\text{C}$  is larger than that under  $-5^{\circ}\text{C}$ , but when the detonation distance is larger than the turning point, the relationship is opposite. During engineering practice, the buildings which need to be protected

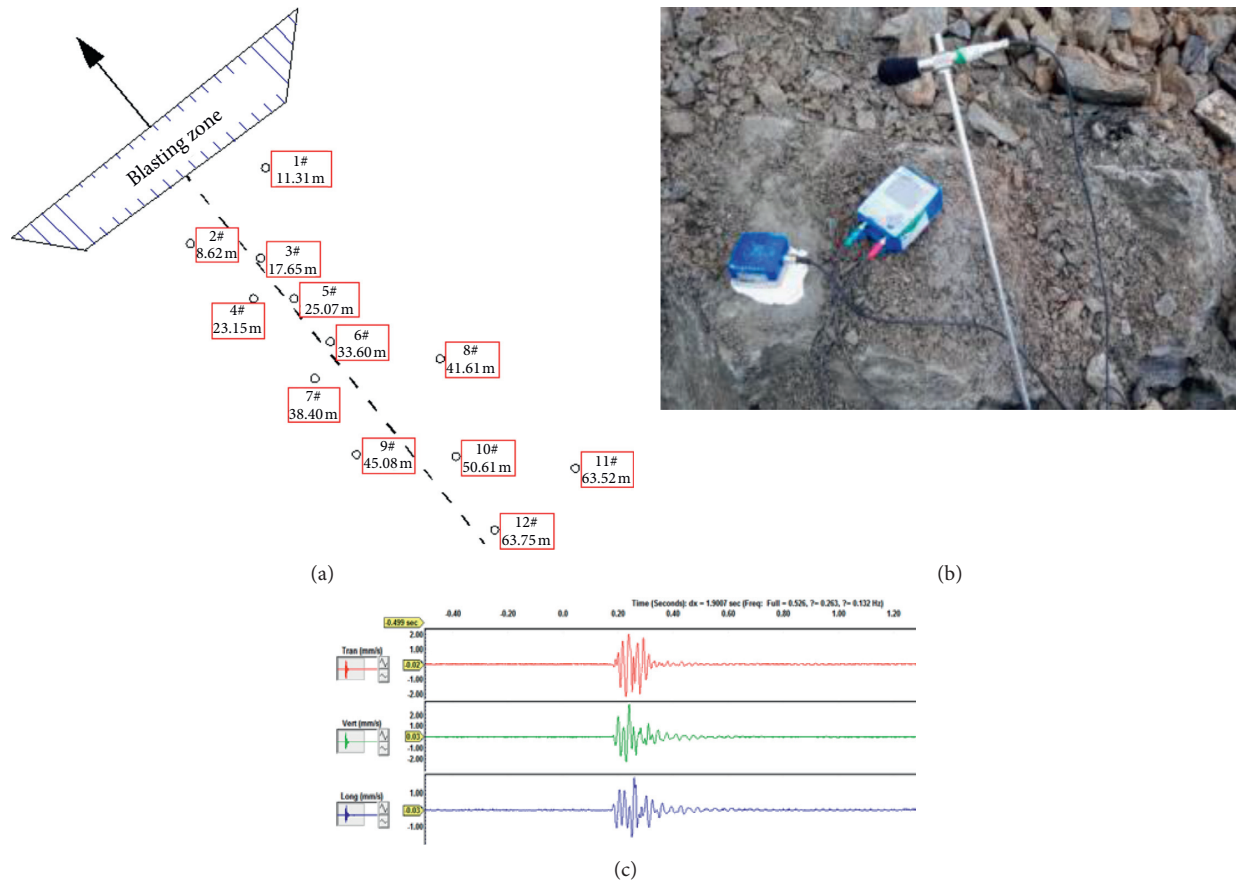


FIGURE 8: The design, equipment, and typical waveform of the site monitoring. (a) Typical layout of measurement. (b) Equipment of blasting vibration. (c) Typical waveform.

are usually located in different detonation distances. Results reveal that when the protected objects are located in the position close to the blast hole, it is dangerous when the rock mass is in the state of  $20^{\circ}\text{C}$ , but if the protected objects are farther than the turning point, the temperature of  $-5^{\circ}\text{C}$  is not helpful for safety. It can be seen that the temperature state of the rock mass could affect the structure security control of blasting vibration significantly, which is rarely noticed in the existed literature.

**3.3. Comparison of PPV Attenuation Law at Different Temperatures.** Estimating the particle velocity and other components of ground vibration with reliable approaches will be very useful in blast design. The most widely used method is the so-called “scaled distance” method, based on the empirical principle that states peak particle velocity (PPV) at a point is inversely proportional to the distance from the blast and shows a square root dependence on the maximum charge per delay. Figures 11 and 12 plot the PPV at different scaled distances of the Y direction in the rock mass under different temperatures.

It can be seen that the relationship between the PPV and scaled distances is clearly because the correlation coefficients exceed 0.9. The attenuation coefficients are quite different when the temperature of the rock mass varies. As the

temperature decreases, the attenuation coefficient  $K$  and  $\alpha$  all decrease by different degrees. The turning points of PPV could be found between two curves of different temperatures, and the location of the turning point has special significance. When the detonation distance of the protective project is less than that of the turning point, the impact of blasting vibration under high temperature is stronger; otherwise, the condition of low temperature is not helpful for the safety of the protective project. The mathematical description of the detonation distance at the turning point is as follows:

$$R^* = Q^{1/3} \left( \frac{K_1}{K_2} \right)^{(1/\alpha_1 - \alpha_2)} \quad (1)$$

If the PPV distribution of  $20^{\circ}\text{C}$  was used as the benchmark, the comparison of the detonation distance versus the maximum charge weight per delay at the turning point is shown in Figure 13.

It can be seen that the special detonation distance is larger when the rock mass is in the temperature state of  $-15^{\circ}\text{C}$ , and the result of the rock mass in  $-5^{\circ}\text{C}$  takes second place, while that of the rock mass under  $-10^{\circ}\text{C}$  is least. When the maximum charge weight per delay is 40 kg, the special detonation distance of the rock mass under  $-5^{\circ}\text{C}$ ,  $-10^{\circ}\text{C}$ , and  $-15^{\circ}\text{C}$  is 29 m, 17 m, and 35 m, respectively. Results

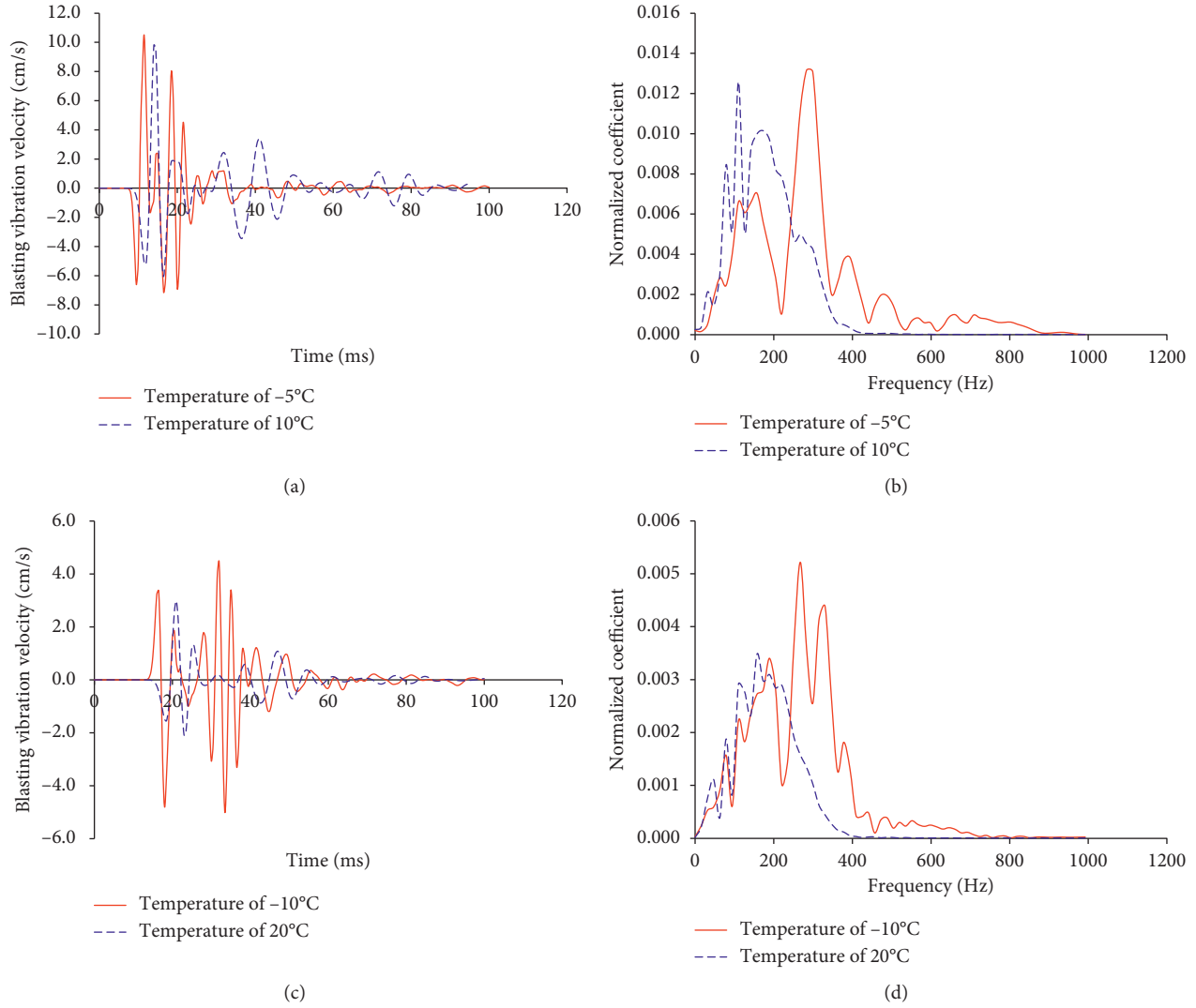


FIGURE 9: Comparison examples of blasting vibration waveform in the conventional and frozen rock mass. (a) Vibration waveform example I. (b) Frequency example I. (c) Vibration waveform example II. (d) Frequency example II.

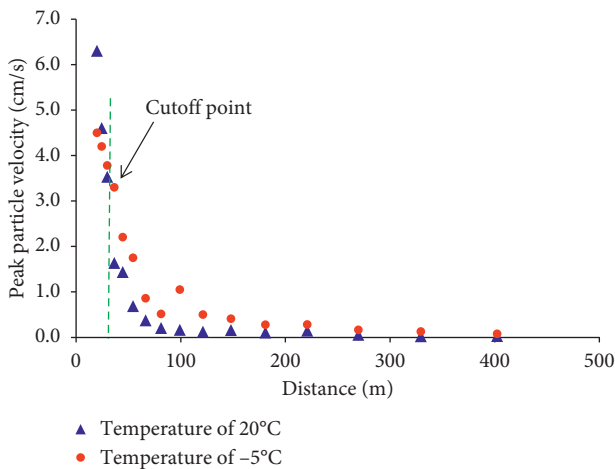


FIGURE 10: Distribution of PPV versus detonation distance at the temperature of -5°C and -20°C.

demonstrate the special detonation distance does not increase with the decrease of temperature strictly. For the same temperature condition, the special detonation distance increases with the maximum charge weight per delay and the relationship obeys the logarithmic function. As the locations of the turning point and protective project are important during the blasting vibration control process, the effect of temperature and the maximum charge weight per delay should be both taken into consideration.

#### 4. Numerical Simulations of the Response and Control in the Structure under Cold Condition

Investigation of rock blasting and its effects by scaled or full size experiment is very expensive and time-consuming. On the other hand, numerical method, derived from sound mechanical principles and validated against experimental data, indicates a promising approach to study the response and control in the structure under cold condition.

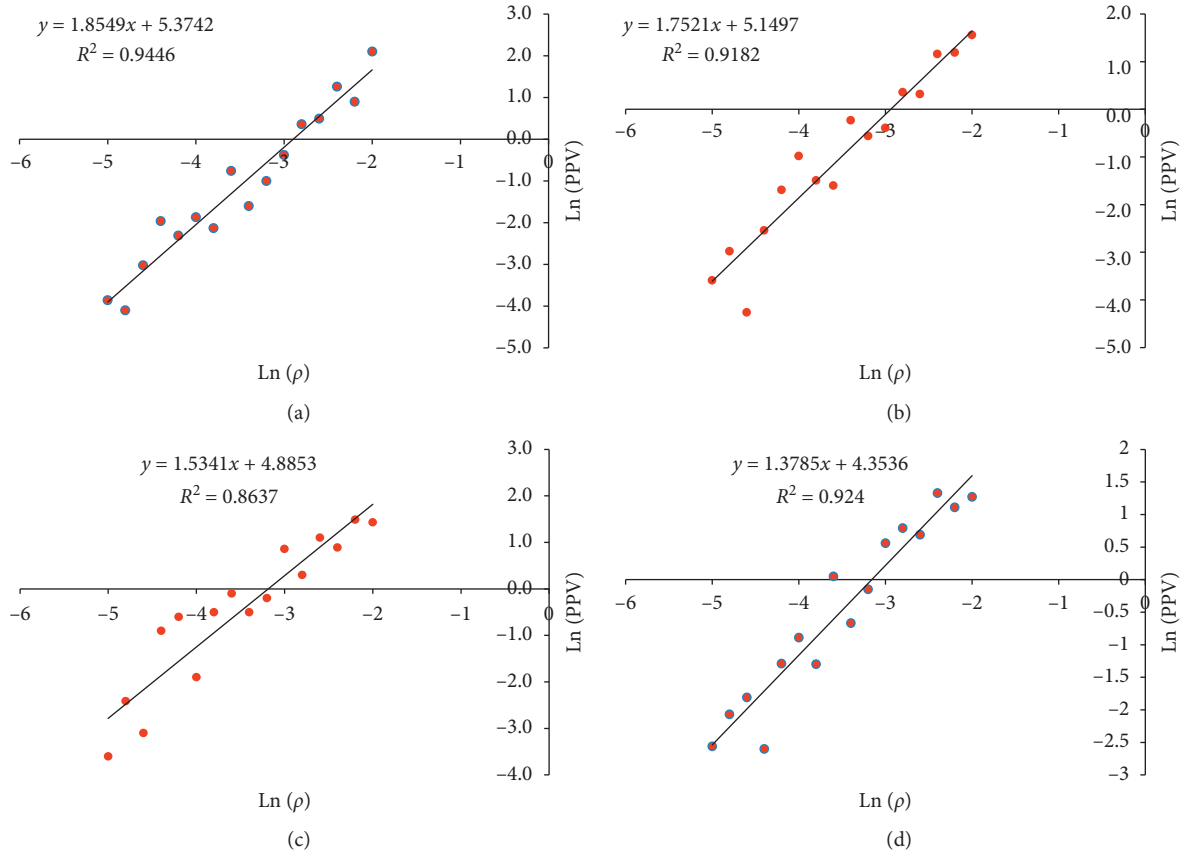


FIGURE 11: Blasting attenuation law curves of different temperatures in rock mass. (a) Temperature of 10°C. (b) Temperature of -5°C. (c) Temperature of -10°C. (d) Temperature of -5°C.

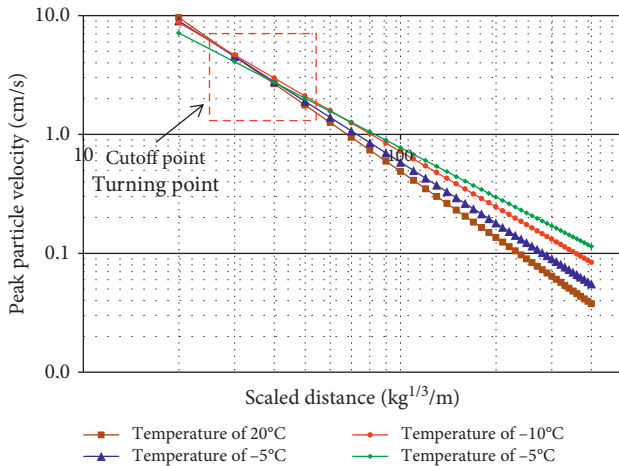


FIGURE 12: Comparison of the blasting attenuation law curves and the schematic of the turning point.

4.1. *The Numerical Tool and Equivalent Freezing Simulation Method.* To achieve a better understanding of this process, numerical simulation was implemented based on the case study of the foundation excavation of Fengman hydropower station. Figure 14 shows the developed numerical model to study the blast wave propagation in rock and structure. The model size was set to be 130 m long, 30 m wide, and 100 m high. A fine grid of elements is used in the vicinity of the

charge to increase the simulation accuracy. The grid increases in size away from the charge, but it should be shorter than 1/8~1/10 of the wavelength in general to properly reduce any wave distortions [23]. There are a total of 317,456 elements and 428,532 nodes in the numerical simulation. The source of the explosive is represented by a detonating cord containing a core load of emulsion explosive. Table 1 shows the used JWL equation of state parameters of the explosive. The contact setting of LS-DYNA was employed in the joint simulation. Nonreflecting boundaries are applied to the other surfaces, except the top surface which has the free boundary condition.

The water in the discontinuities in the rock mass close to the surface may change into ice under the low temperature. The numerous numbers of discontinuities in a rock mass in terms of the cracks and joints and their properties such as positions, orientations, strength, and stiffness are impossible to be known exactly, so the equivalent material property approach still remains the most popular and valuable means in practice in engineering. In the present study, the equivalent freezing simulation method was proposed, and detailed steps are as follows: firstly, the frozen depth and the temperature were determined according to the meteorological data; secondly, the physical-mechanical parameters of the frozen rock mass were obtained according to the laboratory test; and thirdly, the elements of the frozen layer in the numerical model were set as the frozen rock mass by



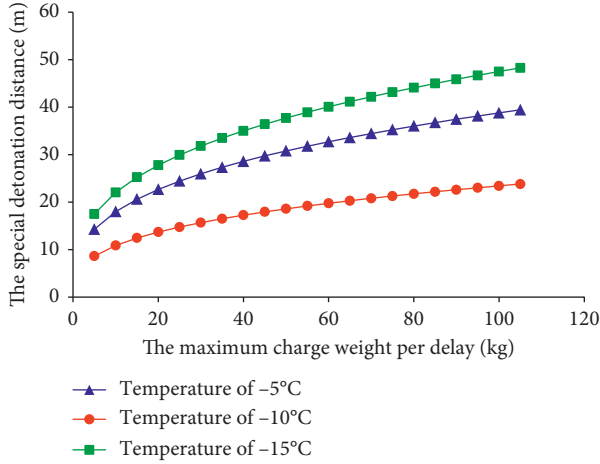


FIGURE 13: Detonation distance versus the maximum charge weight per delay at the turning point.

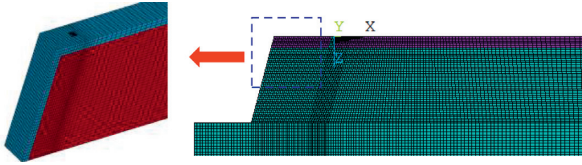


FIGURE 14: Numerical model to study the blast wave propagation.

adopting the different physical-mechanical parameters. Based on the laboratory test of the longitudinal wave velocity in the frozen rock mass, the elasticity modulus could be determined with equation (2). The density could be obtained directly with laboratory test. Table 2 shows the material constants for the constitutive model. Figure 15 plots the elasticity modulus increment versus the porosity in the frozen sandstone.

$$E = \frac{V_p^2 \rho (1 + \mu) (1 - 2\mu)}{(1 - \mu)}. \quad (2)$$

To reveal the rationality of this equivalent simulation approach, the comparison between the site experiment and numerical simulation was implemented. Figure 16 plots the comparison results of vibration waveform and the attenuation law.

It can be seen that the waveform of numerical simulation matches well with that of test results. The development process of blasting vibration waveform is quite similar, and the error of PPV is within 8%. The attenuation law of PPV was also comprised of different conditions. As can be seen from Figure 16, the numerical curves of blasting attenuation law agree well with that of the site experiment when the temperatures are  $-5^\circ\text{C}$  and  $20^\circ\text{C}$ . The error of the attenuation parameters of  $K$  and  $\alpha$  are both within 6%. Results demonstrate that the numerical results agree well with the experiment data, which indicates that the equivalent simulation approach could predict the blasting vibration of the frozen rock mass under blasting.

4.2. *The Determination of the Maximum Charge Weight per Delay in the Frozen Rock Mass.* Numerical simulation could reproduce more kinds of working conditions compared with the site experiment. Figure 17 plots the relationship of attenuation coefficients such as  $K$  and  $\alpha$  versus the frozen depth, respectively, while the results of site experiment were also used as the comparison.

It can be seen that the linear relationship between the attenuation parameters and frozen depth could be obviously found, and the coefficient of correlation could reach as much as 0.9. The mathematical descriptions are shown in equations (3) and (4). Results demonstrate that as the frozen depth of the rock mass increases, the attenuation parameters of  $K$  and  $\alpha$  decrease obviously, which indicates that the blasting seismic wave in rock mass attenuates slower after the rock mass was frozen. It can also be seen that the results of numerical simulation match well with that of site experiments.

$$K_2 = 0.87K_1 - 65 d, \quad (3)$$

$$\alpha_2 = \alpha_1 - 0.30 d. \quad (4)$$

During the engineering practice, the maximum charge weight per delay is one of the most important indexes during the blasting vibration control. Usually, it could be determined with equation (5). But when the rock mass was in the frozen state, the attenuation parameters of  $K$  and  $\alpha$  change obviously, which indicates that maximum charge weight per delay needs to be taken seriously. The description of the maximum charge weight per delay of the rock mass in the frozen state is shown in equation (6).

$$Q = R^3 \left( \frac{V}{K} \right)^{3/\alpha}, \quad (5)$$

$$Q = \frac{R^3 V^{3/(\alpha_1 - 0.30 d)}}{(0.87K_1 - 64 d)^{3/(\alpha_1 - 0.30 d)}}. \quad (6)$$

Assuming that the vibration safety control standard of the building remains unchanged after the rock mass was frozen, the maximum charge weight per delay of the rock mass in the frozen state could be determined according to the above mathematical descriptions. Figure 18 plots the comparison of  $Q_{\max}$  when the rock mass was in conventional and frozen states.

It can be seen that the maximum charge weight per delay change is less than that of conventional condition. The relationship between the frozen depth and the maximum charge weight per delay presents as the parabola characteristics. A minimum charge weight per delay could be found when the frozen depth is about 1.8 m. If the frozen depth is less than 1.8 m, the allowed charge weight per delay decreases with the frozen depth; otherwise, the maximum charge weight per delay increases with the frozen depth. Results demonstrate that the maximum charge weight per delay was limited more strictly during the frozen condition, and a most adverse depth exists. So it is necessary to pay



TABLE 1: JWL equation of state parameters of the explosive used.

Density ( $\text{kg/m}^3$ )	VoD (m/s)	$P_{CJ}$ (GPa)	$A$ (GPa)	$B$ (GPa)	$R1$	$R2$	$\omega$	$E0$ (GPa)
1000	3600	3.24	220	0.2	4.5	1.1	0.35	4.2

VoD: velocity of detonation.

TABLE 2: Material constants for the constitutive model.

Classes	Density ( $\text{kg/m}^3$ )	Elasticity modulus (GPa)	Poisson's ratio	Dynamic tensile strength (MPa)	Damage constants $k$	Damage constants $m$	$K_{IC}$ ( $\text{MN} \cdot \text{m}^{-3/2}$ )	Damage constants $\lambda$ (kg/J)	Material constants ( $\beta$ )
Rock mass	2530	25	0.23	2	$2.33 \cdot 10^{24}$	7	0.92	0.0001	0.5

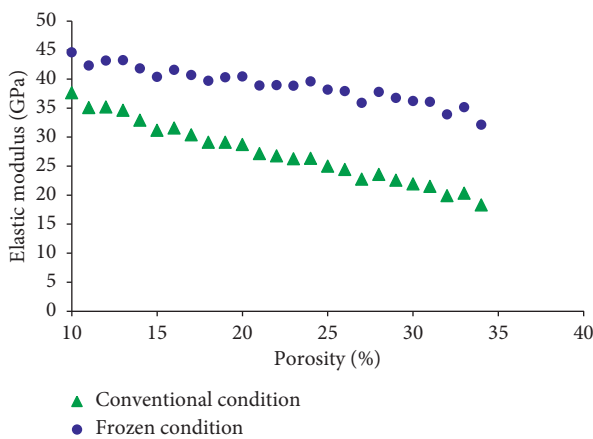


FIGURE 15: Elastic modulus increment versus the porosity in the frozen sandstone.

more attention to the control of the maximum charge weight per delay when the rock mass is in the frozen state.

**4.3. Comparison of the Dynamic Response of the Project of Frozen and Conventional Conditions.** The attenuation characteristic of blasting seismic wave is changed obviously in the frozen rock mass, which also affects the dynamic response of structures. To investigate the blasting vibration characteristic in the structure, the comparison of the structure response of blasting in frozen and conventional conditions was implemented with numerical simulation. Figure 19 plots the schematic diagram of the numerical structure model.

Figure 20 plots the comparison of the maximum principal stress, the minimum principal stress, the radial blasting vibration velocity, and the resultant blasting vibration velocity, respectively.

It can be seen that the stress in the frozen rock mass is larger than that in conventional condition. The maximum principal stress in frozen condition exceeds that in conventional condition by nearly 20%, while that is about 10% for the minimum principal stress. The radial and resultant PPV of the frozen rock mass are also larger than those of the conventional rock mass. The resultant PPV of the

conventional rock mass is only about 75% of that in frozen condition. Results demonstrate that the degree of dynamic response in structure under frozen condition is much stronger. This could be explained that the damping characteristic and geology were changed in the frozen rock mass, which makes the attenuation speed of blasting seismic wave slower.

During the engineering practice, the blasting vibration control standard was adopted as the threshold to limit the dynamic response in the structure within the allowed value. It is known that the tensile strength of the concrete is less than the compressive strength, so the tensile damage could be induced by blasting more easily. The blasting vibration control standard was determined based on the tensile stress control. The detailed steps are as follows: firstly, the numerical simulation of dynamic response in structure was implemented; then the relationship between the PPV at the foundation of structure and the maximum tensile stress of the structure was established; at last, when the maximum tensile stress is equal to the tensile strength, the corresponding PPV is the blasting vibration control standard. Figure 21 plots the comparison of the blasting vibration control standard under the cold and conventional conditions.

It can be seen that the typical linear relationship between the PPV and the maximum tensile stress could be both found under the conventional and frozen conditions. Results reveal that the blasting vibration control standard of the frozen rock mass is larger than that of conventional condition, which indicates that the frozen is beneficial for the blasting vibration safety control. But it should be pointed that the results do not mean the safety control of the blasting vibration in the frozen state is looser. As mentioned in Section 4.2, the maximum charge weight per delay in the frozen rock mass is obviously less than that in the conventional condition. Under the conventional condition, the blasting vibration control standard is 9.6 cm/s, but for the rock mass in the frozen state, that is 10.7 cm/s. During the blasting vibration safety control of the Fengman hydropower station reconstruction project, the blasting vibration control standard was determined as 10 cm/s. A total of 676 monitoring was completed, and no case of excessive measurement could be found.

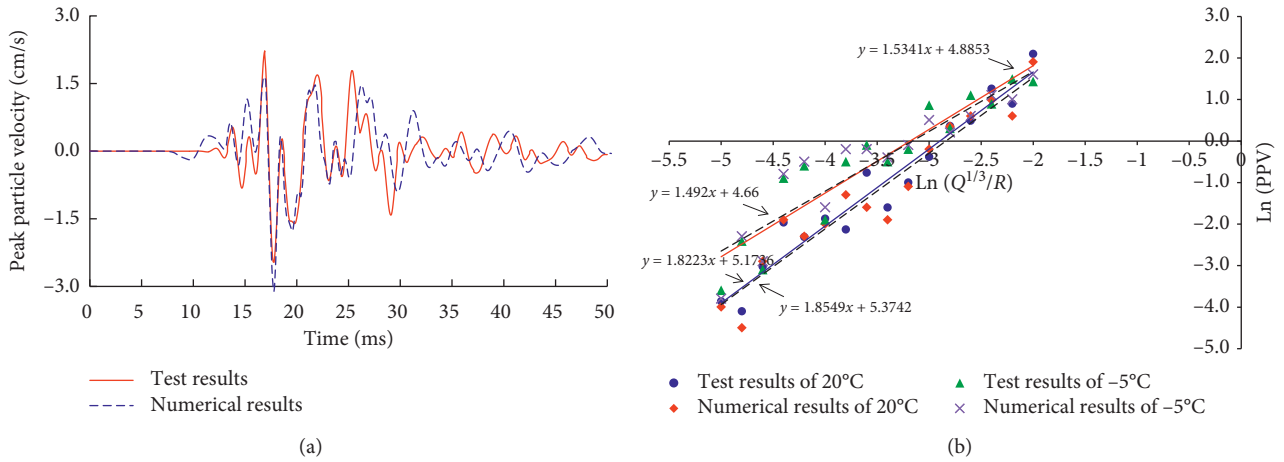


FIGURE 16: Comparison results of vibration waveform and the attenuation law.

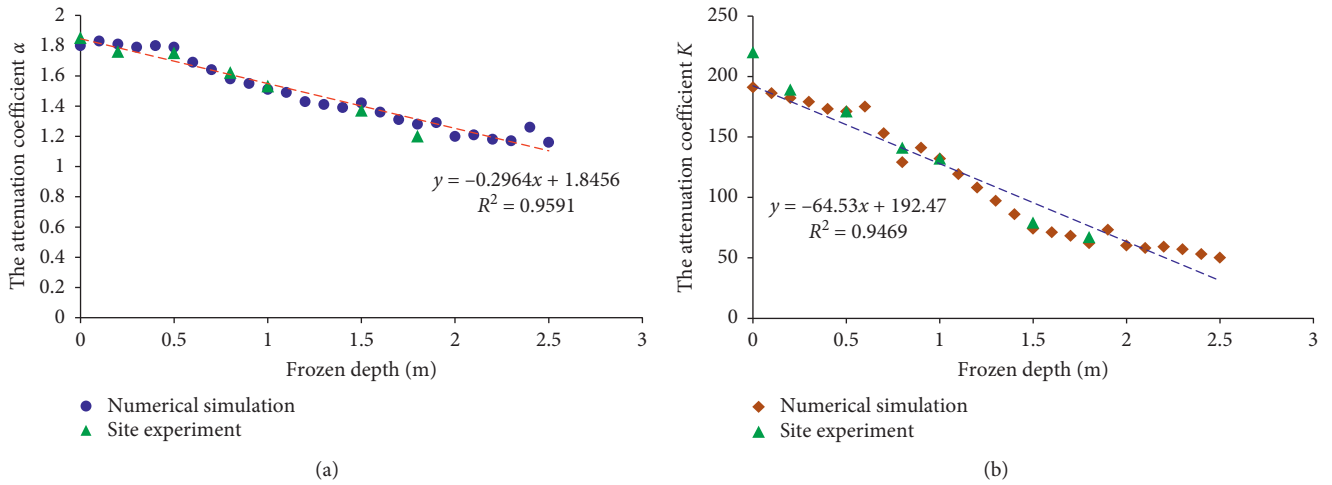


FIGURE 17: Variation law of vibration attenuation parameters versus frozen depth. (a) Coefficient  $\alpha$ . (b) Coefficient  $K$ .

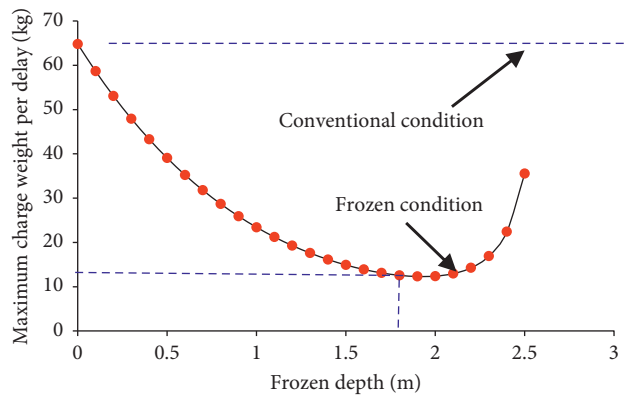


FIGURE 18: Comparison of  $Q_{max}$  when the rock mass was in conventional and frozen states.

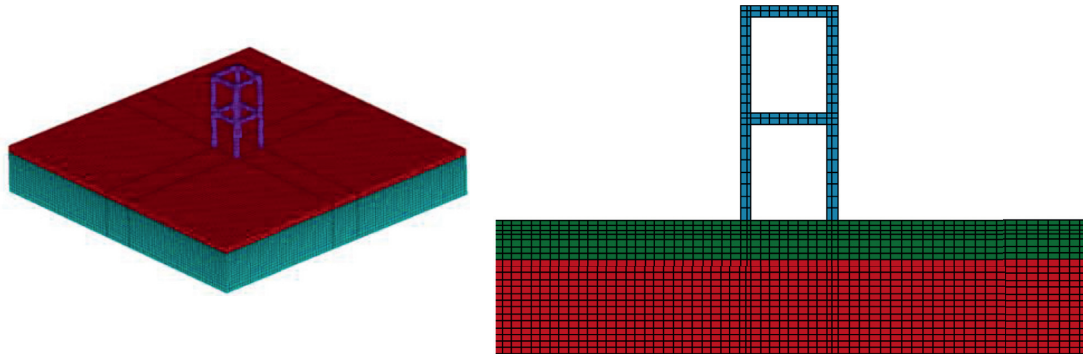


FIGURE 19: Schematic diagram of the numerical model for structural response analysis.

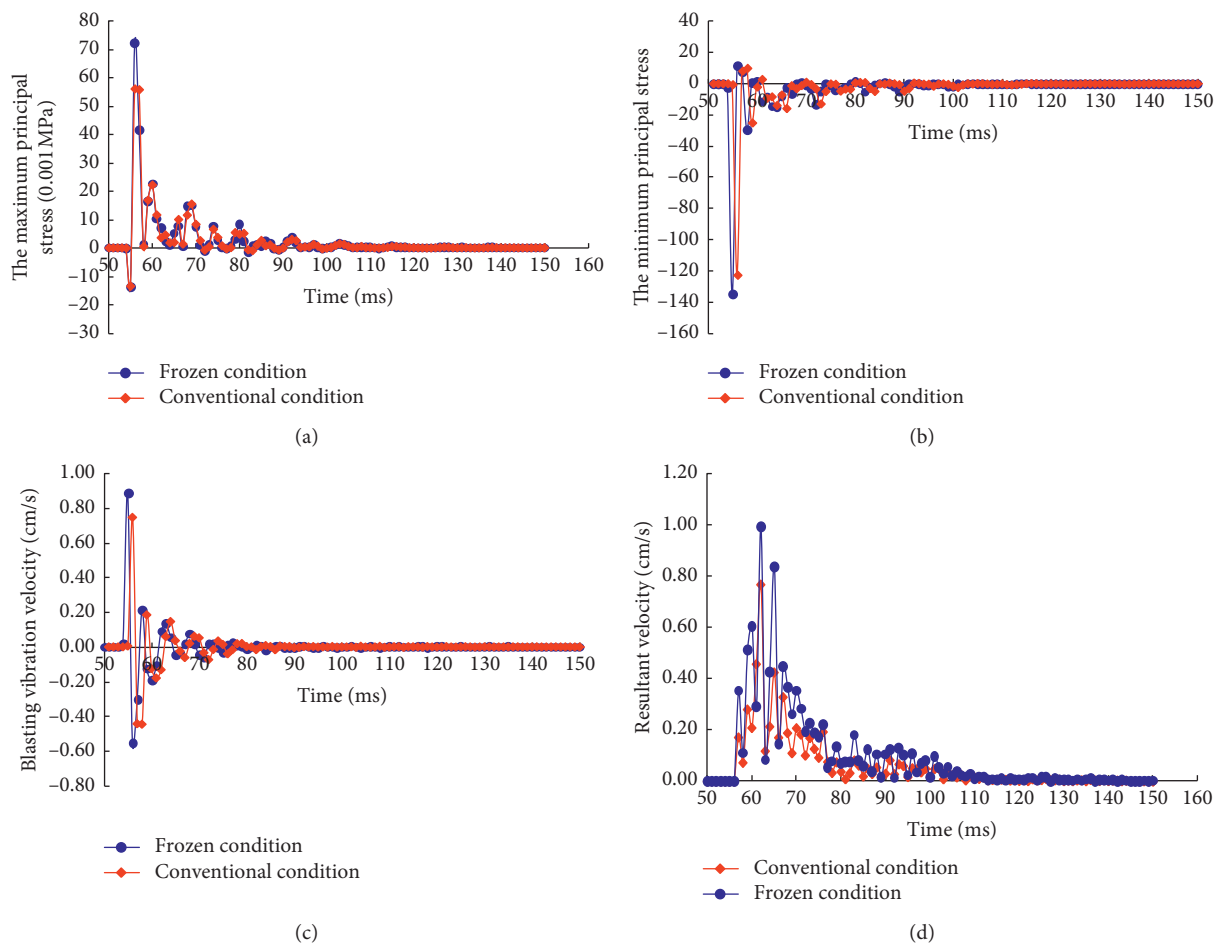


FIGURE 20: Comparison of the dynamic response in the frozen and conventional conditions. (a) The maximum principal stress. (b) The minimum principal stress. (c) The radial blasting vibration velocity. (d) The resultant blasting vibration velocity.

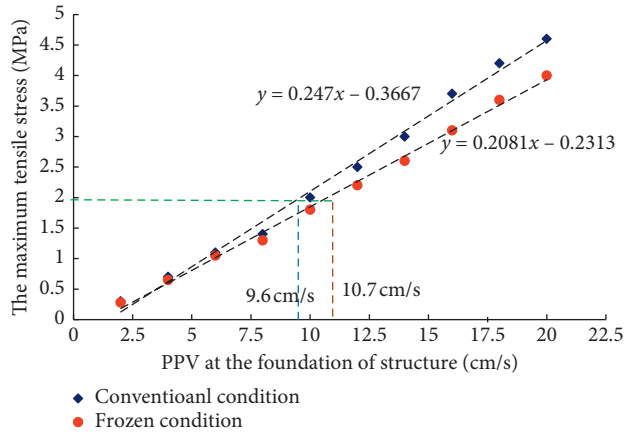


FIGURE 21: Comparison of the blasting vibration control standard under the cold and conventional conditions.

## 5. Conclusions and Discussions

This paper focuses on the blasting vibration control technology of the frozen rock mass under cold condition. Laboratory tests were implemented to investigate the change of mechanical performance for rock mass at the frozen, saturated, normal, and drying states. Then long-term monitoring of blasting vibration was implemented based on the blasting excavation of Fengman hydropower station reconstruction project in China to study the vibration attenuation law of the rock mass at different seasons. The blasting vibration declines slower in winter for the frozen rock mass. At last, numerical simulation of blasting vibration attenuation at different states was finished and suggestion of blasting vibration control of rock mass excavation under cold condition was proposed. The following conclusions and understandings may be drawn from the present study.

The longitudinal wave velocity in the frozen state is the biggest, and the wet saturated state takes the second place, while the natural state is third and the dry state is the least. The longitudinal wave velocity exceeds that of the natural state by about 10%~35% in the Fengman hydropower station area, and the difference between the frozen and natural state increases with the porosity obviously. The ability to conduct the stress waves is enlarged when the rock mass is frozen, especially in the rock medium with high porosity. The wave impedance increment and the porosity obey the exponential relationships obviously.

Results demonstrate the PPV attenuates slower when the rock mass is frozen, which indicates that the quality of the rock mass becomes better. The frequency of the blasting vibration in the frozen rock mass is also larger than that in the conventional condition. As the temperature decreases, the attenuation coefficient  $K$  and  $\alpha$  all decrease by different degrees. The obvious turning points of PPV could be found between different temperatures, where the change of the PPV relationship happens.

The equivalent freezing simulation method was proposed to simulate the response in the frozen rock mass and structures. Results demonstrate that the waveform of numerical simulation matches well with that of test results. The

development process of blasting vibration waveform is quite similar and the error of PPV is within 8%. The relationship of attenuation coefficients such as  $K$  and  $\alpha$  versus the frozen depth was determined, respectively. The linear relationship between the attenuation parameters and frozen depth could be obviously found, and as the frozen depth of the rock mass increases, the attenuation parameters of  $K$  and  $\alpha$  decrease obviously.

The maximum charge weight per delay and blasting vibration control standard were investigated in the frozen rock mass to control the blasting vibration. The relationship between the frozen depth and the maximum charge weight per delay presents as the parabola characteristics. The maximum charge weight per delay was limited more strictly during the frozen condition, and a most adverse depth exists. The degree of dynamic response in structure under frozen condition is much stronger. The blasting vibration control standard in the frozen condition is larger than that in the conventional condition. With the above control approaches, a total of 676 monitoring was completed in the Fengman reconstruction project, and no case of excessive measurement could be found.

## Data Availability

The data supporting the results of this study can be obtained upon request to the corresponding author.

## Conflicts of Interest

The authors declare that they have no conflicts of interest regarding the publication of this paper.

## Acknowledgments

This work was supported by the Chinese National Natural Science Foundation (52079009) and the Central Scientific Research Operating Expenses (CKSF2019477/YT, CKSF2019193/YT). The authors wish to express their thanks to all supporters.

## References

- [1] O. Dogan, Ö. Anil, S. O. Akbas, E. Kantar, and R. Tuğrul Erdem, "Evaluation of blast-induced ground vibration effects in a new residential zone," *Soil Dynamics and Earthquake Engineering*, vol. 50, pp. 168–181, 2013.
- [2] D. Park, B. Jeon, and S. Jeon, "A numerical study on the screening of blast-induced waves for reducing ground vibration," *Rock Mechanics and Rock Engineering*, vol. 42, no. 3, pp. 449–473, 2008.
- [3] G. Ma, H. Hao, and Y. Lu, "Modelling damage potential of high-frequency ground motions," *Earthquake Engineering & Structural Dynamics*, vol. 32, no. 10, pp. 1483–1503, 2003.
- [4] J. H. Yang, J. H. Dai, C. Yao, S. H. Jiang, C. B. Zhou, and Q. H. Jiang, "Estimation of rock mass properties in excavation damage zones of rock slopes based on the Hoek-Brown criterion and acoustic testing," *International Journal of Rock Mechanics and Mining Sciences*, vol. 126, 2020.
- [5] H. R. M. Azizabadi, H. Mansouri, and O. Fouché, "Coupling of two methods, waveform superposition and numerical, to

- model blast vibration effect on slope stability in jointed rock masses,” *Computers and Geotechnics*, vol. 61, pp. 42–49, 2014.
- [6] H. Ak, M. Iphar, M. Yavuz, and A. Konuk, “Evaluation of ground vibration effect of blasting operations in a magnesite mine,” *Soil Dynamics and Earthquake Engineering*, vol. 29, no. 4, pp. 669–676, 2009.
- [7] I. A. Onederra, J. K. Furtney, E. Sellers, and S. Iverson, “Modelling blast induced damage from a fully coupled explosive charge,” *International Journal of Rock Mechanics and Mining Sciences*, vol. 58, pp. 73–84, 2013.
- [8] E. Wang and A. Shukla, “Analytical and experimental evaluation of energies during shock wave loading,” *International Journal of Impact Engineering*, vol. 37, no. 12, pp. 1188–1196, 2010.
- [9] J. Yang, J. Cai, C. Yao, P. Li, Q. Jiang, and C. Zhou, “Comparative study of tunnel blast-induced vibration on tunnel surfaces and inside surrounding rock,” *Rock Mechanics and Rock Engineering*, vol. 52, no. 11, pp. 4747–4761, 2019.
- [10] R. E. Goodman and D. S. Kieffer, “Behavior of rock in slopes,” *Journal of Geotechnical and Geoenvironmental Engineering*, vol. 126, no. 8, pp. 675–684, 2000.
- [11] S. A. Ashford, N. Sitar, J. Lysmer, and N. Deng, “Topographic effects on the seismic response of steep slopes,” *Bulletin of the Seismological Society of America*, vol. 87, pp. 701–709, 1997.
- [12] A. Kesimal, B. Ercikdi, and F. Cihangir, “Environmental impacts of blast-induced acceleration on slope instability at a limestone quarry,” *Environmental Geology*, vol. 54, no. 2, pp. 381–389, 2007.
- [13] M. Chen, W. B. Lu, P. Yan, and C. B. Zhou, “New method for dynamic stability analysis of rock slope under blasting vibration based on equivalent acceleration and Sarma method,” *Canadian Geotechnical Journal*, vol. 51, pp. 441–448, 2013.
- [14] W.-B. Lu, Y.-G. Hu, J.-H. Yang, M. Chen, and P. Yan, “Spatial distribution of excavation induced damage zone of high rock slope,” *International Journal of Rock Mechanics and Mining Sciences*, vol. 64, pp. 181–191, 2013.
- [15] J. Torano, R. Rodríguez, I. Diego, J. M. Rivas, and M. D. Casal, “FEM models including randomness and its application to the blasting vibrations prediction,” *Computers and Geotechnics*, vol. 33, no. 1, pp. 15–28, 2006.
- [16] W. B. Lu, J. H. Yang, M. Chen, and C. B. Zhou, “An equivalent method for blasting vibration simulation,” *Simulation Modelling Practice Theory*, vol. 19, pp. 2050–2062, 2011.
- [17] C. Kuzu, “The importance of site-specific characters in prediction models for blast-induced ground vibrations,” *Soil Dynamics and Earthquake Engineering*, vol. 28, no. 5, pp. 405–414, 2008.
- [18] T.-C. Pan, K. S. Goh, and K. Megawati, “Empirical relationships between natural vibration period and height of buildings in Singapore,” *Earthquake Engineering & Structural Dynamics*, vol. 43, no. 3, pp. 449–465, 2014.
- [19] Y. Lu, H. Hao, G. Ma, and Y. Zhou, “Simulation of structural response under high-frequency ground excitation,” *Earthquake Engineering & Structural Dynamics*, vol. 30, no. 3, pp. 307–325, 2001.
- [20] I.-S. Ha, “Estimation of shear wave velocity of earth dam materials using artificial blasting test,” *Soil Dynamics and Earthquake Engineering*, vol. 55, pp. 120–129, 2013.
- [21] F. Jalayer, D. Asprone, A. Prota, and G. Manfredi, “Multi-hazard upgrade decision making for critical infrastructure based on life-cycle cost criteria,” *Earthquake Engineering & Structural Dynamics*, vol. 40, no. 10, pp. 1163–1179, 2011.
- [22] P. Li, W. B. Lu, X. X. Wu, M. Chen, P. Yan, and Y. G. Hu, “Spectral prediction and control of blast vibrations during the excavation of high dam abutment slopes with millisecond-delay blasting,” *Soil Dynamics and Earthquake Engineering*, vol. 94, pp. 116–124, 2017.
- [23] R. L. Kuhlemeyer and J. Lysmer, “Finite element method accuracy for wave propagation problems,” *Journal of the Soil Mechanics and Foundations Division*, vol. 99, no. 5, pp. 421–427, 1973.



## Research Article

# Influence of Cavity Width on Attenuation Characteristic of Gas Explosion Wave

Dengke Xu <sup>1</sup>, Chaomin Mu <sup>2,3</sup>, Zhongqing Li<sup>2,3</sup> and Wenqing Zhang<sup>2,3</sup>

<sup>1</sup>School of Civil Engineering and Architecture, Anhui University of Science & Technology, Huainan 232001, Anhui, China

<sup>2</sup>School of Energy and Safety, Anhui University of Science & Technology, Huainan 232001, Anhui, China

<sup>3</sup>Key Lab of Mining Coal Safety and Efficiently Constructed by Anhui Province and Ministry of Education, Huainan 232001, Anhui, China

Correspondence should be addressed to Chaomin Mu; [chmmu@mail.ustc.edu.cn](mailto:chmmu@mail.ustc.edu.cn)

Received 3 November 2020; Revised 14 January 2021; Accepted 18 February 2021; Published 26 February 2021

Academic Editor: Bangbiao Wu

Copyright © 2021 Dengke Xu et al. This is an open access article distributed under the Creative Commons Attribution License, which permits unrestricted use, distribution, and reproduction in any medium, provided the original work is properly cited.

This study aimed to investigate the influence of cavity width on the attenuation characteristic of gas explosion wave. Attenuation mechanism of gas explosion wave through cavity was obtained by numerical simulation. The gas explosion shock wave energy can be greatly attenuated through the cavity structure in five stages, namely, plane wave, expansion, oblique reflection, Mach reflection, and reflection stack, to ensure that it is eliminated. Cavities with various width sizes, namely, 500 \* 300 \* 200, 500 \* 500 \* 200, and 500 \* 800 \* 200 (length \* width \* height, unit: mm), were experimented to further investigate the attenuation characteristics through a self-established large-size pipe gas explosion experimental system with 200 mm diameter and 36 m length. Results showed an evident attenuation effect on flame duration light intensity (FDLI) and peak overpressure with increasing cavity width. Compared with 300 mm, the overall FDLI decreased by 83.0%, and the peak overpressure decreased by 71.2% when the cavity width was 800 mm. The fitting curves of the FDLI and peak overpressure attenuation factors to width-diameter demonstrated that the critical width-diameter was 2.19 when the FDLI attenuation factor was 1. The FDLI attenuation factor sharply decreased at the width-diameter ratio range from 1.5 to 2.5 and basically remained steady at 0.17 at the width-diameter ratio range from 2.7 to 4.0. The peak overpressure attenuation factor gradually decreased with the increase of width-diameter ratio and changed from 0.93 to 0.28 with width-diameter ratio from 1.5 to 4.0. The research results can serve as a good reference for the design of gas explosion wave-absorbing structures.

## 1. Introduction

Gas explosion is a dynamic disaster phenomenon that occurs in the coal-mining process when gas enrichment reaches its limit and meets a fire source. The high-temperature and high-pressure shock wave generated by the explosion propagates along the tunnel pipe network, causing heavy casualties and serious damage to roadways, support structures, and equipment [1–5]. Gas explosion prevention mainly includes preventive technical measures to counteract the gas accumulation and fire source generation in coal mines and mitigating measures (such as explosion isolation and suppression) to limit or control the gas explosion shock wave propagation. Many scholars have focused on theoretical and experimental research on

gas explosion suppression. Yoshida et al. [6], Xu et al. [7], Parra et al. [8], Song and Zhang [9], and Nakahara et al. [10] pointed out that water mist has a good effect on gas explosion suppression under certain conditions and the combination of different additives to achieve a suppression effect. Dry powders, such as  $\text{NH}_4\text{H}_2\text{P}_2\text{O}_4$  [11, 12], ABC [13], and  $\text{NaHCO}_3$ /red-mud [14], have been used in explosion suppression studies. The results demonstrated that powder concentration, explosion suppression dose, powder pyrolysis characteristics, and thermal decomposition products can have a different influence on gas explosion inhibition. A number of studies have been conducted to suppress gas explosion overpressure and quench flame propagation by using porous materials, including porous media [15], foam ceramics [16], wire

mesh [17, 18], metal foam [19, 20], and combined wire mesh and foam ceramics [21, 22]. The results showed that the foam iron nickel with great thickness, small aperture, and high nickel content are beneficial to the flame wave attenuation. The effect of combining wire mesh and foam ceramics on attenuation of explosion overpressure and flame temperature is better than that of each. Foam ceramics can attenuate the maximum overpressure of gas explosion by up to 50%, inhibit flame propagation, and quench flames.

Many studies on various pipeline structures and vacuum chambers have reported the influence of these mechanisms on gas explosion propagation. Shao et al. [23–25] conducted experimental research on the influencing factors of the vacuum chamber on explosion suppression. The results showed that the vacuum chamber can effectively suppress the explosion flame and overpressure with any vacuum degree. The vacuum chamber with different diaphragm thicknesses has a variable suppression effect. The explosion suppression effect is related to the break-up time of the diaphragm and the position of the explosion flame front. Niu et al. [26] established a complex transversal pipe network to study the overpressure evolution laws and flame propagation characteristics after methane explosion; these researchers found that a high-pressure area exists in the middle of the transversal branch, and the flame sustaining time and surface damage are minimal at the transversal branch. Sun et al. [27] used numerical methods to investigate the explosion-proof distance and the propagation characteristics of gas explosions with four types of pipe cross-sectional areas. The results demonstrated that maximum overpressure, density, temperature, gas velocity, explosion-proof distance, and combustion rate decrease with the increase of the equivalent pipe diameter. Lin et al. [28] conducted an experiment on the effect of premixed methane-air explosion overpressure by using three different types of bifurcation pipe; the result showed that the peak overpressure had a downtrend before the bifurcation, a sharp increase after the bifurcation until the maximum was reached, and a downtrend at the pipe end. The pipe shapes, such as 90° bends [29, 30], U-bend [31, 32], open-ended pipe [33], pipe with holes [34], and vortex shedding [35] are used to investigate the characteristics of gas explosion propagation.

Previous studies have focused on the propagation characteristics of gas explosion with different absorbing energy materials, pipe network structure, pipe shape, and vacuum chamber. The cavity structure exhibits several characteristics, such as strong damage resistance and reuse, but it is rarely reported to suppress gas explosion propagation using the cavity structure. In this work, the numerical simulation and experimental research are performed to investigate the relevant parameter evolution laws of the gas explosion shock wave through the cavity structure and reveal the quantitative relationship between shock wave attenuation and width of the cavity structure. The research results present a new technique for reducing gas explosion hazard.

## 2. Cavity Attenuation Wave Numerical Analysis

**2.1. Continuous Differential Equation of Gas Explosion.** The kinetic process of a gas explosion in a pipe network is expressed by the conservation of mass, momentum, energy, and component. The equations in the Cartesian coordinate are as follows:

The mass conservation equation is

$$\frac{\partial \rho}{\partial t} + \frac{\partial}{\partial x_i} (\rho u_i) = 0. \quad (1)$$

The momentum conservation equation is

$$\frac{\partial}{\partial t} (\rho u_i) + \frac{\partial}{\partial x_j} (\rho u_i u_j) = -\frac{\partial p}{\partial x_i} + \frac{\partial \tau_{ij}}{\partial x_j}. \quad (2)$$

The energy conservation equation is

$$\frac{\partial}{\partial t} (\rho E) + \frac{\partial}{\partial x_i} (\rho u_i E) = -\frac{\partial}{\partial x_i} (p u_i) + \frac{\partial \tau_{ij}}{\partial x_i} \left( \Gamma_g \frac{\partial E}{\partial x_i} \right) + \tau_{ij} \frac{\partial u_i}{\partial x_{ij}}. \quad (3)$$

The component conservation equation is

$$\frac{\partial}{\partial t} (\rho m_g) + \frac{\partial}{\partial x_i} (\rho u_i m_g) = \frac{\partial}{\partial x_i} \left( \Gamma_g \frac{\partial m_g}{\partial x_i} \right) + R_g. \quad (4)$$

The other formulas are as follows:

$$\tau_{ij} = \mu_t \left( \frac{\partial u_i}{\partial x_j} + \frac{\partial u_j}{\partial x_i} \right) - \frac{2}{3} \delta_{ij} \left( \rho k + \mu_t \frac{\partial u_j}{\partial x_j} \right),$$

$$E = c_v T + \frac{u_i u_i}{2} = \frac{1}{\gamma - 1} \frac{p}{\rho} + \frac{u_i u_i}{2}, \quad (5)$$

$$R_g = C_t \rho \frac{S_t}{\Gamma_g} R_m,$$

$$R_m = \min \left\{ m_g, \frac{m_{\text{air}}}{S}, \frac{m_{\text{pro}}}{1 + S} \right\},$$

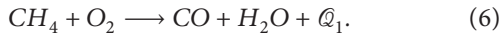
where  $\rho$  is gas density;  $t$  is time;  $u$  is gas explosion propagation velocity,  $i$  and  $j$  are coordinate directions;  $p$  is gas pressure;  $\mu_t$  is turbulent viscosity;  $\delta_{ij}$  is the Kronecker operator;  $E$  is per-unit mass gas total energy;  $T$  is temperature;  $\gamma$  is the adiabatic index;  $c_v$  is constant volume specific heat;  $m_g$  is the  $g$  component mass fraction;  $\Gamma_*$  is the turbulent diffusion coefficient expressing transport characteristic;  $R_g$  is the unit volume  $g$  component ignition rate;  $C_t$  is the dimensionless combustion model coefficient;  $R_m$  is the minimum mass fraction of gas, oxygen, and explosion product; and  $s$  is the stoichiometric ratio of oxygen required for a 1 kg gas complete reaction.

A gas explosion is a chain reaction process that consists of complex physical and chemical processes. The shock wave propagation process exhibits complex change parameters, including the propagation and evolution of explosion combustion flame and shock wave, excitation feedback of flame front and shock wave front, and turbulence. The model is simplified as follows and hypothesized to effectively conduct numerical research:

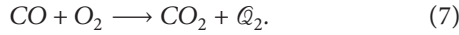
- (1) The gas explosion is simplified as the ideal gas expansion process by heat.
- (2) The pipe and cavity inner wall are regarded as an adiabatic surface without heat exchange. The radiative heat release in the propagation process of the blast wave and the fluid-solid coupling effect between the solid wall and shock flow are ignored.
- (3) The gas and air are evenly mixed in accordance with Moore's law and in a static state before ignition.
- (4) The gas explosion process is realized in two steps, and the gas mixture of wave front is still in a static state.
- (5) The Mach stem is a plane shock wave and perpendicular to the solid wall.

**2.2. Gas Explosion Chemical Reaction Model.** As this study does not simultaneously include the detonation cellular structure part and consider the calculation amount of the elementary reaction model, a two-step reaction model with higher accuracy is adopted, which can be written as follows.

*Step 1.*



*Step 2.*



The energy release is small in Step 1 and large in Step 2. The chemical reaction rate formulas corresponding to the reaction model are presented as follows:

The induced reaction rate is expressed by

$$\omega_\alpha = -K_1 \rho \exp\left(\frac{-E_1}{RT}\right). \quad (8)$$

The rate of exothermic chemical reaction is calculated by

$$\omega_\beta = \begin{cases} -K_2 p^2 \left\{ \beta^2 \exp\left(\frac{-E_2}{RT}\right) - (1 - \beta)^2 \exp\left(\frac{-E_2 + q}{RT}\right) \right\}, & \alpha \leq 0, \\ 0, & 0 < \alpha < 1, \end{cases} \quad (9)$$

where  $K_1$  and  $K_2$  are the rate characteristic constants of the induced and exothermic chemical reactions;  $\alpha$  is the induction progress degree and dimensionless quantity,  $\alpha = 1$  means that the induction reaction has not started yet, and  $\alpha = 0$  means that the induction reaction has been performed;  $\beta$  is the reaction progress degree and dimensionless quantity,  $\beta = 1$  means that the exothermic chemical reaction has not started yet, and  $\beta = 0$  means that the exothermic chemical reaction has been performed;  $\rho$  is density;  $E_1$  and  $E_2$  are the induced reaction and exothermic chemical reaction activation energies, respectively;  $p$  is mixed gas pressure;  $R$  is gas constant;  $T$  is temperature; and  $q$  is unit mass mixed gas heat release.

In this study, the Steger-Warming method [36] is used to construct the difference scheme for physical quantities, and the equation is as follows:

$$\frac{\partial}{\partial t} (\rho\Phi) + \frac{\partial}{\partial x_i} \left( \rho u_i \Phi - \Gamma_\Phi \frac{\partial \Phi}{\partial x_i} \right)^+ + \frac{\partial}{\partial x_i} \left( \rho u_i \Phi - \Gamma_\Phi \frac{\partial \Phi}{\partial x_i} \right)^- - \varphi_\Phi = 0. \quad (10)$$

In spatial dimension, the WENO format [37] is used for discretization. In time dimension, the LU-SSOR method [38] is adopted for discretization and the time discretization equation:

$$\frac{\Delta \widehat{\mathcal{Q}}_g^n}{\Delta \tau} = -c^{n+1} + q^n + \widehat{\mathcal{S}}^{n+1}. \quad (11)$$

The equation, with the retained first-order accuracy  $O(\Delta \widehat{\mathcal{Q}}_g^n)$ , can be expressed as follows:

$$\begin{aligned} c^{n+1} &= \frac{\partial}{\partial \xi} (\widehat{E}_g^n + \widehat{A}^n \cdot \Delta \widehat{\mathcal{Q}}_g^n) + \frac{\partial}{\partial \eta} (\widehat{F}_g^n + \widehat{B}^n \cdot \Delta \widehat{\mathcal{Q}}_g^n) \\ &\quad + \frac{\partial}{\partial \zeta} (\widehat{G}_g^n + \widehat{C}^n \cdot \Delta \widehat{\mathcal{Q}}_g^n) \\ &= \frac{\partial}{\partial \xi} (\widehat{A}^n \cdot \Delta \widehat{\mathcal{Q}}_g^n) + \frac{\partial}{\partial \eta} (\widehat{B}^n \cdot \Delta \widehat{\mathcal{Q}}_g^n) + \frac{\partial}{\partial \zeta} (\widehat{C}^n \cdot \Delta \widehat{\mathcal{Q}}_g^n) + c^n, \end{aligned} \quad (12)$$

where  $c$  is the convection term,  $\widehat{A} = (\partial \widehat{E}_g / \partial \widehat{\mathcal{Q}}_g)$ ,  $\widehat{B} = (\partial \widehat{F}_g / \partial \widehat{\mathcal{Q}}_g)$ , and  $\widehat{C} = (\partial \widehat{G}_g / \partial \widehat{\mathcal{Q}}_g)$  are the Jacobian matrix corresponding to the convection term;  $q$  is the viscous term; and  $\Delta \xi$ ,  $\Delta \eta$ , and  $\Delta \zeta$  are the space steps in the corresponding three coordinate directions in any coordinate system. Correspondingly,  $c$  is discretized as

$$\begin{aligned} c &= \frac{1}{2\Delta \xi} \left[ (E_{g,i+1,j,k}^n - E_{g,i-1,j,k}^n) - (F_{g,i,j+1,k}^n - F_{g,i,j-1,k}^n) \right. \\ &\quad \left. - (G_{g,i,j,k+1}^n - G_{g,i,j,k-1}^n) + (R_{i+1/2,j,k}^n \varphi_{i+1/2,j,k}^n - R_{i-1/2,j,k}^n \varphi_{i-1/2,j,k}^n) \right. \\ &\quad \left. + (R_{i,j+1/2,k}^n \varphi_{i,j+1/2,k}^n - R_{i,j-1/2,k}^n \varphi_{i,j-1/2,k}^n) \right. \\ &\quad \left. + (R_{i,j,k+1/2}^n \varphi_{i,j,k+1/2}^n - R_{i,j,k-1/2}^n \varphi_{i,j,k-1/2}^n) \right], \end{aligned} \quad (13)$$

where the column vectors of  $R_{i \pm 1/2,j,k}^n$ ,  $R_{i,j \pm 1/2,k}^n$ , and  $R_{i,j,k \pm 1/2}^n$  are the right eigenvectors of  $(\partial \widehat{E} / \partial \widehat{U})$ ,  $(\partial \widehat{F} / \partial \widehat{U})$ , and  $(\partial \widehat{G} / \partial \widehat{U})$ , respectively; and  $\varphi$  is the viscosity factor, which is adjusted by numerical viscosity to eliminate the oscillation dispersion in the shock wave in the oscillation-prone area and ensure the simulation accuracy.

**2.3. Numerical Simulation Model.** The gas explosion simulation pipe was designed with a 200 mm inner diameter, 11 m length initiation detonation section, 2.5 m length stable section, and 22.5 m length propagation. The numerical monitoring sample points, called 1#, 2#, and 3#, were arranged at different positions before and after the cavity structure to investigate the parameter variation of the gas

explosion propagation process. The gas explosion propagations in the cavities with dimensions of  $500 * 300 * 200$ ,  $500 * 500 * 200$ , and  $500 * 800 * 200$  were simulated, and the data of representative cavity ( $500 * 500 * 200$ ) were chosen for analyzing the attenuation wave mechanism. The numerical simulation geometric model is shown in Figure 1.

In order to determine the grid size, the step length of iteration time was 0.00001 s, and grid size of  $0.5 * 0.5$  mm,  $1.0 * 1.0$  mm, and  $2.0 * 2.0$  mm was set, respectively, to analyze the grid independence. When the grid size was refined from  $2.0 * 2.0$  mm, and  $1.0 * 1.0$  mm to  $0.5 * 0.5$  mm, the maximum overpressure increased by 8.4% and 0.5%, respectively. The simulation results were very close when the grid size was  $1.0 * 1.0$  mm and  $0.5 * 0.5$  mm. Considering the calculation efficiency, storage space, and accuracy, the tetrahedral grid was used for numerical simulation, the grid size was  $1.0 * 1.0$  mm. The numerical simulation grid diagram is shown in Figure 2.

In this study, the difference scheme was constructed for physical quantities via the finite volume method and Steger-Warming method. The spatial dimension was discretized in the format of WENO, and the time dimension was discretized through the LU-SSOR method. Material properties were as follows: gas concentration and oxygen concentration were 9.5% and 20.9%, respectively,  $\gamma = 1.25$ ,  $C_t = 70$ , and  $\mu = 2.5 \times 10^{-5}$ . The initial conditions were  $P_0 = 2.5 \times 10^{-5}$ ,  $T_0 = 293$  K, and  $v = 0$  m/s. The boundary conditions were: the wall surfaces of pipeline and cavity were adiabatic, without slippage.

**2.4. Numerical Simulation Results and Analysis of Shock Wave.** The numerical simulation results of the gas explosion shock wave overpressure before and after the  $500 * 500 * 200$  cavity structure are shown in Figure 3.

The five main stages can be observed from the simulation results with gas explosion shock wave passes through the cavity structure, as follows:

- (1) Figure 3(a) shows that the gas explosion shock wave propagates forward in the form of a plane wave, and the overpressure of the shock wave changes in a uniform gradient, which enters the cavity structure before.
- (2) Figures 3(b) and 3(c) show that when the gas explosion shock wave enters the cavity structure, the plane wave becomes spherical and forms the vortex area in the propagation process due to the sudden expansion of the propagation section. Under the combined action of diffraction and expansion, the overpressure distribution displays phenomena such as concentrated enhancement zone at the center of the cavity structure, vortex attenuation zone at both sides, and gradient spherical diffusion zone at the front of the shock wave.
- (3) In Figure 3(d), along with the combined effects of reflection and superposition in the gas explosion shock wave propagation process within the cavity structure, the gas explosion shock wave high-

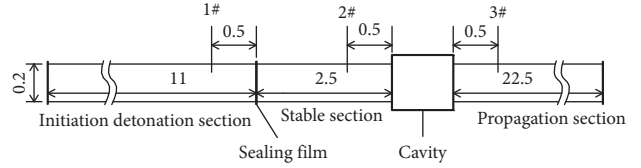


FIGURE 1: Numerical simulation geometric model (unit: m).

pressure area transmits to both sides of the cavity structure, and sparse waves generate in the cavity structure center. The Mach reflection appears, the overpressure concentrated area forms on both sides of the cavity structure, and the concentrated area repeatedly reflects in the propagation process due to the superposition of the shock wave reflection on both sides of the wall.

- (4) Figure 3(e) shows that when the gas explosion shock wave propagates to the cavity structure outlet because of the section reduction, the overpressure concentrated area on both sides of the cavity structure is blocked and reflected. The shock wave attenuation area after the outlet of the cavity structure is simultaneously formed.
- (5) Figures 3(f) and 3(g) show that the overpressure of the gas explosion shock wave gradually attenuates with the forward propagation in the pipe. The reflection wave gradually attenuates in the backward propagation process and generates a local overpressure concentrated area under the reflection superposition and other comprehensive effects after encountering the cavity wall. Accordingly, the local overpressure oscillation occurs.

The simulation results of shock wave pressure over time with  $500 * 500 * 200$  cavity are shown in Figure 4. The peak overpressure at 2# and 3# were 0.852 and 0.709, respectively, and the overpressure decreased by approximately 16.7%. In addition, according to the numerical simulation results of  $500 * 300 * 200$  and  $500 * 800 * 200$  cavities, the peak overpressure decreased by approximately 4.1% and 80%, respectively. In conclusion, the gas explosion shock wave energy can be greatly attenuated through the cavity structure by the aforementioned five stages, namely, plane wave, expansion, oblique reflection, Mach reflection, and reflection stack.

**2.5. Numerical Simulation Results and Analysis of Flame.** The numerical simulation results of the gas explosion flame temperature (temperature scale: K) before and after the  $500 * 500 * 200$  cavity structure are shown in Figure 5.

The four main characteristics can be summarized from the simulation results with gas explosion flame passes through the cavity structure, as follows:

- (1) After the premixed gas is ignited, it forms a spherical flame and spreads forward. Part of the flame directly enters the straight pipe through the cavity, and the flame in the cavity is stretched along the axial direction, as shown in Figure 5(a).



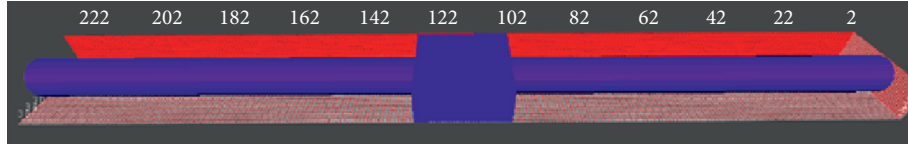


FIGURE 2: Numerical simulation grid diagram.

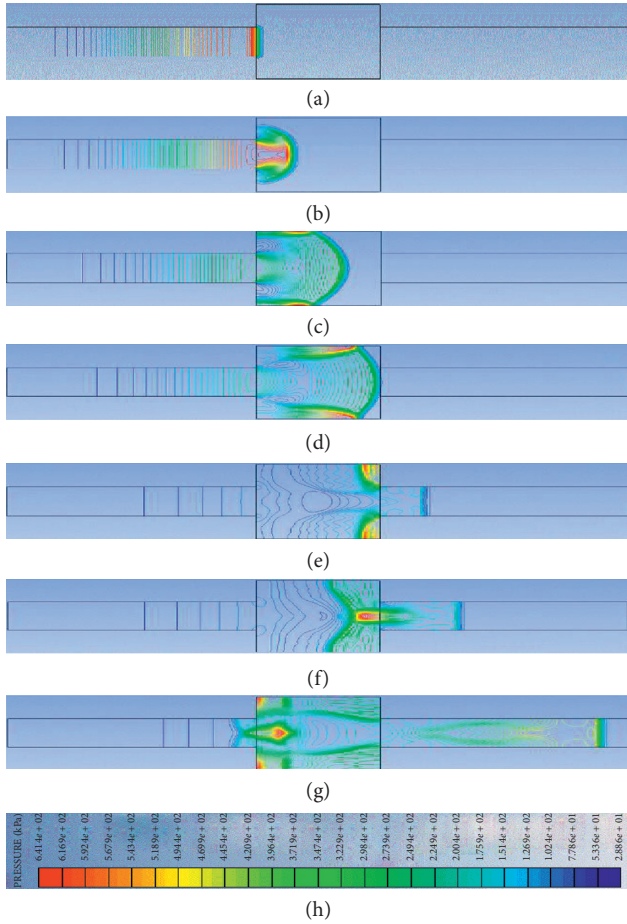


FIGURE 3: Diagram of overpressure distribution at different moments before and after 500 \* 500 \* 200 cavity structure. (a) 1 ms. (b) 1.5 ms. (c) 2 ms. (d) 2.5 ms. (e) 3 ms. (f) 3.5 ms. (g) 4 ms. (h) Scale.

- (2) The flame passing through the cavity continues to propagate forward along the straight pipe, and the other part is blocked by the cavity outlet wall due to the sudden contraction of the propagation section, as shown in Figure 5(b).
- (3) The blocked flame generates reflection on the outlet wall surface and diffuses along the cavity wall surface. As the contact area between the flame and the cavity wall surface increases, the energy consumed for friction increases greatly, as shown in Figures 5(c) and 5(d).
- (4) The flame diffracts in the cavity and the formed reverse propagation flame spreads to the inlet of the cavity, and the flame turbulence increases; however,

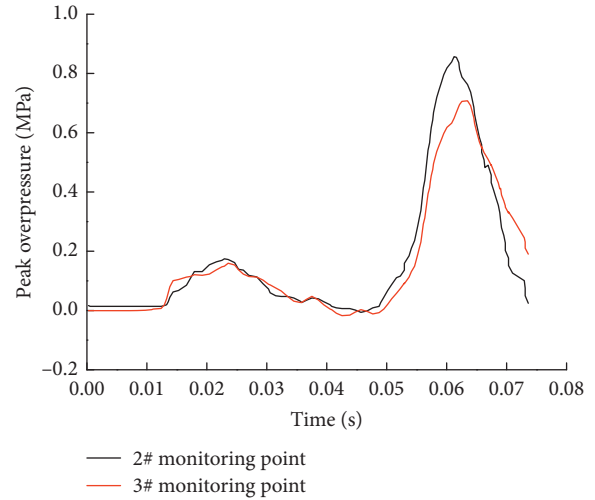


FIGURE 4: Shock wave pressure time travel curve.

the excessive turbulence is not conducive to the flame propagation, as shown in Figure 5(e).

The explosion flame has the occurrence of expansion and dissipation after entering the cavity. The siphon effect of the explosion causes the flame to be stretched. Part of the flame directly passes through the outlet of the cavity, and the other part is propagated back by the cavity wall surface. Due to the different reflection angles, part of the flame enters the cavity inlet and the other part is blocked by the cavity wall and reflects again. The repeated friction between the flame and the cavity wall consumes a lot of energy, and the flame gradually disappears with the depletion of premixed gas. The temperature curve of the explosion flame before and after passing through the cavity size of 500 \* 500 \* 200 is shown in Figure 6. It can be seen that the maximum flame temperature at 2# measuring point in front of the cavity is 1195 K and suddenly drops to 682 K at 3# measuring point after the cavity. The explosion flame energy is greatly attenuated, which shows that this size cavity has a good suppression effect on the explosion flame.

### 3. Gas Explosion Experimental Systems

The experimental system is shown in Figure 7, which mainly consists of the pipe network, distribution gas, ignition, and data collection subsystems. The literature [39] showed that the detonation wave can be generated and propagated when the pipe diameter  $D \geq \lambda/\pi$  ( $\lambda$  is the detonation cell size of the gas).  $\lambda$  is about 340 mm for gas, so the pipe size needs to be



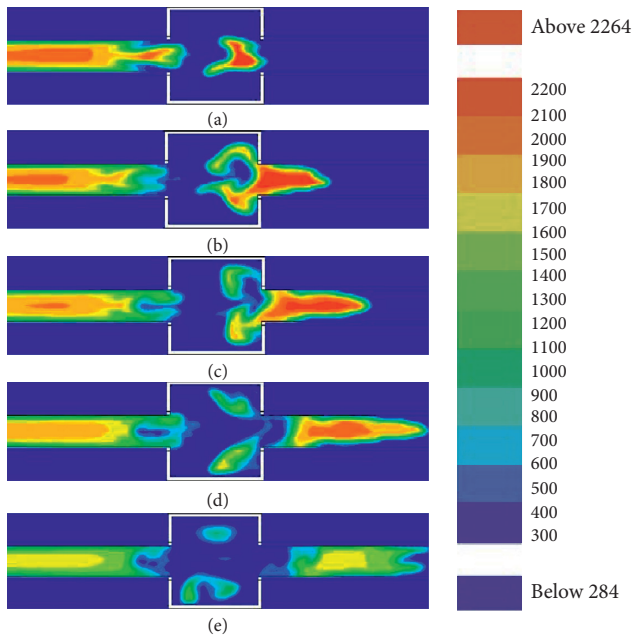


FIGURE 5: The flame propagation process of gas explosion before and after  $500 * 500 * 200$  cavity structure. (a) 0.089 (s). (b) 0.099 (s). (c) 0.105 (s). (d) 0.114 (s). (e) 0.148 s.

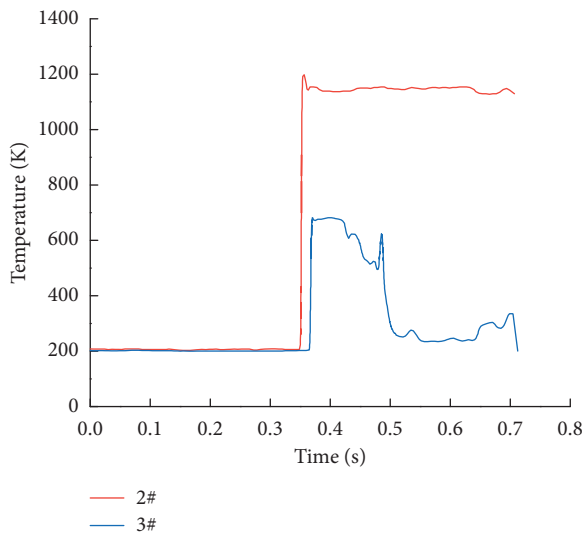


FIGURE 6: Curve of temperature at different measurement points with time.

greater than 108 mm. About the pipe wall thickness, the gas explosion pressure generally does not exceed 3 MPa. According to the requirements of pressure vessel specifications, the wall thickness should be greater than 7 mm. The designed explosion pipe is a 200 mm diameter steel round pipe with 10 mm thickness and 36 m length. The arrangement of a certain number of orifices on the pipe is intended for gas distribution, pressure collection, and flame signal collection, i.e., pressure and flame sensor installation. Figure 8 shows a photograph of the gas explosion experimental system.

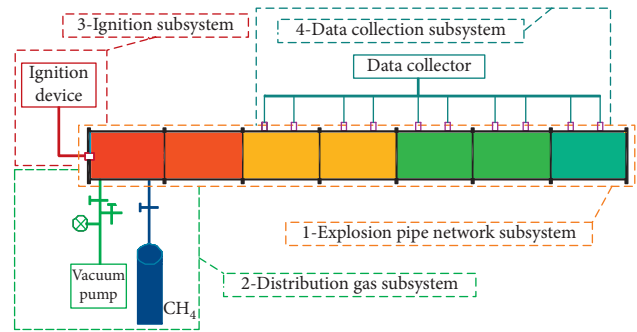


FIGURE 7: Components of gas explosion experimental system.



FIGURE 8: Photograph of gas explosion experimental system.

#### 4. Cavity Attenuation Wave Experiment

The cavities with different width sizes, namely,  $500 * 300 * 200$ ,  $500 * 500 * 200$ , and  $500 * 800 * 200$ , were made of 10 mm thick steel. The cavity structure was connected to the explosion pipe before and after and 13.5 m far from the ignition electrode. The flame sensor is a photo-sensitive triode induction element, its on-state current is positively correlated with the light intensity, and light signal changes to an electrical signal. The flame sensor information was used with the flame light intensity integration against time to represent the flame strength in the flame propagation process, which is defined as the flame duration light intensity (FDLI). Pressure and flame sensors were arranged before and behind the explosion tube and cavity to collect the shock wave overpressure and FDLI information. The flame sensor is the photosensitive triode sensor CKG100, and the response time is less than  $100 \mu\text{s}$ . The pressure sensor is the high frequency piezoelectric sensor CYG1401 F, and the response time is less than 1 ms. The experimental gas concentration is 9.5%. The initiation detonation section and the stability section were separated by 0.4 mm thickness polyethylene sealing film. The pre-mixed gas was filled before the film and stirred evenly by circulating pump for 25 min. During the experiment, the end of the pipeline system was closed. The ignition was used 36 V safety voltage and ignition energy is 10 J. The installation of the three cavities is shown in the photograph in Figure 9. Figure 10 shows the layout of sensors and cavity. The flame and pressure sensors were numbered F1, F2, F3, P1, and P2 from near to far according to the position of the ignition electrode. The specific parameters of distance ( $L$ ) and length-diameter ratio ( $L/D$ ) are shown in Table 1.

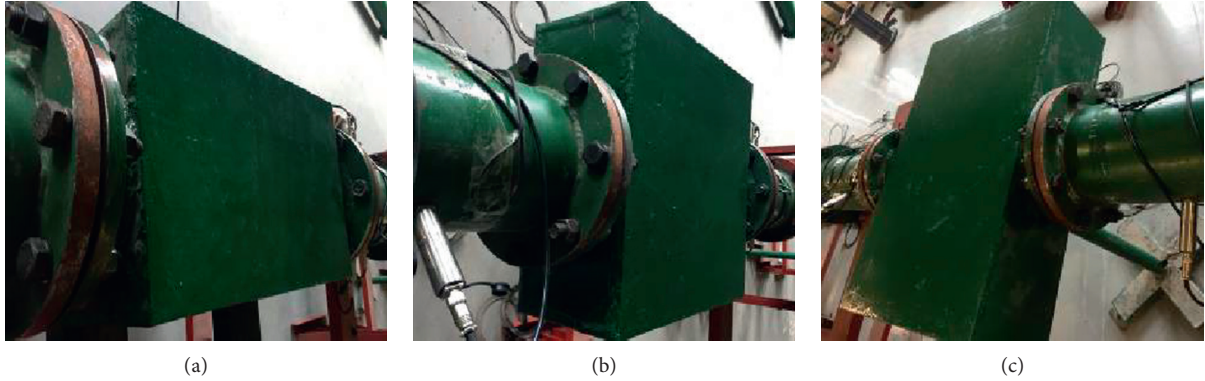


FIGURE 9: Photographs of different width cavities. (a) 500 \* 300 \* 200. (b) 500 \* 500 \* 200. (c) 500 \* 800 \* 200.

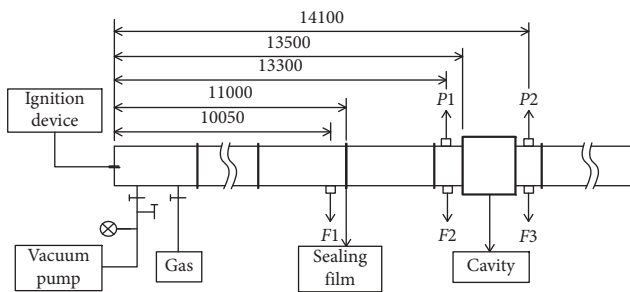


FIGURE 10: Layout of sensor and cavity structure (unit: mm).

TABLE 1: Arrangement of flame and pressure sensors.

Flame sensor		F1	F2	F3
Location	L (m)	10.05	13.3	14.1
	L/D	50.25	66.5	70.5
Pressure sensor		/	P1	P2
Location	L (m)	/	13.3	14.1
	L/D	/	66.5	70.5

## 5. Attenuation Wave Results and Discussion

This approach was conducted to investigate the effects of cavity structures with different widths on the gas explosion shock wave overpressure and FDLI. Three sets of gas explosion experiment were carried out for each cavity structure, and one typical set of experimental data was selected for result analysis.

**5.1. Flame Duration Light Intensity Influence of Different Width Cavities.** The FDLI attenuation rate of gas explosion is defined as the ratio of FDLI attenuation value at measuring points F2 and F3 in front of and behind the cavity to the FDLI at F2.

As shown in Figure 11(a) and Table 2, in the gas explosion propagation experiment of 500 \* 300 \* 200 cavity, the FDLIs at F2 and F3 were 0.0340 and 0.1342, respectively, and the FDLI attenuation was -294% after the shock wave passed through the cavity. The oscillation on the frontal surface of primary flame was severe behind the

cavity, and the secondary flame was obviously increased, and the FDLI at the cavity outlet was increased by 2.94 times, indicating that the cavity width was small, the gas not fully exploded was propagated into the cavity for continuous reaction, the energy released in the reaction zone was larger than the energy dissipated by local resistance of the cavity, and the explosive reaction was still in an accelerated phase, so the FDLI at the cavity outlet was increased.

From Figure 11(b) and Table 2, in the gas explosion propagation experiment of 500 \* 500 \* 200 cavity, the FDLIs at F2 and F3 were 0.0173 and 0.0071, respectively, and the attenuation rate of FDLI was 58.9% after the explosion wave passed through the cavity. The average speed of flame was obtained by dividing the interval between the two measuring points by the time difference for the flame signal to reach the two measuring points. As shown in Figure 11(b), the average flame speed between F1 and F2 was 358 m/s, indicating that the explosion already reached the detonation state in front of the cavity. With the increase in the cavity width, the swelling capacity and disturbance time of flame were increased, so was its energy dissipation. Even though the secondary flame was enhanced, the FDLI behind the cavity was obviously weakened, which was similar to the influence of the change in pipeline section on the gas explosion propagation characteristic in the literature [27].

As shown in Figure 11(c), in the gas explosion propagation experiment of 500 \* 800 \* 200 cavity, the FDLIs at F2 and F3 were 0.0384 and 0.0065, respectively, and the FDLI attenuation rate was 83.0% behind the cavity was passed. With the further increase in the cavity width, the transverse diffusion space of the cavity was enlarged, the Mach number and oblique reflection presented backward and forward oscillation, and the energy sharply dropped in front of the cavity outlet.

From the numerical simulation of the gas explosion flame propagation passing through the cavity, the temperature at the cavity outlet declined with the increase in the cavity width. Although the temperature during the explosion process could not be measured, it could be found that the FDLI at the outlet of cavity with width of greater than 500 mm was reduced, indicating that FDLI is correlated with the temperature, and the increase in the cavity width contributes to the energy dissipation.

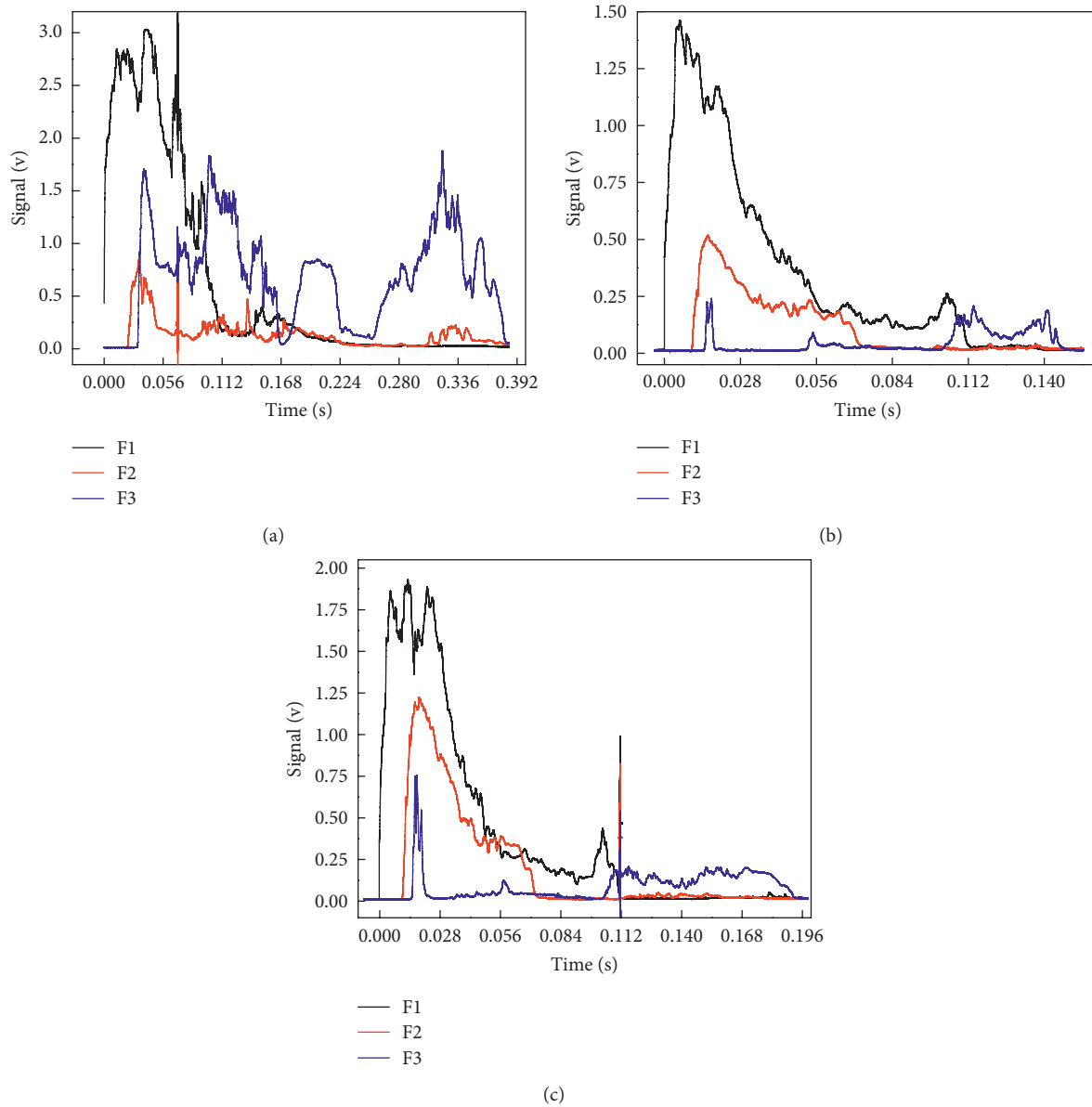


FIGURE 11: Experimental flame duration light intensity information of cavity with different widths. (a) 500 \* 300 \* 200. (b) 500 \* 500 \* 200. (c) 500 \* 800 \* 200.

TABLE 2: Experimental flame duration light intensity of cavity with different widths.

Flame sensor number	F2	F3
500 * 300 * 200	0.0340	0.1342
500 * 500 * 200	0.0173	0.0071
500 * 800 * 200	0.0384	0.0065

**5.2. Peak Overpressure Influence of Different Width Cavities.** The peak overpressure attenuation rate of gas explosion is defined as the ratio of the attenuation value of peak overpressure of shock waves at measuring points  $P1$  and  $P2$  in front of and behind the cavity to the peak overpressure at  $P1$ .

As shown in Figure 12(a) and Table 3, the peak overpressures at  $P1$  and  $P2$  were 0.744 and 0.694, respectively, in the gas exploration propagation experiment of 500 \* 300 \* 200

cavity, and the peak overpressure attenuation rate was 6.7%. Based on the abovementioned simulation and theoretical analysis, the shock wave would experience repeated multiform reflection after passing through the suddenly expanded section and rigid wall surface, and partial reflected wave would be transferred from cavity outlet and inlet, but partial energy also presented vortical attenuation, and the total energy was small. As the ratio of cavity width to pipe diameter was small (300/

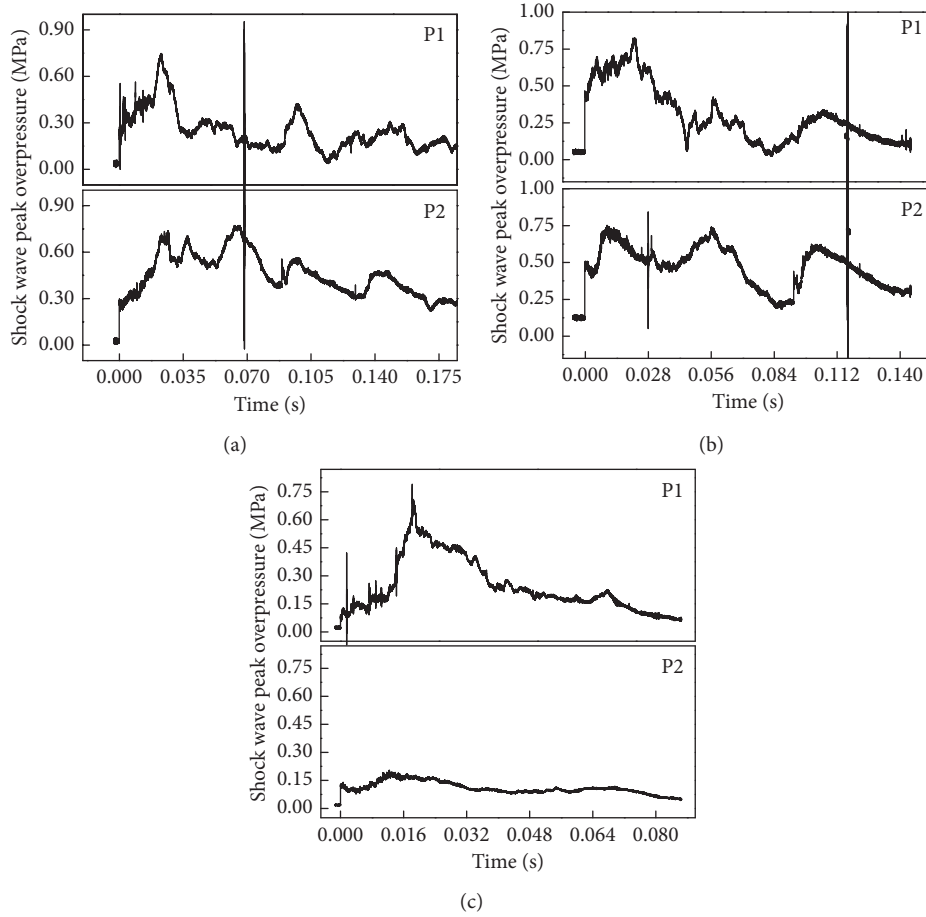


FIGURE 12: Shock wave time pressure travel curve of cavity with different widths. (a) 500 \* 300 \* 200. (b) 500 \* 500 \* 200. (c) 500 \* 800 \* 200.

TABLE 3: Shock wave peak overpressure information before and behind different width cavities.

Flame sensor number		P1	P2
Peak overpressure information ( MPa )	500 * 300 * 200	0.744	0.694
	500 * 500 * 200	0.820	0.730
	500 * 800 * 200	0.706	0.203

200 = 1.5), most of the shock wave entering the cavity would present inertial propagation along the axial direction of pipeline, and although the peak overpressure at the cavity outlet was reduced, the attenuation amplitude was not large.

From Figure 12(b) and Table 3, the peak overpressures at P1 and P2 were 0.820 and 0.730, respectively, in the gas explosion propagation experiment of 500 \* 500 \* 200, and the peak overpressure attenuation rate was 10.9% after passing through the cavity. With the increase in the ratio of cavity width to pipe diameter ( $500/200 = 2.5$ ), the angle between the spherical wave formed inside the cavity and the side wall of the cavity became small, and the possible oblique reflection was increased, thus aggravating the local overpressure oscillation. Because most of the reflected wave on the wall surface at the cavity inlet would still be transferred to the outlet, the attenuation rate of peak overpressure at the cavity outlet would be increased somehow.

It could be known from Figure 12(c) and Table 3 that in the gas explosion propagation experiment of 500 \* 800 \* 200 cavity, the peak overpressures at P1 and P2 were 0.706 and 0.203, respectively, and the overpressure attenuation rate was 71.2% after passing through the cavity. The cavity width was 4 times of pipe diameter, the oscillation space of shock wave inside the cavity was larger, and under the action of superposed reflection, the overpressure of shock wave was transferred to the wall surface of the cavity and dissipated. The ratio of the area of pipeline outlet to the area of cavity wall surface became small, so the peak overpressure at cavity outlet was obviously attenuated.

In conclusion, the shock wave passing through the suddenly enlarged section can occur in the aforementioned five processes. Accordingly, the energy is rapidly consumed. The larger the cavity width is, the larger the spherical wave front becomes. The angle between the spherical wave and

cavity wall is small, and Mach and oblique reflections are more likely to occur. Consequently, substantial shock wave energy is consumed. The larger the cavity size is, the more energy is confined inside the cavity when the converging shock wave passes through the cavity outlet. The shock wave reflects back and forth, thereby resulting in additional oscillations in the cavity. The abovementioned phenomenon is the physical essence of reducing the gas explosion shock wave energy using the cavity.

The overpressure attenuation rates obtained through the experiment and simulation of cavity 300 mm in width were 6.7% and 4.1%, respectively, those of cavity with width of 500 mm were 10.9% and 16.7%, respectively, and those of cavity with width of 800 mm were 71.2% and 80%, respectively. By comparison, the maximum deviation of overpressure attenuation rate between experiment and simulation was 8.8%, and the results are in good agreement. Therefore, the numerical simulation results are reliable, and the calculation model and algorithm used are reasonable.

### 5.3. Quantization Relation of Cavity Width on Gas Explosion Effect.

The width-diameter ratio is defined as the ratio of the cavity width to the pipe diameter, which is a characteristic quantity of a certain diameter pipe and the different width cavities and length-diameter and the height-diameter ratios, to study the quantitative relation of the cavity width on the gas explosion effect. The ratio of the same explosion parameters before and after the cavity is defined as attenuation factor  $D$ , which represents the characteristic quantity of the explosion parameter attenuation.  $D > 1$  is parameter enhancement, and  $D < 1$  is parameter attenuation. The length-diameter and height-diameter ratios of the aforementioned experimental cavity are 2.5 and 1, respectively. The experimental data under cavity widths of 400 mm and 600 mm were added for the curve fitting, in an effort to more reliably quantify the relationship between the cavity width change and attenuation of gas explosion wave. The width-diameter ratio is taken as the x-coordinate, and the attenuation factor of the FDLI and shock wave peak overpressure are taken as the y-coordinate; and the quantitative relation of the different width-diameter ratio cavity on the gas explosion effect is obtained, as shown in Figure 13. The fitting equation for the FDLI change is expressed

as  $y = 0.177 + 3.935 / (1 + \exp((x - 2.026) / 0.171))$  and that for the peak overpressure change is expressed as  $y = 0.614 + 0.387x - 0.118x^2$ . When the width-diameter is small, the peak overpressure presents an attenuation phenomenon, but the effect is insignificant. The FDLI exhibits no attenuation but presents an enhancement effect. The measured peak overpressure attenuation factor is 0.93, and the FDLI attenuation factor is 3.94 with the width-diameter ratio as 1.5. When the width-diameter ratios range from 1.5 to 2.5, the peak overpressure attenuation factor slightly decreases, and the FDLI attenuation factor sharply decreases. The measured peak overpressure attenuation factor is 0.89, and the FDLI attenuation factor is 0.41 with the width-diameter ratio as 2.5. When the width-

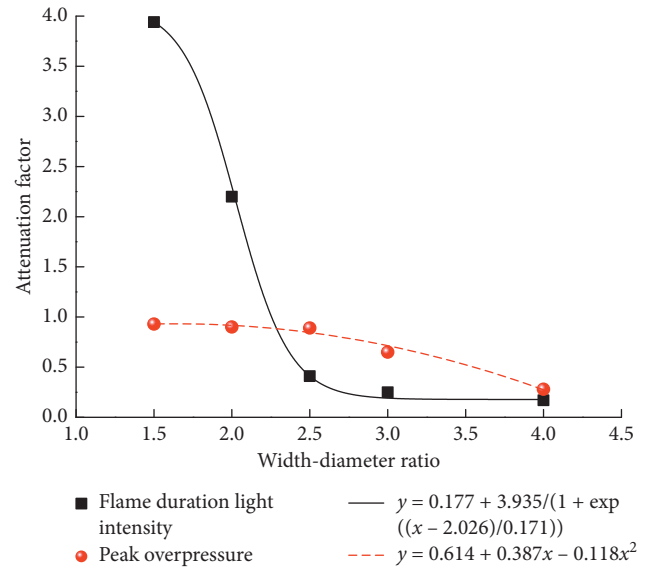


FIGURE 13: Quantitative relation of width-diameter ratio to gas explosion wave attenuation.

diameter ratio is larger than 2.7, the peak overpressure attenuation gradually decreased, and the FDLI attenuation factor basically remained the same. The measured peak overpressure attenuation factor is 0.28, and the FDLI attenuation factor is 0.17 with the width-diameter ratio as 4.0. When the FDLI attenuation factor is equal to one, the width-diameter ratio is 2.19, which is the critical width-diameter ratio. The peak overpressure and FDLI have attenuation with the width-diameter ratio larger than the critical one. The fitting curve illustrates that the attenuation wave effect is evident with the width-diameter ratio larger than 2.7 and tends to be optimal with the width-diameter ratio of approximately 4.0.

## 6. Conclusions

- (1) The explosion wave passing through the cavity occur five stages of plane wave, expansion, oblique reflection, Mach reflection, and reflection stack. Due to the process of expansion and reflection in the above five stages, the shock wave energy is significantly weakened, which could be reflected in the experiment and numerical simulation, and also proved the reasonability of the calculation model and algorithm.
- (2) When the cavity width is smaller, the energy released from the reaction zone is greater than that consumed by the local resistance of the cavity, and the flame energy increases. With the increase of the cavity width, the expansion capacity and disturbance time of the flame increase, the transverse diffusion space of the cavity increase, and the energy dissipation of the flame also increases for oscillating back and forth of the Mach reflection and the oblique reflection, resulting in a sharp drop in energy before the cavity outlet. Compared with the cavity width of 300 mm, when the cavity width is 500 mm and 800 mm, the



attenuation of the overall FDLI is 58.9% and 83.0%, respectively.

- (3) The larger the cavity width is, the larger the spherical wave front becomes, the angle between the spherical wave and cavity wall is smaller, and Mach and oblique reflections are more likely to occur. Meanwhile, with the decrease of the energy inside the cavity and the reflection back and forth of the converging shock wave at the cavity outlet, the additional oscillations occur inside the cavity. The above phenomenon is the physical essence of reducing the gas explosion shock wave energy using the cavity. Compared with the cavity width of 300 mm, when the cavity width is 500 mm and 800 mm, the attenuation of the peak overpressure is 10.9% and 71.2%, respectively. Therefore, increasing the cavity width can significantly improve the attenuation wave effect.
- (4) The fitting equation of the FDLI attenuation factor and width-diameter ratio is expressed as  $y = 0.177 + 3.935/(1 + \exp((x - 2.026)/0.171))$  and shows a positive correlation. Meanwhile, the fitting equation of the peak overpressure attenuation factor and width-diameter ratio is expressed as  $y = 0.614 + 0.387x - 0.118x^2$ . The critical width-diameter ratio is 2.19 when the FDLI attenuation factor is equal to one. The attenuation wave effect is evident with a width-diameter ratio larger than 2.7. The attenuation wave effect tends to be optimal with a 4.0 width-diameter ratio. The peak overpressure attenuation factor is approximately 0.28, and the FDLI attenuation factor is 0.17.

## Data Availability

All data included in this study are available upon request by contacting the corresponding author.

## Conflicts of Interest

The authors declare that there are no conflicts of interest regarding the publication of this paper.

## Acknowledgments

This work was supported by the National Natural Science Foundation of China (11472007) and University Natural Science Research Project in Anhui Province (KJ2019A0098 and 1808085ME160).

## References

- [1] W. Yin, G. Fu, C. Yang, Z. Jiang, K. Zhu, and Y. Gao, "Fatal gas explosion accidents on Chinese coal mines and the characteristics of unsafe behaviors: 2000-2014," *Safety Science*, vol. 92, pp. 173-179, 2017.
- [2] L. Wang, Y.-P. Cheng, and H.-Y. Liu, "An analysis of fatal gas accidents in Chinese coal mines," *Safety Science*, vol. 62, pp. 107-113, 2014.
- [3] H. Chen, H. Qi, and Q. Feng, "Characteristics of direct causes and human factors in major gas explosion accidents in Chinese coal mines: case study spanning the years 1980-2010," *Journal of Loss Prevention in the Process Industries*, vol. 26, no. 1, pp. 38-44, 2013.
- [4] J. J. Zhang, D. Cliff, K. L. Xu et al., "Focusing on the patterns and characteristics of extraordinarily severe gas explosion accidents in Chinese coal mines," *Process Safety and Environmental Protection*, vol. 117, pp. 390-398, 2018.
- [5] X. B. Zhang, J. L. Gao, J. Z. Ren et al., "Analysis of the characteristics and influencing factors of gas explosion in heading face," *Shock and Vibration*, vol. 2020, Article ID 8871865, 11 pages, 2020.
- [6] A. Yoshida, T. Okawa, W. Ebina, and H. Naito, "Experimental and numerical investigation of flame speed retardation by water mist," *Combustion and Flame*, vol. 162, no. 5, pp. 1772-1777, 2015.
- [7] Y.-l. XU, L.-y. Wang, M.-g. Yu, S.-j. Wan, Z.-p. Song, and S.-k. Wang, "Study on the characteristics of gas explosion affected by induction charged water mist in confined space," *Journal of Loss Prevention in the Process Industries*, vol. 40, pp. 227-233, 2016.
- [8] T. Parra, F. Castro, C. Villafruela, and M. A. Rodríguez, "Extinction of premixed methane-air flames by water mist," *Fire Safety Journal*, vol. 39, no. 7, pp. 581-600, 2004.
- [9] Y. Song and Q. Zhang, "Quantitative research on gas explosion inhibition by water mist," *Journal of Hazardous Materials*, vol. 363, pp. 16-25, 2019.
- [10] K. Nakahara, A. Yoshida, and M. Nishioka, "Experiments and numerical simulation on the suppression of explosion of propane/air mixture by water mist," *Combustion and Flame*, vol. 223, pp. 192-201, 2021.
- [11] Z. Luo, T. Wang, J. Ren et al., "Effects of ammonia on the explosion and flame propagation characteristics of methane-air mixtures," *Journal of Loss Prevention in the Process Industries*, vol. 47, pp. 120-128, 2017.
- [12] W. Kordylewski and J. Amrogowicz, "Comparison of NaHCO<sub>3</sub> and NH<sub>4</sub>H<sub>2</sub>PO<sub>4</sub> effectiveness as dust explosion suppressants," *Combustion and Flame*, vol. 90, no. 3-4, pp. 344-345, 1992.
- [13] B. Jiang, Z. Liu, M. Tang, K. Yang, P. Lv, and B. Lin, "Active suppression of premixed methane/air explosion propagation by non-premixed suppressant with nitrogen and ABC powder in a semi-confined duct," *Journal of Natural Gas Science and Engineering*, vol. 29, pp. 141-149, 2016.
- [14] Y. Wang, Y.-s. Cheng, M.-g. Yu et al., "Methane explosion suppression characteristics based on the NaHCO<sub>3</sub>/red-mud composite powders with core-shell structure," *Journal of Hazardous Materials*, vol. 335, pp. 84-91, 2017.
- [15] V. S. Babkin, A. A. Korzhavin, and V. A. Bunev, "Propagation of premixed gaseous explosion flames in porous media," *Combustion and Flame*, vol. 87, no. 2, pp. 182-190, 1991.
- [16] B. Nie, X. He, R. M. Zhang, R. Zhang, W. Chen, and J. Zhang, "The roles of foam ceramics in suppression of gas explosion overpressure and quenching of flame propagation," *Journal of Hazardous Materials*, vol. 192, no. 2, pp. 741-747, 2011.
- [17] Y. Y. Cui, Z. R. Wang, K. B. Zhou, L. S. Ma, M. H. Liu, and J. C. Jiang, "Effect of wire mesh on double-suppression of CH<sub>4</sub>/air mixture explosions in a spherical vessel connected to pipelines," *Journal of Loss Prevention in the Process Industries*, vol. 45, pp. 69-77, 2017.
- [18] H. Hojo, K. Tsuda, M. Arai, and Y. Kano, "Behavior of flame propagation in circular pipe and quenching ability of flame

- arrester," *Kagaku Kogaku Ronbunshu*, vol. 12, no. 2, pp. 153–158, 1986.
- [19] Y. Wang, S. Jiang, Z. Wu, H. Shao, K. Wang, and L. Wang, "Study on the inhibition influence on gas explosions by metal foam based on its density and coal dust," *Journal of Loss Prevention in the Process Industries*, vol. 56, pp. 451–457, 2018.
- [20] P. Chen, F. Huang, Y. Sun, and X. Chen, "Effects of metal foam meshes on premixed methane-air flame propagation in the closed duct," *Journal of Loss Prevention in the Process Industries*, vol. 47, pp. 22–28, 2017.
- [21] R. Zalosh, "Deflagration suppression using expanded metal mesh and polymer foams," *Journal of Loss Prevention in the Process Industries*, vol. 20, no. 4-6, pp. 659–663, 2007.
- [22] J. H. Sun, Y. Zhao, C. R. Wei et al., "Experimental study on combination of metal wire mesh and foam ceramic for suppressing the gas explosion," *Journal of China Coal Society*, vol. 37, pp. 1156–1160, 2012.
- [23] H. Shao, S. Jiang, X. Zhang, Z. Wu, K. Wang, and W. Zhang, "Influence of vacuum degree on the effect of gas explosion suppression by vacuum chamber," *Journal of Loss Prevention in the Process Industries*, vol. 38, pp. 214–223, 2015.
- [24] H. Shao, S. Jiang, Q. Li, and Z. Wu, "Analysis of vacuum chamber suppressing gas explosion," *International Journal of Mining Science and Technology*, vol. 23, no. 5, pp. 653–657, 2013.
- [25] H. Shao, S. Jiang, Q. Wu, W. Zhang, and K. Wang, "Suppression of gas explosion using vacuum chamber at different break-up times of diaphragm," *Journal of Loss Prevention in the Process Industries*, vol. 31, pp. 1–9, 2014.
- [26] Y. Niu, B. Shi, and B. Jiang, "Experimental study of overpressure evolution laws and flame propagation characteristics after methane explosion in transversal pipe networks," *Applied Thermal Engineering*, vol. 154, pp. 18–23, 2019.
- [27] L. Sun, B. Jiang, and F. Gu, "Effects of changes in pipe cross-section on the explosion-proof distance and the propagation characteristics of gas explosions," *Journal of Natural Gas Science and Engineering*, vol. 25, pp. 236–241, 2015.
- [28] B.-q. Lin, C. Guo, Y.-m. Sun, C.-j. Zhu, Y.-d. Hong, and H. Yao, "Effect of bifurcation on premixed methane-air explosion overpressure in pipes," *Journal of Loss Prevention in the Process Industries*, vol. 43, pp. 464–470, 2016.
- [29] R. Blanchard, D. Arndt, R. Grätz, M. Poli, and S. Scheider, "Explosions in closed pipes containing baffles and 90 degree bends," *Journal of Loss Prevention in the Process Industries*, vol. 23, no. 2, pp. 253–259, 2010.
- [30] H. Xiao, X. He, Q. Wang, and J. Sun, "Experimental and numerical study of premixed flame propagation in a closed duct with a 90° curved section," *International Journal of Heat and Mass Transfer*, vol. 66, pp. 818–822, 2013.
- [31] S. M. Frolov, V. S. Aksenov, and I. O. Shamshin, "Reactive shock and detonation propagation in U-bend tubes," *Journal of Loss Prevention in the Process Industries*, vol. 20, no. 4-6, pp. 501–508, 2007.
- [32] S. M. Frolov, V. S. Aksenov, and I. O. Shamshin, "Shock wave and detonation propagation through U-bend tubes," *Proceedings of the Combustion Institute*, vol. 31, no. 2, pp. 2421–2428, 2007.
- [33] C. Lv and Z. Wu, "Flame thickness and propagation characteristics of premixed methane-air explosion with a small filling ratio in an open-ended steel pipe," *Applied Thermal Engineering*, vol. 119, pp. 617–621, 2017.
- [34] G. Zhang, "Experimental study on shock wave propagation of the explosion in a pipe with holes by high-speed schlieren method," *Shock and Vibration*, vol. 2020, Article ID 8850443, 9 pages, 2020.
- [35] H. Hisken, G. A. Enstad, and V. D. Narasimhamurthy, "Suppression of vortex shedding and its mitigation effect in gas explosions: an experimental study," *Journal of Loss Prevention in the Process Industries*, vol. 43, pp. 242–254, 2016.
- [36] J. L. Steger and R. F. Warming, "Flux vector splitting of the inviscid gasdynamic equations with application to finite-difference methods," *Journal of Computational Physics*, vol. 40, no. 2, pp. 263–293, 1981.
- [37] G.-S. Jiang and C.-W. Shu, "Efficient implementation of weighted ENO schemes," *Journal of Computational Physics*, vol. 126, no. 1, pp. 202–228, 1996.
- [38] J. S. Shuen and S. Yoon, "Numerical study of chemically reacting flows using a lower-upper symmetric successive overrelaxation scheme," *AIAA Journal*, vol. 27, no. 12, pp. 1752–1760, 1989.
- [39] I. O. Moen, M. Donato, R. Knystautas, and J. H. Lee, "The influence of confinement on the propagation of detonations near the detonability limits," *Symposium (International) on Combustion*, vol. 18, no. 1, pp. 1615–1622, 1981.

## Research Article

# Time-Frequency Analysis and Application of a Vibration Signal of Tunnel Excavation Blasting Based on CEEMD-MPE-HT

Chen-yang Ma <sup>1</sup>, Li Wu <sup>1</sup>, Miao Sun <sup>1</sup> and Qing Yuan <sup>2</sup>

<sup>1</sup>Engineering Research Center of Rock-Soil Drilling & Excavation and Protection of the Ministry of Education, Faculty of Engineering, China University of Geosciences, Wuhan 430074, Hubei, China

<sup>2</sup>CCCC Second Harbour Engineering Co., Ltd., National Enterprise Technology Center, Wuhan, China

Correspondence should be addressed to Li Wu; [lwu@cug.edu.cn](mailto:lwu@cug.edu.cn)

Received 21 December 2020; Revised 11 January 2021; Accepted 25 January 2021; Published 4 February 2021

Academic Editor: Qi ZHAO

Copyright © 2021 Chen-yang Ma et al. This is an open access article distributed under the Creative Commons Attribution License, which permits unrestricted use, distribution, and reproduction in any medium, provided the original work is properly cited.

The traditional empirical mode decomposition method cannot accurately extract the time-frequency characteristic parameters contained in the noisy seismic monitoring signals. In this paper, the time-frequency analysis model of CEEMD-MPE-HT is established by introducing the multiscale permutation entropy (MPE), combining with the optimized empirical mode decomposition (CEEMD) and Hilbert transform (HT). The accuracy of the model is verified by the simulation signal mixed with noise. Based on the project of Loushan two-to-four in situ expansion tunnel, a CEEMD-MPE-HT model is used to extract and analyze the time-frequency characteristic parameters of blasting seismic signals. The results show that the energy of the seismic wave signal is mainly concentrated in the frequency band above 100 Hz, while the natural vibration frequency of the adjacent existing tunnel is far less than this frequency band, and the excavation blasting of the tunnel will not cause the resonance of the adjacent existing tunnel.

## 1. Introduction

As is known to all, the physical quantities such as peak velocity of particle vibration (PPV), acceleration ( $a$ ), and displacement ( $s$ ) are usually used to measure and determine the degree of influence of structures under blasting vibration [1]. However, the safety standard of blasting vibration of existing regulations is relatively broad and empirical. Therefore, many scholars have proposed and improved safety control criteria for blasting engineering from the perspectives of numerical calculation [2], stress wave propagation theory [3], and maximum instantaneous input energy angle of structure [4]. In engineering practices, in addition to the blasting peak vibration velocity as the basis for controlling blasting hazards, the influencing factors of the vibration degradation of the protected construction (building) on the duration of blasting vibration, frequency of blasting vibration, the energy released by blasting vibration, and type of adjacent structures cannot be ignored [5].

However, blasting seismic waves is a typical nonstationary and nonlinear signal, and only with the help of the time-frequency analysis method can the monitored time-domain signals be transformed into frequency-domain signals. Further interpretation of signal frequency-domain information and energy distribution characteristics is of great significance for blasting seismic wave hazard control. Common time-frequency analysis methods include the short-time Fourier transformation, Wigner-Ville distribution, continuous wavelet transform, etc. [6, 7]. The theoretical basis of the abovementioned methods is Fourier transform, which inevitably leads to false frequencies and redundant signal components [8, 9]. In view of this problem, Huang et al. [10] proposed empirical mode decomposition (EMD) in 1998, which fundamentally broke through the limitation of Fourier transform theory and established a signal analysis method based on instantaneous frequency for the first time [11, 12]. The process of decomposition retained the characteristics of the data itself.

But, there are some problems with EMD. Considering that the monitoring signals of blasting seismic waves are mostly noisy signals, the mixing of noise makes the EMD results produce modal confusion [13], which makes it difficult to identify the time-frequency characteristics of measured blasting seismic wave signals. To solve the abovementioned problems, the efficient random signal detection method of multiscale permutation entropy (MPE) is introduced in this paper. Combined with the optimized EMD, complementary ensemble empirical mode decomposition (CEEMD), the joint algorithm of CEEMD-MPE is obtained. The time-frequency analysis model of CEEMD-MPE-HT can be established by applying the Hilbert transform (HT) to IMF obtained by the CEEMD-MPE joint algorithm. This model can realize the time-frequency analysis of the noise signal and extract the real energy and frequency information of the signal.

This paper discusses the application of the CEEMD-MPE-HT time-frequency analysis model in the blasting project of the Loushan tunnel, which is a separated tunnel with a large span and small clear distance. Compared with other time-frequency analysis methods, the proposed time-frequency algorithm not only preserves the real information of the signal but also has the advantage of effectively suppressing the mode confusion. The advantages of this time-frequency analysis model are compared and verified in the mixed simulation signals and successfully applied in practical engineering. According to the time-frequency characteristic parameters obtained by the proposed model algorithm, the influence of expanding blasting on one side of a super-large and small clear distance separated tunnel on the other side is discussed. The time-frequency algorithm provides a useful idea for solving the identification of blasting seismic wave signals, the analysis of time-frequency characteristic parameter law, and the control of blasting vibration hazards in engineering practices.

## 2. CEEMD-MPE-HT Time-Frequency Analysis Model

*2.1. The Principle of CEEMD.* CEEMD [14] is the method of adding two white noise signals  $n(t)$  in opposite directions to the original monitoring signal  $S(t)$ . Generally, 0.2 times of the standard deviation of  $S(t)$  is taken as the white noise signals, and empirical mode decomposition (EMD) [10] is performed, respectively.

The specific implementation steps of CEEMD are as follows:

Step 1: white noises are added in opposite directions to  $S(t)$  in pairs to get two new signal sources,  $S(t) + n(t)$  and  $S(t) - n(t)$ , respectively

Step 2: EMD decomposition of  $S(t) + n(t)$  and  $S(t) - n(t)$

Step 3: step 1 and step 2 are repeated until the set number of adding white noise is reached

Step 4: the overall average of all the results obtained in Step 2 is carried out, and the obtained result is the CEEMD result

Since white noise in opposite directions is added in pairs and the IMF is averaged many times, it can be considered that the artificially introduced white noise has been eliminated. This method is an improvement of ensemble empirical mode decomposition (EEMD), which not only ensures that the decomposition effect is equivalent to EEMD [15] but also reduces the reconstruction error caused by white noise at the same time.

*2.2. The Principle of MPE.* Permutation entropy (PE) [16] is a method to detect randomness and dynamic mutation in time series. It has the advantages of a simple concept, fast calculation speed, and strong anti-interference ability, especially suitable for the analysis of nonlinear data.

MPE [17] is an optimization method of combining multiple scales with PE. It can analyze the time series more efficiently.

Suppose the length of the any one-dimensional time series  $x(i)$  is  $L$ .  $X(i)$  can be expressed as  $x_L(i) = \{x_1, x_2, x_3, \dots, x_L\}$ . Equation (1) is obtained by coarsening  $x_L(i)$  with a multiscale:

$$y_j^s = \frac{1}{s} \sum_{i=(j-1) \cdot s+1}^{j \cdot s} x_i, \quad 1 \leq j \leq \frac{L}{s} \quad (1)$$

In equation (1),  $s$  is the scale factor and  $y_j^s$  is the multiscale time series. When  $s = 1$ ,  $x(i)$  does not change. The core of multiscale coarse granulation is to segment the time series and take the average value of each segment to improve the operation accuracy. So, the value of  $s$  is critical. When  $s$  is too large, it cannot reflect the complexity of the time series. When  $s$  is too small, it is difficult to extract fragments and the analysis effect is poor. According to [18], this paper takes  $s = 10$ . The MPE value [19, 20] of  $x(i)$  can be obtained by calculating the PE value of  $y_j^s$  in equation (1).

According to the definition of MPE and [21, 22], when the MPE of  $x(i)$  is greater than 0.6, it can be considered as an abnormal component with great randomness and needs to be eliminated.

*2.3. The Principle of HT.* The detailed process of HT is introduced in [10]. The Hilbert marginal spectrum is mainly discussed in this paper, which is obtained by integrating the Hilbert time spectrum with respect to time, as shown in equation (2). The marginal spectrum is the global amplitude of each frequency, which represents the total cumulative amplitude in the statistical sense.  $H(w, t)$  is the spectrum of Hilbert time [23], where  $w$  denotes frequency.

$$h(w) = \int_0^T H(w, t) dt. \quad (2)$$

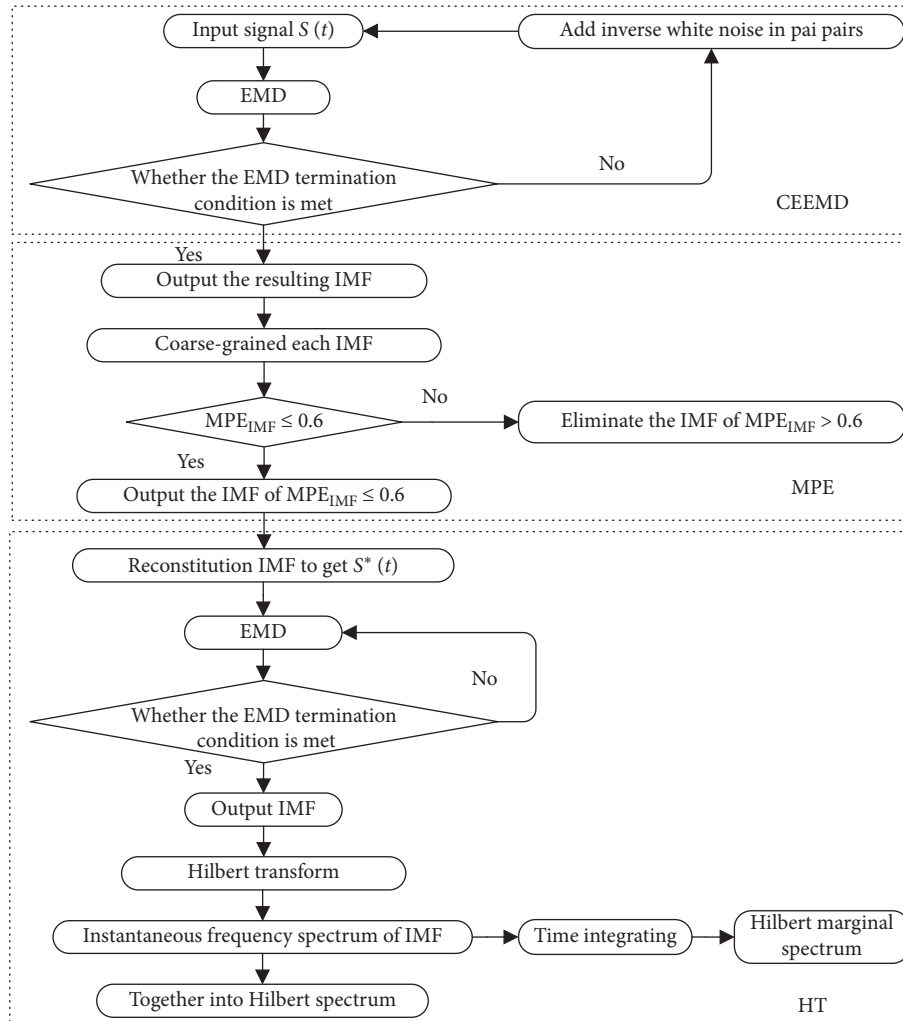


FIGURE 1: Flow chart of the CEEMD-MPE-HT time-frequency analysis model.

Therefore, the flow chart of the CEEMD-MPE-HT time-frequency analysis model of seismic wave vibration signal can be established (Figure 1). For the termination conditions of EMD, refer [10].

### 3. Time Frequency Analysis of a Simulation Signal with Noise

**3.1. The Establishment of a Simulation Signal with Noise.** The noise simulation signal is composed of Gaussian white noise with a power of 0.2 and sinusoidal steady-state signal with a frequency of 120. The number of samples  $N=1028$ , and  $t$  is a time series with a total length of 1 s and a unit time interval of  $1/N$ . Figure 2 shows the waveform of the simulation signal.

**3.2. Comparison of the Time-Frequency Analysis Results of the Simulation Signal with Noise.** Three time-frequency analysis methods were used to analyze the simulation signal shown in Figure 2. The results can be seen in Figures 3–5, among which Figures 3(b), 4(b), and 5(b) are the results of the

modal decomposition of the IMF marginal spectrum. The Y-axis coordinate is  $ESD$  represents the energy spectral density.

By observing Figures 3–5, the following conclusions can be drawn:

- (1) There is an obviously one-to-one correspondence between the results of modal decomposition and the IMF marginal spectrum.
- (2) The IMF high-frequency modes obtained by EMD are seriously confused. The addition of white noise results in the appearance of false IMF components in the decomposition, such as the IMF1 and IMF2 components with frequencies greater than 120 Hz. The low-frequency decomposition is relatively stable.
- (3) The high-frequency modal confusion of IMF obtained by CEEMD is somewhat reduced, but there is a slight modal split at low frequencies [24], such as IMF6 and IMF7.
- (4) The phenomenon of IMF modal confusions obtained by CEEMD-MPE was inhibited. The components are arranged from high frequency to low frequency, and the decomposition results are good. From the



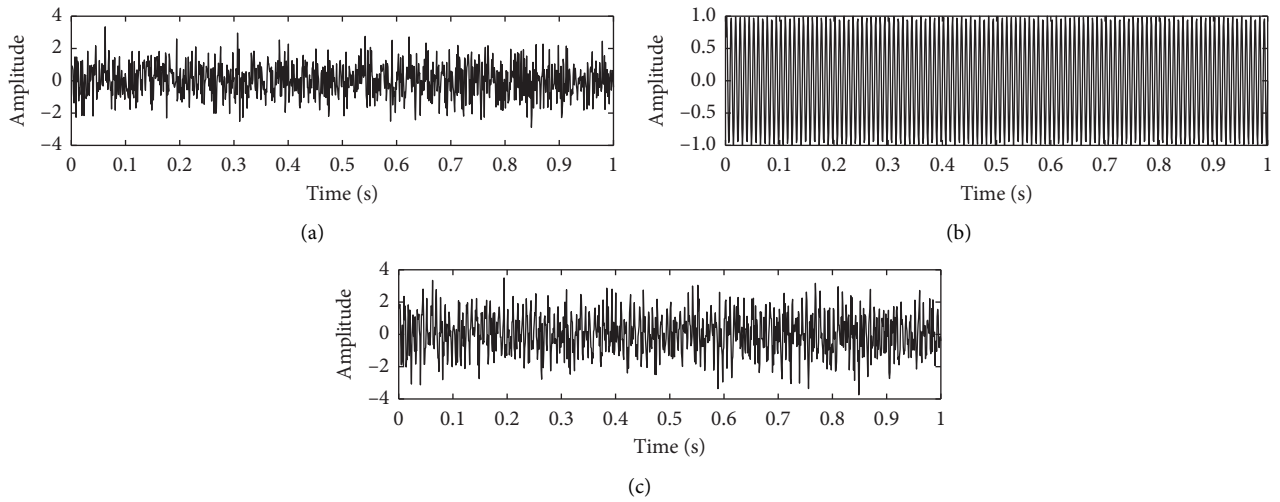


FIGURE 2: Waveform of the simulation signal. (a) Gaussian white noise with power of 0.2. (b) Sinusoidal steady-state signal with frequency 120 Hz. (c) The simulation signal.

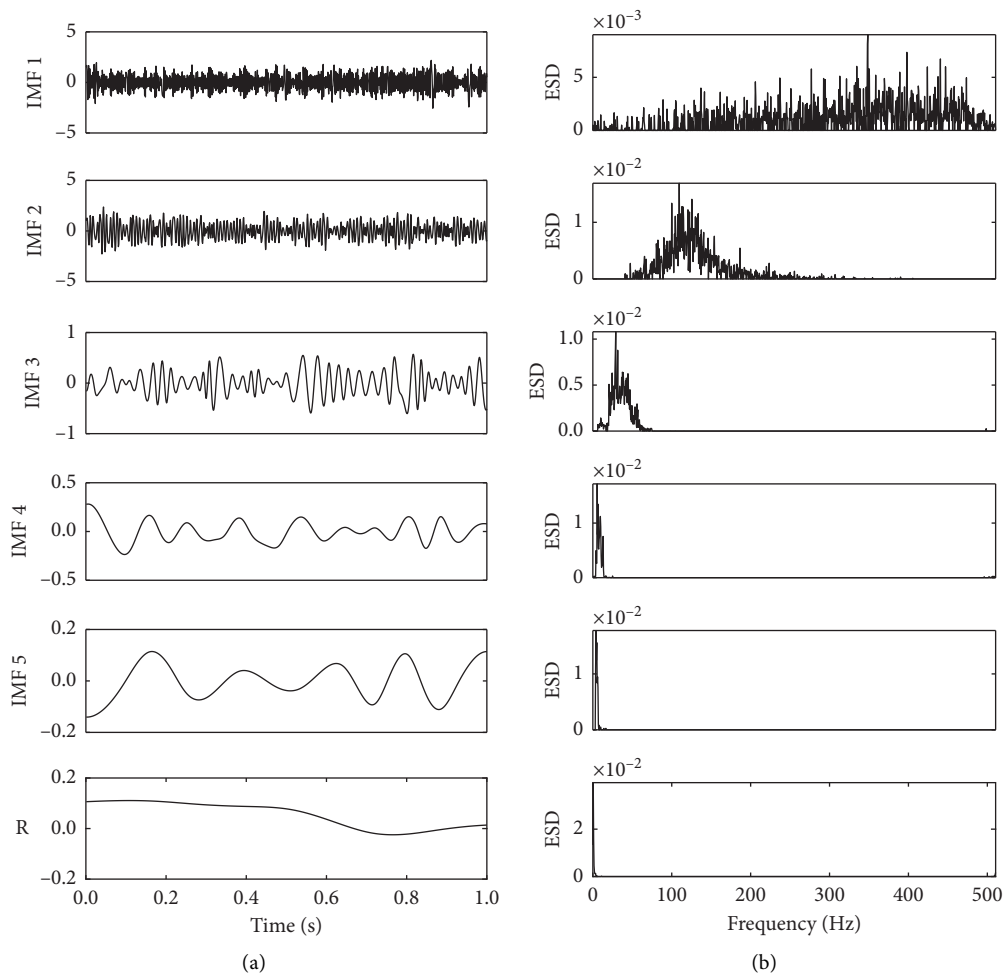


FIGURE 3: Results of EMD-HT time-frequency analysis. (a) Decomposition results of EMD. (b) IMF marginal spectrum.

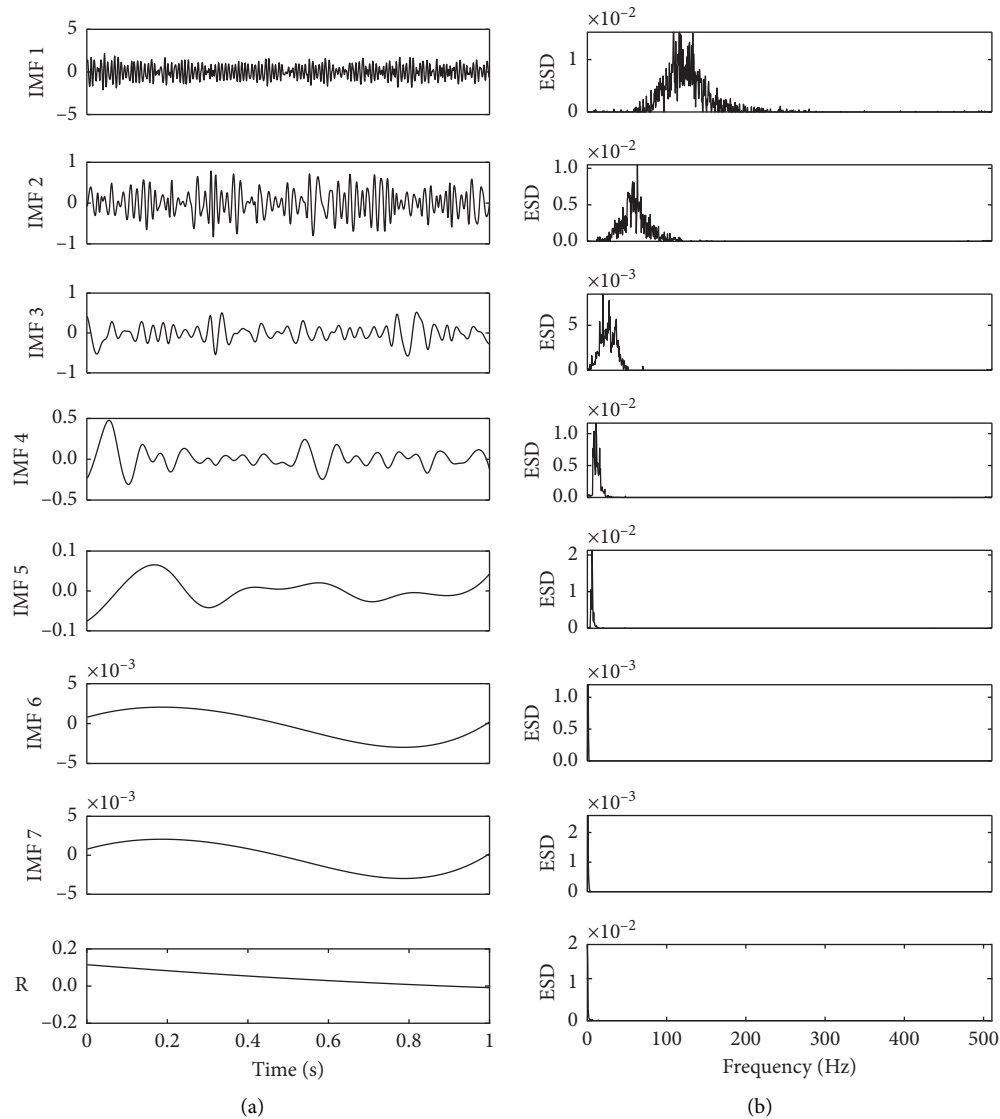


FIGURE 4: Results of CEEMD-HT time-frequency analysis. (a) Decomposition results of EMD. (b) IMF marginal spectrum.

marginal spectrum, it can be clearly concluded that the 120 Hz sinusoidal steady-state signal energy of the original signal is mainly contained in IMF1~IMF4.

The processed results of the simulation signal with noise obtained by the abovementioned time-frequency analysis models are compared. It can be found that the IMF mode confusion obtained by EMD is serious; compared with EMD, the mode confusion of CEEMD in high frequency has been greatly improved, but there is still a mode splitting phenomenon in low frequency; the IMF obtained by CEEMD-MPE has good stability in both high frequency and low frequency. At the same time, it can be found that the CEEMD-MPE-HT model can reflect the real energy and

frequency information of the signal and is more suitable for time-frequency analysis of noisy signals.

## 4. Engineering Application

**4.1. Engineering Application.** The Loushan tunnel is part of the first construction section of the highway project from Jiaojiang to the east of Wenling City. It is a separate tunnel. In order to meet the traffic demand, the original two-way four-lane tunnel was expanded into a two-way eight-lane tunnel in situ. During the closed construction of the right tunnel, the left tunnel shall remain open to traffic normally. Relevant design parameters are shown in Table 1. Therefore, dynamic monitoring must be carried out for the existing left

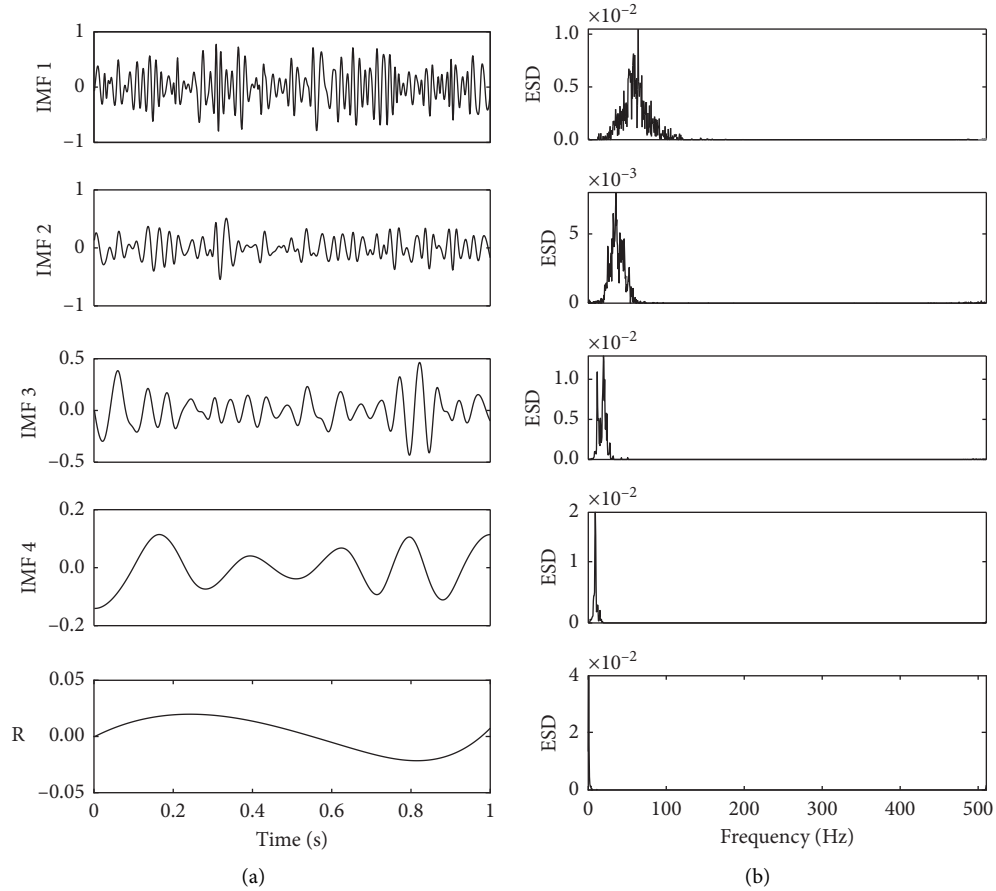


FIGURE 5: Results of CEEMD-MPE-HT time-frequency analysis. (a) Decomposition results of EMD. (b) IMF marginal spectrum.

TABLE 1: Basic design parameters of expanded excavation of the Loushan tunnel (unit: m).

Project	Loushan tunnel after expansion	Loushan tunnel before expansion
Section form	Two-way eight-lane	Two-way four-lane
Width of carriageway (m)	$2 \times 3.50 + 2 \times 3.75$	$2 \times 3.75$
Lateral dimension (m)	0.50	0.50
Width of maintaining roadway (m)	0.75	0.75
Total width (m)	17.25	10.25
Tunnel clearance (m)	5.00	5.00

tunnels to ensure normal traffic during the right tunnel expansion blasting construction. Besides, the influence of the right tunnel expansion blasting on the left tunnel must be strictly controlled.

**4.2. Blasting Monitoring Program.** The purpose of blasting vibration monitoring is to ascertain the impact of blasting vibration on surrounding structures, timely feedback of the dynamic monitoring information, and to provide a reliable basis for improving the blasting design, controlling the blasting scale, and guiding the blasting construction. The Ubox-5016 intelligent blasting vibration monitor is adopted for blasting vibration monitoring, and the layout of measuring points is shown in Figure 6.

**4.3. Analysis of the Measured Blasting Vibration Signal Based on CEEMD-MPE-HT.** In order to analyze the time-frequency characteristics and energy characteristics of blasting seismic wave signals in tunnel expansion and excavation, a typical blasting vibration signal is selected as the analysis object in combination with the on-site blasting vibration monitoring scheme, as shown in Figure 7.

Time-frequency analysis based on CEEMD-MPE-HT was performed for radial seismic wave signals in Figure 7(a), and the result is shown in Figure 8. From Figure 8(a), it can be seen that the IMFs decomposed by radial seismic wave signal CEEMD-MPE rank from high to low frequencies. Each IMF component is relatively stable, and the result is consistent with the simulation signal CEEMD-MPE decomposition result. Combined with the IMF marginal

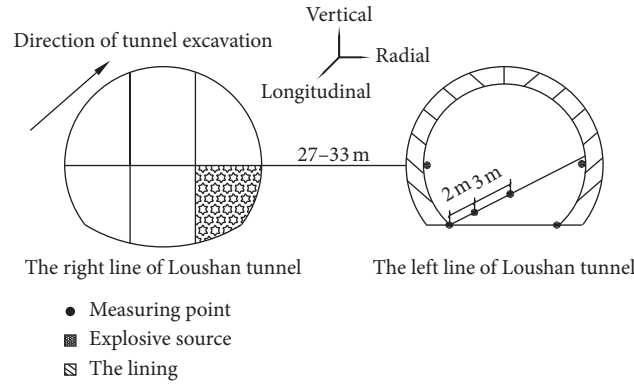


FIGURE 6: Layout of measuring points.

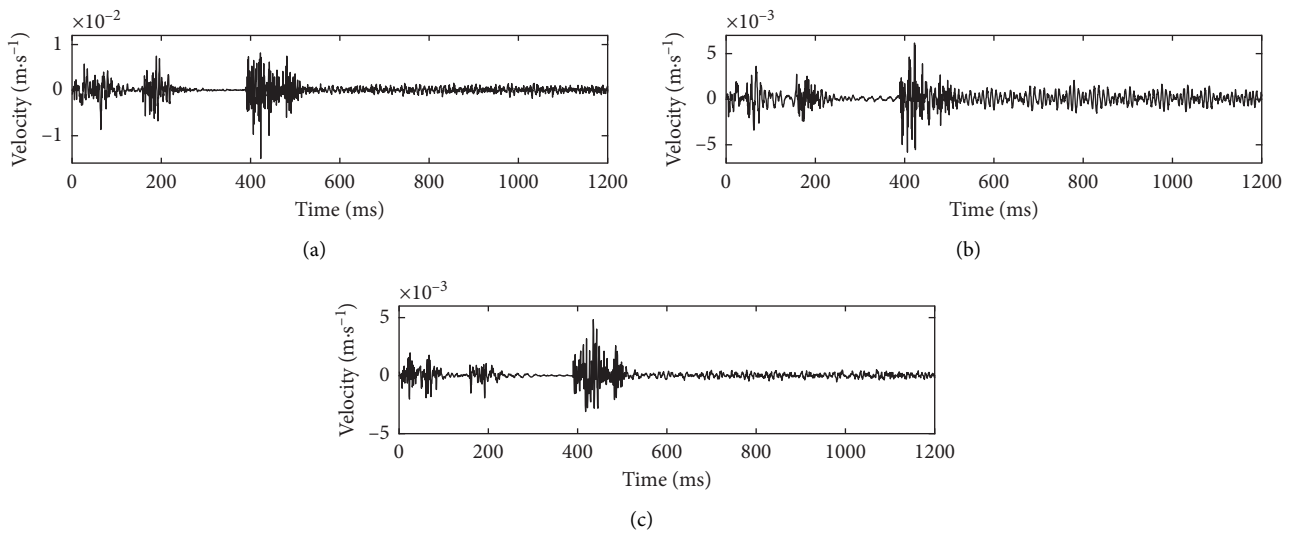


FIGURE 7: Measured typical seismic wave signal map. (a) Radial seismic wave signals. (b) Longitudinal seismic wave signals. (c) Vertical seismic wave signals.

spectrum of the radial seismic wave signal in Figure 8(b), it can be seen that the IMF1 and IMF2 are high-frequency components distributed in the frequency range above 100 Hz and carry the main energy of the radial seismic wave signal. IMF3 ~ IMF5 are middle- and low-frequency components, and the energy contained in them is relatively small compared with IMF1 and IMF2.  $R$  is both the residual term and the trend term. In Hilbert transformation, the residual component is generally not considered.

According to the marginal spectrum of each IMF of Figure 8(b) and the marginal spectrum of radial seismic wave signals in Figure 9, the energy distribution of each frequency band can be obtained. For the convenience of analyzing the energy carried by each frequency band, the whole frequency domain is divided into four frequency bands of 500–800 Hz, 300–500 Hz, 100–300 Hz, and 0–100 Hz. After squaring the  $H(\omega, t)$  in equation (2) and then integrating the frequency, the Hilbert instantaneous energy can be obtained:

$$IE(t) = \int_{\omega_1}^{\omega_2} H^2(\omega, t) d\omega. \quad (3)$$

According to equation (3), the instantaneous energy proportion of each frequency band of the radial seismic wave signal can be calculated. Similarly, the instantaneous energy proportion of each frequency band of the longitudinal and vertical seismic wave signals in Figure 7 can also be obtained by the same method, and the calculation results are shown in Table 2.

It can be seen from Table 2 that the signal energy of the seismic wave of tunnel expansion blasting is mainly concentrated in the frequency band above 100 Hz. The frequency band of 500–800 Hz occupies the largest proportion of energy, accounting for 51.560% of the total energy. The energy of 100–300 Hz frequency band accounts for 31.016% of the total energy. The energy proportion of 0–100 Hz is very small, only accounting for 2.850% of the total energy, which is consistent with the research results in [25].

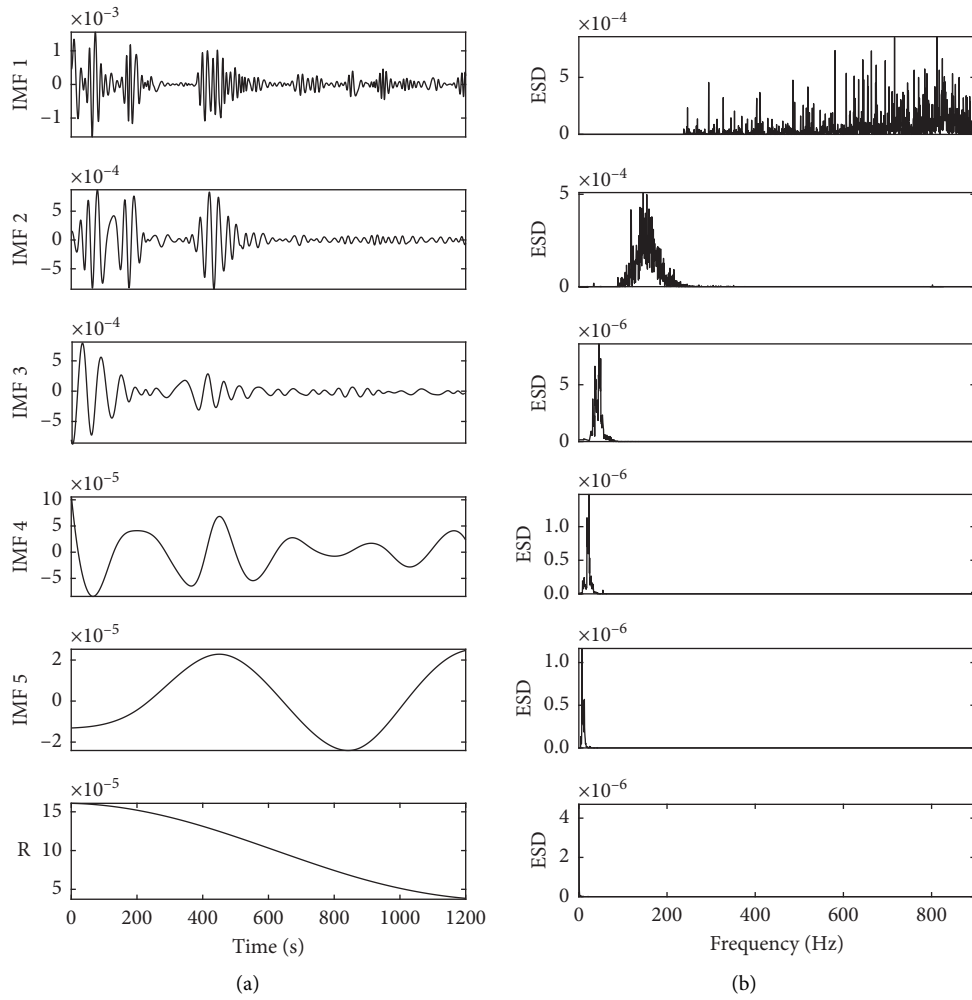


FIGURE 8: Results of CEEMD-MPE-HT time-frequency analysis. (a) Decomposition results of EMD. (b) IMF marginal spectrum.

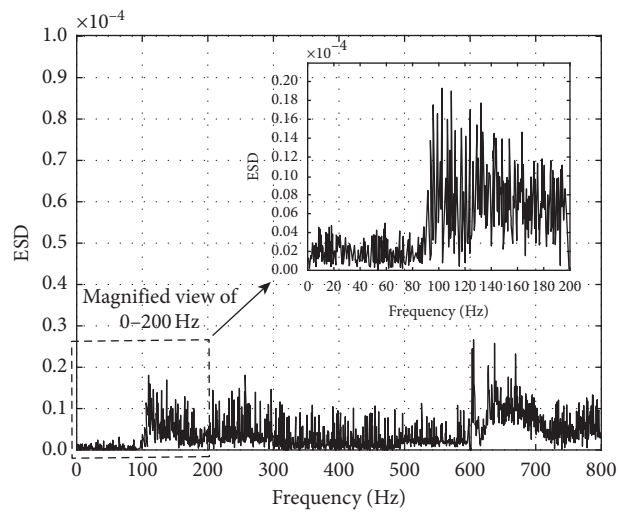


FIGURE 9: Marginal spectrum of the radial seismic wave signal.



TABLE 2: Energy values of typical seismic wave signals in each frequency band.

The frequency distribution		0–100 Hz	100–300 Hz	300–500 Hz	500–800 Hz
Size of the energy ( $\text{m}^2/\text{s}^2$ )	Radial seismic wave signal	$1.686 \times 10^{-6}$	$1.764 \times 10^{-5}$	$0.887 \times 10^{-5}$	$2.847 \times 10^{-5}$
	Longitudinal seismic wave signal	$1.334 \times 10^{-6}$	$1.421 \times 10^{-5}$	$0.654 \times 10^{-5}$	$2.365 \times 10^{-5}$
	Vertical seismic wave signal	$1.027 \times 10^{-6}$	$1.243 \times 10^{-5}$	$0.542 \times 10^{-5}$	$2.149 \times 10^{-5}$
Summary of the energy of each frequency band		$4.047 \times 10^{-6}$	$4.428 \times 10^{-5}$	$2.083 \times 10^{-5}$	$7.361 \times 10^{-5}$
Energy ratio of each frequency band to the total energy		2.850%	31.016%	14.590%	51.560%

According to [26], the natural frequency of the highway tunnel is about 50 Hz. Therefore, it can be preliminarily judged that the seismic wave signal generated by the expansion blasting of the tunnel on the right side of Loushan will not cause resonance of the existing tunnel on the left side, and the normal operation of the existing tunnel on the left side can be ensured during the blasting construction of the right-side tunnel.

## 5. Conclusions

In tunnel blasting engineering, the hazard effect of blasting vibration can be evaluated by analyzing the time-frequency characteristic parameters contained in seismic wave monitoring signals. To extract the time-frequency information and energy characteristic distribution law contained in blasting signals more truly, the CEEMD-MPE-HT time-frequency analysis model is proposed. Conclusions can be drawn as follows:

- (1) CEEMD-MPE algorithm combines the self-adaptability of CEEMD and the ability of MPE to detect the randomness of time series, so that the decomposition results not only retain the original signal characteristic parameters but also suppress the modal confusion phenomenon.
- (2) Based on the time-frequency analysis model of the CEEMD-MPE-HT blasting seismic wave signal, the corresponding relationship between frequency and energy contained in the blasting seismic wave signal can be clearly displayed, which is helpful for the identification of blasting vibration signal characteristics.
- (3) In the tunnel expansion blasting seismic wave signal, the radial signal has the highest energy, followed by the vertical signal and the longitudinal signal having the lowest energy.
- (4) The energy of seismic wave of tunnel expansion blasting is relatively dispersed with frequency distribution, mainly concentrated in a frequency band above 100 Hz, which is much higher than the natural vibration frequency of the adjacent existing tunnel. The energy proportion of 0–100 Hz is very small, only accounting for 2.850% of the total energy. The excavation blasting of the tunnel will not cause the resonance of the adjacent existing tunnel.

## Data Availability

All data included in this study are available upon request by contacting the corresponding author.

## Conflicts of Interest

The authors declare that there are no conflicts of interest regarding the publication of this paper.

## Acknowledgments

This work was supported by the Chinese National Natural Science Foundation (Grant no. 41672260).





## References

- [1] C.-B. Zhou, N. Jiang, K.-W. Xia, X.-D. Luo, S.-W. Lu, and S.-Y. Hu, *Dynamic Action Mechanism and Response Characteristics of Rock Blasting*, Science Press, Beijing, China, 2017.
- [2] N. Jiang and C. Zhou, "Blasting vibration safety criterion for a tunnel liner structure," *Tunnelling and Underground Space Technology*, vol. 32, p. 52, 2012.
- [3] N. Jiang, C.-B. Zhou, G. Luo, and G.-J. Miao, "Blasting vibration safety criterion of railway tunnel concrete lining," *Journal of Central South University (Science and Technology)*, vol. 43, no. 7, pp. 2746–2750, 2012.
- [4] M. Zhao, D. Huang, M. Cao, A. Chi, J. Liu, and Q. Kang, "An energy-based safety evaluation index of blast vibration," *Shock and Vibration*, vol. 2015, Article ID 698193, 9 pages, 2015.
- [5] Y. Peng, Y. Su, L. Wu, and C. Chen, "Study on the attenuation characteristics of seismic wave energy induced by underwater drilling and blasting," *Shock and Vibration*, vol. 2019, Article ID 4367698, 13 pages, 2019.
- [6] H.-X. He, K. Chen, and W.-M. Yan, "Structural seismic-damage assessment based on wavelet packet transformation and time-varying frequencies," *Journal of Vibration and Shock*, vol. 35, no. 7, pp. 23–30, 2016.
- [7] X.-Z. Shi, J.-G. Xue, and S.-R. Chen, "Quadratic time frequency distribution analysis of blasting vibration signal based on bilinear transformation," *Journal of Vibration and Shock*, vol. 27, no. 12, pp. 131–134, 2008.
- [8] X.-B. Li, Y.-P. Zhang, Z.-X. Liu, Y.-J. Zuo, and W.-H. Wang, "Wavelet analysis and Hilbert Huang transform of blasting vibration signal," *Explosion and Shock Waves*, vol. 25, no. 6, pp. 528–535, 2005.
- [9] X.-L. Guan and J.-L. Yan, "The HHT time-frequency power spectrum analysis of the blasting vibration signal," *Journal of Vibration and Shock*, vol. 32, no. 5, pp. 535–541, 2012.
- [10] N.-E. Huang, S. Zheng, S.-R. Luo et al., "The empirical mode decomposition and the Hilbert spectrum for nonlinear and

- non-stationary time series analysis,” *Proceedings of the Royal Society A*, vol. 454, no. 3, pp. 903–995, 1998.
- [11] J.-P. Zhao and H. Lin, “Energy distribution and separation of blast wave based on time-frequency energy analysis technology,” *Chinese Journal of Rock Mechanics and Engineering*, vol. 31, no. S1, pp. 3278–3285, 2012.
- [12] C.-W. Li, X.-Y. Sun, T.-B. Gao, B.-J. Xie, and X.-M. Xu, “Coal and rock vibration failure and the characteristics of micro-seismic signals,” *Journal of China Coal Society*, vol. 40, no. 08, pp. 1834–1844, 2015.
- [13] T. Wang, M. Zhang, Q. Yu, and H. Zhang, “Comparing the applications of EMD and EEMD on time-frequency analysis of seismic signal,” *Journal of Applied Geophysics*, vol. 83, pp. 29–34, 2012.
- [14] J.-R. Yeh and J.-S. Shieh, “Complementary ensemble empirical mode decomposition: a noise enhanced data analysis method,” *Advances in Adaptive Data Analysis*, vol. 2, no. 2, pp. 35–156, 2010.
- [15] Z. Wu and N. E. Huang, “Ensemble empirical mode decomposition: a noise-assisted data analysis method,” *Advances in Adaptive Data Analysis*, vol. 01, no. 01, pp. 1–41, 2009.
- [16] C. Bandt and B. Pompe, “Permutation entropy: a natural complexity measure for time series,” *Physical Review Letters*, vol. 88, no. 17, pp. 1–5, 2002.
- [17] W. Aziz and M. Arif, “Multiscale permutation entropy of physiological time series,” in *Proceedings of 2005 Pakistan Section Multitopic Conference*, Karachi, Pakistan, December 2007.
- [18] J.-D. Zheng, T. Liu, R. Meng, and Q.-Y. Liu, “Generalized composite multiscale permutation entropy and PCA based fault diagnosis of rolling bearings,” *Journal of Vibration and Shock*, vol. 37, no. 20, pp. 61–66, 2018.
- [19] B.-X. Wang, H.-T. Yang, Q. Wang, X. Gao, and X.-X. Chen, “Bridge vibration signal optimization filtering method based on improved CEEMD-multiscale permutation entropy analysis,” *Journal of Jilin University (Engineering and Technology Edition)*, vol. 50, no. 1, pp. 216–226, 2020.
- [20] D.-C. Yao, J.-W. Yang, X.-Q. Cheng, and X. Wang, “Railway rolling bearing fault diagnosis based on multi-scale IMF permutation entropy and SA-SVM classifier,” *Journal of Mechanical Engineering*, vol. 54, no. 09, pp. 168–176, 2018.
- [21] J.-D. Zheng, J.-S. Cheng, and Y. Yang, “Modified EEMD algorithm and its applications,” *Explosion and Shock Waves*, vol. 32, no. 21, pp. 21–26, 2013.
- [22] J. Li and Q. Li, “Medium term electricity load forecasting based on CEEMDAN-permutation entropy and ESN with leaky integrator neurons,” *Electric Machines and Control*, vol. 19, no. 8, pp. 71–80, 2015.
- [23] Y.-P. Zhang and X.-B. Li, “Application of Hilbert-Huang transform in blasting vibration signal analysis,” *Journal of South China University of Technology (Natural Science Edition)*, vol. 5, pp. 168–173, 2005.
- [24] X. Zheng, Z.-Y. Hao, Z.-G. Lu, and J. Yang, “Separation of piston-slap and combustion shock excitations via MEEMD method,” *Journal of Vibration and Shock*, vol. 31, no. 06, pp. 109–113, 2012.
- [25] X.-G. Yang, D.-Q. Shu, W.-B. Lu, and X.-J. Gao, “Study on energy distribution characteristics of seismic waves induced by different forms of blasting resource,” *Journal of Sichuan University(Engineering Science Edition)*, vol. 42, no. 1, pp. 30–34, 2010.
- [26] Y. Fan, F. Wang, W.-B. Lu et al., “Safety evaluation of deep tunnel blasting excavation vibration considering low-frequency amplification effect of transient unloading of in-situ stress,” *Chinese Journal of Rock Mechanics and Engineering*, vol. 37, no. s2, pp. 4184–4197, 2018.

## Research Article

# Modelling on Shock-Induced Energy Release Behavior of Reactive Materials considering Mechanical-Thermal-Chemical Coupled Effect

Baoyue Guo <sup>1</sup>, Kerong Ren <sup>2</sup>, Zhibin Li <sup>1</sup>, and Rong Chen <sup>1</sup>

<sup>1</sup>National University of Defense Technology, College of Liberal Art and Sciences, Changsha 410008, China

<sup>2</sup>Air Force Engineering University, Aviation Maintenance NCO Academy, Xinyang 464000, China

Correspondence should be addressed to Kerong Ren; [ren\\_kerong@163.com](mailto:ren_kerong@163.com) and Rong Chen; [r\\_chen@nudt.edu.cn](mailto:r_chen@nudt.edu.cn)

Received 21 November 2020; Revised 25 December 2020; Accepted 6 January 2021; Published 23 January 2021

Academic Editor: Nan Jiang

Copyright © 2021 Baoyue Guo et al. This is an open access article distributed under the Creative Commons Attribution License, which permits unrestricted use, distribution, and reproduction in any medium, provided the original work is properly cited.

Reactive material (RM) is a new type of energetic material, which is widely used in the military technology fields such as fragmentation warheads and shaped charge warheads. Violent chemical reactions take place in the impact process of reactive materials, and how to realize the macro numerical simulation of shock-induced energy release behavior of reactive materials is one of the most urgent problems to be solved for its future military applications. In this study, a numerical simulation approach and procedure is proposed, which can simulate the shock-induced energy release behavior of reactive materials on a macro scale. Firstly, program implementation of the mechanical-thermal-chemical coupled effect model for RM is realized in the second-development interface of LS-DYNA software. Then, the adaptive simulated annealing algorithm is used to fit the chemical reaction kinetic parameters of RM using the direct ballistics test data. Finally, the simulation calculation of the fragment penetrating upon steel plate is carried out to expand the applicability of the numerical simulation approach proposed in this study. The results show that the numerical simulation approach proposed in this study can reproduce the results of the direct ballistics test more accurately, which assumes practical significance for the engineering application of reactive materials in the military field in the future.

## 1. Introduction

Reactive material (RM) is a special energetic material, which is inert under normal temperature and pressure, while upon strong impact it can react dramatically and release a lot of chemical energy. Reactive materials are usually prepared by hot pressing of metal/nonmetal powder (Al, Ni, W, PTFE, Fe<sub>2</sub>O<sub>3</sub>, etc.) [1]. Warhead fragments made of reactive material can release a large amount of chemical energy on the target in addition to the kinetic energy damage [2, 3]. The inner core of PELE bombs made of reactive materials can enhance the cracking of shells after penetration, resulting in both physical and chemical damage to the target [4]. The metal shape charge of armor penetration warhead made of reactive material can form a reactive jet containing chemical reactions and thus enhance the penetration effect of the jet [5, 6]. In addition, reactive materials have many other

applications in antibiological war agents, underwater explosion, and so on [7].

Compared with the inert materials, the biggest advantage of reactive materials is their shock-induced energy release. To accurately describe the shock-induced energy release behavior of reactive materials, it is necessary to probe the chemical reaction mechanism and identify the chemical kinetic parameters. In theory, the chemical kinetic parameters can be obtained through differential scanning calorimetry (DSC). However, under impact loading, the temperature in reactive material rises very fast (in microseconds), accompanied by strong mechanical effects such as plastic deformation, shear, and friction between the particles [8, 9], bringing about different reaction conditions, which are completely different from the boundary conditions of DSC experiments. Taking Al/PTFE reactive material as an example, Miao [10] finds at the heating rate of 30 K/min that

micron Al powder cannot react with PTFE due to the coating of oxidation film on the surface while according to [11], the oxidation film on the surface of Al particles can be destroyed by the mechanical effect of the shock wave, causing the temperature threshold of impact reaction between Al and PTFE to be only 411k. Therefore, it is necessary to find other ways to obtain reaction parameters. Xiong [12] obtained the shock-induced temperature rise and chemical reaction threshold of reactive materials through theoretical calculation employing results of direct ballistic tests; he also derived the chemical kinetic parameters by fitting test data, which proved the effectiveness of this method. Ren [13] used Xiong's theoretical method to fit the chemical kinetic parameters of three Al/Ni reactive materials and used a self-developed constitutive program to calculate the shock-induced energy release behavior of reactive materials. The simulation results (calculated with Xiong's method) showed a certain difference from the direct ballistic test results.

In this study, a numerical simulation scheme and procedure is proposed, which can simulate the shock-induced energy release behavior of reactive materials on a macro scale. In the first step of this study, the chemical kinetics equation of reactive materials is built into LS-DYNA in the form of a user-defined equation of state (EOS), which realizes the program implementation of the mechanical-thermal-chemical coupled effect model. Then, the adaptive simulated annealing algorithm is used to fit direct ballistics test data, which yields chemical reaction kinetic parameters of the reactive material. Finally, the simulation calculation of fragment penetrating upon steel plate is carried out, and a comparison is made between the damage effect of reactive material fragments and that of inert material fragments, which further expands the applicability of the numerical simulation method proposed in this study.

## 2. Mechanical-Thermal-Chemical Coupled Effect Model for Reactive Materials and Its Program Implementation

In the impact process of reactive materials, violent chemical reactions take place, which is called shock-induced energy release behavior. With complex chemical reaction chain and diversity of reaction products, the shock-induced energy release behavior is hard to be represented by accurate chemical reaction equations. For this reason, we consider that the reactive material during the partial reaction is a mixture of reactants (unreacted reactive material) and reaction products (reactive material with complete reaction). A parameter  $y$ , standing for the extent of chemical reaction, is introduced to represent the mixing of reactant substances and reaction products. The relative volume and internal energy meet the following mixing rules:

$$\begin{cases} v_m = (1 - y)v_r + yv_p, \\ E_m = (1 - y)E_r + yE_p, \end{cases} \quad (1)$$

where  $v$  represents the relative volume and  $E$  represents the internal energy per element of the initial volume. The subscript  $m$  stands for the mixture,  $r$  for the reactants, and  $p$

for the reaction products. Meanwhile, it is assumed that the pressure  $P$  and temperature  $T$  of reactants and products are in equilibrium:

$$\begin{cases} P_m = P_r = P_p, \\ T_m = T_r = T_p. \end{cases} \quad (2)$$

Due to the assumption of temperature equilibrium, it is very important to obtain the temperature of reactants and reaction products in the calculation process. So, we need to take temperature as an independent variable in the EOS to facilitate temperature calculation of the mixture. The JWL equation [14] in the form of pressure-relative volume-temperature ( $P$ - $v$ - $T$ ) takes temperature and relative volume as independent variables. Therefore, in this study, JWL equations are adopted as EOS for reactants and products during the impact process:

$$\begin{aligned} P(v, T) &= Ae^{-R_1 v} + Be^{-R_2 v} + \frac{\omega}{v} C_v T, \\ e(v, T) &= \frac{A}{R_1} e^{-R_1 v} + \frac{B}{R_2} e^{-R_2 v} + C_v T, \end{aligned} \quad (3)$$

where  $C_v$  represents the specific heat capacity of the material and  $A, B, \omega, R_1,$  and  $R_2$  are related parameters of the material. The extent of chemical reaction  $y$  is controlled by chemical kinetics equation. Therefore, if the JWL equation for the reactant and the reaction product and the chemical kinetics equation of the reactive material are known, the EOS that describe the reaction behavior of the reactive material can be constructed, so as to calculate the physical quantities of the reactive material under different impact conditions.

In LS-DYNA, a second-development interface is reserved, allowing users to perform second development on material models such as constitutive equations and EOS, so as to help the users define the updating modes of physical quantities such as stress-strain, pressure, and internal energy by themselves. In this study, the JWL EOS of the reactants and products and the chemical kinetics equation is embedded into LS-DYNA in the form of user-defined EOS, and then the numerical simulation is carried out. In this way, program implementation of the mechanical-thermal-chemical coupled effect model for reactive materials is realized. In the program flow of the user-defined EOS, which considers mechanical-thermal-chemical coupled effect, updating of each physical quantity is shown in Figure 1.

The calculation process for the user-defined EOS is divided into the following seven steps:

Step 1: Enter  $T^t, P^t, y^t$ , and so forth into LS-DYNA main program.

Step 2: Calculate the predicted temperature value,  $T^{*t+1}$  in the current time step (i.e.,  $t+1$  step).

In the iterative scheme of the procedure, the temperature can be calculated through the predictor-corrector method. The prediction value in  $t+1$  step can be calculated based on the values in the previous time step (i.e.,  $t$  step) with the following equation:

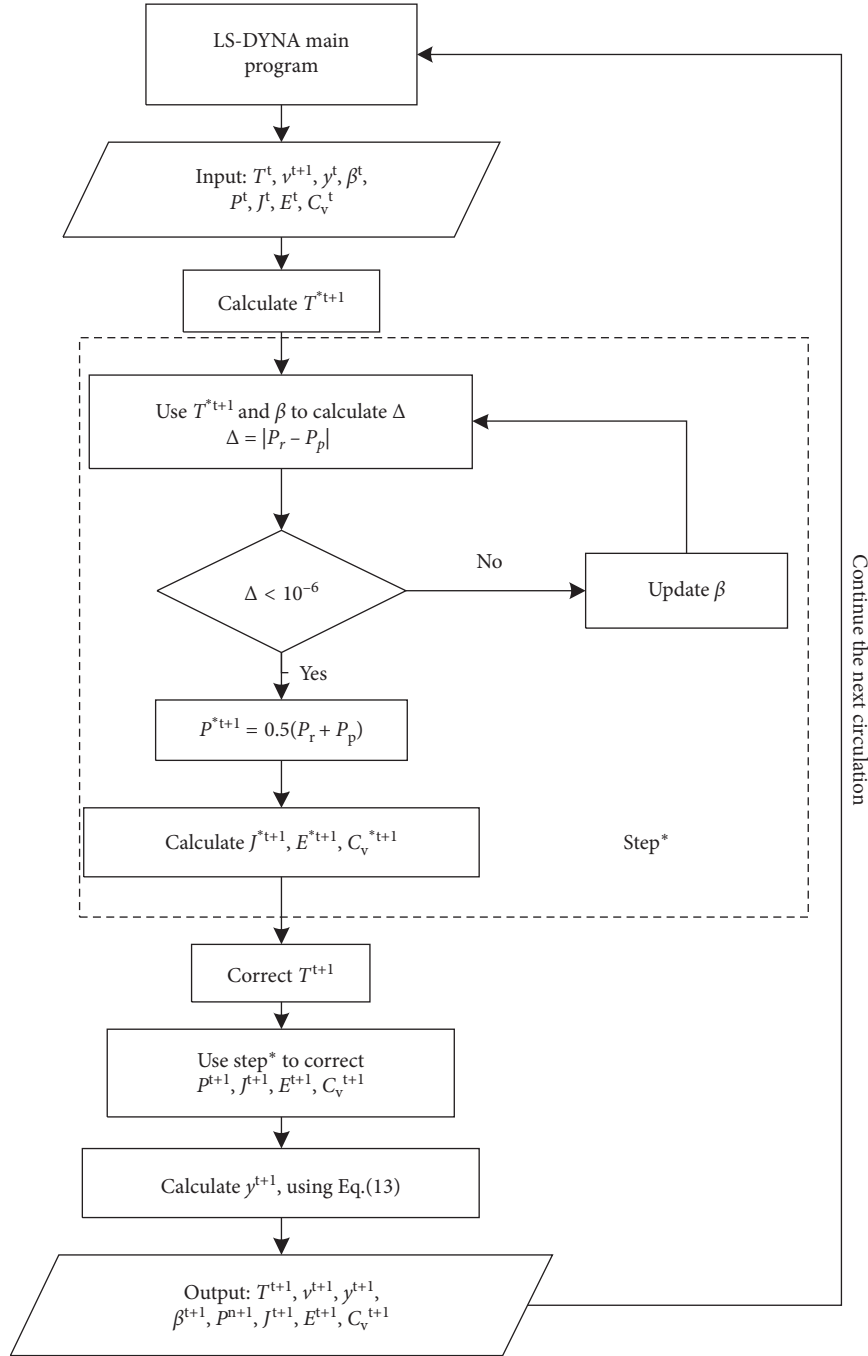


FIGURE 1: Program flow of user-defined EOS.

$$T^{*t+1} = T^t + \Delta T_s^t - (P^t + J^t + q) \left( \frac{\Delta v}{C_v^t} \right), \quad (4)$$

where  $\Delta T_s$  represents the temperature rise due to plastic deformation.  $q = 0.5(q^t + q^{t+1})$  represents the artificial viscous force.  $J$  represents the partial derivative of internal energy with volume.  $\Delta v$  represents the increment of the relative volume of the material in the current time step. In equation (4), some variables cannot be directly obtained in the LS-DYNA main program, so the form of equation (4) needs to be

changed. In LS-DYNA, the element's specific internal energy,  $E = e/v_0$ , represents the internal energy per element's initial relative volume, where  $e$  is the element's internal energy and  $v(\cdot)_0$  is the element's initial relative volume. In  $t+1$  step,  $E$  is calculated as follows:

$$E^{t+1} = \frac{1}{2} (\sigma^t + \sigma^{t+1}) \Delta \varepsilon - \frac{1}{2} (P^t + q^t + P^{t+1} + q^{t+1}) \Delta v + E^t, \quad (5)$$

$\sigma$  stands for deviatoric stress. The first term of equation (5) represents the plastic work, the second term



represents the volume compression work, and the last term represents the element's specific internal energy of  $t$  step. Equation (5) is rearranged as

$$E^{t+1} = \tilde{E} - \frac{P^{t+1}\Delta v}{2}, \quad (6)$$

where  $\tilde{E}$  is transferred into the user-defined EOS subroutine by the dummy argument, `specen`. Combining equations (4), (5), and (6) yields the temperature prediction value:

$$T^{*t+1} = T^t + \frac{\tilde{E} - E^t}{C_v^t} - \left(\frac{1}{2}P^t + J^t\right)\left(\frac{\Delta v}{C_v^t}\right). \quad (7)$$

Step 3: Calculate the predicted pressure  $P^{*t+1}$  and other physical quantities.

According to [15], an intermediate variable  $\beta=(1-y)v_r/v_m$  can be defined to assist the calculation, where  $\beta$  means the reactant volume fraction in the total volume of the mixture. Based on the definition of  $\beta$ , the following relationship can be derived:

$$\begin{cases} v_r = \frac{\beta}{1-y}v_m, \\ v_p = \frac{1-\beta}{y}v_m. \end{cases} \quad (8)$$

Firstly, the pressure of reactants and products is calculated using the initial value of  $\beta$ . Then, the Newton iteration method is employed to iterate  $\beta$ :

$$\beta^{*t+1} = \beta^t - \frac{P_r^t - P_p^t}{(\partial P_r / \partial \beta)^t - (\partial P_p / \partial \beta)^t}, \quad (9)$$

where  $P_r^{*t+1}$  and  $P_p^{*t+1}$  are calculated based on  $\beta^{*t+1}$ . When  $|P_r^{*t+1} - P_p^{*t+1}| \leq 10^{-6}$  iteration stops and  $P_r^{*t+1} = (P_r^{*t+1} + P_p^{*t+1})/2$  is taken as the predicted pressure value for the current time step, then  $T^{*t+1}$ ,  $P^{*t+1}$ , and  $\beta^{*t+1}$  are used to calculate  $J^{*t+1}$ ,  $C_v^{*t+1}$ , and  $E^{*t+1}$ .

Step 4: Calculate the corrected temperature,  $T^{t+1}$ .

When  $T^{*t+1}$ ,  $P^{*t+1}$ ,  $J^{*t+1}$ , and  $C_v^{*t+1}$  are obtained, the corrected value of temperature,  $T^{t+1}$  can be calculated as follows:

$$T^{t+1} = T^t - 0.5(a^{*t+1} - a^t)\Delta v, \quad (10)$$

where  $a^t = (P^t + J^t + q)/C_v^t$  and  $a^{*t+1} = (P^{*t+1} + J^{*t+1} + q)/C_v^{*t+1}$ .

Step 5: Refer to the process in step 3 to update other physical quantities.

Step 6: Calculate  $y^{t+1}$ .

According to the reaction kinetics model given by Arrhenius [16], the chemical reaction rate ( $dy/dt$ ) follows the form

$$\frac{dy}{dt} = A_0 \exp\left(-\frac{E_a}{R_u T}\right) f(y), \quad (11)$$

where  $t$  is the reaction time,  $A_0$  is the preexponential factor,  $E_a$  is the apparent activation energy,  $T$  is the thermodynamic temperature, and  $R_u$  is the universal gas constant.  $f(y)$  is the reaction mechanism function, and its form is determined by the specific reaction type. The n-dimensional control reaction model proposed by Avrami–Erofeev can be employed to describe the solid reaction under rapid temperature rise [16]:

$$f(y) = n(1-y)[- \ln(1-y)]^{1/(1-n)}, \quad (12)$$

where  $n$  is the reaction index. Zhang et al. [12, 17] derived the first-order differential relationship between the thermodynamic temperature,  $T$ , and the extent of reaction,  $y$ , by assuming that the reaction rate is positively correlated with time:

$$\frac{dT}{dy} = \frac{R_u T^2}{E_a} \left[ \frac{1}{2y} - \frac{n \ln(1-y) + n - 1}{n(1-y)[- \ln(1-y)]} \right]. \quad (13)$$

Given the reaction critical temperature,  $T_{cr}$ , and the critical extent of reaction,  $y_{cr}$  (assuming a minimum,  $10^{-4}$  in this study), the differential equation of equation (13) can be used to calculate  $y$  through numerical integration. Here, the fourth-order Runge–Kutta method is adopted:

$$\begin{cases} y_{t+1} = y_t + \frac{6}{h}(K_1 + K_2 + K_3 + K_4), \\ K_1 = f(T_t, y_t), \\ K_2 = f\left(T_t + \frac{h}{2}, y_t + \frac{h}{2}K_1\right), \\ K_3 = f\left(T_t + \frac{h}{2}, y_t + \frac{h}{2}K_2\right), \\ K_4 = f(T_t + h, y_t + hK_3), \end{cases} \quad (14)$$

where

$$\begin{aligned} f(T, y) &= \frac{E_a}{R_u T^2 g(T, y)}, \\ g(T, y) &= \frac{1}{2y} - \frac{n \ln(1-y) + n - 1}{n(1-y)[- \ln(1-y)]}. \end{aligned} \quad (15)$$

Step 7: Feed the updated variables to LS-DYNA main program.

### 3. Fitting of Chemical Reaction Kinetic Parameters Using the Adaptive Simulated Annealing Algorithm

To fully model the mechanical-thermal-chemical coupled behavior of the reactive material, it is necessary to identify the chemical kinetic parameters of the material first. In the chemical kinetics equation (equation (13)), there are three parameters to be determined by experimental fitting. They are the activation energy  $E_a$ , reaction index  $n$ , and reaction critical temperature,  $T_{cr}$ . The fitting process of the above chemical reaction kinetic parameters is as follows in this study.

Firstly, the experimental conditions are simulated by using the solver obtained in the second section; then adaptive simulated annealing algorithm is used to adjust the parameters so that the calculated value and the experimental value of the extent of the reaction for the reactive material will match. In this way, the exact values of the above kinetic parameters can be obtained. Exploiting the existing data of the direct ballistic test (DBT), the application process of the above-mentioned parameter fitting method is described in detail below.

The direct ballistic test data and material parameters used in this section are taken from [13, 18]. References [13, 18] chose the Al/Ni reactive material. This material has good mechanical properties and is easy to prepare, so it is often used to make reactive warhead fragments. The direct ballistic test results for some Al/Ni reactive material are shown in Table 1. In the direct ballistics test setting, the front end of the sealed chamber (volume: 27 L) is made of steel sheet, and the back end is steel target plate. The projectile (cylindrical,  $\Phi 10 \text{ mm} \times 10 \text{ mm}$ ) made of Al/Ni reactive material is launched through a ballistic gun. The projectile first penetrates the steel sheet and the impacts on the steel target. In the process of projectile impact, a large amount of heat will be released and the air pressure in the chamber will be increased. By measuring the quasi-static pressure of the air in the chamber, the chemical energy released by the reactive material projectile can be calculated; and then  $y$  can be calculated by comparing the complete reaction heat of the reactive material. Applying polynomial fitting to the direct ballistic test data shown in Table 1, we find that the impact velocity threshold for the reaction of Al/Ni reactive material is  $1054 \text{ m s}^{-1}$ .

**3.1. Finite Element Model.** The finite element model (Figure 2(a)) to simulate the direct ballistic test is constructed in LS-DYNA software (version 971 smp *d* R8.0.0, Livermore Software Technology Corp., Livermore, CA, U.S.). The model is a two-dimensional axisymmetric model, which simplifies calculation by using two-dimensional axisymmetric elements. The blue area represents the projectile, with a radius of 0.5 cm, a height of 1 cm, and a side length of 0.05 cm of each element; the red area stands for the steel target with a thickness of 2.5 cm, a radius of 2 cm, and a side length of 0.05 cm of each element. The velocity of the projectile is along the positive direction of the  $Y$ -axis, and the

TABLE 1: The direct ballistic test data from [13].

Test #	$v \text{ [m}\cdot\text{s}^{-1}]$	$y$
1#	1730	0.0929
2#	1785	0.1132
3#	1445	0.0419
4#	1437	0.0249
5#	1250	0.0205
6#	1191	0.0111
7#	1097	0.0073
8#	1516	0.0687
9#	1532	0.0500

upper end of the steel target is a fixed boundary, which constrains the displacement of all nodes on this boundary in all degrees of freedom.

The steel target plate is modeled with Johnson–Cook (J–C) constitutive model and Gruneisen EOS (see Appendix A), whose parameters are taken from Tables 2 and 3. Meanwhile, the projectile made of Al/Ni mixture is modeled with J–C constitutive model and user-defined EOS. The parameters (Table 4) for the J–C constitutive model of the Al/Ni mixture are taken from [13].

**3.2. Parameters for JWL Equation Obtainment.** The parameters for the user-defined EOS of reactive materials fall into two parts. The first part is the parameters for the JWL equation of reactants and products, and the other part is the parameters for equation (13). The JWL equation parameters ( $A$ ,  $B$ ,  $R_1$ ,  $R_2$ ,  $\omega$ , and  $C_v$ , altogether six parameters) of reactants and products can be obtained by fitting Hugoniot data of reactive materials. According to [14], the parameters for JWL equations follow these two constraint relations:

$$Ae^{-R_1} + Be^{-R_2} + 298\omega C_v = 0, \quad (16)$$

$$-\rho_0 C_0^2 = A \left( \frac{2\omega + R_1\omega + \omega^2 - 2R_1^2}{2R_1} \right) e^{-R_1} + B \left( \frac{2\omega + R_2\omega + \omega^2 - 2R_2^2}{2R_2} \right) e^{-R_2}, \quad (17)$$

where  $C_v$  represents material specific heat, which can be calculated with the mass ratios of the components. At the same time, it is generally assumed that  $R_2 = R_1/10$ . Thus, we can assume a set of values of  $R_1$  and  $\omega$  to calculate the pressure in the object at each relative volume, and then compare it with the impact adiabat based on the Hugoniot data. Fit the parameters with genetic algorithms, and finally obtain the parameters for the JWL equation [14, 19].

The projectiles used in the direct ballistic test are made of Al/Ni mixtures, and the mass ratio is approximately 1 : 1. Because there are some voids in the mixture, the EOS of the porous mixture with voids is taken as the EOS of reactants. On the other hand, because there is no gas production and the overall  $y$  in the direct ballistic is not high, the EOS of the dense mixture is employed as the EOS of the reaction products.

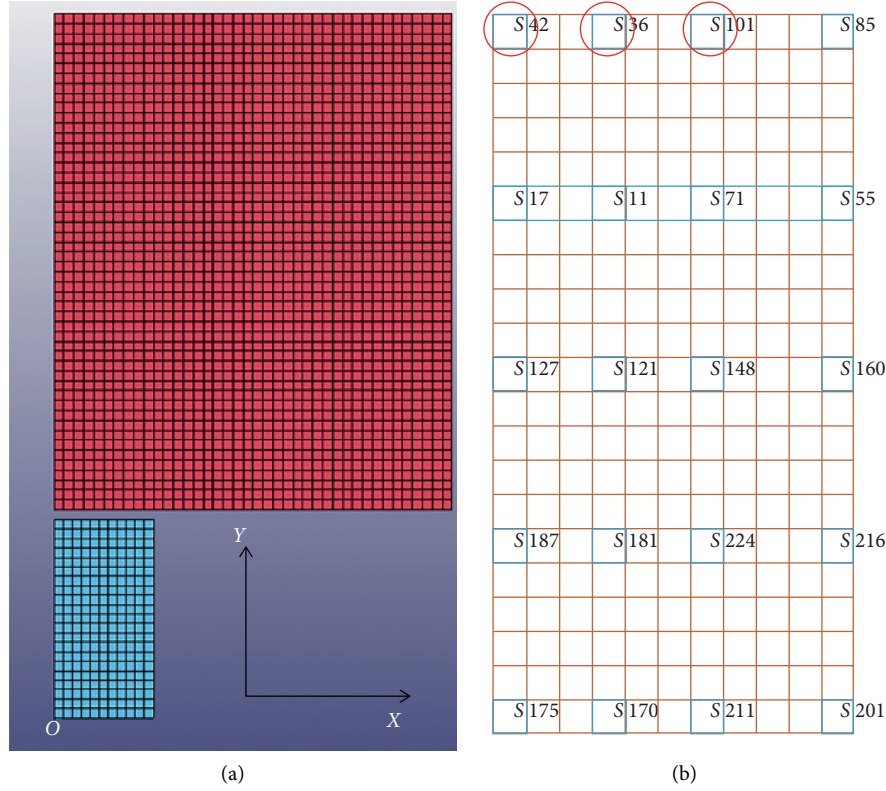


FIGURE 2: Finite element model. (a) Overview. (b) Elements selection for (y) data extraction.

TABLE 2: Parameters of the Johnson–Cook constitutive model for #45 steel.

$T_{\text{melt}}$ (K)	$K$ (GPa)	$A$ (MPa)	$B$ (MPa)	$C$	$N$	$M$
1793	157.8	792	298	0.014	0.26	1.03

TABLE 3: Parameters of the Gruneisen equation of state for #45 steel.

$\rho$ [ $\text{g}\cdot\text{cm}^{-3}$ ]	$c$ [ $\text{km}\cdot\text{s}^{-1}$ ]	$S_1$	$S_2$	$S_3$	$\gamma_0$
7.89	5.13	1.86	0	0	2.77

TABLE 4: Al/Ni reactive material parameters of the J–C constitutive model [13].

$\rho$ [ $\text{g}\cdot\text{cm}^{-3}$ ]	$K$ (GPa)	$A$ (MPa)	$B$ (MPa)	$C$	$N$	$M$
4.098	38.3	202	57	0.03	0.24	0.37

Note.  $K$  is the bulk modulus and  $c_0$  is the sound speed.

Hugoniot data of dense and loose Al/Ni reactive materials [13] can be fitted with genetic algorithms to obtain the JWL equation parameters corresponding to reactants and products, as shown in Table 5.

**3.3. Chemical Reaction Extent Extraction.** For comparison with the direct ballistic test data, it is necessary to extract the calculation results of  $y$  of the projectile. In this study, the data for  $y$  in 20 selected elements in the projectile model are extracted. Then, the data are processed through the weighted

TABLE 5: Hugoniot data of reactive materials and fitting results of JWL equation parameters.

State of material	$c$ [ $\text{km}\cdot\text{s}^{-1}$ ]	$s$	$A$ [100 Gpa]	$B$ [100 Gpa]
Reactants	4.417	1.464	57.1173	-0.2639
Products	4.691	1.324	35.3559	-0.3223
$R_1$	$R_2$	$\omega$	$C_v$ [100Gpa·K <sup>-1</sup> ]	
5.980	0.598	0.103	$2.44 \times 10^{-5}$	
5.224	0.5224	0.1	$2.52 \times 10^{-5}$	

mean method according to the radius scale at each element, resulting in the overall extent of reaction in the projectile. Elements selection is shown in Figure 2(b).

**3.4. Chemical Reaction Kinetic Parameters Fitting.** When the calculated  $y$  of the projectile is obtained, it may be different from the direct ballistic test data, so it is necessary to continuously optimize the chemical kinetic parameters to make the calculated results consistent with the test data. In this study, the adaptive simulated annealing (ASA) algorithm is used to fit the parameters. It is a global random optimization algorithm based on the Monte Carlo iterative strategy. The ASA algorithm is built on the similarity between the annealing process of solid material and the general combinatorial optimization problem: the internal energy of the material is replaced by the objective function, and the annealing time is replaced by the control parameters. A simulated annealing algorithm can jump over the trap of the local optimal solution with a certain probability to find the

global optimal solution. This is a mature method to solve nonlinear optimization problems [20, 21]. LS-OPT (version 6.0.0, Livermore Software Technology Corp., Livermore, CA, USA) is a simulation-based optimization design tool [22], which integrates the ASA algorithm and can solve complex problems such as parameter identification and system optimization. In addition, LS-OPT can directly extract numerical simulation data from LS-DYNA, so as to realize the fitting of material parameters efficiently and conveniently.

In equation (13), there are three parameters to be identified, namely,  $E_a$ ,  $n$ , and  $T_{cr}$ .  $T_{cr}$  can be obtained through numerical simulation for the case that the impact velocity threshold,  $v_{cr} = 1054 \text{ m s}^{-1}$ , and the corresponding simulation result is,  $T_{cr} = 406 \text{ K}$ . Moreover, the other two parameters,  $E_a$  and  $n$ , can be fitted by the ASA algorithm using the data of direct ballistics tests.

The calculation procedure of LS-OPT is designed to incorporate ASA to fit parameters  $E_a$  and  $n$ , as shown in Figure 3. Firstly, enter the values of  $T_{cr}$ , and set  $E_a$  and  $n$  as the variables to be fitted. Secondly, the space-filling sampling method in Radial Basis Function Method is employed to conduct sampling in the variable space, which can select a large number of experimental points for simulation calculation, and avoid errors caused by excessive assumptions. Thirdly, three sets of tests are simulated (2#, 3#, 7# are selected in this study) to extract calculation results of  $y$ . Fourthly, the optimization objective  $S$  is constructed, which needs to be minimized. Fifthly, an adaptive simulated annealing algorithm (ASA) is used to iterate and finally obtain the reaction kinetic parameters. The optimization objective  $S$  is

$$S = (Y_2 - y_2)^2 + (Y_3 - y_3)^2 + (Y_7 - y_7)^2, \quad (18)$$

where  $Y_i$  represents the data of numerical results and  $y_i$  represents the direct ballistic test data.

The chemical kinetic parameters of the reactive material are obtained after 10 iterations (when  $S = 1.546 \times 10^{-4}$ ) (refer to Table 6).

#### 4. Results Analysis

In order to verify the validity of the fitting approach, the mechanical parameters and chemical kinetic parameters of the material (listed in Tables 4–6), which are calculated based on the test data, are used to perform numerical simulation calculation for #6 and #9 tests.  $y$  of the projectile calculated by simulation is shown in Figure 4.

It can be seen from Figure 4 that the chemical reaction is obviously enhanced with increased impact velocity. And the area with high  $y$  gradually shrinks along the radial direction of the projectile. This is due to the attenuation of shock wave propagation and the influence of lateral rarefaction wave, which lowers the temperature of elements on the edge, leading to a reduced extent of reaction.

For the case that the impact velocity is  $1532 \text{ m s}^{-1}$ , the pressure-time curves (Figure 5) of elements 42#, 36#, 101# (red circle in Figure 2(b)) are extracted, and the peak value of the shock pressure is obtained as 24 GPa. The shock pressure is calculated with the one-dimensional shock wave theory to be 21 GPa [13]. Considering the error of JWL equation fitting results and the error of the numerical method, we hold that the pressure calculation of numerical simulation is effective.

The baseline operation function in LS-OPT is employed to calculate  $y$  for all test impact velocities. The calculation results are shown in Table 7 and Figure 6. In Figure 6, the numerical simulation results in this study (triangles in Figure 6) are compared with the direct ballistic test data (rectangles in Figure 6) and Ren's numerical simulation results [13] (circles in Figure 6). It can be found that the results obtained with the numerical approach in this study are closer to the test data, which gains an obvious advantage over Ren's numerical approach. Table 7 shows the relative error (RE) between the slope and interception of the three fitting curves.

The chemical parameters fitted in [13] are  $T_{cr} = 422 \text{ K}$ ,  $E_a = 20880 \text{ J mol}^{-1}$ , and  $n = 1.6$ .  $y$  calculated with these parameters is obviously too large for high impact velocities. The reason for the difference is that the temperature used in the fitting is the overall temperature (473 K at the current impact velocity), which is calculated by employing one-dimensional shock wave theory and shock Hugoniot, without considering the influence of shock wave attenuation and rarefaction wave. By contrast, in finite element simulation, the temperature is expressed for individual elements, so the temperature inside the projectile is not uniform (in Figure 7, red represents temperatures greater than 473 K, pure blue represents 298 K, and the selected time is the moment when the initial shock wave is unloaded). When the temperature reaches a certain threshold, the extent of reaction increases rapidly with the increase of temperature. Therefore, the overall extent of reaction is mainly contributed by the elements at high temperature. Simultaneously, when the bullet hits the target plate, strong plastic deformation occurs in front of the bullet and it expands to the radial direction, so the problem cannot be simply reduced to a one-dimensional problem. The parameters fitted with a numerical method based on LS-DYNA and LS-OPT in this study can be readily applied to numerical simulation of reactive materials.

#### 5. Further Discussion

In order to further verify the ability of the numerical approach constructed in this study to simulate the shock-induced energy release behavior of reactive materials, a numerical simulation is carried out on the penetration of a  $\Phi 7.5 \text{ mm}$  spherical reactive material fragment into a steel plate, as shown in Figure 8. The impact velocity is  $2000 \text{ m s}^{-1}$ , and the velocity direction is along the negative direction of the  $Y$ -axis.

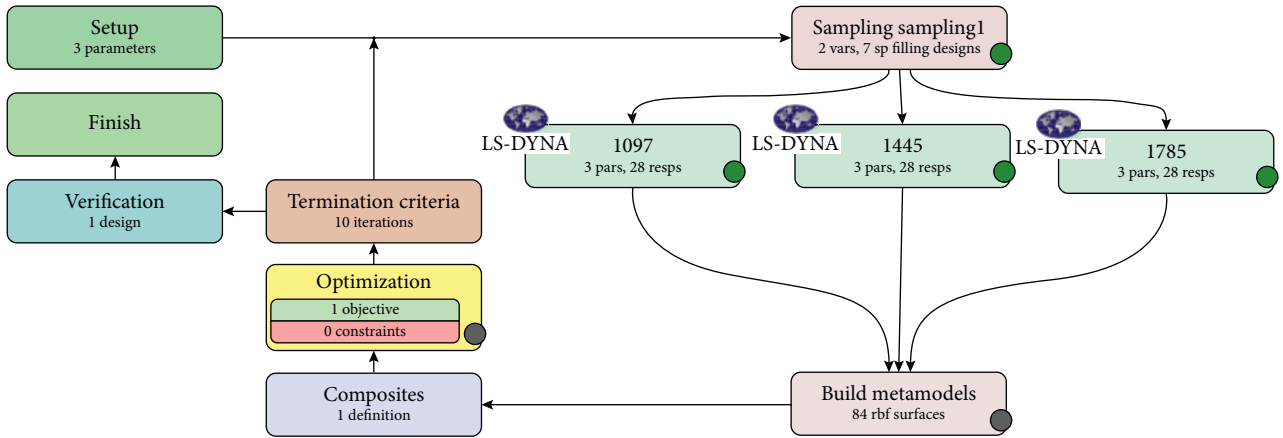
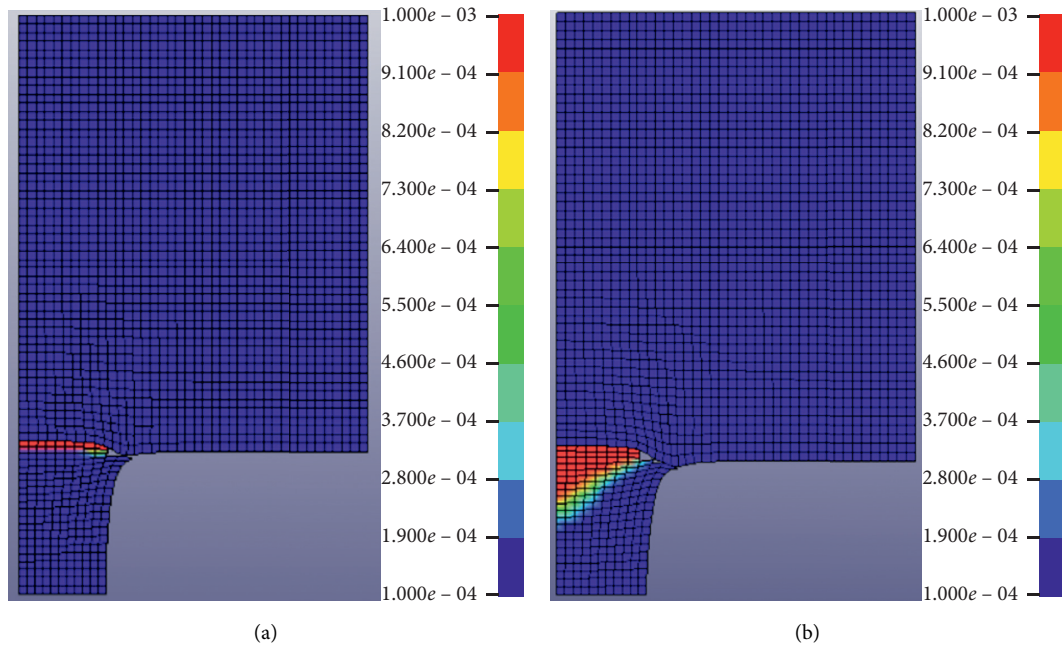


FIGURE 3: LS-OPT optimization program flowchart.

TABLE 6: Chemical reaction kinetic parameters of reactive materials obtained by fitting with adaptive simulated annealing algorithm.

$E_a$ [ $\text{J}\cdot\text{mol}^{-1}$ ]	$n$	$T_{cr}$ (K)
9280	1.609	406

FIGURE 4: Contour of  $\gamma$  (running to  $2\mu\text{s}$ ). (a) Impact velocity is  $1191\text{ m s}^{-1}$ . (b) Impact velocity is  $1532\text{ m s}^{-1}$ .

The parameters of the reactive material are taken from Tables 4–6, and the parameters of the steel plate are taken from Tables 2 and 3. Considering the relatively large deformation of the fragment, we adopt the Smoothed Particle Hydrodynamics (SPH) method [23] for the simulation. The SPH numerical model is shown in Figure 8, where the blue particles stand for the steel plate and the red particles for the spherical fragment.

On the basis of the SPH model above, inert material fragment and reactive material fragment with the same mechanical properties are, respectively, used for numerical simulation. The simulation results are shown in Figure 9. Figure 9(a) is the changing temperature contours of both two fragments during penetration. Figure 9(b) shows the average bulk temperature-time curves of both two fragments during penetration (red for reactive material, blue for inert



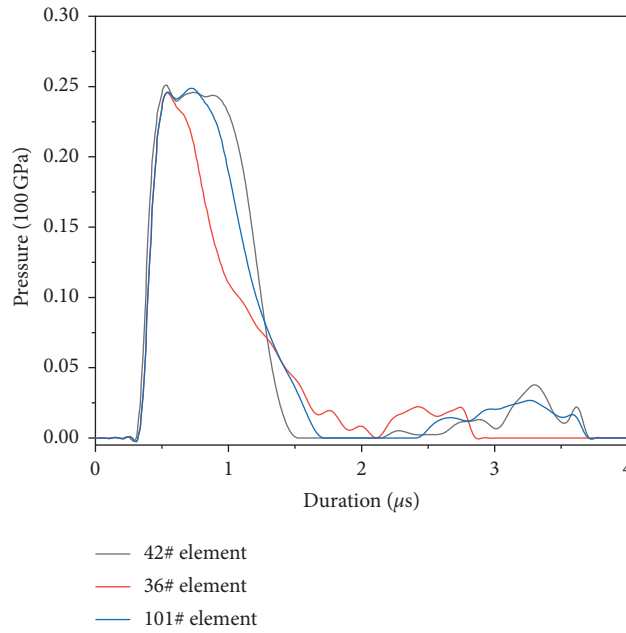


FIGURE 5: Pressure-time curves of typical elements.

TABLE 7: Comparison of linear fitting curves for simulation results and test data.

Linear parameters	Experiments result	Simulations result	Simulations result from [13]
Slope/ $m^{-1}$	$1.41 \times 10^{-4}$	$1.47 \times 10^{-4}$	$1.86 \times 10^{-4}$
RE of slope	—	4.29%	24.49%
Intercept	-0.157	-0.161	-0.207
RE of interception	—	2.53%	19.72%

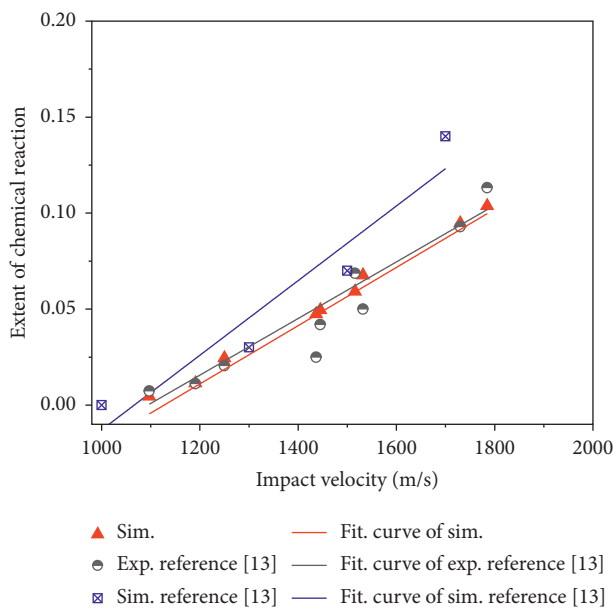


FIGURE 6: Direct ballistic test data [13], and numerical simulation results in this study and [13], for different impact velocities.

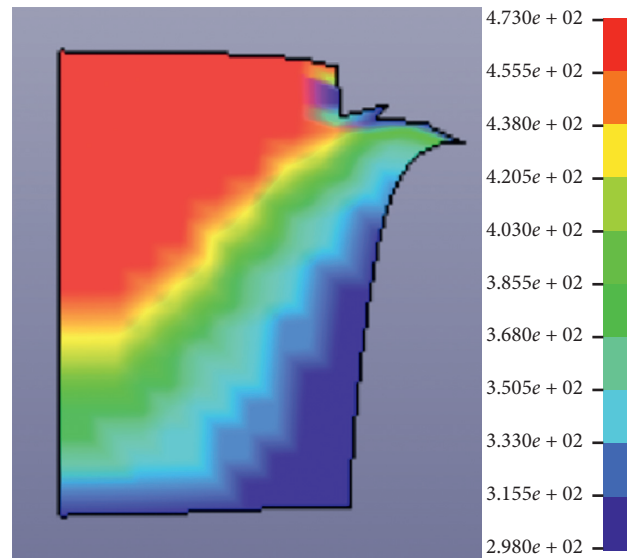


FIGURE 7: Temperature contour of the reactive material projectile.

material). According to the simulation results, it can be seen that the reactive material can release a large amount of chemical energy upon impact, which makes the average bulk temperature of the reactive fragment as high as about 1000K, compared with a temperature of 400K for the inert fragment. This means the surface temperature (red area in Figure 9(a)) of the reactive fragment exceeds the melting point of steel (~1750 K), meaning a stronger ignition and detonation effect on military targets such as fuel tanks and explosives. Therefore, compared with the inert fragment, the damage effect of the reactive fragment is greatly reinforced, which is consistent with [7].

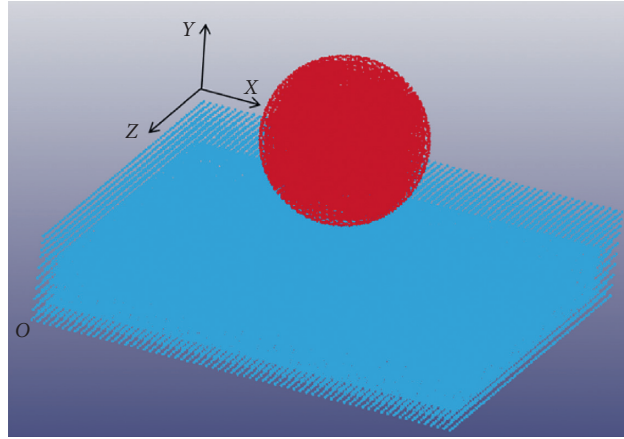


FIGURE 8: SPH numerical model.

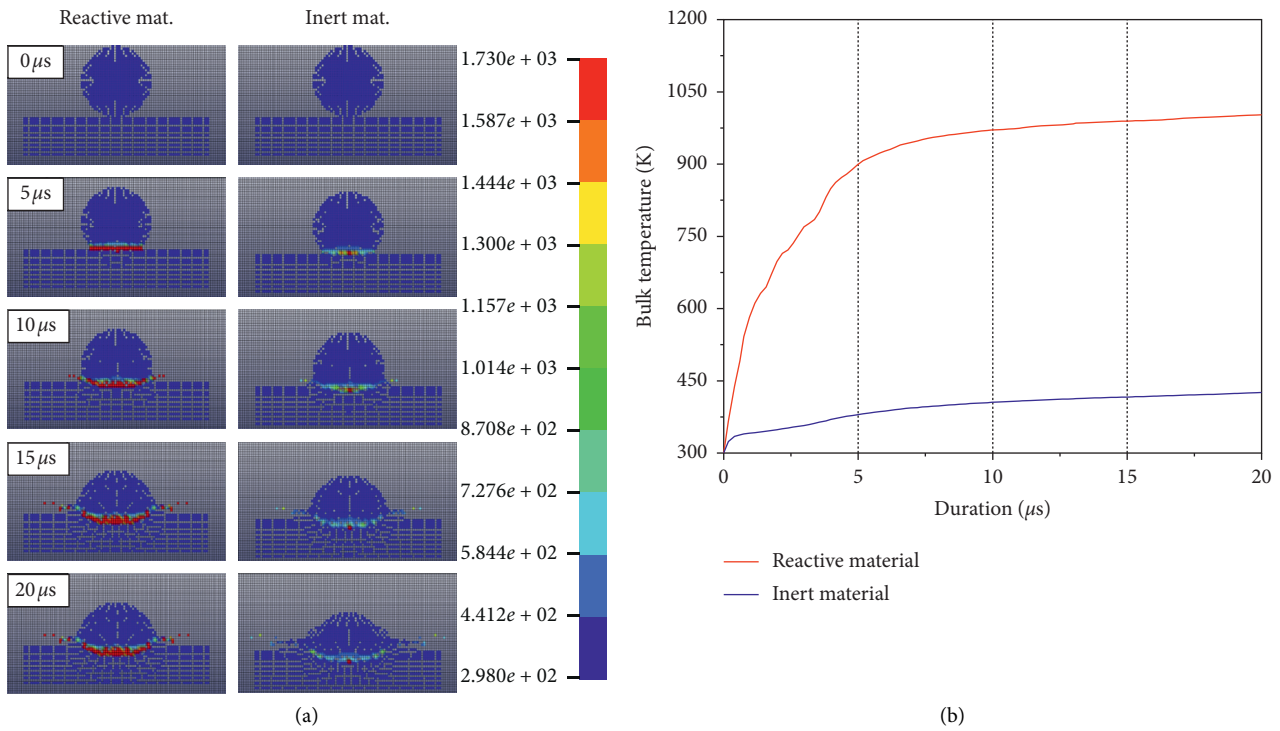


FIGURE 9: Comparison of temperature between the reactive fragment and inert fragment. (a) Time-dependent temperature contour of reactive fragment (left) and inert fragment (right) during the penetration. (b) Comparison of bulk temperature between the reactive fragment and inert fragment.

## 6. Conclusion

- (1) The second-development interface of LS-DYNA is exploited to incorporate the user-defined EOS, including the chemical kinetics equation of reactive materials. The user-defined EOS can characterize the mechanical-thermal-chemical coupled behavior of reactive materials during its shock-induced energy release process. Thus, the constructed solver with the user-defined EOS incorporated can be used to perform finite element simulation on shock-induced

energy release behavior of reactive materials. The simulation results can provide guidance for relevant experimental design.

- (2) A method based on the finite element method and ASA algorithm is proposed to fit the chemical kinetic parameters of reactive materials. The parameters fitted with this method can effectively reproduce the results of direct ballistic tests. Compared with the parameters obtained by theoretic formula fitting, the parameters obtained with this method can reproduce

the direct ballistic tests more accurately, which assumes practical significance for the engineering application of reactive materials in the military field in the future.

## Appendix

In general, for metal materials upon high speed impact, the J-C constitutive model and Gruneisen EOS can be used to describe their mechanical behavior.

The J-C constitutive model [24] describes the relationship between the flow stress  $\sigma_y$  and the effective plastic strain  $\bar{\epsilon}_p$ :

$$\sigma_y = (A + B\bar{\epsilon}_p^N)(1 + C \ln \dot{\epsilon}^*)(1 - T_H^M), \quad (\text{A.1})$$

where  $\dot{\epsilon}^* = \dot{\bar{\epsilon}}^p / \dot{\epsilon}_0$  is the normalized effective plastic strain rate;  $A$  is the initial yield stress of the material under reference strain rate,  $\dot{\epsilon}_0$ , and reference temperature,  $T_{\text{room}}$ ; and  $B$  and  $N$  are the strain hardening modulus and the hardening exponent of the material, respectively.  $C$  is the strain rate hardening parameter and  $M$  is the thermal softening parameter. If the room temperature is  $T_{\text{room}}$  and the melting point is  $T_{\text{melt}}$ , the relative temperature  $T_H$  is defined as

$$T_H = \frac{(T - T_{\text{room}})}{(T_{\text{melt}} - T_{\text{room}})}. \quad (\text{A.2})$$

The pressure change of common materials under pressure can be described by Gruneisen EOS [24] in the form of pressure-specific volume-internal energy ( $P$ - $v$ - $E$ ):

$$P = \frac{\rho_0 C_0^2 u [1 + (1 - (\gamma_0/2))u - (a/2)u^2]}{[1 - (S_1 - 1)u - S_2(u^2/u + 1) - S_3(u^3/(u + 1)^2)]} + (\gamma_0 + au)E, \quad (\text{A.3})$$

where  $C_0$  is sound velocity;  $S_1$ ,  $S_2$ ,  $S_3$  are the material parameters;  $\gamma_0$  is the Gruneisen coefficient;  $a$  is the first-order volume-correction coefficient of  $\gamma_0$ ; and  $u = v_0/v - 1$ . The J-C constitutive model parameters and Gruneisen EOS parameters of steel 45 are listed in Tables 2 and 3, respectively.

## Data Availability

The datasets generated and analyzed in the current study may be obtained from the corresponding author upon reasonable request.

## Conflicts of Interest

The authors declare no conflicts of interest regarding the publication of this paper.

## Acknowledgments

This work was financed and fully supported by the National Science Foundation of China (Grant no.11672328), which is greatly appreciated by the authors.

## References

- [1] P. Chen, B. H. Yuan, J. Chen et al., "Research progress of metal/fluoropolymer reactive materials," *Aerodynamic Missile Journal*, vol. 10, 2018.
- [2] H. F. Wang, Z. W. Liu, W. M. Yu et al., "Experimental investigation of energy release characteristics of reactive fragments," *Transactions of Beijing Institute of Technology*, vol. 29, no. 8, pp. 663–666, 2009.
- [3] H. F. Wang, Y. F. Zheng, Q. B. Yu et al., "Experimental research on igniting the aviation kerosene by reactive fragment," *Acta Armamentarii*, vol. 33, no. 9, pp. 1148–1152, 2012.
- [4] L. L. Ding, *Research on the Reactive Inner Core Formulation and Structural Design as Well as Damage Mechanism of Pele Projectile*, National University of Defense Technology, Changsha, China, 2019.
- [5] J. T. Waddell, T. H. Bootes, G. D. Budy et al., *Reactive Shaped Charge, Reactive Liner, and Method for Target Penetration Using a Reactive Shaped Charge*, 2011.
- [6] F. H. Li, H. T. Liu, and Y. W. Xiao, "Study of the impact energy releasing characteristics of Al/PTFE/W energetic jets," *Shock and Vibration*, vol. 2020, Article ID 8942523, 11 pages, 2020.
- [7] Y. Yang, Y. Zhang, and K. Wang, "Development progress of high density reactive materials and their damage effect," *Ordnance Material Science and Engineering*, vol. 36, no. 4, pp. 81–85, 2013.
- [8] N. N. Thadhani, "Shock-induced and shock-assisted solid-state chemical reactions in powder mixtures," *Journal of Applied Physics*, vol. 76, no. 4, pp. 2129–2138, 1994.
- [9] N. N. Thadhani, R. A. Graham, T. Royal, E. Dunbar, M. U. Anderson, and G. T. Holman, "Shock-induced chemical reactions in titanium-silicon powder mixtures of different morphologies: time-resolved pressure measurements and materials analysis," *Journal of Applied Physics*, vol. 82, no. 3, pp. 1113–1128, 1997.
- [10] L. Mao, S. Ye, W. X. Hu et al., "Thermochemical reaction characteristics of PTFE/Al reactive material," 2020, <https://kns-cnki-net-s.nudtproxy.yitlink.com:443/kcms/detail/11.2176.TJ.20200509.1500.012.html>.
- [11] K. R. Ren, J. Chen, H. Qing et al., "Study on shock-induced chemical energy release behavior of Al/W/PTFE reactive material with mechanical-thermal-chemical coupling SPH approach," *Propellants, Explosives, Pyrotechnics*, vol. 21, 2009, <https://onlinelibrary.wiley.com/doi/10.1002/prep.202000152>.
- [12] W. Xiong, X. Zhang, M. Tan, C. Liu, and X. Wu, "The energy release characteristics of shock-induced chemical reaction of Al/Ni composites," *The Journal of Physical Chemistry C*, vol. 120, no. 43, pp. 24551–24559, 2016.
- [13] K. Ren, R. Chen, Y. Lin, S. Li, X. Zhang, and J. Dong, "Probing the impact energy release behavior of Al/Ni-based reactive metals with experimental and numerical methods," *Metals*, vol. 9, no. 5, p. 499, 2019.
- [14] L. J. Wen, *Research on Mesoscopic Reaction Rate Model of Shock Initiation of PBX*, Beijing Institute of Technology, Beijing, China, 2011.
- [15] F. C. Miao, L. Zhou, X. R. Zhang et al., "Implantation and application of ignition and growth reaction rate equation in ls-dyna software," *Acta Armamentarii*, vol. 40, no. 7, pp. 1411–1417, 2019.
- [16] Y. W. Ding, *Fundamentals of Thermal Analysis*, University of Science and Technology of China Press, Beijing, China, 2020.
- [17] X. F. Zhang, A. S. Shi, J. Zhang, L. Qiao, Y. He, and Z. W. Guan, "Thermochemical modeling of temperature controlled shock-induced chemical reactions in

- multifunctional energetic structural materials under shock compression,” *Journal of Applied Physics*, vol. 111, no. 12, Article ID 123501, 2012.
- [18] K. R. Ren, *Probing the Impact Release Behavior of Al/Ni-Based Energetic Structural Materials Adopting Experimental and Numerical Method*, National University of Defense Technology, Changsha, China, 2018.
- [19] Z. D. Tian, *A Mesomechanic Model of Shock Initiation in Solid Heterogeneous Explosives*, National University of Defense Technology, Changsha, China, 2003.
- [20] A. E. W. Jones and G. W. Forbes, “An adaptive simulated annealing algorithm for global optimization over continuous variables,” *Journal of Global Optimization*, vol. 6, no. 1, pp. 1–37, 1995.
- [21] L. Ingber, “Adaptive simulated annealing (ASA): lessons learned,” *Control & Cybernetics*, vol. 25, no. 1, pp. 33–54, 2002.
- [22] I. Henchi, G. Daehn, Y. Zhang et al., “Material constitutive parameter identification using an electromagnetic ring expansion experiment coupled with LS-DYNA and LS-OPT,” in *Proceedings of the 10th International LS-DYNA Users’ Conference*, Dearborn, MI, USA, 2008.
- [23] S. K. Roy, M. Trabia, B. O’Toole et al., “Study of hypervelocity projectile impact on thick metal plates,” *Shock and Vibration*, vol. 2016, Article ID 4313480, 11 pages, 2016.
- [24] Livermore Software Technology Corporation (LSTC), *LS-DYNA Keyword User’s Manual*, Livermore Software Technology Corporation (LSTC), Livermore, CA, USA, 2007.